Alma Mater Studiorum
Università degli Studi di Bologna

SCUOLA DI SCIENZE

Dipartimento di Fisica e Astronomia

Dottorato di ricerca in Astrofisica
Ciclo XXXII

Galaxy clusters in different dynamical state: a multiband view from MeerKAT and uGMRT

Tesi di Dottorato

Supervisore:
Chiar.mo Prof.
Daniele Dallacasa

Candidata:
Beatrice Terni de Gregory

Co-supervisori:
Dott.ssa Tiziana Venturi
Dott. Mario Nonino

Coordinatore Dottorato:
Chiar.mo Prof.
Francesco Rosario Ferraro

Esame finale anno 2020

Settore concorsuale: 02/C1-Astronomia, Astrofisica, Fisica della Terra e dei Pianeti
Settore scientifico-disciplinare: FIS/05-Astronomia e Astrofisica

This Thesis work was done as part of the research activity of the Istituto di Radioastronomia - Istituto Nazionale di Astrofisica (INAF) in Bologna.

Ai miei genitori

Contents

List of Tables

List of Figures

Abstract

Galaxy clusters are the largest gravitationally bound systems in the Universe, they are special laboratories where is it possible to investigate the evolution and the properties of galaxies in different environments, starting from their centre, going out to the virial radius and beyond.
The properties of radio galaxies can be related to their environment and its dynamical status: nowdays, understand whether the observed properties of radio galaxies arise at formation (*nature* scenario), or they are an end-product of physical processes (*nurture* scenario) coming into play after galaxies have become part of a 'group' or a 'cluster' is difficult and much debated.
We started this work, analyzing a sample of eleven Brightes Cluster Galaxies (BCGs) from ten galaxy clusters in the redshift range $0.2 \leq z \leq 0.4$. They were selected because of the overlap between the Extended GMRT Radio Halo Survey (EGRHS) and the Cluster Lensing and Supernovae Survey with Hubble (CLASH). The main aim is to examine the radio properties of these galaxies considered 'special' because of their position at the very centre of galaxy cluster potential well. In particular, to understand whether the main mechanism responsible for the radio emission, when detected, is mainly due to AGN activity or to Star Formation activity and which is the interplay between the two mechanisms, since both are of fundamental importance for the feedback phenomena.
From the initial sample we then selected two clusters in order to perform a detailed radio-optical analysis on their radio galaxy population. They are representative of two opposite dynamical stages and at comparable redshift and richness class: Abell 1300 (z=0.31) is a post-merging cluster and MACSJ1931-2634 (z=0.35) is a relaxed cool core cluster. Their study is based on new data from MeerKAT at 1.2 GHz and uGMRT at 640 MHz interferometers, both considered SKA precursors.
We analyzed the statistical properties of the population of radio galaxies within a field of 30 arcmin radius from the cluster centre. We performed the clusters statistical source counts comparing it with the background.
A consistent part of the work consisted into the spectroscopical analysis performed in order to identify galaxy cluster members.
We estimated the Radio Luminosity Function for both the clusters, comparing our results with literature. Our result is consistent with the fact that the radio emission could be triggered by the merging.

We estimated galaxy cluster members stellar mass and Star Formation Rate (SFR) and we studied some correlation such as the radio power with stellar mass, radio power with SFR, SFR with stellar mass.
Our results confirm that the cold gas could be the source of fuel for both the AGN and Star Formation activity.
The future aim and perspective are to enlarge our statistics by means of more spectroscopical information and analyze a wider sample of galaxies in clusters in different dynamical state.

Introduction

This thesis is part of a comprehensive project, which we named the RadioCLASH-GCAV project, that involves a collaboration included in the infrared Galaxy Cluster at Vircam survey (GCAV, Nonino M. 2016). The main aim of this thesis is to investigate radio galaxies and galaxy evolution in clusters and to compare multiband properties of galaxies in different environments. Galaxy clusters are the largest gravitationally bound systems in the Universe, indeed they are ideal for studying how our Universe and large scale structures were formed. Clusters are important tracers for dark matter and they act as efficient gravitational lenses. They are also special laboratories to investigate the evolution of galaxies in different environments, not only in their center but also at higher distance, out of the virial radius. Throughout the three years of my PhD, we studied different objects in galaxy clusters related to discrete emission (radio galaxies), and to diffuse emission (halos, relics, mini-halos). We started our work selecting a sample of eleven clusters in the redshift range between $0.2 < z < 0.4$ because of the strong overlap between the Extended GMRT Radio Halo Survey (EGRHS; Venturi et al. 2007, 2008; Kale et al. 2013, 2015) and the Cluster Lensing and Supernovae Survey with Hubble (CLASH).
Reprocessing archival VLA data at 1.4 GHz, in different configurations of the array (possibly A or B to get the maximum resolution), we studied first the radio and the optical-infrared properties of eleven Brightest Cluster Galaxies (BCGs), belonging to the clusters selected, and we compared our results with previous results in literature. BCGs are the most massive, luminous, centrally located, galaxies in clusters. Understanding their formation and evolution can tell us a quantity of information on galaxy clusters in which they are found.
As a further step of this thesis, from our initial sample we extracted two targets, representative of two opposite dynamical stages and with a comparable redshift. A1300 (z=0.31) is a turbulent post-merging cluster, whereas MACSJ1931-2634 (z=0.35) is a relaxed cool core system. Since they are opposite in terms of dynamics the aim was to compare the multiband properties of their radio galaxy population, in order to better understand how the environment can act and influence their formation and evolution.
To reach our purpose the method used was based on the acquisition of new data from forefront instruments such as the upgraded GMRT (uGMRT) and the MeerKAT

interferometers, both considered Square Kilometer Array (SKA) precursors. Moreover, the analysis was completed with the exploitation of reprocessed archival radio data from the Very Large Array (VLA) and the Giant Metrewave Radio Telescope (GMRT), and on the optical Hubble-CLASH (PI Postman M. 2012) data. An added value to this thesis is related to the data analysis from MeerKAT interferometer, a completely new instrument, which made it possible to test new tools and packages for the radio data reduction.
Here we provide a brief summary of what is reported in the following chapters:

• In **Chapter 1** we provide a description of the general properties of galaxy clusters: we describe their general features in a brief introduction; we describe the two main different morphological types in which they are classified as merging or relaxed in relation to their dynamical state. We then analyze their properties in different wavebands: optical, X-ray and radio bands, focusing our attention in the X-ray band on the Sunyaev-Zel'dovich effect and in the radio band on the diffuse emission from halos, relics and mini-halos and on different kind of radio galaxies, in particular on Narrow-Angle Tails. We describe the importance of the Radio Luminosity Function as a statistical tool to study the properties of radio galaxies in relation with the environment in which they are located. Finally, we mention the cluster magnetic fields, whose presence in clusters is nowadays well-established and fundamental to justify the synchrotron emission observed.
• In **Chapter 2** we focus on the Brightest Cluster Galaxies, which are the most massive and luminous galaxies found at the very center of clusters potential well. We describe the kinematic and photometric properties of BCGs, the implications of their central position, theoretical simulations on how they form and the origin of their radio emission. This is the focal point of my analysis: to understand whether the radio emission detected is mainly due to AGN activity or Star Formation activity and which is the level of the interplay between these two phenomena, that is still a matter of debate. In the second part of this chapter, I describe my analysis illustrating the sample, the data reduction and the main results in comparison with the most important results published in literature.
• In **Chapter 3** we present an illustration of the two instruments used for our observations and analysis which are the upgraded GMRT (uGMRT; Pune, India) and the MeerKAT array (Karoo Region, South Africa), which is a SKA precursor. New data were collected during Spring-Summer 2018, at 640 MHz and 1.2 GHz with uGMRT and MeerKAT respectively, during the second year of my PhD. I report also which are the most important science cases for which the instruments are exploited.
• In **Chapter 4** we describe the data reduction steps and we present the images obtained and used for our analysis. In the second part of this chapter, is presented the optical-infrared and spectroscopic analysis performed in order to cross match the radio sources detected and to assess the properties of the cluster member galax-

ies. The optical analysis was made by means of Subaru images, from the archive for MACSJ1931-2634 and entirely reprocessed from the raw images for A1300. We analyzed the GCAV IR data to get the infrared images of A1300 in Y,J,Ks bands and we exploited CLASH VIMOS-VLT spectroscopy (PI Rosati P.) for MACSJ1931-2634 and VIMOS data from VLT ESO GO Large Programme (PI Böringer) for A1300.

• In **Chapter 5** we report a detailed analysis on MACSJ1931-2634 radio galaxy population. We first analyzed from a statistical point of view, exploiting the wide-area images obtained, the field surrounding MACSJ1931-2634 galaxy cluster. We extracted two catalogues at 1.2 GHz and 640 MHz and characterized the spectral properties of the radio sources detected within 30 arcmin radius from the cluster centre. We estimated the statistical source counts in comparison with the background considering a restricted area of 12 arcmin radius, corresponding to two virial radii. We performed the radio-optical crossmatch of the sources, characterizing their properties (color, magnitude). We analyzed the spectra of the galaxies within this area and we obtained 32 spectroscopic redshifts. By means of the spectral analysis we found that six galaxies are consistent with being cluster members. We dedicate a section of this chapter to the extended sources reporting the radio-optical overlays and their main properties. We estimated the Radio Luminosity Function for MACSJ1931-2634 radio galaxies and we compared our result with a local case (A3558, z=0.04 from Venturi et al. 2000) and with a case at comparable redshift (z=0.3 from Branchesi et al. 2006). Finally, we focused on the central regions of the cluster, analyzing the BCG and the Narrow-Angle tail located at $\sim$ 150 kpc from the BCG.

• In **Chapter 6** we report a detailed analysis on A1300 radio galaxy population. We first analyzed from a statistical point of view, exploiting the wide-area images obtained, the field surrounding A1300 galaxy cluster. We extracted two catalogues at 1.2 GHz and 640 MHz and characterized the spectral properties of the radio sources detected within 30 arcmin radius from the cluster centre. As for MACSJ1931-2634, we estimated the statistical source counts in comparison with the background considering a restricted area of 12 arcmin radius, corresponding to two virial radii. We performed the radio optical crossmatch of the sources, characterizing their optical properties. By means of the spectral analysis we found that nine galaxies are consistent with being cluster members. We dedicate a section of this chapter to the extended sources reporting the radio-optical overlays and their main properties. We estimated the Radio Luminosity Function for A1300 radio galaxies and we compared our result with the local case of A3558 at z=0.04 from Venturi et al. 2000 and with Branchesi et al. 2006 at a comparable redshift z=0.3. Finally, we focused on the central region of the cluster, analyzing the 'dumb-bell' BCG properties.

• In **Chapter 7** we compare and discuss the statistical properties and the spectral properties of the radio galaxies detected within the field surrounding A1300 and MACSJ1931-2634 galaxy clusters. Moreover, since our main goal is to compare the

galaxy properties analyzed in two different environments, we examine the statistical source counts and the RLF. Indeed we found that both seem to confirm that the merging activity could be a trigger for the radio emission in agreement with previous literature results. Finally, we get the Stellar Masses and the Star Formation Rate (SFR) for the cluster member galaxies and we compare the radio-optical properties by means of some important correlations: Power vs Stellar Mass, Power vs SFR, Stellar Mass vs SFR.
The future aim and perspective are to enlarge our statistics by means of more spectroscopical information and analyze a wider sample of clusters in different dynamical state.

Chapter 1

Clusters of galaxies

Clusters of galaxies are the most massive and large gravitationally bound systems in the Universe. Their masses are typically of the order of M=$10^{14}\,M_{\odot}$, even if the most massive clusters exceed M=$10^{15}\,M_{\odot}$, and they cover linear sizes typically of few Mpc (up to 3-4 Mpc). Most of the matter in clusters is in the form of dark matter ($\sim$ 80%), which exhibits itself only through dynamical activity and lensing effects; some of the luminous matter is in galaxies ($\sim 3-5\%$), the rest is in form of diffuse hot gas ($\sim 15-17\%$), detected in X-ray through its thermal Bremsstrahlung emission. This thermal plasma, consisting of particles of energies of several keV ($T \sim 10^7 - 10^8 K$), is commonly referred to as Intra-Cluster Medium (ICM). This tenuous hot gas has a density of $\sim 10^{-3} - 10^{-4} cm^{-3}$.
Being large concentrations of galaxies, galaxy clusters have been first discovered, studied and classified in the optical band: the earliest catalogues were indeed based on the visual inspection of photographic plates (e.g. Abell, 1958).
The study of cluster formation and evolution is important to constrain models on the origin and history of large scale structures. According to the current picture of structure formation in the Universe, galaxy clusters form by gravitational collapse starting from small density fluctuations. The existence of such density perturbations can be inferred from the temperature perturbations of the Cosmic Microwave Background (CMB), firstly observed with the COsmic Background Explorer (COBE) satellite (Bennett et al. 1996). Once that the collapse started, matter is accumulated and grows hierarchically via accretion of smaller systems (e.g. Press & Schechter 1974). In this scenario, smaller units like galaxies, groups and small clusters formed first and merged under gravitational pull to larger and larger units in the course of time.
Cluster mergers are the mechanism by which clusters are assembled. The kinetic energy associated with two colliding substructures reaches $10^{63} - 10^{64}$ erg, making cluster mergers the most energetic events in the Universe since the Big Bang (Sarazin, 2002a). During a merger, a major fraction of this energy dissipates into the heating of the ICM via shocks and turbulence and generates non-thermal components. Non-thermal components can be revealed by radio observations of diffuse

synchrotron sources in clusters, such as radio halos and relics, that prove the existence of magnetic fields and relativistic particles mixed with the thermal ICM (Brunetti & Jones, 2014).
The merger activity appears to be continuing at the present time and explains the relative abundance of substructure and temperature gradients detected in clusters of galaxies by optical and X-ray observations.
The physical properties of galaxy clusters, such as the luminosity and temperature, the radial structure of both dark and baryonic matter, are a challenging test for our understanding of how these objects grow from primordial density fluctuations. There are two different regimes of growth of the perturbations: linear and non-linear. The two regimes can be distinguished defining the density fluctuation (or overdensity):

$$\delta = \frac{\rho - \bar{\rho}}{\bar{\rho}} = \frac{\delta\rho}{\bar{\rho}} \tag{1.1}$$

where ρ is the density of the Universe at a given position and $\bar{\rho}$ in the mean unperturbed density of the Universe. In the linear regime the growth of the perturbation can be described with the Jeans theory, who first demonstrated that small density fluctuations in an homogeneous, isotropic and stationary fluid can grow with time, become unstable and collapse. The linear regime acts as long as $\delta << 1$ and can be indeed easily treated (Peebles 1980, 1983; Coles & Lucchin 1995, 2002). Neverthless, galaxy clusters are highly non-linear objects ($\delta >> 1$), and this requires more complex approaches for studying the evolution of perturbations in this particular regime.
There are different ways to model the cosmic structure formation: analytic, semi-analytic and numerical techniques. The analytic techniques were first developed in the '70s and pose the basis of the present models for structure formation (White & Rees, 1978; Fall & Efstathiou, 1980). The semi-analytic techniques (Cole, 1991; White & Frenk, 1991; Kauffmann et al., 1993; Cole et al., 1994) are based on the model of the gravitational clustering developed by Press & Schechter (1974) and its extensions (Bower, 1991; Bond et al., 1991; Lacey & Cole, 1993). This formalism is extensively used to build up, via Monte Carlo methods, synthetic populations of DM halos which evolve with time due to mergers and hierarchical clustering. Numerical methods allow a detailed study of the relevant physical processes and of the matter distribution on different scales (Davis et al., 1995; Steinmetz & Muller, 1995; Katz et al., 1996; Springel et al., 2006). They are the unique instrument to describe the non-linear evolution of the perturbations. Among the largest runs, we mention the Millennium simulation (Springel et al., 2006) and its updates: Millennium II, (Boylan-Kolchin et al. 2009), Millennium-XXL (Angulo et al. 2012), and the Illustris simulation (Vogelsberger et al., 2014), which complements the N-body simulation with hydrodynamic simulations, required to model radiative processes such as cooling and feedback (Fig. 1.1).

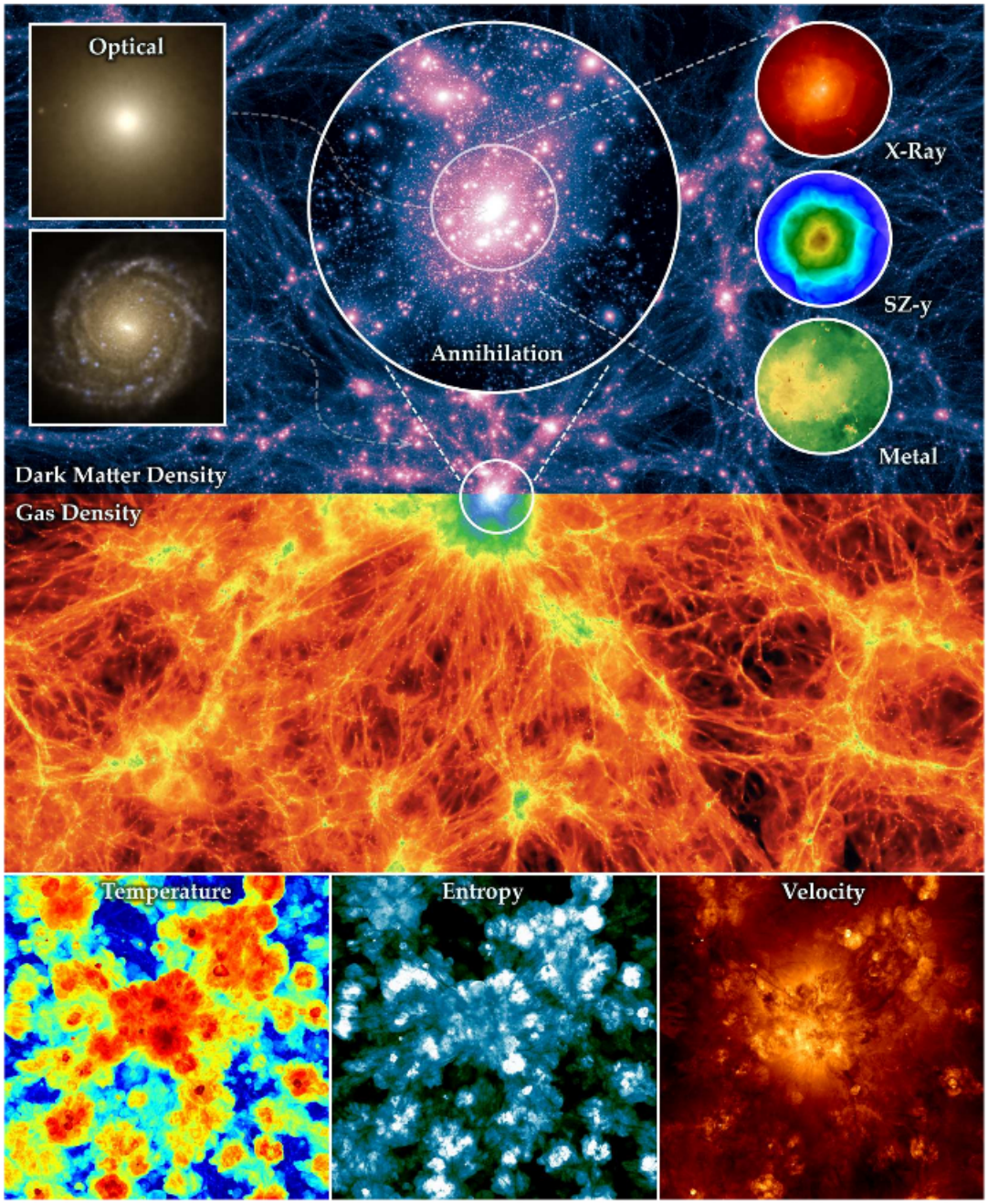

Figure 1.1: Simulated present-day dark and baryonic matter structures. Top panel: Dark matter mass distribution in a slice centered on the most massive halo. Lower panels: gas distribution shown in density, temperature, entropy, and velocity. On the right in the top panel are shown (from top to bottom): X-ray emission of hot intra-cluster gas; thermal Sunyaev-Zel'dovich signal; and the distribution of metals in the gas (all within one virial radius). The central circle shows the expected annihilation signal from self-annihilating DM particles within three virial radii. On the left in the top panel we present optical images of the central galaxy of the cluster (top) and a random disk field galaxy (bottom). (See Vogelsberger et al. (2014) for details).

1.1 Estimate of the cluster mass

From an historical point of view, the dynamics traced by member galaxies has been the first method applied to measure masses of galaxy clusters (Zwicky, 1937). Under the assumption of virial equilibrium, the mass of the cluster can be estimated by knowing the position and redshift for a high enough number of member galaxies:

$$M \propto \frac{3\sigma_v^2 R_V}{G} \tag{1.2}$$

where σ_v is the galaxy velocity dispersion along the line of sight and R_V is the virial radius, i.e. the radius within which the virial theorem applies, which depends on the positions of the galaxies (recognised as true cluster members) with measured redshifts (see Walker et al., 2019, for a review).
The condition of hydrostatic equilibrium determines the balance between the pressure force and gravitational force: $\bigtriangledown P_{gas} = -\rho_{gas} \bigtriangledown \phi$, where P_{gas} and ρ_{gas} are the gas pressure and density and ϕ is the gravitational potential. Under the assumption of spherically symmetric gas distribution, the previous equation becomes:

$$\frac{dP_{gas}}{dr} = -\rho_{gas}\frac{d\phi}{dr} = -\rho_{gas}\frac{GM(<r)}{r^2} \tag{1.3}$$

where r is the distance from the cluster centre and $M(<r)$ is the mass contained within r. Thus, using the equation of state of an ideal gas to relate pressure to gas density and temperature, $P = (K_B\rho T)/\mu m_p$, the mass is given by:

$$M(<r) = \frac{rK_BT}{G\mu m_p}\left(\frac{d\ ln\ \rho_{gas}}{d\ ln\ r} + \frac{d\ ln\ T}{d\ ln\ r}\right) \tag{1.4}$$

where μ is the mean molecular weight of the gas and m_p is the proton mass, and the density ρ and the temperature T profiles can be inferred from X-ray observations (see Ettori et al., 2013, for a review). The gas density profile is generally well described assuming the β model (Cavaliere & Fusco-Femiano, 1976):

$$\rho_{gas}(r) = \frac{\rho_0}{[1 + (r/r_c)^2]^{3\beta/2}} \tag{1.5}$$

where r_c is the core radius (i.e. the radius at which the temperature begins to drop) and $\beta = \mu m_p \sigma_v^2/(k_BT)$. If we assume the gas to be isothermal, the combination of Eq. 1.4 and 1.5 gives:

$$M(<r) = \frac{3K_BTr^3\beta}{\mu m_p G}\left(\frac{1}{r^2 + r_c^2}\right) \tag{1.6}$$

A third independent method to estimate the cluster mass is based on weak and/or strong gravitational lensing, i.e. on the images of distant objects that result distorted by the gravitational potential of the cluster. A simple spherical lensing model

provides a good estimate of the cluster mass within the radius r_{arc} which is the distance between the arc-like image and the cluster centre (e.g. Bartelmann et al., 2003):

$$M_{lens}(< r_{arc}) \approx \pi r^2 \Sigma_{crit} \tag{1.7}$$

where

$$\Sigma_{crit} = \frac{c^2}{4\pi G} \frac{D_S}{D_{LS} D_L} \tag{1.8}$$

D_L, D_{LS} and D_S are respectively the distances from the observer to the lens, from the lens to the source and from the observer to the source, respectively. Observations of weak lensing aim at reconstructing the cluster mass distribution from the weak ellipticity that the cluster gravity induces on faint background galaxies. This method is challenging since galaxies are intrinsically elliptical, therefore it requires several source images to be averaged, under the assumption of random orientation of these sources.
In addition, if a large number of redshift measurements is available, the mass of a cluster of galaxies can be inferred from the dynamical analysis of member galaxies. One method is to fit the velocity dispersion data to the solution of the Jeans equations (e.g. Sanchis et al., 2004; Łokas et al., 2006).
Another method is the "caustic technique". In the line of sight velocity - projected radius diagram, cluster galaxies distribute in a characteristic trumpet shape. The edges of the trumpet are called caustic and, under the assumption of spherical symmetry, they trace the escape velocity profile of the cluster and can thus be used to determine the cluster mass profile (e.g. Diaferio, 1999; Diaferio et al., 2005; Geller et al., 2013; Maughan et al., 2016).
Finally, the mass of clusters can be inferred from the total energy of the gas combined with other observational constraints. This energy budget can be measured directly via scaling relations with other observational properties (Pratt et al., 2009), such as the X-ray luminosity or the Sunyaev-Zel'dovich effect.

1.2 The Sunyaev-Zel'dovich (SZ) effect

The ICM is a hot gas containing extremely energetic electrons. When photons from the Cosmic Microwave Background (CMB) interact with these electrons, they can undergo the Inverse Compton scattering (IC): the photons gain energy interacting with the hot electrons and hence they are scattered and blueshifted. The Sunyaev-Zel'dovich effect (S-Z effect Sunyaev & Zeldovich, 1972) is a small distortion of the CMB spectrum caused by the IC scattering of the CMB photons with the energetic ICM electrons (Fig. 1.2). In particular, thanks to the new state-of-the-art high

angular resolution instruments working in the millimeter waves, the study of substructures in the ICM through SZ effect is entering in a new era (e.g. Korngut et al., 2011; Planck Collaboration et al., 2016; Adam et al., 2017, 2018, b). The distortion of the CMB spectrum appears as a decrement in the CMB intensity at frequencies ≤ 218 GHz ($\lambda \geq 1.4$ mm) and as an increment for frequencies ≥ 218 GHz.

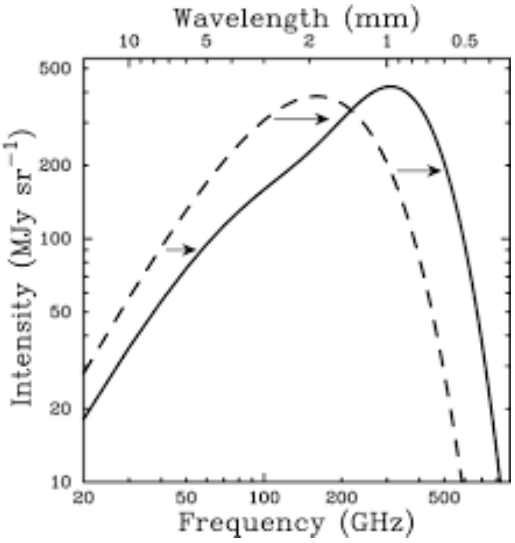

Figure 1.2: Standard CMB spectrum (dashed line) and distorted by SZ effect (solid line). This is just a schematic representation. To emphasize the effect, the SZ distortion shown is for a fictional cluster 1000 times more massive than a typical massive galaxy cluster (From Carlstrom, 2002).

The so-called Compton y-parameter is defined as:

$$y \propto \int_0^\infty n_e T_e dl \tag{1.9}$$

where T_e is the electron temperature and n_e is the electron density, and it is defined for a given direction in the sky. The y-parameter is strictly connected to the surface brightness of the X-ray emission, which is the key quantity to determine whether a galaxy cluster is detectable or not. The Compton y-parameter is independent from the redshift, it depends only on the physical properties of the ICM.
In terms of intensity, the SZ effect can be written as:

$$\Delta I_{SZ} \propto I_0 y \tag{1.10}$$

where I_0 is the CMB intensity unaffected by the IC scattering.
A crucial characteristic of the SZ effect is its correlation with the cluster mass, due to the fact that the SZ signal integrated over the solid angle of the cluster provides the sum of the electrons weighted by temperature, which is a measure of the total

thermal energy of the cluster:

$$\text{SZ flux} \propto Y \equiv \int_{\Omega} y \, d\Omega \propto \frac{1}{D_A^2} \int_0^{\infty} dl \int_A n_e T_e dA \tag{1.11}$$

in this relation A is the area of the cluster in the plane of the sky and D_A is the angular diameter distance.

1.3 Merging clusters vs cool-core clusters

Clusters of galaxies show a variety of morphologies but it is possible to identify two main cases according to their dynamical status: merging clusters, which are characterized by irregular morphology and by the presence of substructures in their X-ray brightness distributions (Fig. 1.3); cool-core clusters, which are in a relaxed state and are characterized by a giant galaxy at their center. They show enhanced X-ray surface brightness in the core.

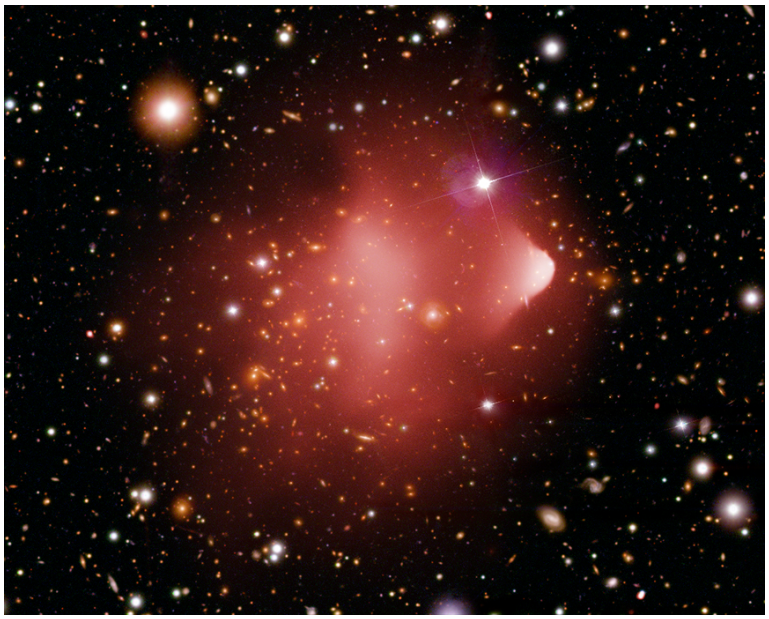

Figure 1.3: A *Chandra* image of the Bullet cluster: the gravity of the merging is displaced from the subcluster gas, this is probably the strongest proof of the existence of dark matter.

1.3.1 Merging clusters

In the X-rays, ROSAT and ASCA observations revealed, for the first time, that many clusters show evidence of the accretion of smaller masses and others undergo major mergers of two nearly equal components (e.g. Briel et al., 1991; Henry &

Briel, 1991; Markevitch et al., 1999). Before the launch of the last generaton of X-ray satellites, namely *Chandra* and *XMM-Newton*, the main information about mergers was based on morphology. With the spatially resolved spectroscopy and high-resolution imaging offered by the new instruments, the situation has radically changed, and sophisticated algorithms have been developed to achieve good and reliable temperature maps (e.g. Peterson et al., 2004; Bourdin et al., 2004; Sanders, 2006), since the temperature is the most accurate tracer of the energy transfer from the collision to the X-ray gas itself.

Mergers are the events by which clusters are formed and major mergers are very energetic events in which clusters collide at velocities of $\sim 2000\ kms^{-1}$. Merger-driven shocks propagate through the ICM and dissipate an amount of energy of $\sim 10^{63}$-10^{64} erg; these hydrodynamical shocks are the major heating source for the ICM and also they can accelerate non-thermal relativistic particles, which give rise to diffuse radio emission associated to the presence of magnetic fields (see Brunetti & Jones, 2014, for a review). Mergers also must significantly affect the emission of the galaxy populations (Ledlow & Owen, 1996; Owen et al., 1999; Dwarakanath & Owen, 1999; Venturi et al., 2000, 2001; Giacintucci et al., 2004).

The kinematics of an individual binary merger collision can be described, following Sarazin 2002, by a simple model in which two subclusters with masses M_1 and M_2 merge at a time t_m after having fallen toghether, with nonzero angular momentum, in the same potential well from a distance d_0. In the model we can assume that the subclusters are pointlike and their radial velocity was zero at the largest separation d_0.

The collapse can be described using the third Kepler's law:

$$d_0 \simeq (2G(M_1 + M_2))^{1/3} \left(\frac{t_m}{\pi}\right)^{2/3} \tag{1.12}$$

the quantity d_0 is called turn-around distance. As the centers of the two subclusters reach a distance of the order of the virial radius of the most massive cluster, R_{max}, the relative impact velocity is given by:

$$v_i \simeq (2G(M_1 + M_2))^{1/2} \left(\frac{1}{R_{max}} - \frac{1}{d_0}\right)^{1/2} \left[1 - \left(\frac{b}{d_0}\right)^2\right]^{-1/2} \tag{1.13}$$

where b is the impact parameter. Most mergers are expected to involve small impact parameters, comparable to the sizes of the gas cores in clusters, but mergers with larger impact parameters may occur. In the simplest case of central collision where b=0:

$$v_i \simeq \left[2G\frac{(M_1 + M_2)}{R_{max}} \left(1 - \frac{1}{\eta_v}\right)\right]^{1/2} \tag{1.14}$$

where $\eta_v \simeq 4 \left(\frac{M_1+M_2}{M_1}\right)^{1/3}$. During a merger, the infall velocities of the subclusters are comparable to the escape velocity, hence $v^2 \approx 2\phi$, and the motion in cluster

mergers are expected to be moderately supersonic: $v^2 \approx 2c_s^2$. Defined the Mach number as $M = \frac{v_s}{c_s}$, one expects weak shocks with Mach numbers of $M \leq 3-5$. Stronger shocks ($\mathrm{M} \sim$ 10-100) associated with the accretion of cold gas onto gravitationally attracting nodes may occur in the outer parts of clusters, or in low mass subclusters merging with more massive clusters (Miniati et al., 2001; Vazza et al., 2009). Shocks represents the imprint of merging events in galaxy clusters, they are now well estabilished as common merger features (e.g. Markevitch & Vikhlinin, 2007, for a review).

1.3.2 Cool-core clusters

As we discussed above, the ICM loses energy emitting X-ray radiation primarily via thermal Bremsstrahlung.
The time-scale for this process can be defined as: $t_{cool} = (d\ lnT/dt)^{-1} = \frac{3(n_e+n_H)kT}{2n_e n_H \Lambda(T)}$.
Being $\Lambda(T) \propto T^{\frac{1}{2}}$, and if the gas cools isobarically, the cooling time is (Sarazin, 1986):

$$t_{cool} \simeq 8.5 \times 10^{10} \left[\frac{n_p}{10^{-3}\mathrm{cm}}\right]^{-1} \left[\frac{T}{10^8\mathrm{k}}\right]^{1/2} \ [\mathrm{yr}] \tag{1.15}$$

which exceeds the Hubble time. The Bremsstrahlung emissivity depends on the square of the gas density, which increases towards the cluster center, and so in some cases t_{cool} becomes $< 10^{10}$ years in the central $\sim$ 100 kpc. In case of lack of balancing heating sources, the gas is compressed by the surrounding ICM, further increasing its X-ray emissivity. To mantain the pressure equilibrium, slow inflows of gas called "cooling flows" are expected. Relaxed clusters were classified as "cooling flow" clusters (Fabian et al., 1994), with predicted gas mass deposition rates in the clusters center up to 1000 $M_\odot yr^{-1}$. This model was challenged by *Chandra* and *XMM-Newton* observations. X-ray and optical studies show that the gas cooling rates were overstimated by an order of magnitude or more (McNamara, 2006). The classical cooling-flow model has finally been replaced by the cool-core model. From the observations, cool-cores are characterized by a strong peak in the surface brightness, a peak in the metal distribution (De Grandi & Molendi, 2001) and a significant drop in the temperature by a factor of $\sim$ 3 (down to 2-3 keV) in the central regions. The gas, however, does not flow towards the center, rather the gas temperature profile seems to be frozen and it seems to has been so for Gyrs (Bauer, 2005). This suggests the presence of a continuous central source of heating which may balance radiative cooling. Several candidates have been proposed, AGNs and Supernovae being the most likely one (Fabian, 2002; Birzan et al., 2004).
Nowdays the term "cool-core" indicates those clusters which are in a relaxed state, characterized by a giant elliptical galaxy at their center (tipically a cD galaxy) and

enhanced X-ray surface brightness peak in the core (Fig. 1.4). The dicotomy between "cool-core" (CC) and "non cool-core" (NCC) clusters depends whether their core region shows a drop in the temperature profile or not (e.g. Molendi & Pizzolato, 2001; Rasia et al., 2015; Li et al., 2015).
The core entropy is of fundamental importance because it controls ICM global properties and controls the thermal history of a cluster. Entropy is therefore an useful quantity for studying the effects of feedback on the cluster environment and investigating any breakdown of cluster self-similarity (Cavagnolo et al., 2009).
It is defined as:

$$K_0 = kTn_e^{-2/3} \tag{1.16}$$

where T is the gas temperature and n_e is the electron number density. Clusters are classified as CC or NCC according to the value of the specific entropy floor in the cluster center (Donahue & Voit, 2004; Donahue et al., 2011; Giacintucci et al., 2017), in particular, clusters with $K_0 < 30$ - 50 keV cm^2 exhibit all the attributes of a cool core (Giacintucci et al., 2017).
Some cool-core clusters show evidence of cavities in X-ray surface brightness, coincident with radio lobes: they are commonly interpreted as bubbles of relativistic gas blown by the AGN into the thermal ICM and they are considered as a signature of the heating mechanism driven by the central source and propagating through the ICM (Birzan et al., 2004; Rafferty et al., 2004; McNamara et al., 2004; McNamara & Nulsen, 2007).

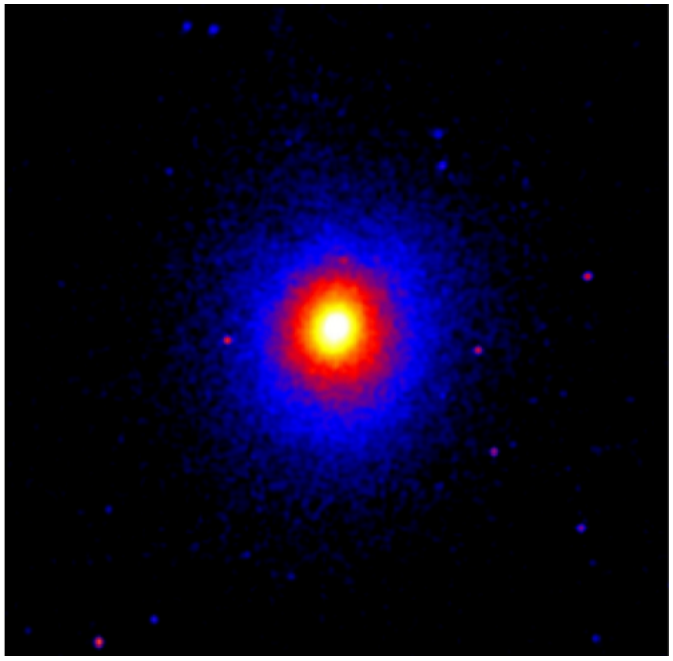

Figure 1.4: *Chandra* image of the cool core galaxy cluster A1835. The X-ray emission peaks in the core and shows a regular morphology.

1.4 Multi-wavelength properties

It is nowdays of fundamental importance to study clusters of galaxies combining data through a multi-wavelength analysis, since every band gives complementary information on their properties and on their different components such as galaxies, diffuse emission, and ICM. In this section the attention is focused on the optical and X-ray properties of clusters. The next section is focused on the radio properties and the radio components. The UV and gamma-ray emission are also present in clusters, deriving from merger-driven shocks propagating through the ICM.

1.4.1 Optical properties

Optical observations of galaxy clusters revealed that galaxies are not uniformly distributed in the sky but rather they are concentrated in large overdensities. Only 20% of galaxies live in clusters, most are in groups or in the "fields" and it is hard to discriminate between groups and clusters: the latters have higher densities than groups, contain a majority of E's and S0's while groups are dominated by spirals. Clusters contain tipically $\sim$ 50-100 luminous galaxies within the central Mpc.
Until the 80's clusters have been modeled as virialized spherically symmetric systems (e.g. Kent & Gunn, 1982). Rather, clusters often contain subsystems of galaxies, usually called substructures or subclusters. Indeed, in the hierarchical scenario of large scale formation it is quite natural to expect that clusters form from the

mergers of small sub-clumps (Colberg et al., 1999). In this context, the presence of substructures is indicative of a cluster in an early phase of the process of dynamical relaxation, or of secondary infall of clumps of galaxies into already virialized clusters (Girardi et al., 1998; Biviano, 2001).
Historically, first systematics catalogues of galaxy clusters were based on optical data (e.g. Abell, 1958; Zwicky et al., 1961). Selected clusters were primarily nearby systems ($z \leq 0.2$), and were also used to define and estimate richness, rough morphological classifications (Rood & Sastry, 1971) as well as distance of the clusters. More recently, clusters searches based on optical data, have been carried out using e.g. Hyper Suprime-Cam, CAMIRA cluster catalogue (Oguri et al., 2018), SDSS (redMaPPer cluster catalogue, Rozo et al., 2015). Similar approaches have been done using Spitzer or WISE 3.6μm and 4.5μm data (e.g. Muzzin et al., 2009; Gonzalez et al., 2019).
Beyond pure galaxy cluster searches, optical and near/mid infared data are used to explore galaxy cluster properties, such as Luminosity Function of cluster galaxies (e.g. De Propris et al., 2013), the stellar mass fraction (e.g. Annunziatella et al., 2014), the radial profile of cluster galaxies distribution, as well as the distribution of galaxy colours (e.g. Zenteno et al., 2016). The multiwavelength observations of sample of galaxy clusters allow to gain insight into galaxy formation and evolution, and the role of the environment and of the cosmic time in these processes (e.g. Wen et al., 2009; Chung et al., 2007; Hennig et al., 2017).
Clusters are important laboratories for investigating the evolution of galaxies in dense environments, e.g. the Butcher-Oemler effect, the morphology-density relation (Dressler, 1980; Butcher & Oemler, 1978a, 1984). This relation is found to extend over five orders of magnitude in space density (Postman & Geller, 1984). Whether it arises at formation (i.e. *nature* scenario) or it is caused by density driven evolutionary effects (i.e. *nurture* scenario) remains a matter of debate (see van Gorkom, 2004, for a review). More recent studies of clusters of galaxies at intermediate redshifts show that both the morphological mix and the star formation rate strongly evolve with redshift (see Finn et al., 2018, and references therein).

1.4.2 X-ray properties

About 17% of the mass of clusters is made of hot gas, the hot plasma which is called ICM. The study of its properties is of fundamental importance: this hot, X-ray emitting gas can trace the global cluster gravitational potential and it is an excellent tool to probe the dynamics, morphology and history of clusters. The ICM is in the form of diffuse, metal-enriched gas, gravitationally heated during the cluster formation. It has a temperature of about $T = 10^7 - 10^8$ K (i.e. $kT \sim 1 - 10$ keV) and a density of $\sim 10^{-1} - 10^{-4} cm^{-3}$. Its luminosity in the X-ray band is about $L_x \sim 10^{43} - 10^{46} ergs^{-1}$ and the typical metallicity is Z $\sim 0.3_{\odot}$.

The ICM emits primarly via thermal Bremsstrahlung, so the emissivity for this process at a frequency ν is given by:

$$\epsilon_\nu \propto n_e n_i g(\nu, T) T^{1/2} exp(-h\nu/k_B T) \tag{1.17}$$

where n_e and n_i are the number density of the electrons and ions respectively, $g(\nu, T) \propto ln(k_B T/h\nu)$ is the Gaunt factor and k_B is the Boltzman constant. The spectral shape of the emissivity $\epsilon_\nu(r)$ provides a measure of $T(r)$ while its normalization gives a misure of n_e (Fig. 1.5).

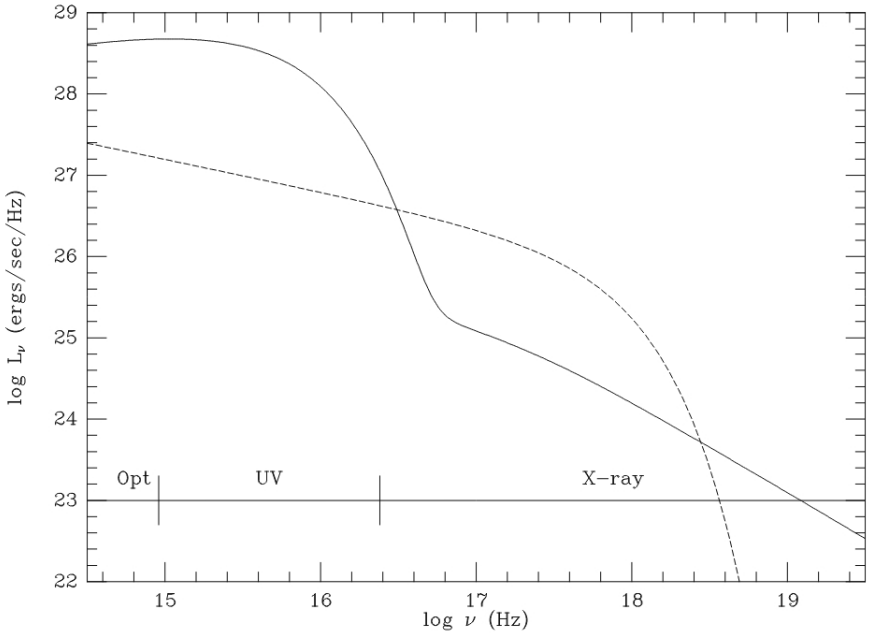

Figure 1.5: The IC spectrum from a typical cluster model (solid line). The dashed curve is a 7 keV thermal Bremsstrahlung spectrum (from Sarazin, 2002b).

The X-ray surface brightness can be used to determine the physical cluster parameters. For a spherical symmetric cluster, the radial X-ray surface brightness distribution is described by the expression (Cavaliere & Fusco-Femiano, 1976):

$$S(r) = S(0) \left[1 + (\frac{r}{r_c})^2\right]^{-3\beta+\frac{1}{2}} \tag{1.18}$$

where S(0) is the central surface brightness, r_c is the cluster core radius and the parameter $\beta = \mu m_p \sigma_v^2/(k_B T)$ is the ratio of the energy per unit mass in the galaxies to that in gas. With the exception of the central cusp in cool core clusters, this expression for the surface brightness distribution has been found to be an adequate tool to describe the gas in clusters. If the surface brightness expression is

deprojected it is possible to obtain the gas density distribution (Vikhlinin, 1999):

$$n(r) = n(0)\left[1 + (\frac{r}{r_c})^2\right]^{-\frac{3}{2}\beta} \tag{1.19}$$

The central electron density n(0) is tipically of the order of $n(0) \simeq 10^{-3} cm^{-3}$ and the total mass of gas in rich clusters ranges from $\sim 5 \times 10^{13} - 5 \times 10^{14} M_{\odot}$.

1.5 Radio emission in galaxy clusters

In the radio band, we can distinguish between two classes of emission in clusters:
- (1) the non-thermal diffuse synchrotron emission (e.g. van Weeren et al., 2019, for reviews) which generates structures such as halos, relics and mini-halos;
- (2) the discrete emission from radio galaxies in clusters, where the synchrotron emission is generated by an Active Galactic Nuclei (AGN).

1.5.1 Diffuse non-thermal emission

During the last years there has been growing evidence for the existence of cluster large scale diffuse radio sources, of synchrotron origin, which have no optical counterpart and therefore associated with the ICM (Giovannini & Feretti, 2002; Feretti & Giovannini, 2008; Ferrari et al., 2008; Feretti et al., 2012). It is now well established that some clusters of galaxies host some particular objects classified as halos, relics and mini-halos (Feretti & Giovannini, 1996; Feretti et al., 2012; Venturi et al., 2007, 2008; Kale et al., 2015) depending on their morphology, origin, location and radio properties. These sources are the direct clue of the existence of clusters magnetic fields and relativistic electrons which affect the thermal state of the ICM (see Brunetti & Jones, 2014, for reviews).
The connection between diffuse radio emission in the ICM and dynamically disturbed systems (Buote, 2001; Cassano et al., 2010, 2013) suggests that cluster mergers play a crucial role in the formation of non-thermal component in galaxy clusters.
The first diffuse radio source detected in a cluster of galaxies (Large et al., 1959) was the giant radio halo in the center of Coma cluster (Fig. 1.6).
Systematic studies of giant diffuse emission in clusters were performed in surveys such as the Giant Metrewave Radio Telescope Radio Halo Survey (GRHS, Venturi et al., 2007, 2008) and its extention (EGRHS, Kale et al., 2013, 2015).
Currently, diffuse radio emission with low surface brightness down to 0.1 μJyarcsec^{-2} at 1.4 GHz is known in about $\sim$ 80 clusters, under different cluster evolutionary conditions (merging and relaxed clusters), at different cluster locations and on very different size scales: from $\sim$100 kpc up to some Mpc. All diffuse radio sources in

clusters share very steep synchrotron spectra ($\alpha > 1$) but there are some peculiar features which characterize them.
The taxonomy of extended radio emission in galaxy clusters is nowdays evolving thanks to the advent of new instruments such as LOFAR (van Haarlem et al., 2013). LOFAR is unveiling the wealth of complex diffuse steep spectrum sources in the ICM (Shimwell et al., 2016; de Gasperin et al., 2017; Bonafede et al., 2018; Brüggen et al., 2018; Kale, 2018).

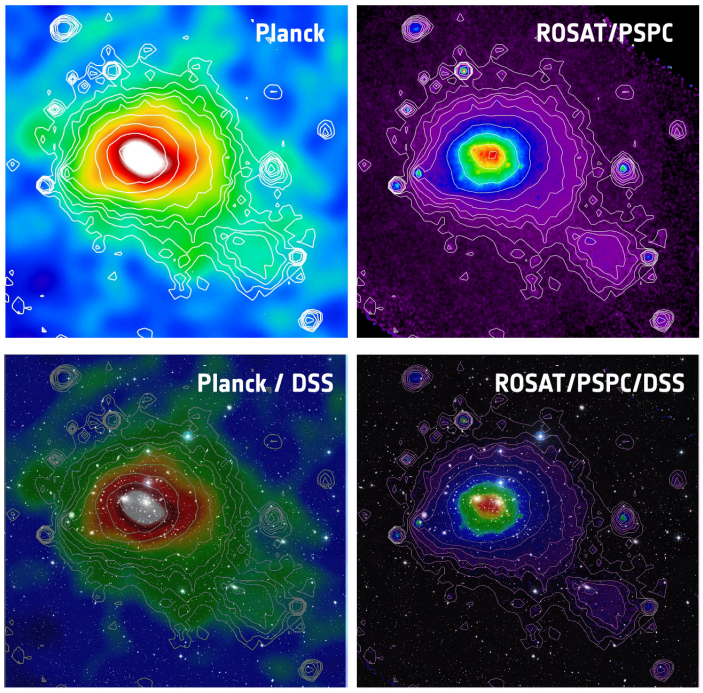

Figure 1.6: The Coma cluster image produced by Planck (top-left) and by ROSAT (top-right). As a comparison, the images are shown superimposed on a wide-field optical image of the Coma cluster from the DSS in the two lower panels.

1.5.2 Radio halos

Radio halos are diffuse extended sources (Fig. 1.7), fairly regular in morphology, of low surface brightness (about 1-0.1 μJyarcsec^{-2} at 1.4 GHz). They are observed at the center of massive dynamically disturbed galaxy clusters (Giovannini et al., 1999; Buote, 2001; Cassano et al., 2010). Their size is typically of the order of $\geq 1 - 2$ Mpc (giant halos, see van Weeren et al., 2019, for a review), unpolarized down to a few percent level.
The prototype of this class is Coma C at the center of the Coma cluster, studied in detail by many authors (Large et al., 1959; Willson, 1970; Giovannini et al., 1993;

Thierbach et al., 2003; Brown & Rudnick, 2011).
The most distant radio halo is found in El Gordo at z=0.87 (Menanteau et al., 2012; Lindner et al., 2014; Botteon et al., 2016). The 1.4 GHz radio powers of observed halos range between about $10^{23} - 10^{26}$ W Hz^{-1}, with the most powerful radio halo ($P_{1.4} = 1.6 \times 10^{26}$ W Hz^{-1}) being present in the quadruple merging cluster MACSJ0717+3745 (Bonafede et al., 2009; van Weeren et al., 2009). Currently, there are about 65 confirmed radio halos (van Weeren et al., 2019).
Halos always show a steep spectrum ($\alpha \geq 1$, with $S(\nu) \propto \nu^{-\alpha}$) but integrated radio spectra are poorly known, so, it is difficult to determine the spectral steepening. Radio halo spectra are usually constrained by only a few data-points, covering a small range of frequencies, and are commonly fitted with a simple single power-low (e.g. Venturi et al., 2013).
An extreme class of radio halos with $\alpha > 1.5$, the so-called *ultra-steep spectrum radio halos* (USSRHs), is also observed (Brunetti et al., 2008; Dallacasa et al., 2009; Macario et al., 2010, 2013; Wilber et al., 2018). USSRHs pose an energy runaway problem requiring that an excessive amount of energy is associated to the relativistic plasma if the steep power-low energy distribution is extrapolated to lower energies. A solution to this problem is that the observed synchrotron radiation comes from electrons whose energy distribution has a high-energy break at energies of a few GeV.
Recent findings obtained with improved statistic suggest that there is a clear separation between relaxed and non-relaxed clusters, in the radio behavior (Venturi et al., 2007, 2008; Kale et al., 2013, 2015). The bi-modality between halo and non-halo clusters (see Brunetti et al., 2007, 2009; Cassano et al., 2010; Kale et al., 2015), reflects the dicotomy between non-relaxed and relaxed clusters, also discussed by Rossetti & Molendi (2011).
What is intriguing is the existence of dynamically disturbed clusters which do not show any evidence of radio halo. It may be possible that giant radio halos are only present above a treshold of mass or temperature. New generation instrument like for instance LOFAR, uGMRT are allowing the detection of low brightness-low power large halos, important to understand if halos are present in all merging clusters or only in the most massive ones (Bonafede et al., 2014; Shimwell et al., 2016; de Gasperin et al., 2017; Hoang et al., 2017; Kale, 2018).

1.5.3 Relics

Cluster radio shocks, commonly referred to as radio relics, are elongated, arc-like radio sources characterized by sharp emission edges (Fig. 1.8). They are generally observed in the outskirts of galaxy clusters and have significant linear polarization (typically up to 30%). The prototype of this class of objects is 1253+275, detected in Coma cluster (Giovannini et al., 1991). In the most impressive cases, symmetric

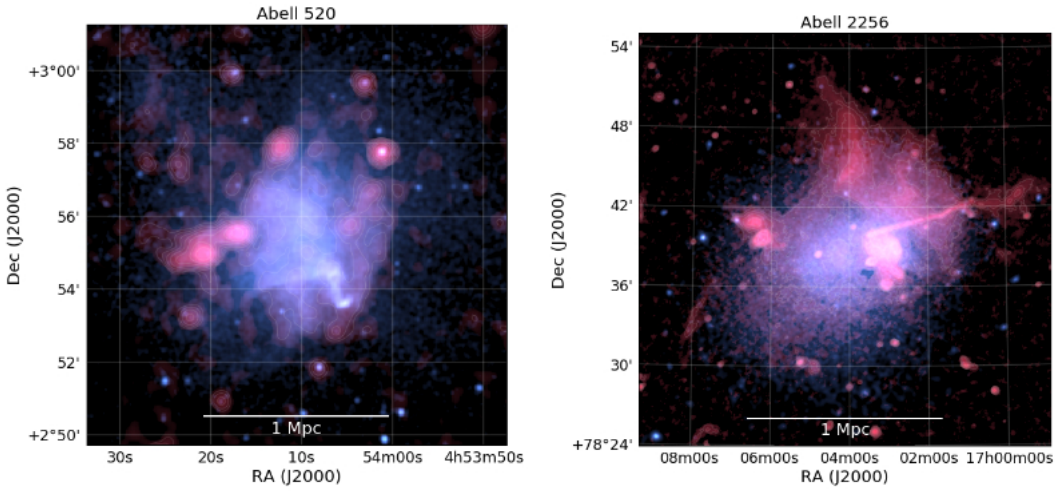

Figure 1.7: A520 (left) and A2256 (right) galaxy clusters hosting giant radio halos. The radio emission is shown in red and the X-ray emission in blue. A520: VLA 1.4 GHz and Chandra 0.5-2.0 keV. A2256: LOFAR 120-170 MHz and XMM-Newton 0.4-1.3 keV. See van Weeren et al. (2019) for reviews.

double relics are observed on opposite sides of clusters (see de Gasperin et al., 2014; Bonafede et al., 2017, and references therein).
Observations of relics provide the evidence of the presence of $\sim \mu G$ level magnetic fields and relativistic particles in cluster outskirts. They provide evidence for the acceleration of relativistic particles at shock fronts at large distance (Mpc scale) from the cluster centers (Brüggen et al., 2011).
Relics shows quite steep integrated spectra, while spectral index maps highlight spectral steepening, indicative of particle aging, toward the cluster center (e.g. Bonafede et al., 2009, 2012; van Weeren et al., 2010; de Gasperin et al., 2015; Hoang et al., 2018).
A single power-law is usually adopted to fit the spectra of relics, and it is still under discussion whether a spectral curvature is present at frequencies $\gtrsim 2$ GHz (see Stroe et al., 2013, 2014, 2016).

There is broad agreement on the hypothesis that radio relics are connected with shocks (e.g. Brüggen et al., 2012; Brunetti & Jones, 2014). The evidence includes (i) the *arc-like* morphology and peripherial location of some relics, which is consistent with numerical simulations of clusters shocks, (ii) the radial spectral gradients and/or spectral curvature, suggesting that the relativistic electrons gain energy at the shock front and lose energy after the shock passage, (iii) the high degree of linear polarization, indicating a magnetic field aligned whithin the shock plane and (iv) the existence of double radio relics, interpreted as tracers of shocks moving outward after an head-on cluster merger in the plane of the sky. The consolidation of the relic-shock connection is supported by the detection in the X-rays of shock fronts underlying some radio relics (Akamatsu & Kawahara, 2013; Shimwell et al.,

2015; Eckert et al., 2016). Although it is clear that shocks play a fundamental role in the formation of radio relics, the details of mechanisms generating the relativistic electrons are still under debate.

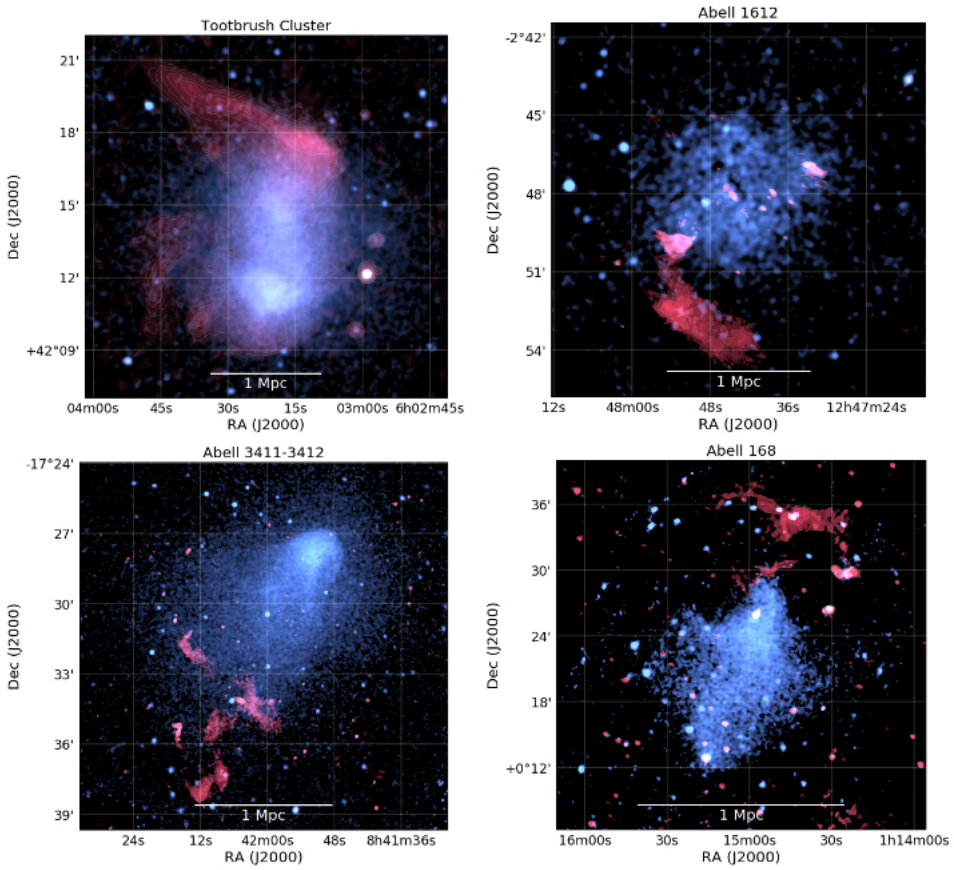

Figure 1.8: Examples of cluster radio shocks from van Weeren et al. 2019. The radio emission is shown in red and the X-ray emission in blue. Toothbrush Cluster: LOFAR 120-180 MHz and Chandra 0.5-2.0 keV. Abell 1612: GMRT 610 MHz and Chandra 0.5-2.0 keV. Abell 3411-3412: GMRT 610 MHz and Chandra 0.5-2.0 keV. Abell 168: GMRT 323 MHz and XMM-Newton 0.4-2.3 keV.

1.5.4 Mini-halos

Radio mini-halos have sizes of $\sim$ 100-500 kpc and are found in relaxed cool core clusters (see van Weeren et al., 2019), with the radio emission surrounding the central radio loud BCG (Giacintucci et al., 2014; Gitti, 2015; Giacintucci et al., 2017). The sizes of mini-halos are comparable to that of the central cluster cooling regions. They have in common with halos and relics a low surface brightness and a steep

spectrum. An example of radio mini-halo is the diffuse source in the Ophiucus cluster (Govoni et al., 2009; Murgia et al., 2010, see Fig. 1.9).
Radio mini-halos have 1.4 GHz radio powers in the range of $10^{23} - 10^{25}$ WHz^{-1}. The most luminous mini-halos known are located in the clusters PKS0745-191 (Baum & O'Dea, 1991) and RXJ1347.5-1145 (Gitti et al., 2007).
Their emission originates from relativistic particles and magnetic fields which are believed to be mixed with the thermal ICM. This physical characteristic can be used to distinguish mini-halos from other kind of steep spectrum radio sources in clusters such as radio bubbles related to AGN activity.
There are some difficulties in the classification of mini-halos, their relatively small angular size combined with a possibly strong emission of the central radio galaxy complicates their detection. Despite these observational difficulties the number of known mini-halos has steadily been increasing (Gitti et al., 2006; Doria et al., 2012; Giacintucci et al., 2011, 2014, 2017).
The origin of these sources is still poorly known, one possible explanation is that mini-halos result from a relic population of relativistic electrons reaccelerated by MHD turbulence via Fermi-like processes, the necessary energetic being supplied by the cool-core region. This is supported by the correlation observed between the mini-halo radio power and the cooling rate power (Gitti et al., 2004; Mazzotta & Giacintucci, 2008).
Cool-core clusters are generally considered relaxed systems but, when analyzed in detail they sometimes reveal peculiar X-ray features in the cluster center which may be indicative of a link between the mini-halo emission and some minor merger activity. Another last consideration regards the sloshing process: cold fronts associated to the core gas sloshing have been observed in some clusters hosting a mini-halo. Thus, the possible explanation is that gas sloshing may generate turbulence in the core, which in turn may reaccelerate the relativistic electrons necessary to form mini-halo (ZuHone et al., 2011, 2013).

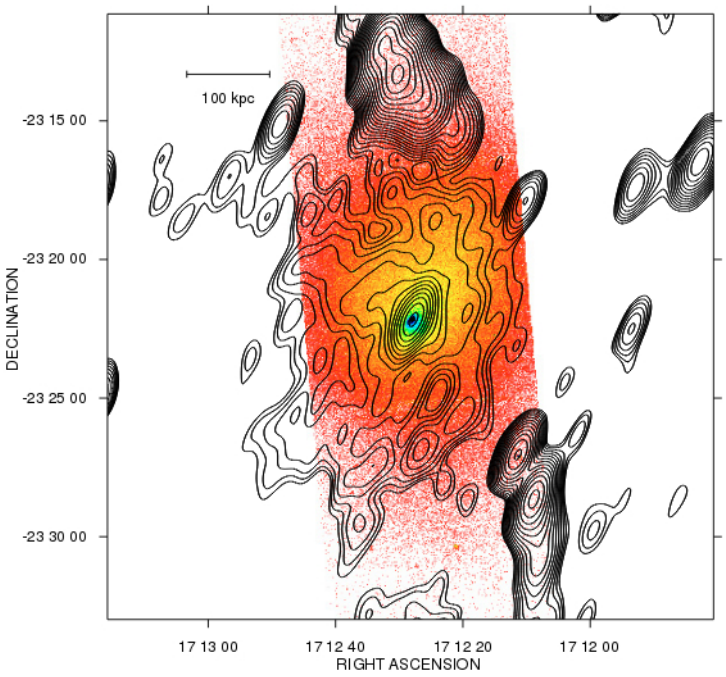

Figure 1.9: Total intensity radio contours of Ophiuchus overlaid on the Chandra X-ray image in the 0.5 - 4 keV band from Govoni et al. (2009).

1.6 Radio galaxies in galaxy clusters

In addition to the diffuse emission related to the ICM, the radio emission in galaxy clusters is from radio galaxies, associated both to the star formation or AGN mechanisms.
Radio galaxies show different properties in connection with the environment in which they are located (Dressler, 1980; Butcher & Oemler, 1984; Dwarakanath & Owen, 1999; Owen et al., 1999; Poggianti et al., 1999; Venturi et al., 2001; Condon et al., 2002; Branchesi et al., 2006; Mauch & Sadler, 2007; Mahony et al., 2016).
Among the radio galaxies in clusters, the so-called Brightest Cluster Galaxies (BCG) occupy a special location, being the most massive and centrally located galaxies with radio properties strongly connected to the host cluster (Best, 2007; Cavagnolo et al., 2009; Kale et al., 2015). We refer to Chapter 2 for the analysis of a sample of eleven BCGs from ten selected galaxy clusters.
Crucial information on the cluster dynamics and on the interaction between the radio plasma and the ICM can be derived from radio galaxy populations (Venturi et al., 2000; Biviano, 2001; Branchesi et al., 2006; Di Gennaro et al., 2018). The external gas can interact in different ways with a radio source: modifying its morphology via ram-pressure, enhancing star formation, feeding the central AGN, confining the radio lobes and exerting stripping effects on the galaxy's gaseous com-

ponent (see van Gorkom, 2004, for a review).
There are different classes of radio galaxies with various structures and morphologies; of fundamental importance for their formation and evolution is the presence of the intracluster gas and of cluster mergers (Ledlow & Owen, 1996; Owen et al., 1999; Dwarakanath & Owen, 1999; Venturi et al., 2000, 2001; Giacintucci et al., 2004).
In the last years our knowledge of the environment of radio galaxies has greatly improved thanks to the high sensitivity achieved by X-ray satellites (Markevitch & Vikhlinin, 2007; Venturi et al., 2008; ZuHone et al., 2013; Giacintucci et al., 2014, 2017).
The effect of the gaseous environment on the extended radio sources can be investigated in detail. The ICM within merging clusters is likely to be in a turbulent dynamical state which may have a significant effect on the radio source morphology and the evolution of clusters radio galaxies (see Oemler, 1977; Butcher & Oemler, 1978b; Feretti & Venturi, 2002; van Gorkom, 2004; Di Gennaro et al., 2018). Mergers generate expansion shocks in the ICM through which individual galaxies may pass. In doing so, they will experience an increase in ram pressure which can induce a burst of star formation changing the observed galaxy's colours and stellar content. The ram pressure may also strip the galaxy of its gas content reducing the potential for future star formation and thus altering the galaxy's observed colour and morphology.

1.6.1 FRI and FRII

The radio emission originating from individual elliptical galaxies frequently extends well beyond the physical size of the host galaxy ($\geq$ 100 kpc). Radio galaxies with different luminosity have quite different radio morphologies on kiloparsec scale.
A very important morphological classification of extended radio structures was made by Fanaroff & Riley (1974) who classified radio sources into two categories, pointing out the fact that low power radio galaxies tend to be brighter close to their nuclei, whereas high power ones are brighter at their outer extremities. These two classes are the so-called FRI and FRII respectively, and they are also known as edge darkened and edge brightened. FRI sources have a radio power $P_{1.4} \leq 10^{24.5} WHz^{-1}$ whereas FRII have $P_{1.4} \geq 10^{24.5} WHz^{-1}$ (Fanaroff & Riley, 1974; Owen & Ledlow, 1994).
Cluster radio galaxies are mostly FR I (Fig. 1.10), so they are edge darkened with low radio power and low brightness lobe. FR Is are associated to giant elliptical galaxies (de Ruiter et al., 1990; Hardcastle et al., 1998) while FR IIs are identified with galaxies of lower optical luminosity and exist in poorer clusters (Prestage & Peacock, 1988; de Ruiter et al., 1990). FR I sources are typically found in regions of significantly enhanced galaxy density, whereas FR II sources appear to differ in

their cluster environments only marginally from elliptical galaxies drawn at random from the whole population. In general, cluster radio sources are characterized by complex structures, with prominent distortions resulting from the interaction between the radio emitting regions and the ambient gas (Parma et al., 1999; van Gorkom, 2004; Liuzzo et al., 2009; Di Gennaro et al., 2018). A common morphology is represented by the so-called tailed radio galaxies, i.e. FR I sources where the large scale low-brightness emission is bent in the same direction, forming features similar to tails. These radio galaxies are classified into two classes: narrow-angle tailed sources (NAT), which are "U" shaped, i.e. they have a small angle between the tails (O'Dea & Owen, 1985), and wide-angle tailed sources (WAT), which are "V" shaped, i.e. with a larger angle between the tails (Miley, 1980; Burns, 1998; Feretti & Venturi, 2002). We discuss this kind of sources in the next Section. FR IIs radio galaxies present a marginal distortion and only in weak structures.

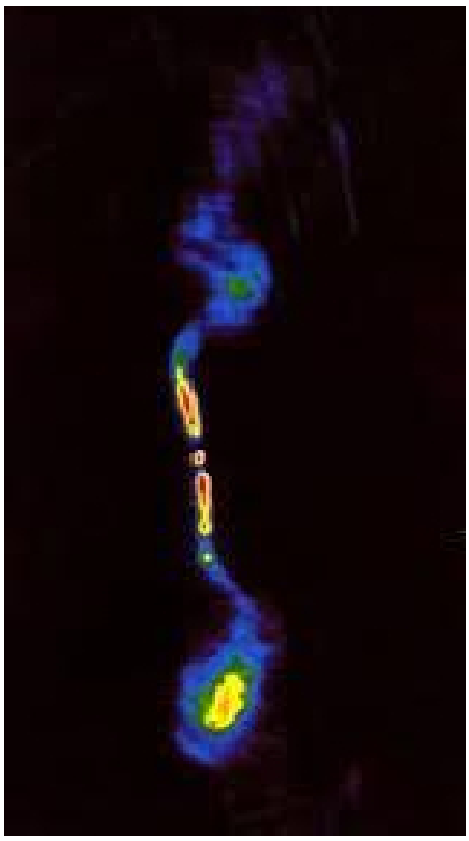

Figure 1.10: The radio galaxy 3C449 is an example of a FRI radio source. The structure consists of two opposite jets, emanating from the central nucleus, and two extended lobes of low brightness.

1.6.2 Narrow-angle tailed radio galaxies (NAT)

Radio galaxies located in dense environments, often show prominent and complex distorted radio structure (Giacintucci & Venturi, 2009). The most striking example of the interaction between the ICM and radio sources is provided by the so-called head-tailed, or NAT, sources (Rudnick & Owen, 1976). This class of radio galaxies presents radio jets which are bent at extreme angles, from their original orientation. They have a luminosity typical of FRI sources and are identified with cluster galaxies located at any projected distance from the cluster center. Generally the NAT radio sources show a very high degree of polarization in the tails, up to $40-50\%$, with the intrinsic magnetic field parallel to the tail direction. The typical age of the electron populations at the end of the tails, derived from the spectral index analysis, is around 5×10^7 years (see Feretti & Venturi, 2002, for a review). The prototypical example of a NAT radio source is NGC 1265 in the Perseus cluster (Wellington et al., 1973). The standard model used to explain the peculiar morphology of the NATs galaxies is the ram pressure model: jets are curved by ram pressure due to the high-velocity host galaxy moving through the dense ICM (Miley et al., 1972; O'Dea & Owen, 1985; Di Gennaro et al., 2018), whereas the low brightness tails are material left behind by the galaxy motion and trace the projected trajectory of the galaxy whithin the cluster. The bending is described by the Euler equation (Begelman et al., 1979; Jones & Owen, 1979):

$$R \sim h \left(\frac{\rho_j}{\rho_e}\right) \left(\frac{v_j}{v_g}\right)^2 \tag{1.20}$$

where R is the curvature radius, ρ_j is the density of the jet, ρ_e the density of the external medium, v_j is the velocity of the jet and v_g the dispersion velocity of the galaxy and h is the scale height over which the ram pressure is transmitted to the jets. Thus, from the jet bending important constrains on both the jet dynamics and the ICM can be placed (Terni de Gregory et al., 2017). Bends can occur very close to the nucleus, indicating that the bulk of interstellar medium has been stripped by the galaxy during its motion.

Studies on the properties of nearby, rich clusters of galaxies revealed that NATs are preferentially found in clusters with X-ray substructure (Bliton et al., 1998); moreover NAT galaxies tend to have, on average, velocities similar to those of typical cluster members, instead of high peculiar motions expected if NATs were bent from ram pressure. Since NATs are associated with dynamically complex clusters with possible recent or ongoing cluster-subcluster mergers, it has been also proposed that the "U" shaped morphology could be produced, at least in part, by merger-induced bulk motion of the ICM bending the jets. As concern the direction of the tails, some analysis found that the direction of NAT tails are consistent with random orientations in clusters (Bliton et al., 1998); however, it is possible to note that some clusters show tailed radio galaxies with the tails oriented in the same direction (Feretti & Venturi, 2002, for review). This would support the interpretation

that bulk gas motion plays a role in the formation of the tailed morphology at least in some clusters.

1.6.3 Wide-angle tailed radio galaxies (WAT)

Wide-angle tailed radio galaxies were originally defined by Owen & Rudnick (1976) as "V" shaped radio sources consisting of two, straight and narrow jets that flare into broad tails (see Fig. 1.11).
Like in NATs, the tails usually extend in a common direction, although forming a much wider angle between them. They are typically associated with cD or giant elliptical galaxies at the centers of cool core clusters (O'Donoghue et al., 1990). They show a radio luminosity in the range between 10^{42} to 10^{43} $ergs^{-1}$, an intermediate value between FRI and FRII. A peculiar characteristic of their jets is that they display a pronounced and abrupt transition from the well-collimated small-scale flow to the extended large-scale lobe structure. This transition is usually identified with a brightness flaring point, where the flow sudden expands by a factor of 3-10 (O'Donoghue et al., 1993). The prototypical example of WAT is 3C465 (Eilek et al., 1984).
Polarization properties and source radiative ages are similar to those of NATs.

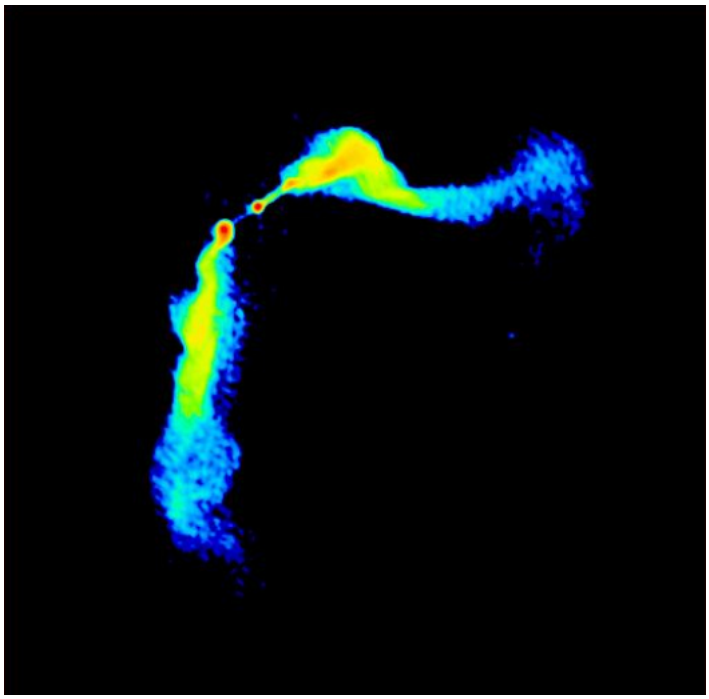

Figure 1.11: The radio galaxy 3C465 is the prototypical example of wide-angle tailed galaxies with "V" shaped radio jets Eilek et al. (1984).

From optical studies it is derived that WAT galaxies are generally moving very

slowly, typically less than 100 kms^{-1}, relatively to the cluster velocity centroid. Such slow motion is insufficient to bend the jets or tails of WATs to their observed curvature by ram pressure. In fact, typical velocities required to provide the necessary ram pressure to bend the jets are about 1000 $\mathrm{km}s^{-1}$, assuming typical central gas densities of $\sim 10^{-3}\mathrm{cm}^{-3}$. Also, it was proposed that jets could be deflected by collisions with dense clouds in the ICM (Eilek et al., 1984), although there is a problem since this process has difficulty in producing the large-scale symmetric structure of WATs. Therefore, WATs must be shaped, at least in part, by other ram pressure gradients not arising from motion of the host galaxy.
It has been suggested that the galaxy motions required to bend WATs by ram pressure are a by-product of mergers between clusters (Pinkney, 1993; Loken et al., 1995; Roettiger et al., 1996; Gomez et al., 1997).
In the hypothesis that the gas is not in a static condition, the "cluster weather" (Burns, 1998; Feretti & Venturi, 2002; Di Gennaro et al., 2018) is invoked to explain the morphology of these galaxies. Major perturbations in merging clusters include shocks, turbulence and bulk flows; during the collision of a cluster with a second comparable system, the two gaseous components will rapidly dissipate their kinetic energy, merging into a single structure. The radio galaxy, on the other hand, will not be decelerated at the same rate as the surrounding ICM, being essentially a collisionless system. Therefore, the motion of the galaxy relative to the ICM will generate the ram pressure necessary to bend the radio jets. Numerical simulations presented by Roettiger et al. (1993) support this idea.
If the merger hypotesis is true, one expect WAT clusters to exhibit other merger signatures, such as elongation of the X-ray morphology in the same direction as the radio tails, absence of cooling flows and velocity substructure. All of these are indeed observed. In addition to the effect of cluster merger, because the fact that the jets lie inside the potential of the surrounding cluster of galaxies, one would expect gravitational forces to affect their dynamics. In particular, if the jets are less dense than their surrounding, then buoyancy forces may play a role in bending the outer radio structures into directions of decreasing external gas pressure.

1.7 Statistics of radio sources: the Radio Luminosity Function

The high density of galaxies within clusters, especially in the innermost cluster regions, and the peculiar velocities of galaxies, most extreme in merging clusters, enhance the probability of galaxy-galaxy interactions (Feretti & Venturi, 2002).
These conditions raised the question whether cluster galaxies have enhanced the probability of developing a radio source, or if they tend to have more powerful and long lived radio emission.

A powerful statistical tool to adress these questions is the Radio Luminosity Function (RLF).
RLF was defined for the first time by Longair (1966) as "the distribution of radio luminosity among a complete sample of galaxies within a unit volume at a given cosmological epoch", ρ (P, z). Later, a fractional Luminosity Function was introduced and estimated by many authors (Fanti, 1984; Ledlow & Owen, 1996; Stocke et al., 1999; Venturi et al., 2000, 2001; Branchesi et al., 2006; Mauch & Sadler, 2007; Kale et al., 2015), defined as:

$$f_i(P, z) = \rho_i(P, z)/\phi_i(z) \tag{1.21}$$

where ϕ_i(z) is the density of objects of a particular class i at the epoch z.
From an operational point of view, we can express the fractional RLF as the probability that a galaxy in a defined sample at a given epoch emits with radio power in the interval P $\pm$ dP:

$$f(P) = \frac{n(\Delta P_i)}{N(\Delta P_i)} \tag{1.22}$$

where n and N are respectively the number of detected radio galaxies in the radio power interval ΔP$_i$ and the total number of optical galaxies which could have been detected in the same power bin.
In order to take into account the correlation between the optical and radio properties of galaxies, it is possible to define a Bivariate Luminosity Function, which represents the probability that a galaxy with magnitude in the range M $\pm$ dM be radio emitting in the radio power range P $\pm$ dP (Fig. 1.12).
The influence of the environment on the radio properties of galaxies should reflect on the Radio Luminosity Function, changing either its shape, its amplitude or both (Venturi et al., 2000, 2001; Branchesi et al., 2006; Kale et al., 2015). In particular, it is reasonable to expect that any difference in the radio properties of a sample of galaxies should be reflected in the shape of the RLF or in the power cutoff. Indeed it is very useful to compare RLFs in different environments and at different redshifts, which is one of the main goals of this thesis work.
Literature results show that the most relevant parameter that counts in the shape and in the cut off is the optical magnitude: i.e. brighter galaxies have a higher probability of developing a radio galaxy within a given power range. The radial distribution of radio galaxies in rich clusters reveals a segregation effect, i.e. powerful radio sources are centrally peaked (more than 50% of radio galaxies with log$P_{1.4GHz} \geqslant 24.5$ are located within 0.2 R_A from the cluster centre), and the distribution flattens at lower powers. This could, at least in part, reflect the segregation in the optical, and could be interpreted as due to the fact that brighter galaxies, which have a higher probability of producing a powerful radio galaxy, tend to be more concentrated towards the cluster centre (Auriemma et al., 1977; Fanti, 1984; Ledlow & Owen, 1996).

Apparently, the enhanced probability of galaxy interaction in merging clusters seems to not have effects on the probability of galaxies to develop a radio active AGN in their centre (Bardelli et al., 1998; Venturi et al., 2000, 2001). Moreover, it seems that no evolution is found out to redshift z $\sim$ 0.8 (Stocke et al., 1999). Whether cluster mergers have any influence in triggering the radio emission in galaxies, the influence of local and large scale environment and if there is any relation with the cosmological epoch are still open questions. Therefore it is important to pursue the investigation on large samples and down to lower power limits, in local Universe and at higher redshifts.

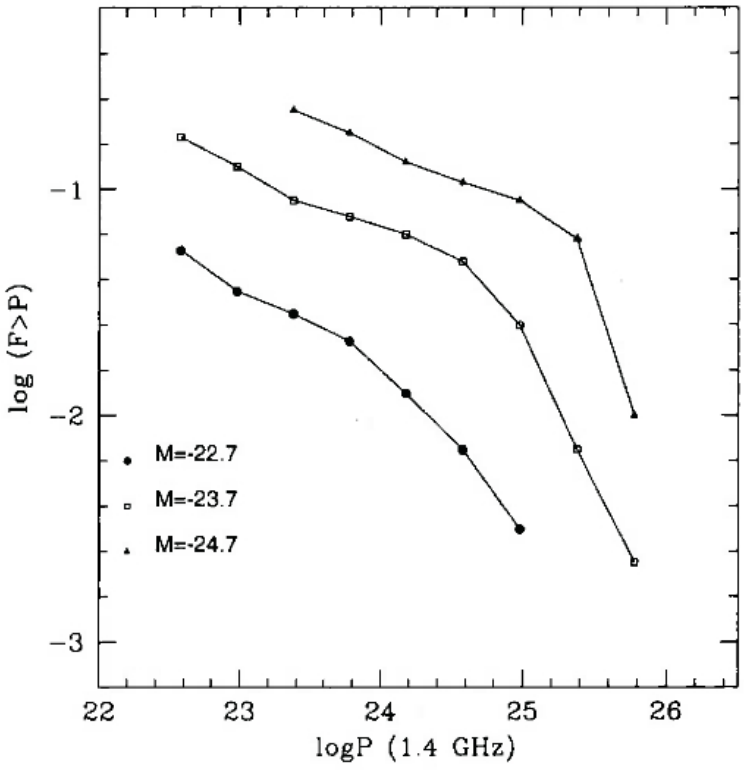

Figure 1.12: The bivariate Luminosity Function for elliptical galaxies given in Ledlow & Owen (1996). The magnitudes are computed in R band.

1.8 Clusters magnetic fields

Thanks to the new observational techniques and the improvement of interpretative models, today the understanding of magnetic fields associated with the intracluster medium has advanced significantly (Bonafede et al., 2010, 2011; Bonafede, 2015), and the presence of μG-level magnetic fields in clusters of galaxies is now widely

acknowledged.
Most of what is known regarding clusters magnetic field derives from the study of cluster diffuse radio sources and Faraday Rotation Measures (Fig. 1.13) of polarized radio galaxies located inside or behind galaxy clusters (Feretti et al., 2012).
Radio halos are objects through which large-scale magnetic fields are studied: they reveal magnetic fields spread over extremely large volumes. Moreover, the brightness fluctuations and polarization level of radio halos are strictly related to the intracluster magnetic field structure.
The most promising technique to derive a detailed view of the intracluster magnetic fields on small spatial scales is the analysis of the Faraday rotation of radio galaxies located inside and beyond clusters. The Farady effect is the rotation suffered by linearly polarized radiation traveling through a magnetized plasma. The intrinsic polarization angle ψ_0 is rotated by an amount:

$$\Delta\psi = \psi - \psi_0 = \lambda^2 RM \tag{1.23}$$

where λ is the radiation wavelenght while RM is the so-called Rotation Measure. The rotation measure is defined as:

$$RM = 812 \int_0^L n_e B_z dl \quad [radm^{-2}] \tag{1.24}$$

where n_e is the thermal electron density in cm^{-3}, B_z is the magnetic field component along the line of sight in μG, and L is the path lenght through the plasma in kpc (Burn, 1966).
With multi-frequency observations of a polarized radio source embedded in or behind a galaxy cluster and then by a linear fit of the λ^2-law in the equation 1.24 it is possible to estimate the RM along that direction. By knowing the RM and given a model for the distribution of the thermal electrons (e.g. from X-ray observations) the intracluster magnetic field can be inferred. But it has to be taken into account that the magnetic field is turbulent and random, so inverting equation 1.24 is not straightforward even in the cases of simple electron density distributions.
There are various techniques to analyze and interpret the RM data, one of them is the RM Synthesis (Brentjens & de Bruyn, 2005), which uses the RM transfer function to solve the nπ ambiguity related to the RM computation, and allows to distinguish the emission as a function of Faraday depth. With this technique detailed RM images of extended radio sources have been obtained; the observed RM fluctuations indicated that the intracluster magnetic field is not regularly ordered but turbulent on scales ranging from tens of kpc to $\leq$ 100 pc.

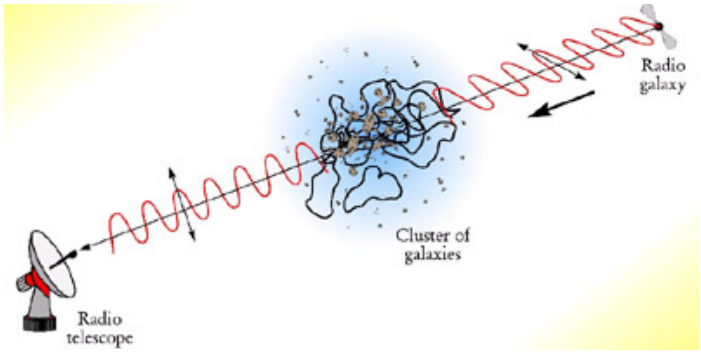

Figure 1.13: The Faraday effect: for the study of cluster magnetic field it is considered the Faraday rotation of radio sources in the background of the cluster.

Chapter 2

Brightest Clusters Galaxies

Brightest Cluster Galaxies (BCGs) are the most massive and luminous elliptical galaxies in the present-day Universe (Lauer et al., 2014, for reviews). They are typically located at the center of galaxy clusters, often but not always found near the bottom of the cluster's gravitational potential well (Donahue et al., 2015).
BCGs generally sit close to the X-ray peak of their hosting cluster. They typically have small peculiar velocities relative to the cluster mean (see Lauer et al., 2014).
The first studies of BCGs focussed on their high luminosity that has small dispersion, which makes them "standard candle" (Hoessel, 1980). This is just one of the very peculiar properties of these galaxies.
The reason why the BCGs are so special is because their formation and evolution is linked to the physical mechanisms of galaxy cluster formation and evolution (Lauer et al., 2014). The properties of BCGs differ from those of the other elliptical galaxies and surely they experienced a different evolution (Poggianti et al., 1999; De Lucia et al., 2007; De Lucia & Blaizot, 2007; Fasano et al., 2010).
Cannibalism, whereby a BCG sitting in the middle of the cluster potential tends to engulf and merge with its neighbors, has been invoked to explain the high luminosity of these systems (e.g. Ostriker & Tremaine, 1975; Hausman & Ostriker, 1978; Richstone, 1975), but it remains unclear why this leads to such uniform properties, expecially when we know that many clusters undergo interactions and merging.
BCG growth by cannibalism does appear to take place in clusters at some level (Lauer, 1988); however, dynamical arguments suggest that most of the BCG assembly takes place outside the cluster (Merritt, 1985).
The position of the BCG with respect to the cluster center gives an important information about the evolutionary state of both the galaxy and the cluster (Rossetti et al., 2016). In short, in many ways the BCG reflects the environment of the cluster that hosts it.

2.1 General properties of BCGs

2.1.1 Kinematic and photometric properties

The average luminosities of BCGs have been known for a long time to have small dispersion, allowing these galaxies to be used as "standard candles" (see Lauer et al., 2014, for reviews). An important refinement of the use of BCGs as distance indicators was developed by Hoessel (1980): the physical concentration of the BCGs is expressed in terms of α, i.e. the logarithmic slope of the variation of L_m, defined as follows:

$$\alpha = dlogL_m/dlogr|r_m \tag{2.1}$$

where r_m is the metric radius and L_m is the metric luminosity (the luminosity within the metric radius, also called M_m in Lauer et al. 2014).
The L_m-α relationship showed that α initially increases with L_m, then plateaus for the more luminous BCGs (Fig. 2.1). The α is used to predict L_m, which in turn is used as "standard candle" to infer the distance of the BCGs.

The metric luminosity L_m correlates with σ, the central stellar velocity dispersion. In particular the slope of their relation has the same trend as for the Faber & Jackson relation $\sigma \propto L^{1/4}$ for normal elliptical galaxies (1976). This suggests that the central portion of the BCG within r_m has a "normal" relationship between σ and L, in contrast to that between the total L and σ (Lauer et al., 2007). The structure and the luminosity of BCGs may be tied to the properties of the clusters as traced by the temperature and the luminosity of the associated X-ray emitting gas. Lauer et al. (2014) found that the BCG luminosity also correlates with the cluster velocity dispersion (see Fig. 2.2), which can serve as a proxy for cluster X-ray luminosity, L_X, given the relationship between the two cluster parameters. There is a relation between α and σ_c that echoes the relation between the shallowness of the BCG surface brightness profile and the cluster X-ray luminosity seen by Schombert (1988) and Brough et al. (2005).
The relation between $L_m - \alpha - \sigma$ offers a BCG-based distance indicator with the effects of the cluster environment removed. Both the metric luminosity and structure of the BCGs may also be related to the peculiar velocities of the BCGs within their hosting clusters.

2.1.2 The position of BCGs within the cluster

The position of the BCG with respect to the center of the cluster gives an important information about the evolutionary state of both the galaxy and the cluster (Nipoti et al., 2003; Rossetti et al., 2016). Martel et al. (2014) emphasize that the BCG offset from the cluster center of mass, as well as the velocity offset is a signature of the assembly of galaxy cluster by hierarchical merging. The BCG itself may be

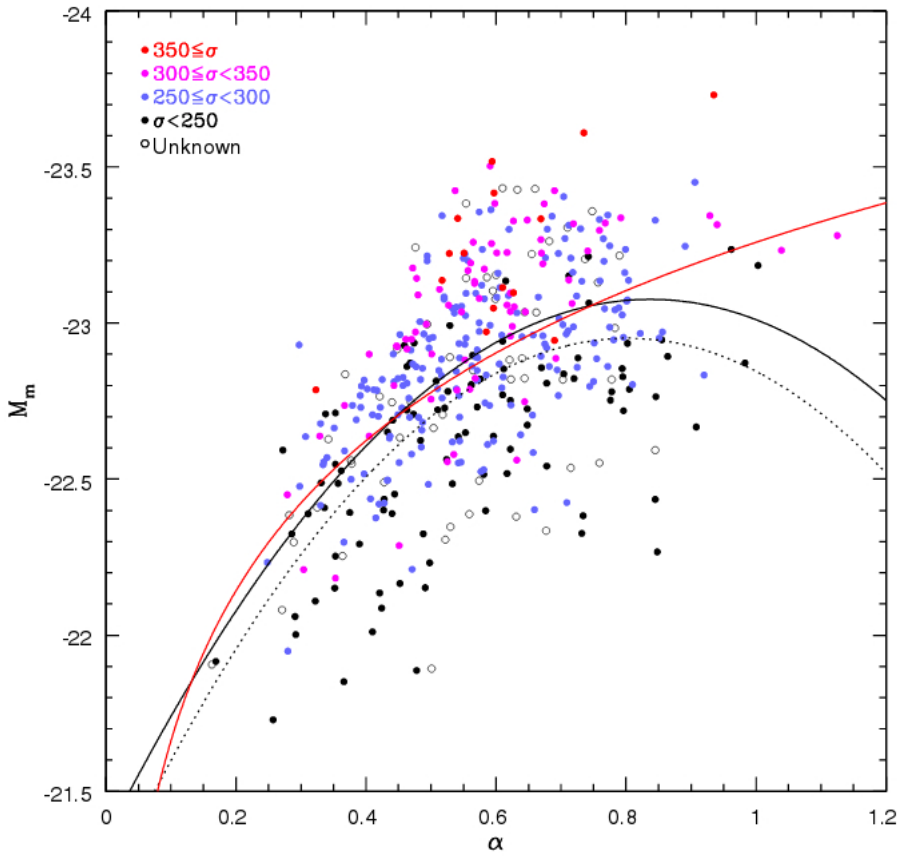

Figure 2.1: Relationship between the metric luminosity M_m and α for BCGs. See Lauer et al. (2014) for more details.

introduced as part of an infalling group into the cluster. A key point is that the galaxies, the X-ray gas and the dark matter halo of the cluster all have different mechanisms and time scales for relaxing after cluster mergers.
The parameter α defined above (2.1) correlates with the offset of the BCG within the cluster relative to the X-ray center (Fig. 2.3): α is larger for BCGs closer to the center of their clusters, consistent with Ascaso et al. (2011).
Hausman & Ostriker (1978) argued that dry mergers (i.e. dissipationless) would cause little central growth of the BCGs, a phenomenon also seen in merger simulations.
The global picture is that the bulk of any given BCG is largely assembled outside of the cluster, before the galaxy is accreted by the cluster.

2.1.3 Star Formation vs AGN activity

The radio emission in galaxies could essentially be due to AGN activity or to Star Formation (SF) activity. Nowdays, the interplay between the two mechanisms is

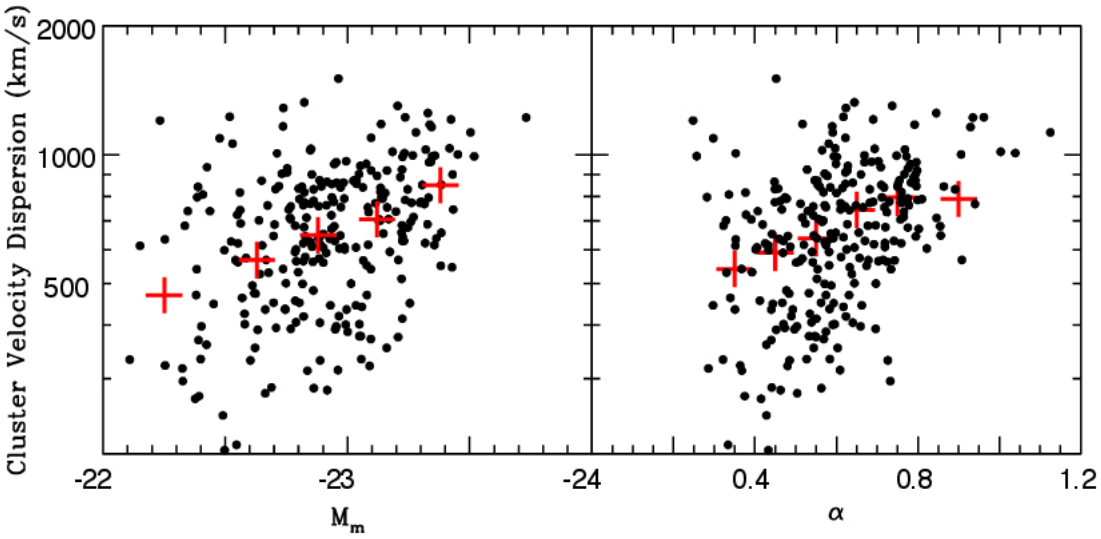

Figure 2.2: The cluster velocity dispersion is plotted as a function of BCG metric luminosity M_m (left panel) and α (right panel). The red crosses give the median velocity dispersion for each 0.25 mag in M_m or 0.2 bin in α. Both parameters increase with velocity dispersion. See (Lauer et al., 2014) for more details.

still a matter of debate. The radio emission from BCGs is mainly due to the AGN activity, however, there is strong observational evidence that SF is not negligible (Fig. 2.4), expecially in cool cores (Fogarty et al., 2015; Donahue et al., 2015). Donahue et al. (2015) exploit the opportunity provided by rest-frame UV imaging of galaxy clusters in the CLASH[1] project to reveal the diversity of UV morphologies in BCGs and to compare them with simulations of the cool, star-forming gas structures produced by precipitation-driven feedback (Fig. 2.5).
All the CLASH BCGs are detected in the rest-frame UV (280 nm). Ultraviolet morphologies among the BCGs with strong UV excesses exhibit distinctive knots, multiple elongated clumps, and extended filaments of emission that distinctly differ from the smooth profiles of the UV-quiet BCGs. From CLASH UV images star-formation rates were found up to $\sim 80\ M_{\odot} yr^{-1}$. Fogarty et al. (2015) found values up to $\sim 100\ M_{\odot} yr^{-1}$, considering also $H\alpha + N$II emission.
The core entropy K_0, defined in Chapter 1 (1.16), is a proxy for the existence of a cool core in a galaxy cluster (Hudson et al., 2010; Giacintucci et al., 2017).
Coupling their data with *Chandra* X-ray measurements, Fogarty et al. (2015) infer that the star formation occurs in low-entropy cluster cores and exhibits a correlation with gas properties related to cooling. SFRs derived in their sample are correlated with the X-ray properties of the ICM.
The BCG activity is observed to occur only in clusters where K_0 is $\lesssim 30$ KeV cm^2

[1]Cluster Lensing and Supernova Survey with Hubble;
http://archive.stsci.edu/prepds/clash/

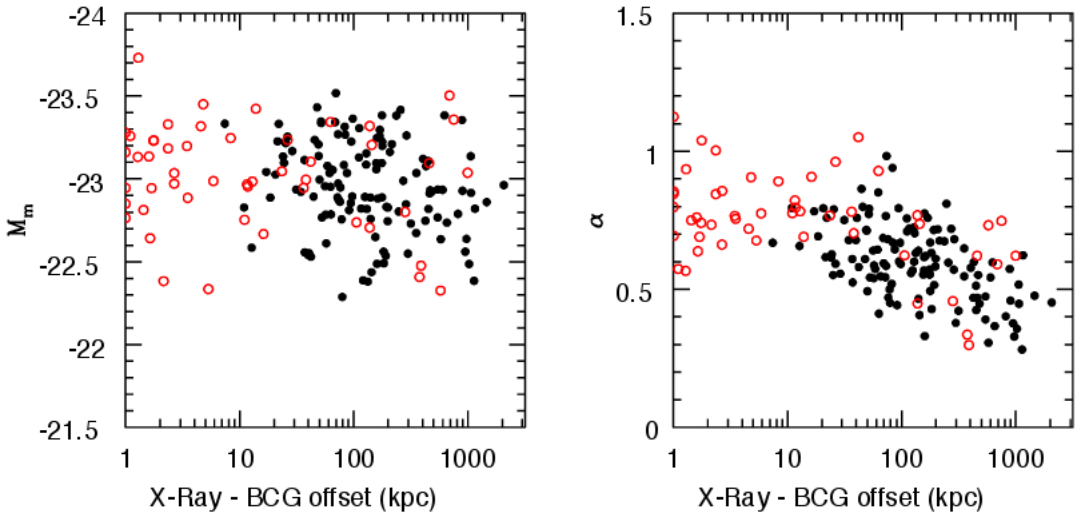

Figure 2.3: From Lauer et al. (2014): the metric luminosity M_m and α are plotted as a function of distance of the BCG from the X-ray defined center of the cluster. Solid black symbols indicate clusters with ROSAT measurements, while the open red symbols indicate cluster with Chandra-based X-ray centers. Little dependence on M_m with distance from the center is seen, while α increases with decreasing distance.

(Cavagnolo et al., 2008; Hoffer et al., 2012; Giacintucci et al., 2017). In Donahue et al. (2015) a similar entropy threshold was found for the UV-NIR color of CLASH BCGs, indicating that the threshold does not change substantially out to z∼0.5. Fogarty et al. (2015) demonstrate that a tight correlation exists between reddening corrected SFRs and K_0. Specifically, all of the BCGs with a SFR $> 10\ M_{\odot} yr^{-1}$ have a core entropy consistent with a value ≤ 30 KeV cm^2.
The star formation activity in BCGs is a diagnostic of the amount of the ICM plasma that cools into molecular gas, while the AGN activity, is invoked to provide the feedback necessary to quench cooling flows in the ICM (McNamara & Nulsen, 2007; Voit et al., 2015).

2.1.4 Properties of BCGs at redshift 0.2 < z < 0.4

The BCGs selected in my sample and discussed in the next Section are in the redshift range between $0.2 < z < 0.4$. At this stage the mergers are typically dry, i.e. dissipationless, which means that they do not involve a large amount of gas (see De Lucia et al., 2006).
It is thought that star formation at this redshift is not the main mechanism by which mass accretes in these galaxies (Cooke et al., 2016). They found no correlation between SFR and stellar mass (Fig. 2.6) neither between stellar mass and redshift (Fig. 2.7).

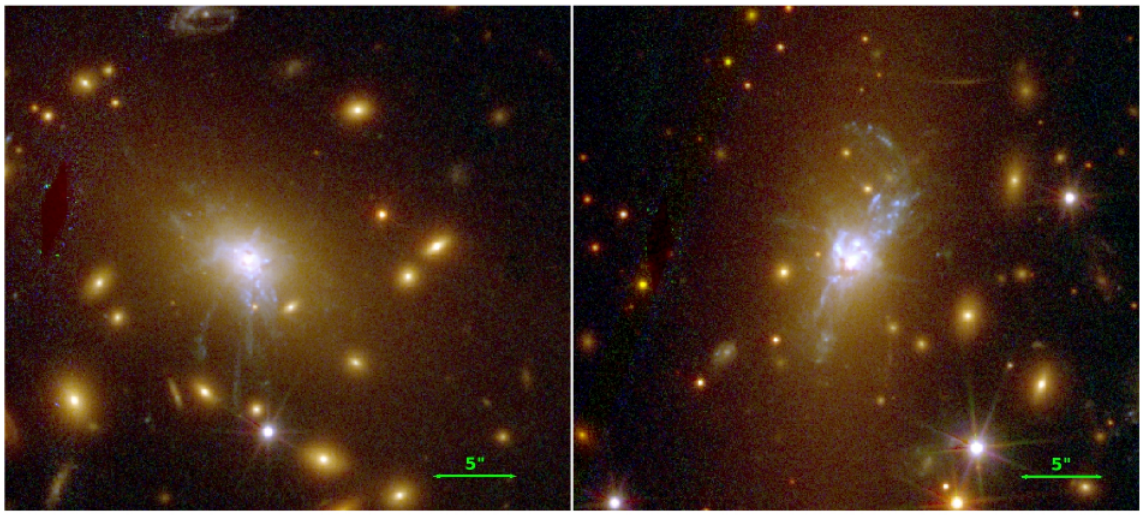

Figure 2.4: Color composite images of amongst the most active star forming BCGs of RXJ1532.9+3021 (z=0.363) on the left and MACSJ1931.8-2653 (z=0.352) on the right. The latter is deeply discussed in this thesis. From Fogarty et al. (2015).

However, the values of the SFR found by Cooke et al. (2016) are not coincident with what found by Fogarty et al. (2015).
From the radio analysis, Cooke et al. (2016) found that the BCGs are radio loud, and that the upper limits are one or two order of magnitude above the radio powers expected if due to solely to star formation (Fig. 2.8). This suggest that the radio emission is being powered by the AGN in these galaxies. The maximum observed radio power increases with galaxy mass. This suggests that the source of fuel for AGN activity correlates with galaxy mass. Cooke et al. (2016) conclude that, in BCGs, the cold gas is the responsible of the fueling of both the AGN and star formation activity. SF is not the main mechanism by which mass accretes in BCGs, even if it is not negligible, expecially in cool cores. (Fogarty et al., 2015; Donahue et al., 2015).

2.1.5 Radio properties of BCGs

From the radio point of view, the emission from BCGs is expected to be mainly AGN contribution dominated.
Cooke et al. (2016) observed that radio powers and upper limits of BCGs are 1-2 orders of magnitude above the radio powers expected if due solely to star formation estimated following Condon (1992). This suggests that the radio emission is being powered by the AGN in their sample (see Fig. 2.8).
BCGs host super massive black holes in their center. They show core emission and often extended emission, well beyond the optical envelope, in terms of jets that rep-

resent the feedback mechanism to the cluster medium. This emission sometimes is bent forming a C-shaped Wide Angle Tailed glaxy, as for example the prototypical case of 3C465 at the center of A2634 (Eilek et al., 1984). WAT radio galaxies are only found in association with brightest cluster galaxies (Feretti & Venturi, 2002). The typical radio power of BCGs is intermediate between the FRI and FRII radio galaxies (Kale et al., 2015, Fig. 2.9). They found that radio loud BCGs are considerably more common in relaxed clusters (71 % against 29 % in merging clusters). Conversely, radio-quiet BCGs are more common in merging systems (81 % to be compared to the 19 % in relaxed clusters).

Previous studies relate the radio emission to the cluster properties. Best (2007) found that the fraction of radio loud BCGs depends on the optical luminosity or the stellar mass of BCGs, but not on the cluster velocity dispersion. Ma et al. (2013) found that the radio power is higher in more massive clusters and at higher redshifts, which implies possible redshift evolution of BCG radio emission power.
More fundamental studies of the BCGs radio emission and their dependence on cluster properties should consider the radio luminosity function, which is a measure of the variation of BCG space density wih the radio luminosity. The radio luminosity functions for AGNs and for star-forming galaxies have been found to be very different (Mauch & Sadler, 2007; Kale et al., 2015; Yuan et al., 2016) but no significant variation is found with the redshift (Fig. 2.10).
Yuan et al. (2016) performed a study considering the largest complete sample of BCGs taken from the NVSS and FIRST surveys to study the possible dependence of BCGs radio emission on BCGs properties and cluster environment. From the radio lumiosity function analysis, their result is that the most powerful BCGs are associated with optically bright BCGs in relaxed clusters.
The same result is obtained by Kale et al. (2015): they calculated the fractional radio luminosity function for two subsamples of merging and relaxed clusters taken from the EGRHS (Venturi et al., 2007, 2008; Kale et al., 2015). BCGs in relaxed clusters show a significantly higher probability to be radio loud than those in merging systems.
The results obtained by Kale et al. (2015) are the starting point of the radio analysis of the BCGs in my sample. The goals are: (i) to investigate the correlation between the BCGs radio emission with the cluster properties, and (ii) to discriminate between the contribution to the radio emission given by AGN activity or Star Formation activity. Starting from these results I performed an analysis onto a sample of eleven BCGs exploiting the overlap between CLASH and EGRHS samples.

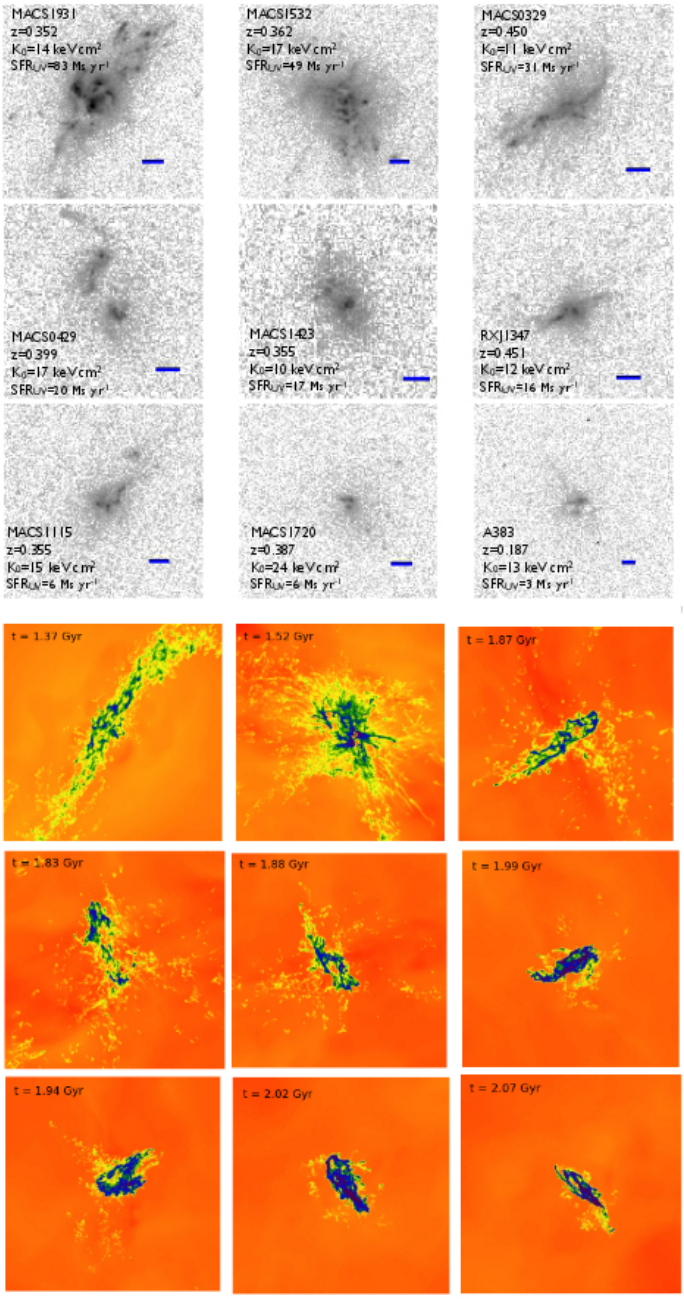

Figure 2.5: From Donahue et al. (2015). The top 9 images show the central 50 kpc × 50 kpc of the 280 nm broad-band HST images for star-forming CLASH BCGs. The blue bar indicates a 1" angul ar scale. The bottom 9 images show gas-temperature maps with similar physical scales from a simulation of a single BCG in which precipitation of cold clouds out of the CGM triggers jets from the central AGN.

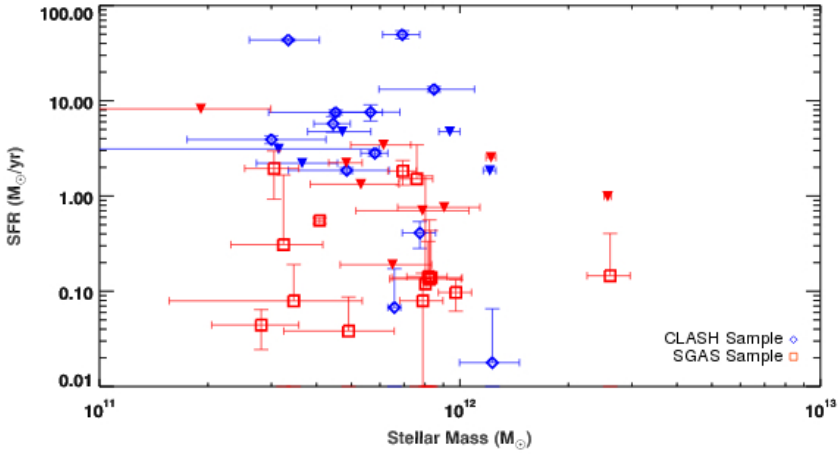

Figure 2.6: Star formation rate versus stellar mass from Cooke et al. (2016). Apparently no Star Formation Main Sequence is seen in their sample.

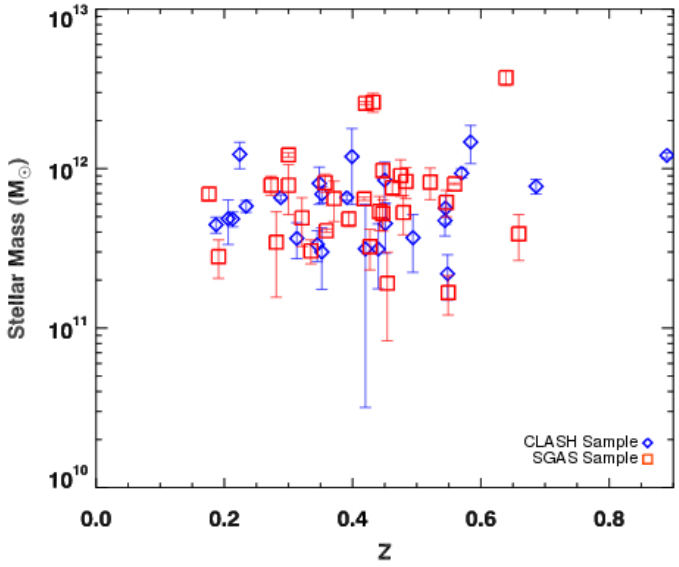

Figure 2.7: BCG stellar mass versus redshift from Cooke et al. (2016). There is no trend of stellar mass with redshift over the range z= 0.2-0.7.

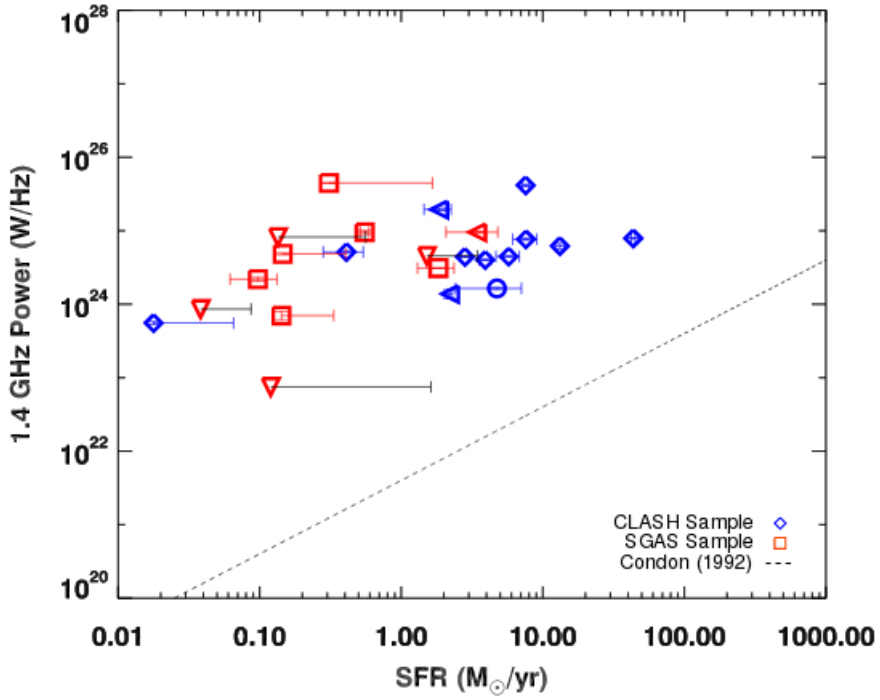

Figure 2.8: FIRST and NVSS 1.4 GHz rest frame emission assuming α=0.75 versus star formation rate from Cooke et al. (2016). The representative radio emission due to a star formation dominated scenario is plotted with the dashed line Condon (1992).

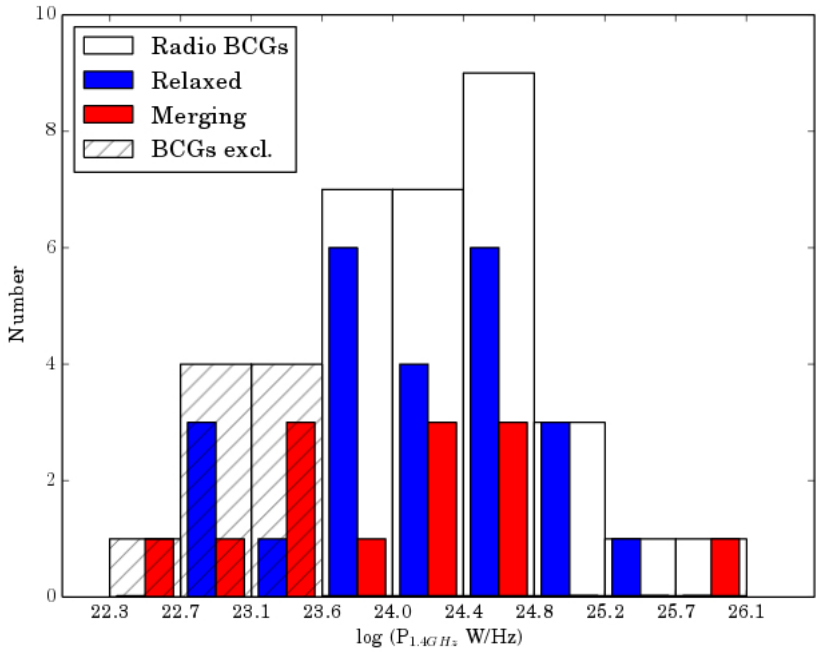

Figure 2.9: Histogram of the radio power of the BCGs in the sample from Kale et al. (2015). The shaded intervals refer to the BCGs that were removed from the statystical analysis. The peak of the distribution is at $\log P_{1.4GHz} \sim 24.5$.

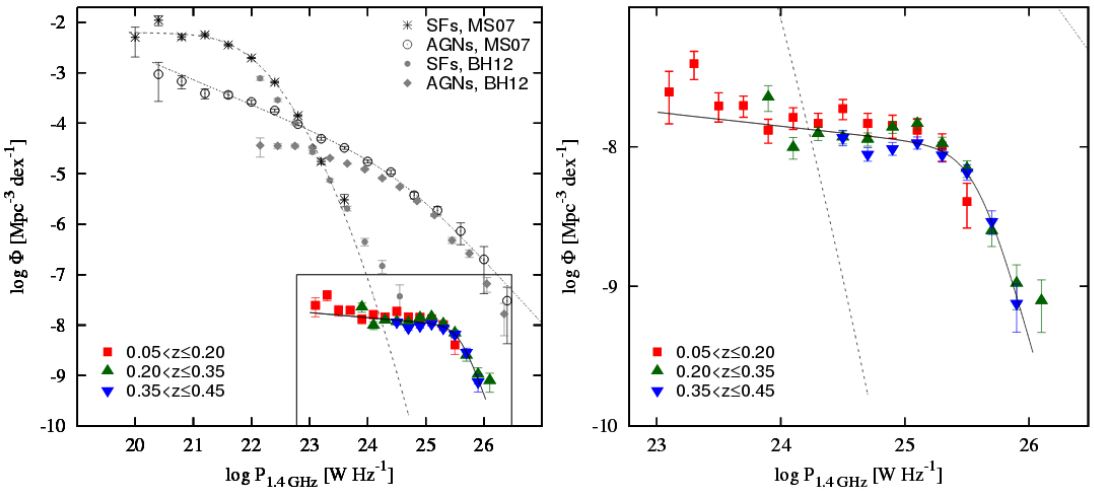

Figure 2.10: Radio luminosity functions from Yuan et al. (2016) of BCGs in their sample compared with radio luminosity functions of star-forming galaxies and AGNs obtained by Mauch & Sadler (2007); Best & Heckman (2012). No evolution with redshift can be found, consistently with previous results.

2.2 Radio properties of the BCGs in a subset of CLASH and EGRHS Clusters

In the first part of the thesis work I performed a morphological and a radio analysis on a sample of eleven BCGs which belong to ten galaxy clusters in the redshift range between $0.2 < z < 0.4$ (which is the redshift limit of the EGRHS). They were selected because of the strong overlap between the radio EGRHS (Venturi et al., 2007, 2008; Kale et al., 2013, 2015) and the optical CLASH (Postman et al., 2012) surveys.
The radio properties of the BCGs are strongly dependent on the central properties of the host cluster, both in the in the local Universe and at intermediate redshift (Kale et al., 2015; Di Gennaro et al., 2018). Indeed our main aim is to study the radio properties of these galaxies in relation with the environment in which they are located, particularly in relation with the cluster dynamical state.
Besides the radio analysis, the intent is to constrain if the radio emission, when detected, is mainly due to the AGN activity or the Star Formation activity, since both are present and not negligible, expecially in cool cores (Fogarty et al., 2015; Donahue et al., 2015).

2.2.1 The sample

The targets were selected from the Extended GMRT radio halo cluster sample (Venturi et al., 2007, 2008; Kale et al., 2015) and from the Cluster Lensing and Supernova Survey with Hubble (CLASH; Postman et al., 2012). There is a strong overlap between the two surveys, moreover, a lot of ancillary data are available for almost all of the targets.
In more details, from the optical point of view, all of them are CLASH clusters except two: A1300 belongs to the Relics[2] (PI Coe D.) and the GCAV[3] (PI Nonino M.) surveys; A2744 is a Frontier Field cluster[4] (FF; PI Lotz J.). A2744 hosts two central BCGs in its centre.
All the clusters selected for our analysis (except MACSJ1931, MACSJ0429 and MACSJ1206), overlap with the EGRHS survey.
The total sample of eleven BCGs is in a redshift range between $0.2 < z < 0.4$.
The clusters are also selected because they are in different dynamical state (Tab. 2.1): A209, A1300 and A2744 are merging clusters, they show diffuse radio emission like central halos and relics. All the others are relaxed (Giacintucci et al., 2014; Kale et al., 2015). Among the relaxed clusters, three host a certain mini-halo: MACSJ1206, RXCJ1115 and RXCJ1532. Additionally, there is an ambiguous as-

[2]https://relics.stsci.edu/
[3]https://www.eso.org/sci/observing/PublicSurveys/
[4]http://www.stsci.edu/hst/

signment to the one in MACSJ1931 (this target is analyzed and discussed in detail in Chapter 5). The presence of mini-halo in this cluster is uncertain (Giacintucci et al., 2017). In Tab. 2.1 are reported in column 1 the cluster name, in columns 2 and 3 the BCGs coordinates (J2000), in columns 4 and 5 the redshifts and the linear scale, in column 6 the cluster dynamical state and in columns 7 and 8 the optical and radio surveys to which they belong to. The coordinates refer to the position of the BCG identified from the radio-optical overlays.

Table 2.1: The sample of eleven BCGs selected

cluster name	RA_{J2000} (hms)	DEC_{J2000} (° ' ")	z	scale (kpc/")	Dynamical state	Optical-IR	Radio
A209	01 31 52.5	-13 36 40.9	0.206	3.3	Merging	CLASH	EGRHS
A611	08 00 56.8	36 03 23.4	0.288	4.3	Relaxed	CLASH	EGRHS
A1300	11 31 54.1	-19 55 40.5	0.307	4.5	Merging	Relics, GCAV	EGRHS
A1423	11 57 17.3	33 36 39.9	0.213	3.4	Relaxed	CLASH	EGRHS
A2744	00 14 20.6	-30 24 01.4	0.308	4.5	Merging	Frontier Field	EGRHS
A2744	00 14 22.1	-30 24 21.8	0.308	4.5	Merging	Frontier Field	EGRHS
MACSJ1931	19 31 49.6	-26 34 34.0	0.352	4.9	Relaxed	CLASH	/
MACSJ0429	04 29 36.1	-02 53 08.0	0.399	5.3	Relaxed	CLASH	/
MACSJ1206	12 06 12.2	-08 48 02.4	0.440	5.6	Relaxed	CLASH	/
RXCJ1115	11 15 52.0	01 29 56.6	0.352	4.9	Relaxed	CLASH	EGRHS
RXCJ1532	15 32 53.7	30 20 58.7	0.362	5.0	Relaxed	CLASH	EGRHS

2.2.2 Data reduction

To perform the radio analysis, I exploited GMRT archival images at the frequencies of 610 MHz and 323 MHz and I reprocessed VLA archival data at 1.4 GHz (L-band). I reduced archival VLA data choosing, when possible, the A or B configurations of the array in order to have the maximum resolution possible and pinpoint the central emission (Tab. 2.2).
The GMRT resolution ranges from 6" to 15" (see Tab. 2.5) whereas the VLA resolution ranges from 1.3" to NVSS 45" (see Tab. 2.4).
I reprocessed VLA archival data by means of the AIPS[5] package, with a standard procedure for calibration, inspecting and editing the data with UVPLT and WIPER tasks, calibrating them using VLACALIB task after running VLAPROCS. After at least three self-calibrations, the final images were generated using the task IMAGR

[5]http://www.aips.nrao.edu/

and were cleaned by interactive deconvolution. The Tables below (2.2 and 2.3) report the observational setup parameters, i.e. the central frequency, the VLA array configuration, the time on source and the bandwidth.

Table 2.2: VLA Observational Setup

cluster name	central frequency (GHz)	IF	configuration	n. antennas	time on source (min)	BW (MHz)
A209	1.4	2	A	27	26	50
A611	1.4	2	C	27	38	50
A1300	1.4	2	B	22	3	50
A1423	1.4	2	A	27	6	50
A2744	1.4	2	C	27	143	50
MACSJ1931	1.4	2	A	22	82	50
MACSJ0429	1.4	2	B	26	47	50
MACSJ1206	1.4	2	B	22	3	50
RXCJ1115	1.4	NVSS	NVSS	NVSS	NVSS	NVSS
RXCJ1532	1.4	2	B	26	35	50

Table 2.3: GMRT Observational Setup

cluster name	central frequency (MHz)	time on source (min)	BW (MHz)
A209	610 MHz	150	32
A611	610 MHz	240	32
A1300	323 MHz	480	32
A1423	610 MHz	240	32
A2744	323 MHz	480	32
MACSJ1931	323 MHz	480	32
MACSJ0429	323 MHz	480	32
MACSJ1206	323 MHz	480	32
RXCJ1115	610 MHz	240	32
RXCJ1532	610 MHz	240	32

2.2.3 Radio-optical overlays

To identify the exact position of the BCG, I exploited optical HST images from the CLASH (PI Postman M.) survey [6].
The CLASH astrometry is based on the ground-based telescope *Subaru*-Suprime and the positional error is < 0.1 arcsec. The radio positional error of our data is on sub-arcsec scale, so we can unambiguously associate the central radio source of our images to the nucleus of the BCG.
In Figure 2.11 and following, I report the BCGs radio VLA (white) at 1.4 GHz and GMRT (green) at 610 or 323 MHz contours overlayed on the optical HST (R,G,B filters). According to our result, we can separate between three different cases: (i) the BCG is not detected in the radio domain (i.e.A209, A1423 and A2744 have no radio counterpart); (ii) the BCG is clearly visible and not surrounded by diffuse emission (i.e. A611, MACSJ0429); (iii) the BCG is detected and surrounded by a diffuse emission, a halo (i.e. A1300 GMRT), a mini-halo (i.e. MACSJ1206, RXCJ1115, RXCJ1532) or, a possible restarted source (i.e MACSJ1931, which is entirely analyzed in Chapter 5). In Tab. 2.4 and Tab. 2.5 we report the observational parameters of the final images.

Table 2.4: Observational parameters of the final VLA images

target name	beam (arcsec)	PA (°)	rms (mJy/b)
A209	1.9 × 1.2	-8.9	∼0.02
A611	14.3 × 13.0	35.6	∼0.03
A1300	6.7 × 4.0	1.7	∼0.05
A1423	1.3 × 1.2	-55.8	∼0.03
A2744	31.8 × 11.9	0.65	∼0.06
MACSJ1931	2.5 × 1.2	4.3	∼0.03
MACSJ0429	4.9 × 4.4	7.7	∼0.01
MACSJ1206	5.3 × 4.2	-10.5	∼0.01
RXCJ1115	NVSS	NVSS	NVSS
RXCJ1532	4.1 × 3.8	-16.8	∼0.01

2.2.4 Spectral analysis

Our sample is composed of eleven BCGs from ten galaxy clusters (A2744 hosts two BCGs). We found that there is no detection in A209, A1423 and A2744. In

[6] https://archive.stsci.edu/prepds/clash/

Table 2.5: Observational parameters of the final GMRT images

target name	beam (arcsec)	PA (°)	rms (mJy/b)
A209	13.0 × 7.5	66	∼0.04
A611	6.0 × 5.2	60	∼0.05
A1300	14.0 × 8.8	7.7	∼0.4
A1423	7.2 × 4.0	76.2	∼0.09
A2744	15.8 × 8.4	37.9	∼0.1
MACSJ1931	10.1 × 6.9	-5.0	∼0.9
MACSJ0429	9.6 × 9.1	31.7	∼0.2
MACSJ1206	9.7 × 6.6	43.8	∼0.1
RXCJ1115	8.0 × 4.0	0.0	∼0.09
RXCJ1532	11.0 × 10.0	51.2	∼0.07

particular, in A2744 a giant diffuse halo contaminates the discrete emission, and we found that the BCGs are undetected even after removing the contribution of the halo emission.
A209 and A1423 host an extended tail radio galaxy which, confirmed from VIMOS spectroscopy (see Yu et al., 2018), belong to the cluster. In particular, the tail in A209 has a projected linear extent of $\sim$ 70 kpc with the VLA at 1.4 GHz in A array, whereas the GMRT linear projected extent at 610 MHz is $\sim$ 250 kpc.
The tail in A1423 has a linear projected extent of $\sim$ 90 kpc with the VLA at 1.4 GHz in A array, whereas it has a linear extent of $\sim$ 140 kpc with the GMRT at 610 MHz.
Both the tails are located at a projected distance of few tens of kpc from the central BCG. In more details, A1423 tail is located at 12 arcsec from the BCG, which corresponds to a projected distance of $\sim$ 41.2 kpc at the cluster redshift; A209 tail is located at 17 arcsec from the BCG, which corresponds to $\sim$ 60 kpc at the cluster redshift.
A very interesting point would be understand the correlation between the dynamical state of the cluster and the presence of such tailed radio galaxies located close to their centre. Indeed, A209 is considered a merging cluster by Venturi et al. (2007); Postman et al. (2012); Giovannini et al. (2009); Kale et al. (2015); Annunziatella et al. (2016); A1423 is, on the contrary, a relaxed cluster (Venturi et al., 2007; Kale et al., 2015).
Tailed radio galaxies are thought to be more frequent in merging clusters (Douglass et al., 2011; Hardcastle et al., 2005), even though exceptions can occur (i.e. A1423).
In order to get information on the radio properties of the BCGs in our sample, we performed a radio analysis estimating the fluxes and the spectral indices of the sources. The upper limits reported for A209, A1423 and A2744 are given at 3σ. All

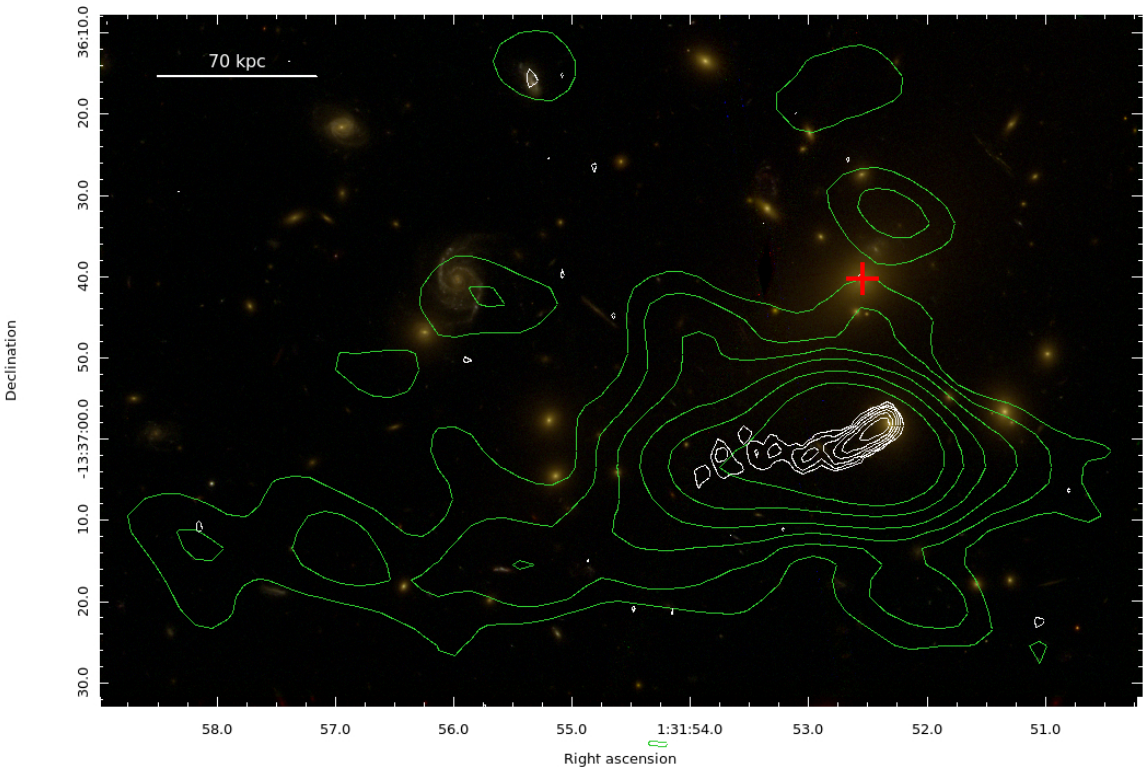

Figure 2.11: **A209**: Composite HST image (f814w, f625w, f435w) with GMRT radio contours (green) at 610 MHz and VLA radio contours (white) at 1.4 GHz. The radio contours are drawn at 3σ, i.e. 0.13 mJy/b and 0.07 mJy/b respectively. The red cross indicates the position of the BCG.

the sources are unresolved at both frequencies: we report their peak fluxes in Tab. 2.6. The estimate of the BCGs flux density is obtained by means of AIPS TVSTAT. RXCJ1115 VLA flux is taken from the NVSS[7]. The flux errors are measured according to the formula from Klein et al. (2003):

$$\Delta F_i = \sqrt{(rms)^2 + (cF_i)^2} \tag{2.2}$$

where the rms is the noise of the image, c is the residual calibration error (conservatively assumed of 2%). The values of the spectral indices are estimated by the equation:

$$\alpha = \frac{log_{10}\left(\frac{F_1}{F_2}\right)}{log_{10}\left(\frac{\nu_2}{\nu_1}\right)} \tag{2.3}$$

we adopted the convention:

$$F_\nu \propto \nu^{-\alpha} \tag{2.4}$$

[7]https://www.cv.nrao.edu/nvss/

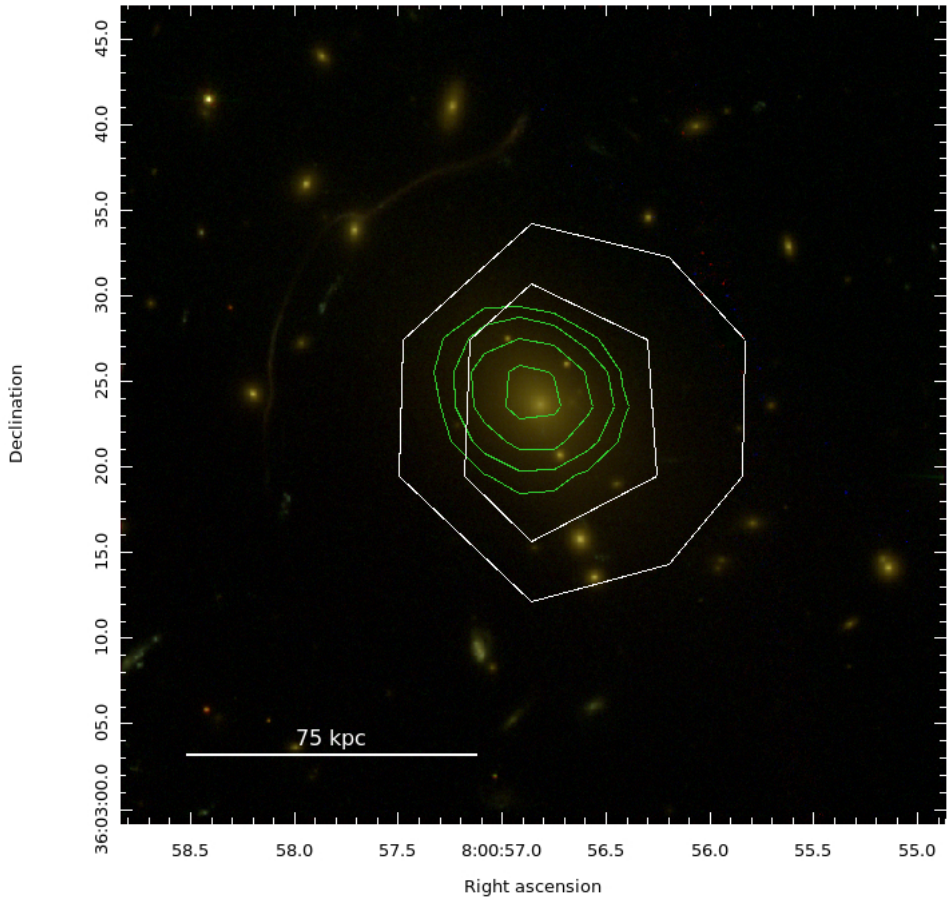

Figure 2.12: **A611**: Composite HST image (f814w, f606w, f435w) with GMRT radio contours (green) at 610 MHz and VLA radio contours (white) at 1.4 GHz. The radio contours are drawn at 3σ, i.e. 0.15 mJy/b and 0.09 mJy/b respectively.

where F_ν is the energy density as a function of the frequency ν.
The errors are calculated according to the formula (Mahony et al., 2016):

$$E_\alpha = \frac{1}{ln\frac{\nu_1}{\nu_2}}\sqrt{\left(\frac{F_{1,err}}{F_1}\right)^2 + \left(\frac{F_{2,err}}{F_2}\right)^2} \tag{2.5}$$

where $\nu_{1,2}$ refers to the frequencies, and $F_{1,2}$ to the corresponding flux densities at those frequencies.
The result of our analysis is reported in Tab. 2.6

The radio spectra of a BCG is usually decomposed into two components: the nuclear component, related to the central AGN, and the extended component, associated with jets or lobe emission and so generated by an older population of relativistic electrons from past nuclear activity (Brunetti & Jones, 2014; Mazzotta

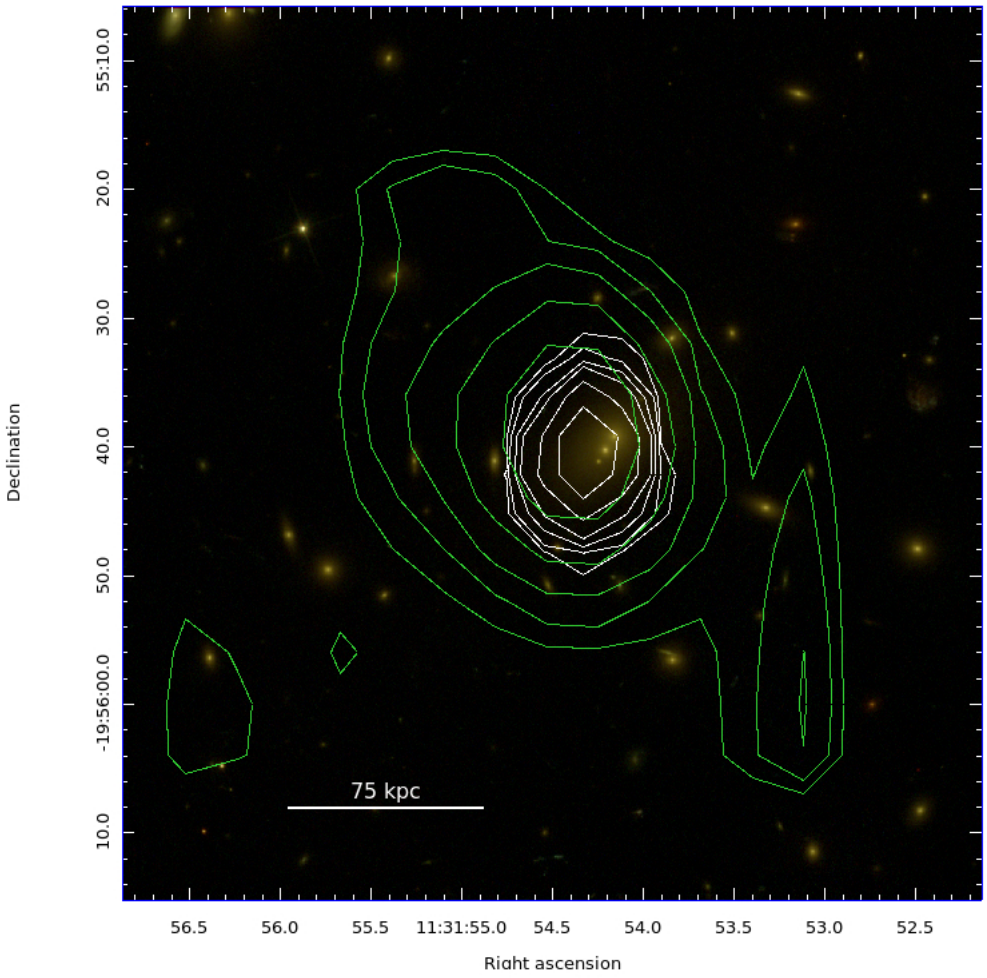

Figure 2.13: **A1300**: Composite HST image (f814w, f606w, f435w) with GMRT radio contours (green) at 323 MHz and VLA radio contours (white) at 1.4 GHz. The radio contours are drawn at 3σ, i.e. 0.15 mJy/b and 0.09 mJy/b respectively. The BCG GMRT radio emission is blended with the halo emission.

& Giacintucci, 2008).
From our analysis, we identified only the nuclear emission of BCGs, associated to the central AGN. There are some cases in which the diffuse emission from a halo or mini-halo could be responsible of a spectral steepening (i.e. A1300, MACSJ1931, MACSJ1206).
The value of the spectral index of MACSJ0429 BCG is quite flat, indicating a very young electron population and a strong AGN, according to the value of the radio power (see Tab. 2.7).
The spectral index distribution is peaked at 0.7 ± 0.06 (Fig. 2.24).
In Fig. 2.21, 2.22 and 2.23 we report the spectra of MACSJ1206, RXCJ1115 and

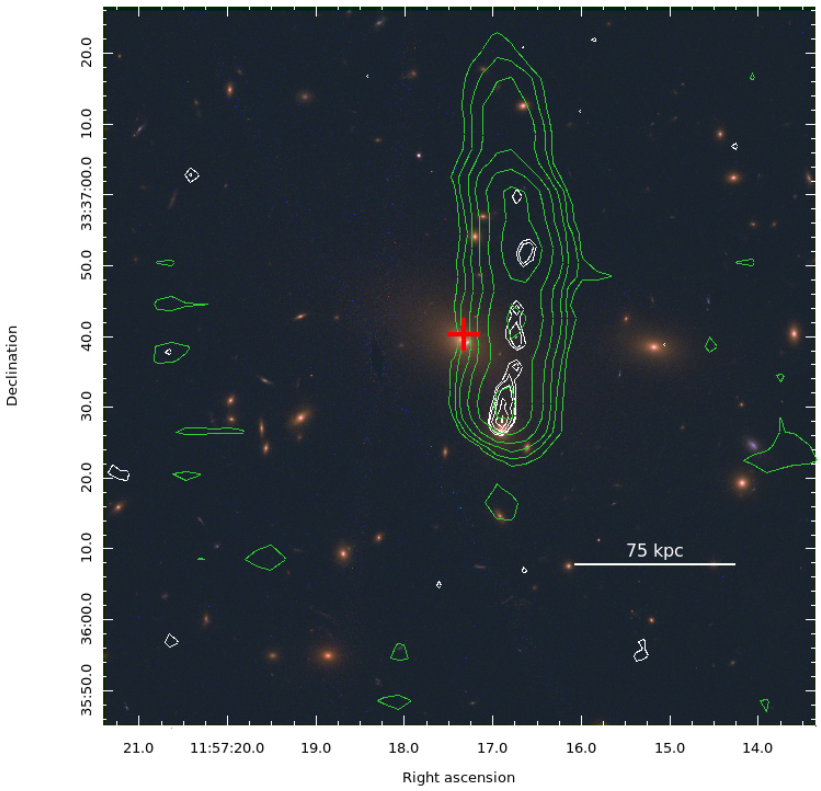

Figure 2.14: **A1423**: Composite HST image (f814w, f606w, f435w) with GMRT radio contours (green) at 610 MHz and VLA radio contours (white) at 1.4 GHz. The radio contours are drawn at 3σ, i.e. 0.27 mJy/b and 0.1 mJy/b respectively. The red cross indicates the position of the BCG.

RXCJ1532. The value at 150 MHz are taken from the TGSS[8]. MACSJ1931 and A1300 BCG spectra are reported in Chapter 5 and 6 respectively. A209, A1423, A2744 are undetected.

The values of the spectral indices from our analysis are consistent with the fact that these galaxies are mainly AGN powered.

In order to fully constrain the radio properties of the BCGs in our sample, we estimated and report in Tab. 2.7 the VLA and the GMRT radio powers respectively. The radio powers are estimated from:

$$L = 4\pi D_l(z)^2 F_{int} \times (1+z)^{-(1+\alpha)} \tag{2.6}$$

In the equation, D_l is the luminosity distance and α is the spectral index of the source. The K-correction is computed as $(1+z)^{-(1+\alpha)}$.

[8]http://tgssadr.strw.leidenuniv.nl/doku.php

Table 2.6: The spectral analysis

target name	$F_{1.4GHz}$ (mJy)	F_{GMRT} (mJy)	ν GMRT MHz	spectral index
A209	< 0.07	< 0.13	610	< 0.7
A611	0.75±0.03	1.5±0.04	610	0.8±0.09
A1300	9±0.06	44±0.9	323	1.08±0.02
A1423	< 0.10	< 0.27	610	< 1.1
A2744	< 0.18	< 0.5	323	< 0.7
A2744	"	"	323	"
MACSJ1931	20±0.03	279±5	323	1.7±0.01
MACSJ0429	127±0.01	150±0.2	323	0.1±0.05
MACSJ1206	130±0.01	664±0.1	323	1.1±0.09
RXCJ1115	14±0.04	9±0.07	610	0.5±0.02
RXCJ1532	15±0.01	24±0.08	610	0.6±0.16

Table 2.7: The VLA and GMRT radio powers

target name	$\log P_{1.4}$ (W/Hz)	$\log P_{GMRT}$ (W/Hz)	ν_{GMRT} (MHz)
A209	<21.93	<22.50	610
A611	23.27	23.57	610
A1300	24.50	25.27	323
A1423	<21.91	<22.43	610
A2744	<24.17	<24.88	323
A2744	"	"	323
MACSJ1931	25.00	26.34	323
MACSJ0429	25.87	25.93	323
MACSJ1206	25.95	26.83	323
RXCJ1115	24.80	24.88	610
RXCJ1532	24.85	25.04	610

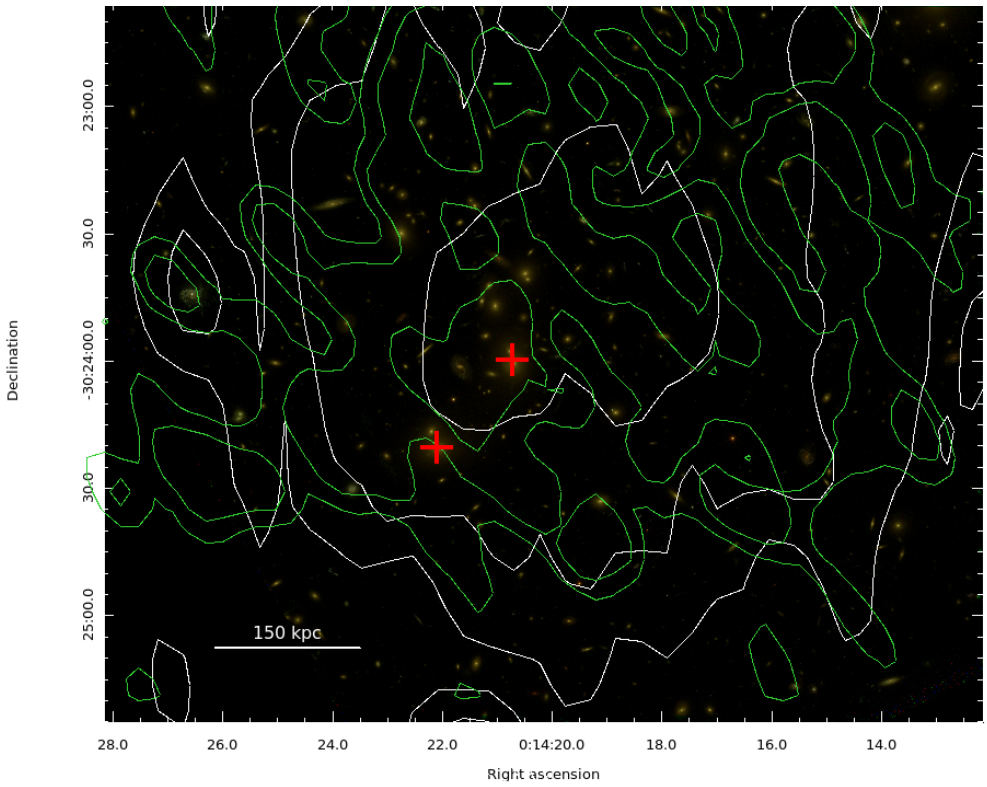

Figure 2.15: **A2744**: Composite HST image (f814w, f606w, f435w) with GMRT radio contours (green) at 323 MHz and VLA radio contours (white) at 1.4 GHz. The radio contours are drawn at 3σ, i.e. 0.5 mJy/b and 0.18 mJy/b respectively. The red crosses indicate the BCGs position.

The radio power ranges between $21.9 < \log P_{1.4} < 25.9$ (W/Hz) for the BCGs detected with the VLA and between $22.4 < \log P_{GMRT} < 26.8$ (W/Hz) for the BCGs detected with the GMRT. The values obtained are consistent with the fact that these galaxies have a power which ranges between FRI and FRII radio galaxies (Fanaroff & Riley, 1974; Kale et al., 2015).

In Fig. 2.25 is reported the histogram of the radio powers in our sample. The peak of the VLA distribution is at $\log P_{1.4} = 24.2$, whereas the peak of GMRT distribution is at $\log P_{GMRT} = 24.7$. The result is consistent with the trend presented in Owen & Laing (1989) and with the fact that, the radio power which discriminates the transition between FRI and FRII is higher for higher optical magnitudes. Indeed BCGs are the brightest galaxies by definition.

Even though the radio emission detected is associated to the AGN emission, Star Formation processes are detected in BCGs and not negligible especially in cool core clusters (Fogarty et al., 2015; Donahue et al., 2015). The interplay between these two mechanisms is still unclear but it is of fundamental importance to better constrain the feedback phenomena. The analysis related to the Star Formation process

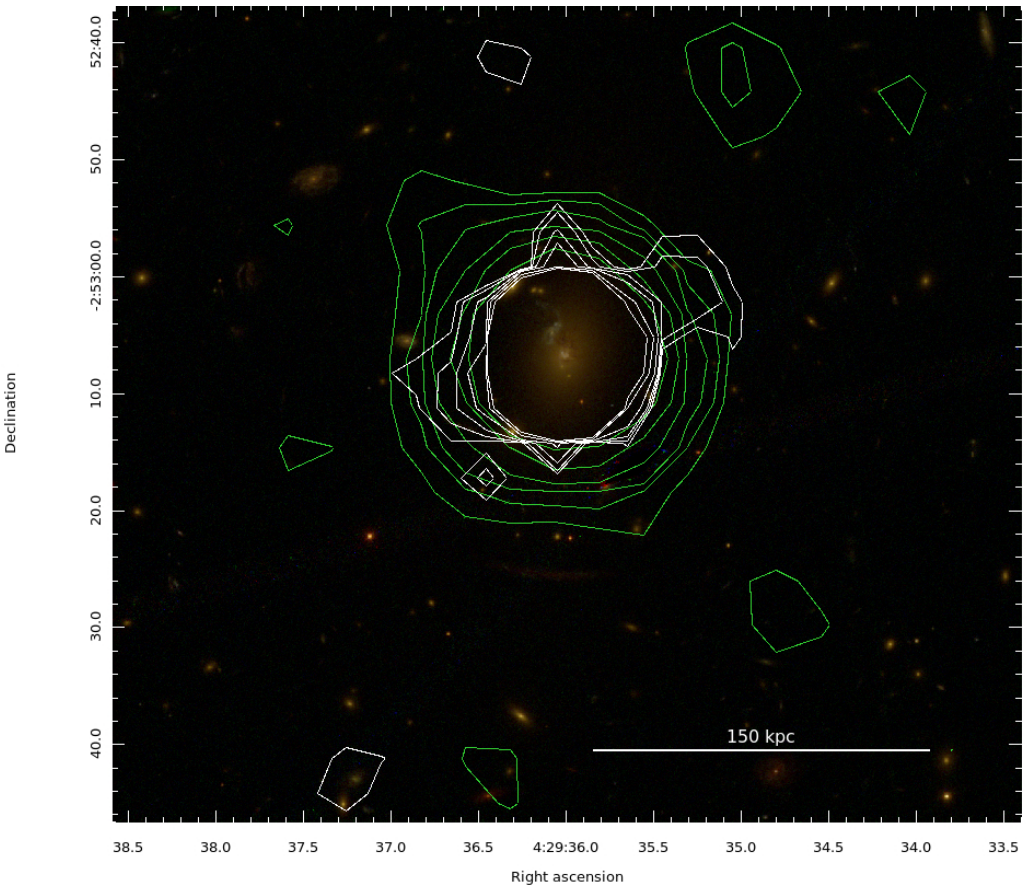

Figure 2.16: **MACSJ0429**: Composite HST image (f814w, f625w, f435w) with GMRT radio contours (green) at 323 MHz and VLA radio contours (white) at 1.4 GHz. The radio contours are drawn at 3σ, i.e. 0.8 mJy/b and 0.03 mJy/b respectively.

in our sample is reported in the next Section.

2.2.5 Star Formation vs AGN emission

One of the most relevant topics of the first part of my analysis is to understand if the radio emission from the BCGs in my sample, when detected, is mainly due to the contribution of AGN activity or Star Formation activity.
These galaxies are giant elliptical and are very bright not only in the optical but also in the radio domain. They host a central SMBH, so the main expectation is that the radio emission is mainly powered by the central AGN accretion mechanism. Indeed from our radio analysis it resulted that the emission is consistent with being powered by a central AGN.
On the contrary, one of the most important result from Yuan et al. (2016) is that the luminosity of the [OIII] 5007 forbidden line, which is a tracer of BH mass, do not

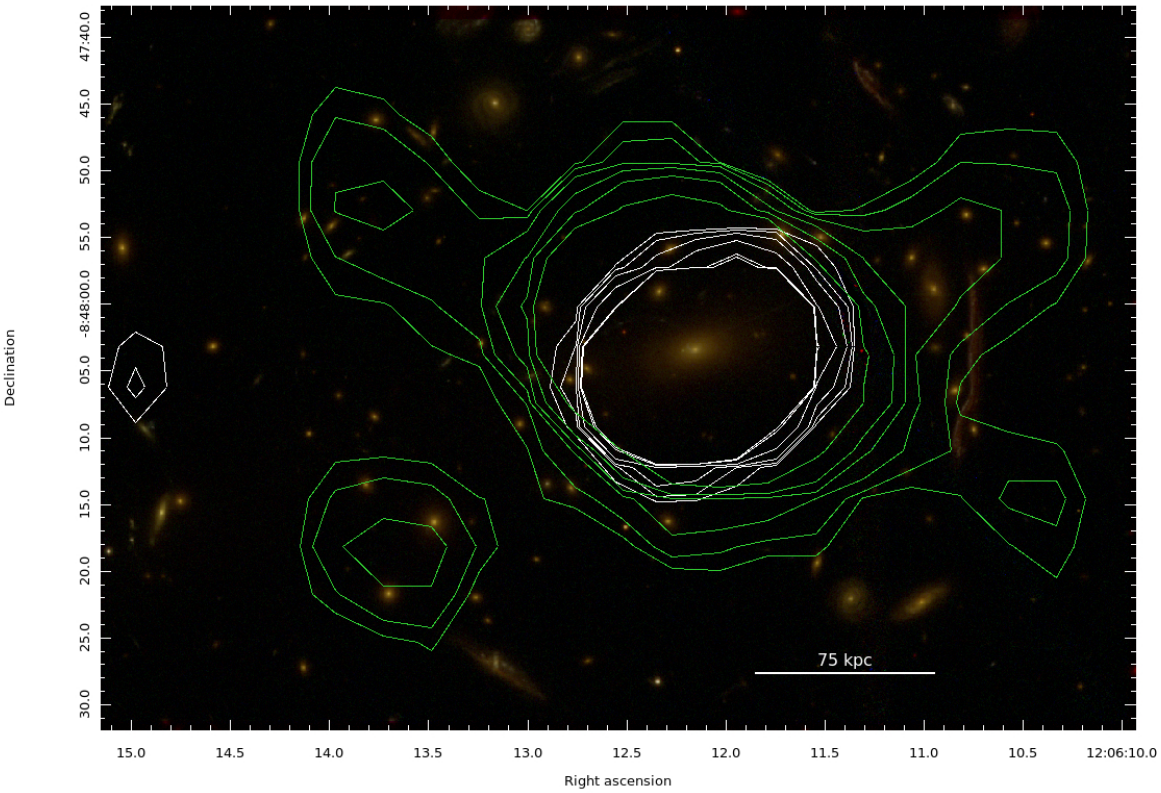

Figure 2.17: **MACSJ1206**: Composite HST image (f814w, f625w, f435w) with GMRT radio contours (green) at 323 MHz and VLA radio contours (white) at 1.4 GHz. The radio contours are drawn at 3σ, i.e. 0.38 mJy/b and 0.06 mJy/b respectively.

correlate or weakly correlate with the radio power at 1.4 GHz, while these correlation is very strong for normal elliptical radio galaxies. At least, this highlight that these galaxies evolve in different way in respect to the normal radio galaxies. Moreover, Donahue et al. (2015); Fogarty et al. (2015) show that in these galaxies there are extended filaments in optical and UV bands, which testify that the Star Formation activity is strong and not negligible, expecially in those galaxies surrounded by a cool core of high pressure and low entropy ($K_0 < 30 \div 50$ keV cm^{-2}).
In particular, Fogarty et al. (2015) show very high SFR values in the UV and $H\alpha$ bands for CLASH BCGs, some of them overcome $100 M_{\odot}$. The highest value is those of the BCG in MACSJ1931 where the SFR in the UV band is $280 M_{\odot}$. This value is higher in respect to the one calculated by Santos et al. (2016) in IR band from Herschel data, which is $\sim$150M$_{\odot}$/yr.
Starting from these different results, I analyzed my sample estimating, first, the q parameter (i.e. the parameter which discriminates between the dominance of AGN or Star Formation activity in galaxies), following Condon et al. (2002) method. The q parameter is defined by Condon et al. (2002) as follows:

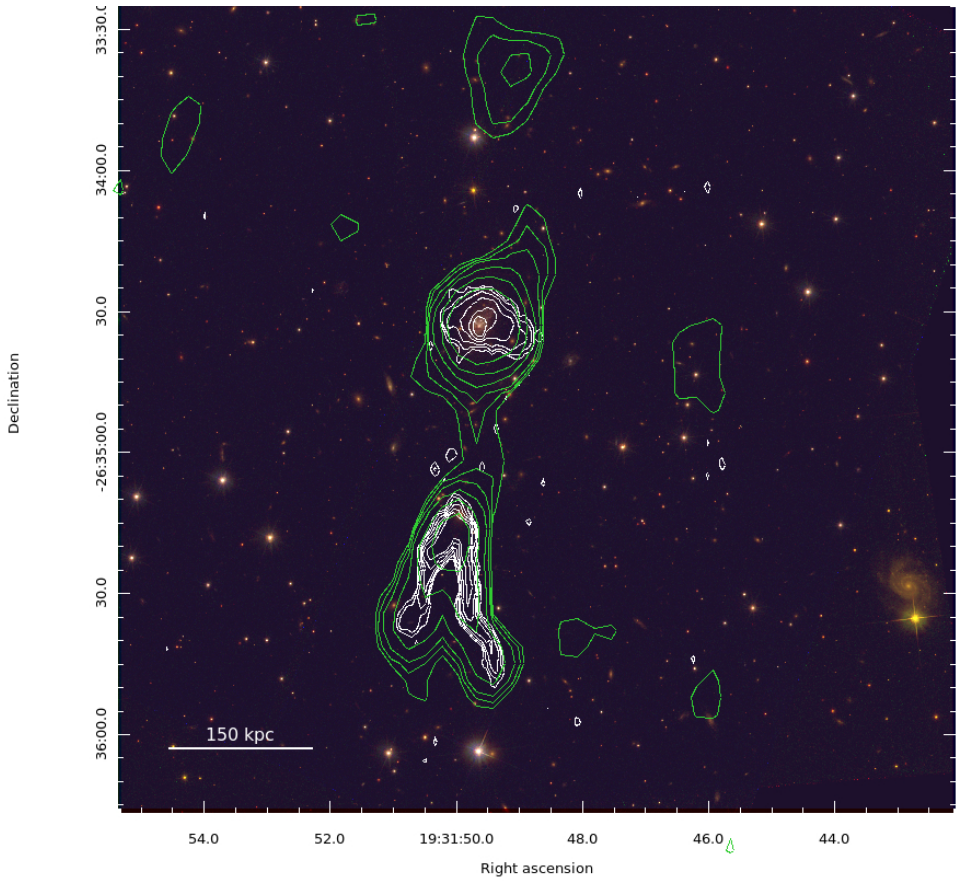

Figure 2.18: **MACSJ1931**: Composite HST image (f814w, f625w, f435w) with GMRT radio contours (green) at 323 MHz and VLA radio contours (white) at 1.4 GHz. The radio contours are drawn at 3σ, i.e. 2.7 mJy/b and 0.09 mJy/b respectively.

$$q = log\left[\frac{FIR/(3.75 \times 10^{12} Hz)}{F_{1.4GHz}(WHz^{-1}m^{-2})}\right] \tag{2.7}$$

where:

$$FIR(Wm^{-2}) = 1.26 \times 10^{-14}\left[2.58 S_{60\mu m}(Jy) + S_{100\mu m}(Jy)\right] \tag{2.8}$$

is the far-infrared flux obtained from the IRAS flux densities at 60 μm and 100 μm (see Carilli & Walter, 2013, for reviews).
In my case, I considered the flux from Herschel/PACS and Spitzer/MIPS, assuming the same caveat as Condon et al. (2002): when they do not have the 100 μm value, they consider it as the double of those measured at $60\mu m$. This assumption introduces a negligible bias to the calculation, since the median value of the logarithmic

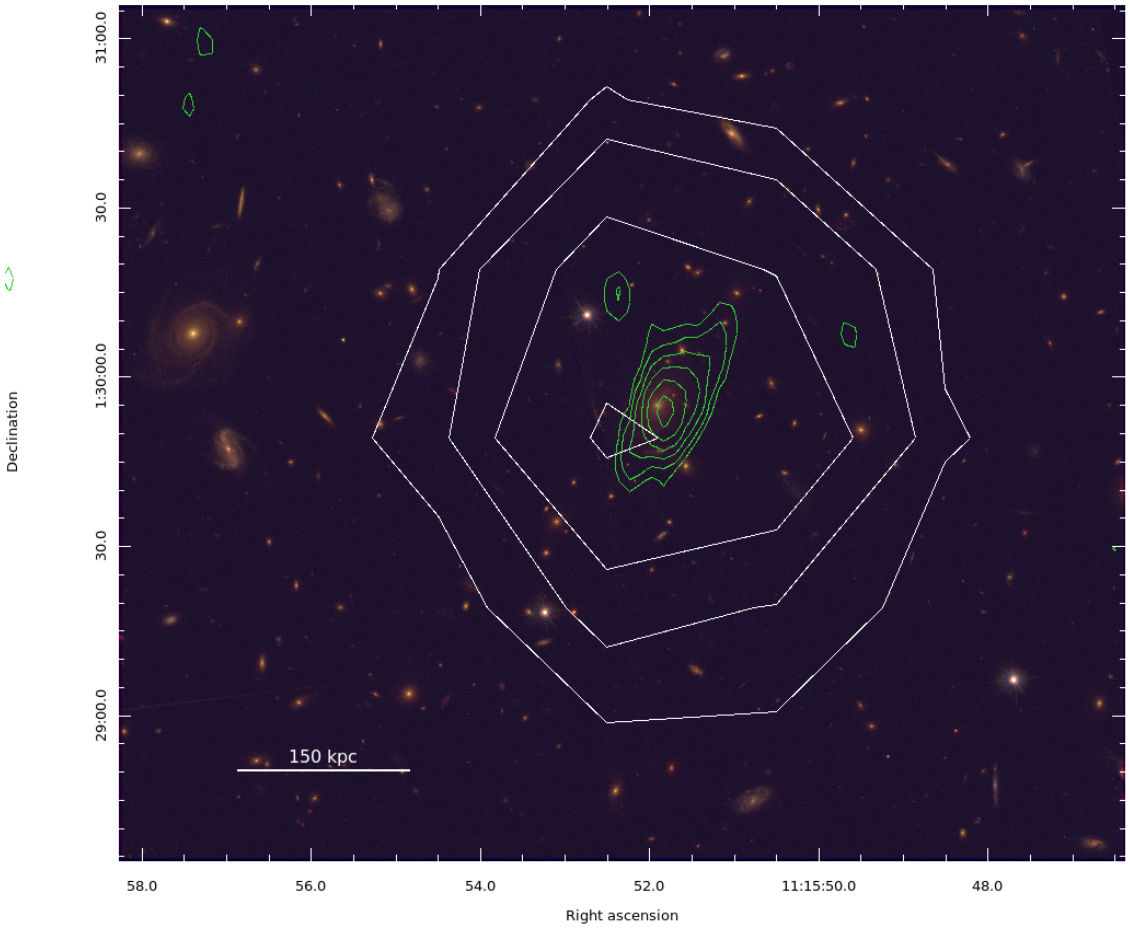

Figure 2.19: **RXCJ1115**: Composite HST image (f814w, f625w, f435w) with GMRT radio contours (green) at 610 MHz and VLA radio contours (white) at 1.4 GHz. The radio contours are drawn at 3σ, i.e. 0.28 mJy/b and 0.45 mJy/b (NVSS) respectively.

ratio between the two fluxes has a small rms scatter.
In Tab. 2.8 I report the q value estimated for the targets in my sample to whom it was possible to calculate it (no FIR is found for A1300, A2744 and A1423).

All the galaxies with q < 1.8 are more than three times more "radio loud" than the mean for star forming galaxies and they are classified as AGN-powered (Condon et al., 2002). In my case, all the targets have q < 1.8 whit the exception of A209. Indeed it has a lower limit on q > 1.4, which resulted consistent with the value of the radio power, typical of a SF galaxy (see Tab. 2.7).
From the relation between the flux and the luminosity (2.6), I derived $L_{60\mu m}$ and hence the SFR from Yun et al. (2001):

$$SFR_{FIR} = \left[\frac{L_{60\mu m}}{5.1 \times 10^{23} W/Hz}\right] M_{\odot} yr^{-1} \tag{2.9}$$

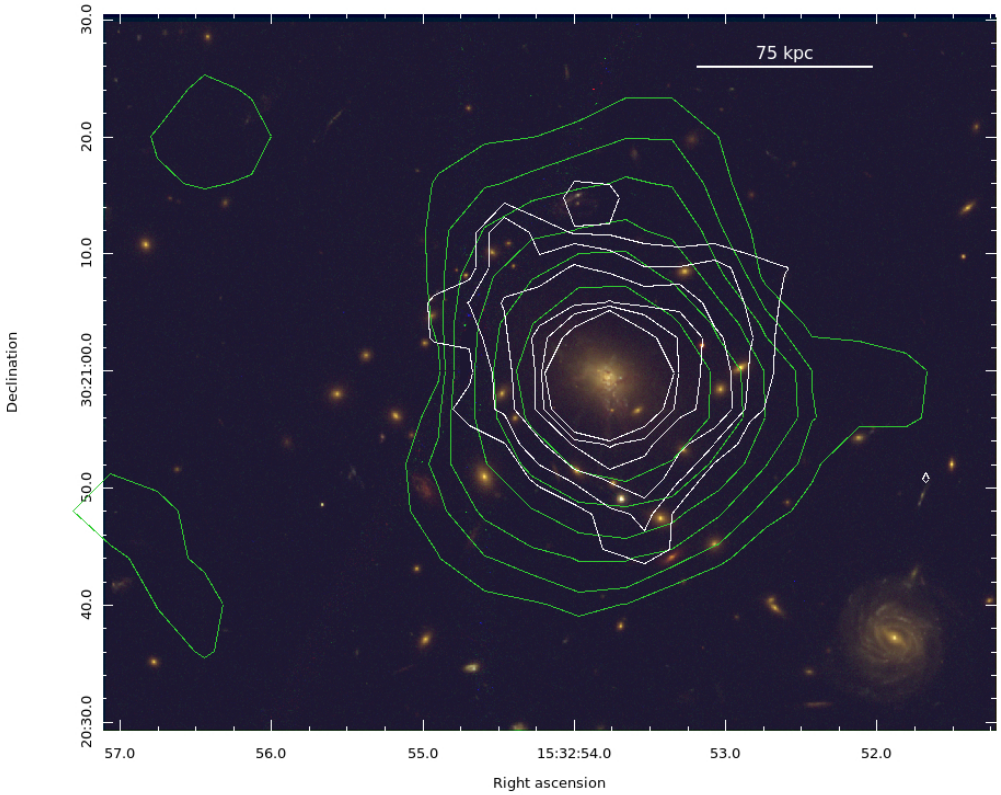

Figure 2.20: **RXCJ1532**: Composite HST image (f814w, f625w, f435w) with GMRT radio contours (green) at 610 MHz and VLA radio contours (white) at 1.4 GHz. The radio contours are drawn at 3σ, i.e. 0.21 mJy/b and 0.03 mJy/b respectively.

The values obtained are reported in Tab. 2.9 and compared with the value from Fogarty et al. (2015). The FIR band should be less affected by biases in respect to the UV and H_α bands.

From the value estimated of $L_{60\mu m}$ I verified the correlation $L_{1.4GHz}$ vs $L_{60\mu m}$ from Yun et al. (2001) in Fig. (2.26).

Only A209 lies on the correlation, consistent with the q value, whereas the other targets lie above the correlation. In particular, considering their luminosities, they can be classified as Luminous IR Galaxies (LIRG), since their luminosity ranges between $10^9 < L_\odot < 10^{11}$.
I considered a representative value of 30 $M_\odot yr^{-1}$ to separate between high and low SFR (i.e. full and empty red circles respectively).
I found that, even if my values are lower than those found from Fogarty et al. (2015), their trend is consistent, confirming the evidence that SFR is higher for cool core clusters.

Table 2.8: The q parameter and the dynamical state

Target name	q	Dynamical state	Diffuse em.
A209	>1.4	Merging	-
A611	∼0.37	Relaxed	-
A1300	-	Merging	H
A1423	-	Relaxed	-
A2744	∼0.1	Merging	H
A2744	∼0.1	Merging	H
MACSJ1931	∼0.85	Relaxed	MH?
MACSJ0429	∼-0.75	Relaxed	-
MACSJ1206	∼-0.36	Relaxed	MH
RXCJ1115	∼0.55	Relaxed	MH
RXCJ1532	∼0.62	Relaxed	MH

Table 2.9: The SFR calculated from my analysis (FIR) compared with Fogarty et al. (2015).

cluster name	$L_{60\mu m}$ (W/Hz)	SFR_{FIR} $M_\odot yr^{-1}$	SFR_{UV} $M_\odot yr^{-1}$	$SFR_{H\alpha}$ $M_\odot yr^{-1}$
A209	$1.5x10^{23}$	0.3 ± 0.02	-0.01 ± 0.04	/
A611	$2.9x10^{23}$	0.6 ± 0.04	< 0.04	/
A1300	/	/	/	/
A1423	/	/	-0.07 ± 0.03	/
A2744	/	/	/	/
MACSJ1931	$4.8x10^{25}$	94 ± 9	280 ± 20	130 ± 40
MACSJ0429	$8.7x10^{24}$	17 ± 1	28 ± 2	33 ± 9
MACSJ1206	$2.6x10^{25}$	51 ± 5	2.9 ± 0.6	/
RXCJ1115	$1.7x10^{25}$	31 ± 3	13 ± 1	3.4 ± 1.0
RXCJ1532	$2.2x10^{25}$	43 ± 2	97 ± 4	140 ± 40

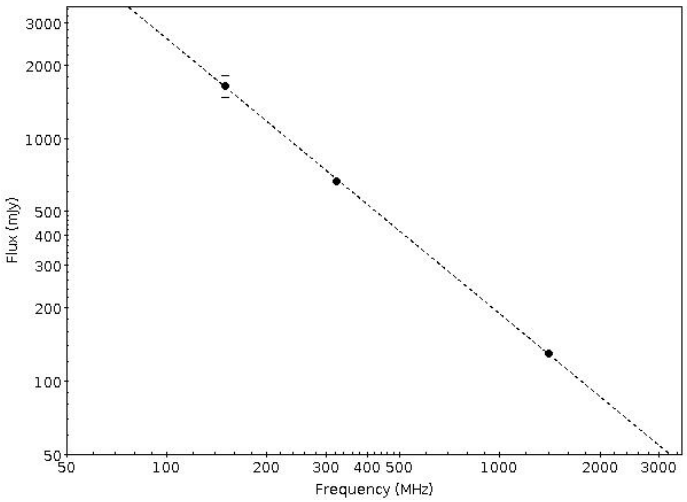

Figure 2.21: Radio spectrum of the BCG in MACSJ1206 from VLA at 1.4 GHz, GMRT at 323 MHz and at 150 MHz from TGSS.

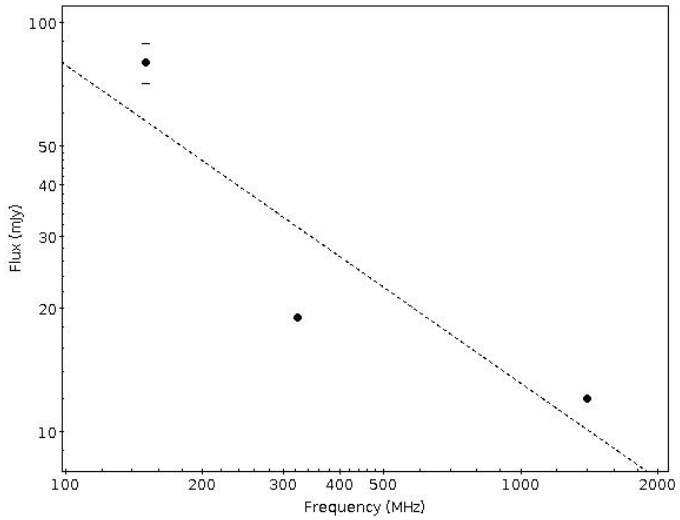

Figure 2.22: Radio spectrum of the BCG in RXCJ1115 from VLA at 1.4 GHz, GMRT at 610 MHz and at 150 MHz from TGSS.

This result is in agreement also with Kale et al. (2015): radio loudness is higher for relaxed clusters. They also found a relation between the concentration parameter (Cassano et al., 2010, 2013) and the radio loudness of BCGs.
Surely in cool core clusters there is a reservoir of cold gas which is both the fuel for the AGN activity but also responsible for high Star Formation activity. We can infer from the analysis that these two mechanisms are strictly related to each other since the fuel which feeds them have same origin but their interplay is still an open issue.

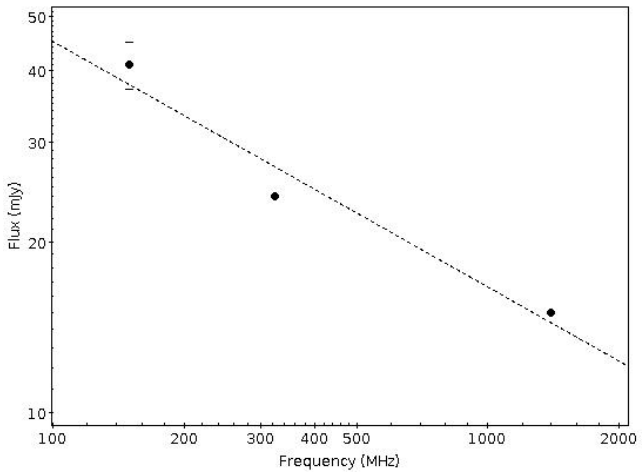

Figure 2.23: Radio spectrum of the BCG in RXCJ1532 from VLA at 1.4 GHz, GMRT at 610 MHz and at 150 MHz from TGSS.

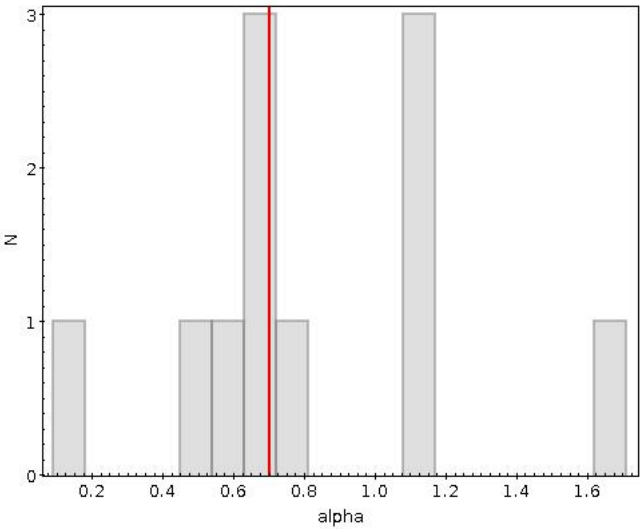

Figure 2.24: Spectral index distribution of the BCGs in our sample. The peak is 0.7 ± 0.06. In some cases, the presence of diffuse emission could be responsible of a spectral steepening.

2.2.6 Correlations measured

One of the goals of our analysis is to constrain the relation between the radio emission detected from the BCGs and the dynamical state of the clusters which host them. In Tab. (2.8) we report the value of q, the parameter which discriminates between the dominance of Star Formation emission and AGN emission, in relation with the dynamical state of the clusters. Even though the poor statistics, we can infer some preliminary considerations. Only A209, a merging cluster, shows a

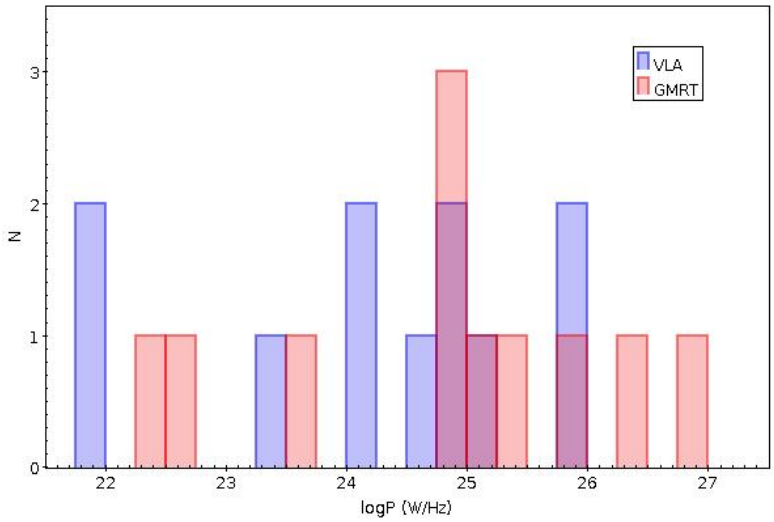

Figure 2.25: Radio power distribution of the BCGs in our sample. The peak is 24.2 and 24.7 for the VLA and GMRT respectively. The result is consistent with Kale et al. (2015) and with the fact that the main mechanism which produces the radio emission detected is the AGN emission.

q value which is consistent with the fact that the Star Formation is the dominant mechanism in its BCG. Indeed it stands on the FIR-radio correlation in Fig. (2.26). On the contrary, A2744, has a q value which is consistent with the fact that the two BCGs are AGN powered, and that the AGN emission is the mechanism which dominates the radio emission. We are aware that this result is derived from many assumptions, however, the robustness of the method adopted for the estimation of q, makes this result reliable. Apparently, it seems that the merging does not influence the prevalence of one of the two mechanisms. The histogram in Fig. (2.27) reports the distribution of q in relation with the cluster dynamical status. It seems that there is no correlation between the AGN emission dominance and the dynamical state of the cluster.
The SFR measured in the FIR band from our analysis differs from Fogarty et al. (2015). In Fig. (2.28) we report the correlation between the SFR in the FIR band, and the SFR in UV band. Even though the values estimated from our analysis resulted different, taking into account the bias that could be introduced in the UV band, the trend is similar, and consistent with the fact that the SFRs is higher in relaxed clusters, according to Donahue et al. (2015); Kale et al. (2015); Fogarty et al. (2015).

In Tab. (2.10) we report the values of the cluster masses taken from Burke et al. (2015) and of the stellar masses of the BCGs. The values of the stellar mass reported for A1300 and MACSJ1931 are estimated by means of MAGPHYS (Cunha et al., 2008), the other values are taken from Burke et al. (2015).

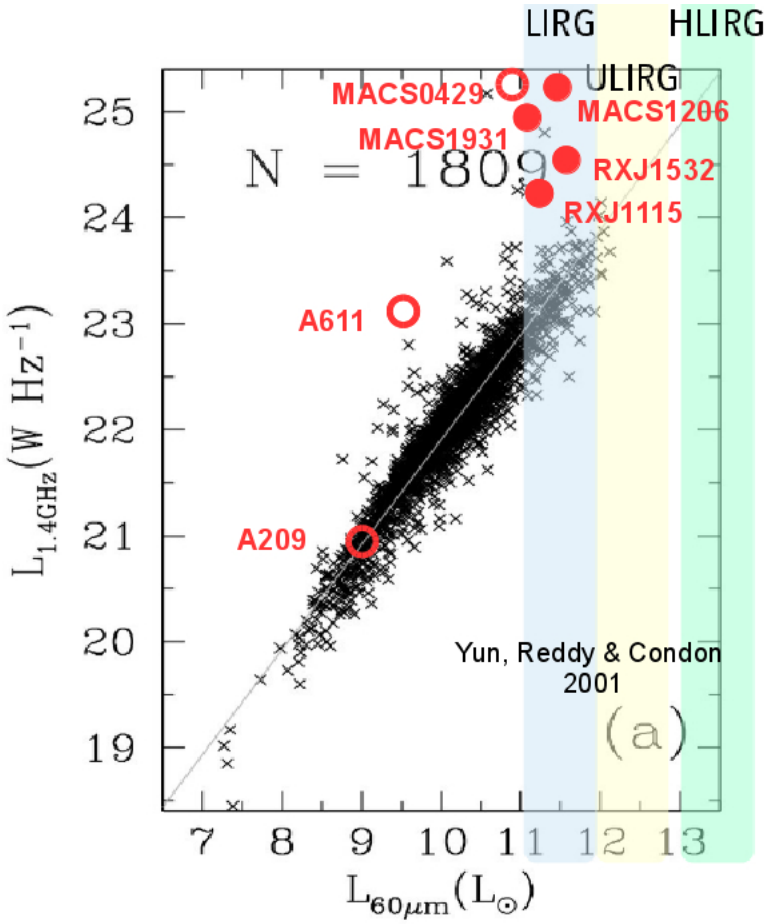

Figure 2.26: The $L_{60\mu m}$ vs $L_{1.4GHz}$ correlation from Yun et al. 2001. The empty red circles indicate those BCGs with SFR lower than $30M_\odot$. The full red circles indicate those BCGs with SFR higher than $30M_\odot$.

In order to investigate the origin of the Star Formation, we report the SFR-Mass correlation in Fig. (2.29). From literature we know that the correlation indicates a gradual assembly of the stellar mass, as opposed to bursty star formation (Davé, 2008; Santini et al., 2009; Vaddi et al., 2016) which introduces a scatter. Moreover, we want to compare our result with Cooke et al. (2016). The tight correlation observed up to z $\sim$ 2 between the SFR and stellar mass has been called Star Formation Main Sequence (SFMS). Cooke et al. (2016) do not observe any SFMS (see Fig. 2.6). We found from our analysis that no correlation is found from the galaxies in our sample.

The core entropy K_0 (see 1.16) is a proxy for the existence of a cool core in galaxy clusters (Cavagnolo et al., 2009; Donahue & Voit, 2004; Giacintucci et al., 2017). Low values of core entropy typically accompany activity in BCGs. Donahue

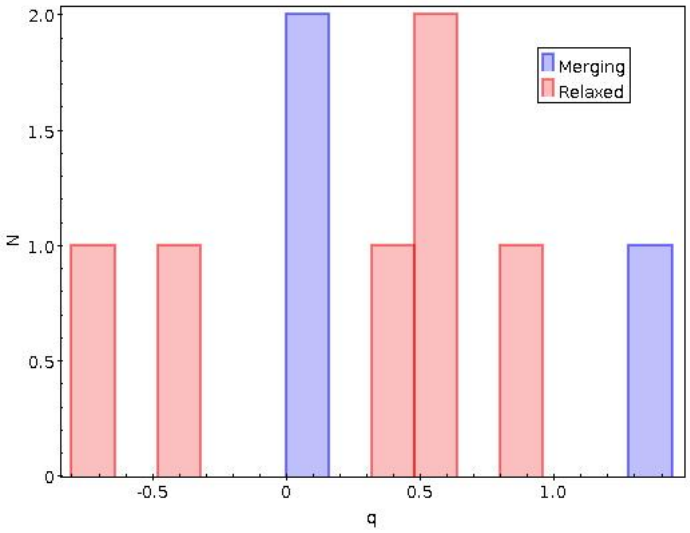

Figure 2.27: The q parameter distribution in relation with the dynamical status of the cluster. Apparently there is no correlation between the AGN emission dominance and the merging status of the cluster.

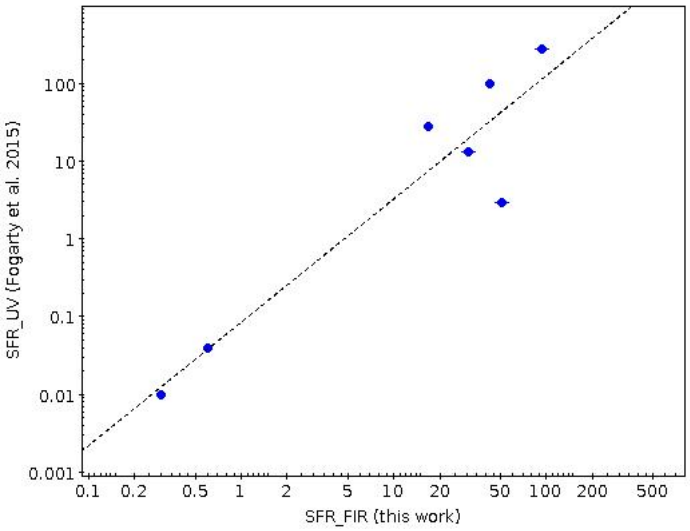

Figure 2.28: The image shows the correlation between the SFR estimated from Fogarty et al. (2015) in the UV and from our analysis in the FIR band. The same trend seems to confirm that the SFR is higher in relaxed clusters.

et al. (2015) report that $K_0 \lesssim 30$ keV cm^2 is the threshold to detect SFR activity > 10 M$_\odot$ yr^{-1} in the UV, in agreement with Cavagnolo et al. (2008, 2009); Hoffer et al. (2012); Fogarty et al. (2015). In order to confirm the result, we estimated correlation between the SFR estimated from FIR in this work with the core entropies taken from ACCEPT (Cavagnolo et al., 2009). The plot reported in Fig. (2.30)

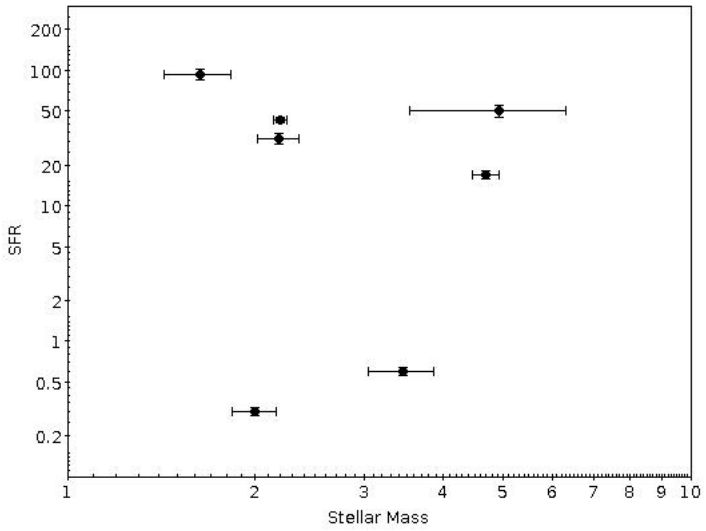

Figure 2.29: The image shows the SFR estimated in this work versus stellar mass of the BCGs. There is no SFMS observed according to the result from Cooke et al. (2016).

Table 2.10: The cluster mass, BCG stellar mass, SFR from this work and the core entropy from ACCEPT (Cavagnolo et al., 2009; Donahue et al., 2015).

Target name	Cluster mass M_{200} $\times 10^{15}$ $M_\odot$	BCG mass $\times 10^{11}$ $M_\odot$	SFR FIR $M_\odot yr^{-1}$	K_0 keVcm^2
A209	1.17 ± 0.07	2.00 ± 0.16	0.3 ± 0.02	106 ± 27
A611	1.03 ± 0.07	3.45 ± 0.42	0.6 ± 0.04	125 ± 18
MACSJ1931	0.99 ± 0.07	1.63 ± 0.20	94 ± 9	14 ± 4
MACSJ0429	0.96 ± 0.14	4.68 ± 0.23	17 ± 1	17 ± 4
MACSJ1206	1.00 ± 0.11	4.93 ± 1.39	51 ± 5	69 ± 10
RXCJ1115	1.13 ± 0.10	2.19 ± 0.17	31 ± 3	15 ± 3
RXCJ1532	0.64 ± 0.09	2.20 ± 0.05	43 ± 2	17 ± 2

confirm this result.
To conclude we can confirm that, from our analysis, the radio emission in BCG is mainly due to AGN activity. Apparently, there is no evidence of correlation between the radio emission and the merging status of the cluster. On the contrary, it seems that the presence of a cool core enhance the Star Formation activity. This is consistent with cold gas being the source of fuel for both the AGN and Star Formation activity (Pizzolato & Soker, 2005; Gaspari et al., 2013, 2015; Tremblay et al., 2016; Cooke et al., 2016).

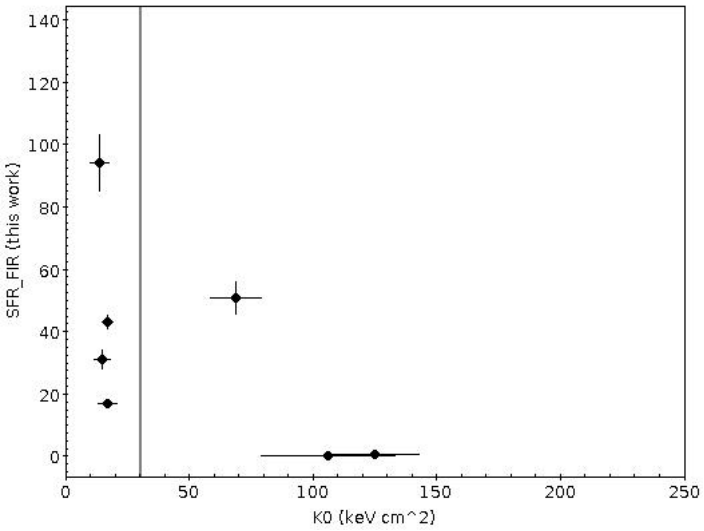

Figure 2.30: BCG SFR estimated in this work compared to cluster core entropies. The grey vertical line indicates the 30 keV cm^2 threshold. Core entropies below $\sim$ 30 keV cm^2 are associated with SFR $>$ 10 M$_\odot$ yr^{-1}. Our result is in agreement with Fogarty et al. (2015).

Chapter 3

The uGMRT and MeerKAT interferometers

After the analysis on a sample of eleven BCGs selected from ten galaxy clusters, belonging to the CLASH and the EGRHS surveys, we extracted two targets from our initial sample in order to perform a statistical analysis on their radio galaxy poupulation.
We selected A1300 (z=0.31) and MACSJ1931-2634 (z=0.35) as representative of a post-merging and a relaxed environment respectively. The aim is to compare the statistical properties (such as the source counts and the Radio Luminosity Function) and the optical properties of the radio galaxies in relation with the environment in which they are located (Dressler, 1980; Dwarakanath & Owen, 1999; Venturi et al., 2000, 2001; Biviano, 2001; Giacintucci et al., 2004; Branchesi et al., 2006; Mahony et al., 2016; Di Gennaro et al., 2018).
To reach our goal, we exploited new data from two SKA precursors[1]: the upgraded GMRT and the MeerKAT interferometers.
The entire analysis on MACSJ1931-2634 and A1300 radio galaxy population is presented in Chapter 5 and 6 respectively.
In this chapter I report a detailed description of the new instruments, I focused on technical details of their construction and on their scientific goals.
The uGMRT (i.e. the upgraded version of the Giant Metrewave Radio Telescope) is one of the largest and most sensitive fully operational low-frequency radio telescopes in the world today (Gupta et al. 2017).
The MeerKAT radio telescope is the largest and most sensitive radio telescope array in the centimeter wavelength regime in the southern sky until SKA1-MID will be operational (Jonas 2016; Camilo et al. 2018).

[1] https://www.skatelescope.org

3.1 The GMRT interferometer

The Giant Metrewave Radio Telescope (GMRT; Swarup, 1991) is a radio interferometer set up by the National Center for Radio Astrophysics (NCRA-TIFR [2]), near Khodad village (Telescope Latitude=19.1°N, Longitude=74.05° E), which is about 80 km North from Pune, Maharashtra (Fig. 3.1).

Figure 3.1: GMRT interferometer.

The array configuration consists of 30 alt-azimuth mounted parabolic antennas, each of 45 m diameter. The elevation limit has been set at 17°, giving a declination coverage from -53° to +90°. The reflecting surface is formed by wire mesh and the efficiency of the antennas varies from 60% to 40%, from the lowest to the highest frequency. Spanning over a region of 25 km diameter, it provides a total collecting area of about 30,000 m^2 at metre wavelenghts, with an angular resolution of about 1 arcsec at 1.4 GHz.
The interferometer has a hybrid configuration with 14 of its 30 antennas located in a central compact array with size ∼1.1 km and the remaining antennas distributed in a roughly "Y" shape, giving a maximum baseline lenght of ∼ 25 km (Fig. 3.2). The shortest baseline is about 100 m.

The baselines obtained from antennas in the central square are similar in lenght to the VLA D-array configuration, while the baselines between the arm antennas are comparable in lenght to the baseline lenghts between VLA A-array and VLA B-array configurations. Hence, a single observation with the GMRT samples the

[2]http://www.ncra.tifr.res.in.

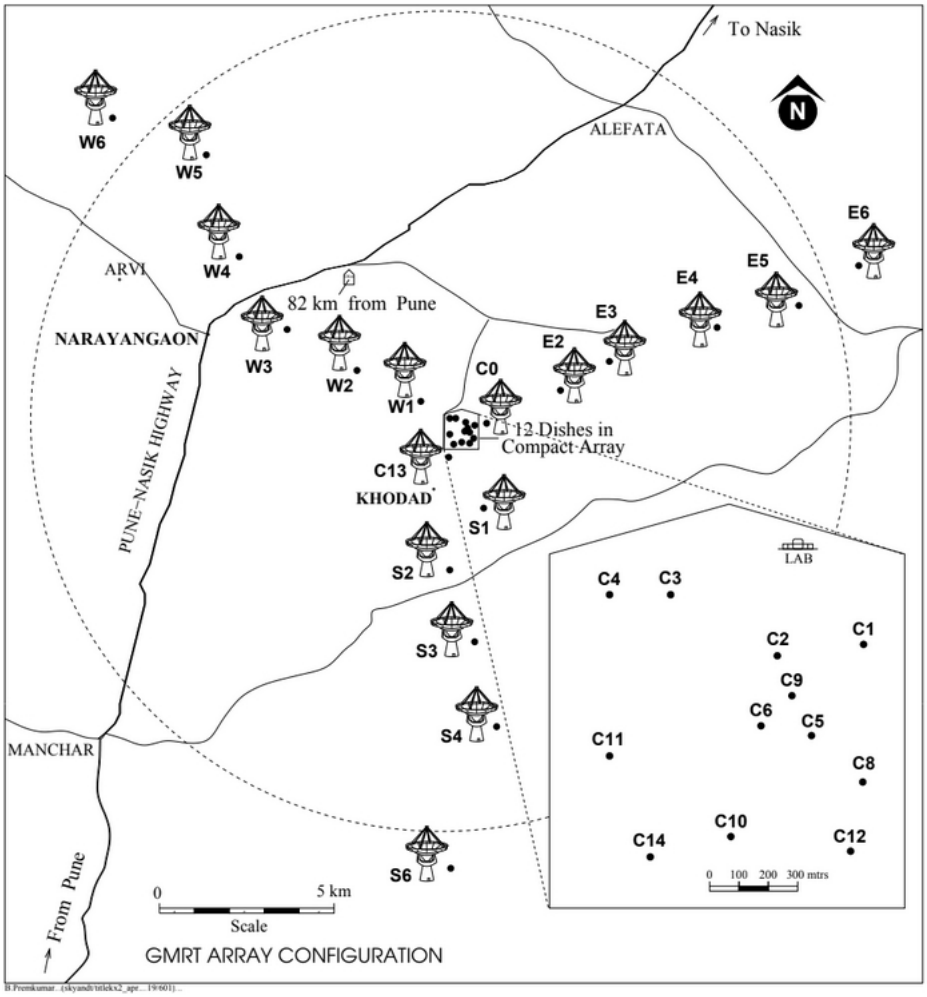

Figure 3.2: The GMRT array configuration.

u,v plane adequately on both short and long baselines with good sensitivities.
The GMRT can also be configured in array mode, where it acts as a single dish by adding the signals from individual dishes. This mode of operation is used for studying compact objects like pulsars, which are effectively point sources even for the largest interferometric baselines.
The 'legacy' GMRT has a maximum istantaneous operating bandwidth at any frequency band of 32 MHz. It can also runs at 33.333 MHz sampling rate, which is useful for cases where the input bandwidth is limited to 16 MHz or less (see Gupta et al. 2017).
Since its commissioning in 2001, the GMRT has produced several new and interesting results in a wide range of topics in astrophysics[3]. The science addressed by the GMRT spans a wide range, from our Sun and nearby stars, to the Epoch of

[3]see the proceedings of **The Metrewavelenght Sky conference.**

Reionisation, Pulsars, redshifted HI 21 cm emission and Galaxy Clusters.

3.2 Main goals of the GMRT upgrade

The GMRT was one of the first in a series of new radio observatories in the 1990s. Shortly after its commissioning, new facilities such as LOFAR (van Haarlem et al., 2013), MWA (Tingay et al., 2013), LWA (Ellingson et al., 2013) were conceived and started becoming operational towards the end of the first decade of this century.
A plan to upgrade the GMRT was proposed during the XI Plan funding period (2007-2012) and the first serious work in this direction was initiated around 2010. The main goal identified was to add extra capability to the existing GMRT array in terms of frequency coverage and sensitivity.
More specifically, the improved frequency coverage, to be achieved by broadbanding the receiver systems, allow spectral line observations over a wider range of the centimetre and metre wavelenght spectrum, allowing for explorations of the Universe over a much wider range of redshifts than is possible with the existing GMRT. The increased sensitivity, achieved by a combination of wider bandwidths and improved technology receivers, improve the capability of the GMRT for continuum imaging, allowing more refined galactic and extra-galactic studies to be carried out, and also make it a more powerful tool for detection and detailed studies of pulsars and transients.
The following are the main goals for the upgraded GMRT (see Gupta et al. 2017):
-**(1)** Seamless frequency coverage, as far as possible, from 50 to 1500 MHz, replacing the five limited bandwidth frequency bands of the original GMRT;
-**(2)** Maximum istantaneous bandwidth of 400 MHz, replacing the 32 MHz bandwidth of the original GMRT design;
-**(3)** Improved receiver systems (Fig. 3.3) with higher G/T_{sys} and better dynamic range;
-**(4)** Versatile digital backend correlator and pulsar receiver catering to the 400 MHz bandwidth;
-**(5)** Modern servo system;
-**(6)** Sophisticated, next-generation monitor and control system;
-**(7)** Matching improvements in mechanical systems and computing resources;
-**(8)** Implementation of the upgrade with minimal disruption to the availability of the existing GMRT for scientific observations.
Full care has been taken in the design of new systems to ensure that the performance of the existing GMRT was not affected as the upgrade was implemented.

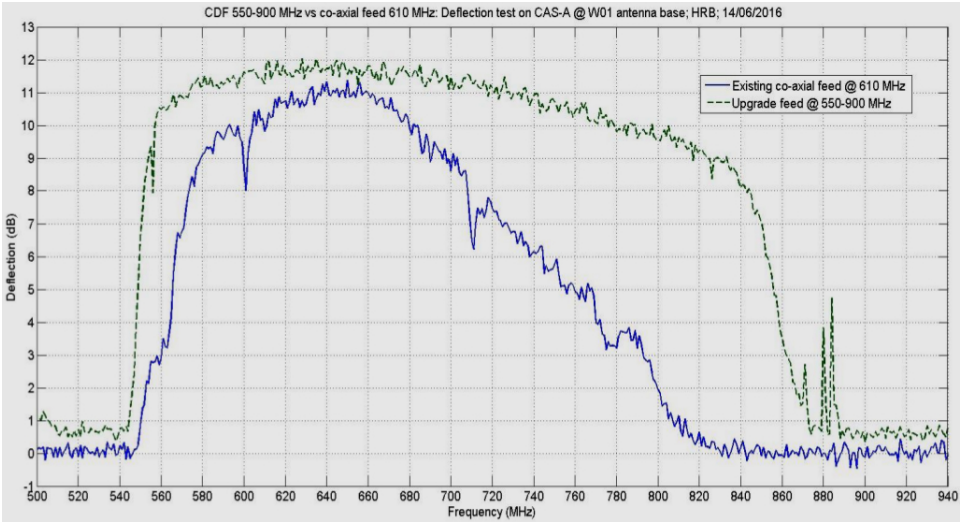

Figure 3.3: Comparison between the pre-existing co-axial feed at 610 MHz and the upgrade at 550-900 MHz (band 4).

3.3 Implementation of the upgrade

The final frequency coverage for the uGMRT after the upgrade is: 50-80 MHz (band-1), 120-250 MHz (band-2), 250-500 MHz (band-3), 550-850 MHz (band-4), 1050-1450 MHz (band-5). The gap in the frequency coverage in this choice of bands is due to constraints of very strong Radio Frequency Interferences (RFI) such as the FM band, TV channels and mobile communication bands. Figure 3.4 shows the frequency coverage targeted with the uGMRT, alongwith the fractional bandwidth for each receiver band (image courtesy: Ruta Kale, NCRA).

3.3.1 System parameters

The main system parameters of the uGMRT, compared with the measured parameters of the GMRT, are summarized in Tables 3.1 and 3.2 as taken from *Observer's manual* updated at June 2018. The uGMRT can, in the ideal situation, achieve sub-milliJansky sensitivities for imaging and detection of pulsars in 10 minutes of observing time. Figure 3.5 compares the targeted sensitivity of the uGMRT with other global facilities already in operation or incoming as SKA-I, for a typical full-synthesis continuum-mode observation. The uGMRT is one of the most sensitive facilities in the 250-1500 MHz frequency range until the SKA Phase-1. Furthermore, the uGMRT at 300-1000 MHz is well matched to JVLA at higher frequencies (3-10 GHz), thereby providing a powerful combination for exploring a wide range of astrophysical phenomena.

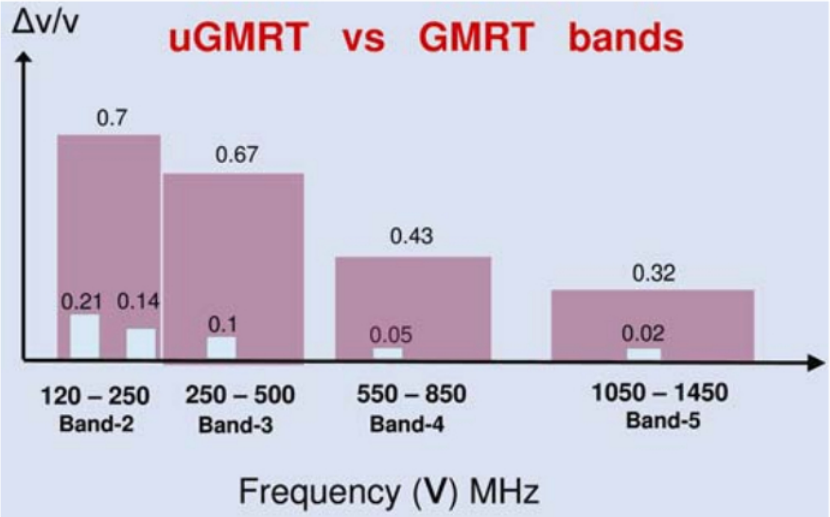

Figure 3.4: Frequency coverage and fractional bandwidth of the four uGMRT bands in comparison with the existing GMRT bands.

Table 3.1: Measured system parameters of the GMRT

	151MHz	235MHz	325MHz	610MHz	1420MHz
Primary Beam (arcmin)	186±6	114±5	81±4	43±3	24±2
Receiver Temperature (T_R)	295	106	53	60	45
Total System Temperature (K)	615	237	106	102	73
Antenna Gain (K/Jy/Antenna)	0.33	0.33	0.32	0.32	0.22
Synt. Beam[1] (arcsec)	20	13	9	5	2
Best rms Sensitivity (mJy)	0.7	0.25	0.04	0.02	0.03

[1]whole array

Table 3.2: System parameters of the uGMRT

Band	Gain	Total T_{sys} (K)	rms (mJy/b)	Synth. Beam (arcsec)
2	0.33	760 to 240	0.19	17.3
3	0.38	165 to 100	0.05	8.3
4	0.35	105 to 100	0.04	4.3
5	0.28	80 to 75	0.04	2.3

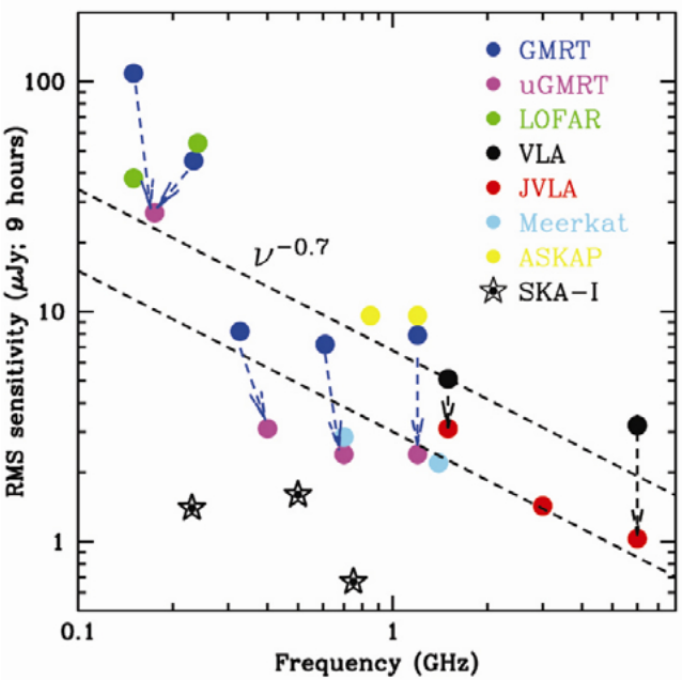

Figure 3.5: Comparison between the continuum sensitivities of existing and upcoming radio interferometers, for a 9 hours on-source integration. As can be seen, uGMRT is the most sensitive interferometer in the world at frequencies 250-1500 MHz until the advent of Phase-1 of SKA.

3.4 Science with the GMRT upgrade

The uGMRT, with the increased frequency coverage, wider bandwidth and improved receiver systems, offers significant potential for new science covering diverse areas. Since the uGMRT is one of the most sensitive instruments operating at centimetre wavelengths until SKA Phase-1 is ready, many of the science projects with the uGMRT will probe new regimes. Here we provide a list of the highlighted possibilities.

- Spectral line science: the increased frequency coverage of the uGMRT offers outstanding near-seamless redshift coverage in the spectral lines of neutral hydrogen HI and hydroxyl OH. This would allow searches for redshifted HI 21 cm absorption from damped Lyman-α absorbers (DLAs) and neutral hydrogen associated with Active Galactic Nuclei (AGNs) out to the highest redshifts at which these systems have been discovered, allowing to probe the redshift evolution of DLA spin temperatures, and the presence and kinematics of neutral gas in AGN environments (see Morganti et al., 2015).
Detections of OH 1667 MHz megamaser emission from hyperluminous infrared galaxies and lensed ultraluminous infrared galaxies should be possible at z $\approx$ 3, allowing one to probe physical conditions in massive starburst galaxies (see Darling & Giovanelli, 2002).
- Blind surveys: the wide frequency coverage will also allow 'blind' surveys for atomic and molecular absorbtion at high redshifts, which should yeld the detection of new absorbers that might be used to study redshift evolution in the fundamental constants of physics (see Chengalur & Kanekar, 2003).
- Molecular transition: The new frequency coverage will provide access to new molecular transitions (e.g. CH at $\approx$ 701 MHz and CH_3OH at 834 MHz), that have not so far been observable with interferometers, allowing one to probe the large-scale spatial structure of molecular clouds in the galaxy.
- Galactic interstellar medium: the significantly higher spectral resolution offered by the GMRT Wider Backend (GWB) also makes the uGMRT a superb instrument for deep, high-velocity resolution absorption studies of the galactic interstellar medium, as would be needed to study the properties of atomic gas in the warm or unstable phases of the interstellar medium (see Roy et al., 2013).

- Continuum imaging science: the improved sensitivity for continuum imaging with large bandwidths has great potential for new science with the uGMRT. Mapping of diffuse, extended, low-surface brightness emission requires a good sampling of the u-v plane (Fig. 3.6) to image the emission over a large range of angular scales (see Feretti et al., 2012). The large fractional bandwidths of the uGMRT bands provide excellent u-v coverage to map such diffuse structures. This, together with the improved sensitivity and arcsecond-scale resolution will open up several areas of study, among which revealing new features in clusters and groups of galaxies, studying radio galaxies at high redshifts, discovering MHz peaked spectrum sources, GHz peaked spectrum sources at high redshift (z $\sim$ 3), detecting weak emission from galaxies, separating thermal versus non-thermal sources in the galactic plane while imaging with the large bandwidths.
Finally, with the wider bands of the uGMRT, like the 250-500 MHz band, an **all sky survey** can be carried out that will be more than an order of magnitude deeper

than the 150 MHz TIFR-GMRT Sky Survey[4].

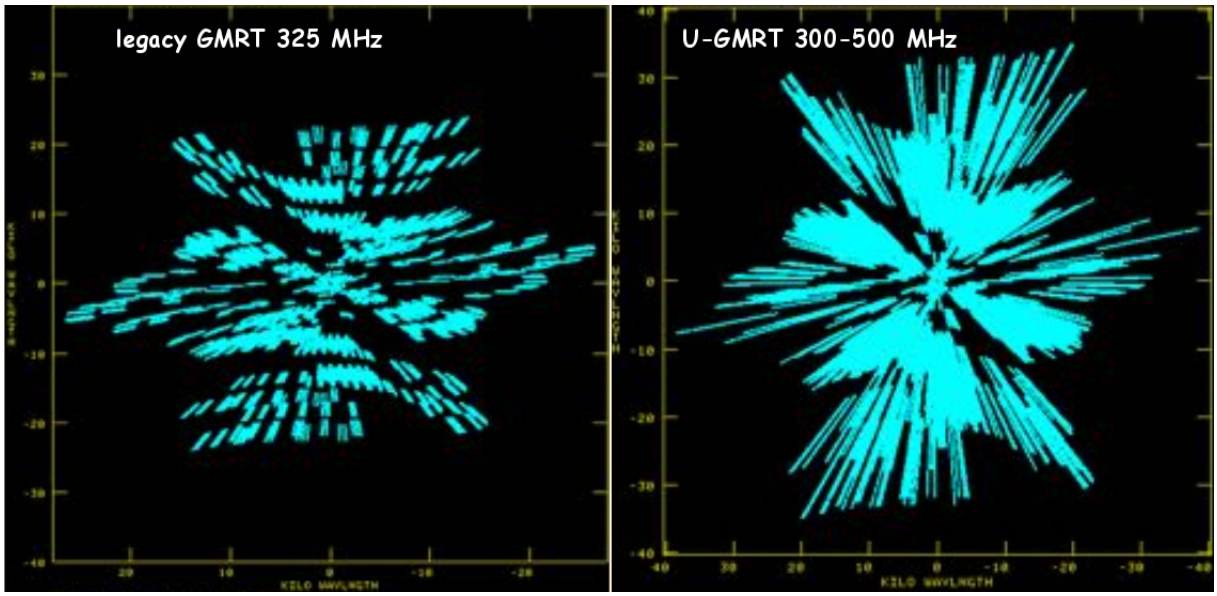

Figure 3.6: Comparison between legacy GMRT and uGMRT u-v coverage at 325 MHz (image courtesy Ishwara-Chandra C.H.).

- Pulsar science: as pulsars are steep spectrum sources, sensitive observations of these objects are well motivated in the 150-1500 MHz frequency range, where the uGMRT opens new possibilities with its wide frequency coverage and improved sensitivity. The higher sensitivity improves also the capabilities for interesting studies of pulsar emission properties that have been attempted with the legacy GMRT system. This, coupled with the ability to observe simultaneously at different bands of the uGMRT using the subarray capability and multiple beams provided by the upgraded 400 MHz digital backend, will enhance the power of the GMRT to carry out multi-frequency studies of pulsars.

3.5 First results and future: the Expanded GMRT

The improvements in the u-v coverage and consequently in the imaging with the uGMRT have been tested thanks to simulations described in details in Deo & Kale (2017). Imaging of the sky with radio interferometers is a general challenge due to the fact that the measurements are limited to the sampled angular scales and the sky distribution is unknown. Thanks to simulations (Deo & Kale, 2017) compared flux and morphology of a simulated ideal extended source and a real one observed

[4]https://tgss.ncra.tifr.res.in

both with the GMRT 32 MHz bandwidth and the uGMRT 400 MHz bandwidth. They found that the increase in bandwidth increases the recovered flux significantly from 45% of the GMRT to 90% from the uGMRT.
Moreover, an observational example on how the improvements can affect the detection of radio emission is given in Kale et al. (2018). They performed a study on A4038 radio relic morphology and spectral curvature, observing the cluster with the uGMRT, during the shared risk phase (Cycle 31), in band 3 and 5, with a bandwidth of 200 MHz and 400 MHz respectively.
Thanks to the sensitivity achieved it was possible to identificate three parts in which the radio relic can be decomposed (Fig. 3.7). Moreover, the deep radio images (Fig. 3.8) from the uGMRT resulted in the detection of faint lobes around a radio core identified with the galaxy PGC072471 (see Kale, 2018).
Finally, in a recent work Patra et al. (2019) show the possibility to expand the existing uGMRT array adding new antennas (EGMRT) and installing focal plane arrays (FPAs) to improve point-source sensitivity, surface brightness sensitivity, angular resolution, field of view, and u-v coverage. There are excellent science arguments to explain the reasons why adding new antennas would be necessary (see Patra et al., 2019, for details). Essentially, the proposed expansion, consists practically in adding 56 antennas, 30 new antennas at short distance (< 2.5 km) and 26 at relatively long distance (5-25 km from the array centre). This will increase the sensitivity and the survey speed of the array, allowing the uGMRT to retain its status as one of the premier low frequency radio interferometer in the world well beyond the next decade, and into the SKA era.

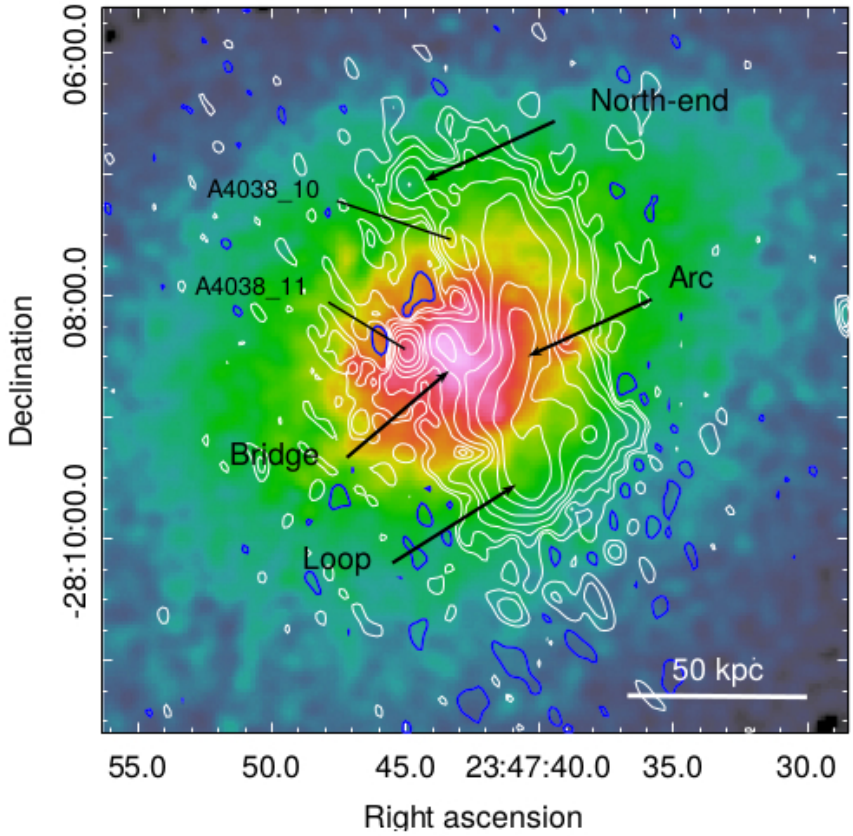

Figure 3.7: The uGMRT 402 MHz image from Kale (2018) is shown in contours overlaid on the Chandra 0.5-7 keV X-ray image (OBSID 04992) in colour. The contour levels start at $\sigma\times$[-3,3,6,12,...], where σ=0.07 mJybeam^{-1} is the rms noise. Positive contours are white and the negative are blue. The discrete sources are *A*4038_11 and *A*4038_10. The components of the radio relic are labelled 'Arc', 'Loop' and 'Bridge'.

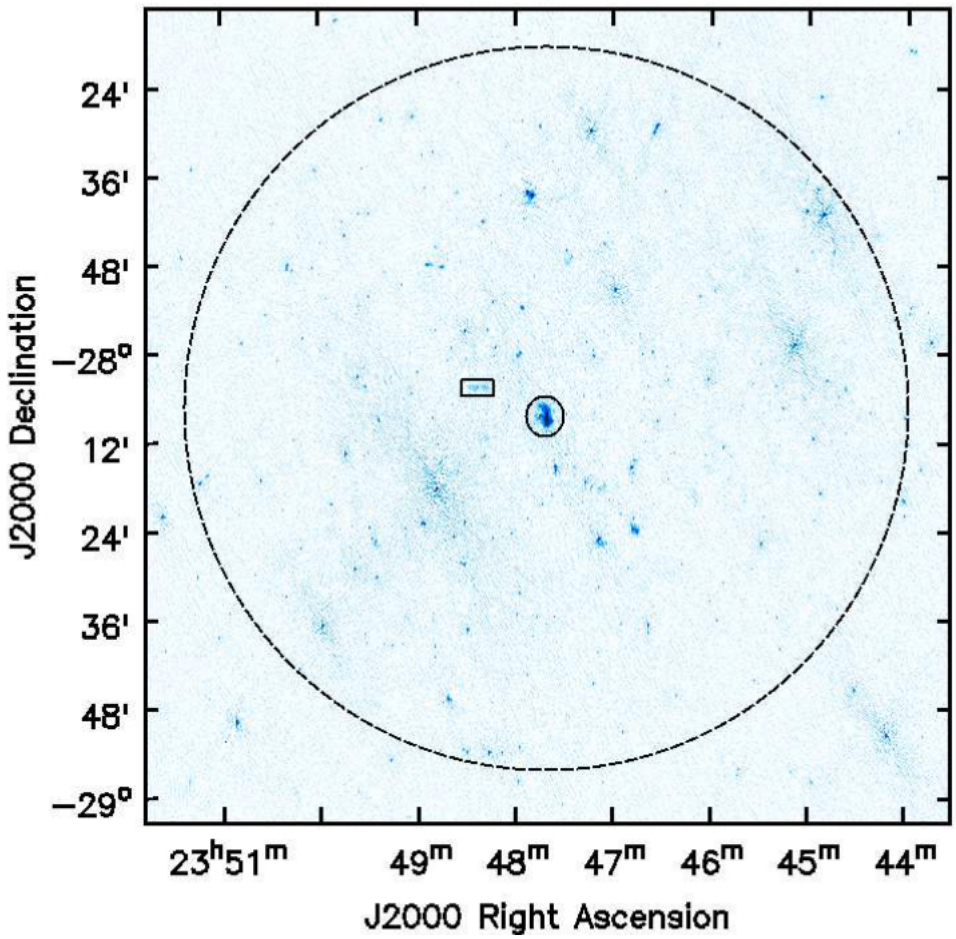

Figure 3.8: The uGMRT 402 MHz image using data between 300-500 MHz from Kale (2018). The rms is 0.07 mJybeam^{-1} near the centre of the field. The central ellipse shows the relic in A4038 and the rectangle marks the detection of diffuse lobes of a radio galaxy.

3.6 The MeerKAT interferometer: generalities

The MeerKAT radio telescope[5] is a precursor for the Square Kilometre Array (SKA) mid-frequency telescope. It will be the most sensitive decimetre-wavelenght radio interferometer array in the world before the advent of SKA1-mid (Jonas & MeerKAT Team, 2016; Camilo et al., 2018).
It is located in the Karoo region of the Northern Cape Province in South Africa (Fig. 3.9), roughly 90 km from the nearest town of Carnarvon. The specifically designed Karoo Array Processor Building (KAPB) is located at short distance from the core of the array at the Losberg site complex and houses the backend systems required to co-ordinate the telescope and process the data derived from it. A support base is located about an hour's drive away from Klerefontein, just outside Carnarvon,

[5]https://www.ska.ac.za

whilst the telescope is operated from a Cape Town based controol room.
The telescope and its associated infrastructure is funded by the government of South Africa through the National Research Foundation (NRF), an agency of the Department of Science and Technology (DST). Construction and commissioning of the telescope has been the responsibility of the SKA South Africa Project Office, which is a business unit of the NRF. Telescope operations are responsibility of the South Africa Radio Astronomy Observatory (SARAO), a National Facility administered by the NFR. MeerKAT will be incorporated into the SKA1-mid array towards the end of the construction phase of SKA1-mid. The MeerKAT project resulted from a DST strategy for South Africa to develop technical and scientific capabilities in academic and industrial sectors in order to be able to fully partecipate to the international SKA project.
A range of technology prototyping activities were undertaken prior to embarking on the final design of MeerKAT. These involved the investigation of novel technologies for use in the SKA and MeerKAT, including phased-array feeds (PAFs), ambient temperature receiver clusters, single-piece composite reflectors, RF-over-fibre analog signal transport and Stirling-cycle cryogenic coolers.
Two prototype telescopes were designed and commissioned as part of the prototyping programme[6]: the single 15 m eXperimental Developement Model (XDM) single dish at HartRAO in 2007 and the seven element Karoo Array Telescope 7 (KAT-7) interferometer array in the Karoo in 2010. Both of these prototype telescopes have been used for productive science programmes (see Bernardi et al., 2017).

[6]the current state is to be found at **http://public.ska.ac.za/meerkat/meerkat-schedule.**

Figure 3.9: MeerKAT interferometer.

3.7 The MeerKAT Large (legacy) Survey Projects

When the DST made the decision to fund the design and construction of a SKA precursor, a directive was issued that the instrument must have science goals related to those of the SKA, and the technologies used to implement the instrument should be applicable to the eventual SKA. The preliminary MeerKAT science case is outlined in Booth et al. (2009). In that year a call was made to the international science community to propose large-scale survey projects (LSPs) that might be carried out on the MeerKAT telescope accordingly with the criteria defined in Booth et al. (2009). This solicitation resulted in 20 survey proposals that were adjudicated by a Time Allocation Committee (TAC). The resulting ten LSPs approved for observing time are briefly described below:

- LADUMA: An ultra-deep atomic hydrogen emission survey out to a redshift of 1.4 to investigate the cosmic evolution of HI in galaxies over the last 9 Gyr.
- MIGHTEE: An extra-galactic continuum survey to investigate the evolution of AGN, star-forming galaxies, and galaxy clusters from the epoch of reionization through the present day. These observations, combined with a lot of ancillary data, will also probe the evolution of cosmic magnetism.
- MHONGOOSE: An HI survey to map the distribution and dynamics of neutral hydrogen in a sample of 30 galaxies located whithin 30 Mpc and spanning five orders of magnitude in HI mass.
- Fornax: A deep HI emission line survey of the Fornax cluster to study the dy-

namics of neutral gas in the cluster and its connection to the cosmic web.
- MALS: An extremely sensitive survey of HI and OH absorbers to map the evolution of cold atomic and molecular gas in galaxies at $0 \leq z \leq 2$. This redshift range probes the evolution in star-formation rate density from near its peak at z ≈2 to the low levels observed in the current universe.
- ThunderKAT: A program to make image-plane detections of multiple populations of Galactic and extra-galactic synchrotron radio sources associated with high energy accretion and explosive events.
- MeerGAL: The deepest and highest resolution 14 GHz survey of the southern Galactic plane, aiming to probe Galactic structure and dynamics, including the study of hyper-compact HII regions and anomalous microwave emission from small spinning dust grains.
- MESMER: A survey targeting redshifted emission originating from the J(1-0) transition of 12CO associated with molecular gas in high-redshift (z≈7) galaxies, to investigate the role of molecular hydrogen in the early universe.
- Pulsar Timing (MeerTime): Long-term timing of various classes of pulsars for a range of scientific goals, including the detection of gravitational wave background, tests of General Relativity and constraining the structure of nuclear matter.
- TRAPUM: Targeted and blind surveys for the detection of fast radio transients and pulsar. The expected discovery of large numbers of Fast Radio Bursts and of pulsars in targets such as unidentified Fermi sources, supernova remnants, and globular clusters, will contribute to understanding of physics in extreme environments and of Galactic dynamics.

3.8 System overview

The science requirements derived from the ten MeerKAT large survey proposals were used to refine the initial telescope specifications provided in the call for proposals in 2009 (see Booth et al., 2009). The specifications and reference design concept of the MeerKAT telescope have evolved further since this early conceptualization.
The antenna diameter, optical configuration, cryogenic cooling technology and receiver technology were determined through a constrained joint electromagnetic and mechanical optimization process. The goal was to maximize point-source sensitivity under the constraints of capital and operational costs. A secondary goal of the optimization was to maximize imaging dynamic range.
The strategy adopted placed tight constraints on the antenna primary beam characteristics (near and far sidelobe levels, circular symmetry, cross-polarization at boresight and within the primary beam) and the RF signal path (passband flatness

Table 3.3: Key MeerKAT system parameters for L-band operation for both the 2009 reference design and the as-built telescope.

	2009 value	As-built value
Number of antennas	80	64
Antenna diameter	12 m	13.5 m
Aperture efficiency	0.7	0.75-0.81 (L-band)
Field of view at 1.4 GHz	1deg^2	0.8deg^2
System temperature	30 K	22-18 K (L-band)
A_e/T_{sys} (array)	200 m^2/K	305-339 m^2/K
Minimum baseline	20 m	29 m
Maximum baseline	8 km	8 km
Frequency range	0.58-2.5 GHz	0.85-1.7GHz
Number of channels	16.384	32.768 (wideband mode)

and stability). Operational issues, such as access to the receivers and the physical volume available for receivers, were also considered in the optimization.
Today the MeerKAT array is formed by 64 antennas, each composed by 13.5 m diameter offset Gregorian dishes, designed to host four receivers spanning a total frequency range from 580 MHz to 14.5 GHz, fully operational, and, in respect to the initial project the sensitivity (see Tab. 3.3) exceed by a large margin thanks also to the Gifford-McMahon (GM) cryogenic coolers. The offset Gregorian dish configuration further enhances sensitivity by providing high aperture efficiency and low spill-over temperature contribution. Moreover this configuration provides a clean optical path that can be designed to produce low overall sidelobe levels and azimuthal symmetry in the inner sidelobes. Low sidelobe levels also provide good rejection of unwanted radio frequency interference from satellites and terrestrial transmitters.

The array configuration is designed with two components: a compact core containing 70% of the dishes, whith the shortest baseline of 29 m and the longest of 1km, and an outer component containing 30% of the dishes with the maximum baseline

of 8 km. The compact core is for pulsars science, transient searching, VLBI and low column density mapping. The extended array is designed for high fidelity imaging performance over a range of resolutions from 4-5 arcsec to approximately 60-100 arcsec.
In addition to the already existing antennas, an additional 7 antennas are planned for phase-2 of the project, in order to have the baselines extended to a maximum of 20 km to reduce the confusion and enhance image fidelity for continuum imaging survey.
The array configuration has been positioned on-site using a site mask to avoid placing antennas close to hills, in gullies, near existing facilities (PAPER or KAT-7), possible future facilities (e.g. SKA), or near the access road. Fig. 3.10 shows the positions of the antennas on the site mask, whereas Fig. 3.11 shows the resulting positions of antennas on a map, also indicating the position of the access roads, site complex and KAT-7 array. The array center is at 30°42'47" S, 21°26'38" E, as taken from Jonas & MeerKAT Team (2016).

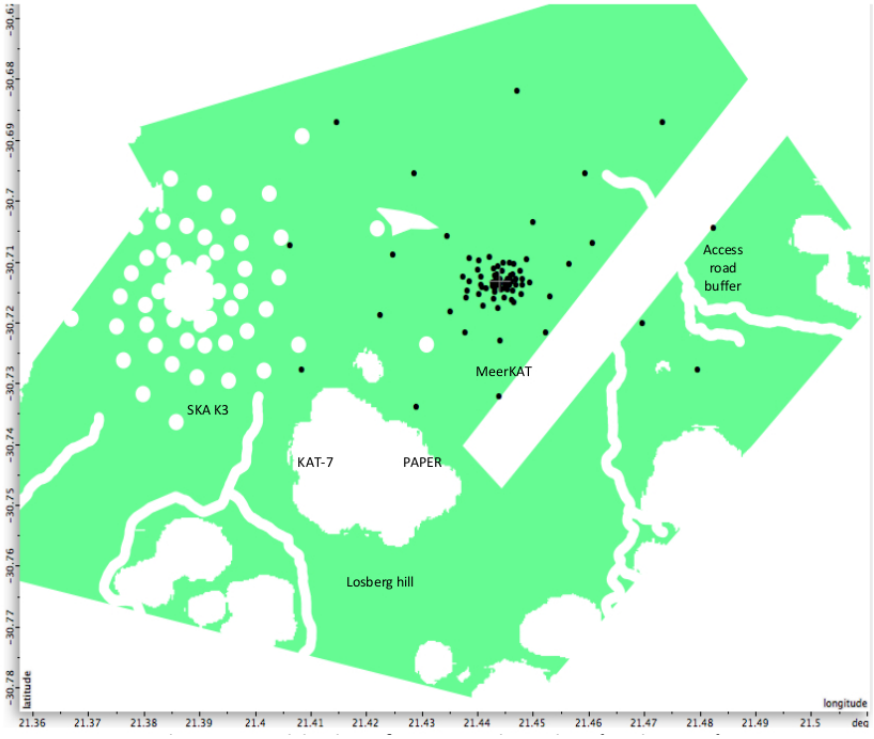

Figure 3.10: Positioning of the MeerKAT array on site using the site mask.

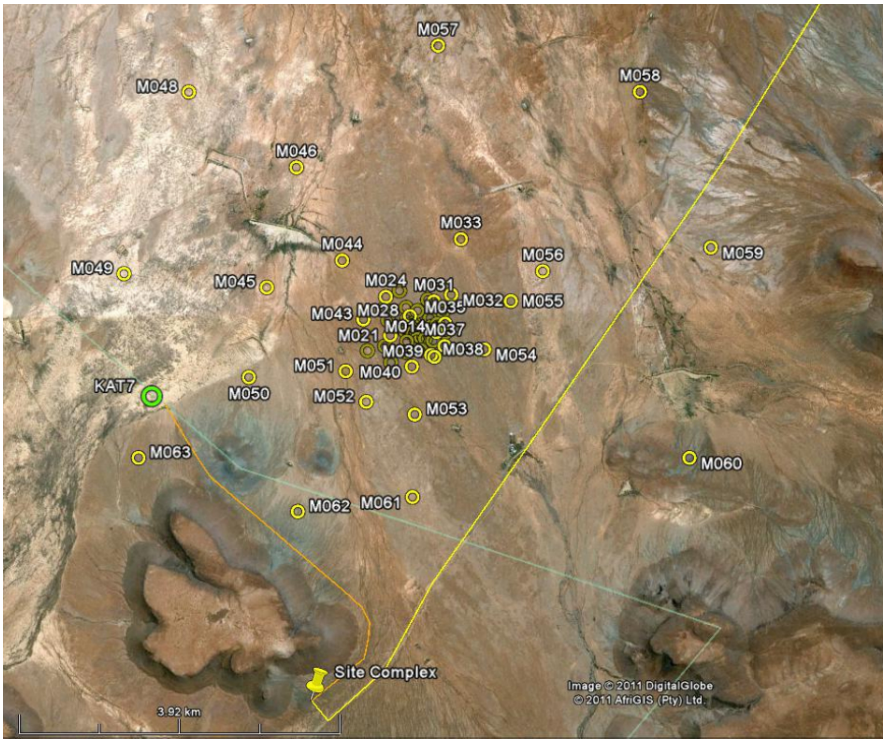

Figure 3.11: Position of the MeerKAT array and site complex.

3.8.1 Dish structure

The final configuration selected for the array dish structure is a 13.5 metre projected diameter, "feed-down" offset Gregorian optical configuration (Fig. 3.12). This choice was a significant developement risk, because it was a new mechanical design and not prototyped.
The key advantage of this choice over the symmetric centre-fed parabola is the unblocked aperture that results in:
- **(1)** A high aperture efficiency ranging from 0.71 to 0.81 across the UHF and L-band frequencies (580 - 1015 MHz and 900 - 1670 MHz respectively), and hence a good sensitivity;
- **(2)** Low far sidelobes, providing some immunity to terrestrial and airborne RFI, and the attenuation of strong cosmic radio sources outside of the imaging field;
- **(3)** An almost circularly-symmetric main beam and inner sidelobe pattern, hence a reduction in the calibration challenges provided by the primary beam rotating relative to the sky (i.e. slow variation of the time and direction dependent beam pattern Jones matrices);
- **(4)** Elimination of ground radiation scattering off of feed legs into the feed, hence reducing the system temperature and thus increasing sensitivity;
- **(5)** The reduction of internal specular reflections and associated passband ripples (i.e. a Jones matrix that is smooth over frequency);

- **(6)** A large volume for locating multiple receiver systems and support services on the receiver index platform that does not compromise the clean optical path, hence increasing the utility of the telescope as a facility instrument.
Moreover, the "feed-down" configuration has these advantages over the "feed-up" configuration:
- **(7)** Reduced spill-over from ground radiation, hence reducing the system temperature and improving the sensitivity;
- **(8)** Easy and safe access to the receiver systems when the antenna is stowed at its lowest elevation.
A disadvantage of the feed-down configuration is that the minimum elevation limit is constrained to 15°. This limit is imposed by the geometry of the optical path and mechanical interference between the elevation structure and the pedestal tower.
High dynamic range, wide-field continuum imaging requires that the Jones matrix for the primary beam pattern remains stable over the characteristic time-scales of the visibility calibration cycle. This requirement was a key driver of the specifications for the MeerKAT dishes.

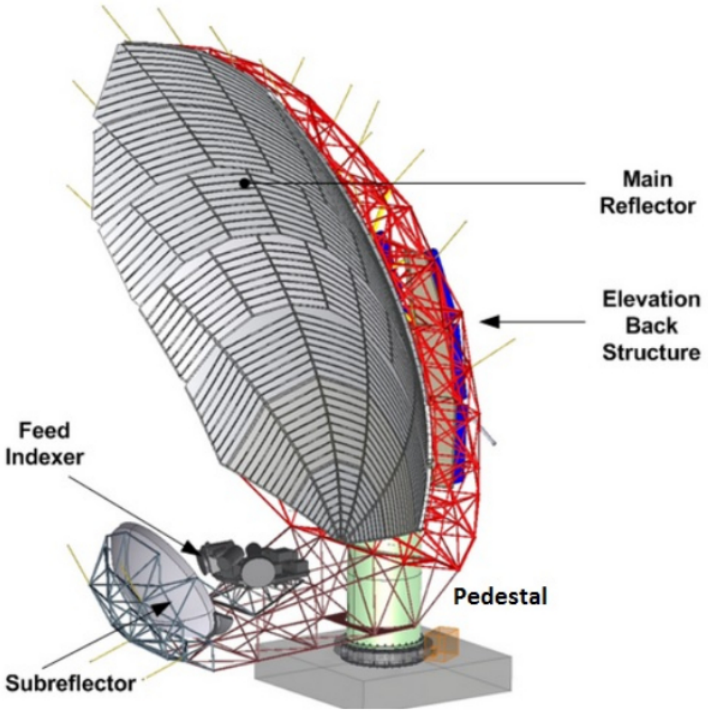

Figure 3.12: A schematic view of the MeerKAT dish structure showing the major elements of the design.

3.8.2 Receivers

The UHF-band and L-band feed horns and receiver systems are of very similar design, with the wavelength dependent scaling of the dimensions of the waveguide and ortho-mode transducer (OMT) components being the largest difference between them. The OMT is made from a pair of orthogonal dipoles in the back of a shorted waveguide as shown in Fig. 3.13.
The L-band receiver (0.9 - 1.67 GHz) is installed from Phase-1, which will be followed by the UHF-band (580 MHz - 1.015 GHz) and X-band (8 - 14.5 GHz) receivers in Phase-2. The receiver indexer allows each dish to carry multiple receivers simultaneously and is able to perform a receiver switchover in less than one minute.
The feed horns have a wide flare angle and employ concentric choke rings to control the feed beam pattern. The feed beam patterns were optimized to provide optimum System Equivalent Flux Density (SEFD), sidelobe and polarization performance across the operating frequency range in the context of the dish optical configuration. The main reason for adopting sub-octave receiver systems in preference to wide-band design was to obtain optimal sensitivity and primary beam performance.
The sidelobe specifications are driven by the requirements for high dynamic range continuum imaging and attenuation of RFI cosmic sources away from the field of view.
The polarization specification is driven from the requirements of precision pulsar timing and high dynamic range continuum imaging.
The improvement in sensitivity resulted from the usage of two-stage Gifford-McMahon (G-M) cryogenic refrigerators to cool the Low Noise Amplifier (LNAs) and OMT component.
The thermal stabilization is necessary to achieve the gain stability specifications derived from the system-level requirement to achieve high imaging dynamic range.

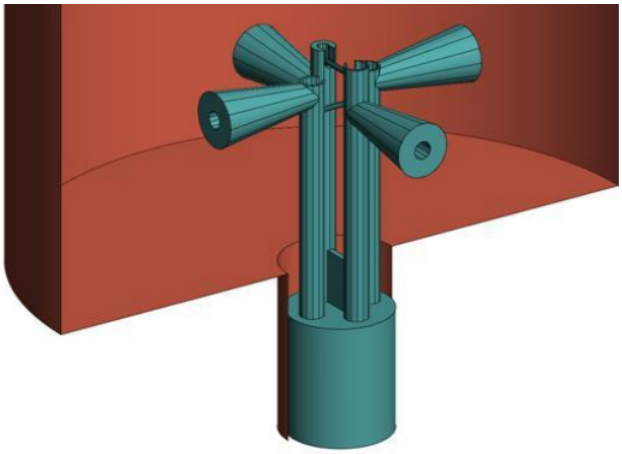

Figure 3.13: MeerKAT L-band OMT as designed schematically.

3.9 Telescope performance

As individual telescope components were assembled into increasingly complex functional units, initial acceptance tests were performed on low-level devices, then more sophisticated tests were performed as subsystems and systems assembly progressed. The majority of the most important MeerKAT performance specifications are allocated to the receptor, comprising the dish structure, feed horn, receiver and digitizer.

MeerKAT was optimized for point-source sensitivity because this was a common requirement for all of the LSPs. The original specification for the MeerKAT aggregate system-equivalent flux density (SEFD) was 12.55 Jy. For the 64-element MeerKAT array this corresponds to a per-receptor SEFD of 800 Jy. Figure 3.14 shows the results of L-band SEFD measurements made with MeerKAT receptor M062, the second receptor that was installed and integrated (the first was M063). The plot shows that the SEFD is far better than the original specification across the entire L-band frequency range, and that the measured curves follow the predicted performance quite well.

The large deviations in the measured curves are due to RFI from satellites and mobile phone base stations, and Galactic HI (at 1420 MHz). The measurements shown were made at relatively low elevation of 37°. Tipping curve measurements show that the SEFD at 15° elevation is less than 20% higher than at zenith over all L-band frequencies.

This improvement in sensitivity over the original specification was a result of the design choiches made at the CoDR and PDR stages of the project, specifically the choice of Gregorian offset optics, sub-octave receivers and G-M cryo-coolers.

The key antenna performance factors affecting imaging dynamic range are telescope pointing accuracy and stability, and the primary beam pattern characteristics.

The characteristics of the antenna L-band primary beam pattern were derived using

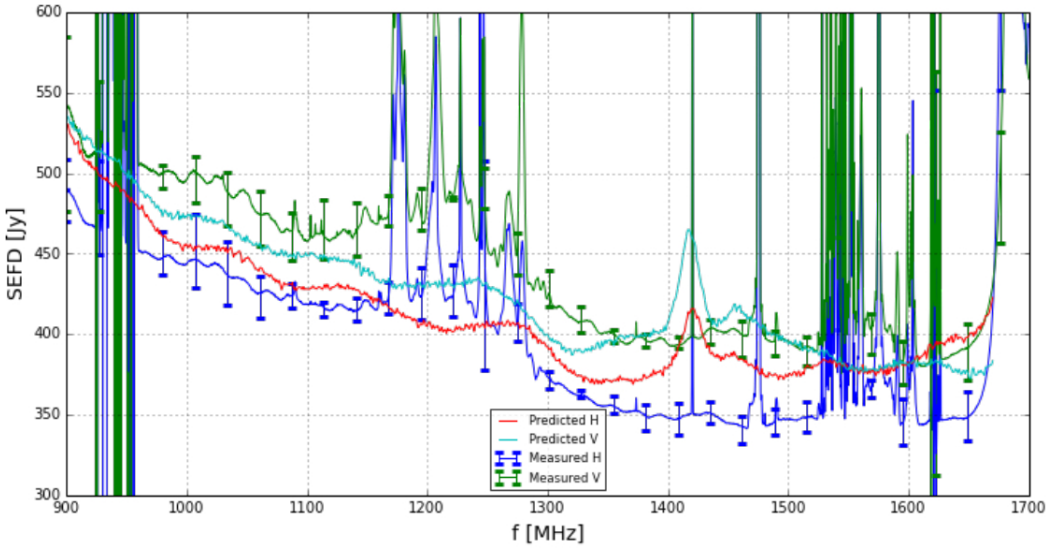

Figure 3.14: The spectrum of the SEFD of a single antenna at 37° elevation derived from L-band measurements made on antenna M062 using three different L-band receivers. The error bars on the measured curves represent the total range of all measurements made with all three receivers.

various techniques, including holography. Figure 3.15 compares the beam pattern at 1350 MHz predicted using a full-wave electromagnetic simulation against the beam pattern of MeerKAT receptor M062 measured using L-band holography (using a satellite beacon). These plots show that the measured beam pattern matches the simulations very closely, despite the fact that M062 was known to have a collimation problem at the time of the measurement. The measured patterns indicate that the second sidelobe is comfortably less than the -23 dB specification, and that the cross-polarization specifications are exceeded by a large margin.
For a very recent study on the MeerKAT primary beam modelling we remand to Asad et al. (2019). They used both the astro-holographic (AH) technique (it was targeted at the astronomical object 3C 273), and the more physical approach based on the electromagnetic (EM) simulation of an antenna. The main goal was to derive a formalism to be applied for the direction dependent calibration and imaging, given any dataset. The diagonal elements on the Jones E matrices, i.e. the matrices that represent the two formalisms, well matched each other, but the off-diagonal elements vary significantly and the difference increases with frequency (see Asad et al., 2019). However, the MeerKAT excellent beam characteristics vindicate the selection of the Gregorian offset optical configuration and sub-octave feeds.

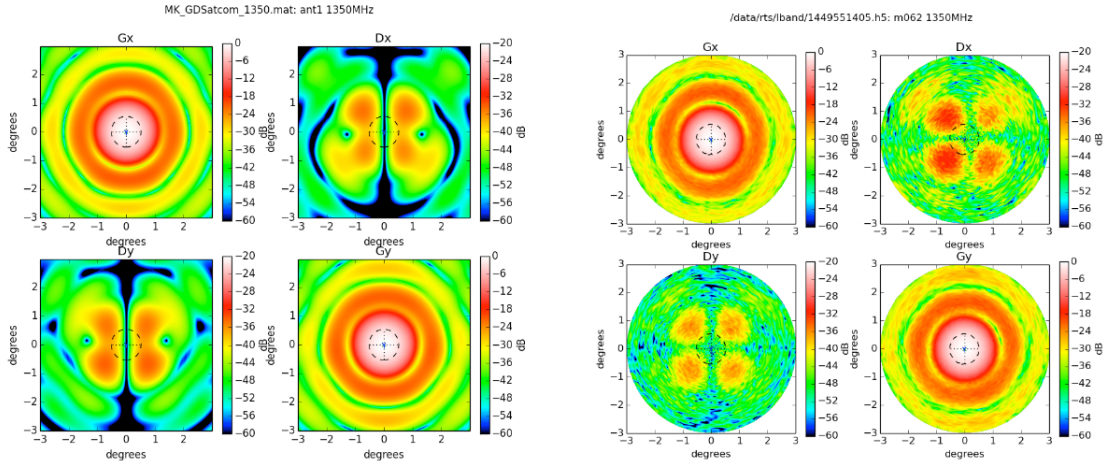

Figure 3.15: Comparison for the simulated MeerKAT L-band (1350 MHz) primary beam derived using electromagnetic simulations (left) and the beam of receptor M062 measured using holography. The measurement was made prior to final collimation of the reflector surfaces and feed receiver indexer.

3.10 Science with MeerKAT

Today MeerKAT is fully operational with 64 antennas in the array, and it is expected to give unprecedent results being the largest and most sensitive radio telescope array in the centimetre wavelenght regime in the southern skies until the SKA-1 MID. Since the first observational tests MeerKAT revealed its high level of performance. On July 13th 2018 the telescope was inaugurated by the presence of Deputy President of Republic of South Africa. During the lounch event the image of the central region of the Milky Way was shown, giving a strong impact demonstration on the science capabilities of the new instrument (see Fig. 3.16).

Another important science case with MeerKAT is related to the study of magnetars, which are the most magnetic objects known in the universe. They are a class of neutron stars with high energy emission powered by the decay of ultra-strong magnetic fields. Radio observations from MeerKAT enabled the first detection of pulsations for the neutron star PSR J1622-4950 (see Camilo et al., 2018).

The examples reported in this section show clearly the high level of science that MeerKAT is able to produce. This results showed also that MeerKAT is positively exceeding the originally planned specifictions and expectations.

The data considered in this thesis are from an early test phase of MeerKAT-16, i.e. only 16 antennas were operational at the time of the observation (April 2018). However, the images obtained and the analysis which we were able to perform, even though on early data, show all the potential of this instrument. Moreover, our analysis will be improved with more statistics and with the follow-up observation by means of MeerKAT 64.

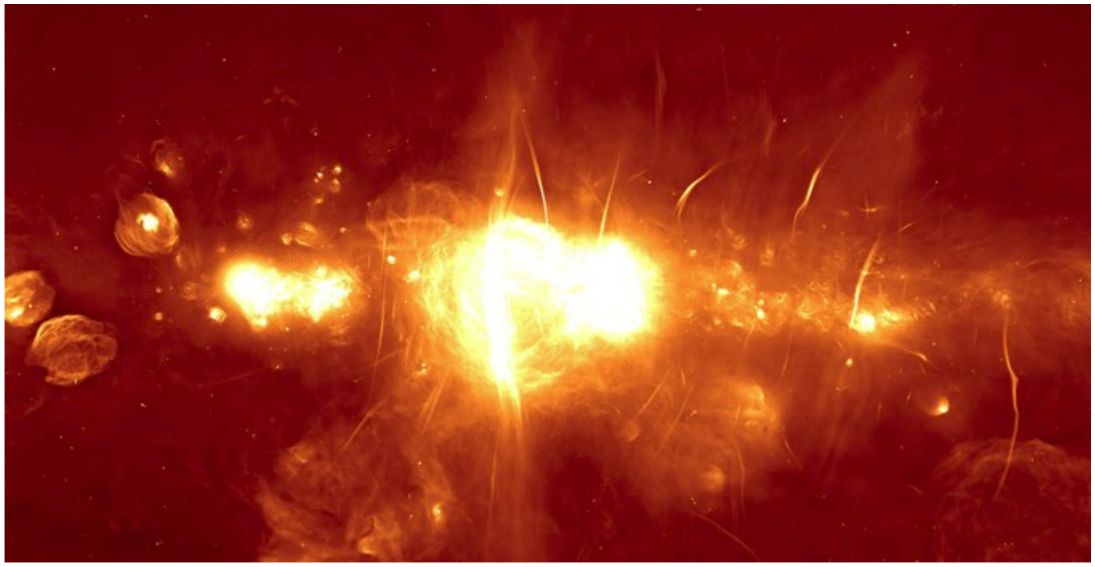

Figure 3.16: The MeerKAT view of the central region of our Galaxy. The area corresponds to about 1.000 light years by 500 light years (credits by South African Radio Astronomy Observatory).

Chapter 4

Data analysis

In this Chapter we present the new radio observations and the analysis performed with the MeerKAT and uGMRT interferometers, two new instruments in phase of construction at the time of our analysis. We report the data reduction steps, the images obtained and the strategy adopted in order to create the final catalogues. In the second part of this Chapter, we report the optical-IR and spectroscopic analysis. The two targets selected from our initial sample, MACSJ1931-2634 and A1300, are analyzed in Chapters 5 and 6 respectively. They were observed in the same period: Spring 2018, i.e. during the second year of my PhD.

4.1 Radio analysis

4.1.1 MeerKAT observations and data reduction

We observed during the AR-1 stage (only 16 antennas were fully operational) MACSJ1931-2634 and A1300 galaxy clusters. The central frequency is 1.2 GHz (i.e. λ= 0.23 m), and the observation covered an area of 2 $\times$ 2 deg^2.
MACSJ1931-2634 was observed on May 2nd 2018, and A1300 was observed on April 21st 2018.
In Tab. 4.1 we report the details of the observations. Each observation was carried out with a 856 MHz bandwidth, the correlation of the signal was carried out using a total of 4096 channels, each 208 kHz wide (4k channelization mode), with 8s integration time. The observation of MACSJ1931-2634 has the resolution of 5" $\times$ 3" in p.a. $\sim$ 136° and the observation of A1300 has the resolution of 12" $\times$ 5" in p.a. $\sim$ 113°. The difference of the beam size is mainly due to the different uv-coverage as visible in Fig. 4.1.

To obtain the final images for our analysis, the data reduction was divided into two parts: we performed the a-priori calibration first, by means of a dedicated piepline mainly based on CASA tasks. Then we performed the self-calibration using

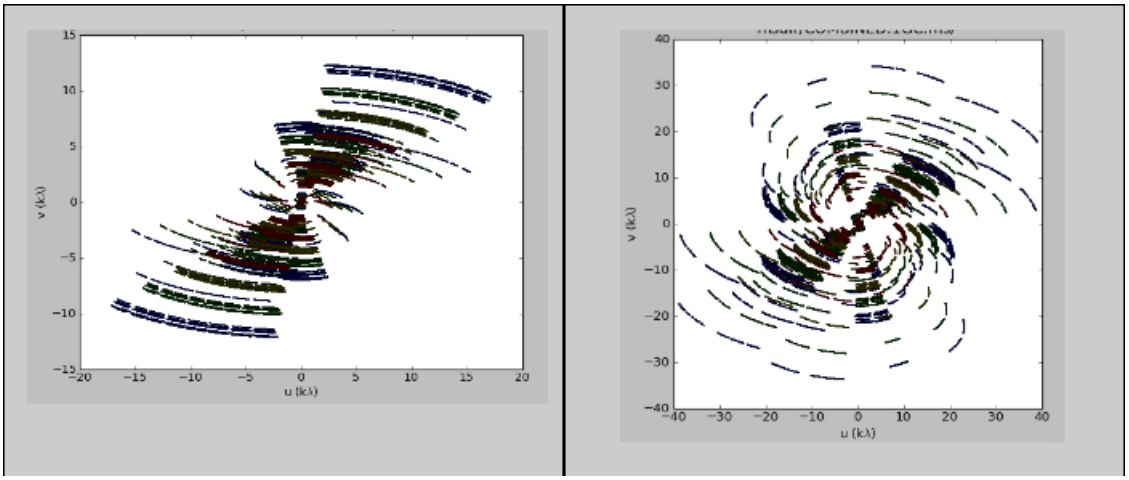

Figure 4.1: The image shows the resulting uv coverage of A1300 (left panel) and of MACSJ1931-2634 (right panel).

Table 4.1: Details on MeerKAT observations

target	α (J2000)	δ (J2000)	ν (MHz)	BW (MHz)	tos (hr)	FWHM; pa (arcsec); (°)	rms (mJy/b)
A1300	11:31:54.4	-19:55:42.0	1283	856	2.40	12×5; 113	0.04
MACSJ1931 -2634	19:31:49.6	-26:34:34.0	1283	856	2	5×3; 136	0.04

a second dedicated pipeline based on WSClean and Cubical packages related each other thanks to Stimela (I will provide a brief description of the packages adopted in the next Section).
In the first pipeline, the initial preprocessing of the data was carried out using 'flagdata' first, in order to flag autocorrelations and the edges of the band. Then, using AOflagger (Offringa et al., 2012, 2013), an automatic flagging of RFI was performed. To set the amplitude scale, we used the primary flux calibrator PKS1934-638 (Reynolds, 1994). We then solved for delay, i.e. for K gain, with 'gaincal'. We solved for B gain, performing the bandpass with the same task 'gaincal' and the same calibrator as used for the amplitude. We then solved for G gain, the G calibrator is J1141-2850, and finally, we transferred the flux scale with the 'fluxscale' task. We applied the solutions with 'applycal' and then we performed another run of automatic flagging on the target source. We then split our dataset containing only the target.

The second pipeline was created to perform the self-calibration, i.e. the attempt to reconcile a model of the target field with the observed visibility data by solving for the direction-independent gains (Cornwell & Wilkinson, 1981; Kenyon et al., 2018). The self-calibration was performed with four iterations with phase-only solutions on the entire band, improving the model of clean components at each step. To perform the self-calibration, we first created a model running WSClean (for every image we adopted the full resolution, i.e. Briggs weighting with "robust -2"). The pixelsize is 1arcsec and the image size is 8192 × 8192 pixels. We cleaned using a combination of a mask manually created and an auto-masking option. The stop criterion is given by the auto-threshold parameter which is set on 0.25 sigma (where sigma is the theoretically estimated noise of the map). The MFS deconvolution mode is obtained in WSClean by the parameter "joinchannels" which is set on True mode. The "mgain" parameter activate the Cotton-Schwab imaging, which is set on 0.85. To keep into account the rms variation throughout the field, we enabled the parameter "local-rms-window"=300.
To perform the self-calibration with CubiCal, we choose first a longer solution interval set by the parameter "g-time-int". In four iterations the "g-time-int" is 40, 30, 20, 5 respectively, meaning 5 minutes, 4 minutes, 2 minutes and 30 seconds, obtained by inspecting the solutions at each steps. We followed for both the targets, MACSJ1931-2634 and A1300, the same strategy.
In order to get the intrinsic fluxes, we performed on MeerKAT images, a primary beam correction to take into account the beam response across the field of view (FOV). The MeerKAT FOV at 1.2 GHz is ~ 1 degree (see Mauch et al., 2020).
At the time of our analysis, a model for MeerKAT primary beam was not available. The primary beam correction was based onto an analitic correction derived by fitting the MeerKAT beam with holographic models (Asad et al., 2019). The analitic correction that we applied to our apparent fluxes is given by:

$$cos^6(a \times \frac{1}{\lambda_c} \times \theta) \tag{4.1}$$

where a is a fitting parameter which is a=7.3 m, λ_c is the central wavelength in m, whereas θ is the distance of each source from the phase center and it is expressed in radians.

4.1.2 Stimela, WSClean and CubiCal

Stimela (the Zulu world for a "train"; Makhathini, 2018) is a platform independent radio interferometry scripting framework based on Docker and Python. In this framework, radio interferometry related tasks such as imaging, calibration and data synthesis, are executed in Docker containers. In fact, whithin this framework, the packages that perform these tasks are Python modules. Stimela does not do any data processing, synthesis or analysis but merely offers a simple interface to

packages that perform these tasks. The aim of Stimela is to provide a user friendly and modular scripting environment that gives general users easy access to novel radio interferometry calibration, imaging and synthesis packages.
WSClean (Offringa et al., 2014) is a wide-field interferometric imager[1], written in c++ language, that uses the w-stacking algorithm [2] and can make use of the w-snapshot algorithm. It has been tested on data from the Murchison Widefield Array (MWA) and it has been found to be an order of magnitude faster than CASA's w-projection. The w-stacking methods grids visibilities on different w-layers and performs the w-corrections after the inverse Fourier transforms. The w-snapshot imaging is a technique that combines warped-snapshot imaging with a w-correcting technique, such as w-projection or w-stacking (Cornwell et al., 2012). Offringa et al. (2014) predicted that the computing cost is reduced and the imaging is 2 to 12 times faster, depending on the arrays configuration.
CubiCal[3] is a Python package which implements several accelerated gain solvers which exploit complex optimization. It can perform both the direction-independent and direction-dependent calibration. It is expanded in Cython, a Python-like language from which C-code can be generated. The use of Cython accelerates the implementation, that is accelerated further by the use of multi-processing strategy. The problem of multi-processing large overheads is mitigated by the use of shared memories. CubiCal is characterized by high modularity. Kenyon et al. (2018) have successfully applied CubiCal for calibration to both simulated and real data, showing to be substantially faster than its most comparable competitor.

4.1.3 The images

The final images that we obtained after the data reduction have sizes 2×2 deg^2. We obtained them by means of WSClean adopting wheighting "Briggs" scheme ad robust "-2" to get the full resolution.
MACSJ1931-2634 resolution is 5×3 arcsec in p.a. $\sim 136°$ whereas A1300 resolution is 12×5 arcsec in p.a. $\sim 113°$.
In Fig. 4.2 and 4.3 we report the A1300 and MACSJ1931-2634 fields in a restricted area of 30 arcmin radius (green circle), i.e. 0.785 deg^2. This is the area of interest for our analysis and the area of the extraction of the catalogues. Moreover, this is the distance within which the primary beam correction that we applied introduces an error of less than 10 % on the flux densities. The central noise level is 0.04 mJy/b in both the images. There are some residual patterns in A1300 field, indicative of some low-level residual RFI. Unfortunately, even though a heavier flagging performed on A1300 it was not possible to entirely remove them. There remain some phase

[1] http://sourceforge.net/p/wsclean
[2] https://www.skatelescope.org/uploaded/59116_132 _Memo_Humphreys.pdf
[3] https://github.com/ratt-ru/CubiCal

artefacts around the brightest sources, which was not possible to entirely remove during the calibration. However, they are localized around the bright sources and have a very little impact on the majority of the map and nearby sources.
The amplitude self-calibration was not performed in order to not introduce any amplitude errors (see Williams et al., 2016).
In Fig. 4.4 we report a zoom-in of the central region of 12 arcmin radius (0.125 deg^2), which is the region that we considered for the radio-optical cross match (see Chapter 5 and 6).

4.1.4 Comparison with the NVSS survey

Given the uncertanties in the preliminary fitted model of MeerKAT primary beam, we compared our flux densities with those from NRAO VLA Sky Survey (NVSS; Condon et al., 1998) even though our fluxes are measured at 1.2 GHz.
We have first degraded the resolution of our MeerKAT images with AIPS task CONVL in order to compare the fluxes at the same resolution of NVSS, which is 45". We then selected only those sources which are isolated (i.e. not blended) to ensure one-to-one matches. We measured integrated flux densities at 20 arcmin, 30 arcmin and 40 arcmin from the field center.
The results of our comparison are shown in Fig. 4.5 for A1300 and MACSJ1931-2634 respectively. Even though it is difficult to compare directly data which have different observational characteristics, and data reduction steps, this test shows that the data have good correlation with each other, and consistent with the error within few tens of percent (see White et al., 2010; Williams et al., 2016, for comparison).

4.1.5 uGMRT observations and data reduction

We observed with the uGMRT interferometer A1300 galaxy cluster on May 24th 2018 and MACSJ1931-2634 galaxy cluster between May 24th and May 25th 2018. The observation covered an area of 2×2 deg^2. The central frequency is 640 MHz (i.e. $\lambda = 0.46$ m).
In Tab. 4.2 we report the details of the observations. Each observation was carried out with a 200 MHz bandwidth, the correlation of the signal was carried out using 2048 channels, each 97 kHz wide, with 10s integration time. The observation of A1300 has the resolution of 5" × 3" in p.a. 43°, and the observation of MACSJ1931-2634 has the resolution of 5" × 4" in p.a. 169°.

To obtain the final images, the data reduction and calibration were divided into two parts: we performed the a-priori calibration first, using a standard procedure performed by CASA package. Then we performed the self-calibration dividing the band into four sub-bands, and considering each separately. The final images were

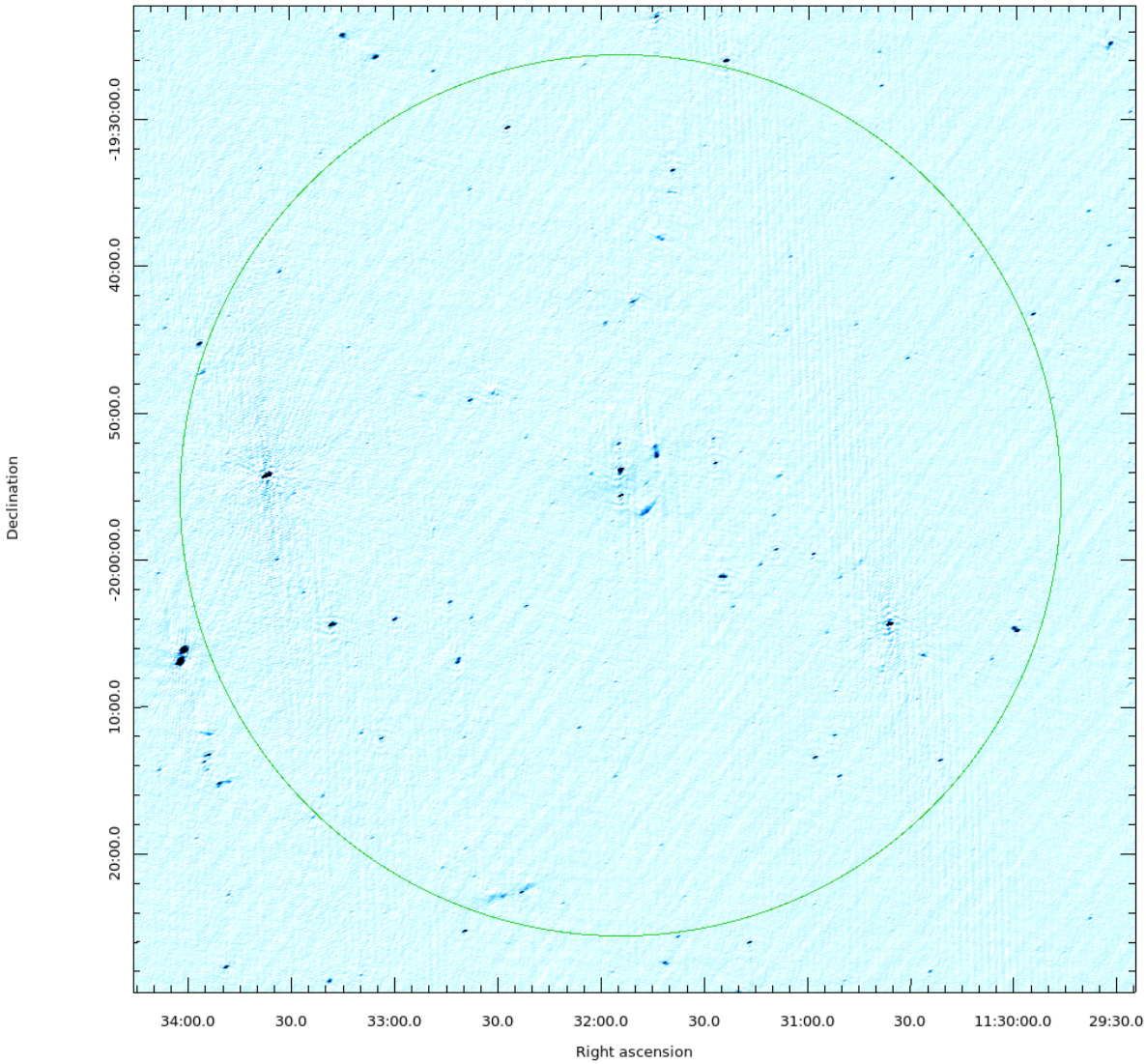

Figure 4.2: The image shows the field surrounding A1300 galaxy cluster at 1.2 GHz which covers an area of 0.785 deg^2 (green circle). This is the area of interest in our analysis (i.e. the area within which we extracted the catalogues), and the area within which the primary beam correction applied introduces an error of less than 10% on the flux density. The noise is 0.04 mJy/b with resolution 12 $\times$ 5 arcsec in p.a. $\sim$ 113°.

obtained merging the four sub-bands self-calibrated separately.
During the a-priori calbration we flagged first with 'flagdata' task the bad antennas (i.e. C12 and W02), the first 15 seconds of each scan and the channel 0. We then set the amplitude scale using as flux calibrator 3C286 for both A1300 and MACSJ1931-2634. We solved for delay K, bandpass B (3C286 is also the bandpass calibrator in both the observations), and G gain, using as phase calibrators J1130-148 for A1300 and J1923-210 for MACSJ1931-2634. We then set the scale of flux with 'fluxscale'

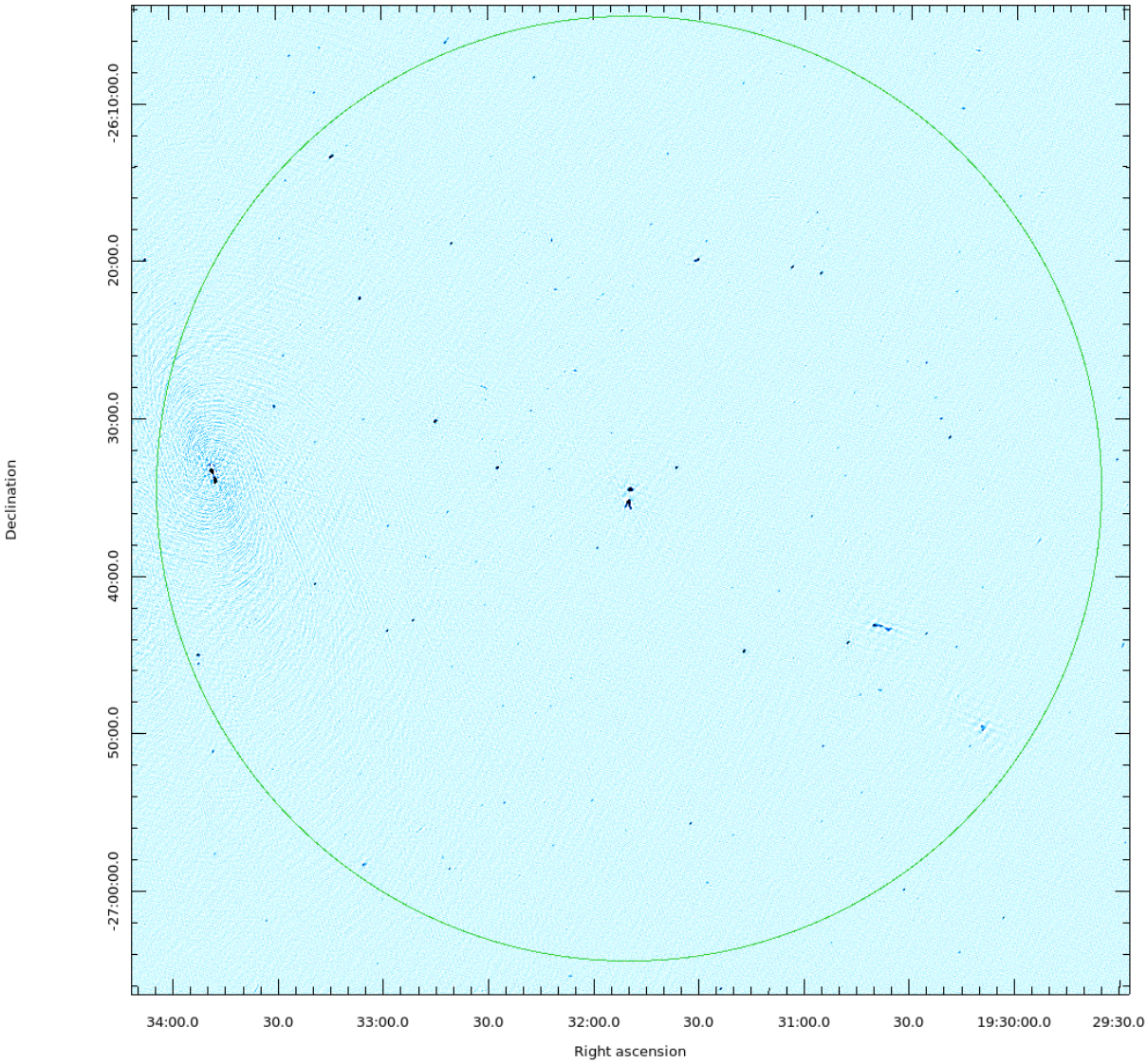

Figure 4.3: The image shows the field surrounding MACSJ1931-2634 galaxy cluster at 1.2 GHz which covers an area of 0.785 deg^2. This is the area of interest in our analysis (i.e. the area within which we extracted the catalogues), and the area within which the primary beam correction applied introduces an error of less than 10% on the flux density. The noise is 0.04 mJy/b with resolution 5 $\times$ 3 arcsec in p.a. $\sim 136°$.

and finally we applied the solutions with 'applycal'. We did more flagging with casa 'rflag' mode and then we splitted the dataset containing only the target.
To perform the self-calibration we run a CASA script alternating 'tclean' task and 'gaincal' task. We splitted the band into four subbands of 50 MHz each and 512 channels and we runned four self-cal separately. The soution interval was shortened from 300s, to 120s, 60s, 30s improving the model of clean components and inspecting

Table 4.2: Details on uGMRT observations

target	α (J2000)	δ (J2000)	ν (MHz)	BW (MHz)	tos (hr)	FWHM; pa (arcsec); (°)	rms (mJy/b)
A1300	11:31:54.4	-19:55:42.0	640	200	2.7	5 × 3; 43	0.03
MACSJ1931 -2634	19:31:49.6	-26:34:34.0	640	200	3.3	5 × 4; 169	0.03

the solutions at every step. The task 'tclean' was used both to produce a model and to perform the imaging. We obtained two final images smaller than those obtained with MeerKAT: the pixelsize is 1 arcsec and the imsize is 5000 × 5000 pixels, i.e. 1.5 deg^2. We cleaned using a manually created mask first and then we runned the last image without the mask, until the threshold of 0.25 σ (theoretically estimated noise). We present the images in the next section.

4.1.6 The images

The final images that we obtained after the data reduction have sizes 1.5 × 1.5 deg^2. MACSJ1931-2634 resolution is 5 × 4 arcsec in p.a. $\sim 169°$, A1300 resolution is 5 × 3 arcsec in p.a. $\sim 43°$.
In Fig. 4.6 and 4.7 we report the A1300 and MACSJ1931-2634 fields in a restricted area of 30 arcmin radius (green circle), i.e. 0.785 deg^2. To be consistent with MeerKAT analysis, this is the area selected for our analysis, i.e. the area within which we extracted the catalogues. The central noise level is 0.03 mJy/b. There remain some phase artefacts around the brightest sources, which was not possible to entirely remove during the calibration. However, they are localized around the bright sources and they have a small impact on the nearby sources.
The amplitude self-calibration was not performed in order to not introduce any amplitude errors (see Williams et al., 2016). This is the reason why the relic in the A1300 image is not fully cleaned. However, the diffuse emission in A1300 (i.e. the halo and the relic) are not considered in the source catalogue.
We performed the primary beam correction to get the intrinsic fluxes, taking into account the beam response across the field of view. The uGMRT Field of View at 640 MHz is 0.6 $\sim$ degree. We did the correction with AIPS PBCOR task, giving the coefficient for the PBPARM parameters for the uGMRT, updated at December 1st 2018 (courtesy: Ruta Kale, NCRA, Pune).
In Fig. 4.8 we report a zoom-in of the central region of 12 arcmin radius (0.125 deg^2), which is the region that we considered for the radio-optical cross match, the

statistical source counts and the estimation of the Radio Luminosity Function (see Chapter 5 and 6).

4.1.7 The radio catalogues

We compiled our source catalogues using PyBDSF (Mohan & Rafferty, 2015), a source extractor package, to detect and characterize sources. We ran PyBDSF on the 'final' images, using the pre-beam-corrected images for MeerKAT (and we applied after the source extraction the analitic correction), and the primary beam-corrected images for uGMRT as the extraction images.
PyBDSF initially builds a noise map from the pixel data using variable mesh boxes. We used the parameters: adaptive_rms_box=True setting rms_box=(60,15) pixels around the bright sources (defined as having peaks exceeding 150σ, where σ is the sigma-clipped rms across the entire field). Using a smaller box near bright sources accounts for the increase in local rms as a result of calibration artefacts (see Williams et al., 2016, for comparison).
PyBDSF extracts sources by first identifying islands of contiguous emission above a given threshold, then decomposing this into Gaussian components. A peak of $5\sigma_{local}$ was used to define sources and an island threshold of $4\sigma_{local}$ was used to define the islands boundary (see Mahony et al., 2016, for comparison).
We used the group_tol parameter with a value of 10.0 to allow larger sources to be formed. This parameter controls how Gaussians within the same island are grouped into sources; this value is a compromise between selecting all Gaussians in a single island as a single source, thus merging too many distinct nearby sources, and selecting them as separate sources, thus separating the radio lobes belonging to the same radio sources (Williams et al., 2016). PyBDSF reports the fitted Gaussian parameters as well as the deconvolved sizes, computed assuming the image restoring beam. Following this method, we obtained four source catalogues, two MeerKAT at 1.2 GHz and two uGMRT at 640 MHz. We summarize in Tab. 4.3 our results. In columns 1 and 2 are reported the target name and the central frequency of the images, in column 3 is reported the catalogue threshold at 5σ (Prandoni et al., 2000; Owen & Morrison, 2008; Fomalont et al., 2006), in columns 4 and 5 the total extraction area and the number of reliable sources within the total area, after the visual inspection and the exclusion of the artefacts, in columns 6 and 7 the restricted area of 30 arcmin and the sources within this area.

4.1.8 Morphology of the sources

After the extraction of four catalogues, we established a criterion to classify morphologically the sources (Condon et al., 1998; Branchesi et al., 2006).

Table 4.3: Details on the radio catalogues

target	frequency (MHz)	threshold(5σ) (mJy)	total area (deg^2)	source total number	area (arcmin)	source final number
A1300	1283	0.20	2×2	339	30	112
MACSJ1931 -2634	1283	0.20	2×2	626	30	192
A1300	640	0.15	1.5×1.5	399	30	318
MACSJ1931 -2634	640	0.15	1.5×1.5	732	30	623

We first have estimated the flux errors, relatively to the peak flux and the integrated flux, according to the formula from (Klein et al., 2003):

$$\Delta F_i = \sqrt{(rms)^2 + (cF_i)^2 + (E_{fit})^2} \tag{4.2}$$

where the rms is the noise of the images, c is the residual calibration error (assumed conservatively of 10%) and E_{fit} is the fit error given by PyBDSF, which is negligible.
We then adopted the following equation to classify the source morphology.

$$|F_t - F_{peak}| < 2\sigma \tag{4.3}$$

where σ is given by:

$$\sigma = \sqrt{\sigma_{peak}^2 + \sigma_t^2} \tag{4.4}$$

We separate between three categories: all the sources for which the equation 4.3 is valid are classified as unresolved (pointlike). The sources for which the equation is not valid are classified as barely resolved, i.e. not pointlike even though a defined morphology is not evident. Finally, we defined as extended, those sources for which a well-defined morphology is visible. In our catalogues, only few sources within 30 arcmin radius are extended (see Chapters 5 and 6).

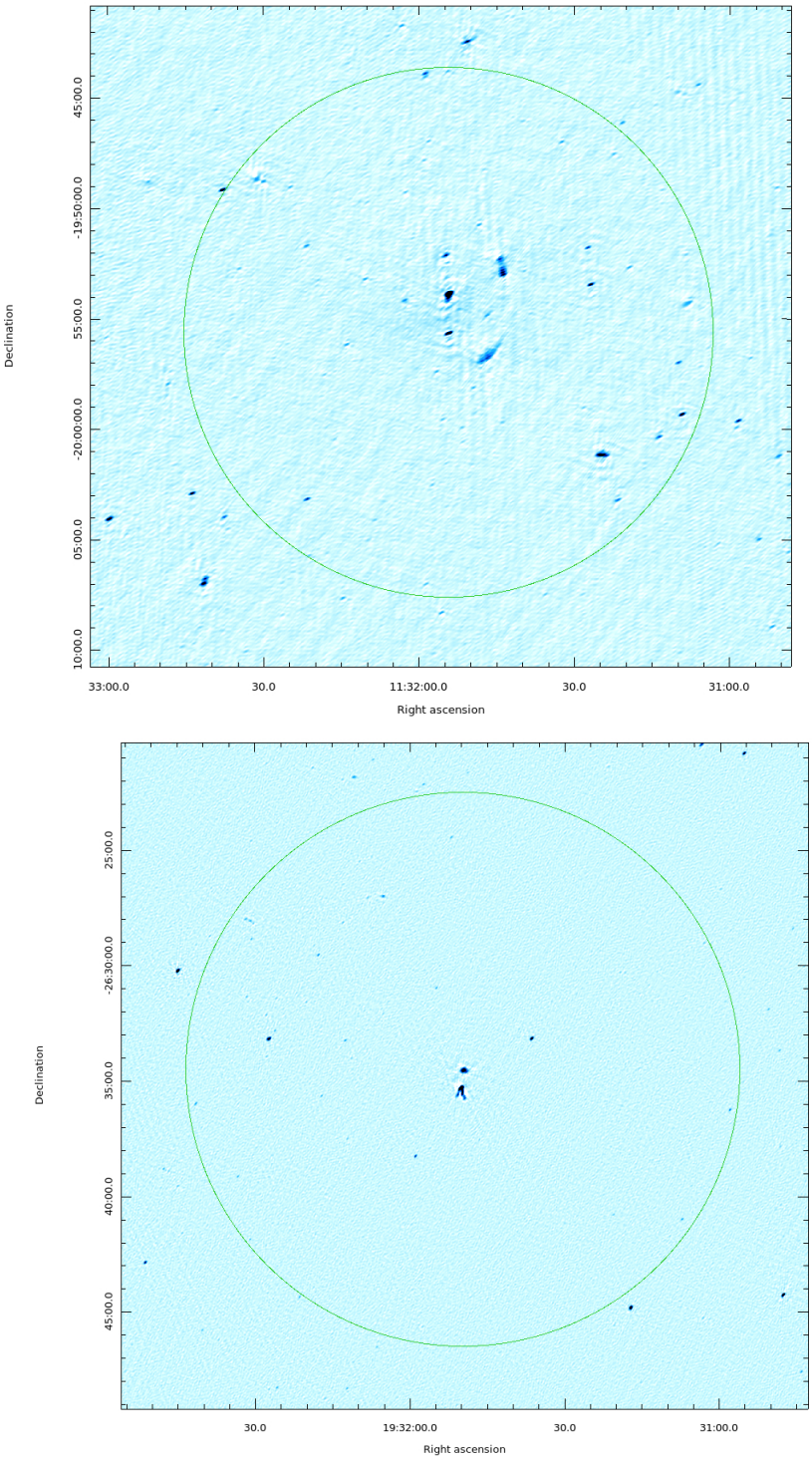

Figure 4.4: A zoom-in of A1300 (top panel) and MACSJ1931-2634 (bottom panel) fields in an area of 12 arcmin radius (green circle). The area corresponds to about two virial radii and was considered to perform the source counts, the radio-optical cross-match and the estimation of the Radio Luminosity Functions (see Chapter 5 and 6).

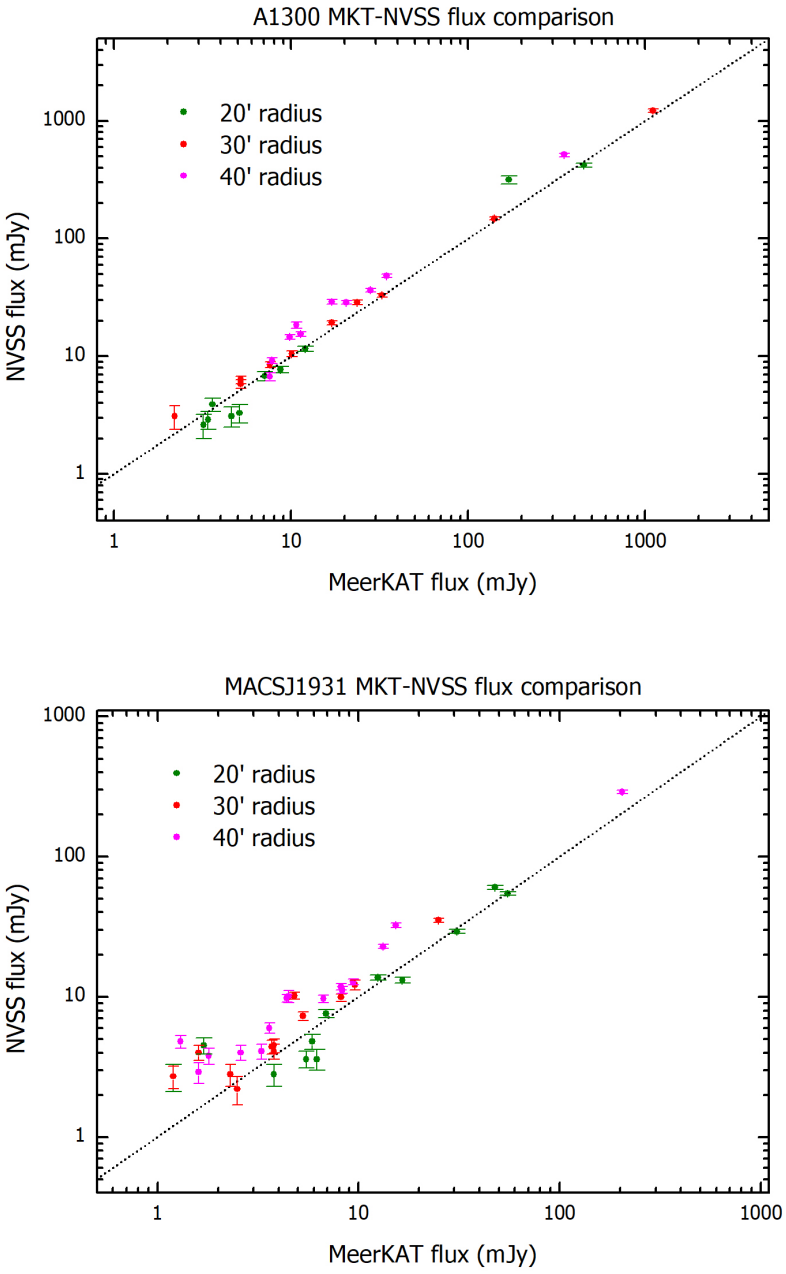

Figure 4.5: Comparison of the integrated flux densities of isolated (i.e not blended) radio sources in common between the NVSS survey and MeerKAT data, for A1300 (top panel) and MACSJ1931-2634 (bottom panel), at the same resolution of 45". The data show good correlation with each other up to 30' radius.

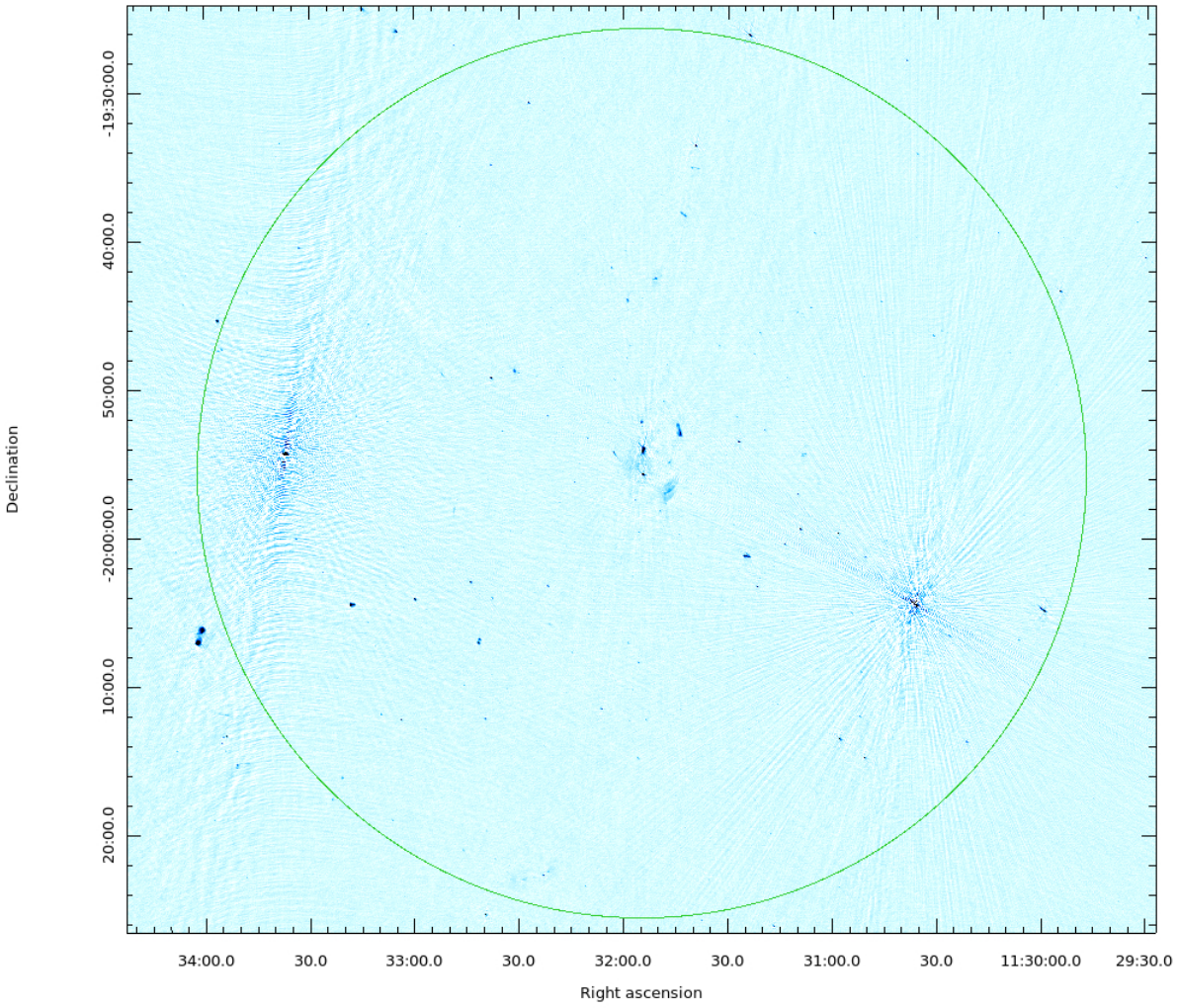

Figure 4.6: The image shows the field surrounding A1300 galaxy cluster at 640 MHz which covers an area of 0.785 deg^2 (green circle). This is the area of interest in our analysis (i.e. the area within which we extracted the catalogues). The noise is 0.03 mJy/b with resolution 5 $\times$ 3 arcsec in p.a. $\sim 43°$.

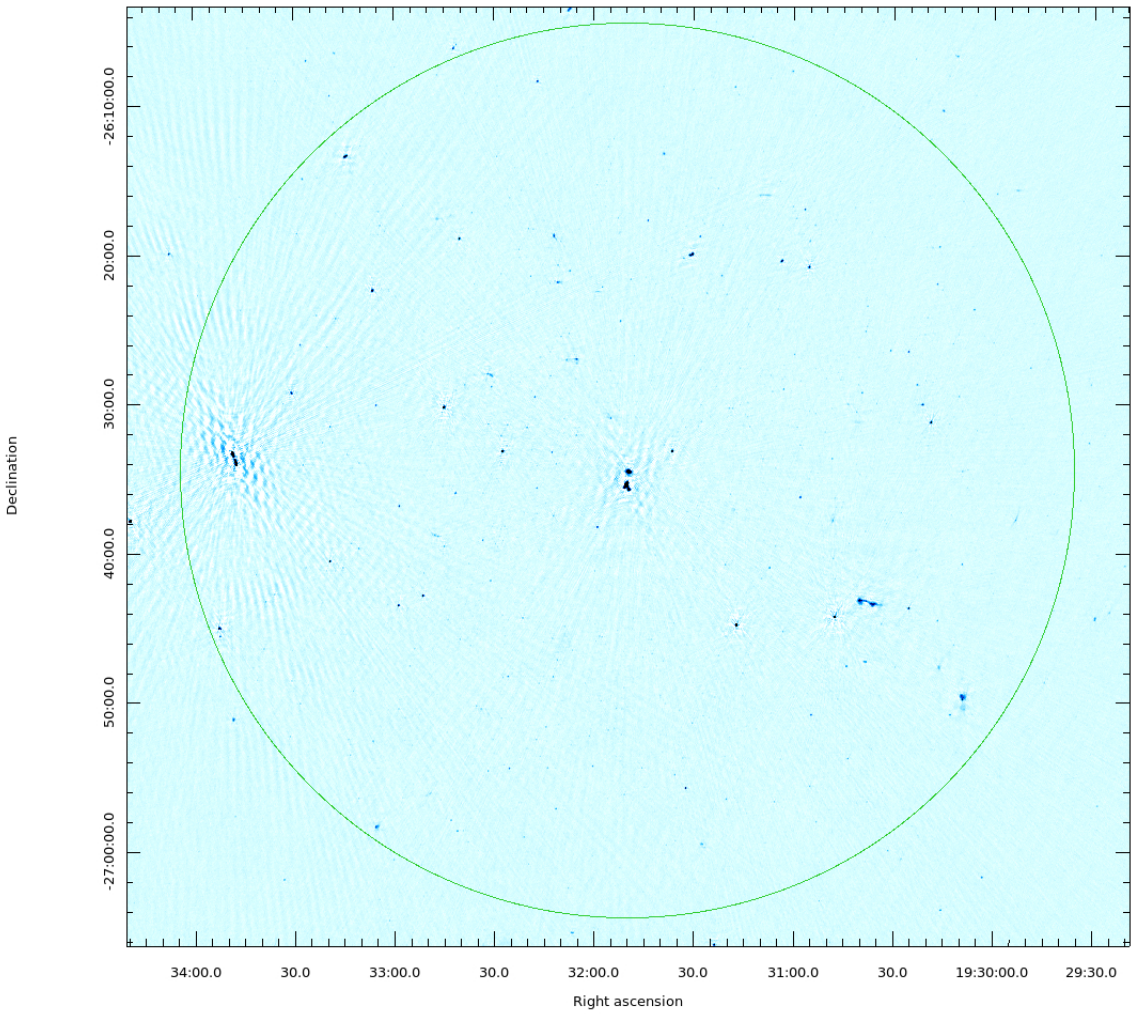

Figure 4.7: The image shows the field surrounding MACSJ1931-2634 galaxy cluster at 640 MHz which covers an area of 0.785 deg^2 (green circle). This is the area within which we extracted the source catalogue. The noise is 0.03 mJy/b and the resolution is 5 $\times$ 4 arcsec in p.a. $\sim 169°$.

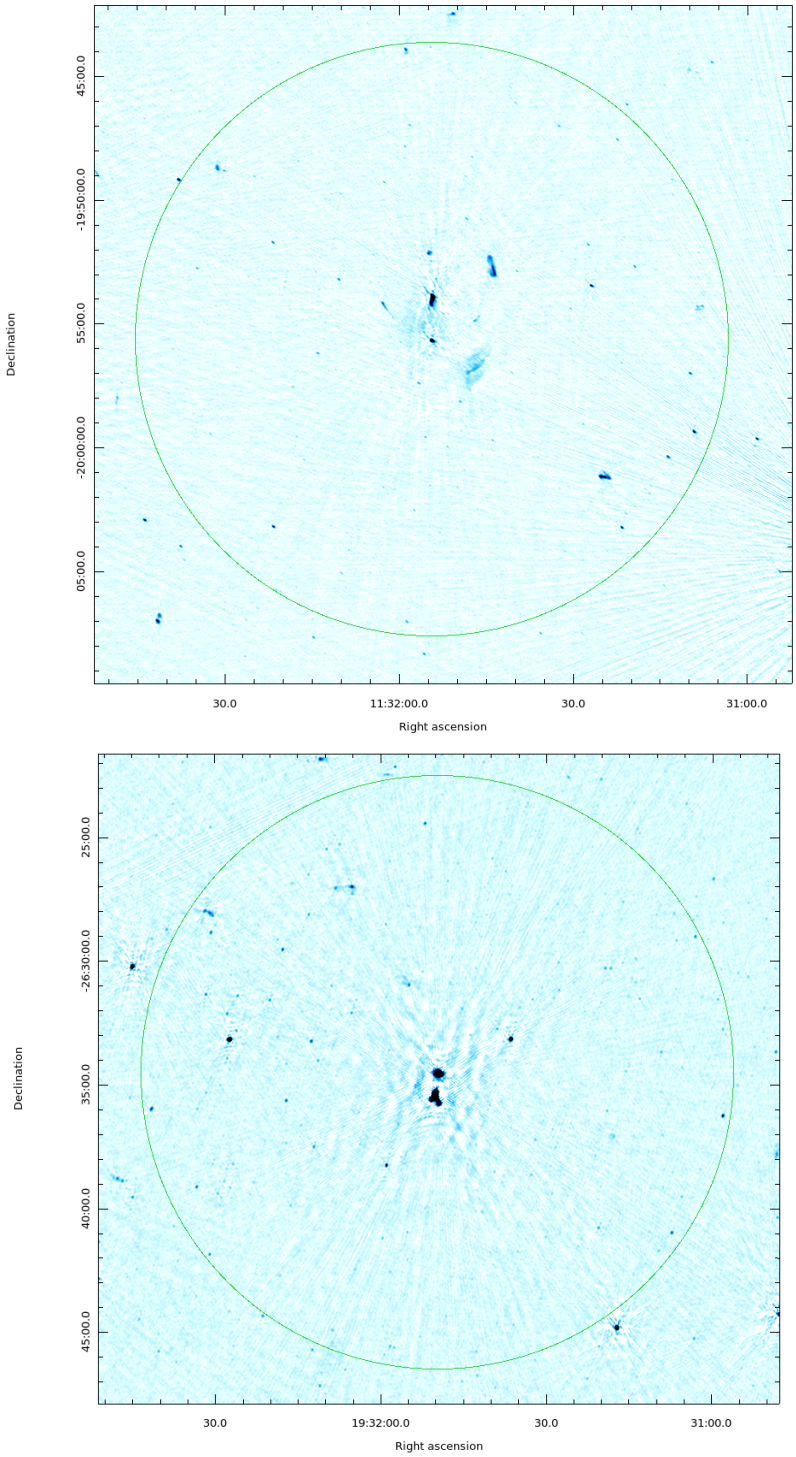

Figure 4.8: A zoom-in of A1300 (top panel) and MACSJ1931-2634 (bottom panel) fields in an area of 12 arcmin radius (green circle). This is the area considered for our statistical analysis and for the radio-optical cross-match.

4.2 Optical-IR Spectroscopic analysis

4.2.1 Suprime Images

Optical counterparts to the radio sources in MACSJ1931-2634 and A1300 were identified from *Subaru*-Suprime images. For MACSJ1931-2634 field, the images were taken from the CLASH project[4]. Images in B, V, RC, IC, Z filters have been used (Fig. 4.9). In Tab. 4.4 we report the details of the optical observations (2012 observation), i.e. the filter, the exposure time, the FWHM and the optical depth. We used in particular the RC and B band filters in order to cross-match our radio catalogues and to identify the optical counterparts.

Table 4.4: MACSJ1931-2634 optical observations

Filter	exposure (s)	FWHM (")	depth*
B	2640	1.20	25.59
V	1275	0.88	25.04
RC	4560	0.81	24.95
IC	1800	0.92	24.54
Z	1950	0.76	24.29

* depth: AB magnitude 5-sigma in 2arcsec-diameter aperture

Subaru-SuprimeCam raw images of A1300 have been retrieved from the SMOKA Science Archive[5]. The *g'* and *r'* datasets were secured by the Merging Cluster Collaboration (MCC)[6] in February 2014.
The images have been overscanned, bias and flat field corrected. The images have been taken in both filters at different position angle. The astrometric solution has been obtained by means of the Astromatic Program SCAMP (Software for Calibrating AstroMetry and Photometry)[7] and a catalogue extracted from the GAIA2 database as reference. The images have been then coadded using the Astromatic Program SWarp[8].

[4]https://archive.stsci.edu/missions/hlsp/clash/macs1931/data/subaru/
[5]https://www.re3data.org/repository/
[6]http://www.mergingclustercollaboration.org/
[7]https://www.astromatic.net/
[8]https://www.astromatic.net/software/swarp

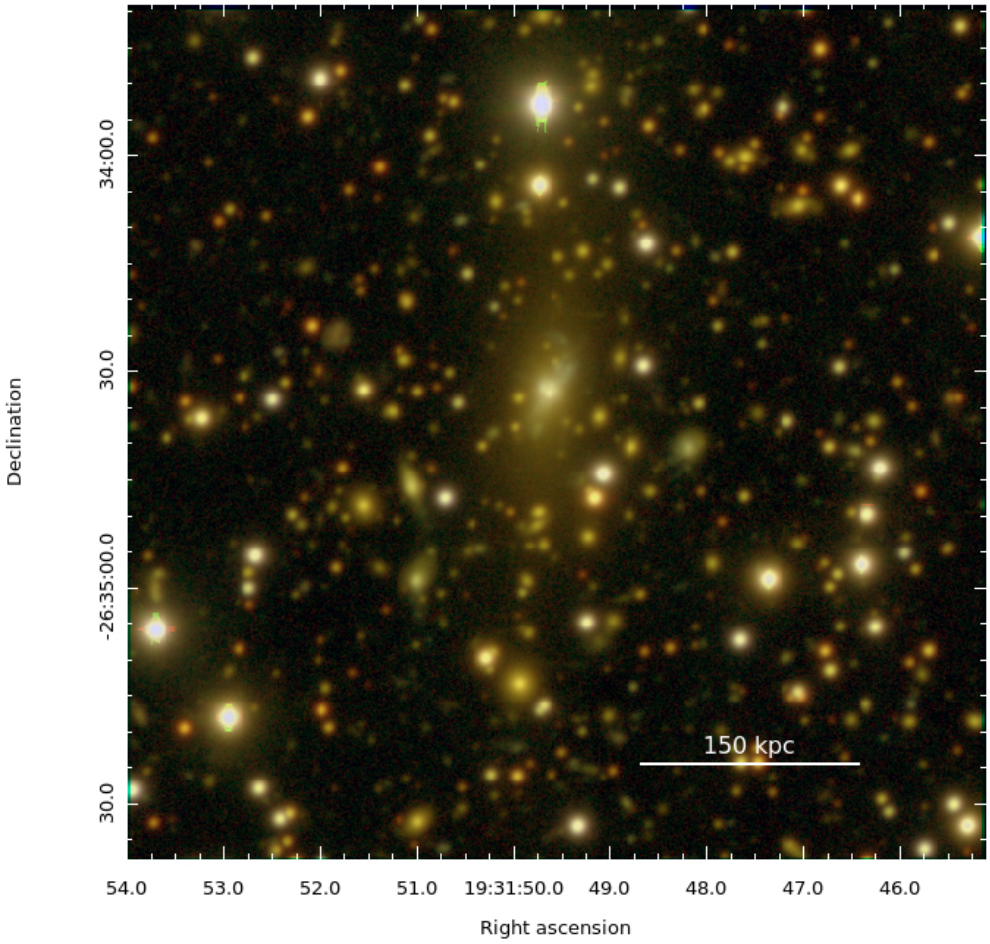

Figure 4.9: Optical image that we obtained combining IC, RC, B *Subaru* filters of MACSJ1931-2634 in an area of $\sim 2 \times 2$ arcmin^2 with BCG in the centre. The BCG envelope is clearly extended in North-South direction.

The final coadded images have been calibrated using point-like sources PSF, aperture corrected, photometry matched against PanStarr PSF photometry, including color $(g\text{-}r)_{Pstarr}$ color term.
Magnitudes have been corrected for galactic extinction following Schlafly & Finkbeiner (2011).
The 5σ depth for the images is ~ 25.69AB for g' and ~ 26.17AB for r' (1" aperture radius). In Fig. 4.10 we report grey scale A1300 *Subaru*-Suprime final image in r'.

4.2.2 Near Infrared Images

Near Infrared images for A1300 have been obtained by the Galaxy Clusters at VIRCAM Survey (GCAV)[9]. The GCAV is a VISTA ESO Public Survey which

[9]https://www.eso.org/sci/observing/PublicSurveys/docs/GCAV_SMP_10012017.pdf

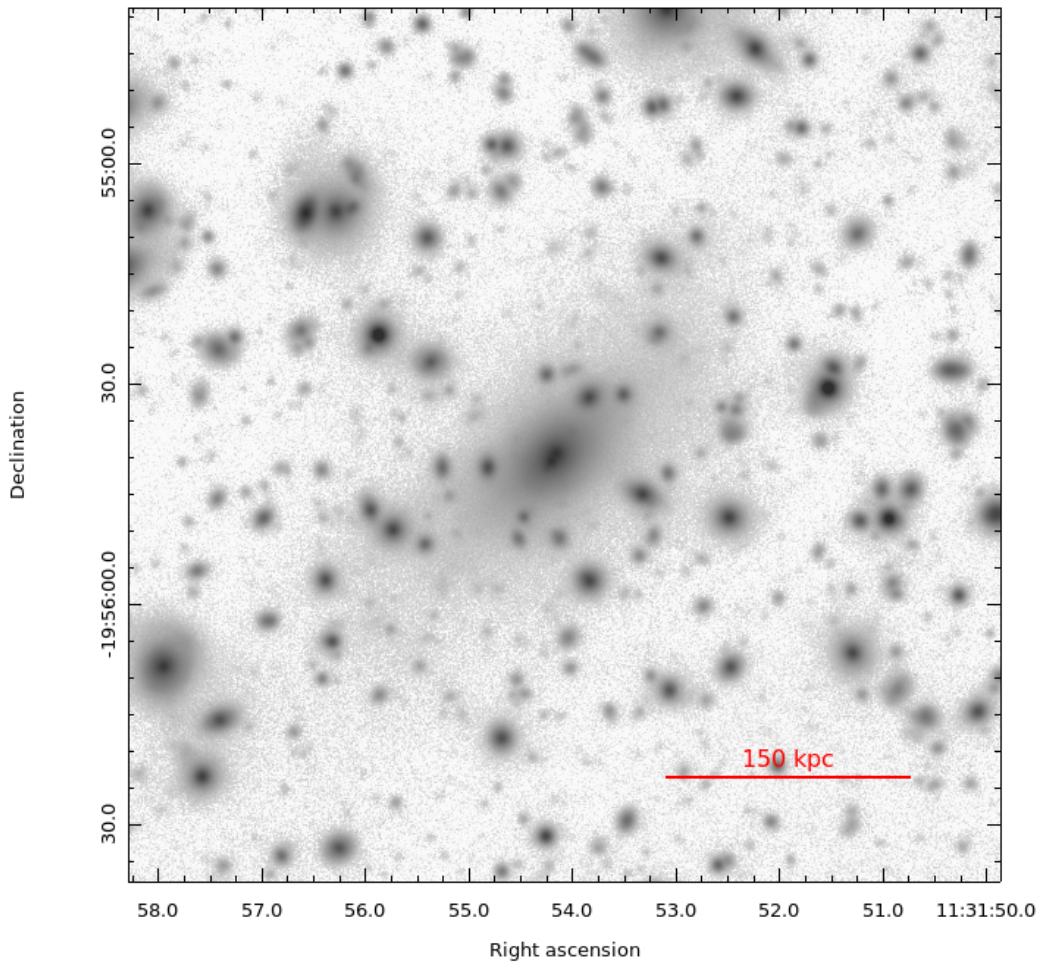

Figure 4.10: Gray scale *Subaru* image of A1300 in *r'* filter within an area of ∼2 × 2 arcmin^2 with BCG in the centre.

consists of 560 hrs observation in Y, J, Ks bands of 20 Clusters of Galaxies in the redshift range $0.2 \leqslant z \leqslant 0.9$. The total coverage of ~ 30 deg^2 allow to sample a wide dynamic range in density from the field to overdense regions in clusters central regions. The goal of this Survey is mainly to explore galaxy evolution in a wide diversity of environments.
The final stacks of A1300 are reported in Tab. 4.5.

Fig. 4.11 shows the final near infrared GCAV image in Ks band of A1300 with the 'Dumb-bell' BCG in its centre.

Table 4.5: A1300 GCAV observations and final stacks

Filter	exposure (hrs)	FWHM (")	depth*
Y	6.4	0.86	24.7
J	5.6	0.84	24.5
Ks	3.5	0.80	22.9

* depth: AB magnitude 5-sigma in 2arcsec-diameter aperture

4.2.3 Spectroscopic redshifts and stellar masses

For MACSJ1931-2634, as well as for A1300, the radio observations discussed in this thesis were obtained much later the spectroscopic campaigns. For the galaxy cluster MACSJ1931-2634, spectra were kindly provided by the CLASH-VLT Collaboration (P.I. P. Rosati), programme number 186.A-0798. I will report in Chapter 5 the details of the observation. For Abell 1300 the spectroscopic data have been obtained starting from the raw VIMOS data from the VLT ESO GO Large Programme (P.I. Böringher) number 169.A-0595 (see Ziparo et al., 2012). I will report in Chapter 6 the details of the observation.
The spectra have been obtained with a combination of IRAF[10] tasks (*apall, (re)identify, dispcor, xcsao*) and custom programs to cope e.g. with the dithering during observations. To assign to each slit the target object, the informations stored in the header of the VIMOS files have been used as first guess. These preliminary positions were then mapped into the SuprimeCam WCS also using IRAF *geomap*.
We collected a total of $\sim$ 400 redshifts for A1300 from our analysis, most obtained from our spectra extraction. After the spectroscopic analysis, which involved a substantial portion of the work, resulted that six galaxies are consistent with being cluster members in MASJ1931-2634 galaxy cluster and nine galaxies are consistent with being cluster members in A1300. In Fig. 4.12 and 4.13 we report the cutouts of the member galaxies for MACSJ1931-2634 and A1300 respectively.

MAGPHYS[11](Cunha et al., 2008) has been used to calculate stellar masses and Star Formation Rate of the cluster members galaxies. For A1300, to give consistent input magnitudes, a correction factor between the SuprimeCam *r'* aperture magnitude, 1".5 radius, and the *r'* total magnitude has been computed. This factor has then been applied to the other, *g',Y,J,Ks* bands. The results from the Spectral Energy Distribution fitting, including an estimate of the specific Star Formation Rate (sSFR), are reported in Chapter 7.

[10]http://ast.noao.edu/data/software
[11]http://www.iap.fr/magphys/

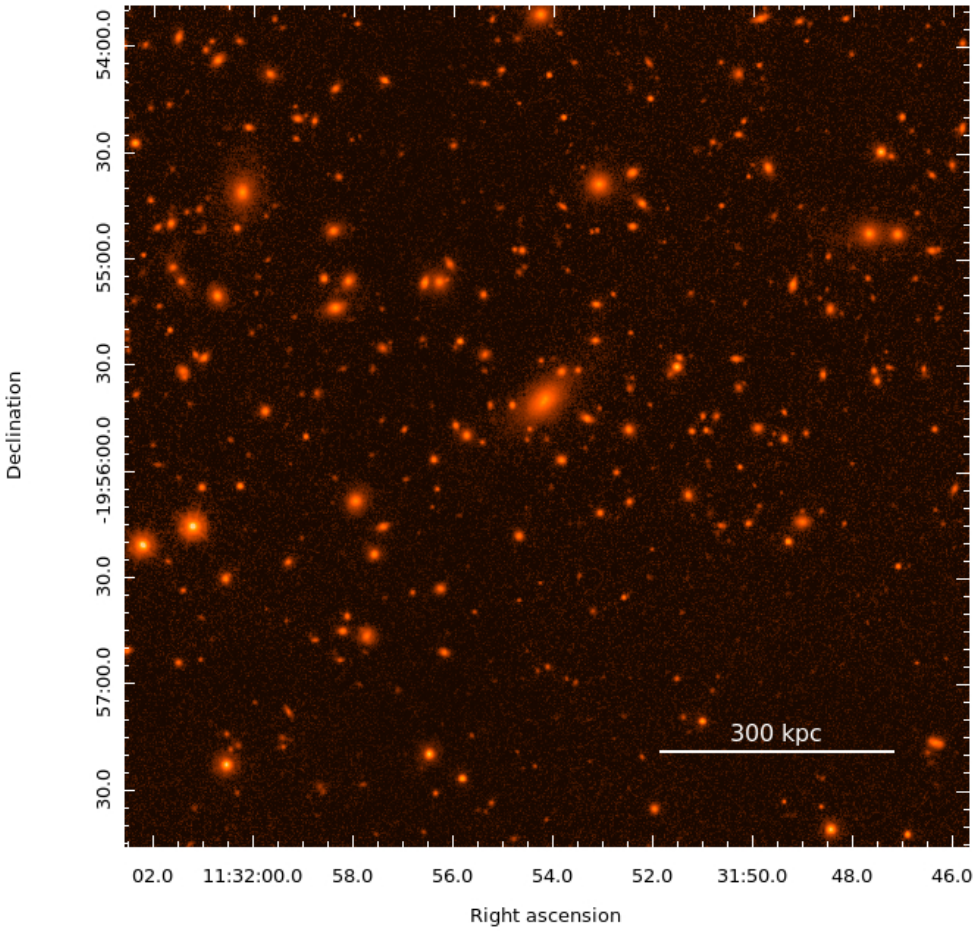

Figure 4.11: GCAV image of A1300 in Ks band within an area of $\sim 4 \times 4$ arcmin^2 with the 'Dumb-bell' BCG in the centre.

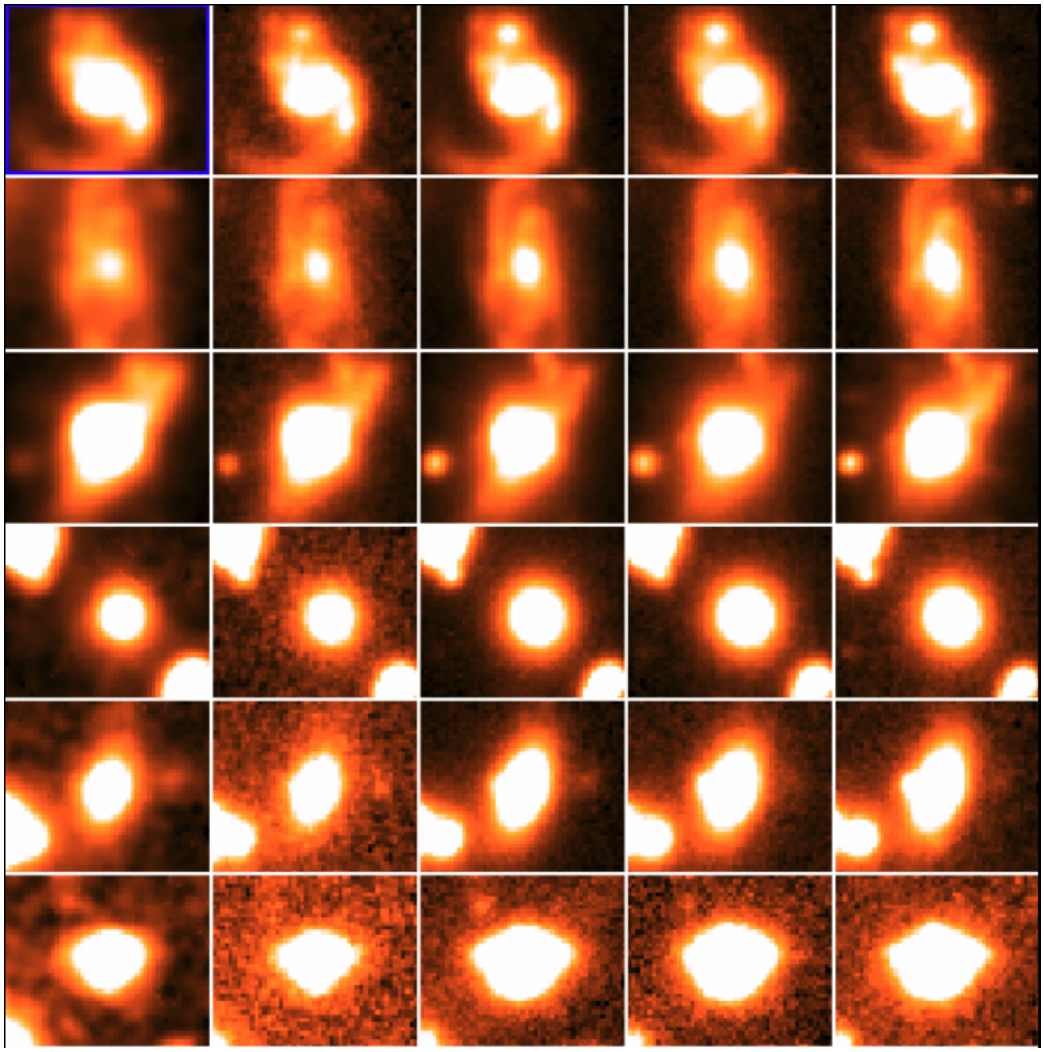

Figure 4.12: From left to right: B,V,RC,IC,Z cutouts of the six cluster members of MACSJ1931-2634. Source ID from top to bottom: 255, 282, 320 (BCG), 500078 (NAT), 500199, 500307. We adopted the same ID used in the tables reported in Chapter 5.

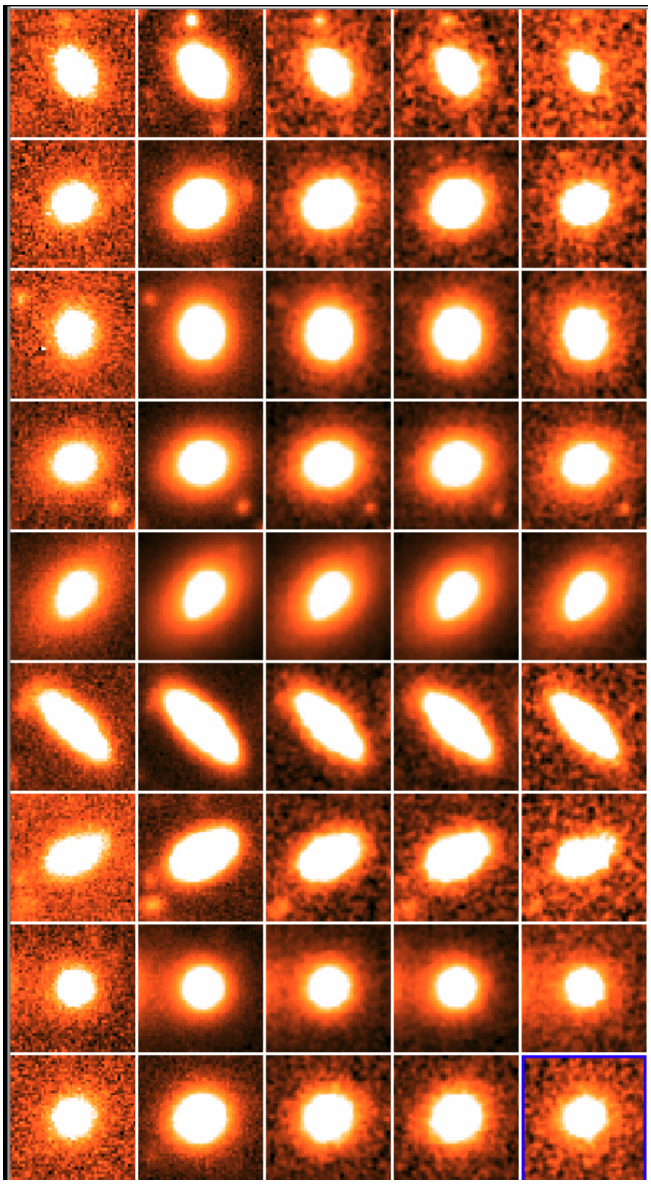

Figure 4.13: From left to right: g',r',Y,J,Ks bands cutouts of the nine cluster members of A1300. Source ID from top to bottom: 166, 168, 196, 200, 201 (BCG), 216, 221, 228, 304. We adopted the same ID used in the tables reported in Chapter 6.

Chapter 5

A multiwavelength analysis of the radio galaxy population in MACSJ1931-2634

This chapter presents a multiwavelength analysis of the radio galaxy population of the galaxy cluster MACSJ1931-2634 and its field. Since our main goal is to investigate the properties of the galaxies and their evolution in relation with the environment in which they are located, we analyzed the radio galaxy population in a wide region surrounding the cluster. We extracted two radio catalogues at 1.2 GHz (MeerKAT-16 L band) and at 640 MHz (uGMRT band 4) within an area of 30 arcmin radius, which corresponds to 9 Mpc at the cluster redshift (z=0.352); we present the two catalogues and the spectral indices of the sources in common. Moreover, we estimated the upper limits on the spectral indices for the sources detected only at 1.2 GHz or only at 640 MHz.
Second, we restricted the area of interest to 12 arcmin radius (i.e. two virial radii), corresponding to 3.5 Mpc at the cluster redshift, to crossmatch with the optical the radio sources in our catalogues and to perform the entire analysis on the galaxy population, i.e. statistical source counts (logN-logS), considerations on radio and optical overdensities and the Color-Magnitude diagram.
Finally, we estimated the Radio Luminosity Functions at 1.2 GHz and at 0.6 GHz in order to investigate the statistical properties of the radio galaxies in relation with the environment. We compared our result with the local RLF in Venturi et al. (2000), in order to see if there is an evolution with z, and with Branchesi et al. (2006) to compare our RLF with a result obtained at the same redshift (z $\sim$0.3).

5.1 MACSJ1931-2634

This massive, X-ray selected (Ebeling et al., 2010) cool core galaxy cluster, located at redshift z=0.352, is part of the Massive Cluster Survey (MACS) sample (see Ebeling et al., 2007, and references therein). The Massive Cluster Survey, launched in 1999, has compiled the first large X-ray selected sample of clusters that are both massive and distant. Based on sources listed in ROSAT All Sky Survey (RASS; Trümper, 1984) and in its Bright Sources Catalogue ((BSC, Voges et al., 1999), MACS covers the entire extragalactic sky observable from Mauna Kea (Hawaii) in a range of declination between -40° $\leq \delta \geq$ 80 °, and on clusters at z $\geq$ 0.3.
MACSJ1931-2634 hosts one of the most X-ray luminous cool cores yet discovered (see Fig. 5.1), with an equivalent mass cooling rate within the central $50h_{70}^{-1}$ kpc of $\sim$ 700 $M_{\odot}yr^{-1}$ (Ehlert et al., 2011).
In a short 12 ks *Chandra* observation of MACSJ1931-2634 taken in October 2002 (Allen et al., 2004; Allen, 2008), X-ray cavities were detected surrounding the bright central AGN. The physical size of these cavities is $\sim$25 kpc and is similar to those observed in the nearby Perseus cluster (Fabian et al., 2003, 2006). Indeed, with its luminous cool core, central bright point source, and very large apparent cooling rate, MACSJ1931-2634 is in many ways a higher redshift analog of the Perseus Cluster (Ehlert et al., 2011).
Deeper *Chandra* observations were taken in August 2008, increasing the total exposure at $\sim$100 ks, giving a surface brightness profile as seen in Figure 5.1.

The central AGN clearly manifests an outburst with an amount of power of the order of $P_{jet} = 4 - 14 \times 10^{45}\ ergs^{-1}$ (Ehlert et al., 2011), making this among the most powerful jet ever observed.
MACSJ1931-2634 is also part of the Cluster Lensing and Supernova Survey with Hubble (CLASH; Postman et al., 2012) sample of 25 massive galaxy clusters used to study the Dark Matter distribution in clusters.
The cluster is dominated by the very large, luminous central BCG that is undergoing a phase of active Star Formation (Fogarty et al., 2015; Donahue et al., 2015). The SFR of the BCG, removing the AGN contribution, is measured to be SFR=150$\pm$15 $M_{\odot}yr^{-1}$ (Santos et al., 2016) with *Herschel* in the FIR band. The main properties of this galaxy cluster are shown in Tab. 5.1.

Table 5.1: MACSJ1931-2634 cluster general properties

Name	z	scale (kpc/")	RA[a] (hms)	DEC[a] (° ' ")	M_{200}[b] $M_\odot$	L_X[c] ($ergs^{-1}$)	kT[c] (KeV)
MACSJ1931-2634	0.352	4.9	19:31:49.6	-26:34:34	9.9 ± 10^{14}	1×10^{45}	7.5 ± 1.4

[a] Ebeling, H., 2010.
[b] Santos, J., 2016.
[c] Giacintucci, S., 2014.

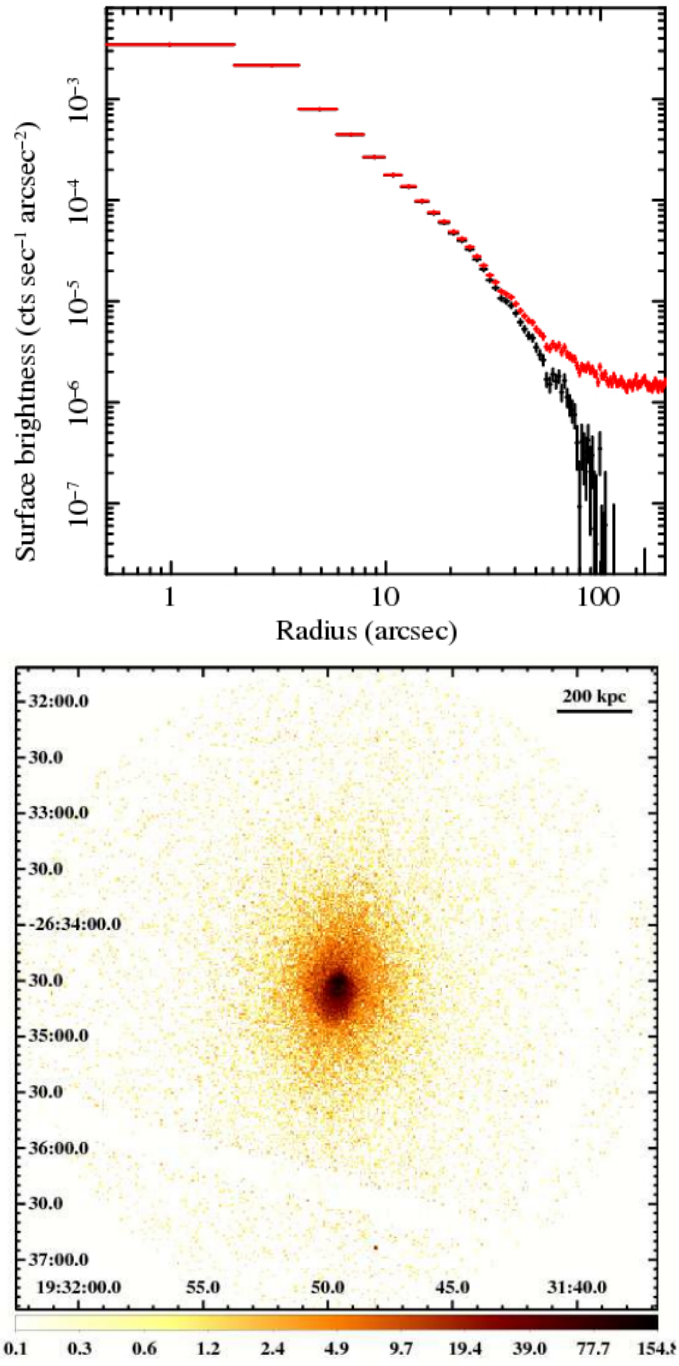

Figure 5.1: Combined X-ray surface brightness profile for MACSJ1931-2634 in the energy range 0.7-2.0 KeV. The red points denote the total surface brightness, while the black denote the background subtracted surface brightness (top panel). *Chandra* view of the cool core of MACSJ1931-2634 in a 5.7' × 5.7' central region (bottom panel), (see Ehlert et al., 2011).

5.2 The multiwavelength analysis

The radio and the optical/IR-spectroscopic data reduction is entirely presented in Chapter 4. In this section, I report a summary of the radio, optical, spectroscopic data used to perform the analysis on the radio galaxy population of MACSJ1931-2634 galaxy cluster and its field.

Radio data

We performed the radio analysis mainly by means of the data taken from new observations with the MeerKAT-16 interferometer at 1.2 GHz and the uGMRT interferometer at 640 MHz (Tab. 5.2). Moreover, to gain a complete view of the cluster galaxy population and its environment, starting from the BCG in the core to the outer regions, we reprocessed archival VLA data at 1.4 GHz (1.2 arcsec resolution, A array); we also used the 323 MHz archival GMRT data. The archival 1.4 GHz VLA and 323 MHz GMRT data were also used to perform the BCGs radio analysis reported in Chapter 2. We inspected finally the VLA Sky Survey[1] (VLASS) data at 3 GHz (see Lacy et al. 2019)[2].

Table 5.2: MACSJ1931-2634 radio data

Instrument	obs. date	central ν (MHz)	BW (MHz)	tos (min)	synt. beam (arcsec)	PA (deg)	rms (mJy/b)
MeerKAT	2 May 2018	1283	800	120	5×3	136	0.04
uGMRT	24 May 2018	640	200	208	5×4	169	0.03
VLA	14 Apr 2006	1400	50	82	2×1	4	0.02
GMRT	17 Nov 2012	323	32	480	10×6	-5	0.17
VLASS	9 Feb 2018	3000	2	ref.[2]	2×1	48	0.1

[1] https://science.nrao.edu/science/surveys/vlass
[2] https://arxiv.org/pdf/1907.01981.pdf

Optical and Photometric data

We analyzed optical data from *Subaru*-SuprimeCam (2012 observations) in a broad-band range of filters: B,V,RC,IC,Z. The details of the optical observations are reported in Table 5.3.
We used these optical data to cross-match our radio catalogues and to inspect the optical features of the cluster. In particular, we cross-matched our radio catalogues with Suprime RC and B bands in order to identify the optical counterparts of the radio galaxies in our sample.
From the composite optical Suprime image that we obtained combining I,RC, and B filters (Fig. 5.2), it is clear that the cluster core has a structure in North-South direction, according to what is detected also in the X-ray (Ehlert et al., 2011).

Table 5.3: MACSJ1931-2634 optical observations

Filter	exposure (s)	FWHM (")	depth*
B	2640	1.20	25.59
V	1275	0.88	25.04
RC	4560	0.81	24.95
IC	1800	0.92	24.54
Z	1950	0.76	24.29

* depth: AB magnitude 5-sigma in 2arcsec-diameter aperture

Spectroscopic data: VIMOS-VLT and FORS2

VIMOS spectra have been collected within the CLASH-VLT ESO Large Programme (PI P. Rosati), 186.A-0798 (Rosati et al., 2014). MACSJ1931 has been observed with the Low Resolution blue Grism, resulting in a spectral coverage $\sim$ 3700 Å-6700 Å, and a spectral resolution of $\sim$ 180.
The cluster has been covered with four partially overlapping pointings, with Observing Blocks 1 hr long, each one splitted in 900s-1200s exposure.
We proposed to observe MACSJ1931-2634 central Narrow-Angle tail radio galaxy in September 2018 (PI B. Terni de Gregory). Observations have been carried out using FORS2/VLT, Programme ID:0101.A-0776, using 300I Grism, covering the 6000 Å-11000 Å interval. A total of 3 hrs where allocated to the programme: 1 hr observation for the bright elliptical galaxy, the most likely counterpart, and two

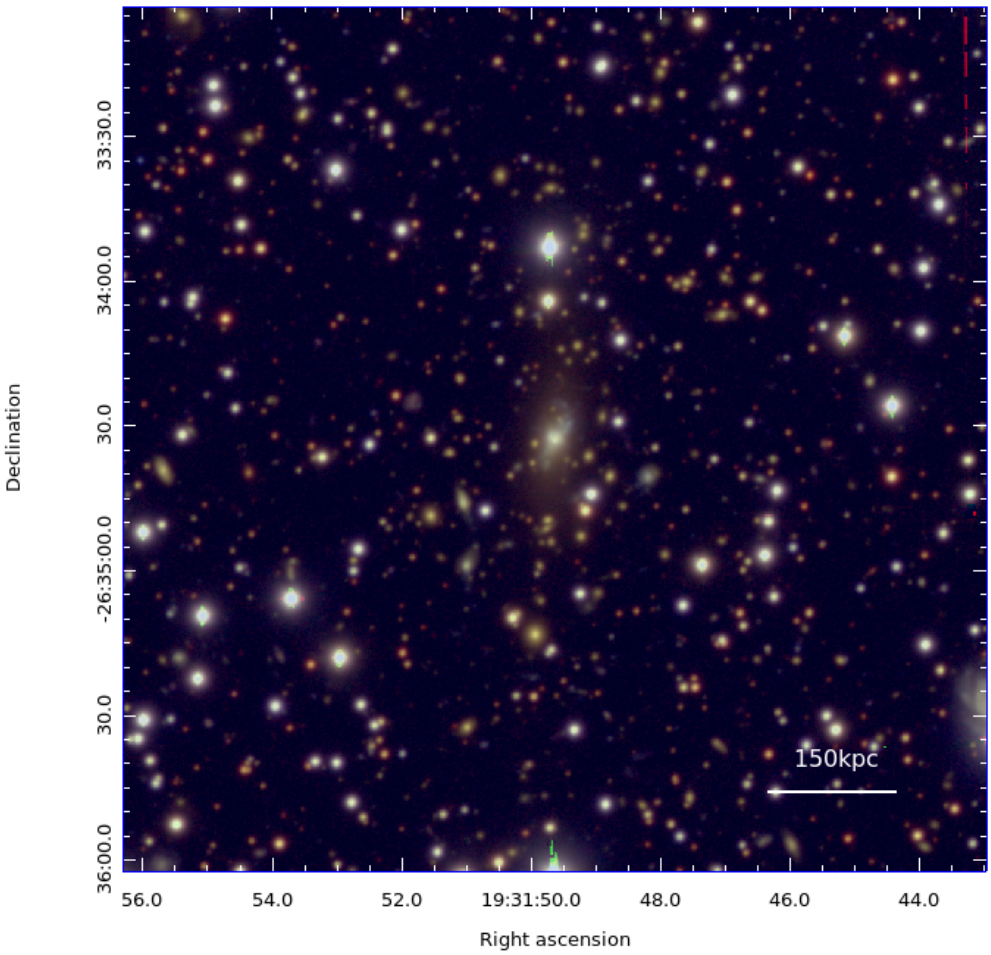

Figure 5.2: Optical image that we obtained combining IC,RC,B *Subaru* filters of MACSJ1931-2634 in an area of $\sim 3 \times 3$ arcmin^2 centered on the BCG. From this image is visible that the BCG envelope is extended in North-South direction.

hours for two very close and fainter sources. Seeing during observations was between 0.5" and 1.3". Each Observing Block, 1 hour of observations, was split into 3 exposures each 850s long. Results from this spectroscopic observation are entirely presented and discussed in the last Section of this chapter.

X-ray data

We reprocessed archival *Chandra* X-ray data taken from an 2008 observation in order to assess the properties of the central object in MACSJ1931-2634 galaxy cluster. We adopted the CIAO software package, 4.11 version, and a standard script to reprocess our data (4.8.3 CALDB version). The details of the observation are

reported in Tab.5.4.
We adopted the unsharp masking technique (Shin et al., 2016) to get our final image (Fig.5.30).

Table 5.4: MACSJ1931-2634 X-ray observations

Observation ID	Observation date	Detector	exposure time* (ks)
9382	21 August 2008	ACIS-I	89.5

* same data used by Ehlert et al. (2011)

5.3 The MeerKAT radio catalogue

The total number of sources detected at 1.2 GHz with MeerKAT-16, above the catalogue threshold of 0.2 mJy (5 sigma), within an area of 30 arcmin radius, is 192 (Fig. 5.3 and 5.4). The list of the sources is given in Table 5.5 and the following, where we report respectively their name, position (J2000), integrated flux density at 1.2 GHz, flux error and indication on the radio morphology. All flux densities are corrected for the primary beam attenuation. The primary beam correction is obtained using the analitic formula derived for MeerKAT primary beam described in Chapter 4. At the time of our analysis an accurate model of the MeerKAT primary beam was not available.
All flux densities are extracted with PyBDSF (Mohan & Rafferty, 2015), according to the criterion adopted and described in Chapter 4; whereas the flux of the extended sources is measured by AIPS TVSTAT, which allows integration of the image brightness values over irregular areas. The flux errors are measured according to the formula from Klein et al. (2003):

$$\Delta F_i = \sqrt{(rms)^2 + (cF_i)^2 + (E_{fit})^2} \tag{5.1}$$

where the rms is the noise of the image, c is the residual calibration error (conservatively assumed of 10%), and E_{fit} is the error of the fit in PyBDSF which is negligible. The dominant term is the calibration error.
To classify the source morphologies we adopted the following criterion (see Condon et al., 1998; Branchesi et al., 2006):

$$|F_t - F_{peak}| < 2\sigma \tag{5.2}$$

where σ is given by:

$$\sigma = \sqrt{\sigma_{peak}^2 + \sigma_t^2} \tag{5.3}$$

i.e. all the sources for which the relation (6.2) is valid are classified unresolved (pointlike). All the sources for which the relation is not valid are classified as barely resolved (i.e. not pointlike even though a clear morphology is not visible). The sources which show a clear extention and a defined morphology are classified extended. We report them in boldface in the catalogue.
According to this morphological classification, the majority of the radio sources is unresolved or barely resolved (see Tab. 5.5 and following); in particular, only four sources are extended (see Sect. 6.10). Among them, two are the central BCG and the NAT, whose flux density is F_{BCG}= 45.4 ± 4.5 mJy and F_{NAT}= 145.2 ± 14.5 mJy respectively. The BCG is contaminated by the unresolved diffuse emission surrounding it in the MeerKAT image. An FRII radio galaxy of flux F=1006 ± 100.6 mJy is located towards East direction from the cluster center (Fig. 5.21) and the fourth extended galaxy detected in our sample is located in the South-West direction. The classification of this galaxy is challenging: it could be an FRI (see Fig. 5.20) or an FRII. Its flux at 1.2 GHz is F=27.1 ± 2.7 mJy.
In the MeerKAT catalogue there are five sources with fluxes $\geq$ 50 mJy, i.e. the 2% of the sample.

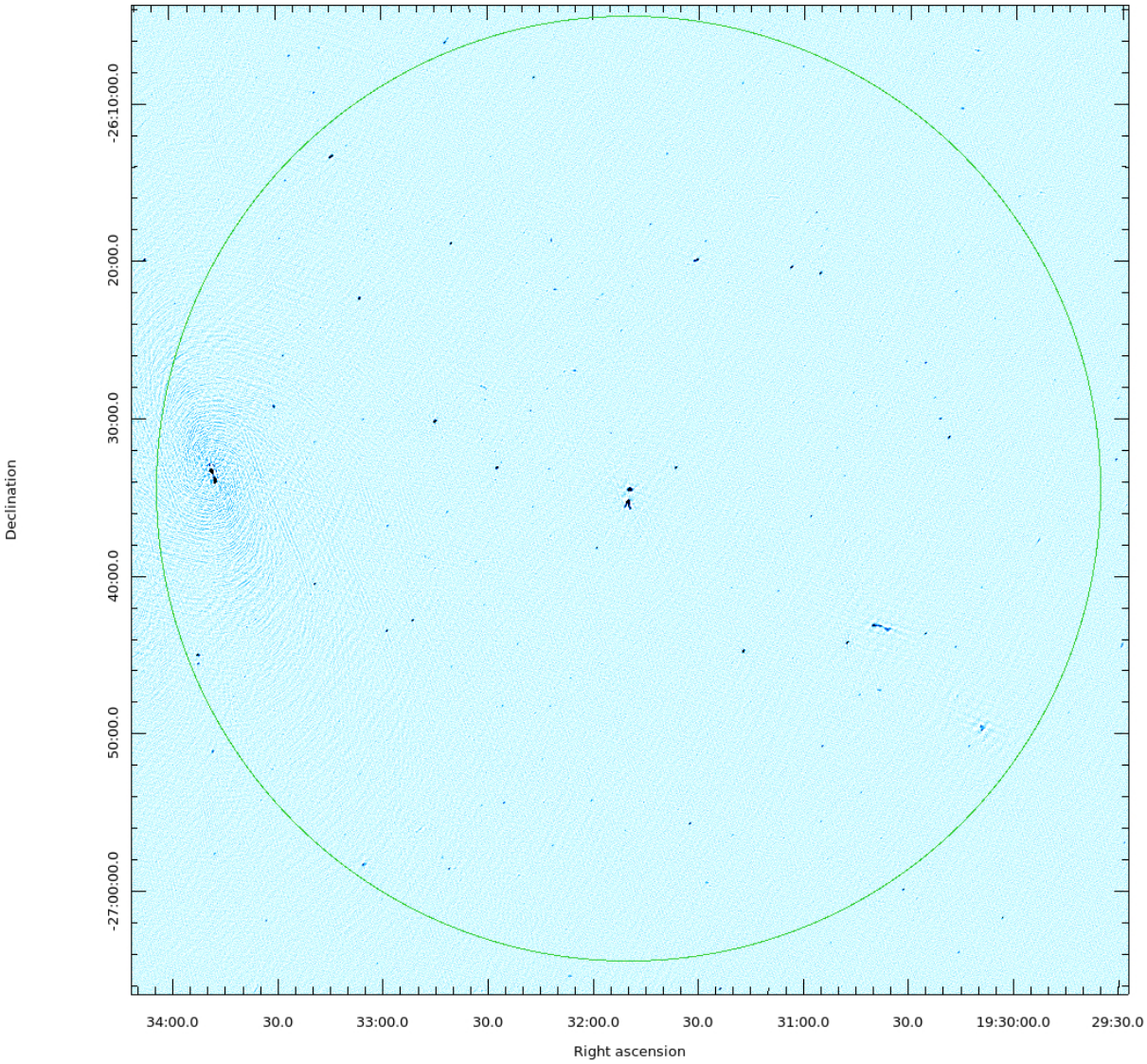

Figure 5.3: The image shows blue-scale view of the MeerKAT field which encompasses an area of 0.785 deg^2 (30 arcmin radius, green circle). This is the area of interest in our analysis and the area within which we extracted our catalogues. The central noise is 0.04 mJy/b with resolution of 5 $\times$ 3 in p.a. $\sim$ 136°.

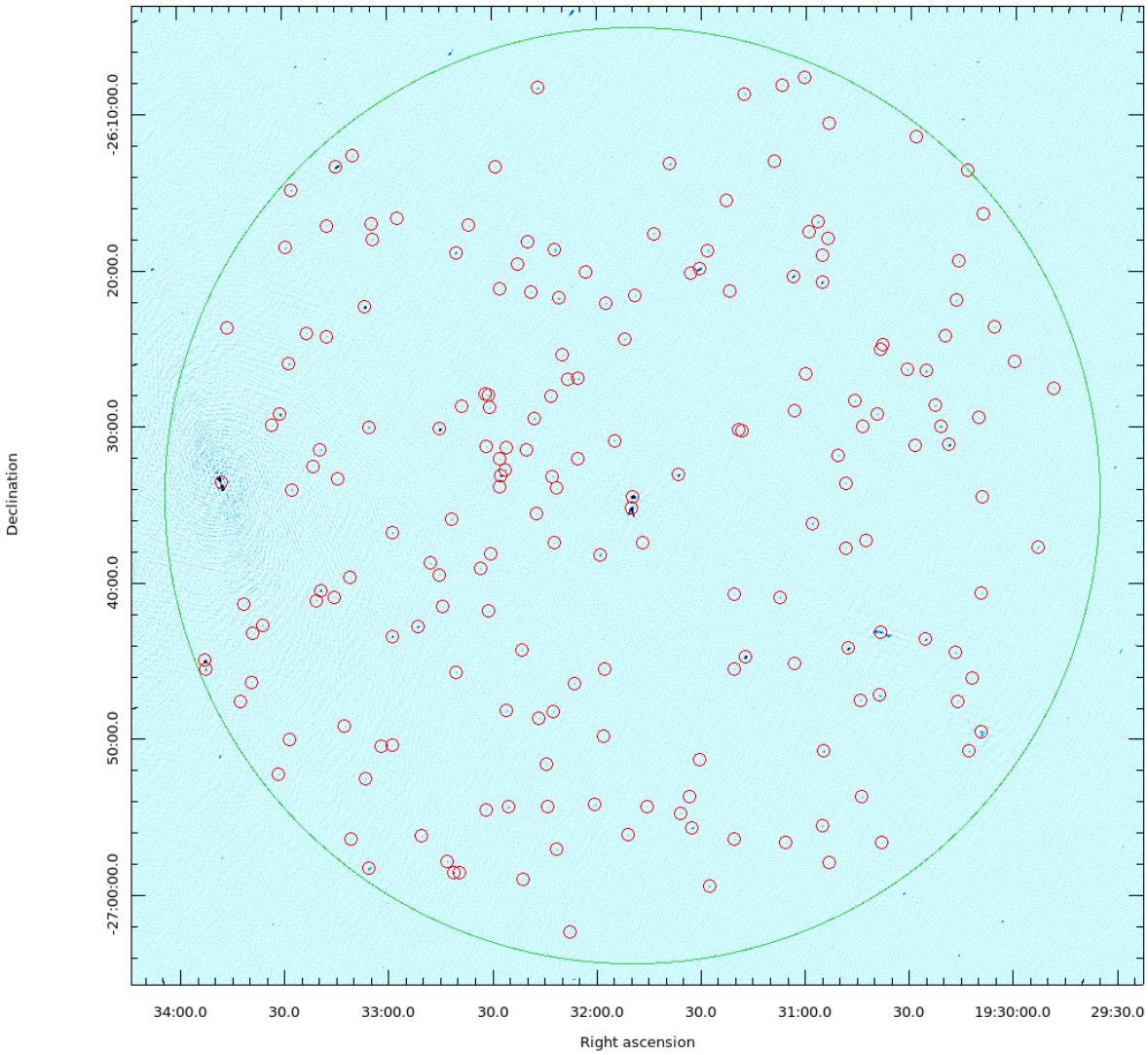

Figure 5.4: The image shows blue-scale view of the same area of 0.785 deg^2 (30 arcmin, green circle). The red circles indicate the radio sources detected over a threshold of 5σ (i.e. 0.2 mJy/b).

Table 5.5: MACSJ1931-2634 MeerKAT radio catalogue

Name	RA_{J2000}	DEC_{J2000}	$F_{1.2GHz}$ (mJy)	ΔF	Morphology
J1929-2627	19:29:48.89	-26:27:32.4	0.60	0.07	unresolved
J1929-2637	19:29:53.29	-26:37:44.8	1.60	0.16	barely
J1930-2625a	19:30:00.09	-26:25:52.2	0.50	0.06	barely
J1930-2623	19:30:05.90	-26:23:38.7	0.70	0.08	unresolved
J1930-2616a	19:30:09.21	-26:16:24.1	0.40	0.05	unresolved
J1930-2640	19:30:09.37	-26:40:43.0	0.60	0.07	unresolved
J1930-2634	19:30:09.37	-26:34:29.6	0.60	0.07	barely
J1930-2649	19:30:09.40	-26:49:34.3	7.60	0.76	barely
J1930-2629a	19:30:10.40	-26:29:27.9	0.40	0.06	barely
J1930-2646	19:30:11.91	-26:46:08.2	0.30	0.05	unresolved
J1930-2650a	19:30:12.87	-26:50:48.9	1.40	0.14	unresolved
J1930-2613	19:30:13.82	-26:13:35.3	0.80	0.09	unresolved
J1930-2619a	19:30:16.27	-26:19:26.8	0.80	0.09	unresolved
J1930-2647a	19:30:16.29	-26:47:38.1	0.60	0.07	barely
J1930-2644a	19:30:16.76	-26:44:30.4	1.40	0.15	unresolved
J1930-2621	19:30:16.91	-26:21:56.2	0.80	0.09	unresolved
J1930-2631a	19:30:18.81	-26:31:12.2	8.00	0.80	unresolved
J1930-2624a	19:30:19.87	-26:24:11.1	0.40	0.05	unresolved
J1930-2630a	19:30:21.31	-26:30:01.2	3.00	0.30	barely
J1930-2628a	19:30:22.95	-26:28:41.5	0.90	0.10	unresolved
J1930-2643a	19:30:25.37	-26:43:40.4	3.80	0.38	unresolved
J1930-2626a	19:30:25.52	-26:26:28.6	2.40	0.24	unresolved
J1930-2611	19:30:28.40	-26:11:29.4	0.40	0.05	unresolved
J1930-2631b	19:30:28.46	-26:31:13.5	0.30	0.05	unresolved
J1930-2626b	19:30:30.91	-26:26:24.0	0.70	0.08	unresolved
J1930-2656	19:30:37.88	-26:56:40.1	0.50	0.06	barely
J1930-2624b	19:30:37.97	-26:24:48.2	0.50	0.06	barely
J1930-2643b	19:30:38.23	-26:43:11.4	27.1	2.71	**FRI-II?**
J1930-2625b	19:30:38.41	-26:25:07.3	0.40	0.05	barely
J1930-2647b	19:30:38.62	-26:47:15.5	0.80	0.09	barely
J1930-2629b	19:30:39.45	-26:29:13.6	0.60	0.07	unresolved
J1930-2637a	19:30:42.69	-26:37:21.1	0.30	0.05	unresolved
J1930-2653	19:30:43.64	-26:53:45.8	0.80	0.09	unresolved
J1930-2630b	19:30:43.70	-26:30:00.9	0.40	0.05	barely
J1930-2647c	19:30:44.09	-26:47:34.8	0.90	0.10	unresolved
J1930-2628b	19:30:45.92	-26:28:23.3	0.50	0.06	unresolved
J1930-2644b	19:30:47.62	-26:44:15.2	47.3	4.73	unresolved
J1930-2637b	19:30:48.27	-26:37:50.0	0.40	0.06	barely
J1930-2633	19:30:48.44	-26:33:39.7	0.60	0.07	unresolved
J1930-2631c	19:30:50.59	-26:31:52.6	0.60	0.07	unresolved
J1930-2658	19:30:53.08	-26:58:00.4	0.40	0.06	unresolved

Table 5.6: continued

Name	RA_{J2000}	DEC_{J2000}	$F_{1.2GHz}$ (mJy)	ΔF	Morphology
J1930-2610	19:30:53.51	-26:10:38.0	0.40	0.05	barely
J1930-2617a	19:30:53.58	-26:17:59.9	0.40	0.06	unresolved
J1930-2650b	19:30:54.68	-26:50:50.4	2.30	0.20	unresolved
J1930-2655	19:30:55.05	-26:55:37.7	0.80	0.09	unresolved
J1930-2619b	19:30:55.14	-26:19:04.5	0.60	0.07	barely
J1930-2620	19:30:55.36	-26:20:48.2	11.3	1.13	unresolved
J1930-2616b	19:30:56.61	-26:16:56.5	1.70	0.18	unresolved
J1930-2636	19:30:57.98	-26:36:14.6	1.70	0.18	unresolved
J1930-2617b	19:30:59.16	-26:17:34.0	0.50	0.06	barely
J1930-2626c	19:30:59.83	-26:26:40.5	0.50	0.06	barely
J1931-2607	19:31:00.31	-26:07:41.4	0.90	0.10	unresolved
J1931-2629	19:31:03.07	-26:29:00.8	0.50	0.06	unresolved
J1931-2645a	19:31:03.17	-26:45:15.6	0.60	0.07	barely
J1931-2620a	19:31:03.59	-26:20:25.0	6.90	0.69	barely
J1931-2656a	19:31:05.64	-26:56:40.7	0.40	0.06	unresolved
J1931-2608a	19:31:06.96	-26:08:09.2	0.50	0.06	unresolved
J1931-2640a	19:31:07.25	-26:40:59.1	0.90	0.09	unresolved
J1931-2613a	19:31:09.17	-26:13:04.0	0.30	0.05	unresolved
J1931-2644	19:31:17.18	-26:44:48.7	28.9	2.89	barely
J1931-2608b	19:31:17.55	-26:08:44.7	1.00	0.10	unresolved
J1931-2630a	19:31:18.35	-26:30:18.3	0.30	0.05	unresolved
J1931-2630b	19:31:19.30	-26:30:17.5	0.30	0.05	unresolved
J1931-2656b	19:31:20.25	-26:56:29.8	0.60	0.07	unresolved
J1931-2645b	19:31:20.42	-26:45:34.4	0.40	0.05	unresolved
J1931-2640b	19:31:20.53	-26:40:46.7	0.40	0.05	unresolved
J1931-2621a	19:31:21.62	-26:21:23.2	0.50	0.06	barely
J1931-2615	19:31:22.64	-26:15:33.8	0.30	0.05	unresolved
J1931-2659	19:31:27.40	-26:59:30.9	1.30	0.13	barely
J1931-2618	19:31:28.05	-26:18:46.2	1.00	0.11	unresolved
J1931-2651	19:31:30.36	-26:51:23.3	0.40	0.05	unresolved
J1931-2619	19:31:30.37	-26:19:56.2	5.60	0.56	barely
J1931-2655	19:31:32.41	-26:55:45.3	3.40	0.35	unresolved
J1931-2620b	19:31:33.10	-26:20:14.0	0.40	0.05	barely
J1931-2653	19:31:33.28	-26:53:45.1	0.20	0.04	unresolved
J1931-2654a	19:31:35.79	-26:54:52.1	0.50	0.07	barely
J1931-2633	19:31:36.44	-26:33:09.6	15.2	1.52	barely
J1931-2613b	19:31:38.93	-26:13:13.7	1.30	0.13	unresolved
J1931-2617	19:31:43.67	-26:17:42.1	1.10	0.11	unresolved
J1931-2654b	19:31:45.56	-26:54:24.4	0.40	0.05	unresolved
J1931-2637	19:31:46.56	-26:37:32.1	0.30	0.05	unresolved
J1931-2621b	19:31:48.83	-26:21:39.0	0.40	0.05	unresolved

Table 5.7: continued

Name	RA_{J2000}	DEC_{J2000}	$F_{1.2GHz}$ (mJy)	ΔF	Morphology
J1931-2634	19:31:49.56	-26:34:32.7	45.4	4.54	**BCG**
J1931-2635	19:31:49.98	-26:35:17.3	145.2	14.5	**NAT**
J1931-2656c	19:31:50.85	-26:56:11.6	0.40	0.06	unresolved
J1931-2624	19:31:51.97	-26:24:26.9	0.80	0.09	unresolved
J1931-2630c	19:31:54.87	-26:30:57.7	0.80	0.09	unresolved
J1931-2622	19:31:57.37	-26:22:09.7	0.70	0.08	unresolved
J1931-2645c	19:31:57.56	-26:45:38.2	0.40	0.05	unresolved
J1931-2649	19:31:57.96	-26:49:55.0	0.30	0.05	unresolved
J1931-2638	19:31:58.93	-26:38:15.7	3.50	0.35	unresolved
J1932-2654a	19:32:00.41	-26:54:17.6	0.90	0.10	unresolved
J1932-2620	19:32:03.07	-26:20:11.0	0.40	0.05	unresolved
J1932-2632a	19:32:05.19	-26:32:05.7	0.30	0.05	barely
J1932-2627a	19:32:05.20	-26:27:00.2	2.30	0.23	barely
J1932-2646	19:32:06.43	-26:46:31.1	0.50	0.06	unresolved
J1932-2702	19:32:07.73	-27:02:27.9	0.40	0.06	unresolved
J1932-2627b	19:32:08.17	-26:27:03.4	0.50	0.07	barely
J1932-2625	19:32:09.74	-26:25:29.4	0.30	0.05	unresolved
J1932-2621a	19:32:10.80	-26:21:50.5	2.00	0.20	barely
J1932-2634	19:32:11.30	-26:34:01.0	0.30	0.05	unresolved
J1932-2657a	19:32:11.49	-26:57:08.6	0.80	0.08	unresolved
J1932-2618a	19:32:11.85	-26:18:43.2	2.50	0.25	barely
J1932-2637	19:32:12.15	-26:37:29.7	0.50	0.06	unresolved
J1932-2648	19:32:12.26	-26:48:18.4	0.60	0.07	unresolved
J1932-2633	19:32:12.54	-26:33:14.4	0.90	0.10	unresolved
J1932-2628	19:32:12.95	-26:28:07.8	0.50	0.06	unresolved
J1932-2654b	19:32:14.01	-26:54:23.9	0.50	0.06	unresolved
J1932-2651	19:32:14.41	-26:51:39.7	0.40	0.06	unresolved
J1932-2648a	19:32:16.53	-26:48:44.6	0.50	0.06	barely
J1932-2608	19:32:16.78	-26:08:22.1	3.50	0.30	unresolved
J1932-2635a	19:32:17.11	-26:35:38.4	0.60	0.07	unresolved
J1932-2629	19:32:17.70	-26:29:32.1	1.30	0.13	unresolved
J1932-2621b	19:32:18.81	-26:21:25.9	0.50	0.06	unresolved
J1932-2618b	19:32:19.55	-26:18:14.5	0.50	0.06	barely
J1932-2631a	19:32:20.07	-26:31:35.1	0.50	0.06	unresolved
J1932-2659	19:32:21.19	-26:59:02.7	0.60	0.07	barely
J1932-2644	19:32:21.42	-26:44:21.0	0.60	0.07	unresolved
J1932-2619	19:32:22.41	-26:19:39.7	0.40	0.05	unresolved
J1932-2654	19:32:25.41	-26:54:26.0	1.90	0.19	unresolved
J1932-2648b	19:32:25.80	-26:48:16.2	0.70	0.08	unresolved
J1932-2631b	19:32:25.84	-26:31:24.5	0.30	0.05	unresolved
J1932-2632b	19:32:26.11	-26:32:48.8	0.50	0.07	unresolved

Table 5.8: continued

Name	RA_{J2000}	DEC_{J2000}	$F_{1.2GHz}$ (mJy)	ΔF	Morphology
J1932-2633a	19:32:27.32	-26:33:10.1	17.7	1.70	barely
J1932-2621c	19:32:27.69	-26:21:15.1	0.30	0.05	barely
J1932-2633b	19:32:27.73	-26:33:56.5	0.40	0.05	unresolved
J1932-2632c	19:32:27.80	-26:32:08.3	0.50	0.07	unresolved
J1932-2613	19:32:29.00	-26:13:24.5	0.50	0.06	unresolved
J1932-2638a	19:32:30.45	-26:38:12.5	0.20	0.04	unresolved
J1932-2628a	19:32:30.69	-26:28:50.8	0.60	0.07	unresolved
J1932-2628b	19:32:30.90	-26:28:03.4	1.00	0.11	barely
J1932-2641a	19:32:31.01	-26:41:51.3	0.50	0.06	unresolved
J1932-2631c	19:32:31.59	-26:31:20.8	0.50	0.06	unresolved
J1932-2627c	19:32:31.75	-26:27:58.9	0.90	0.10	barely
J1932-2654c	19:32:31.80	-26:54:36.1	0.50	0.06	unresolved
J1932-2639a	19:32:33.36	-26:39:08.1	0.60	0.07	unresolved
J1932-2617	19:32:36.55	-26:17:10.6	0.60	0.07	barely
J1932-2628c	19:32:38.69	-26:28:43.1	0.70	0.08	barely
J1932-2658	19:32:39.40	-26:58:36.4	0.50	0.06	unresolved
J1932-2618c	19:32:40.26	-26:18:54.8	6.30	0.60	unresolved
J1932-2645	19:32:40.28	-26:45:47.1	0.40	0.06	unresolved
J1932-2658	19:32:41.10	-26:58:37.8	2.60	0.26	unresolved
J1932-2635b	19:32:41.51	-26:35:58.3	1.20	0.13	barely
J1932-2657b	19:32:43.01	-26:57:54.3	0.70	0.08	unresolved
J1932-2641b	19:32:44.15	-26:41:34.6	0.30	0.05	unresolved
J1932-2630	19:32:44.91	-26:30:13.1	52.7	5.20	unresolved
J1932-2639b	19:32:44.96	-26:39:32.6	0.60	0.07	unresolved
J1932-2638b	19:32:47.76	-26:38:47.4	0.60	0.07	unresolved
J1932-2656	19:32:50.31	-26:56:16.5	0.50	0.06	barely
J1932-2642	19:32:51.32	-26:42:51.0	5.80	0.58	barely
J1932-2616	19:32:57.15	-26:16:42.1	0.60	0.07	barely
J1932-2636	19:32:58.44	-26:36:50.4	1.50	0.16	unresolved
J1932-2650	19:32:58.63	-26:50:26.2	0.30	0.05	unresolved
J1932-2643	19:32:58.69	-26:43:29.7	5.30	0.53	unresolved
J1933-2650a	19:33:01.88	-26:50:30.5	0.30	0.05	unresolved
J1933-2618a	19:33:04.10	-26:18:01.8	0.60	0.07	barely
J1933-2617a	19:33:04.42	-26:17:05.6	0.40	0.05	unresolved
J1933-2630	19:33:05.31	-26:30:04.6	1.30	0.14	unresolved
J1933-2658	19:33:05.62	-26:58:21.1	4.40	0.44	barely
J1933-2622	19:33:06.31	-26:22:22.9	11.9	1.19	barely
J1933-2652a	19:33:06.41	-26:52:35.9	0.60	0.07	unresolved
J1933-2612	19:33:09.92	-26:12:41.5	0.60	0.07	unresolved
J1933-2639	19:33:10.60	-26:39:41.3	0.40	0.06	unresolved
J1933-2656	19:33:10.77	-26:56:26.3	0.60	0.07	unresolved

Table 5.9: continued

Name	RA_{J2000}	DEC_{J2000}	$F_{1.2GHz}$ (mJy)	ΔF	Morphology
J1933-2649	19:33:12.34	-26:49:14.4	0.60	0.07	barely
J1933-2633a	19:33:14.15	-26:33:22.7	0.40	0.05	unresolved
J1933-2613	19:33:14.52	-26:13:24.9	31.1	3.11	barely
J1933-264a0	19:33:15.35	-26:40:58.4	0.50	0.06	barely
J1933-2617b	19:33:17.36	-26:17:11.3	0.30	0.05	unresolved
J1933-2624a	19:33:17.37	-26:24:15.7	0.70	0.08	unresolved
J1933-2631	19:33:19.15	-26:31:30.8	0.80	0.09	unresolved
J1933-2640b	19:33:19.22	-26:40:31.4	4.90	0.49	unresolved
J1933-2641a	19:33:20.27	-26:41:10.5	0.50	0.07	unresolved
J1933-2632	19:33:21.33	-26:32:34.2	0.50	0.06	unresolved
J1933-2624b	19:33:23.13	-26:24:03.3	0.80	0.09	unresolved
J1933-2614	19:33:27.27	-26:14:53.6	1.40	0.14	barely
J1933-2634	19:33:27.33	-26:34:04.0	1.20	0.12	unresolved
J1933-2626	19:33:28.06	-26:26:00.9	1.70	0.17	unresolved
J1933-2650b	19:33:28.31	-26:50:03.4	0.40	0.06	barely
J1933-2618b	19:33:28.99	-26:18:34.2	1.10	0.12	unresolved
J1933-2629	19:33:30.74	-26:29:13.1	10.2	1.02	barely
J1933-2652b	19:33:31.37	-26:52:17.1	0.70	0.08	unresolved
J1933-2629	19:33:33.18	-26:29:58.6	0.20	0.04	barely
J1933-2642	19:33:35.92	-26:42:44.8	1.00	0.11	unresolved
J1933-2643	19:33:38.57	-26:43:13.9	0.70	0.08	unresolved
J1933-2646	19:33:39.15	-26:46:23.6	0.90	0.10	barely
J1933-2641b	19:33:41.41	-26:41:25.6	0.70	0.08	barely
J1933-2647	19:33:42.46	-26:47:39.9	0.60	0.07	unresolved
J1933-2623	19:33:45.83	-26:23:41.4	0.50	0.06	unresolved
J1933-2633b	19:33:47.67	-26:33:35.0	1006	100.6	**FRII**
J1933-2645a	19:33:52.32	-26:45:33.1	3.60	0.36	unresolved
J1933-2645b	19:33:52.52	-26:45:00.1	23.1	2.31	unresolved

5.4 The uGMRT radio catalogue

The total number of sources detected at 640 MHz with the uGMRT interferometer, above the catalogue threshold of 0.15 mJy (5 sigma), within an area of 30 arcmin radius, is 623 (Fig. 5.5 and 5.6). The list of the sources is given in Table 5.10 and following, where we report respectively their name, position (J2000), integrated flux density at 640 MHz, flux error and indication on the radio morphology. All flux densities given are corrected for the primary beam attenuation. The primary beam correction is obtained by PBCOR task in AIPS giving the PBPARM parameters for the uGMRT updated at December 1st 2018 (see Chapter 4, courtesy by Ruta Kale; NCRA).
All flux densities are extracted with PyBDSF (Mohan & Rafferty, 2015), whereas we measured by AIPS TVSTAT the fluxes of the extended sources. The flux errors are measured, as for the MeerKAT sample, according to the formula (6.1) from Klein et al. (2003). The residual calibration error is conservatively assumed of 10% and it is the dominating term.
We adopted the same method that we used for the MeerKAT catalogue to define the morphology of the sources. As clear from Table 5.10 and following, the majority of the sources is unresolved or barely resolved; in particular, only six sources are extended. Among the extended sources, two are the BCG and the NAT in the field center, which have fluxes of 183.7 ± 18.3 mJy and 354.7 ± 35.4 mJy respectively. Also in the uGMRT image the BCG is contaminated by the unresolved diffuse emission surrounding it. The FRII radio galaxy located toward East from the BCG has a flux density of 3526 ± 352.6 mJy, the uncertain FRI-II located at South-West has a flux density of 118.3 ± 11.8 mJy. There are two more extended sources with respect to the MeerKAT catalogue reported in Fig.5.22 and 5.23 of fluxes 109 ± 10.9 mJy and 5.84 ± 0.58 mJy respectively.

Table 5.10: MACSJ1931-2634 uGMRT radio catalogue

Name	RA_{J2000}	DEC_{J2000}	F_{640MHz} (mJy)	ΔF	Morphology
J1929-2633a	19:29:38.38	-26:33:47.1	0.65	0.07	barely
J1929-2642	19:29:40.24	-26:42:10.1	0.60	0.06	unresolved
J1929-2638	19:29:40.89	-26:38:31.5	1.69	0.17	barely
J1929-2635a	19:29:41.91	-26:35:59.4	0.61	0.06	unresolved
J1929-2626a	19:29:43.72	-26:26:58.5	1.29	0.13	barely
J1929-2637a	19:29:43.83	-26:37:26.6	1.07	0.11	barely
J1929-2625	19:29:45.10	-26:25:24.4	0.89	0.09	barely
J1929-2624	19:29:48.06	-26:24:34.1	0.74	0.08	barely
J1929-2647	19:29:48.68	-26:47:29.7	0.77	0.08	unresolved
J1929-2627	19:29:48.95	-26:27:32.5	2.17	0.21	unresolved
J1929-2633b	19:29:50.75	-26:33:58.3	0.42	0.05	unresolved
J1929-2631	19:29:51.04	-26:31:36.4	0.54	0.06	barely
J1929-2635b	19:29:52.68	-26:35:18.3	0.37	0.04	unresolved
J1929-2637b	19:29:53.30	-26:37:41.4	8.87	0.88	barely
J1929-2630	19:29:54.64	-26:30:58.0	0.53	0.06	unresolved
J1929-2646	19:29:55.61	-26:46:53.0	0.75	0.08	unresolved
J1929-2626b	19:29:57.27	-26:26:40.3	0.38	0.04	unresolved
J1929-2639	19:29:57.55	-26:39:05.4	0.24	0.03	unresolved
J1929-2635c	19:29:58.56	-26:35:17.9	0.88	0.09	barely
J1930-2630a	19:30:00.02	-26:30:41.6	0.29	0.04	unresolved
J1930-2642	19:30:00.06	-26:42:40.1	0.49	0.05	unresolved
J1930-2625a	19:30:00.11	-26:25:51.9	0.75	0.08	unresolved
J1930-2641a	19:30:00.58	-26:41:20.0	0.63	0.07	barely
J1930-2631a	19:30:02.03	-26:31:21.3	0.33	0.04	unresolved
J1930-2625b	19:30:02.95	-26:25:25.1	0.47	0.05	unresolved
J1930-2631b	19:30:05.00	-26:31:45.7	0.59	0.06	unresolved
J1930-2623a	19:30:05.95	-26:23:38.6	2.94	0.29	unresolved
J1930-2650a	19:30:06.24	-26:50:46.8	0.70	0.07	unresolved
J1930-2619a	19:30:06.33	-26:19:24.5	0.56	0.06	unresolved
J1930-2621a	19:30:07.26	-26:21:38.3	0.38	0.04	unresolved
J1930-2634a	19:30:07.75	-26:34:22.9	0.54	0.06	unresolved
J1930-2635a	19:30:07.84	-26:35:35.5	0.51	0.05	barely
J1930-2649a	19:30:09.14	-26:49:43.3	109.0	10.9	**FRII**
J1930-2616a	19:30:09.26	-26:16:23.5	1.13	0.11	barely
J1930-2634b	19:30:09.38	-26:34:29.3	1.34	0.13	barely
J1930-2640a	19:30:09.41	-26:40:42.8	2.16	0.21	unresolved
J1930-2630b	19:30:09.41	-26:30:21.2	0.25	0.03	unresolved
J1930-2634c	19:30:09.47	-26:34:50.3	0.31	0.04	unresolved
J1930-2629a	19:30:10.45	-26:29:28.1	1.25	0.12	barely
J1930-2625c	19:30:10.56	-26:25:20.1	0.49	0.05	unresolved
J1930-2625d	19:30:10.80	-26:25:41.8	0.28	0.04	unresolved

Table 5.11: continued

Name	RA_{J2000}	DEC_{J2000}	F_{640MHz} (mJy)	ΔF	Morphology
J1930-2653a	19:30:11.03	-26:53:19.3	0.82	0.08	barely
J1930-2646	19:30:11.90	-26:46:08.1	0.85	0.09	unresolved
J1930-2625e	19:30:12.22	-26:25:56.4	0.82	0.08	unresolved
J1930-2637a	19:30:12.70	-26:37:25.3	0.36	0.04	unresolved
J1930-2650b	19:30:12.92	-26:50:48.9	4.30	0.43	unresolved
J1930-2631c	19:30:13.25	-26:31:18.9	0.49	0.05	unresolved
J1930-2613a	19:30:13.89	-26:13:35.2	2.44	0.24	unresolved
J1930-2622a	19:30:15.50	-26:22:20.0	0.75	0.08	barely
J1930-2647a	19:30:16.29	-26:47:38.3	5.85	0.58	barely
J1930-2619b	19:30:16.34	-26:19:26.4	2.47	0.24	unresolved
J1930-2644a	19:30:16.79	-26:44:30.1	1.95	0.19	unresolved
J1930-2621b	19:30:17.00	-26:21:56.5	3.07	0.30	unresolved
J1930-2625f	19:30:17.75	-26:25:15.6	0.33	0.04	unresolved
J1930-2628a	19:30:18.33	-26:28:31.0	0.31	0.04	unresolved
J1930-2653b	19:30:18.38	-26:53:07.6	0.51	0.05	unresolved
J1930-2619c	19:30:18.48	-26:19:29.8	1.05	0.11	barely
J1930-2640b	19:30:18.87	-26:40:54.1	0.40	0.05	barely
J1930-2631d	19:30:18.88	-26:31:12.1	27.0	2.70	barely
J1930-2633a	19:30:18.89	-26:33:06.7	0.29	0.04	unresolved
J1930-2616b	19:30:19.44	-26:16:02.7	0.46	0.05	barely
J1930-2632a	19:30:19.72	-26:32:46.2	0.43	0.05	barely
J1930-2624	19:30:19.94	-26:24:11.5	0.62	0.06	unresolved
J1930-2619d	19:30:20.24	-26:19:27.9	0.38	0.04	unresolved
J1930-2628b	19:30:20.45	-26:28:25.3	0.43	0.05	unresolved
J1930-2625g	19:30:20.70	-26:25:19.8	0.58	0.06	barely
J1930-2632b	19:30:20.78	-26:32:13.3	0.38	0.04	unresolved
J1930-2630j	19:30:21.38	-26:30:01.3	8.74	0.87	barely
J1930-2641b	19:30:22.81	-26:41:35.6	0.40	0.05	barely
J1930-2628c	19:30:23.02	-26:28:41.1	1.83	0.10	unresolved
J1930-2639	19:30:23.30	-26:39:46.4	0.84	0.08	barely
J1930-2625h	19:30:23.42	-26:25:36.6	0.23	0.02	unresolved
J1930-2626a	19:30:24.35	-26:26:43.3	0.15	0.01	unresolved
J1930-2626b	19:30:25.34	-26:26:19.0	0.28	0.02	unresolved
J1930-2643a	19:30:25.41	-26:43:40.4	13.1	1.30	unresolved
J1930-2626c	19:30:25.59	-26:26:28.6	5.97	0.50	unresolved
J1930-2637b	19:30:27.78	-26:37:16.4	0.44	0.04	unresolved
J1930-2611	19:30:28.43	-26:11:29.3	1.13	0.10	unresolved
J1930-2631e	19:30:28.48	-26:31:13.4	0.31	0.03	unresolved
J1930-2615	19:30:28.72	-26:15:07.1	0.41	0.04	unresolved
J1930-2647b	19:30:29.45	-26:47:37.4	0.56	0.05	unresolved
J1930-2626d	19:30:30.96	-26:26:24.0	1.86	0.10	unresolved

Table 5.12: continued

Name	RA_{J2000}	DEC_{J2000}	F_{640MHz} (mJy)	ΔF	Morphology
J1930-2638a	19:30:32.21	-26:38:00.3	0.26	0.02	unresolved
J1930-2637c	19:30:32.59	-26:37:45.2	0.34	0.03	unresolved
J1930-2618a	19:30:32.79	-26:18:47.8	0.47	0.04	unresolved
J1930-2656a	19:30:33.24	-26:56:02.9	0.72	0.07	unresolved
J1930-2626e	19:30:33.30	-26:26:32.3	0.26	0.02	unresolved
J1930-2644b	19:30:33.62	-26:44:44.1	0.91	0.09	barely
J1930-2614	19:30:33.71	-26:14:01.2	0.84	0.08	barely
J1930-2632c	19:30:33.93	-26:32:22.8	0.19	0.02	unresolved
J1930-2651	19:30:33.99	-26:51:40.6	0.41	0.04	unresolved
J1930-2629b	19:30:35.16	-26:29:57.6	0.48	0.05	unresolved
J1930-2620a	19:30:35.69	-26:20:15.3	0.40	0.05	barely
J1930-2639b	19:30:36.03	-26:39:57.7	0.53	0.05	barely
J1930-2653c	19:30:36.58	-26:53:07.8	0.67	0.06	barely
J1930-2618b	19:30:36.64	-26:18:29.2	0.36	0.04	unresolved
J1930-2630c	19:30:36.89	-26:30:25.4	0.24	0.03	unresolved
J1930-2616c	19:30:37.15	-26:16:30.0	0.29	0.03	unresolved
J1930-2656b	19:30:37.91	-26:56:39.4	1.48	0.15	unresolved
J1930-2623b	19:30:37.93	-26:23:26.4	0.76	0.07	unresolved
J1930-2624b	19:30:38.00	-26:24:47.3	0.56	0.05	unresolved
J1930-2643b	19:30:38.01	-26:43:17.5	118.3	11.8	**FRI-II?**
J1930-2622b	19:30:38.17	-26:22:51.3	0.26	0.04	unresolved
J1930-2623c	19:30:38.27	-26:23:01.4	0.38	0.04	barely
J1930-2634d	19:30:38.31	-26:34:51.4	0.20	0.03	unresolved
J1930-2625i	19:30:38.46	-26:25:07.4	0.86	0.09	unresolved
J1930-2638b	19:30:38.50	-26:38:31.7	0.37	0.04	unresolved
J1930-2647c	19:30:38.51	-26:47:16.1	5.36	0.53	barely
J1930-2610a	19:30:39.36	-26:10:02.7	0.73	0.07	barely
J1930-2629c	19:30:39.51	-26:29:13.9	1.76	0.17	unresolved
J1930-2631f	19:30:39.91	-26:31:48.5	0.21	0.03	unresolved
J1930-2634e	19:30:40.15	-26:34:42.4	0.25	0.03	unresolved
J1930-2626f	19:30:40.48	-26:26:51.2	0.31	0.04	unresolved
J1930-2631g	19:30:40.58	-26:31:13.5	1.08	0.11	barely
J1930-2628d	19:30:40.58	-26:28:42.2	0.40	0.05	unresolved
J1930-2612a	19:30:41.06	-26:12:24.6	0.44	0.05	unresolved
J1930-2630d	19:30:41.14	-26:30:31.5	0.69	0.07	unresolved
J1930-2634f	19:30:41.14	-26:34:01.8	0.16	0.03	unresolved
J1930-2616d	19:30:41.67	-26:16:49.2	0.51	0.05	unresolved
J1930-2608	19:30:42.17	-26:08:55.0	0.61	0.06	unresolved
J1930-2653d	19:30:42.95	-26:53:30.2	0.40	0.05	unresolved
J1930-2639c	19:30:43.43	-26:39:19.9	0.35	0.04	unresolved
J1930-2653e	19:30:43.67	-26:53:45.7	1.92	0.19	unresolved

Table 5.13: continued

Name	RA_{J2000}	DEC_{J2000}	F_{640MHz} (mJy)	ΔF	Morphology
J1930-2630e	19:30:43.72	-26:30:00.5	0.79	0.08	barely
J1930-2647d	19:30:44.12	-26:47:34.5	2.74	0.27	unresolved
J1930-2620b	19:30:44.49	-26:20:35.3	0.54	0.06	unresolved
J1930-2636a	19:30:45.18	-26:36:33.6	0.25	0.03	unresolved
J1930-2628e	19:30:45.94	-26:28:22.3	0.45	0.05	unresolved
J1930-2613b	19:30:46.61	-26:13:51.0	0.44	0.05	barely
J1930-2627a	19:30:46.65	-26:27:52.8	0.22	0.03	unresolved
J1930-2649b	19:30:46.72	-26:49:46.3	0.59	0.06	unresolved
J1930-2636b	19:30:47.25	-26:36:54.7	0.29	0.04	unresolved
J1930-2638c	19:30:47.41	-26:38:42.0	0.24	0.03	unresolved
J1930-2617a	19:30:47.50	-26:17:39.0	0.42	0.05	unresolved
J1930-2636c	19:30:47.60	-26:36:17.8	0.50	0.05	barely
J1930-2641c	19:30:47.60	-26:41:42.8	0.49	0.05	unresolved
J1930-2644c	19:30:47.66	-26:44:15.0	70.6	7.06	unresolved
J1930-2640c	19:30:48.16	-26:40:20.8	0.63	0.06	unresolved
J1930-2637d	19:30:48.30	-26:37:47.3	2.37	0.23	barely
J1930-2633b	19:30:48.48	-26:33:39.3	0.98	0.10	unresolved
J1930-2630f	19:30:48.56	-26:30:17.7	0.27	0.04	unresolved
J1930-2649c	19:30:48.86	-26:49:13.5	0.55	0.06	barely
J1930-2627b	19:30:48.99	-26:27:27.3	0.18	0.03	unresolved
J1930-2657c	19:30:49.21	-26:57:12.0	0.43	0.05	unresolved
J1930-2628f	19:30:50.26	-26:28:17.0	0.28	0.04	unresolved
J1930-2612b	19:30:50.39	-26:12:27.5	0.32	0.04	unresolved
J1930-2631h	19:30:50.60	-26:31:52.7	0.32	0.04	unresolved
J1930-2700a	19:30:52.15	-27:00:42.3	0.52	0.06	unresolved
J1930-2633c	19:30:52.35	-26:33:27.7	0.23	0.03	unresolved
J1930-2647e	19:30:52.48	-26:47:09.3	0.35	0.04	unresolved
J1930-2634g	19:30:52.83	-26:34:37.1	0.18	0.03	unresolved
J1930-2658	19:30:53.11	-26:58:00.4	1.58	0.16	unresolved
J1930-2627d	19:30:53.47	-26:27:37.7	0.22	0.03	unresolved
J1930-2630g	19:30:53.48	-26:30:37.7	0.32	0.04	unresolved
J1930-2610b	19:30:53.55	-26:10:37.9	0.74	0.08	unresolved
J1930-2617b	19:30:53.66	-26:17:59.7	0.82	0.08	unresolved
J1930-2616e	19:30:53.96	-26:16:23.6	0.46	0.05	unresolved
J1930-2650c	19:30:54.69	-26:50:12.0	0.27	0.04	barely
J1930-2650d	19:30:54.71	-26:50:50.1	3.88	0.38	unresolved
J1930-2634h	19:30:54.84	-26:34:32.0	0.22	0.03	unresolved
J1930-2655	19:30:55.06	-26:55:37.3	1.29	0.13	unresolved
J1930-2619e	19:30:55.18	-26:19:04.1	1.40	0.14	barely
J1930-2630h	19:30:55.30	-26:30:28.4	0.22	0.03	unresolved
J1930-2635b	19:30:55.41	-26:35:00.7	0.28	0.04	unresolved

Table 5.14: continued

Name	RA_{J2000}	DEC_{J2000}	F_{640MHz} (mJy)	ΔF	Morphology
J1930-2620c	19:30:55.43	-26:20:48.2	24.5	2.45	unresolved
J1930-2616f	19:30:56.68	-26:16:56.6	4.57	0.45	unresolved
J1930-2618c	19:30:57.06	-26:18:35.7	0.35	0.04	barely
J1930-2700b	19:30:57.28	-27:00:43.4	0.51	0.05	unresolved
J1930-2632d	19:30:57.55	-26:32:57.3	0.22	0.03	unresolved
J1930-2650e	19:30:57.90	-26:50:16.5	0.30	0.04	unresolved
J1930-2628	19:30:57.97	-26:28:26.7	0.23	0.03	unresolved
J1930-2636d	19:30:58.04	-26:36:14.6	3.88	0.38	unresolved
J1930-2632e	19:30:58.07	-26:32:44.7	0.49	0.05	unresolved
J1930-2630i	19:30:58.35	-26:30:19.4	0.16	0.03	unresolved
J1930-2631i	19:30:59.00	-26:31:32.5	0.37	0.04	unresolved
J1930-2617c	19:30:59.25	-26:17:33.4	0.78	0.08	barely
J1930-2626g	19:30:59.78	-26:26:40.0	0.77	0.08	unresolved
J1930-2617d	19:30:59.80	-26:17:03.6	0.35	0.04	barely
J1930-2649d	19:30:59.99	-26:49:38.8	0.37	0.04	barely
J1931-2616a	19:31:00.25	-26:16:45.9	0.67	0.07	unresolved
J1931-2607	19:31:00.37	-26:07:41.3	3.48	0.35	barely
J1931-2638a	19:31:02.03	-26:38:24.4	0.18	0.03	unresolved
J1931-2628a	19:31:02.76	-26:28:10.0	0.25	0.03	unresolved
J1931-2627a	19:31:02.93	-26:27:23.2	0.25	0.03	unresolved
J1931-2656a	19:31:02.99	-26:56:30.8	0.28	0.04	unresolved
J1931-2629a	19:31:03.10	-26:29:00.1	0.86	0.09	unresolved
J1931-2645a	19:31:03.23	-26:45:14.9	0.69	0.07	unresolved
J1931-2628b	19:31:03.45	-26:28:19.5	0.24	0.03	unresolved
J1931-2620a	19:31:03.67	-26:20:25.0	15.4	1.54	barely
J1931-2653a	19:31:03.92	-26:53:48.8	0.39	0.04	unresolved
J1931-2615a	19:31:04.11	-26:15:04.0	0.51	0.05	unresolved
J1931-2623a	19:31:04.73	-26:23:38.1	0.42	0.05	unresolved
J1931-2634a	19:31:05.46	-26:34:17.8	0.23	0.03	unresolved
J1931-2639	19:31:05.51	-26:39:31.7	0.42	0.05	barely
J1931-2656b	19:31:05.70	-26:56:40.0	1.06	0.11	unresolved
J1931-2629b	19:31:06.44	-26:29:09.7	0.38	0.04	unresolved
J1931-2650a	19:31:06.80	-26:50:43.4	0.22	0.03	unresolved
J1931-2628c	19:31:06.96	-26:28:04.3	0.34	0.04	unresolved
J1931-2608a	19:31:07.02	-26:08:09.5	0.79	0.08	unresolved
J1931-2640a	19:31:07.28	-26:40:58.5	1.39	0.14	unresolved
J1931-2659a	19:31:08.47	-26:59:25.0	0.54	0.06	unresolved
J1931-2622a	19:31:08.56	-26:22:20.0	0.29	0.04	unresolved
J1931-2615b	19:31:08.70	-26:15:59.6	5.84	0.58	**FRI-II?**
J1931-2637a	19:31:08.97	-26:37:01.5	0.31	0.04	barely
J1931-2613a	19:31:09.25	-26:13:04.3	0.44	0.05	unresolved

Table 5.15: continued

Name	RA_{J2000}	DEC_{J2000}	F_{640MHz} (mJy)	ΔF	Morphology
J1931-2633a	19:31:09.26	-26:33:40.2	0.48	0.05	unresolved
J1931-2641a	19:31:09.65	-26:41:42.0	0.42	0.05	unresolved
J1931-2628d	19:31:10.05	-26:28:07.0	0.16	0.03	unresolved
J1931-2651	19:31:11.12	-26:51:47.0	0.30	0.04	unresolved
J1931-2631a	19:31:13.16	-26:31:31.0	0.39	0.04	unresolved
J1931-2624a	19:31:13.20	-26:24:49.4	0.22	0.03	unresolved
J1931-2624b	19:31:13.60	-26:24:39.4	0.44	0.05	barely
J1931-2646a	19:31:13.61	-26:46:48.1	0.26	0.04	unresolved
J1931-2629c	19:31:13.84	-26:29:54.1	0.38	0.04	barely
J1931-2630a	19:31:13.89	-26:30:50.8	0.23	0.03	unresolved
J1931-2618a	19:31:13.98	-26:18:12.6	0.32	0.04	barely
J1931-2657a	19:31:14.03	-26:57:26.4	0.31	0.04	unresolved
J1931-2623b	19:31:14.13	-26:23:36.4	0.22	0.03	unresolved
J1931-2634b	19:31:15.05	-26:34:14.0	0.15	0.03	unresolved
J1931-2648a	19:31:15.27	-26:48:02.8	0.61	0.06	barely
J1931-2649	19:31:15.30	-26:49:32.4	0.30	0.04	unresolved
J1931-2634c	19:31:15.64	-26:34:27.2	0.25	0.03	unresolved
J1931-2627b	19:31:16.13	-26:27:36.4	0.27	0.04	unresolved
J1931-2630b	19:31:16.19	-26:30:04.1	0.22	0.03	unresolved
J1931-2609a	19:31:16.52	-26:09:15.6	0.85	0.09	unresolved
J1931-2655a	19:31:16.73	-26:55:08.3	0.27	0.04	unresolved
J1931-2624c	19:31:16.84	-26:24:54.3	0.20	0.03	unresolved
J1931-2644a	19:31:17.22	-26:44:48.5	61.5	6.15	unresolved
J1931-2656a	19:31:17.56	-26:56:24.2	0.30	0.04	unresolved
J1931-2608b	19:31:17.59	-26:08:44.4	2.90	0.29	unresolved
J1931-2637b	19:31:17.85	-26:37:04.8	1.99	0.20	barely
J1931-2630c	19:31:18.37	-26:30:17.5	0.53	0.06	unresolved
J1931-2612a	19:31:18.96	-26:12:56.0	0.39	0.04	unresolved
J1931-2636a	19:31:19.02	-26:36:02.9	0.36	0.04	unresolved
J1931-2652a	19:31:19.20	-26:52:19.6	0.32	0.04	unresolved
J1931-2630d	19:31:19.38	-26:30:17.3	0.60	0.06	unresolved
J1931-2627c	19:31:19.38	-26:27:17.3	0.17	0.03	unresolved
J1931-2620b	19:31:19.55	-26:20:46.4	0.36	0.04	barely
J1931-2622b	19:31:20.15	-26:22:39.1	0.61	0.06	barely
J1931-2656b	19:31:20.22	-26:56:29.3	1.33	0.13	unresolved
J1931-2645b	19:31:20.41	-26:45:33.9	0.42	0.05	unresolved
J1931-2640b	19:31:20.53	-26:40:46.2	0.63	0.07	unresolved
J1931-2653b	19:31:20.64	-26:53:37.7	0.33	0.04	unresolved
J1931-2701a	19:31:21.10	-27:01:12.9	0.63	0.06	barely
J1931-2637c	19:31:21.11	-26:37:51.3	0.23	0.03	unresolved
J1931-2618b	19:31:21.29	-26:18:00.6	0.62	0.06	unresolved

Table 5.16: continued

Name	RA_{J2000}	DEC_{J2000}	F_{640MHz} (mJy)	ΔF	Morphology
J1931-2621a	19:31:21.62	-26:21:23.5	1.08	0.11	unresolved
J1931-2646b	19:31:22.55	-26:46:52.0	0.34	0.04	unresolved
J1931-2615c	19:31:22.69	-26:15:33.4	0.58	0.06	unresolved
J1931-2628e	19:31:23.24	-26:28:49.7	0.19	0.03	unresolved
J1931-2649a	19:31:23.68	-26:49:39.1	0.38	0.04	unresolved
J1931-2614a	19:31:24.88	-26:14:50.0	0.31	0.04	unresolved
J1931-2622c	19:31:26.08	-26:22:34.2	0.69	0.07	barely
J1931-2617a	19:31:26.85	-26:17:54.7	0.49	0.05	barely
J1931-2650b	19:31:27.12	-26:50:54.5	0.37	0.04	unresolved
J1931-2617b	19:31:27.35	-26:17:41.2	0.32	0.04	barely
J1931-2649b	19:31:27.41	-26:49:24.6	0.36	0.04	unresolved
J1931-2659b	19:31:27.44	-26:59:32.8	7.07	0.70	barely
J1931-2631b	19:31:27.77	-26:31:10.6	0.34	0.04	unresolved
J1931-2630e	19:31:27.85	-26:30:03.6	0.31	0.04	unresolved
J1931-2627d	19:31:28.06	-26:27:41.3	0.31	0.04	unresolved
J1931-2618c	19:31:28.11	-26:18:45.9	2.34	0.23	unresolved
J1931-2637d	19:31:28.34	-26:37:31.7	0.20	0.03	unresolved
J1931-2631c	19:31:28.70	-26:31:29.9	0.24	0.03	unresolved
J1931-2636b	19:31:28.89	-26:36:48.3	0.19	0.03	unresolved
J1931-2641b	19:31:30.12	-26:41:08.9	0.23	0.03	unresolved
J1931-2608c	19:31:30.15	-26:08:55.6	0.73	0.07	unresolved
J1931-2651b	19:31:30.41	-26:51:23.3	0.77	0.08	unresolved
J1931-2619a	19:31:30.69	-26:19:58.7	34.2	3.42	barely
J1931-2643	19:31:31.00	-26:43:37.9	0.23	0.03	unresolved
J1931-2637e	19:31:32.03	-26:37:13.1	0.34	0.04	unresolved
J1931-2646c	19:31:32.06	-26:46:09.1	0.23	0.03	unresolved
J1931-2618d	19:31:32.33	-26:18:05.0	0.25	0.03	unresolved
J1931-2655	19:31:32.43	-26:55:45.0	8.51	0.85	unresolved
J1931-2631d	19:31:32.52	-26:31:33.1	0.26	0.03	unresolved
J1931-2638b	19:31:32.76	-26:38:38.8	0.35	0.04	barely
J1931-2620c	19:31:33.04	-26:20:14.1	1.24	0.12	barely
J1931-2649b	19:31:33.11	-26:49:14.3	0.16	0.03	unresolved
J1931-2653c	19:31:33.28	-26:53:44.3	0.64	0.07	unresolved
J1931-2623c	19:31:33.37	-26:23:37.3	0.24	0.03	unresolved
J1931-2623d	19:31:33.69	-26:23:46.7	0.19	0.03	unresolved
J1931-2650c	19:31:34.31	-26:50:32.0	0.29	0.04	unresolved
J1931-2631e	19:31:34.86	-26:31:52.3	0.38	0.04	barely
J1931-2641c	19:31:35.17	-26:41:44.3	0.21	0.03	unresolved
J1931-2657b	19:31:35.23	-26:57:05.6	0.47	0.05	unresolved
J1931-2659c	19:31:35.54	-26:59:16.9	0.68	0.07	barely
J1931-2654	19:31:35.75	-26:54:51.4	1.31	0.13	unresolved

Table 5.17: continued

Name	RA_{J2000}	DEC_{J2000}	F_{640MHz} (mJy)	ΔF	Morphology
J1931-2623e	19:31:35.82	-26:23:07.6	0.25	0.03	unresolved
J1931-2644b	19:31:35.94	-26:44:41.7	0.37	0.04	unresolved
J1931-2633b	19:31:36.49	-26:33:09.3	24.1	2.41	unresolved
J1931-2622d	19:31:36.60	-26:22:52.5	0.24	0.03	unresolved
J1931-2627e	19:31:36.74	-26:27:18.0	0.19	0.03	unresolved
J1931-2626a	19:31:37.35	-26:26:22.3	0.28	0.04	unresolved
J1931-2609b	19:31:37.58	-26:09:33.4	0.33	0.04	unresolved
J1931-2615d	19:31:38.15	-26:15:30.2	0.29	0.04	unresolved
J1931-2659d	19:31:38.32	-26:59:34.3	0.62	0.06	unresolved
J1931-2650d	19:31:38.56	-26:50:05.2	0.19	0.03	unresolved
J1931-2632	19:31:38.93	-26:32:44.6	0.46	0.05	unresolved
J1931-2644c	19:31:38.95	-26:44:37.8	0.22	0.03	unresolved
J1931-2609c	19:31:39.01	-26:09:40.9	0.33	0.04	unresolved
J1931-2613b	19:31:39.02	-26:13:13.4	8.87	0.88	barely
J1931-2608d	19:31:39.08	-26:08:42.9	0.94	0.09	unresolved
J1931-2614b	19:31:39.16	-26:14:11.4	0.29	0.04	unresolved
J1931-2647	19:31:39.25	-26:47:13.7	0.29	0.04	unresolved
J1931-2638c	19:31:39.38	-26:38:31.0	0.24	0.03	unresolved
J1931-2625	19:31:39.76	-26:25:51.2	0.25	0.03	unresolved
J1931-2649c	19:31:40.03	-26:49:33.4	0.35	0.04	unresolved
J1931-2619b	19:31:40.71	-26:19:23.4	0.20	0.03	unresolved
J1931-2621b	19:31:41.37	-26:21:57.4	0.30	0.04	unresolved
J1931-2640c	19:31:41.60	-26:40:08.1	0.36	0.04	barely
J1931-2606	19:31:41.84	-26:06:11.1	0.42	0.05	unresolved
J1931-2646d	19:31:42.55	-26:46:45.2	0.38	0.04	unresolved
J1931-2645c	19:31:42.71	-26:45:47.1	0.31	0.04	unresolved
J1931-2628f	19:31:42.84	-26:28:26.3	0.20	0.03	unresolved
J1931-2642a	19:31:43.42	-26:42:51.4	0.20	0.03	unresolved
J1931-2617c	19:31:43.73	-26:17:42.0	2.77	0.27	unresolved
J1931-2621c	19:31:44.43	-26:21:30.0	0.28	0.04	unresolved
J1931-2655b	19:31:44.78	-26:55:41.6	0.57	0.06	barely
J1931-2646e	19:31:44.79	-26:46:31.1	0.17	0.03	unresolved
J1931-2702	19:31:45.22	-27:02:42.3	0.66	0.07	barely
J1931-2631f	19:31:45.27	-26:31:55.6	0.38	0.04	unresolved
J1931-2646f	19:31:45.29	-26:46:58.9	0.29	0.04	unresolved
J1931-2654	19:31:45.54	-26:54:24.0	0.80	0.08	unresolved
J1931-2648b	19:31:45.92	-26:48:04.0	0.18	0.03	unresolved
J1931-2626b	19:31:47.87	-26:26:46.3	0.24	0.03	unresolved
J1931-2644d	19:31:48.15	-26:44:21.5	0.22	0.03	unresolved
J1931-2621d	19:31:48.90	-26:21:38.6	0.65	0.07	unresolved
J1931-2619c	19:31:49.35	-26:19:45.3	0.21	0.03	unresolved

Table 5.18: continued

Name	RA_{J2000}	DEC_{J2000}	F_{640MHz} (mJy)	ΔF	Morphology
J1931-2634d	19:31:49.58	-26:34:32.9	183.7	18.3	**BCG**
J1931-2650e	19:31:49.98	-26:50:18.9	0.24	0.03	unresolved
J1931-2635	19:31:50.10	-26:35:25.4	354.7	35.4	**NAT**
J1931-2656c	19:31:50.91	-26:56:11.5	1.00	0.10	unresolved
J1931-2649	19:31:50.97	-26:49:01.2	0.35	0.04	unresolved
J1931-2652b	19:31:50.97	-26:52:10.8	0.23	0.03	unresolved
J1931-2650f	19:31:51.64	-26:50:27.0	0.39	0.04	barely
J1931-2652	19:31:51.82	-26:52:10.1	0.47	0.05	unresolved
J1931-2624d	19:31:51.97	-26:24:26.4	1.39	0.14	unresolved
J1931-2653d	19:31:52.06	-26:53:57.0	0.58	0.06	barely
J1931-2701b	19:31:52.28	-27:01:05.7	0.58	0.06	unresolved
J1931-2618e	19:31:52.32	-26:18:31.2	0.58	0.06	barely
J1931-2617d	19:31:52.68	-26:17:31.9	0.43	0.05	unresolved
J1931-2645d	19:31:52.92	-26:45:10.7	0.23	0.03	unresolved
J1931-2650g	19:31:53.27	-26:50:24.4	0.58	0.06	unresolved
J1931-2653e	19:31:53.38	-26:53:38.3	0.28	0.04	unresolved
J1931-2651c	19:31:53.94	-26:51:44.8	0.56	0.06	barely
J1931-2612	19:31:53.99	-26:12:12.9	0.64	0.07	unresolved
J1931-2613c	19:31:54.92	-26:13:53.1	0.58	0.06	barely
J1931-2630f	19:31:55.05	-26:30:56.6	3.71	0.37	barely
J1931-2621e	19:31:55.15	-26:21:10.7	0.39	0.04	unresolved
J1931-2640d	19:31:55.20	-26:40:57.7	0.26	0.03	unresolved
J1931-2614c	19:31:55.43	-26:14:17.7	0.46	0.05	barely
J1931-2612b	19:31:55.63	-26:12:45.6	0.55	0.06	unresolved
J1931-2651d	19:31:55.70	-26:51:52.2	0.57	0.06	barely
J1931-2656d	19:31:55.86	-26:56:26.9	0.19	0.03	unresolved
J1931-2615e	19:31:56.13	-26:15:03.4	0.28	0.04	unresolved
J1931-2616b	19:31:56.49	-26:16:45.3	0.22	0.03	unresolved
J1931-2614d	19:31:57.31	-26:14:21.9	0.32	0.04	unresolved
J1931-2622	19:31:57.40	-26:22:09.1	0.94	0.09	unresolved
J1931-2645e	19:31:57.61	-26:45:37.2	0.43	0.05	unresolved
J1931-2617e	19:31:57.76	-26:17:43.6	0.19	0.03	unresolved
J1931-2649d	19:31:57.91	-26:49:54.2	0.42	0.05	unresolved
J1931-2649e	19:31:58.28	-26:49:33.4	0.27	0.04	barely
J1931-2645f	19:31:58.33	-26:45:34.4	0.67	0.07	barely
J1931-2642b	19:31:58.36	-26:42:33.2	0.24	0.03	unresolved
J1931-2625b	19:31:58.36	-26:25:57.6	0.22	0.03	unresolved
J1931-2622e	19:31:58.82	-26:22:27.9	1.52	0.15	barely
J1931-2615	19:31:58.95	-26:15:19.1	0.38	0.04	unresolved
J1931-2638d	19:31:58.96	-26:38:15.3	3.74	0.37	barely
J1931-2628g	19:31:59.06	-26:28:30.8	0.36	0.04	unresolved

Table 5.19: continued

Name	RA_{J2000}	DEC_{J2000}	F_{640MHz} (mJy)	ΔF	Morphology
J1931-2645g	19:31:59.42	-26:45:54.4	0.22	0.03	unresolved
J1931-2641d	19:31:59.73	-26:41:11.7	0.32	0.04	unresolved
J1932-2654a	19:32:00.42	-26:54:16.9	1.56	0.15	unresolved
J1932-2700a	19:32:00.48	-27:00:18.0	0.69	0.07	barely
J1932-2617a	19:32:01.06	-26:17:57.5	0.16	0.03	unresolved
J1932-2609a	19:32:01.18	-26:09:14.9	0.66	0.07	barely
J1932-2652a	19:32:01.42	-26:52:15.3	0.62	0.06	unresolved
J1932-2648a	19:32:02.61	-26:48:43.2	0.24	0.03	unresolved
J1932-2606a	19:32:03.12	-26:06:03.7	0.61	0.06	unresolved
J1932-2631a	19:32:04.37	-26:31:34.2	0.21	0.03	unresolved
J1932-2642a	19:32:04.68	-26:42:28.1	0.32	0.04	unresolved
J1932-2606b	19:32:05.03	-26:06:41.1	0.45	0.05	unresolved
J1932-2626a	19:32:05.25	-26:26:59.9	3.87	0.38	barely
J1932-2632	19:32:05.27	-26:32:05.9	0.66	0.07	unresolved
J1932-2628	19:32:05.34	-26:28:18.5	0.28	0.04	unresolved
J1932-2610a	19:32:06.32	-26:10:06.8	0.42	0.05	barely
J1932-2646a	19:32:06.45	-26:46:30.5	0.35	0.04	unresolved
J1932-2652b	19:32:06.92	-26:52:50.9	0.44	0.05	unresolved
J1932-2621a	19:32:07.17	-26:21:04.5	1.19	0.12	unresolved
J1932-2625a	19:32:07.42	-26:25:16.4	0.53	0.06	unresolved
J1932-2702a	19:32:07.77	-27:02:27.4	1.30	0.13	unresolved
J1932-2627	19:32:08.15	-26:27:02.8	1.23	0.12	barely
J1932-2624a	19:32:08.33	-26:24:55.1	0.19	0.03	unresolved
J1932-2633a	19:32:08.59	-26:33:23.4	0.47	0.05	barely
J1932-2619a	19:32:08.77	-26:19:26.8	0.28	0.04	unresolved
J1932-2644a	19:32:08.78	-26:44:54.4	0.43	0.05	barely
J1932-2645a	19:32:08.82	-26:45:25.2	0.42	0.05	barely
J1932-2630a	19:32:08.86	-26:30:59.7	0.30	0.04	unresolved
J1932-2625b	19:32:09.78	-26:25:28.7	0.53	0.06	unresolved
J1932-2619b	19:32:09.87	-26:19:05.8	0.50	0.05	unresolved
J1932-2647a	19:32:10.11	-26:47:29.3	0.23	0.03	unresolved
J1932-2651a	19:32:10.68	-26:51:29.5	0.16	0.03	unresolved
J1932-2620	19:32:10.73	-26:20:41.1	0.81	0.08	unresolved
J1932-2621b	19:32:10.79	-26:21:50.4	3.43	0.34	barely
J1932-2646b	19:32:10.80	-26:46:38.8	0.27	0.04	unresolved
J1932-2647b	19:32:11.06	-26:47:09.8	0.70	0.07	unresolved
J1932-2634a	19:32:11.34	-26:34:01.2	0.45	0.05	unresolved
J1932-2657a	19:32:11.48	-26:57:08.0	2.26	0.22	unresolved
J1932-2654b	19:32:11.56	-26:54:24.8	0.27	0.04	unresolved
J1932-2621c	19:32:11.67	-26:21:46.2	0.43	0.05	unresolved
J1932-2647c	19:32:11.80	-26:47:44.1	0.27	0.04	unresolved

Table 5.20: continued

Name	RA_{J2000}	DEC_{J2000}	F_{640MHz} (mJy)	ΔF	Morphology
J1932-2649a	19:32:11.83	-26:49:57.4	0.16	0.03	unresolved
J1932-2618a	19:32:11.84	-26:18:44.7	8.42	0.84	barely
J1932-2637a	19:32:12.13	-26:37:29.7	0.75	0.08	unresolved
J1932-2648b	19:32:12.26	-26:48:17.5	0.92	0.09	unresolved
J1932-2645b	19:32:12.45	-26:45:42.8	0.59	0.06	unresolved
J1932-2633b	19:32:12.57	-26:33:14.1	1.44	0.14	unresolved
J1932-2648c	19:32:12.77	-26:48:33.6	0.29	0.04	unresolved
J1932-2628b	19:32:12.99	-26:28:06.9	0.53	0.06	unresolved
J1932-2626b	19:32:13.03	-26:26:30.0	0.30	0.04	unresolved
J1932-2621d	19:32:13.13	-26:21:54.5	0.42	0.05	unresolved
J1932-2654c	19:32:13.99	-26:54:23.6	0.91	0.09	unresolved
J1932-2651b	19:32:14.41	-26:51:39.2	1.03	0.10	unresolved
J1932-2636	19:32:14.42	-26:36:38.5	0.31	0.04	barely
J1932-2617b	19:32:14.88	-26:17:43.1	0.32	0.04	barely
J1932-2645c	19:32:15.13	-26:45:57.9	0.21	0.03	unresolved
J1932-2626c	19:32:16.02	-26:26:51.4	0.41	0.05	barely
J1932-2653a	19:32:16.22	-26:53:37.6	0.41	0.05	unresolved
J1932-2639	19:32:16.33	-26:39:52.5	0.28	0.04	unresolved
J1932-2648d	19:32:16.54	-26:48:43.7	0.58	0.06	unresolved
J1932-2608a	19:32:16.84	-26:08:21.9	13.2	1.32	barely
J1932-2634b	19:32:17.08	-26:34:08.6	0.24	0.03	unresolved
J1932-2637b	19:32:17.10	-26:37:21.3	0.23	0.03	unresolved
J1932-2635a	19:32:17.11	-26:35:37.7	1.20	0.12	unresolved
J1932-2652c	19:32:17.31	-26:52:30.0	0.73	0.07	unresolved
J1932-2629a	19:32:17.72	-26:29:31.6	1.49	0.15	unresolved
J1932-2618b	19:32:18.13	-26:18:17.0	0.50	0.05	unresolved
J1932-2642b	19:32:18.26	-26:42:41.8	0.27	0.04	unresolved
J1932-2633c	19:32:18.66	-26:33:04.1	0.39	0.04	barely
J1932-2629b	19:32:18.67	-26:29:07.6	0.29	0.04	unresolved
J1932-2650a	19:32:18.73	-26:50:29.8	0.26	0.03	unresolved
J1932-2621e	19:32:18.85	-26:21:25.7	0.80	0.08	unresolved
J1932-2615a	19:32:19.05	-26:15:17.2	0.30	0.04	unresolved
J1932-2618c	19:32:19.59	-26:18:14.4	0.78	0.08	unresolved
J1932-2700b	19:32:19.70	-27:00:50.6	0.79	0.08	unresolved
J1932-2700c	19:32:19.90	-27:00:02.5	0.55	0.06	barely
J1932-2631b	19:32:20.06	-26:31:34.5	0.84	0.08	unresolved
J1932-2653b	19:32:20.22	-26:53:06.0	0.42	0.05	barely
J1932-2649b	19:32:20.86	-26:49:47.7	0.28	0.04	unresolved
J1932-2659a	19:32:21.06	-26:59:02.3	1.66	0.16	barely
J1932-2644b	19:32:21.41	-26:44:20.3	0.78	0.08	unresolved
J1932-2615b	19:32:21.73	-26:15:40.7	0.43	0.05	unresolved

Table 5.21: continued

Name	RA_{J2000}	DEC_{J2000}	F_{640MHz} (mJy)	ΔF	Morphology
J1932-2607a	19:32:21.78	-26:07:11.7	0.55	0.06	unresolved
J1932-2628c	19:32:22.10	-26:28:32.2	0.21	0.03	unresolved
J1932-2620b	19:32:22.29	-26:20:10.1	0.29	0.04	unresolved
J1932-2616a	19:32:22.33	-26:16:40.3	0.33	0.04	barely
J1932-2619c	19:32:22.44	-26:19:38.5	0.43	0.05	unresolved
J1932-2606c	19:32:22.85	-26:06:00.7	0.77	0.08	barely
J1932-2638a	19:32:23.02	-26:38:56.3	0.22	0.03	unresolved
J1932-2614	19:32:23.74	-26:14:09.6	0.34	0.04	unresolved
J1932-2616b	19:32:25.17	-26:16:10.6	0.68	0.07	unresolved
J1932-2654d	19:32:25.43	-26:54:25.6	3.71	0.37	unresolved
J1932-2648e	19:32:25.82	-26:48:15.8	1.49	0.15	unresolved
J1932-2631c	19:32:25.87	-26:31:23.8	0.61	0.06	unresolved
J1932-2615	19:32:25.95	-26:15:36.1	0.22	0.03	unresolved
J1932-2632b	19:32:26.15	-26:32:48.1	0.67	0.07	unresolved
J1932-2616c	19:32:26.62	-26:16:44.3	0.27	0.04	barely
J1932-2638b	19:32:26.79	-26:38:12.1	0.37	0.04	unresolved
J1932-2645d	19:32:26.79	-26:45:32.4	0.17	0.03	unresolved
J1932-2646c	19:32:26.88	-26:46:05.7	0.18	0.03	unresolved
J1932-2654e	19:32:27.00	-26:54:11.3	0.44	0.05	unresolved
J1932-2639b	19:32:27.29	-26:39:09.4	0.27	0.04	unresolved
J1932-2648f	19:32:27.34	-26:48:19.6	0.50	0.05	unresolved
J1932-2633d	19:32:27.35	-26:33:09.7	35.5	3.55	unresolved
J1932-2644	19:32:27.51	-26:44:09.0	0.32	0.04	barely
J1932-2621f	19:32:27.77	-26:21:16.1	0.34	0.04	unresolved
J1932-2633e	19:32:27.79	-26:33:55.7	0.41	0.05	unresolved
J1932-2632c	19:32:27.80	-26:32:07.8	0.78	0.08	unresolved
J1932-2651c	19:32:27.83	-26:51:04.0	0.48	0.05	unresolved
J1932-2638c	19:32:27.91	-26:38:23.1	0.20	0.03	unresolved
J1932-2609b	19:32:28.32	-26:09:21.8	0.60	0.06	unresolved
J1932-2638d	19:32:28.38	-26:38:53.2	0.31	0.04	unresolved
J1932-2608b	19:32:28.93	-26:08:40.3	0.67	0.07	barely
J1932-2639	19:32:28.93	-26:39:33.7	0.23	0.03	unresolved
J1932-2613	19:32:29.05	-26:13:24.4	0.78	0.08	unresolved
J1932-2635b	19:32:29.07	-26:35:00.4	0.21	0.03	unresolved
J1932-2639c	19:32:29.13	-26:39:51.8	0.24	0.03	unresolved
J1932-2639d	19:32:29.52	-26:39:22.9	0.39	0.04	unresolved
J1932-2652d	19:32:30.41	-26:52:29.3	0.60	0.06	unresolved
J1932-2638e	19:32:30.46	-26:38:11.8	0.26	0.04	unresolved
J1932-2628d	19:32:30.73	-26:28:50.3	1.23	0.12	unresolved
J1932-2634c	19:32:30.78	-26:34:41.8	0.22	0.03	unresolved
J1932-2624b	19:32:30.82	-26:24:35.4	0.39	0.04	unresolved

Table 5.22: continued

Name	RA_{J2000}	DEC_{J2000}	F_{640MHz} (mJy)	ΔF	Morphology
J1932-2641a	19:32:31.04	-26:41:50.8	0.90	0.09	unresolved
J1932-2628e	19:32:31.08	-26:28:02.6	6.12	0.61	barely
J1932-2631d	19:32:31.63	-26:31:20.3	0.92	0.09	unresolved
J1932-2635c	19:32:31.63	-26:35:18.8	0.34	0.04	unresolved
J1932-2650a	19:32:31.71	-26:50:46.8	0.70	0.07	barely
J1932-2654f	19:32:31.81	-26:54:35.7	1.54	0.15	unresolved
J1932-2650b	19:32:32.60	-26:50:27.3	0.36	0.04	barely
J1932-2615c	19:32:32.87	-26:15:46.1	0.31	0.04	unresolved
J1932-2635d	19:32:33.25	-26:35:58.0	0.31	0.04	unresolved
J1932-2639e	19:32:33.36	-26:39:07.4	1.16	0.12	unresolved
J1932-2643a	19:32:33.47	-26:43:32.1	0.21	0.03	unresolved
J1932-2650b	19:32:33.93	-26:50:26.7	1.00	0.10	barely
J1932-2702b	19:32:34.39	-27:02:34.9	0.84	0.08	unresolved
J1932-2650c	19:32:35.33	-26:50:14.4	0.67	0.07	unresolved
J1932-2621g	19:32:35.81	-26:21:57.0	0.37	0.04	unresolved
J1932-2644c	19:32:36.47	-26:44:12.8	0.21	0.03	unresolved
J1932-2617c	19:32:36.57	-26:17:10.0	1.12	0.11	unresolved
J1932-2642c	19:32:36.79	-26:42:06.6	0.28	0.04	unresolved
J1932-2646d	19:32:37.10	-26:46:11.6	0.32	0.04	unresolved
J1932-2652e	19:32:37.49	-26:52:12.2	0.41	0.05	unresolved
J1932-2640a	19:32:37.52	-26:40:42.0	0.26	0.03	unresolved
J1932-2623	19:32:37.55	-26:23:38.5	0.27	0.04	unresolved
J1932-2659b	19:32:37.83	-26:59:21.3	0.78	0.08	unresolved
J1932-2609c	19:32:38.62	-26:09:10.2	0.60	0.06	barely
J1932-2628f	19:32:38.69	-26:28:42.7	0.75	0.08	barely
J1932-2658e	19:32:39.38	-26:58:36.1	0.72	0.07	unresolved
J1932-2656	19:32:40.08	-26:56:46.7	0.49	0.05	barely
J1932-2645e	19:32:40.27	-26:45:46.0	0.59	0.06	unresolved
J1932-2618d	19:32:40.31	-26:18:54.4	15.3	1.53	unresolved
J1932-2624c	19:32:40.55	-26:24:54.4	0.40	0.05	unresolved
J1932-2648g	19:32:40.86	-26:48:01.2	0.29	0.04	unresolved
J1932-2658b	19:32:41.09	-26:58:37.2	3.09	0.31	unresolved
J1932-2642d	19:32:41.17	-26:42:17.3	0.16	0.03	unresolved
J1932-2629	19:32:41.42	-26:29:05.3	0.37	0.04	unresolved
J1932-2635e	19:32:41.54	-26:35:57.9	2.62	0.26	barely
J1932-2617d	19:32:42.96	-26:17:22.1	1.16	0.12	barely
J1932-2657b	19:32:43.01	-26:57:53.9	2.12	0.21	unresolved
J1932-2644d	19:32:43.85	-26:44:28.0	0.44	0.05	unresolved
J1932-2641b	19:32:44.15	-26:41:32.6	0.25	0.03	unresolved
J1932-2642e	19:32:44.21	-26:42:26.2	0.24	0.03	unresolved
J1932-2657c	19:32:44.57	-26:57:47.9	0.60	0.06	unresolved

Table 5.23: continued

Name	RA_{J2000}	DEC_{J2000}	F_{640MHz} (mJy)	ΔF	Morphology
J1932-2639f	19:32:44.93	-26:39:32.0	0.92	0.09	unresolved
J1932-2630b	19:32:44.94	-26:30:12.7	59.4	5.94	unresolved
J1932-2640b	19:32:45.36	-26:40:02.1	0.27	0.04	unresolved
J1932-2635f	19:32:45.41	-26:35:30.5	0.40	0.05	unresolved
J1932-2656b	19:32:46.06	-26:56:31.5	0.35	0.04	unresolved
J1932-2617e	19:32:46.96	-26:17:35.0	3.07	0.30	barely
J1932-2607b	19:32:46.97	-26:07:55.5	1.72	0.17	unresolved
J1932-2638f	19:32:47.56	-26:38:47.9	4.32	0.43	barely
J1932-2656c	19:32:49.30	-26:56:06.1	2.09	0.21	barely
J1932-2634d	19:32:50.11	-26:34:26.9	0.19	0.03	unresolved
J1932-2625c	19:32:50.97	-26:25:07.1	0.33	0.04	unresolved
J1932-2641c	19:32:51.06	-26:41:19.5	0.60	0.06	unresolved
J1932-2632d	19:32:51.07	-26:32:25.3	0.20	0.03	unresolved
J1932-2642f	19:32:51.34	-26:42:50.6	11.7	1.17	unresolved
J1932-2700d	19:32:51.99	-27:00:53.8	1.29	0.13	unresolved
J1932-2659c	19:32:52.23	-26:59:32.0	0.59	0.06	unresolved
J1932-2650c	19:32:52.42	-26:50:48.3	0.35	0.04	unresolved
J1932-2646e	19:32:53.89	-26:46:23.3	0.65	0.07	barely
J1932-2642g	19:32:54.53	-26:42:17.6	0.33	0.04	unresolved
J1932-2652f	19:32:54.67	-26:52:52.2	0.56	0.06	unresolved
J1932-2647d	19:32:55.32	-26:47:33.3	0.69	0.07	unresolved
J1932-2640c	19:32:55.67	-26:40:53.1	0.38	0.04	unresolved
J1932-2643b	19:32:55.82	-26:43:40.7	0.38	0.04	unresolved
J1932-2619	19:32:56.41	-26:19:04.2	0.49	0.05	unresolved
J1932-2651d	19:32:56.78	-26:51:01.3	0.60	0.06	barely
J1932-2652g	19:32:56.88	-26:52:32.3	0.35	0.04	unresolved
J1932-2616	19:32:57.17	-26:16:41.2	0.62	0.06	unresolved
J1932-2609d	19:32:57.33	-26:09:51.8	0.38	0.04	unresolved
J1932-2656d	19:32:57.53	-26:56:23.0	0.71	0.07	unresolved
J1932-2649c	19:32:58.43	-26:49:48.6	0.38	0.04	unresolved
J1932-2636	19:32:58.45	-26:36:50.0	3.76	0.37	unresolved
J1932-2643c	19:32:58.71	-26:43:29.2	12.6	1.26	unresolved
J1932-2650d	19:32:58.74	-26:50:25.9	0.66	0.07	unresolved
J1932-2622	19:32:59.40	-26:22:46.4	0.63	0.07	barely
J1933-2622a	19:33:01.38	-26:22:25.0	0.46	0.05	unresolved
J1933-2643a	19:33:02.00	-26:43:26.1	0.40	0.05	unresolved
J1933-2618a	19:33:02.64	-26:18:24.8	0.73	0.07	unresolved
J1933-2618b	19:33:04.12	-26:18:01.3	1.21	0.12	unresolved
J1933-2617a	19:33:04.55	-26:17:05.0	1.38	0.14	barely
J1933-2618c	19:33:04.75	-26:18:38.0	0.57	0.06	unresolved
J1933-2630a	19:33:05.35	-26:30:04.2	3.78	0.37	unresolved

Table 5.24: continued

Name	RA_{J2000}	DEC_{J2000}	F_{640MHz} (mJy)	ΔF	Morphology
J1933-2658	19:33:05.42	-26:58:19.8	21.6	2.16	barely
J1933-2622b	19:33:06.35	-26:22:22.7	30.9	3.09	barely
J1933-2652a	19:33:06.41	-26:52:36.0	2.06	0.20	barely
J1933-2638	19:33:08.51	-26:38:19.1	0.27	0.04	unresolved
J1933-2647a	19:33:08.94	-26:47:27.6	0.31	0.04	unresolved
J1933-2624a	19:33:09.77	-26:24:26.5	0.55	0.06	barely
J1933-2612	19:33:09.97	-26:12:40.9	0.94	0.09	unresolved
J1933-2647b	19:33:10.10	-26:47:10.2	0.52	0.06	unresolved
J1933-2633a	19:33:10.46	-26:33:56.5	0.59	0.06	unresolved
J1933-2630b	19:33:10.56	-26:30:45.4	0.41	0.05	unresolved
J1933-2639a	19:33:10.59	-26:39:40.3	1.35	0.13	unresolved
J1933-2656	19:33:10.77	-26:56:25.4	1.26	0.12	unresolved
J1933-2636	19:33:11.35	-26:36:26.5	0.39	0.04	unresolved
J1933-2649	19:33:12.30	-26:49:13.6	0.81	0.08	unresolved
J1933-2639b	19:33:12.92	-26:39:20.4	0.86	0.09	barely
J1933-2652b	19:33:13.20	-26:52:48.4	1.19	0.12	barely
J1933-2653	19:33:13.27	-26:53:30.9	1.33	0.13	unresolved
J1933-2633b	19:33:13.64	-26:33:24.7	0.41	0.05	unresolved
J1933-2652c	19:33:13.85	-26:52:28.7	1.00	0.10	unresolved
J1933-2633c	19:33:14.16	-26:33:21.7	0.67	0.07	unresolved
J1933-2613	19:33:14.31	-26:13:22.7	90.5	9.05	barely
J1933-2640a	19:33:15.30	-26:40:57.4	0.89	0.09	unresolved
J1933-2617b	19:33:17.36	-26:17:11.3	0.73	0.07	barely
J1933-2624b	19:33:17.39	-26:24:14.7	2.02	0.20	unresolved
J1933-2631	19:33:19.15	-26:31:29.9	2.12	0.21	unresolved
J1933-2640b	19:33:19.25	-26:40:31.0	13.8	1.38	unresolved
J1933-2626a	19:33:19.99	-26:26:09.9	0.88	0.09	unresolved
J1933-2632	19:33:21.40	-26:32:34.0	0.71	0.07	unresolved
J1933-2614a	19:33:22.95	-26:14:49.1	0.85	0.09	unresolved
J1933-2624c	19:33:23.16	-26:24:02.5	1.28	0.13	unresolved
J1933-2614b	19:33:27.31	-26:14:53.2	4.47	0.44	barely
J1933-2634a	19:33:27.33	-26:34:03.6	1.22	0.12	unresolved
J1933-2626b	19:33:28.07	-26:26:00.4	4.01	0.40	unresolved
J1933-2650	19:33:28.28	-26:50:03.5	1.36	0.13	unresolved
J1933-2634b	19:33:28.63	-26:34:28.4	1.16	0.12	barely
J1933-2618d	19:33:29.02	-26:18:33.6	2.54	0.25	unresolved
J1933-2629	19:33:30.70	-26:29:14.1	17.0	1.70	barely
J1933-2648a	19:33:30.84	-26:48:32.3	0.90	0.09	unresolved
J1933-2652d	19:33:31.33	-26:52:16.0	1.77	0.17	unresolved
J1933-2642	19:33:35.91	-26:42:43.9	1.86	0.18	unresolved
J1933-2643b	19:33:38.59	-26:43:13.6	2.22	0.22	barely

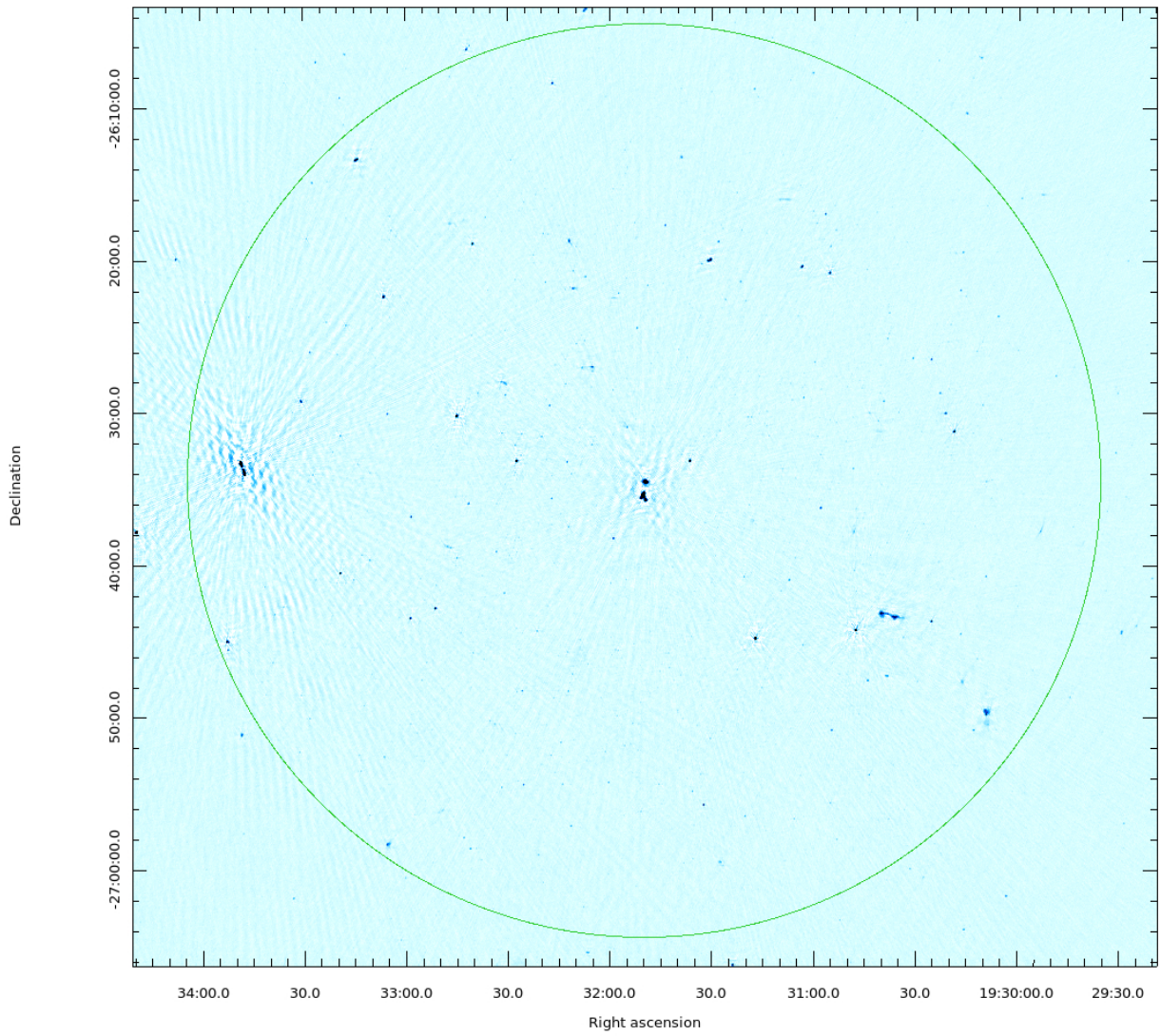

Figure 5.5: The image shows blue-scale view of the uGMRT field which encompasses an area of 0.785 deg^2 (30 arcmin, green circle). This is the area of interest in our analysis and the area within which we extracted our catalogues. The noise is 0.03 mJy/b and the resolution is 5 $\times$ 4 arcsec in p.a. $\sim$ 169°.

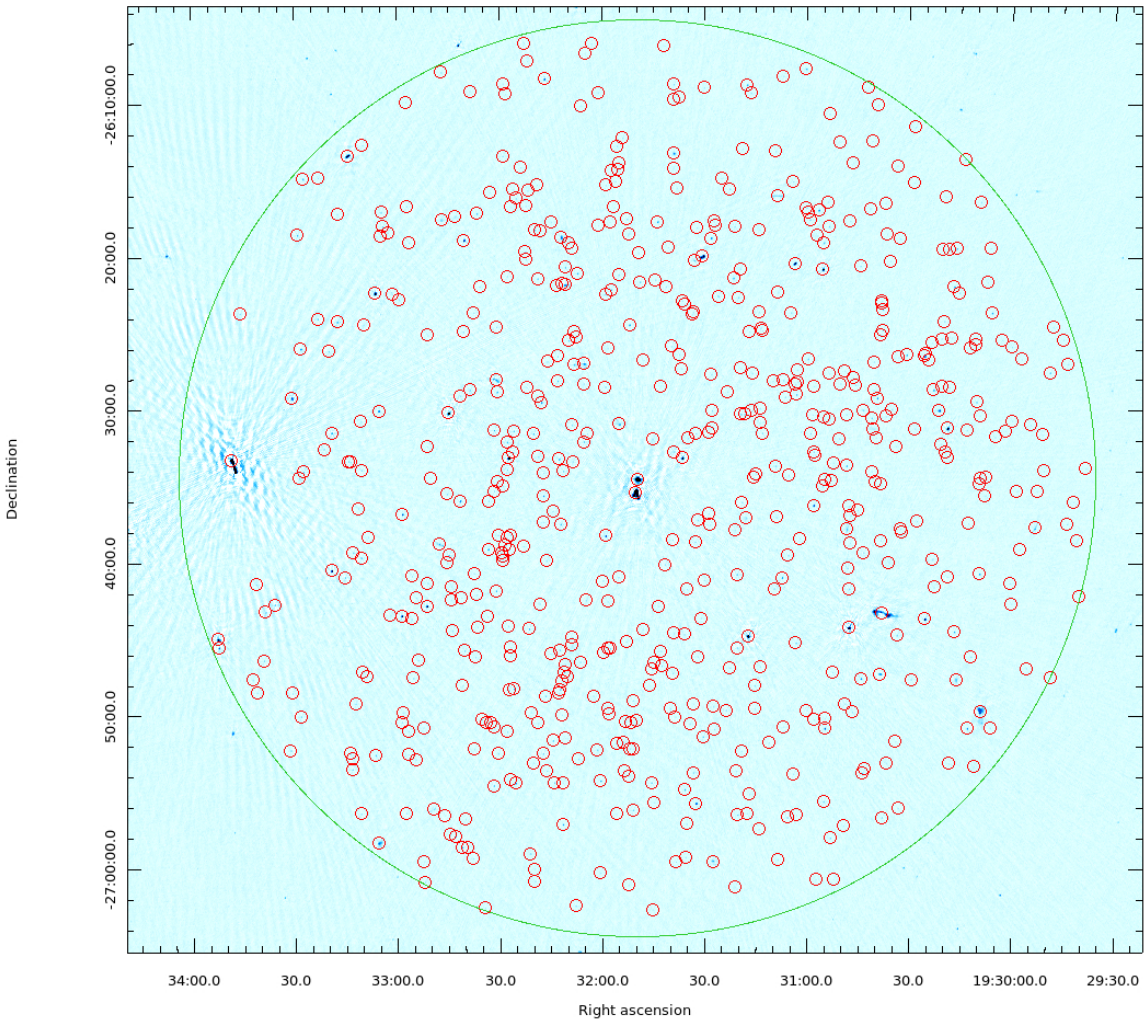

Figure 5.6: The image shows blue-scale view of uGMRT field which encompasses an area of 0.785 deg^2 (30 arcmin, green circle). The red circles indicate the radio sources detected over a threshold of 5σ (i.e. 0.15 mJy/b).

Table 5.25: continued

Name	RA_{J2000}	DEC_{J2000}	F_{640MHz} (mJy)	ΔF	Morphology
J1933-2646	19:33:39.14	-26:46:23.4	1.96	0.19	barely
J1933-2648b	19:33:41.16	-26:48:29.4	0.95	0.10	barely
J1933-2641	19:33:41.38	-26:41:24.4	1.39	0.14	unresolved
J1933-2647c	19:33:42.40	-26:47:38.8	1.24	0.12	barely
J1933-2623	19:33:45.88	-26:23:41.5	1.26	0.12	unresolved
J1933-2633d	19:33:48.45	-26:33:16.4	3526.7	352.6	**FRII**
J1933-2645	19:33:52.35	-26:45:32.6	9.86	0.98	unresolved
J1933-2644	19:33:52.52	-26:44:59.6	79.4	7.94	unresolved

5.5 Summary of the MeerKAT and the uGMRT radio catalogues

A summary of the MeerKAT and the uGMRT radio catalogues is shown in Tab. 5.26 and 5.27. We report the number (N) of the sources and the percentage (%) of the unresolved, barely resolved or extended sources in the samples.
According to our morphological criterion, in the MeerKAT catalogue, the sources which are unresolved are the 69%, the barely resolved sources are 29%, whereas the extended sources are only the 2% of the sample.
In the uGMRT catalogue, the unresolved sources are 77% of the sample, the barely resolved are 22%, and the extended sources are only the 1% of the sample.
In Fig.5.7 and 5.8 we show the histograms of the integrated flux density distribution from the MeerKAT and uGMRT catalogues respectively: there is evidence of statistical incompleteness in both the samples, consistent with what we found from the statistical source counts (logN-logS).

Table 5.26: MACSJ1931-2634 MeerKAT radio catalogue

	Unresolved	**Barely**	**Extended**
N	132	56	4
%	69	29	2

Table 5.27: MACSJ1931-2634 uGMRT radio catalogue

	Unresolved	**Barely**	**Extended**
N	480	137	6
%	77	22	1

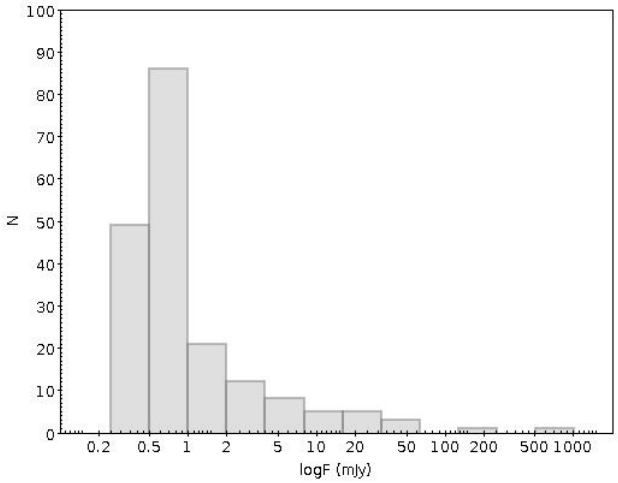

Figure 5.7: The histogram shows the distribution of the integrated flux density for the sources in the MeerKAT radio catalogue. The incompleteness at low fluxes is consistent with the result from the statistical source counts (logN-logS).

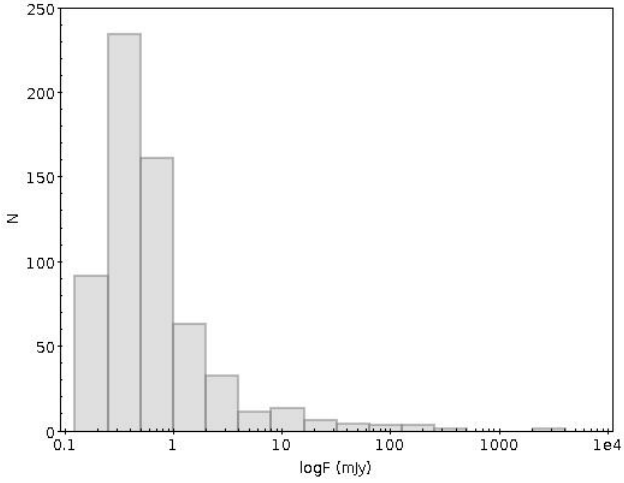

Figure 5.8: The histogram shows the distribution of the integrated flux density for the sources in the uGMRT radio catalogue. The incompleteness of the sample is consistent with what resulted from the statistical source counts (logN-logS).

5.6 Spectral analysis

We crossmatched our catalogues in order to get a spectral index information on the radio sources detected within 30 arcmin radius from the field center. We performed a test to determine the optimal radius for the matches, following the same method adopted in Mahony et al. (2016). We matched our catalogues several times, choosing different separation radii, in order to investigate how the number of matches varies with the separation radius. The optimal matching radius was found to be 5 arcsec, which corresponds to the radius after which the number of matches drops. The result of our test is reported in Fig. 5.9.

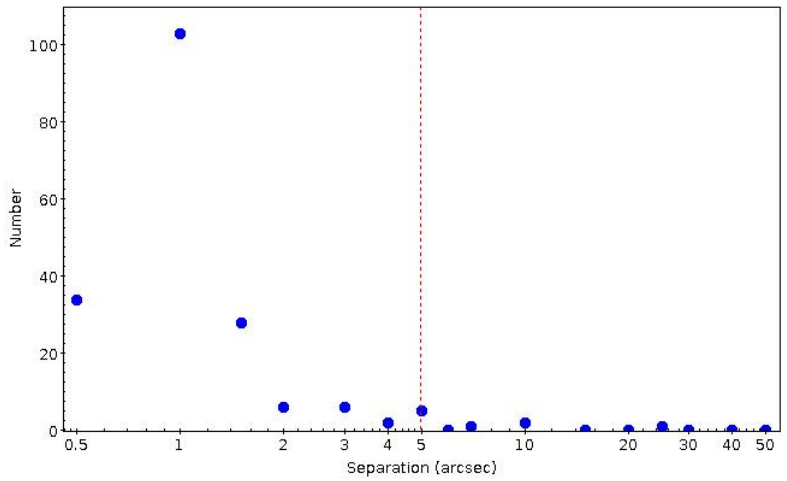

Figure 5.9: The image shows our test to determine the optimal matching radius between the two catalogues. The blue dots are the number of matches as a function of the search radius. The dotted line marks the search radius choosen for the final best match.

We report in Fig.5.10 the offset between the MeerKAT sources and the uGMRT sources. This shows a systematic offset, not uncommon when doing phase-only self-calibration (Mahony et al., 2016). The median values of the offset are -0.45 arcsec in right ascension and -0.4 in declination, well below the pixel size (1 arcsec). The sources which show a higher offset were further visually inspected to assess the reliability of the crossmatch.

To estimate the spectral indices we considered the central frequencies of 1.2 GHz and 640 MHz.
First, we report the spectral indices of the sources in common (Table 5.28 and following), which are 184. Then, we give an upper limit for the sources detected only at 1.2 GHz (Table 5.33), which are 8, or only at 640 MHz (Table 5.34 and following), which are 439. The spectral index of the extended sources is calculated separately, according to the measure of the fluxes separately with AIPS TVSTAT.

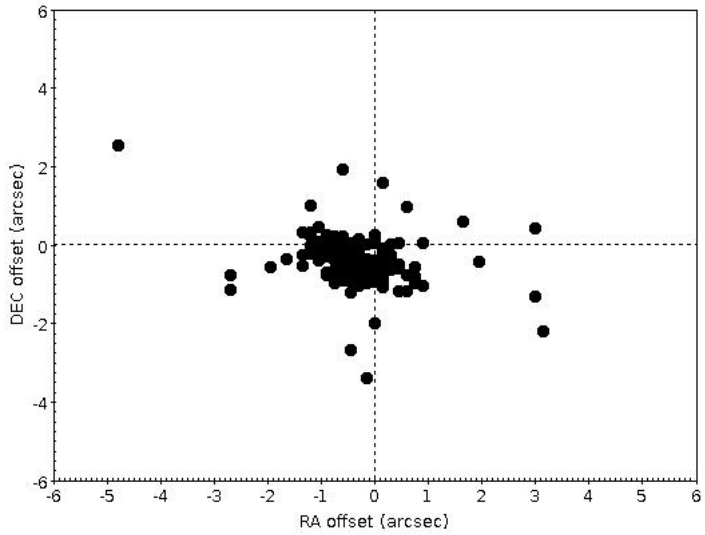

Figure 5.10: The image shows the offset in right ascension and declination between the MeerKAT positions and the uGMRT positions. There is a clear systematic offset, primarly in declination for all sources.

We adopted the convention: $F_\nu \propto \nu^{-\alpha}$.
The values of the spectral indices are estimated by the equation:

$$\alpha = \frac{log_{10}\left(\frac{F_1}{F_2}\right)}{log_{10}\left(\frac{\nu_2}{\nu_1}\right)} \tag{5.4}$$

The errors are calculated according to the formula (Mahony et al., 2016):

$$E_\alpha = \frac{1}{ln\frac{\nu_1}{\nu_2}}\sqrt{\left(\frac{F_{1,err}}{F_1}\right)^2 + \left(\frac{F_{2,err}}{F_2}\right)^2} \tag{5.5}$$

where $\nu_{1,2}$ refers to the frequencies, and $F_{1,2}$ to the corresponding flux densities at those frequencies.

In Figure 5.11 we report the spectral index distribution of the sources in common which has a median spectral index of 0.93 ± 0.2. This value is steeper than what was found in previous studies (Williams et al., 2016; Intema et al., 2011; Ishwara-Chandra et al., 2010). The typical spectral index over these frequencies is around 0.78, but can range from 0.76 to 0.85 (Hardcastle et al., 2016). Mahony et al. (2016) found a steep value of 0.82 ± 0.02 in their work from sources in the Lockman-wide sample between 1.4 GHz and 150 MHz. Steep values are also found in Sirothia et al. (2009) of 0.82 ± 0.01 and in Williams et al. (2013) of 0.87 ± 0.01. We can separate the sample of the sources in common into three primary categories,

Table 5.28: Spectral indices of the common sources

RA_{J2000}	DEC_{J2000}	$F_{1.2GHz}$ (mJy)	F_{640MHz} (mJy)	α	E_α
19:29:48.89	-26:27:32.4	0.60	2.17	1.848	0.22
19:29:53.29	-26:37:44.8	1.65	8.87	2.401	0.20
19:30:00.09	-26:25:52.2	0.50	0.75	0.582	0.24
19:30:05.90	-26:23:38.7	0.70	2.94	2.063	0.21
19:30:09.21	-26:16:24.1	0.44	1.13	1.356	0.24
19:30:09.37	-26:40:43.0	0.69	2.16	1.640	0.22
19:30:09.37	-26:34:29.6	0.65	1.34	1.040	0.22
19:30:10.40	-26:29:27.9	0.49	1.25	1.346	0.23
19:30:11.91	-26:46:08.2	0.39	0.85	1.120	0.25
19:30:12.87	-26:50:48.9	1.41	4.30	1.603	0.20
19:30:13.82	-26:13:35.3	0.84	2.44	1.533	0.21
19:30:16.27	-26:19:26.8	0.86	2.47	1.517	0.20
19:30:16.29	-26:47:38.1	0.65	5.85	3.159	0.22
19:30:16.76	-26:44:30.4	1.47	1.95	0.406	0.20
19:30:16.91	-26:21:56.2	0.82	3.07	1.898	0.20
19:30:18.81	-26:31:12.2	8.00	27.0	1.748	0.20
19:30:19.87	-26:24:11.1	0.43	0.62	0.526	0.20
19:30:21.31	-26:30:01.2	3.00	8.74	1.537	0.20
19:30:22.95	-26:28:41.5	0.95	1.83	0.942	0.20
19:30:25.37	-26:43:40.4	3.87	13.1	1.753	0.20
19:30:25.52	-26:26:28.6	2.40	5.97	1.310	0.20
19:30:28.40	-26:11:29.4	0.43	1.13	1.389	0.24
19:30:28.46	-26:31:13.5	0.35	0.31	-0.17	0.29
19:30:30.91	-26:26:24.0	0.72	1.86	1.364	0.21
19:30:37.88	-26:56:40.1	0.56	1.48	1.397	0.22
19:30:37.97	-26:24:48.2	0.51	0.76	0.573	0.20
19:30:38.23	-26:43:11.4	27.1	118.3	2.119	0.20
19:30:38.41	-26:25:07.3	0.44	0.86	0.963	0.24
19:30:38.62	-26:47:15.5	0.89	5.36	2.565	0.20
19:30:39.45	-26:29:13.6	0.64	1.76	1.454	0.21
19:30:43.64	-26:53:45.8	0.84	1.92	1.188	0.21
19:30:43.70	-26:30:00.9	0.41	0.79	0.943	0.24
19:30:44.09	-26:47:34.8	0.96	2.74	1.507	0.21
19:30:45.92	-26:28:23.3	0.51	0.45	-0.17	0.20
19:30:47.62	-26:44:15.2	47.39	70.6	0.573	0.20
19:30:48.27	-26:37:50.0	0.48	2.37	2.296	0.20
19:30:48.44	-26:33:39.7	0.60	0.98	0.705	0.22
19:30:50.59	-26:31:52.6	0.61	0.32	-0.92	0.24
19:30:53.08	-26:58:00.4	0.48	1.58	1.713	0.23
19:30:53.51	-26:10:38.0	0.41	0.74	0.849	0.25
19:30:53.58	-26:17:59.9	0.45	0.82	0.862	0.20

Table 5.29: Spectral indices of the common sources (continued)

RA_{J2000}	DEC_{J2000}	$F_{1.2GHz}$ (mJy)	F_{640MHz} (mJy)	α	E_α
19:30:54.68	-26:50:50.4	2.34	3.88	0.727	0.20
19:30:55.05	-26:55:37.7	0.81	1.29	0.669	0.21
19:30:55.14	-26:19:04.5	0.68	1.40	1.038	0.22
19:30:55.36	-26:20:48.2	11.36	24.5	1.105	0.20
19:30:56.61	-26:16:56.5	1.78	4.57	1.355	0.20
19:30:57.98	-26:36:14.6	1.79	3.88	1.112	0.20
19:30:59.16	-26:17:34.0	0.56	0.78	-0.14	0.20
19:30:59.83	-26:26:40.5	0.52	0.77	0.564	0.23
19:31:00.31	-26:07:41.4	0.94	3.48	1.881	0.21
19:31:03.07	-26:29:00.8	0.51	0.86	0.751	0.23
19:31:03.17	-26:45:15.6	0.62	0.69	0.153	0.21
19:31:03.59	-26:20:25.0	6.91	15.4	1.152	0.20
19:31:05.64	-26:56:40.7	0.45	1.06	1.232	0.20
19:31:06.96	-26:08:09.2	0.50	0.79	0.657	0.23
19:31:07.25	-26:40:59.1	0.91	1.39	0.609	0.21
19:31:09.17	-26:13:04.0	0.33	0.44	0.413	0.20
19:31:17.18	-26:44:48.7	28.96	61.5	1.082	0.20
19:31:17.55	-26:08:44.7	1.01	2.90	1.516	0.21
19:31:18.35	-26:30:18.3	0.35	0.53	0.596	0.27
19:31:19.30	-26:30:17.5	0.37	0.60	0.695	0.20
19:31:20.25	-26:56:29.8	0.67	1.33	0.985	0.21
19:31:20.42	-26:45:34.4	0.41	0.42	0.034	0.26
19:31:20.53	-26:40:46.7	0.42	0.63	0.582	0.25
19:31:21.62	-26:21:23.2	0.52	1.08	1.05	0.23
19:31:22.64	-26:15:33.8	0.36	0.58	0.685	0.26
19:31:27.40	-26:59:30.9	1.33	7.07	2.402	0.21
19:31:28.05	-26:18:46.2	1.07	2.34	1.125	0.20
19:31:30.36	-26:51:23.3	0.41	0.77	0.906	0.25
19:31:30.37	-26:19:56.2	5.61	34.2	2.599	0.20
19:31:32.41	-26:55:45.3	3.49	8.51	1.281	0.20
19:31:33.10	-26:20:14.0	0.44	1.24	1.489	0.23
19:31:33.28	-26:53:45.1	0.25	0.64	1.351	0.31
19:31:35.79	-26:54:52.1	0.58	1.31	1.171	0.22
19:31:36.44	-26:33:09.6	15.29	24.1	0.654	0.20
19:31:38.93	-26:13:13.7	1.30	8.87	2.75	0.20
19:31:43.67	-26:17:42.1	1.13	2.77	1.289	0.20
19:31:45.56	-26:54:24.4	0.42	0.80	0.926	0.24
19:31:48.83	-26:21:39.0	0.42	0.65	0.628	0.20
19:31:49.56	-26:34:32.7	45.4	183.7	2.006	0.20
19:31:49.98	-26:35:17.3	145.2	354.7	1.284	0.20

Table 5.30: Spectral indices of the common sources (continued)

RA_{J2000}	DEC_{J2000}	$F_{1.2GHz}$ (mJy)	F_{640MHz} (mJy)	α	E_α
19:31:50.85	-26:56:11.6	0.45	1.00	1.148	0.24
19:31:51.97	-26:24:26.9	0.88	1.39	0.657	0.21
19:31:54.87	-26:30:57.7	0.85	3.71	2.119	0.20
19:31:57.37	-26:22:09.7	0.74	0.94	0.343	0.21
19:31:57.56	-26:45:38.2	0.41	0.43	0.068	0.20
19:31:57.96	-26:49:55.0	0.31	0.42	0.436	0.20
19:31:58.93	-26:38:15.7	3.51	3.74	0.091	0.20
19:32:00.41	-26:54:17.6	0.97	1.56	0.683	0.20
19:32:05.19	-26:32:05.7	0.36	0.66	0.871	0.20
19:32:05.20	-26:27:00.2	2.36	3.87	0.711	0.20
19:32:06.43	-26:46:31.1	0.50	0.35	-0.51	0.24
19:32:07.73	-27:02:27.9	0.48	1.30	1.432	0.23
19:32:08.17	-26:27:03.4	0.59	1.23	1.056	0.22
19:32:09.74	-26:25:29.4	0.34	0.53	0.638	0.27
19:32:10.80	-26:21:50.5	2.03	3.43	0.754	0.20
19:32:11.30	-26:34:01.0	0.36	0.45	0.32	0.26
19:32:11.49	-26:57:08.6	0.80	2.26	1.493	0.21
19:32:11.85	-26:18:43.2	2.52	8.42	1.734	0.21
19:32:12.15	-26:37:29.7	0.50	0.75	0.582	0.23
19:32:12.26	-26:48:18.4	0.63	0.92	0.544	0.22
19:32:12.54	-26:33:14.4	0.93	1.44	0.628	0.20
19:32:12.95	-26:28:07.8	0.67	0.93	0.471	0.20
19:32:14.01	-26:54:23.9	0.56	0.91	0.698	0.22
19:32:14.41	-26:51:39.7	0.49	1.03	1.068	0.23
19:32:16.53	-26:48:44.6	0.53	0.58	0.129	0.23
19:32:16.78	-26:08:22.1	3.57	13.2	1.88	0.20
19:32:17.11	-26:35:38.4	0.63	1.20	0.926	0.22
19:32:17.70	-26:29:32.1	1.31	1.49	0.185	0.20
19:32:18.81	-26:21:25.9	0.54	0.80	0.565	0.22
19:32:19.55	-26:18:14.5	0.50	0.78	0.639	0.23
19:32:20.07	-26:31:35.1	0.53	0.84	0.662	0.22
19:32:21.19	-26:59:02.7	0.60	1.66	1.463	0.20
19:32:21.42	-26:44:21.0	0.64	0.78	0.284	0.22
19:32:22.41	-26:19:39.7	0.41	0.44	0.101	0.20
19:32:25.41	-26:54:26.0	1.92	3.71	0.947	0.20
19:32:25.80	-26:48:16.2	0.76	1.49	0.967	0.21
19:32:25.84	-26:31:24.5	0.35	0.61	0.798	0.26
19:32:26.11	-26:32:48.8	0.59	0.67	0.182	0.22
19:32:27.32	-26:33:10.1	17.75	35.5	0.996	0.20
19:32:27.69	-26:21:15.1	0.33	0.34	0.042	0.20
19:32:27.73	-26:33:56.5	0.44	0.41	-0.1	0.20

Table 5.31: Spectral indices of the common sources (continued)

RA_{J2000}	DEC_{J2000}	$F_{1.2GHz}$ (mJy)	F_{640MHz} (mJy)	α	E_α
19:32:27.80	-26:32:08.3	0.58	0.78	0.425	0.22
19:32:29.00	-26:13:24.5	0.50	0.78	0.639	0.23
19:32:30.45	-26:38:12.5	0.25	0.26	0.056	0.35
19:32:30.69	-26:28:50.8	0.62	1.23	0.984	0.22
19:32:30.90	-26:28:03.4	1.03	6.12	-0.77	0.20
19:32:31.01	-26:41:51.3	0.51	0.90	0.816	0.23
19:32:31.59	-26:31:20.8	0.57	0.92	0.688	0.22
19:32:31.80	-26:54:36.1	0.57	1.54	1.429	0.22
19:32:33.36	-26:39:08.1	0.67	1.16	0.789	0.22
19:32:36.55	-26:17:10.6	0.63	1.12	0.827	0.22
19:32:38.69	-26:28:43.1	0.74	0.75	0.019	0.22
19:32:39.40	-26:58:36.4	0.51	0.72	0.495	0.23
19:32:40.26	-26:18:54.8	6.32	15.3	1.271	0.20
19:32:40.28	-26:45:47.1	0.49	0.59	0.267	0.20
19:32:41.10	-26:58:37.8	2.60	3.09	0.248	0.20
19:32:41.51	-26:35:58.3	1.24	2.62	1.075	0.20
19:32:43.01	-26:57:54.3	0.73	2.12	1.532	0.21
19:32:44.15	-26:41:34.6	0.39	0.45	0.205	0.20
19:32:44.91	-26:30:13.1	52.77	59.4	0.17	0.20
19:32:44.96	-26:39:32.6	0.61	0.92	0.59	0.22
19:32:47.76	-26:38:47.4	0.64	4.32	2.746	0.21
19:32:51.32	-26:42:51.0	5.85	11.7	0.996	0.20
19:32:57.15	-26:16:42.1	0.66	0.62	-0.08	0.21
19:32:58.44	-26:36:50.4	1.59	3.76	1.237	0.20
19:32:58.63	-26:50:26.2	0.32	0.66	1.041	0.20
19:32:58.69	-26:43:29.7	5.33	12.6	1.237	0.20
19:33:04.10	-26:18:01.8	0.63	1.21	0.938	0.22
19:33:04.42	-26:17:05.6	0.40	1.38	1.78	0.20
19:33:05.31	-26:30:04.6	1.38	3.78	1.448	0.20
19:33:05.62	-26:58:21.1	4.47	21.06	2.228	0.20
19:33:06.31	-26:22:22.9	11.94	30.9	1.367	0.20
19:33:06.41	-26:52:35.9	0.68	2.06	1.593	0.21
19:33:09.92	-26:12:41.5	0.68	0.94	0.465	0.21
19:33:10.60	-26:39:41.3	0.49	1.35	1.457	0.21
19:33:10.77	-26:56:26.3	0.66	1.26	0.929	0.21
19:33:12.34	-26:49:14.4	0.61	0.81	0.407	0.22
19:33:14.15	-26:33:22.7	0.43	0.67	0.637	0.24
19:33:14.52	-26:13:24.9	31.1	90.5	1.536	0.20
19:33:15.35	-26:40:58.4	0.50	0.89	0.829	0.20
19:33:17.36	-26:17:11.3	0.33	0.73	1.141	0.26
19:33:17.37	-26:24:15.7	0.70	2.02	1.524	0.21

Table 5.32: Spectral indices of the common sources (continued)

RA_{J2000}	DEC_{J2000}	$F_{1.2GHz}$ (mJy)	F_{640MHz} (mJy)	α	E_α
19:33:19.15	-26:31:30.8	0.84	2.12	1.331	0.21
19:33:19.22	-26:40:31.4	4.95	13.8	1.474	0.20
19:33:21.33	-26:32:34.2	0.50	0.71	0.504	0.23
19:33:23.13	-26:24:03.3	0.87	1.28	0.555	0.21
19:33:27.27	-26:14:53.6	1.43	4.47	1.638	0.20
19:33:27.33	-26:34:04.0	1.23	1.22	-0.01	0.20
19:33:28.06	-26:26:00.9	1.74	4.01	1.2	0.20
19:33:28.31	-26:50:03.4	0.47	1.36	1.527	0.23
19:33:28.99	-26:18:34.2	1.17	2.54	1.114	0.20
19:33:30.74	-26:29:13.1	10.2	17.0	0.734	0.20
19:33:31.37	-26:52:17.1	0.71	1.77	1.313	0.20
19:33:35.92	-26:42:44.8	1.07	1.86	0.795	0.20
19:33:38.57	-26:43:13.9	0.72	2.22	1.619	0.21
19:33:39.15	-26:46:23.6	0.94	1.96	1.056	0.20
19:33:41.41	-26:41:25.6	0.72	1.39	0.945	0.20
19:33:42.46	-26:47:39.9	0.60	1.24	1.043	0.20
19:33:45.83	-26:23:41.4	0.52	1.26	1.272	0.22
19:33:47.67	-26:33:35.0	1006.0	3526.0	1.803	0.20
19:33:52.32	-26:45:33.1	3.66	9.86	1.424	0.20
19:33:52.52	-26:45:00.1	23.18	79.4	1.77	0.20

according to Mahony et al. (2016): sources with $\alpha\ ^{1283}_{640} < 0.5$ are flat, sources with $0.5 < \alpha\ ^{1283}_{640} < 1.2$ are steep, whereas sources with $\alpha\ ^{1283}_{640} > 1.2$ are ultra-steep.
According to this separation, our sample is dominated by steep sources ($0.5 < \alpha\ ^{1283}_{640} < 1.2$), which is expected from sources at these frequencies. They are the 48 % of the sample, whereas the ultra-steep and the flat are the 32% and the 20% of the sample respectively.
Fig 5.12 and 5.13 report the spectral index distributions of the upper limits, i.e. the sources detected only at 1.2 GHz or only at 640 MHz respectively.
The median value of the MeerKAT distribution is -1.3 whereas the median value of the uGMRT distribution is 0.92.

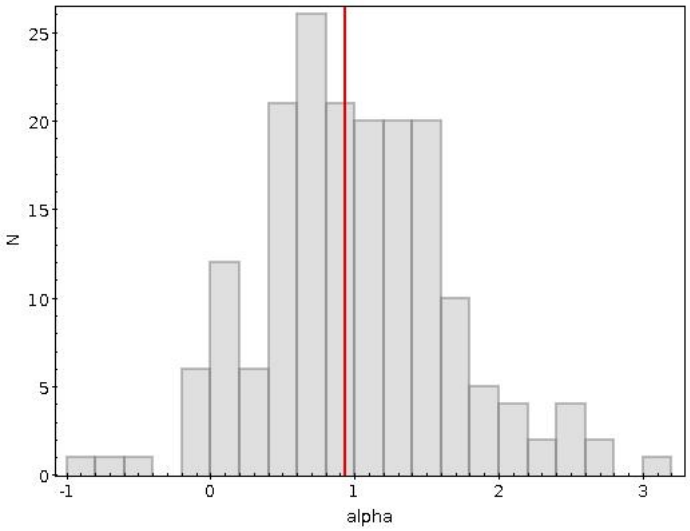

Figure 5.11: Histogram of the spectral indices from 640 MHz-1.2 GHz for sources in the MACSJ1931-2634 field detected both at 1.2 GHz and 640 MHz. The red line indicates the median value, steeper in respect to the previous studies, which is 0.93 ± 0.2. The source population is dominated by steep spectra sources.

Table 5.33: Spectral index upper limits of the MeerKAT (only) sources

RA_{J2000}	DEC_{J2000}	$F_{1.2GHz}$ (mJy)	ΔF	α u.l.
19:30:42.69	-26:37:21.1	0.38	0.05	<-1.33
19:31:46.56	-26:37:32.1	0.39	0.05	<-1.37
19:32:03.07	-26:20:11.0	0.40	0.05	<-1.41
19:32:31.75	-26:27:58.9	0.96	0.10	<-2.66
19:32:50.31	-26:56:16.5	0.50	0.06	<-1.73
19:33:01.88	-26:50:30.5	0.34	0.05	<-1.17
19:33:20.27	-26:41:10.5	0.58	0.07	<-1.94
19:33:33.18	-26:29:58.6	0.20	0.04	<-0.41

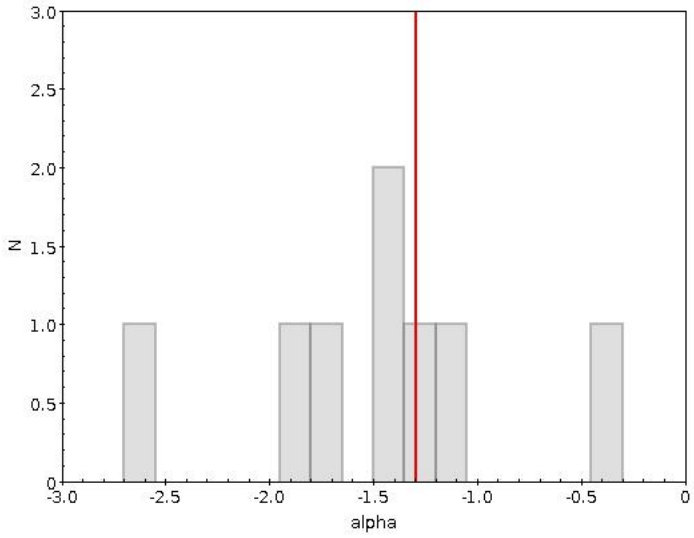

Figure 5.12: Histogram of the upper limits of the spectral indices for sources in MACSJ1931-2634 field detected only at 1.2 GHz. For the 640 MHz fluxes we assumed an upper limit of 5σ (i.e. 0.15 mJy). The red line indicates the median value which is -1.3.

Table 5.34: Spectral index upper limits of the uGMRT (only) sources

RA_{J2000}	DEC_{J2000}	F_{640MHz} (mJy)	ΔF	α u.l.
19:29:38.38	-26:33:47.1	0.65	0.07	<1.69
19:29:40.24	-26:42:10.1	0.60	0.06	<1.57
19:29:40.89	-26:38:31.5	1.69	0.17	<3.06
19:29:41.91	-26:35:59.4	0.61	0.06	<1.60
19:29:43.72	-26:26:58.5	1.29	0.13	<2.68
19:29:43.83	-26:37:26.6	1.07	0.11	<2.41
19:29:45.10	-26:25:24.4	0.89	0.09	<2.14
19:29:48.06	-26:24:34.1	0.74	0.08	<1.88
19:29:48.68	-26:47:29.7	0.77	0.08	<1.93
19:29:50.75	-26:33:58.3	0.42	0.05	<1.06
19:29:51.04	-26:31:36.4	0.54	0.06	<1.42
19:29:52.68	-26:35:18.3	0.37	0.04	<0.88
19:29:54.64	-26:30:58.0	0.53	0.06	<1.40
19:29:55.61	-26:46:53.0	0.75	0.08	<1.90
19:29:57.27	-26:26:40.3	0.38	0.04	<0.92
19:29:57.55	-26:39:05.4	0.24	0.03	<0.26
19:29:58.56	-26:35:17.9	0.88	0.09	<2.13
19:30:00.02	-26:30:41.6	0.29	0.04	<0.53
19:30:00.06	-26:42:40.1	0.49	0.05	<1.28
19:30:00.58	-26:41:20.0	0.63	0.07	<1.64
19:30:02.03	-26:31:21.3	0.33	0.04	<0.71
19:30:02.95	-26:25:25.1	0.47	0.05	<1.22
19:30:05.00	-26:31:45.7	0.59	0.06	<1.55
19:30:06.24	-26:50:46.8	0.70	0.07	<1.80
19:30:06.33	-26:19:24.5	0.56	0.06	<1.48
19:30:07.26	-26:21:38.3	0.38	0.04	<0.92
19:30:07.75	-26:34:22.9	0.54	0.06	<1.42
19:30:07.84	-26:35:35.5	0.51	0.05	<1.34
19:30:09.41	-26:30:21.2	0.25	0.03	<0.32
19:30:09.47	-26:34:50.3	0.31	0.04	<0.63
19:30:10.56	-26:25:20.1	0.49	0.05	<1.28
19:30:10.80	-26:25:41.8	0.28	0.04	<0.48
19:30:11.03	-26:53:19.3	0.82	0.08	<2.02
19:30:12.22	-26:25:56.4	0.82	0.08	<2.02
19:30:12.70	-26:37:25.3	0.36	0.04	<0.84
19:30:13.25	-26:31:18.9	0.49	0.05	<1.28
19:30:15.50	-26:22:20.0	0.75	0.08	<1.90
19:30:17.75	-26:25:15.6	0.33	0.04	<0.71
19:30:18.33	-26:28:31.0	0.31	0.04	<0.63
19:30:18.38	-26:53:07.6	0.51	0.05	<1.34

Table 5.35: Spectral index upper limits of the uGMRT sources (continued)

RA_{J2000}	DEC_{J2000}	F_{640MHz} (mJy)	ΔF	α u.l.
19:30:18.48	-26:19:29.8	1.05	0.11	<2.38
19:30:18.87	-26:40:54.1	0.40	0.05	<0.99
19:30:18.89	-26:33:06.7	0.29	0.04	<0.53
19:30:19.44	-26:16:02.7	0.46	0.05	<1.19
19:30:19.72	-26:32:46.2	0.43	0.05	<1.10
19:30:20.24	-26:19:27.9	0.38	0.04	<0.92
19:30:20.45	-26:28:25.3	0.43	0.05	<1.10
19:30:20.70	-26:25:19.8	0.58	0.06	<1.53
19:30:20.78	-26:32:13.3	0.38	0.04	<0.92
19:30:22.81	-26:41:35.6	0.40	0.05	<0.99
19:30:23.30	-26:39:46.4	0.84	0.08	<2.06
19:30:23.42	-26:25:36.6	0.23	0.03	<0.20
19:30:24.35	-26:26:43.3	0.15	0.03	<-0.4
19:30:25.34	-26:26:19.0	0.28	0.04	<0.48
19:30:27.78	-26:37:16.4	0.44	0.05	<1.13
19:30:28.72	-26:15:07.1	0.41	0.05	<1.03
19:30:29.45	-26:47:37.4	0.56	0.06	<1.48
19:30:32.21	-26:38:00.3	0.26	0.04	<0.37
19:30:32.59	-26:37:45.2	0.34	0.04	<0.76
19:30:32.79	-26:18:47.8	0.47	0.05	<1.22
19:30:33.24	-26:56:02.9	0.72	0.07	<1.84
19:30:33.30	-26:26:32.3	0.26	0.04	<0.37
19:30:33.62	-26:44:44.1	0.91	0.09	<2.17
19:30:33.71	-26:14:01.2	0.84	0.08	<2.06
19:30:33.93	-26:32:22.8	0.19	0.03	<-0.07
19:30:33.99	-26:51:40.6	0.41	0.05	<1.03
19:30:35.16	-26:29:57.6	0.48	0.05	<1.25
19:30:35.69	-26:20:15.3	0.40	0.05	<0.99
19:30:36.03	-26:39:57.7	0.53	0.06	<1.40
19:30:36.58	-26:53:07.8	0.67	0.07	<1.73
19:30:36.64	-26:18:29.2	0.36	0.04	<0.84
19:30:36.89	-26:30:25.4	0.24	0.03	<0.26
19:30:37.15	-26:16:30.0	0.29	0.04	<0.53
19:30:38.00	-26:24:47.3	0.56	0.06	<1.48
19:30:38.17	-26:22:51.3	0.26	0.04	<0.37
19:30:38.27	-26:23:01.4	0.38	0.04	<0.92
19:30:38.31	-26:34:51.4	0.20	0.03	<2.14
19:30:38.50	-26:38:31.7	0.37	0.04	<0.88
19:30:39.36	-26:10:02.7	0.73	0.07	<1.86
19:30:39.91	-26:31:48.5	0.21	0.03	<0.07

Table 5.36: Spectral index upper limits of the uGMRT sources (continued)

RA_{J2000}	DEC_{J2000}	F_{640MHz} (mJy)	ΔF	α u.l.
19:30:40.15	-26:34:42.4	0.25	0.03	<0.32
19:30:40.48	-26:26:51.2	0.31	0.04	<0.63
19:30:40.58	-26:31:13.5	1.08	0.11	<2.42
19:30:40.58	-26:28:42.2	0.40	0.05	<0.99
19:30:41.06	-26:12:24.6	0.44	0.05	<1.13
19:30:41.14	-26:30:31.5	0.69	0.07	<1.78
19:30:41.14	-26:34:01.8	0.16	0.03	<-0.3
19:30:41.67	-26:16:49.2	0.51	0.05	<1.34
19:30:42.17	-26:08:55.0	0.61	0.06	<1.60
19:30:42.95	-26:53:30.2	0.40	0.05	<0.99
19:30:43.43	-26:39:19.9	0.35	0.04	<0.80
19:30:44.49	-26:20:35.3	0.54	0.06	<1.42
19:30:45.18	-26:36:33.6	0.25	0.03	<0.32
19:30:46.61	-26:13:51.0	0.44	0.05	<1.13
19:30:46.65	-26:27:52.8	0.22	0.03	<0.13
19:30:46.72	-26:49:46.3	0.59	0.06	<1.55
19:30:47.25	-26:36:54.7	0.29	0.04	<0.53
19:30:47.41	-26:38:42.0	0.24	0.03	<0.26
19:30:47.50	-26:17:39.0	0.42	0.05	<1.06
19:30:47.60	-26:36:17.8	0.50	0.05	<1.31
19:30:47.60	-26:41:42.8	0.49	0.05	<1.28
19:30:48.16	-26:40:20.8	0.63	0.06	<1.64
19:30:48.56	-26:30:17.7	0.27	0.04	<0.43
19:30:48.86	-26:49:13.5	0.55	0.06	<1.45
19:30:48.99	-26:27:27.3	0.18	0.03	<-0.1
19:30:49.21	-26:57:12.0	0.43	0.05	<1.10
19:30:50.26	-26:28:17.0	0.28	0.04	<0.48
19:30:50.39	-26:12:27.5	0.32	0.04	<0.67
19:30:52.15	-27:00:42.3	0.52	0.06	<1.37
19:30:52.35	-26:33:27.7	0.23	0.03	<0.20
19:30:52.48	-26:47:09.3	0.35	0.04	<0.80
19:30:52.83	-26:34:37.1	0.18	0.03	<-0.1
19:30:53.47	-26:27:37.7	0.22	0.03	<0.13
19:30:53.48	-26:30:37.7	0.32	0.04	<0.67
19:30:53.96	-26:16:23.6	0.46	0.05	<1.19
19:30:54.69	-26:50:12.0	0.27	0.04	<0.43
19:30:54.84	-26:34:32.0	0.22	0.03	<0.13
19:30:55.30	-26:30:28.4	0.22	0.03	<0.13
19:30:55.41	-26:35:00.7	0.28	0.04	<0.48

Table 5.37: Spectral index upper limits of the uGMRT sources (continued)

RA_{J2000}	DEC_{J2000}	F_{640MHz} (mJy)	ΔF	α u.l.
19:30:57.06	-26:18:35.7	0.35	0.04	<0.80
19:30:57.28	-27:00:43.4	0.51	0.05	<1.34
19:30:57.55	-26:32:57.3	0.22	0.03	<0.13
19:30:57.90	-26:50:16.5	0.30	0.04	<0.58
19:30:57.97	-26:28:26.7	0.23	0.03	<0.20
19:30:58.07	-26:32:44.7	0.49	0.05	<1.28
19:30:58.35	-26:30:19.4	0.16	0.03	<-0.3
19:30:59.00	-26:31:32.5	0.37	0.04	<0.88
19:30:59.80	-26:17:03.6	0.35	0.04	<0.80
19:30:59.99	-26:49:38.8	0.37	0.04	<0.88
19:31:00.25	-26:16:45.9	0.67	0.07	<1.73
19:31:02.03	-26:38:24.4	0.18	0.03	<-0.1
19:31:02.76	-26:28:10.0	0.25	0.03	<0.32
19:31:02.93	-26:27:23.2	0.25	0.03	<0.32
19:31:02.99	-26:56:30.8	0.28	0.04	<0.48
19:31:03.45	-26:28:19.5	0.24	0.03	<0.26
19:31:03.92	-26:53:48.8	0.39	0.04	<0.96
19:31:04.11	-26:15:04.0	0.51	0.05	<1.34
19:31:04.73	-26:23:38.1	0.42	0.05	<1.06
19:31:05.46	-26:34:17.8	0.23	0.03	<0.20
19:31:05.51	-26:39:31.7	0.42	0.05	<1.06
19:31:06.44	-26:29:09.7	0.38	0.04	<0.92
19:31:06.80	-26:50:43.4	0.22	0.03	<0.13
19:31:06.96	-26:28:04.3	0.34	0.04	<0.76
19:31:08.47	-26:59:25.0	0.54	0.06	<1.42
19:31:08.56	-26:22:20.0	0.29	0.04	<0.53
19:31:08.97	-26:37:01.5	0.31	0.04	<0.63
19:31:09.25	-26:13:04.3	0.44	0.05	<1.13
19:31:09.26	-26:33:40.2	0.48	0.05	<1.25
19:31:09.65	-26:41:42.0	0.42	0.05	<1.06
19:31:10.05	-26:28:07.0	0.16	0.03	<-0.3
19:31:11.12	-26:51:47.0	0.30	0.04	<0.58
19:31:13.16	-26:31:31.0	0.39	0.04	<0.96
19:31:13.20	-26:24:49.4	0.22	0.03	<0.13
19:31:13.60	-26:24:39.4	0.44	0.05	<1.13
19:31:13.61	-26:46:48.1	0.26	0.04	<0.37
19:31:13.84	-26:29:54.1	0.38	0.04	<0.92
19:31:13.89	-26:30:50.8	0.23	0.03	<0.20

Table 5.38: Spectral index upper limits of the uGMRT sources (continued)

RA_{J2000}	DEC_{J2000}	F_{640MHz} (mJy)	ΔF	α u.l.
19:31:13.98	-26:18:12.6	0.32	0.04	<0.67
19:31:14.03	-26:57:26.4	0.31	0.04	<0.63
19:31:14.13	-26:23:36.4	0.22	0.03	<0.13
19:31:15.05	-26:34:14.0	0.14	0.03	<-0.5
19:31:15.27	-26:48:02.8	0.61	0.06	<1.60
19:31:15.30	-26:49:32.4	0.30	0.04	<0.58
19:31:15.64	-26:34:27.2	0.25	0.03	<0.32
19:31:16.13	-26:27:36.4	0.27	0.04	<0.43
19:31:16.19	-26:30:04.1	0.22	0.03	<0.13
19:31:16.52	-26:09:15.6	0.85	0.09	<2.08
19:31:16.73	-26:55:08.3	0.27	0.04	<0.43
19:31:16.84	-26:24:54.3	0.20	0.03	<2.14
19:31:17.56	-26:56:24.2	0.30	0.04	<0.58
19:31:17.85	-26:37:04.8	1.99	0.20	<3.30
19:31:18.96	-26:12:56.0	0.39	0.04	<0.96
19:31:19.02	-26:36:02.9	0.36	0.04	<0.84
19:31:19.20	-26:52:19.6	0.32	0.04	<0.67
19:31:19.38	-26:27:17.3	0.17	0.03	<-0.2
19:31:19.55	-26:20:46.4	0.36	0.04	<0.84
19:31:20.15	-26:22:39.1	0.61	0.06	<1.60
19:31:20.64	-26:53:37.7	0.33	0.04	<0.71
19:31:21.10	-27:01:12.9	0.63	0.06	<1.64
19:31:21.11	-26:37:51.3	0.23	0.03	<0.20
19:31:21.29	-26:18:00.6	0.62	0.06	<1.62
19:31:22.55	-26:46:52.0	0.34	0.04	<0.76
19:31:23.24	-26:28:49.7	0.19	0.03	<-0.0
19:31:23.68	-26:49:39.1	0.38	0.04	<0.92
19:31:24.88	-26:14:50.0	0.31	0.04	<0.63
19:31:26.08	-26:22:34.2	0.69	0.07	<1.78
19:31:26.85	-26:17:54.7	0.49	0.05	<1.28
19:31:27.12	-26:50:54.5	0.37	0.04	<0.88
19:31:27.35	-26:17:41.2	0.32	0.04	<0.67
19:31:27.41	-26:49:24.6	0.36	0.04	<0.84
19:31:27.77	-26:31:10.6	0.34	0.04	<0.76
19:31:27.85	-26:30:03.6	0.31	0.04	<0.63
19:31:28.06	-26:27:41.3	0.31	0.04	<0.63
19:31:28.34	-26:37:31.7	0.20	0.03	<2.14
19:31:28.70	-26:31:29.9	0.24	0.03	<0.26
19:31:28.89	-26:36:48.3	0.19	0.03	<-0.07
19:31:30.12	-26:41:08.9	0.23	0.03	<0.20
19:31:30.15	-26:08:55.6	0.73	0.07	<1.86

Table 5.39: Spectral index upper limits of the uGMRT sources (continued)

RA_{J2000}	DEC_{J2000}	F_{640MHz} (mJy)	ΔF	α u.l.
19:31:31.00	-26:43:37.9	0.23	0.03	<0.20
19:31:32.03	-26:37:13.1	0.34	0.04	<0.76
19:31:32.06	-26:46:09.1	0.23	0.03	<0.20
19:31:32.33	-26:18:05.0	0.25	0.03	<0.32
19:31:32.52	-26:31:33.1	0.26	0.03	<0.37
19:31:32.76	-26:38:38.8	0.35	0.04	<0.80
19:31:33.11	-26:49:14.3	0.16	0.03	<-0.3
19:31:33.37	-26:23:37.3	0.24	0.03	<0.26
19:31:33.69	-26:23:46.7	0.19	0.03	<-0.07
19:31:34.31	-26:50:32.0	0.29	0.04	<0.53
19:31:34.86	-26:31:52.3	0.38	0.04	<0.92
19:31:35.17	-26:41:44.3	0.21	0.03	<0.07
19:31:35.23	-26:57:05.6	0.47	0.05	<1.22
19:31:35.54	-26:59:16.9	0.68	0.07	<1.75
19:31:35.82	-26:23:07.6	0.25	0.03	<0.32
19:31:35.94	-26:44:41.7	0.37	0.04	<0.88
19:31:36.60	-26:22:52.5	0.24	0.03	<0.26
19:31:36.74	-26:27:18.0	0.19	0.03	<-0.07
19:31:37.35	-26:26:22.3	0.28	0.04	<0.48
19:31:37.58	-26:09:33.4	0.33	0.04	<0.71
19:31:38.15	-26:15:30.2	0.29	0.04	<0.53
19:31:38.32	-26:59:34.3	0.62	0.06	<1.62
19:31:38.56	-26:50:05.2	0.19	0.03	<-0.07
19:31:38.93	-26:32:44.6	0.46	0.05	<1.19
19:31:38.95	-26:44:37.8	0.22	0.03	<0.13
19:31:39.01	-26:09:40.9	0.33	0.04	<0.71
19:31:39.08	-26:08:42.9	0.94	0.09	<2.22
19:31:39.16	-26:14:11.4	0.29	0.04	<0.53
19:31:39.25	-26:47:13.7	0.29	0.04	<0.53
19:31:39.38	-26:38:31.0	0.24	0.03	<0.26
19:31:39.76	-26:25:51.2	0.25	0.03	<0.32
19:31:40.03	-26:49:33.4	0.35	0.04	<0.80
19:31:40.71	-26:19:23.4	0.20	0.03	<2.14
19:31:41.37	-26:21:57.4	0.30	0.04	<0.58
19:31:41.60	-26:40:08.1	0.36	0.04	<0.84
19:31:41.84	-26:06:11.1	0.42	0.05	<1.06
19:31:42.55	-26:46:45.2	0.38	0.04	<0.92
19:31:42.71	-26:45:47.1	0.31	0.04	<0.63
19:31:42.84	-26:28:26.3	0.20	0.03	<2.14
19:31:43.42	-26:42:51.4	0.20	0.03	<2.14

Table 5.40: Spectral index upper limits of the uGMRT sources (continued)

RA_{J2000}	DEC_{J2000}	F_{640MHz} (mJy)	ΔF	α u.l.
19:31:44.43	-26:21:30.0	0.28	0.04	<0.48
19:31:44.78	-26:55:41.6	0.57	0.06	<1.50
19:31:44.79	-26:46:31.1	0.17	0.03	<-0.2
19:31:45.22	-27:02:42.3	0.66	0.07	<1.71
19:31:45.27	-26:31:55.6	0.38	0.04	<0.92
19:31:45.29	-26:46:58.9	0.29	0.04	<0.53
19:31:45.92	-26:48:04.0	0.18	0.03	<-0.1
19:31:47.87	-26:26:46.3	0.24	0.03	<0.26
19:31:48.15	-26:44:21.5	0.22	0.03	<0.13
19:31:49.35	-26:19:45.3	0.21	0.03	<0.07
19:31:49.98	-26:50:18.9	0.24	0.03	<0.26
19:31:50.97	-26:49:01.2	0.35	0.04	<0.80
19:31:50.97	-26:52:10.8	0.23	0.03	<0.20
19:31:51.64	-26:50:27.0	0.39	0.04	<0.96
19:31:51.82	-26:52:10.1	0.47	0.05	<1.22
19:31:52.06	-26:53:57.0	0.58	0.06	<1.53
19:31:52.28	-27:01:05.7	0.58	0.06	<1.53
19:31:52.32	-26:18:31.2	0.58	0.06	<1.53
19:31:52.68	-26:17:31.9	0.43	0.05	<1.10
19:31:52.92	-26:45:10.7	0.23	0.03	<0.20
19:31:53.27	-26:50:24.4	0.58	0.06	<1.53
19:31:53.38	-26:53:38.3	0.28	0.04	<0.48
19:31:53.94	-26:51:44.8	0.56	0.06	<1.48
19:31:53.99	-26:12:12.9	0.64	0.07	<1.67
19:31:54.92	-26:13:53.1	0.58	0.06	<1.53
19:31:55.15	-26:21:10.7	0.39	0.04	<0.96
19:31:55.20	-26:40:57.7	0.26	0.03	<0.37
19:31:55.43	-26:14:17.7	0.46	0.05	<1.19
19:31:55.63	-26:12:45.6	0.55	0.06	<1.45
19:31:55.70	-26:51:52.2	0.57	0.06	<1.50
19:31:55.86	-26:56:26.9	0.19	0.03	<-0.07
19:31:56.13	-26:15:03.4	0.28	0.04	<0.48
19:31:56.49	-26:16:45.3	0.22	0.03	<0.13
19:31:57.31	-26:14:21.9	0.32	0.04	<0.67
19:31:57.76	-26:17:43.6	0.19	0.03	<-0.07
19:31:58.28	-26:49:33.4	0.27	0.04	<0.43
19:31:58.33	-26:45:34.4	0.67	0.07	<1.73
19:31:58.36	-26:42:33.2	0.24	0.03	<0.26
19:31:58.36	-26:25:57.6	0.22	0.03	<0.13
19:31:58.82	-26:22:27.9	1.52	0.15	<2.91

Table 5.41: Spectral index upper limits of the uGMRT sources (continued)

RA_{J2000}	DEC_{J2000}	F_{640MHz} (mJy)	ΔF	α u.l.
19:31:58.95	-26:15:19.1	0.38	0.04	<0.92
19:31:59.06	-26:28:30.8	0.36	0.04	<0.84
19:31:59.42	-26:45:54.4	0.22	0.03	<0.13
19:31:59.73	-26:41:11.7	0.32	0.04	<0.67
19:32:00.48	-27:00:18.0	0.69	0.07	<1.78
19:32:01.06	-26:17:57.5	0.16	0.03	<-0.3
19:32:01.18	-26:09:14.9	0.66	0.07	<1.71
19:32:01.42	-26:52:15.3	0.62	0.06	<1.62
19:32:02.61	-26:48:43.2	0.24	0.03	<0.26
19:32:03.12	-26:06:03.7	0.61	0.06	<1.60
19:32:04.37	-26:31:34.2	0.21	0.03	<0.07
19:32:04.68	-26:42:28.1	0.32	0.04	<0.67
19:32:05.03	-26:06:41.1	0.45	0.05	<1.16
19:32:05.34	-26:28:18.5	0.28	0.04	<0.48
19:32:06.32	-26:10:06.8	0.42	0.05	<1.06
19:32:06.92	-26:52:50.9	0.44	0.05	<1.13
19:32:07.17	-26:21:04.5	1.19	0.12	<2.56
19:32:07.42	-26:25:16.4	0.53	0.06	<1.40
19:32:08.33	-26:24:55.1	0.19	0.03	<-0.07
19:32:08.59	-26:33:23.4	0.47	0.05	<1.22
19:32:08.77	-26:19:26.8	0.28	0.04	<0.48
19:32:08.78	-26:44:54.4	0.43	0.05	<1.10
19:32:08.82	-26:45:25.2	0.42	0.05	<1.06
19:32:08.86	-26:30:59.7	0.30	0.04	<0.58
19:32:09.87	-26:19:05.8	0.50	0.05	<1.31
19:32:10.11	-26:47:29.3	0.23	0.03	<0.20
19:32:10.68	-26:51:29.5	0.16	0.03	<-0.3
19:32:10.73	-26:20:41.1	0.81	0.08	<2.01
19:32:10.80	-26:46:38.8	0.27	0.04	<0.43
19:32:11.06	-26:47:09.8	0.70	0.07	<1.80
19:32:11.56	-26:54:24.8	0.27	0.04	<0.43
19:32:11.67	-26:21:46.2	0.43	0.05	<1.10
19:32:11.80	-26:47:44.1	0.27	0.04	<0.43
19:32:11.83	-26:49:57.4	0.16	0.03	<-0.3
19:32:12.45	-26:45:42.8	0.59	0.06	<1.55
19:32:12.77	-26:48:33.6	0.29	0.04	<0.53
19:32:13.03	-26:26:30.0	0.30	0.04	<0.58
19:32:13.13	-26:21:54.5	0.42	0.05	<1.06
19:32:14.42	-26:36:38.5	0.31	0.04	<0.63
19:32:14.88	-26:17:43.1	0.32	0.04	<0.67

Table 5.42: Spectral index upper limits of the uGMRT sources (continued)

RA_{J2000}	DEC_{J2000}	F_{640MHz} (mJy)	ΔF	α u.l.
19:32:15.13	-26:45:57.9	0.21	0.03	<0.07
19:32:16.02	-26:26:51.4	0.41	0.05	<1.03
19:32:16.22	-26:53:37.6	0.41	0.05	<1.03
19:32:16.33	-26:39:52.5	0.28	0.04	<0.48
19:32:17.08	-26:34:08.6	0.24	0.03	<0.26
19:32:17.10	-26:37:21.3	0.23	0.03	<0.20
19:32:17.31	-26:52:30.0	0.73	0.07	<1.86
19:32:18.13	-26:18:17.0	0.50	0.05	<1.31
19:32:18.26	-26:42:41.8	0.27	0.04	<0.43
19:32:18.66	-26:33:04.1	0.39	0.04	<0.96
19:32:18.67	-26:29:07.6	0.29	0.04	<0.53
19:32:18.73	-26:50:29.8	0.26	0.03	<0.37
19:32:19.05	-26:15:17.2	0.30	0.04	<0.58
19:32:19.70	-27:00:50.6	0.79	0.08	<1.97
19:32:19.90	-27:00:02.5	0.55	0.06	<1.45
19:32:20.22	-26:53:06.0	0.42	0.05	<1.06
19:32:20.86	-26:49:47.7	0.28	0.04	<0.48
19:32:21.73	-26:15:40.7	0.43	0.05	<1.10
19:32:21.78	-26:07:11.7	0.55	0.06	<1.45
19:32:22.10	-26:28:32.2	0.21	0.03	<0.07
19:32:22.29	-26:20:10.1	0.29	0.04	<0.53
19:32:22.33	-26:16:40.3	0.33	0.04	<0.71
19:32:22.85	-26:06:00.7	0.77	0.08	<1.93
19:32:23.02	-26:38:56.3	0.22	0.03	<0.13
19:32:23.74	-26:14:09.6	0.34	0.04	<0.76
19:32:25.17	-26:16:10.6	0.68	0.07	<1.75
19:32:25.95	-26:15:36.1	0.22	0.03	<0.13
19:32:26.62	-26:16:44.3	0.27	0.04	<0.43
19:32:26.79	-26:38:12.1	0.37	0.04	<0.88
19:32:26.79	-26:45:32.4	0.17	0.03	<-0.2
19:32:26.88	-26:46:05.7	0.18	0.03	<-0.1
19:32:27.00	-26:54:11.3	0.44	0.05	<1.13
19:32:27.29	-26:39:09.4	0.27	0.04	<0.43
19:32:27.34	-26:48:19.6	0.50	0.05	<1.31
19:32:27.51	-26:44:09.0	0.32	0.04	<0.67
19:32:27.83	-26:51:04.0	0.48	0.05	<1.25
19:32:27.91	-26:38:23.1	0.20	0.03	<2.14
19:32:28.32	-26:09:21.8	0.60	0.06	<1.57
19:32:28.38	-26:38:53.2	0.31	0.04	<0.63
19:32:28.93	-26:08:40.3	0.67	0.07	<1.73

Table 5.43: Spectral index upper limits of the uGMRT sources (continued)

RA_{J2000}	DEC_{J2000}	F_{640MHz} (mJy)	ΔF	α u.l.
19:32:28.93	-26:39:33.7	0.23	0.03	<0.20
19:32:29.07	-26:35:00.4	0.21	0.03	<0.07
19:32:29.13	-26:39:51.8	0.24	0.03	<0.26
19:32:29.52	-26:39:22.9	0.39	0.04	<0.96
19:32:30.41	-26:52:29.3	0.60	0.06	<1.57
19:32:30.78	-26:34:41.8	0.22	0.03	<0.13
19:32:30.82	-26:24:35.4	0.39	0.04	<0.96
19:32:31.63	-26:35:18.8	0.34	0.04	<0.76
19:32:31.71	-26:50:46.8	0.70	0.07	<1.80
19:32:32.60	-26:50:27.3	0.36	0.04	<0.84
19:32:32.87	-26:15:46.1	0.31	0.04	<0.63
19:32:33.25	-26:35:58.0	0.31	0.04	<0.63
19:32:33.47	-26:43:32.1	0.21	0.03	<0.07
19:32:33.93	-26:50:26.7	1.00	0.10	<2.31
19:32:34.39	-27:02:34.9	0.84	0.08	<2.06
19:32:35.33	-26:50:14.4	0.67	0.07	<1.73
19:32:35.81	-26:21:57.0	0.37	0.04	<0.88
19:32:36.47	-26:44:12.8	0.21	0.03	<0.07
19:32:36.79	-26:42:06.6	0.28	0.04	<0.48
19:32:37.10	-26:46:11.6	0.32	0.04	<0.67
19:32:37.49	-26:52:12.2	0.41	0.05	<1.03
19:32:37.52	-26:40:42.0	0.26	0.03	<0.37
19:32:37.55	-26:23:38.5	0.27	0.04	<0.43
19:32:37.83	-26:59:21.3	0.78	0.08	<1.95
19:32:38.62	-26:09:10.2	0.60	0.06	<1.57
19:32:40.08	-26:56:46.7	0.49	0.05	<1.28
19:32:40.55	-26:24:54.4	0.40	0.05	<0.99
19:32:40.86	-26:48:01.2	0.29	0.04	<0.53
19:32:41.17	-26:42:17.3	0.16	0.03	<-0.3
19:32:41.42	-26:29:05.3	0.37	0.04	<0.88
19:32:42.96	-26:17:22.1	1.16	0.12	<2.52
19:32:43.85	-26:44:28.0	0.44	0.05	<1.13
19:32:44.21	-26:42:26.2	0.24	0.03	<0.26
19:32:44.57	-26:57:47.9	0.60	0.06	<1.57
19:32:45.36	-26:40:02.1	0.27	0.04	<0.43
19:32:45.41	-26:35:30.5	0.40	0.05	<0.99
19:32:46.06	-26:56:31.5	0.35	0.04	<0.80
19:32:46.96	-26:17:35.0	3.07	0.30	<3.92
19:32:46.97	-26:07:55.5	1.72	0.17	<3.09
19:32:49.30	-26:56:06.1	2.09	0.21	<3.37

Table 5.44: Spectral index upper limits of the uGMRT sources (continued)

RA_{J2000}	DEC_{J2000}	F_{640MHz} (mJy)	ΔF	α u.l.
19:32:50.11	-26:34:26.9	0.19	0.03	<-0.07
19:32:50.97	-26:25:07.1	0.33	0.04	<0.71
19:32:51.06	-26:41:19.5	0.60	0.06	<1.57
19:32:51.07	-26:32:25.3	0.20	0.03	<2.14
19:32:51.99	-27:00:53.8	1.29	0.13	<2.68
19:32:52.23	-26:59:32.0	0.59	0.06	<1.55
19:32:52.42	-26:50:48.3	0.35	0.04	<0.80
19:32:53.89	-26:46:23.3	0.65	0.07	<1.69
19:32:54.53	-26:42:17.6	0.33	0.04	<0.71
19:32:54.67	-26:52:52.2	0.56	0.06	<1.48
19:32:55.32	-26:47:33.3	0.69	0.07	<1.78
19:32:55.67	-26:40:53.1	0.38	0.04	<0.92
19:32:55.82	-26:43:40.7	0.38	0.04	<0.92
19:32:56.41	-26:19:04.2	0.49	0.05	<1.28
19:32:56.78	-26:51:01.3	0.60	0.06	<1.57
19:32:56.88	-26:52:32.3	0.35	0.04	<0.80
19:32:57.33	-26:09:51.8	0.38	0.04	<0.92
19:32:57.53	-26:56:23.0	0.71	0.07	<1.82
19:32:58.43	-26:49:48.6	0.38	0.04	<0.92
19:32:59.40	-26:22:46.4	0.63	0.07	<1.64
19:33:01.38	-26:22:25.0	0.46	0.05	<1.19
19:33:02.00	-26:43:26.1	0.40	0.05	<0.99
19:33:02.64	-26:18:24.8	0.73	0.07	<1.86
19:33:04.75	-26:18:38.0	0.57	0.06	<1.50
19:33:08.51	-26:38:19.1	0.27	0.04	<0.43
19:33:08.94	-26:47:27.6	0.31	0.04	<0.63
19:33:09.77	-26:24:26.5	0.55	0.06	<1.45
19:33:10.10	-26:47:10.2	0.52	0.06	<1.37
19:33:10.46	-26:33:56.5	0.59	0.06	<1.55
19:33:10.56	-26:30:45.4	0.41	0.05	<1.03
19:33:11.35	-26:36:26.5	0.39	0.04	<0.96
19:33:12.92	-26:39:20.4	0.86	0.09	<2.09
19:33:13.20	-26:52:48.4	1.19	0.12	<2.56
19:33:13.27	-26:53:30.9	1.33	0.13	<2.72
19:33:13.64	-26:33:24.7	0.41	0.05	<1.03
19:33:13.85	-26:52:28.7	1.00	0.10	<2.31
19:33:19.99	-26:26:09.9	0.88	0.09	<2.13
19:33:22.95	-26:14:49.1	0.85	0.09	<2.08
19:33:28.63	-26:34:28.4	1.16	0.12	<2.52
19:33:30.84	-26:48:32.3	0.90	0.09	<2.16
19:33:41.16	-26:48:29.4	0.95	0.10	<2.24

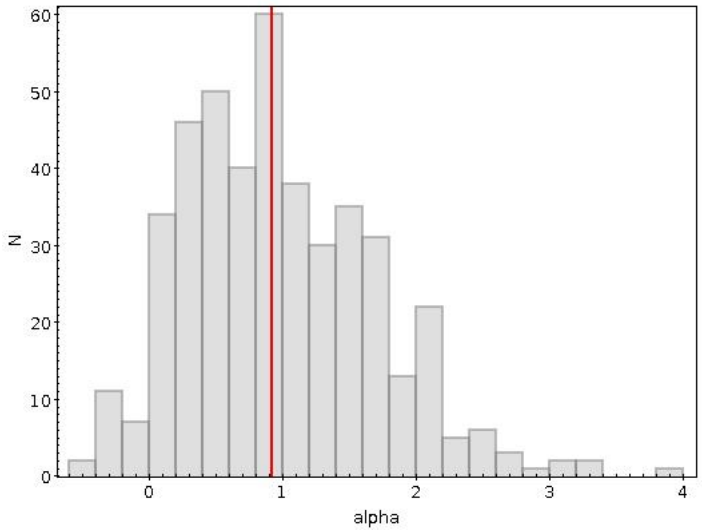

Figure 5.13: Histogram of the upper limits of the spectral indices for sources in MACSJ1931-2634 field detected only at 640 MHz. For the 1.2 GHz fluxes we assumed an upper limit of 5σ (i.e. 0.2 mJy). The red line indicates the median value of the distribution which is 0.92.

5.7 Radio source counts

After the radio analysis performed on the entire sample distributed on an area of 30 arcmin radius centered on the BCG, we restricted the statistical analysis and the radio-optical crossmatch on an area of 12 arcmin radius. As estimated from lensing (Santos et al., 2016), the MACSJ1931-2634 virial radius is 1.8 Mpc. The area of our analysis corresponds to two virial radii, a distance within which the galaxy properties could be still influenced by the dynamics of the cluster.
We computed the source counts for our radio samples and we compared them with the background in order to study if the dynamical properties of this region result in an enhanced number of radio sources or vice-versa, in a reduced number of radio sources (Venturi et al., 2000, 2001; Giacintucci et al., 2004; Prandoni et al., 2006; Mahony et al., 2016). We computed the two logN-logS distributions both for the sources detected with MeerKAT (Fig. 5.14) and those detected with uGMRT (Fig. 5.15).
The MeerKAT logN-logS (black counts) is computed on an area corresponding to 0.125 deg^2. The noise in this area is homogeneus, so we considered a flux limit of F $\geq$ 0.2 mJy, (i.e. 5σ), which is the source detection threshold of the MeerKAT catalogue. The flux density ranges from 0.2 mJy to 145.2 mJy, which is the flux density of the NAT radio galaxy in the center.
The total number of sources detected within this area over the flux density threshold is 38. The resulting logN-logS is shown in Figure 5.14. The differential number of sources in each bin is given in N deg^{-2} and the errors are poissonian. The width of each bin is ΔF=F $\times$ log(2.5) (following Venturi et al., 2000, 2001).
For the background estimate (red counts), we considered an integrating area of 0.66 deg^2, obtained by subtracting the area of 12 arcmin radius to the total area of 30 arcmin radius (0.785 deg^2) of our complete sample. In order to take into account the primary beam attenuation at this distance, for the background estimate, we considered a subsample with a higher flux density limit of F $\geq$ 0.25 mJy. The total number of sources in the sub-sample for the background counts is 153.
As clear from Fig.5.14 the counts in the cluster area and in the background have the same shape, and we can conclude that the number of radio sources in MACSJ1931-2634 is in good agreement with the background radio source counts. However, it is evident that, at fluxes $>$ 10 mJy, the sources dominate the background. This result is also true for the uGMRT sample and it is consistent with what we found in previous studies (see Venturi et al., 2000, 2001; Giacintucci et al., 2004).
The cluster counts are below the background for fluxes F $<$ 0.25 mJy, indicating that our sample is incomplete below this limit, consistent with what is found in literature (Prandoni et al., 1999, 2006; Venturi et al., 2000, 2001; Giacintucci et al., 2004).
The same method is followed also for the source counts in the uGMRT sample, integrating over the same total area of 0.125 deg^2, within which the noise is uniform.

We considered a flux limit of F $\geq$ 0.15 mJy (i.e. 5σ), which is the source detection threshold of the uGMRT catalogue. The total number of sources within the integrating area is 129. We plot the background (red counts) for comparison obtained, as for the MeerKAT sample, by subtracting the integrating area of 12 arcmin radius to the total area of 30 arcmin radius. The background area is 0.66 deg^2. We take into account the primary beam attenuation at this distance, considering, as we did for the MeerKAT sample, an higher threshold of 0.2 mJy for the background computation. The sources in the reduced sub-sample for the background integration are 392. The resulting logN-logS is shown in Fig.5.15.
Also at 640 MHz, it is evident that the counts in the cluster area and in the background have the same shape, and for F $>$ 10 mJy, the sources dominate the background. The cluster counts are below the background for F $<$ 0.5 mJy, indicating the statistical incompleteness of our sample.

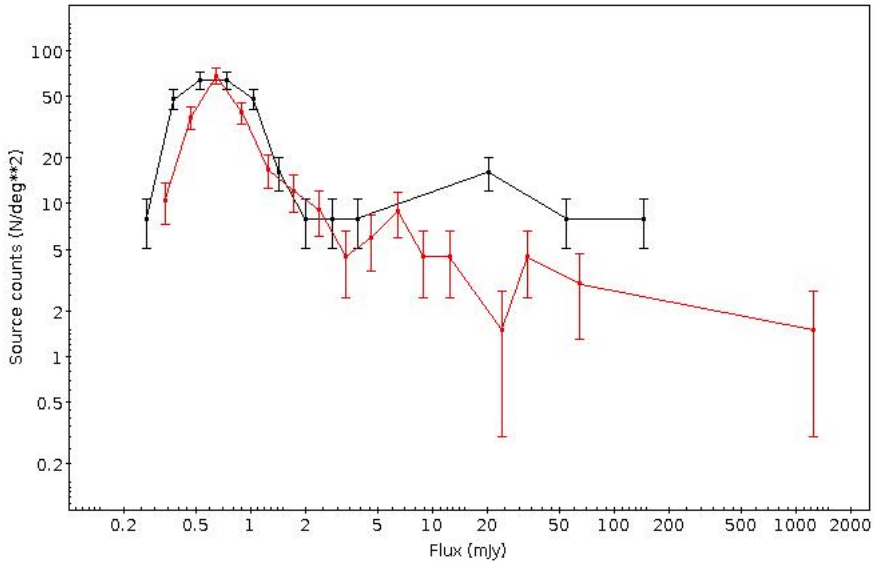

Figure 5.14: Differential radio source counts in MACSJ1931-2434 at 1.2 GHz. The total integrating area, equivalent to 2 virial radii, is of 0.125 deg^2 (black counts). The background integrating area is of 0.66 deg^2 (red counts). The sources dominate the background for fluxes $>$ 10 mJy.

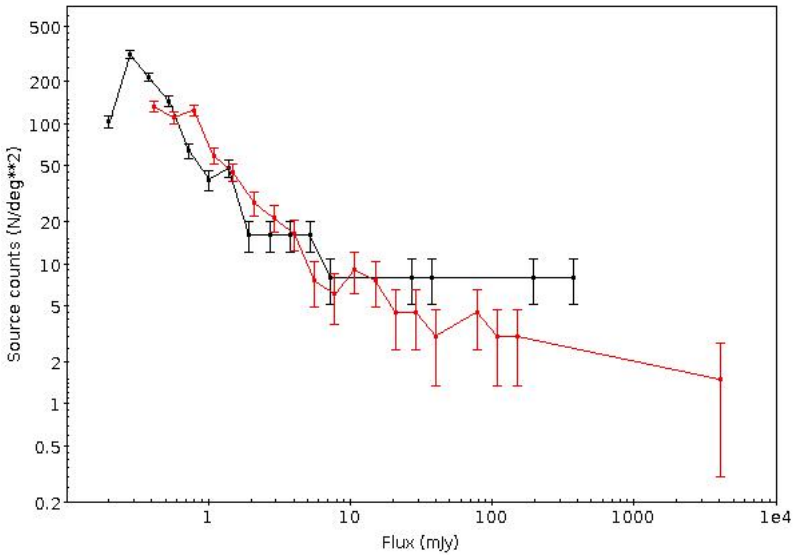

Figure 5.15: Differential radio source counts in MACSJ1931-2434 at 640 MHz. The total integrating area, equivalent to 2 virial radii, is of 0.125 deg^2 (black counts). The background integrating area is of 0.66 deg^2 (red counts). As for MeerKAT, the sources dominate the background for fluxes > 10 mJy.

5.8 Optical identifications

We searched for optical counterparts of the radio sources detected in our catalogues using *Subaru*-SuprimeCam photometric catalogues[3], limited by magnitude $m_{B_{AB}}$= 25.6 and $m_{R_{AB}}$= 24.9 (values given at 5σ). Magnitudes have been corrected for the galactic extinction. Consistently with the computation of the statistical source counts, we performed our search within 2 virial radii (i.e. 3.5 Mpc) from the cluster center.

The radio positional error is given by the ratio (HPBW/2×SNR) of the faintest source (5σ) according to the method adopted in Prandoni et al. (2000). In both the MeerKAT and the uGMRT samples the radio positional error is ~ 0.5". The optical positional error is of the order of ~ 0.02 arcsec. To crossmatch our catalogues, according to the method used in Giacintucci et al. (2004), we considered the parameter R, defined as:

$$R^2 = \frac{\Delta^2_{r-o}}{\sigma^2_r + \sigma^2_g} \tag{5.6}$$

Here, Δ^2_{r-o} is the offset between the radio and the optical positions, σ^2_g is the uncertainty in the galaxy position, and σ^2_r is the uncertainty in the radio position. For our radio sources we considered reliable identifications those with R < 3, which

[3]https://archive.stsci.edu/prepds/clash/

corresponds to an offset of the order of 2". In Fig.5.16 we report the offset between the radio and the optical coordinates. After the crossmatch we further visually inspected each source in order to assess the reliability of the matches.

There is only one case of uncertainty in the identification of the optical counterparts (source radio ID 141). In this case we considered the closest source the most reliable counterpart.
Among the radio sources, within the radius considered, 36 are in common at both frequencies, only 2 belong to the MeerKAT catalogue only and 94 belong to the uGMRT catalogue only. The total number of radio galaxies crossmatched with Suprime RC and B bands resulted 132.
After a cut in magnitude of $m_{R_{AB}} < 25$ in RC, we found 97 optical counterparts in RC and 89 in B, i.e. $\sim 73\%$ and 67% of our sample. We report upper limits ($>$) in the blue magnitude for the missing 8 sources.
The result of our cross-match is shown in Table.5.45 and following, where we report in columns 1 and 2 the Suprime RC coordinates (J2000), in column 3 the radio ID as derived from the original initial catalogues, in 4 and 5 we report the radio coordinates (J2000) and in column 6, 7, 8 the photometric information.
In boldface we report those sources that are consistent with being cluster members. The BCG (ID 320), of colour 0.7, is highlighted with an asterisk.
In order to test the reliability of our match, we shifted the radio coordinates of tens arcsec and we repeated the match step. We get on average 12 matching, meaning that about 8-10% of the associations could be random.

The redshift information for the optical counterparts are taken from VIMOS-VLT spectra (see Sect. 1.2) within the CLASH-VLT ESO Large Programme (P.I. P.Rosati), 186.A-0798 (Rosati et al., 2014). The slits originally selected where preferentially placed on red galaxies, this could introduce a selection bias against blue galaxies.
After the analysis, we found 36 slits and we found that 32 sources have spectroscopic redshift, among which, 6 are consistent with being cluster members.
They are reported in boldface in Table 5.48 and following. The BCG is indicated with an asterisk.
The result of our spectroscopic analysis is shown in Table 5.48 and following. We report in columns 1 and 2 the radio coordinates (J2000), in column 3 the original radio ID, in 4 and 5 we report the fluxes at 1.2 GHz and 640 MHz respectively, in column 6 the spectral index, in column 7 we report the spectroscopic redshifts that we found, whereas in columns 8 and 9 we report the radio powers.
We can distinguish between two cases to classify the radio powers: we report for those sources which have the radio flux density and the redshift information a true power; we report an upper limit ($<$) of the radio power at 5σ for those sources with redshift but for which the radio flux is undetected; the sources with no redshifts are indicated with a symbol -.

Table 5.45: Optical identifications

RA Suprime (RC)	DEC Suprime (RC)	Radio ID	RA radio hms	DEC radio dms	Bmag	Rmag	(B-R)
19:30:57.53	-26:32:57.18	495	19:30:57.55	-26:32:57.31	24.96	22.32	2.64
19:30:57.97	-26:36:14.37	489	19:30:57.97	-26:36:14.39	> 25.6	23.86	> 1.74
19:30:58.04	-26:32:44.23	491	19:30:58.07	-26:32:44.74	23.7	21.76	1.94
19:31:01.96	-26:38:23.84	482	19:31:02.03	-26:38:24.47	19.71	18.49	1.22
19:31:03.04	-26:28:59.84	478	19:31:03.08	-26:29:00.19	25.45	23.58	1.87
19:31:05.45	-26:34:17.54	471	19:31:05.46	-26:34:17.88	> 25.6	22.1	> 3.50
19:31:05.47	-26:39:31.51	470	19:31:05.51	-26:39:31.73	20.22	19.17	1.05
19:31:06.38	-26:29:09.19	468	19:31:06.44	-26:29:09.77	23.85	23.24	0.61
19:31:07.24	-26:40:58.54	462	19:31:07.24	-26:40:58.87	> 25.6	23.95	> 1.65
19:31:09.21	-26:33:40.18	454	19:31:09.25	-26:33:40.20	23.28	20.77	2.51
19:31:09.60	-26:41:41.84	453	19:31:09.65	-26:41:42.06	21.33	19.8	1.53
19:31:09.85	-26:28:07.07	452	19:31:10.05	-26:28:07.09	23.01	20.79	2.22
19:31:13.11	-26:31:30.77	447	19:31:13.16	-26:31:31.09	23.93	23.58	0.35
19:31:13.81	-26:29:55.14	444	19:31:13.83	-26:29:54.18	> 25.6	24.58	> 1.02
19:31:13.86	-26:30:50.20	443	19:31:13.89	-26:30:50.80	20.8	19.14	1.66
19:31:14.99	-26:34:14.17	439	19:31:15.05	-26:34:14.02	24.52	22.49	2.03
19:31:15.64	-26:34:26.90	436	19:31:15.64	-26:34:27.22	25.04	22.06	2.98
19:31:16.08	-26:27:36.00	435	19:31:16.13	-26:27:36.45	21.5	20.42	1.08
19:31:16.16	-26:30:03.89	434	19:31:16.19	-26:30:04.15	26.37	24.95	1.42
19:31:18.30	-26:30:17.62	426	19:31:18.34	-26:30:18.14	22.36	22.18	0.18
19:31:18.97	-26:36:02.86	424	19:31:19.02	-26:36:02.92	20.96	19.89	1.07
19:31:19.33	-26:30:16.85	500328	19:31:19.30	-26:30:17.39	24.65	22.94	1.71
19:31:19.35	-26:27:17.06	423	19:31:19.38	-26:27:17.29	22.387	20.9	1.49
19:31:20.51	-26:40:46.09	416	19:31:20.54	-26:40:46.53	18.84	18.78	0.06
19:31:21.05	-26:37:50.80	414	19:31:21.11	-26:37:51.32	26.03	22.92	3.11
19:31:23.23	-26:28:49.09	407	19:31:23.24	-26:28:49.76	22.38	20.59	1.79
19:31:27.75	-26:31:11.06	395	19:31:27.77	-26:31:10.65	22.23	21.39	0.84
19:31:28.01	-26:27:41.02	394	19:31:28.06	-26:27:41.35	20.72	19.35	1.37
19:31:28.31	-26:37:31.92	391	19:31:28.34	-26:37:31.71	22.915	21.403	1.51
19:31:30.16	-26:41:09.79	387	19:31:30.12	-26:41:08.97	16.6	17.42	-0.82
19:31:30.99	-26:43:37.93	382	19:31:30.99	-26:43:37.92	20.89	19.52	1.37
19:31:32.04	-26:37:13.58	379	19:31:32.03	-26:37:13.17	22.732	20.434	2.30
19:31:32.51	-26:31:33.24	376	19:31:32.52	-26:31:33.19	22.59	20.79	1.80
19:31:33.29	-26:23:37.24	371	19:31:33.36	-26:23:37.31	22.94	21.54	1.40
19:31:33.65	-26:23:46.86	369	19:31:33.69	-26:23:46.70	24.288	24.073	0.22
19:31:35.16	-26:41:44.13	367	19:31:35.17	-26:41:44.33	23.55	22.33	1.22
19:31:35.76	-26:23:07.68	364	19:31:35.82	-26:23:07.63	22.08	20.79	1.29
19:31:35.91	-26:44:41.70	362	19:31:35.94	-26:44:41.76	22.83	21.42	1.41
19:31:36.43	-26:33:09.10	359	19:31:36.45	-26:33:09.32	24.21	21.9	2.31
19:31:36.71	-26:27:18.70	360	19:31:36.74	-26:27:18.08	25.42	23.43	1.99
19:31:38.89	-26:32:44.56	352	19:31:38.93	-26:32:44.61	22.44	20.53	1.91

Table 5.46: Optical identifications (continued)

RA Suprime (RC)	DEC Suprime (RC)	Radio ID	RA radio hms	DEC radio dms	Bmag	Rmag	(B-R)
19:31:38.94	-26:44:38.15	351	19:31:38.95	-26:44:37.84	24.44	24.07	0.37
19:31:39.73	-26:25:51.11	345	19:31:39.76	-26:25:51.29	20.21	18.38	1.83
19:31:41.58	-26:40:08.34	341	19:31:41.59	-26:40:08.12	20.15	18.55	1.60
19:31:42.71	-26:45:47.21	337	19:31:42.71	-26:45:47.11	23.62	22.4	1.22
19:31:43.38	-26:42:50.50	336	19:31:43.42	-26:42:51.41	23.72	22.77	0.95
19:31:45.23	-26:31:55.65	332	19:31:45.27	-26:31:55.66	19.47	18.92	0.55
19:31:46.53	**-26:37:31.02**	**500307**	**19:31:46.60**	**-26:37:31.73**	**21.95**	**19.67**	**2.28**
19:31:47.86	-26:26:46.58	326	19:31:47.87	-26:26:46.32	24.03	23.39	0.64
19:31:48.14	-26:44:21.75	325	19:31:48.15	-26:44:21.54	21.9	20.14	1.76
19:31:49.63	**-26:34:32.58**	**320***	**19:31:49.56**	**-26:34:32.75**	**18.84***	**18.14***	**0.70***
19:31:50.00	**-26:35:17.10**	**500078**	**19:31:49.98**	**-26:35:17.34**	**21.54**	**19.27**	**2.27**
19:31:52.88	-26:45:11.39	307	19:31:52.92	-26:45:10.72	20.53	19.36	1.17
19:31:54.86	**-26:30:56.99**	**500199**	**19:31:54.88**	**-26:30:57.13**	**21.66**	**19.46**	**2.20**
19:31:57.55	-26:45:37.45	500350	19:31:57.56	-26:45:38.09	24.37	22.92	1.45
19:31:58.32	**-26:45:33.62**	**282**	**19:31:58.33**	**-26:45:34.42**	**20.85**	**19.33**	**1.52**
19:31:58.36	-26:25:57.39	284	19:31:58.36	-26:25:57.69	22.66	21.1	1.56
19:31:58.93	-26:38:15.22	278	19:31:58.94	-26:38:15.04	23.5	22.08	1.42
19:31:59.02	-26:28:30.72	279	19:31:59.06	-26:28:30.86	22.6	22.27	0.33
19:31:59.45	-26:45:54.76	277	19:31:59.42	-26:45:54.44	21.41	20.27	1.14
19:31:59.70	-26:41:11.96	275	19:31:59.73	-26:41:11.77	25.43	24.61	0.82
19:32:04.34	-26:31:33.80	267	19:32:04.37	-26:31:34.26	> 25.6	24.74	> 0.86
19:32:04.67	-26:42:28.11	266	19:32:04.68	-26:42:28.12	24.823	23.587	1.24
19:32:05.24	-26:32:05.83	262	19:32:05.20	-26:32:06.07	24.49	24.41	0.08
19:32:07.35	**-26:25:16.31**	**255**	**19:32:07.42**	**-26:25:16.45**	**20.52**	**19.22**	**1.30**
19:32:08.80	-26:44:54.36	248	19:32:08.78	-26:44:54.44	21.19	19.43	1.76
19:32:09.74	-26:25:28.76	500290	19:32:09.72	-26:25:29.38	22.61	21.47	1.14
19:32:12.11	-26:37:29.46	230	19:32:12.11	-26:37:29.46	20.07	18.81	1.26
19:32:12.99	-26:26:29.60	225	19:32:13.02	-26:26:30.02	20.14	19.03	1.11
19:32:14.38	-26:36:38.32	221	19:32:14.42	-26:36:38.53	24.6	22.72	1.88
19:32:15.98	-26:26:51.56	217	19:32:16.02	-26:26:51.40	22.64	20.67	1.97
19:32:16.30	-26:39:53.13	215	19:32:16.33	-26:39:52.54	20.48	19.29	1.19
19:32:17.02	-26:34:08.44	213	19:32:17.07	-26:34:08.61	21.05	20.13	0.92
19:32:17.08	-26:37:21.15	212	19:32:17.10	-26:37:21.33	21.62	20.26	1.36
19:32:17.70	-26:29:31.57	208	19:32:17.71	-26:29:31.53	22.33	20.31	2.02
19:32:18.23	-26:42:42.49	206	19:32:18.26	-26:42:41.86	23.69	22.44	1.25
19:32:18.62	-26:29:07.19	204	19:32:18.67	-26:29:07.63	22.51	20.21	2.30
19:32:18.63	-26:33:03.42	203	19:32:18.66	-26:33:04.10	21.56	19.96	1.60
19:32:20.04	-26:31:34.38	197	19:32:20.07	-26:31:34.92	19.9	18.86	1.04
19:32:22.10	-26:28:32.24	191	19:32:22.09	-26:28:32.28	21.19	19.63	1.56
19:32:23.02	-26:38:57.08	186	19:32:23.02	-26:38:56.36	21.88	20.47	1.41
19:32:26.13	-26:32:48.38	179	19:32:26.14	-26:32:48.46	21.8	20.22	1.58

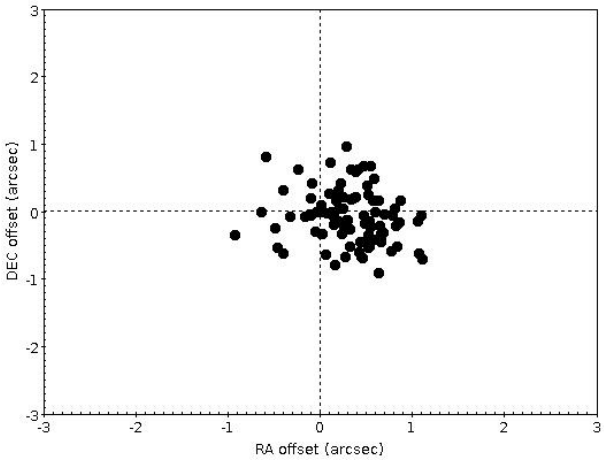

Figure 5.16: The image shows the radio positions compared to the optical positions. We choosed 2" as the reliable distance for the crossmatches further visually inspecting each match.

Table 5.47: Optical identifications (continued)

RA Suprime (RC)	DEC Suprime (RC)	Radio ID	RA radio hms	DEC radio dms	Bmag	Rmag	(B-R)
19:32:26.75	-26:38:12.58	176	19:32:26.79	-26:38:12.10	19.87	18.76	1.11
19:32:27.25	-26:39:09.71	174	19:32:27.29	-26:39:09.47	23.42	21.43	1.99
19:32:27.77	-26:33:55.56	170	19:32:27.80	-26:32:08.30	> 25.6	24.16	> 1.44
19:32:27.84	-26:32:08.00	167	19:32:27.80	-26:32:08.00	> 25.6	24.16	> 1.44
19:32:28.39	-26:38:53.85	165	19:32:28.38	-26:38:53.22	20.23	19.98	0.25
19:32:28.89	-26:39:34.07	163	19:32:28.92	-26:39:33.70	23.98	22.1	1.88
19:32:29.04	-26:35:01.15	161	19:32:29.07	-26:35:00.47	20.47	19.4	1.07
19:32:29.11	-26:39:52.03	160	19:32:29.13	-26:39:51.85	23.35	22.08	1.27
19:32:30.44	-26:38:11.71	156	19:32:30.46	-26:38:11.55	20.94	19.6	1.34
19:32:30.91	-26:28:02.82	500065	19:32:30.90	-26:28:02.89	25.98	22.33	3.65
19:32:31.04	-26:41:51.09	151	19:32:31.03	-26:41:51.09	> 25.6	24.2	> 1.4
19:32:31.49	-26:27:58.66	500064	19:32:31.79	-26:27:58.99	17.32	17.77	-0.45
19:32:31.61	-26:31:20.42	148	19:32:31.61	-26:31:20.22	24.24	23.49	0.75
19:32:33.21	-26:35:57.33	141	19:32:33.24	-26:35:58.01	24.18	23.31	0.87
19:32:33.31	-26:35:57.67	141	19:32:33.24	-26:35:58.01	24.9	23.38	1.52

Table 5.48: Redshift identifications and radio powers

RA radio (hms)	DEC radio (dms)	Radio ID	$F_{1.2GHz}$ (mJy)	$F_{0.6GHz}$ (mJy)	α	zspec	$logP_{1.2}$	$logP_{0.6}$
19:30:57.55	-26:32:57.31	495	0.2	0.22	0.13	/	-	-
19:30:57.97	-26:36:14.39	489	1.79	3.88	1.11	/	-	-
19:30:58.07	-26:32:44.74	491	0.2	0.49	1.28	0.814	<23.87	24.11
19:31:02.03	-26:38:24.47	482	0.2	0.18	-0.13	0.205	<22.4	22.43
19:31:03.08	-26:29:00.19	478	0.51	0.86	0.75	/	-	-
19:31:05.46	-26:34:17.88	471	0.2	0.23	0.20	/	-	-
19:31:05.51	-26:39:31.73	470	0.2	0.42	1.06	0.218	<22.47	22.76
19:31:06.44	-26:29:09.77	468	0.2	0.38	0.92	/	-	-
19:31:07.24	-26:40:58.87	462	0.91	1.39	0.60	/	-	-
19:31:09.26	-26:33:40.20	454	0.2	0.48	1.25	0.513	<23.36	23.64
19:31:09.65	-26:41:42.06	453	0.2	0.42	1.06	0.208	<22.42	22.71
19:31:10.05	-26:28:07.09	452	0.2	0.16	-0.32	0.382	<23.04	23.09
19:31:13.16	-26:31:31.09	447	0.2	0.39	0.96	/	-	-
19:31:13.84	-26:29:54.18	444	0.2	0.38	0.92	/	-	-
19:31:13.89	-26:30:50.81	443	0.2	0.23	0.20	/	-	-
19:31:15.05	-26:34:14.02	439	0.2	0.15	-0.41	/	-	-
19:31:15.64	-26:34:27.23	436	0.2	0.25	0.32	/	-	-
19:31:16.13	-26:27:36.45	435	0.2	0.27	0.43	0.215	<22.45	22.61
19:31:16.19	-26:30:04.15	434	0.2	0.22	0.13	/	-	-
19:31:18.34	-26:30:18.14	426	0.35	0.53	0.59	/	-	-
19:31:19.02	-26:36:02.92	424	0.2	0.36	0.84	0.203	<22.45	22.64
19:31:19.30	-26:30:17.39	500328	0.35	0.53	0.59	/	-	-
19:31:19.38	-26:27:17.30	423	0.2	0.17	-0.23	/	-	-
19:31:20.54	-26:40:46.53	416	0.42	0.63	0.58	/	-	-
19:31:21.11	-26:37:51.32	414	0.2	0.23	0.20	/	-	-
19:31:23.24	-26:28:49.76	407	0.2	0.19	-0.07	0.292	<22.76	22.83
19:31:27.77	-26:31:10.65	395	0.2	0.34	0.76	/	-	-
19:31:28.06	-26:27:41.35	394	0.2	0.31	0.63	0.292	<22.77	22.96
19:31:28.34	-26:37:31.72	391	0.2	0.2	/	/	-	-
19:31:30.12	-26:41:08.98	387	0.2	0.23	0.20	/	-	-
19:31:31.00	-26:43:37.92	382	0.2	0.23	0.20	0.201	<22.39	22.48
19:31:32.03	-26:37:13.17	379	0.2	0.34	0.76	/	-	-
19:31:32.52	-26:31:33.19	376	0.2	0.26	0.37	/	-	-
19:31:33.37	-26:23:37.31	371	0.2	0.24	0.26	/	-	-
19:31:33.69	-26:23:46.70	369	0.2	0.19	-0.07	/	-	-
19:31:35.17	-26:41:44.33	367	0.2	0.21	0.07	/	-	-
19:31:35.82	-26:23:07.63	364	0.2	0.25	0.32	/	-	-
19:31:35.94	-26:44:41.76	362	0.2	0.37	0.88	0.417	<23.14	23.38
19:31:36.45	-26:33:09.32	359	15.29	24.1	0.65	/	-	-
19:31:36.74	-26:27:18.08	360	0.2	0.19	-0.07	/	-	-
19:31:38.93	-26:32:44.61	352	0.2	0.46	1.19	0.288	<22.75	23.06

Table 5.49: Redshift identifications and radio powers (continued)

RA radio (hms)	DEC radio (dms)	Radio ID	$F_{1.2GHz}$ (mJy)	$F_{0.6GHz}$ (mJy)	α	zspec	$logP_{1.2}$	$logP_{0.6}$
19:31:38.95	-26:44:37.84	351	0.2	0.22	0.13	/	-	-
19:31:39.76	-26:25:51.29	345	0.2	0.25	0.32	/	-	-
19:31:41.60	-26:40:08.12	341	0.2	0.36	0.84	0.206	<22.41	22.66
19:31:42.71	-26:45:47.12	337	0.2	0.31	0.63	/	-	-
19:31:43.42	-26:42:51.41	336	0.2	0.2	/	/	-	-
19:31:45.27	-26:31:55.67	332	0.2	0.38	0.92	0.230	<22.52	22.78
19:31:46.60	**-26:37:31.73**	**500307**	**0.39**	**0.15**	**-1.3**	**0.342**	**23.22**	**<23.06**
19:31:47.87	-26:26:46.33	326	0.2	0.24	0.26	/	-	-
19:31:48.15	-26:44:21.54	325	0.2	0.22	0.13	0.314	<22.84	22.95
19:31:49.62	**-26:34:32.65**	**320***	**45.46**	**183.7**	**1.97**	**0.352***	**25.31***	**25.74***
19:31:50.02	**-26:35:17.23**	**500078**	**145.2**	**354.7**	**1.28**	**0.351**	**25.81**	**26.13**
19:31:52.92	-26:45:10.72	307	0.2	0.23	0.20	0.29	<22.76	22.87
19:31:54.88	**-26:30:57.13**	**500199**	**0.88**	**1.39**	**0.65**	**0.351**	**23.60**	**23.80**
19:31:57.56	-26:45:38.09	500350	3.51	3.74	0.09	/	-	-
19:31:58.33	**-26:45:34.42**	**282**	**0.2**	**0.67**	**1.73**	**0.359**	**<22.98**	**23.37**
19:31:58.36	-26:25:57.69	284	0.2	0.22	0.13	/	-	-
19:31:58.94	-26:38:15.04	278	3.51	3.74	0.09	/	-	-
19:31:59.06	-26:28:30.87	279	0.2	0.36	0.84	/	-	-
19:31:59.42	-26:45:54.44	277	0.2	0.22	0.13	/	-	-
19:31:59.73	-26:41:11.77	275	0.2	0.32	0.67	/	-	-
19:32:04.37	-26:31:34.26	267	0.2	0.21	0.07	/	-	-
19:32:04.68	-26:42:28.12	266	0.2	0.32	0.67	/	-	-
19:32:05.20	-26:32:06.07	262	2.36	3.87	0.71	/	-	-
19:32:07.42	**-26:25:16.46**	**255**	**0.2**	**0.53**	**1.40**	**0.349**	**<22.95**	**23.28**
19:32:08.78	-26:44:54.44	248	0.2	0.43	1.10	0.213	<22.45	22.74
19:32:09.72	-26:25:29.38	500290	0.34	0.53	0.63	/	-	-
19:32:12.11	-26:37:29.46	230	0.5	0.75	0.58	0.207	22.81	23.00
19:32:13.03	-26:26:30.03	225	0.2	0.3	0.58	0.116	<21.86	22.04
19:32:14.42	-26:36:38.53	221	0.2	0.31	0.63	/	-	-
19:32:16.02	-26:26:51.40	217	0.2	0.41	1.03	/	-	-
19:32:16.33	-26:39:52.54	215	0.2	0.28	0.48	0.212	<22.44	22.61
19:32:17.08	-26:34:08.61	213	0.2	0.24	0.26	0.246	<22.59	22.71
19:32:17.10	-26:37:21.33	212	0.2	0.23	0.20	/	-	-
19:32:17.71	-26:29:31.53	208	1.31	1.49	0.18	/	-	-
19:32:18.26	-26:42:41.87	206	0.2	0.27	0.43	/	-	-
19:32:18.66	-26:33:04.10	203	0.2	0.39	0.96	/	-	-
19:32:18.67	-26:29:07.63	204	0.2	0.29	0.53	0.405	<23.11	23.29
19:32:20.07	-26:31:34.92	197	0.53	0.84	0.66	0.145	22.49	22.69
19:32:22.10	-26:28:32.28	191	0.2	0.21	0.07	/	-	-
19:32:23.02	-26:38:56.36	186	0.2	0.22	0.13	/	-	-
19:32:26.14	-26:32:48.46	179	0.59	0.67	0.18	/	-	-
19:32:26.79	-26:38:12.10	176	0.2	0.37	0.88	0.212	<22.44	22.69
19:32:27.29	-26:39:09.47	174	0.2	0.27	0.43	/	-	-

Table 5.50: Redshift identifications and radio powers (continued)

RA radio (hms)	DEC radio (dms)	Radio ID	$F_{1.2GHz}$ (mJy)	$F_{0.6GHz}$ (mJy)	α	zspec	$logP_{1.2}$	$logP_{0.6}$
19:32:27.80	-26:32:08.00	167	0.58	0.78	0.42	/	-	-
19:32:27.80	-26:32:08.30	170	0.58	0.78	0.42	/	-	-
19:32:28.38	-26:38:53.22	165	0.2	0.31	0.63	/	-	-
19:32:28.93	-26:39:33.70	163	0.2	0.23	0.20	/	-	-
19:32:29.07	-26:35:00.47	161	0.2	0.21	0.07	0.212	<22.44	22.51
19:32:29.13	-26:39:51.85	160	0.2	0.24	0.26	/	-	-
19:32:30.46	-26:38:11.55	156	0.25	0.26	0.05	/	-	-
19:32:30.90	-26:28:02.89	500065	1.03	6.12	2.5	/	-	-
19:32:31.03	-26:41:51.09	151	0.51	0.9	0.81	/	-	-
19:32:31.61	-26:31:20.22	148	0.57	0.92	0.68	/	-	-
19:32:31.79	-26:27:58.99	500064	0.96	0.15	-2.6	/	-	-
19:32:33.25	-26:35:58.02	141	0.2	0.31	0.63	/	-	-
19:32:33.25	-26:35:58.02	141	0.2	0.31	0.63	/	-	-

5.9 Radio-optical overdensities

In order to explore the properties of the radio galaxies in our sample and the dynamical properties of the environment in which they are located, we evaluated their distribution on the Color-Magnitude diagram (Fig.5.17) and we analyzed their spatial distribution within a magnitude range $19.7 < m_{RC} < 21.7$ (Fig.5.18).
The Color-Magnitude diagram shows the distribution of the galaxies (the entire sample belonging to VIMOS-VLT) divided into the red sequence, i.e. $(B\text{-}RC)_{AB}$ higher than 1.5-1.7, and the blue sequence. The dotted line represents the central value of 2.5 whereas the dashed lines represent a $\pm$ 3σ scatter from the central value. The green dots are the radio galaxies detected in our samples (either the MeerKAT galaxies and the uGMRT galaxies). The purple firebricks represent those galaxies whose redshift is not consistent with being cluster members. The triangles represent those galaxies with redshifts consistent with being cluster members: in particular, the black triangle is the NAT (consistent with being a giant elliptical AGN galaxy), with colour 2.27. The blue triangle is the BCG (a star forming galaxy) with colour= 0.7, the other four galaxies belonging to the cluster (red triangles) are symmetrically distributed into two AGNs on the red sequence and two Star Forming galaxies on the blue sequence.
It is interesting to point out that there is a group of galaxies located at z=0.21, belonging to a foreground group. They are highlighted within a black circle in Fig. 5.17.

The spatial distribution of the galaxies in our sample is shown in Fig.5.18. The color scale represents the source spatial density, being the yellow-white region the densest region. The black lines are isodensity curves. The smaller black dots indicate all the optical galaxies, whereas the bigger dots indicate the common MeerKAT and uGMRT sources (green circles), the uGMRT only (cyan) and the MeerKAT only (pink circles, only two galaxies) respectively. The biggest dots represent those galaxies with redshift consistent with being cluster members. The BCG and the NAT are respectively the green and the red dots in the field center. There is absence of an offset between the BCG and the centre of the spatial distribution.
From the optical galaxies distribution and the cluster galaxy distribution, there is evidence of a real elongated North-South spatial distribution.
Finally, inspecting the images at our disposal, we found no evidence of filaments in the field surrounding MACSJ1931-2634.

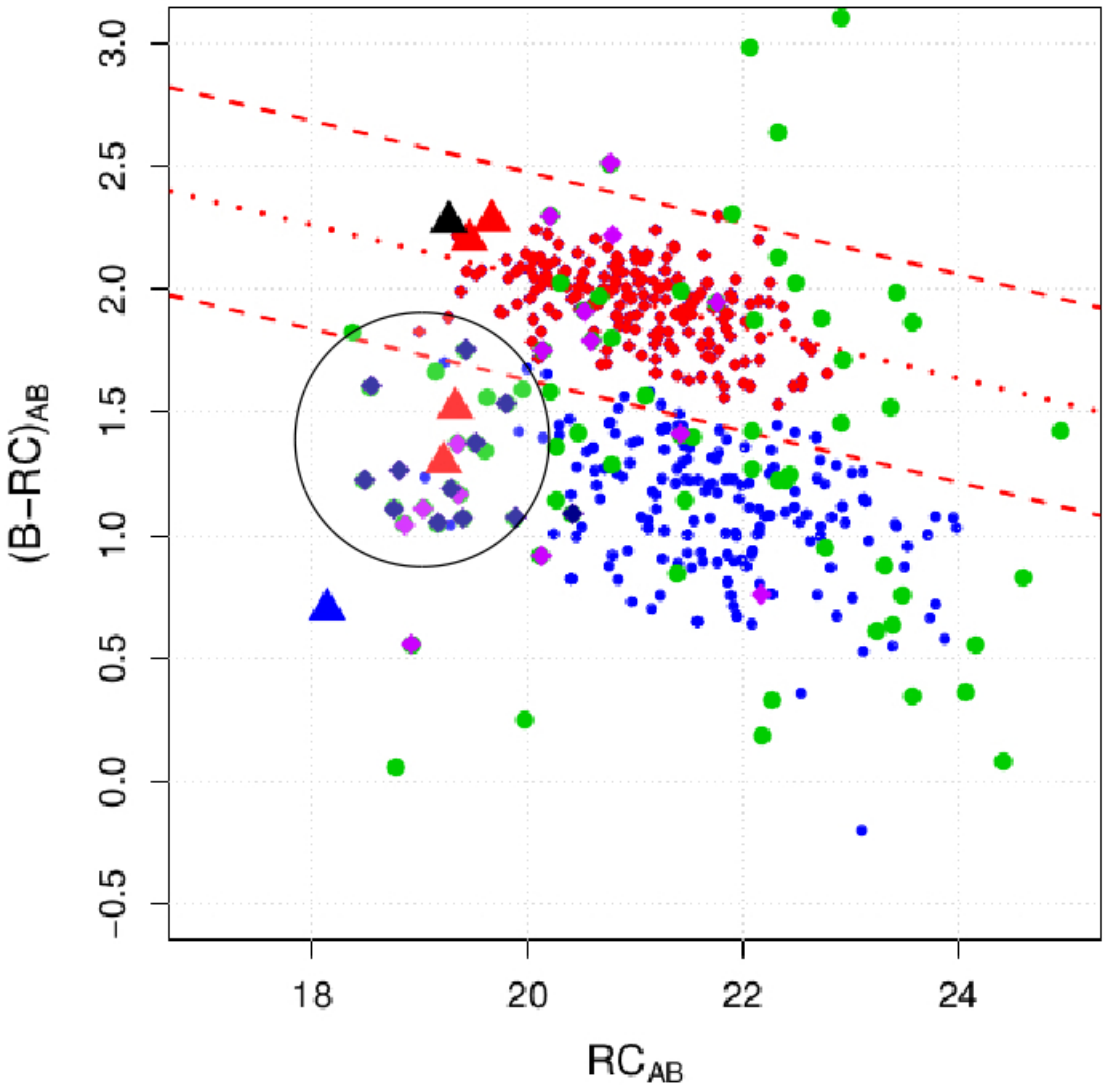

Figure 5.17: The Color-Magnitude diagram shows the galaxies distributed on the red (AGN galaxies) and blue (SF galaxies) sequence. The green dots represent the galaxies from our samples (MeerKAT and uGMRT). The triangles are the galaxies belonging to the cluster; the BCG is the blue triangle and the NAT is the black triangle. Within the black circle are highlighted the galaxies located at z=0.21 which represent a foreground group.

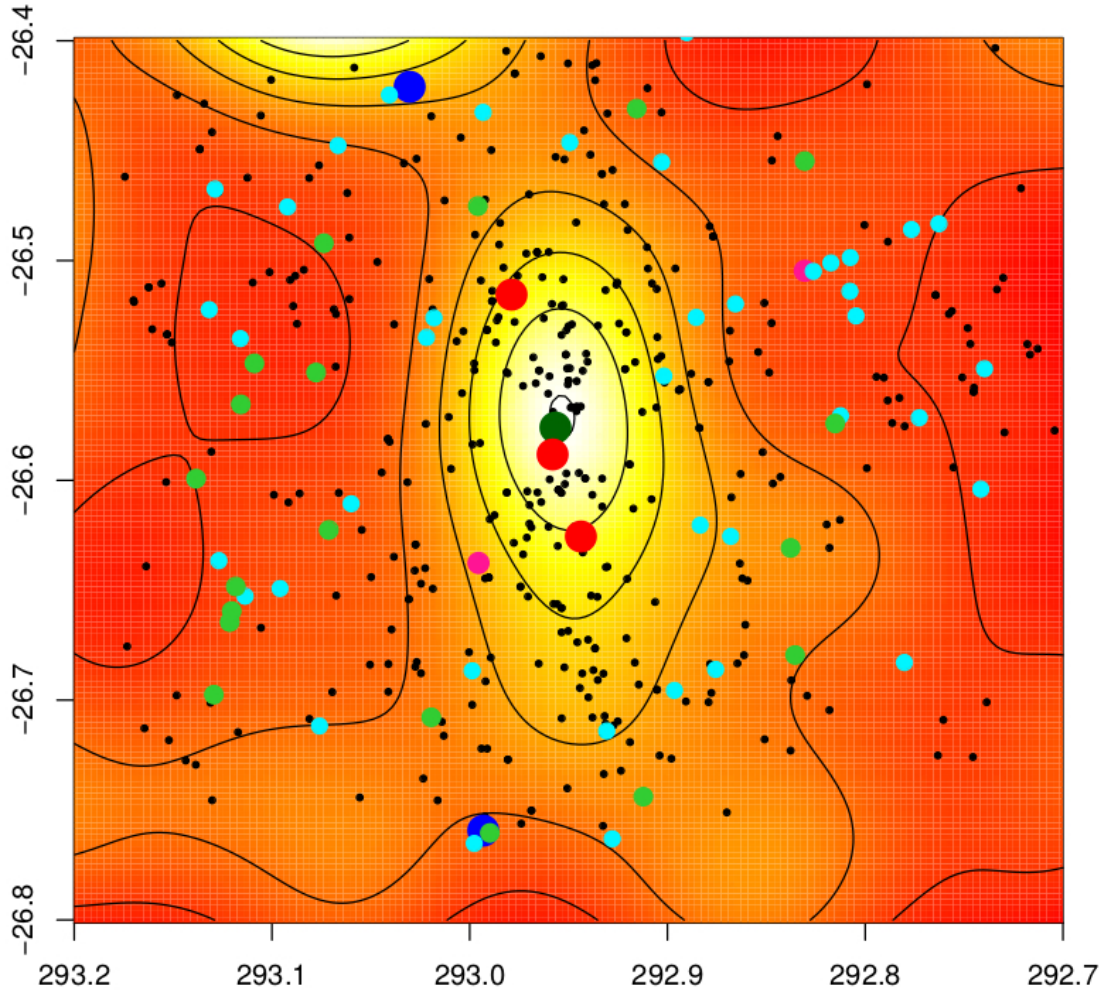

Figure 5.18: Spatial distribution of galaxies within a magnitude range $19.7 < m_{RC} < 21.7$. From the optical galaxies (black dots) and the cluster galaxies there is evidence of an elongated North-South spatial distribution, which is real and intrinsically related to the dynamical state of the cluster.

5.10 Properties of the extended radio galaxies

According to our morphological criterion, four radio galaxies are extended in the MeerKAT sample, whereas six galaxies are extended in the uGMRT sample. Among them, four sources are in common whereas two are uGMRT only. In this section we report their radio contours, possibly overlayed on optical *Subaru*-Suprime images (if they are not in Suprime, we report the radio image), to show their morphology. The name of the radio sources in common and the coordinates reported are taken from the MeerKAT radio catalogue.

The BCG and the NAT

MACSJ1931-2634 is dominated by two central bright objects which are the Brightest Cluster Galaxy and a Narrow-Angle tailed radio galaxy detected at about 150 kpc in projected linear distance from the BCG. We refer to the last Section for a detailed description of these two objects, reporting here the radio contours at 1.2 GHz (green) and at 640 MHz (white). They are overlayed on an optical *Subaru*-Suprime image, that we obtained combining IC, RC, and B filters (Fig.5.19).

J1930-2643b

This radio galaxy of coordinates RA=19:30:38.2 δ=-26:43:11.4 is located at a projected distance of $\sim$ 18' South-West from the BCG (Fig.5.20). The classification of this galaxy is challenging: it could be an FRI or an FRII. The integrated flux at 1.2 GHz is F=27.1 $\pm$ 2.7 mJy whereas the flux at 640 MHz is 118.3 $\pm$ 11.8 mJy.

J1933-2633b

The radio galaxy J1933-2633b has coordinates RA=19:33:45.83 δ=-26:33:35.00. It is located at $\sim$ 30' in projected distance from the central BCG towards East. We report the MeerKAT radio contours (green) and the uGMRT contours (white) overlayed on the MeerKAT image tho show the morphology and the extent of this galaxy. The morphology is consistent with being an FRII, with two hot spots clearly visible in Figure 5.21. J1933-2633b is the brightest source in our samples, with F= 1 $\pm$ 0.1 Jy at 1.2 GHz and F= 3.5 $\pm$ 0.3 Jy at 640 MHz. The radio fluxes are consistent with those we found in the archive.[4].

[4]https://ned.ipac.caltech.edu/

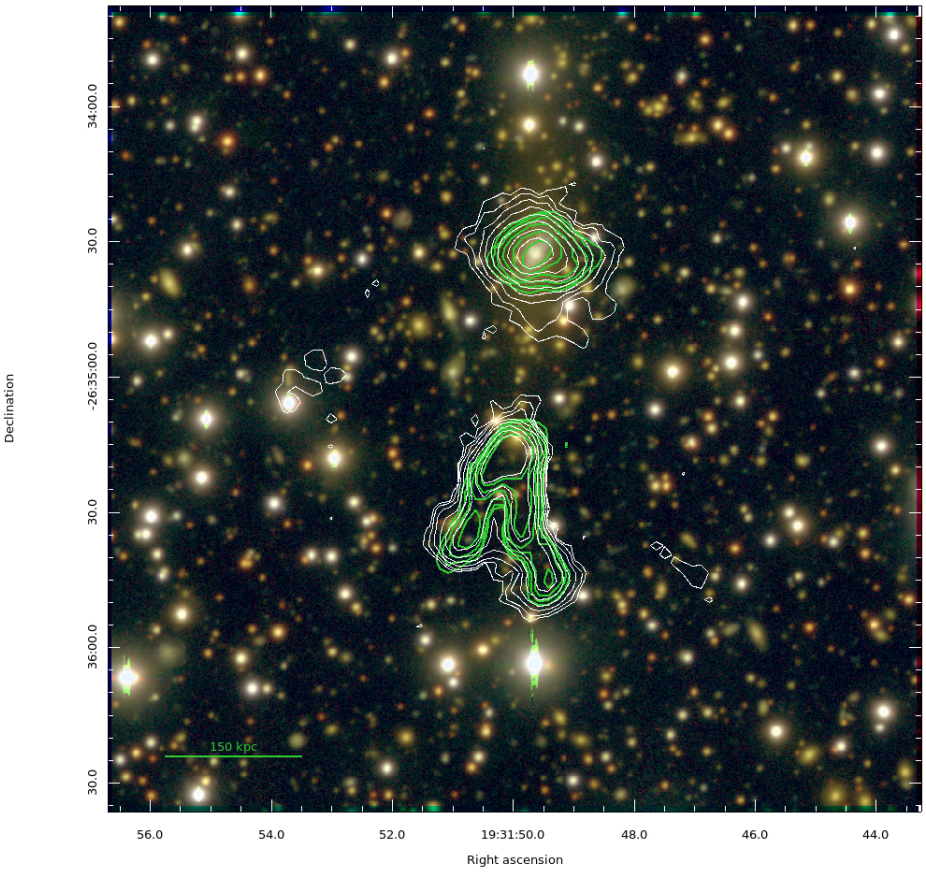

Figure 5.19: The Brightest Cluster Galaxy in MACSJ1931-2634 and the Narrow-Angle tailed radio galaxy located at 150 kpc in linear distance towards South. Green contours are MeerKAT at 1.2 GHz drawn at 5 sigma × (1,2,4,8,16,32,64) mJy/beam. The resolution is 5 × 3 arcsec in PA=139°. White contours are uGMRT at 640 MHz drawn at 5 sigma × (1,2,4,8,16,32,64) mJy/beam. The resolution is 5 × 4 arcsec in PA=169°.

J1930-2649a

This radio galaxy of coordinates RA=19:30:09.14 δ=-26:49:43.33 is detected only in the uGMRT image. In Figure 5.22 we report the uGMRT radio contours (white). Its location is at $\sim$ 27' from the central BCG in projected distance towards South-West. We classified it as a FRII radio galaxy, with a flux at 640 MHz of F=109 $\pm$ 10 mJy. In the image, a probable hot spot is visible at the extremity of the Southern tail.

J1931-2615b

The radio galaxy J1931-2615b is detected only in the uGMRT image at 640 MHz. It has coordinates RA=19:31:08.56 δ=-26:15:59.65. In Figure 5.23 we report the

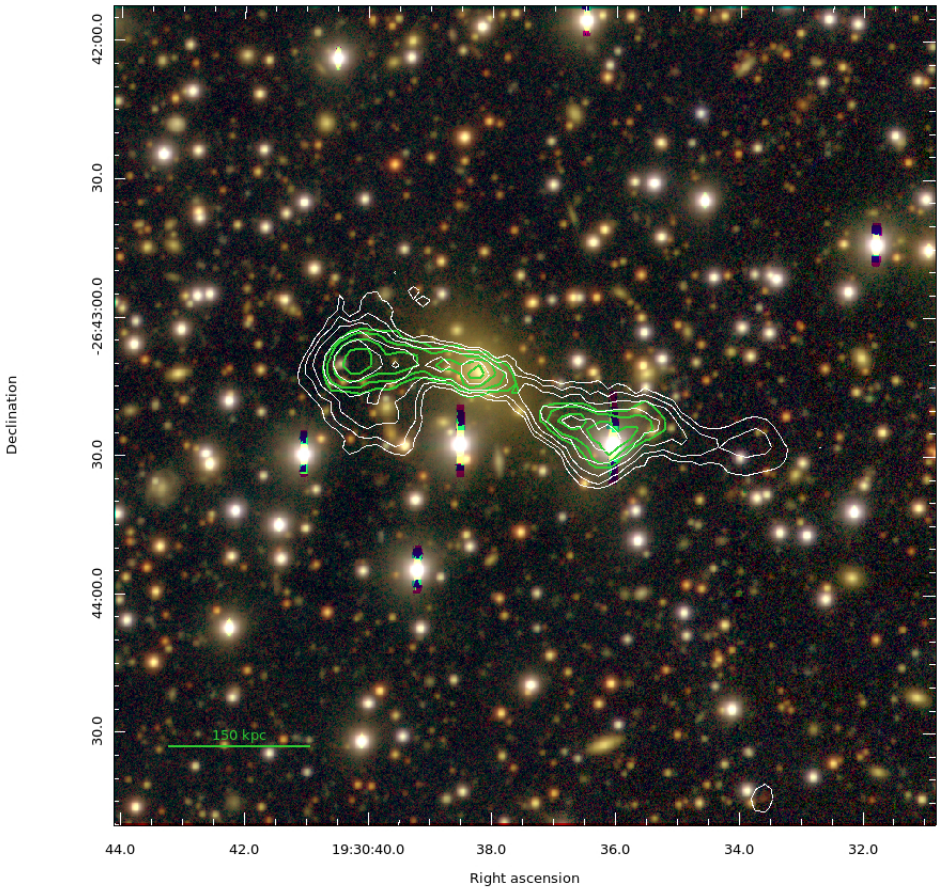

Figure 5.20: The radio galaxy **J1930 − 2643b** is located at 18' in projected distance towards South-West from the BCG. Green contours are MeerKAT at 1.2 GHz drawn at 5 sigma × (1,2,4,8,16,32,64) mJy/beam. The resolution is 5 × 3 arcsec in PA=139°. White contours are uGMRT at 640 MHz drawn at 5 sigma × (1,2,4,8,16,32,64) mJy/beam. The resolution is 5 × 4 arcsec in PA=169°.

uGMRT radio contours (white). It is located at ∼ 20' in projected distance from the BCG towards North-West. It is the faintest among the extended sources in the sample with a flux density at 640 MHz of 5.84 ± 0.5 mJy.

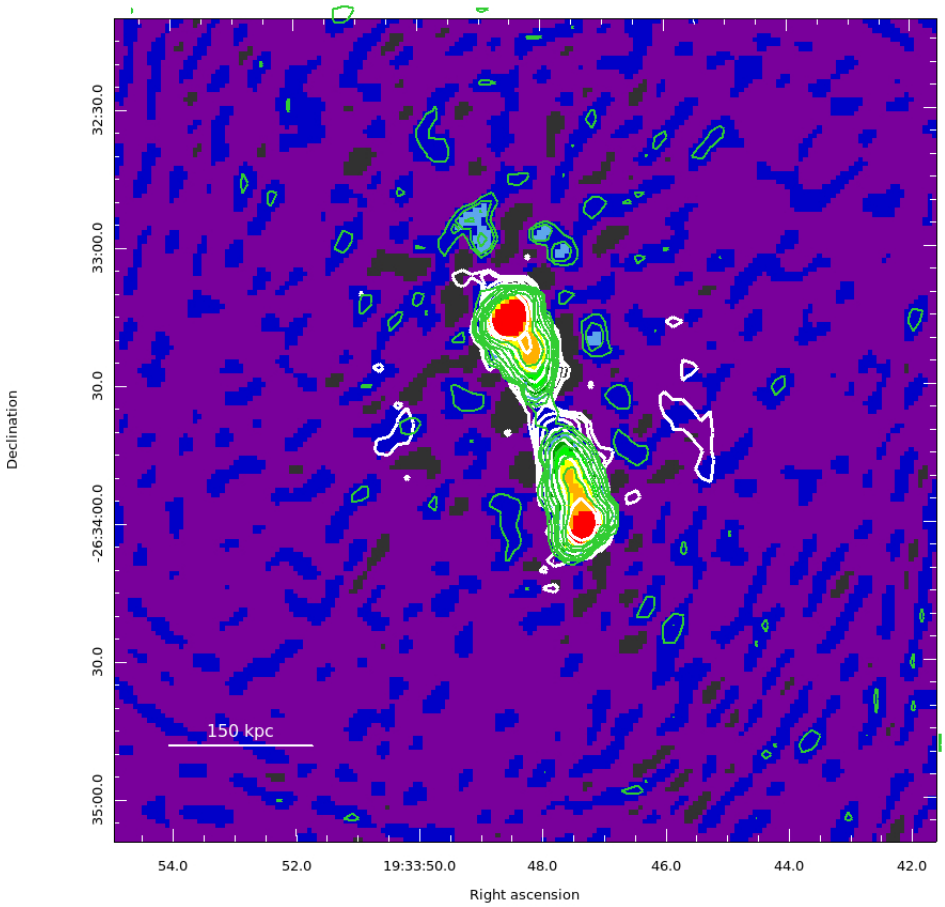

Figure 5.21: The radio galaxy **J1933 − 2633b** is located at 30' in projected distance towards East from the BCG. Green contours are MeerKAT at 1.2 GHz drawn at 5 sigma × (1,2,4,8,16,32,64) mJy/beam. The resolution is 5 ×3 arcsec in PA=139°. White contours are uGMRT at 640 MHz drawn at 5 sigma × (1,2,4,8,16,32,64) mJy/beam. The resolution is 5 × 4 arcsec in PA=169°.

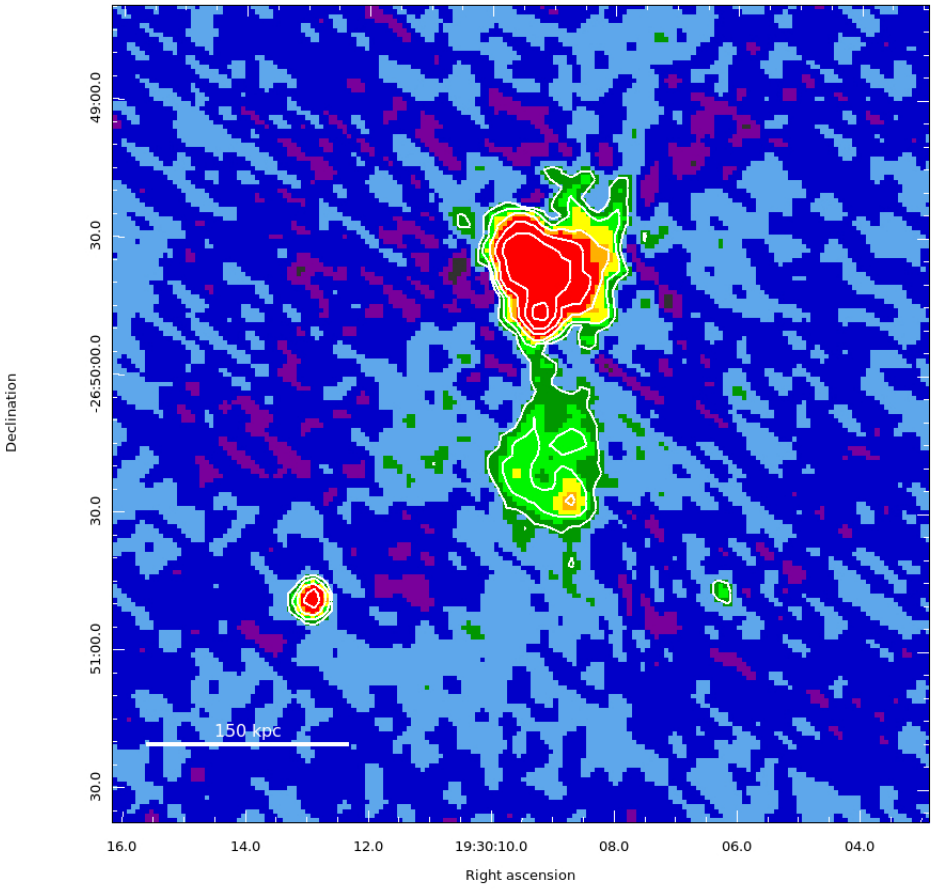

Figure 5.22: The radio galaxy **J1930 − 2649a** is located at 27' in projected distance towards South-West from the BCG. White contours are uGMRT at 640 MHz drawn at 5 sigma × (1,2,4,8,16,32,64) mJy/beam. The resolution is 5 × 4 arcsec in PA=169°.

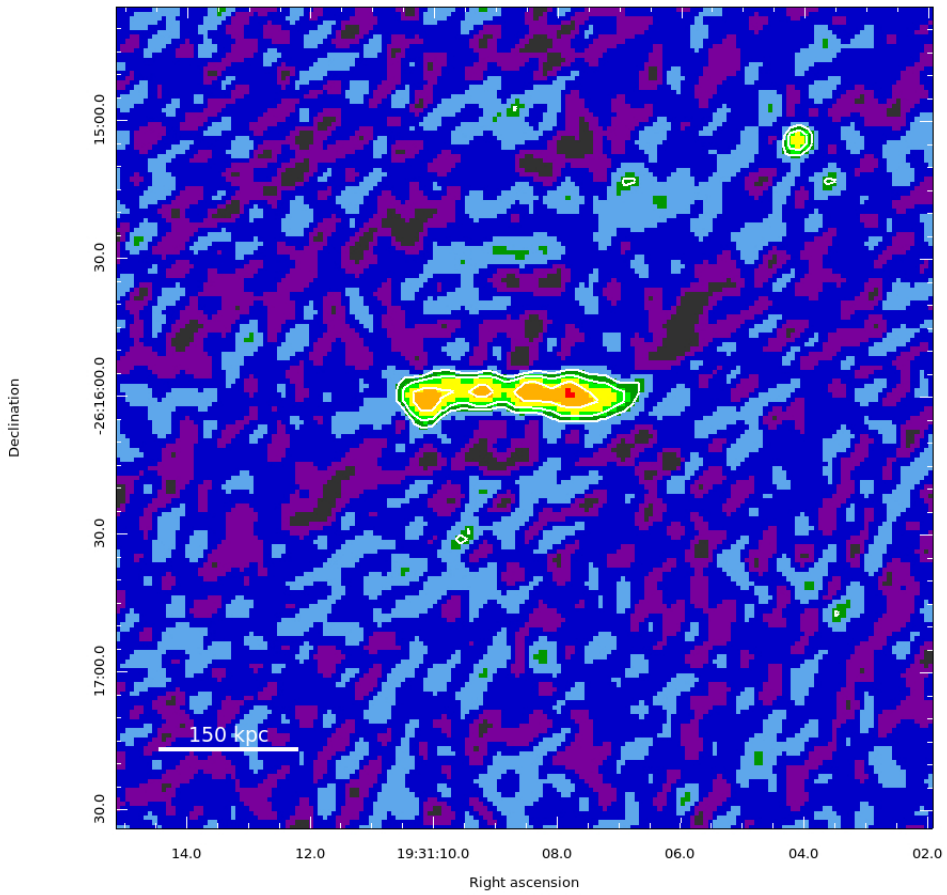

Figure 5.23: The radio galaxy **J1931 − 2615b** is located at 20' in projected distance towards North-West from the BCG. White contours are uGMRT at 640 MHz drawn at 5 sigma × (1,2,4,8,16,32,64) mJy/beam. The resolution is 5 × 4 arcsec in PA=169°.

5.11 The Radio Luminosity function

The influence of the environment on the radio properties of galaxies should reflect on the Radio Luminosity Function (RLF), changing either its shape, its amplitude or both (Venturi et al., 2001; Branchesi et al., 2006).
The Radio Luminosity Function is a powerful tool for investigating the statistical properties of a population of objects. It provides the probability of a galaxy to be radio loud with a radio power higher than a given value of P.
The cumulative fractional Radio Luminosity Function could be described as follow (Kale et al., 2015):

$$F(\geq P_k) = \sum_{j=1}^{k} f(P_j) \tag{5.7}$$

with

$$f(P_k) = \frac{1 - \sum_{j=1}^{k-1} f(P_j)}{n_u(P_i < P_k) + n_d(P \leq P_k)} \tag{5.8}$$

The equation reports the ratio between the fraction of detections in the jth radio power interval and the number of upper limits (n_u, i.e. undetections) for ($P_i < P_k$), and n_d ($P \leq P_k$), the number of detections for $P \leq P_k$.
In order to see if the dynamical state affects the radio emission of the galaxies, we calculated the bivariate Luminosity Function at 1.2 GHz and at 640 MHz for our sample of galaxies following eq 5.7 and 5.8, i.e. the same method used by Venturi et al. (2000, 2001), derived from Ledlow & Owen (1996). We compared our 1.2 GHz Bivariate Luminosity Function with the result in Venturi et al. (2000), rescaled to our cosmology.
Moreover, Branchesi et al. (2006) derived the RLF for a sample of objects within the redshift range $0.3 < z < 0.8$ taken from ROSAT North Ecliptic Pole (NEP) survey (Gioia et al., 2003). They followed the same method adopted in Fanti (1984), considering the sum of the contribution of each source within each logarithmic bin of total luminosity. We reanalyzed our samples according to this method reporting a comparison of our RLF with Branchesi et al. (2006). We are aware that our cases are different in terms of detection limits, sample selection, and data analysis. However, Branchesi et al. (2006) considered a redshift range which is consistent with our redshift ($z \geq 0.3$), moreover, their radio power interval ($22.5 < \Delta\log P_{1.4} < 26.0$) is consistent with the radio power interval of our sample ($22.9 < \Delta\log P_{1.2} < 25.9$) even though we have less statistics.
Venturi et al. (2000) calculated the Radio Luminosity Function for a population of galaxies located in A3558 cluster, i.e. at a local (z=0.04) redshift. We compared our RLF reanalyzing their sample in order to verify if any similarities exist in the radio properties of local and distant clusters of galaxies. There is an overlap in terms of

radio powers due to the different detection limits. In A3558 fainter objects not visible in MACSJ1931-2634 are detected, however, in MACSJ1931-2634 are detected more powerful radio galaxies that in A3558 are missing. From the comparison with literature resulted that, even though the Radio Luminosity Functions show different amplitudes, their shape seems to confirm that, apparently, there is no evolution with z.
Radio Luminosity Functions are necessarly bivariate in the sense that redshift determination is based on optical spectroscopy, and thus the spectroscopic completeness factors into the derived RLF (Miller et al., 2009).
We calculated our total Radio Luminosity Functions both for MeerKAT and uGMRT samples, not separating between the AGN population and SF galaxies, due to the poor statistics: only six galaxies in our sample are confirmed cluster members. However, for comparison, the number of galaxies used by Venturi et al. (2001) is similar. They computed the RLF with 11 confirmed cluster members for A3528.
Nowdays, there are still few literature works on the Radio Luminosity Functions at redshifts higher than z > 0.3 (see Stocke et al., 1999; Branchesi et al., 2006), so this work could set grounds for future studies.
The confirmed cluster member radio galaxies used for our computation, considering the total integrating area of 12 arcmin radius, have optical counterparts with magnitude $18.1 < m_{R_{AB}} < 19.7$, which corresponds to the range between the brightest BCG and the faintest galaxy in the radio sample. The power ranges from $\log P_{1.2GHz}$(W Hz^{-1})= 22.95 to $\log P_{1.2GHz}$(W Hz^{-1})= 25.95 for MeerKAT and from $\log P_{0.6GHz}$(W Hz^{-1})= 22.83 to $\log P_{0.6GHz}$(W Hz^{-1})= 26.43 for uGMRT (see Tab.5.51 and 5.52). A standard convention is to bin each luminosity interval (ΔlogP) of 0.4 dex in size (Miller et al., 2009; Kale et al., 2015), however, due to the low number of sources we adopted larger bins of 0.6 dex in size.
In this range of magnitude, the total number of optical galaxies in the considered integrating area is 2956. Considering a color selection, the optical galaxies having color redder than 0.7 (BCG) are 1181. From spectroscopy, there are 86 galaxies which satisfy the magnitude and colour selection criterion, among them, 16 have $0.33 < z_{spec} < 0.37$, thus obtaining that the number of optical galaxies for our normalization is 220. For comparison, the number obtained by Venturi et al. (2000) following the same method is 185.
The resulting integral Radio Luminosity Functions obtained from our analysis for MeerKAT at 1.2 GHz and uGMRT at 0.6 GHz are shown in Figure 5.24, 5.25 and Figure 5.26.
The shape of the RLFs are similar until $\log P_{1.4GHz} \sim 24.3$ (W/Hz), however, the amplitude of MACSJ1931-2634 is higher then A3558 and Branchesi et al. (2006). MACSJ1931-2634 RLF at 640 MHz remains constant for $\log P_{1.4GHz} > 24.3$ (W/Hz).

Table 5.51: MACSJ1931-2634 Bivariate Luminosity Function at 1.2 GHz

$\Delta\log P_{1.2}$	Fractional BLF	Integral BLF
22.95-23.55	3/220	0.0271
23.55-24.15	1/220	0.0135
24.15-24.75	0/220	0.009
24.75-25.35	1/220	0.009
25.35-25.95	1/220	0.0045

Table 5.52: MACSJ1931-2634 Bivariate Luminosity Function at 0.6 GHz

$\Delta\log P_{0.6}$	Fractional BLF	Integral BLF
22.83-23.43	3/220	0.026
23.43-24.03	1/220	0.013
24.03-24.63	0/220	0.009
24.63-25.23	0/220	0.009
25.23-25-83	0/220	0.009
25.83-26.43	2/220	0.009

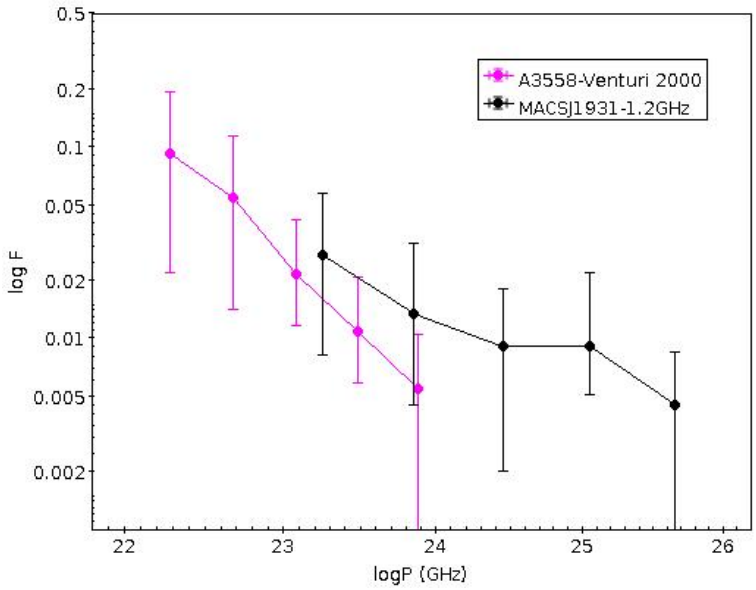

Figure 5.24: Radio integral Luminosity Function, expressed as the fraction of galaxies emitting with radio power $\geq$ logP, for the MeerKAT sample at 1.2 GHz (black) compared with Venturi et al. (2000) Luminosity Function of A3558 (magenta) rescaled to our cosmology.

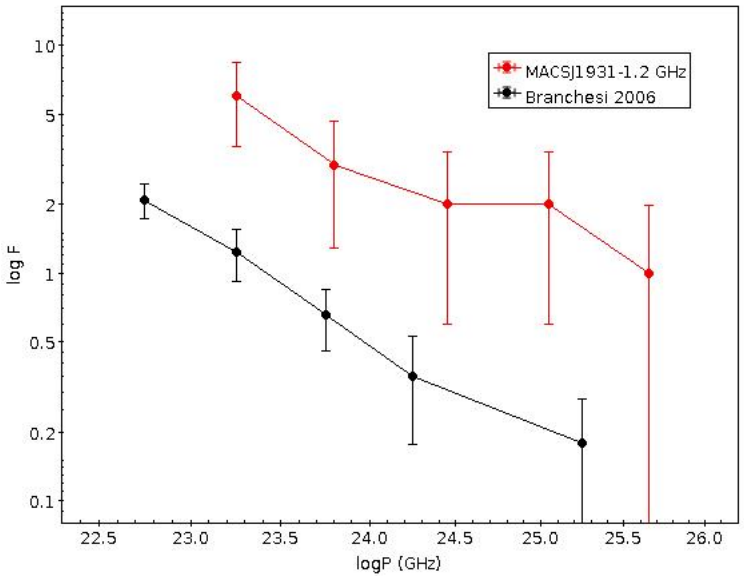

Figure 5.25: Radio integral Luminosity Function, expressed as the fraction of galaxies emitting with radio power $\geq$ logP, for the MeerKAT sample at 1.2 GHz (red) compared with Branchesi et al. (2006) (black) calculated following their method.

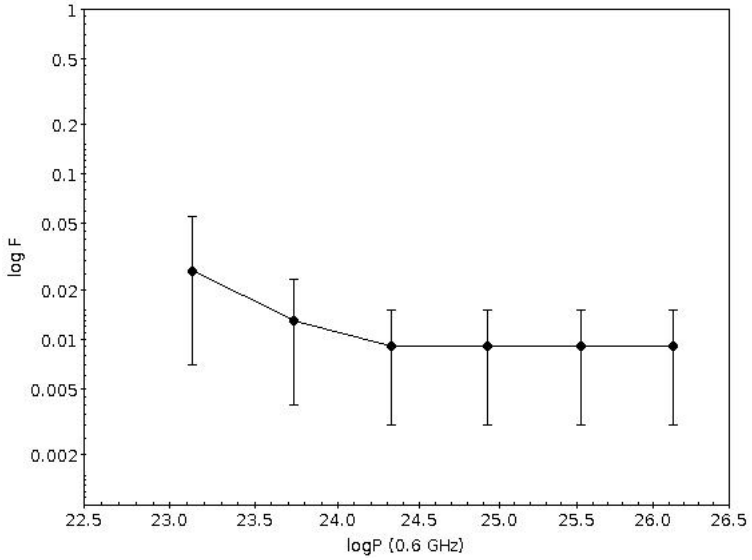

Figure 5.26: Radio integral Luminosity Function, expressed as the fraction of galaxies emitting with radio power $\geq$ logP, for the uGMRT sample at 640 MHz (black).

5.12 Properties of the central regions of MACSJ1931-2634 galaxy cluster

In the radio domain, MACSJ1931-2634 is dominated by two bright central objects: the Brightest Cluster Galaxy (BCG) and a Narrow-angle tailed (NAT) galaxy, located at about 150 kpc in projection towards South direction from the BCG.
In Figure 5.27 we report a zoom of $\sim 2 \times 2$ arcmin^2 on the central region with white radio contours of our reprocessed archival VLA data at 1.4 GHz with resolution of 2 arcsec overlayed on HST-CLASH[5] image obtained combining f814w, f625w, f435w filters.

5.12.1 The Brightest Cluster Galaxy (BCG)

The central BCG in MACSJ1931-2634 has been studied in detail by many authors (i.e. Giacintucci et al., 2014; Fogarty et al., 2015; Donahue et al., 2015; Santos et al., 2016; Fogarty et al., 2019). BCGs are early-type galaxies typically fuelled by a central powerful AGN. Indeed this is the case for MACSJ1931-2634 BCG. Moreover, it is evident from observations, that the BCG in MACSJ1931-2634 is very active in terms of star formation (Santos et al., 2016; Fogarty et al., 2019). This is due to the presence of a cold gas reservoir which condensate then precipitates onto the galactic nucleus, fuelling starburst and further AGN activity (Gaspari et al., 2013; Voit et al., 2017). The presence of a large ($1.9 \pm 0.3 \times 10^{10}$ M$_\odot$) reservoir of molecular gas has been confirmed from ALMA observations by Fogarty et al. (2019).
We refer to Chapter 2 for our results on the radio properties of the BCG obtained reprocessing archival VLA data at 1.4 GHz and GMRT at 323 MHz.
In this Section, we report the results from our radio analysis exploiting new MeerKAT and uGMRT data. According to our morphological criterion the BCG in our MeerKAT and uGMRT samples is extended. However, as visible from Fig.5.28 the discrete AGN radio emission is barely separable from the diffuse emission surrounding the BCG. The AGN emission appears to be directed towards North-South, whereas the diffuse emission is directed perpendicularly to it, towards Est-West (green contours).
The BCG projected linear size results $\sim$ 35 kpc at 1.2 GHz. The extended emission surrounding it, classified as an uncertain mini-halo by (Giacintucci et al., 2014), is $\sim$ 100 kpc in size. At 640 MHz, with the uGMRT, at a resolution of 5 arcsec, it is not possible to separate the two components (Fig.5.28). The radio emission detected extends $\sim$ 150 kpc towards Est-West (white contours).
In Tab.5.53 we report the radio properties of the BCG and the diffuse component from our new MeerKAT and uGMRT data. The fluxes reported are F_{peak} for the BCG and the flux obtained by subtracting the peak (BCG contribution) to the total emission for the diffuse component.

[5]https://archive.stsci.edu/prepds/clash/

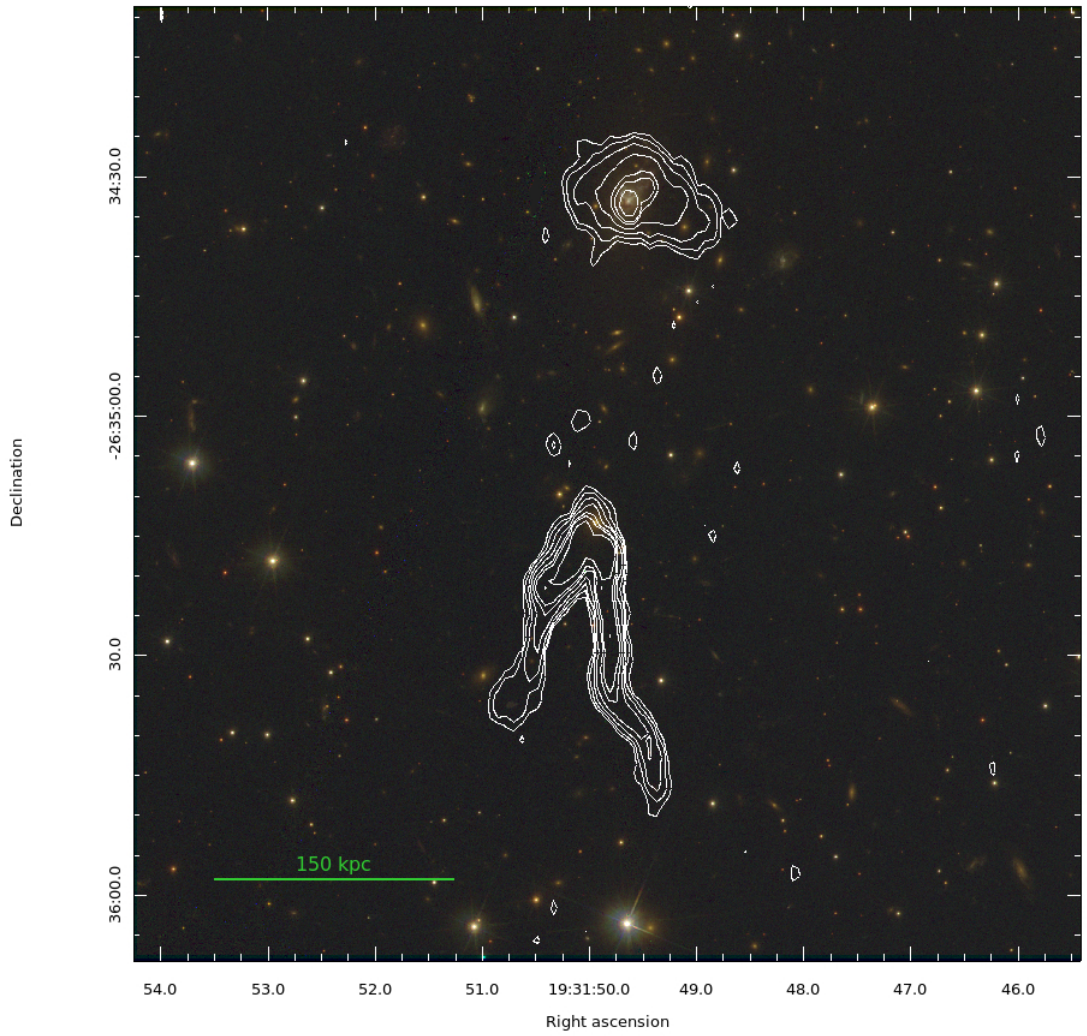

Figure 5.27: White radio contours at 3 sigma (i.e. 0.08 mJy/beam) of the central BCG and the NAT radio galaxy in MACSJ1931-2634 obtained reprocessing archival VLA data at 1.4 GHz (A array, i.e. 2 × 1 arcsec resolution in PA= 4°) overlayed on HST-CLASH image obtained combining f814w, f625w, f435w filters (i.e. R, G, B).

From VLASS data, new MeerKAT and uGMRT data and from archival GMRT at 323 MHz data we derived the BCG radio spectrum reported in Fig.5.29.

In order to assess the properties of the diffuse emission surrounding the BCG (see Giacintucci et al., 2014), we reprocessed archival Chandra data (observation ID: 9382) by means of the standard Chandra processing pipeline (see Ehlert et al., 2011). We adopted the unsharp masking technique to detect X-ray cavities, as previously used in other studies (Diehl et al., 2008; Dong et al., 2010; Shin et al., 2016). Our result is shown in Fig.5.30. At least two regions where a surface brightness

Table 5.53: Radio properties of the BCG and the diffuse emission surrounding it from our new MerKAT and uGMRT data.

	$F_{1.2GHz}$ (mJy)	$F_{0.6GHz}$ (mJy)	$logP_{1.2}$	$logP_{0.6}$	α
BCG	20	54	24.9	25.3	1.4
diffuse em.	25.4	129.7	25.1	25.7	2.2

depression is clearly visible are detected (East-West direction), moreover, a third possible surface brightness depression feature is visible towards South. We overlayed VLA 1.4 GHz radio contours (white) regridding the radio and X-ray images at the same scale (i.e. 1 pxl=0.5").
By means of the unsharp masking technique the linear size of the cavities is difficult to estimate, they could extend several hundreds of kpc (Shin et al., 2016). X-ray cavities are considered signposts of radio mode feedback (McNamara et al., 2000; Fabian, 2002; Giacintucci et al., 2011) because they are often filled with radio lobes, implying that the cavities originates from the interaction between the radio jets and the intergalactic medium. From our result, we infer that the central object in MACSJ1931-2634 could be a case of a restarted radio galaxy, more than a Mini-Halo.

5.12.2 The Narrow-angle tail (NAT)

Narrow-angle tailed radio galaxies are FRI galaxies (Fanaroff & Riley, 1974), typically located in clusters and found at any distance from the cluster center. According to their definition, they have radio powers below $10^{24.5}$ (W Hz^{-1}). Their morphology gives the most striking example of the interaction between the Intra-Cluster medium (ICM) and the radio source (Rudnick & Owen, 1977). Indeed they are interpreted as the result of ram pressure exerted by the intergalactic medium on the double-sided radio emission (Feretti & Venturi, 2002).
In the case of MACSJ1931-2634, the NAT radio galaxy is located very close to the center of a cluster which is defined dynamically relaxed. The morphology of its two tails is quite peculiar: they show a clear asymmetry and remain tight even at larger distance from the origin of the emission.
The radio properties of the NAT galaxy are reported in Table 5.54 and 5.55.
At 1.4 GHz, with the VLA (2" resolution, i.e. A array) the two tails are resolved,

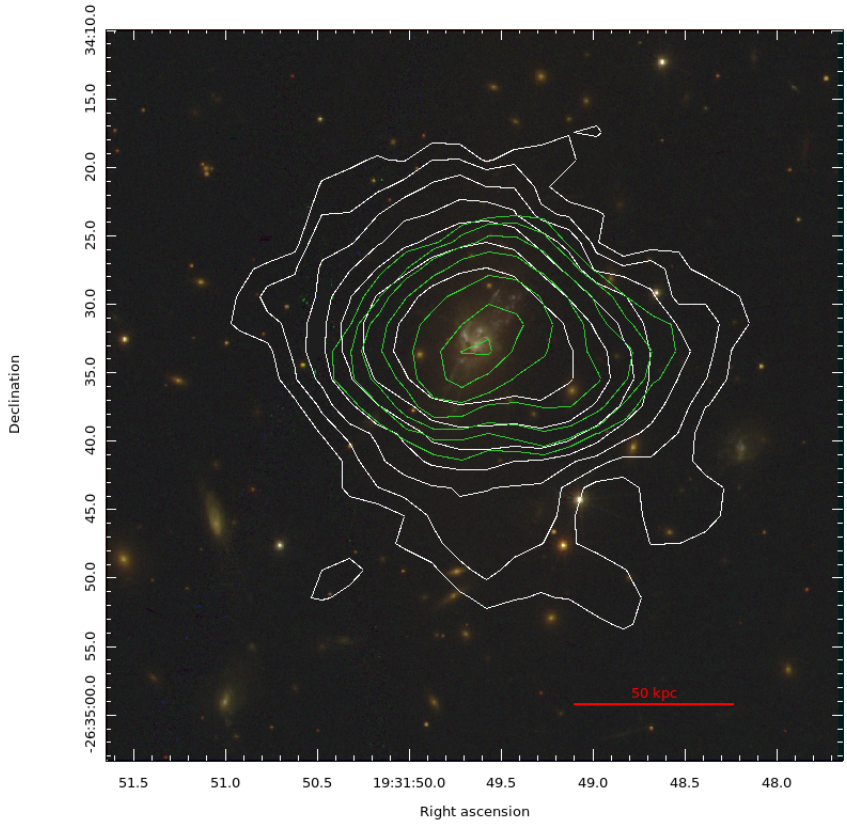

Figure 5.28: Radio contours at 3 sigma from new MeerKAT (i.e. 0.28 mJy/beam) and uGMRT (i.e. 0.26 mJy/beam) data at 1.2 GHz (green) and 640 MHz (white) respectively, overlayed on HST-CLASH image obtained by combining f814w, f625w, f435w filters (R,G,B).

so we considered the East and West tails separately. The Western tail, which is the brightest, has a linear size of $\sim$ 180 kpc at the cluster redshift. The Eastern tail, the faintest, has a linear size of $\sim$ 130 kpc. Tab.5.54 and 5.55 show that the NAT is more powerful than the typical FRI galaxies.
We report the NAT radio spectra in Fig. 5.31, estimated from our reprocessed VLA at 1.4 GHz data, uGMRT at 640 MHz and archival GMRT at 323 MHz data.

To investigate the origin and the nature of the intriguing radio morphology observed, we submitted an ESO proposal (PI Terni de' Gregory) in 2018 and we obtained 3hrs observing time with FORS-2 in order to get the spectra of the three possible candidate optical counterparts. After the spectra extraction and the analysis, we identify the brightest elliptical galaxy as the most probable counterpart, indicated with a red cross in Figure 5.32. The FORS-2 spectra extracted are shown in Figure 5.33. From ground-based observations the spectra of the two faintest candidates are blended, so we report only one of the two. From the spectroscopic analysis we found that the brightest candidate has a redshift z=0.352, consistent

Table 5.54: Radio properties of the NAT from the archival VLA and GMRT data.

	$F_{1.4GHz}$ (mJy)	$P_{1.4}$ (W Hz^{-1}) 10^{25}	F_{323MHz} (mJy)	P_{323} (W Hz^{-1}) 10^{26}	α
total	145.2	6.5	371.8	2.5	0.6
East tail	72.1	3.2	/	/	-
West tail	72.9	3.3	/	/	-

Table 5.55: Radio properties of the NAT from new MeerKAT and uGMRT data.

	$F_{1.2GHz}$ (mJy)	$P_{1.2}$ (W Hz^{-1}) 10^{25}	F_{640MHz} (mJy)	P_{640} (W Hz^{-1}) 10^{26}	α
total	145.2	6.5	354.7	1.6	1.2

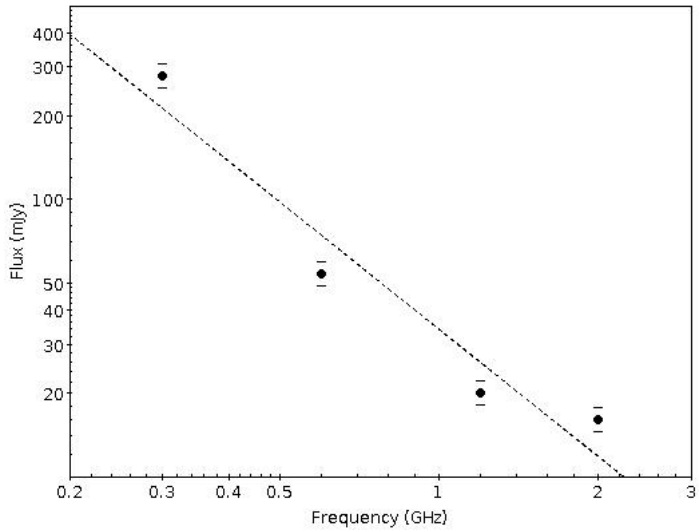

Figure 5.29: Radio spectrum of the BCG derived from VLASS (2GHz), MeerKAT at 1.2 GHz, uGMRT at 640 MHz and archival GMRT at 323 MHz.

with the cluster redshift. The difference in radial velocity is $\leq$ 200 km s^{-1}. The other two fainter objects have redshifts of z= 0.268, so they belong to a foreground group.

From our analysis resulted that the spectra of the optical counterpart is typical of an elliptical galaxy with no emission lines or any peculiar features (Fig.5.33). From the radio power we conclude that the host galaxy is consistent with being a powerful AGN, even though the typical features and the emission lines (i.e. OII,OIII) are not observed in the spectra. Moreover, from the dynamical point of view, the difference in radial velocity among the galaxy and the cluster resulted $\leq$ 200km/s. If we consider that the morphology observed is due to the interaction between the galaxy and the ICM surrounding the galaxy, then we can infer that the tangential component of motion should be dominant. The cluster weather can be invoked to explain such morphology (Burns, 1998; Feretti & Venturi, 2002), even though the combination of bulk motions of the ICM and the cluster weather is typically associated to the WAT radio galaxies (Di Gennaro et al., 2018).
To complete our dynamical analysis, we can use the Euler equation (Begelman et al., 1979; Jones & Owen, 1979) to describe the jet bending conditions:

$$R \sim h \left(\frac{\rho_j}{\rho_e}\right) \left(\frac{v_j}{v_g}\right)^2 \tag{5.9}$$

where R is the jet curvature radius, ρ_j/ρ_e is the ratio between the jet density and the external density, v_j/v_g is the ratio between the jet and the galaxy velocity and h is the scale height over which the ram pressure is transmitted to the jets.

For the galaxy velocity, v_g, we consider the value from the spectra in Fig. 5.33 (top panel), we assume the value of 0.2c for v_j (from Wu et al., 1999). The jet density is unknown, so we consider the possibility of a light jet with $(\rho_j/\rho_g) = 0.1$ (Clarke et al., 1986). Finally, h is $\sim$ 18 kpc as estimated from the VLA at 1.4 GHz image (corresponding roughly to the transversal size of the jet). In this way, we obtain the value of the jet curvature radius, which is R $\sim$ 0.6 kpc. The estimated value of R is indicative, because of several assumptions, but, if we compare the value obtained with the one taken from the radio image (i.e. $\sim$ 9 kpc), we can see that there is one order of magnitude of difference (see Terni de Gregory et al., 2017, for comparison). Therefore we deduce that projection effects could play a role into make the observed jets/tails narrow even at large distance.

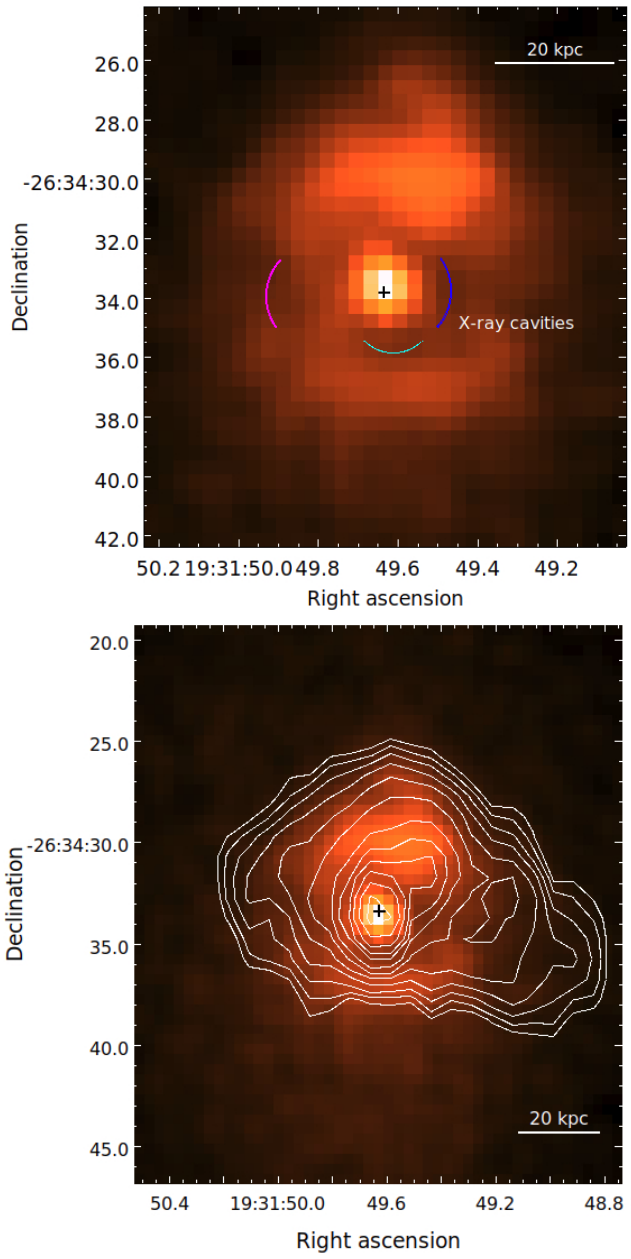

Figure 5.30: Chandra X-ray image of MACSJ1931-2634 cavities obtained with the unsharp masking technique. There are at least two regions of surface brightness depression coincident with radio lobes. Moreover, a third depression is evident towards South, coincident with the cavity detected by Shin et al. (2016).

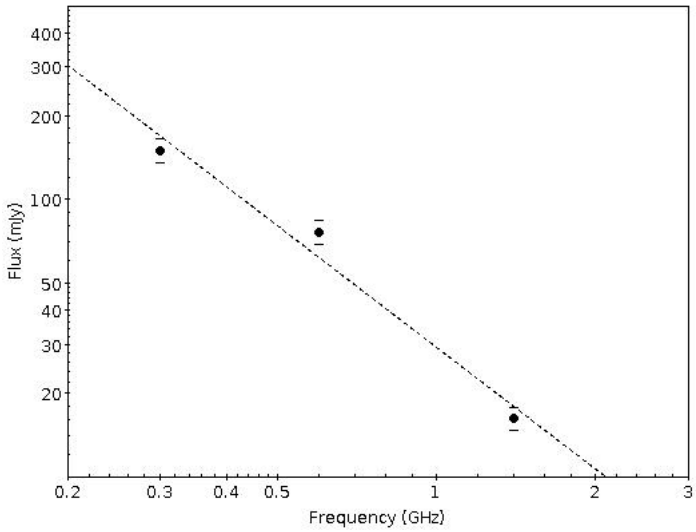

Figure 5.31: Radio spectrum of the NAT derived from VLA at 1.4 GHz, uGMRT at 640 MHz and archival GMRT at 323 MHz.

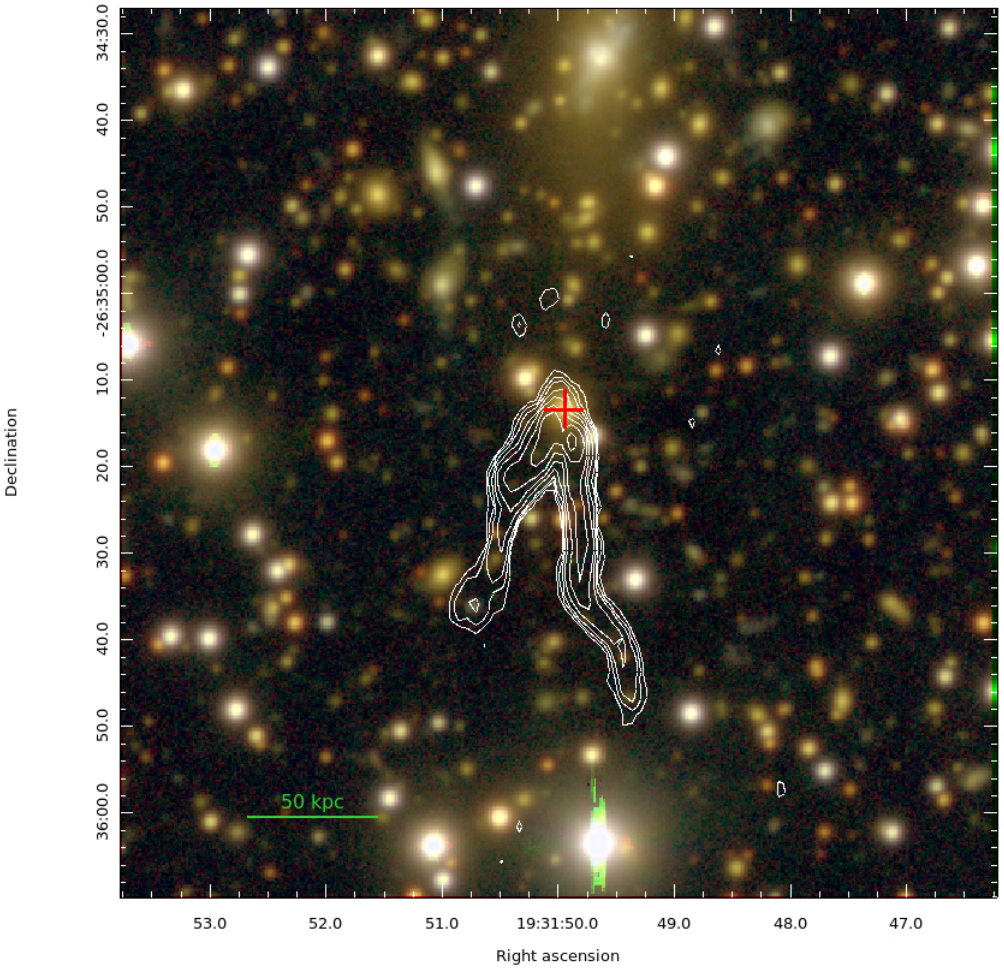

Figure 5.32: A zoom on the NAT radio galaxy in MACSJ1931-2634 galaxy cluster with radio VLA contours (white) at 1.4 GHz overlayed on an optical image from *Subaru*-Suprime obtained combining IC, RC, B filters. The red cross indicates the elliptical galaxy considered as the optical counterpart.

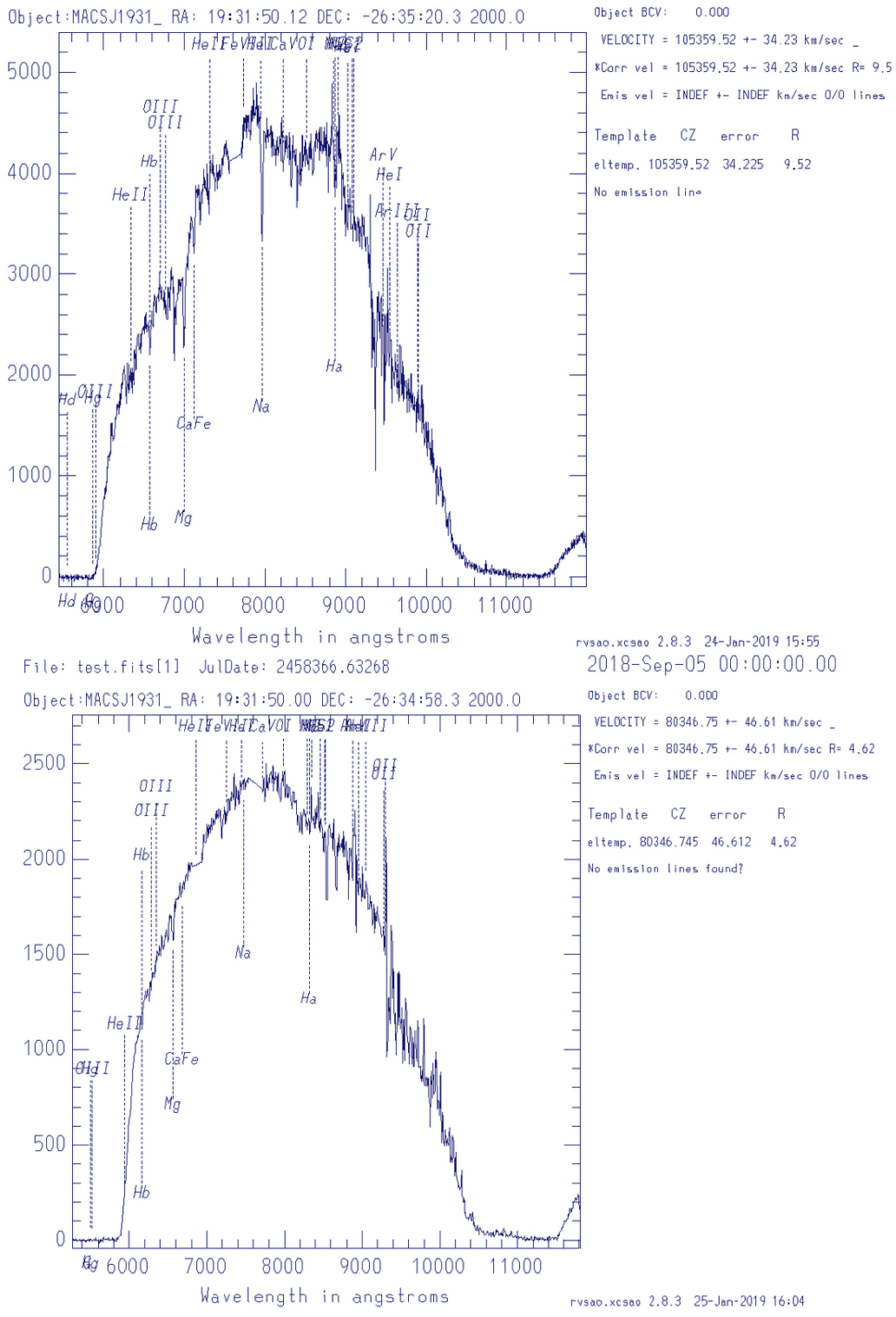

Figure 5.33: FORS-2 spectra of the brightest (top panel) and the faintest (bottom panel) candidate counterparts. We found that the brightest candidate is consistent with being a cluster member.

Chapter 6

A multiwavelength analysis of the radio galaxy population in A1300

This chapter presents a multiwavelength analysis of the radio galaxy population of the galaxy cluster A1300 and its field. This cluster was selected from our original sample in order to perform a comparison with the MACSJ1931-2634 galaxy population. We extracted two radio catalogues at 1.2 GHz (MeerKAT-16, L band) and at 640 MHz (uGMRT, band 4) within an area of 30 arcmin radius, which corresponds to 8.1 Mpc at the cluster redshift (z=0.31); we present the two catalogues and the spectral indices of the sources in common.
Moreover, we estimated the upper limits on the spectral indices for the sources detected only at 1.2 GHz or at 640 MHz.
Second, to be consistent with the analysis in MACSJ1931-2634, we restricted the area of interest within two virial radii, corresponding to an area of 12 arcmin radius (3.2 Mpc). This is the area within which we crossmatched the optical and the radio sources detected in our samples and we performed the analysis on the radio galaxy population, i.e. statistical source counts (logN-logS), radio and optical overdensities, and the Radio Luminosity Function.

6.1 A1300

The galaxy cluster A1300 is described as a richness class 1 object by Abell et al. (1989). It was observed for the first time in X-ray during the Rosat All Sky Survey (RASS; Pierre et al., 1994) in which it is identified with RXJ1131.9-1955. It has an X-ray luminosity of $L_x \sim 1.7 \times 10^{45}$ ergs^{-1} in the 0.1-2.4 keV band (Lemonon et al., 1997; Reid et al., 1999) and a mass $M_{tot} \sim 1.3 \times 10^{15}$ $M_\odot$ (Lemonon et al., 1997) at a radius $\sim$ 2.2 Mpc.
The results from the optical (Pierre et al., 1997) and the X-ray (Lemonon et al., 1997) suggest that A1300 is in a post-merging phase. Indeed, in this massive sys-

tem a major merging occurred about 3 Gyr ago (Ziparo et al., 2012) and additional minor merging events happen at different times via filaments, which will lead to an increase of the cluster mass up to 60 per cent in the next Gyr (Ziparo et al., 2012). A1300 hosts a 'dumb-bell' cD galaxy in its centre (Pierre et al., 1997) and prominent filaments visible in the galaxy density distribution (Ziparo et al., 2012).
The radio observations of A1300 revealed that the cluster is very active in the radio band (Reid et al., 1999; Venturi et al., 2013). A1300 hosts a giant radio halo and a relic (Reid et al., 1999) located in the south-west periphery of the cluster (Fig. 6.1), and a number of radio galaxies with extended emission are found at the cluster centre (Reid et al., 1999; Venturi et al., 2013).
Ziparo et al. (2012) report on a possible shock front, consistent with a Mach number $M = 1.2 \pm 0.1$, and on a sharp edge in the galaxy distribution at the location of the relic.
An elongated, thin structure, referred to as *bridge* (Venturi et al., 2013), connects the head-tail radio galaxy to the central BCG (A2 and A1 objects respectively, following Reid et al. (1999) nomenclature). It is not clear whether such a feature is an extention of the tail of A2 or a brightness peak of the diffuse radio halo (Fig. 6.1).
The radio halo brightness distribution is fairly uniform and there is little gradient going from the central part to the periphery (Giacintucci et al., 2011; Venturi et al., 2013). Its shape is similar to the higher frequency images, and the linear extention of $\sim$ 890 kpc is also comparable with the one reported in (Reid et al., 1999). The south-western relic too, is similar in shape, extent and brightness distribution to the earlier images, and its largest linear size (i.e. LLS) is $\sim$ 450 kpc at 325 MHz (Venturi et al., 2013).
A1300 is one of the clusters belonging to the Merging Cluster Collaboration (MCC)[1], an international working group estabilished to perform observations and simulations of merging galaxy clusters.
A1300 also belongs to the Galaxy Cluster at VIRCAM (GCAV) Survey[2] (PI M. Nonino), an Infra-red, 560 hrs, ESO Public Survey in the Y, J, K_s bands, whose aim is to explore galaxy evolution over a large variety of environments.
The main properties of this galaxy cluster are summarized in Tab. 6.1.

[1] http://www.mergingclustercollaboration.org/
[2] https://www.eso.org/sci/observing/PublicSurveys/docs/GCAV_SMP_10012017.pdf

Table 6.1: A1300 cluster general properties

Name	z	scale (kpc/")	RA[a] (hms)	DEC[a] (° ' ")	M_{200}[b] $M_\odot$	L_X[c] (ergs^{-1})	kT[c] (KeV)
A1300	0.31	4.5	11:31:56.3	-19:55:37	1.3×10^{15}	1.7×10^{45}	11.0

[a] Venturi, T., 2013.
[b] Lemonon, L., 1997.
[c] Pierre, M., 1997.

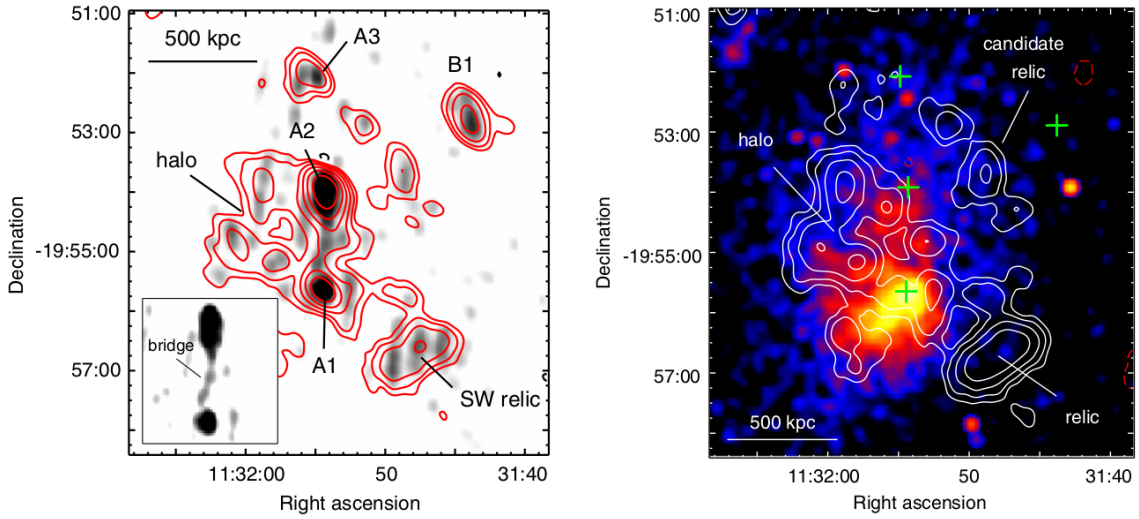

Figure 6.1: This image is taken from Venturi et al. (2013). Left: GMRT 325 MHz radio contours of the emission from A1300 at the resolution of 27 × 18 arcsec, in PA = 43° overlaid on the gray-scale full resolution image (14 × 8 arcsec, PA = 8°). The 1σ noise level is 0.6 mJybeam^{-1}. Right: radio contours of the central cluster region after subtracting the discrete radio sources (28 × 28 arcsec in PA = 0°). The 1σ noise level is 0.5 mJybeam^{-1}.

6.2 The multiwavelength analysis

In this section we report a summary of the radio, optical, spectroscopic and Infrared data that we used to perform the entire analysis on the radio galaxy population in A1300 galaxy cluster and its field.

Radio data

We performed the radio analysis by means of the data taken from the new observations with the MeerKAT-16 interferometer at 1.2 GHz and the uGMRT interferometer at 640 MHz (Tab.6.2). Moreover, we exploited the archival GMRT data at 323 MHz.

Table 6.2: A1300 radio data

Instrument	obs. date	central ν (MHz)	BW (MHz)	tos (min)	synt. beam (arcsec)	PA (deg)	rms (mJy/b)
MeerKAT	2 May 2018	1283	800	120	5×3	136	0.04
uGMRT	24 May 2018	640	200	208	5×4	169	0.03
GMRT	21 Mar 2007	323	32	480	14×8	7	0.3

Optical and Photometric data

We analyzed optical data from *Subaru*-Suprime Cam (2014 observations) in g' and r' filters. The g' and r' datasets were secured by the Merging Cluster collaboration (MCC)[3] in February 2014. The raw images were retrived from the SMOKA Science archive[4]. We used these optical data to cross-match our radio catalogues and to inspect the optical features of the cluster. In particular, we cross-matched our radio catalogues with Suprime g' and r' bands in order to identify the optical counterparts of the radio galaxies in our samples. The details of the optical observations are reported in Tab. 6.3.

Spectroscopic data

VIMOS spectra have been collected from the VLT ESO GO Large Programme (PI Böringher) number 169.A-0595 (see Ziparo et al., 2012).
A1300 has been observed with the Low Resolution blue Grism (Le Fèvre et al.,

[3]http://www.mergingclustercollaboration.org/
[4]https://www.re3data.org/repository/r3d100010166

Table 6.3: A1300 optical observations

Observation date	Filter	exposure (s)	FWHM (")	depth*
Feb 2014	g'	720	1.06	25.69
Feb 2014	r'	2880	0.94	26.17

* depth: AB magnitude 5-sigma in 2arcsec-diameter aperture

2003), mounted on VLT-UT3 at Paranal Observatory (ESO), Chile.
The cluster was observed with three pointings that partially overlap in the centre and reach beyond a distance of 4 Mpc in the east-west (EW) direction from the cluster X-ray centre (see Ziparo et al., 2012, for more details).

IR data

In order to get the mass estimate of the galaxies identified as cluster members, we exploited the new data from the Galaxy Cluster at VIRCAM survey (GCAV; PI M. Nonino). The GCAV is an Infra-red, 560 hrs, ESO Public survey in Y, J, Ks bands aimed at studying galaxy properties and their evolution in a variety of environments.

Table 6.4: A1300 IR observations

Filter	exposure (hrs)	FWHM (")	depth*
Y	6.4	0.86	24.7
J	5.6	0.84	24.5
Ks	3.5	0.80	22.9

* depth: AB magnitude 5-sigma in 2arcsec-diameter aperture

6.3 The MeerKAT radio catalogue

The total number of sources detected at 1.2 GHz with MeerKAT-16, above the catalogue threshold of 0.2 mJy (5 sigma), within an area of 30 arcmin radius, is

112 (Fig. 6.2 and 6.3). The list of the sources is given in Table 6.5 and following, where we report respectively their name, position (J2000), integrated flux density at 1.2 GHz, flux error and indication on the radio morphology. All flux densities are corrected for the primary beam attenuation. The primary beam correction is obtained using the analytic formula derived for MeerKAT primary beam described in Chapter 4.
As for MACSJ1931-2634, all flux densities are extracted with PYBDSF (Mohan & Rafferty, 2015), according to the method adopted and described in Chapter 4; whereas the flux density of the extended sources are measured by AIPS TVSTAT, which allows integration of the image brightness values over irregular areas. The flux errors are measured according to the formula (5.1) from Klein et al. (2003). The dominant term in the error estimate is the residual calibration error, conservatively assumed of 10% (see Chapter 4).
To classify the source morphologies we adopted the same criterion as for MACSJ1931-2634 samples, using the equation (5.2), consistent with what we found in (Condon et al., 1998; Branchesi et al., 2006).
According to the morphological classification that we adopted, the majority of the radio sources are classified unresolved (i.e. pointlike) or barely resolved. The BCG, of coordinates RA=11:31:54.30 δ=-19:55:39.05, is unresolved at 1.2 GHz and has a flux density of F=12.1 $\pm$ 1.2 mJy.
The extended sources are five: they are reported in boldface in Tab. 6.5 and following. We describe their radio properties in Sect. 6.10.
In the MeerKAT catalogue, there are two sources with flux $>$ 50 mJy, i.e. 2% of the sample.

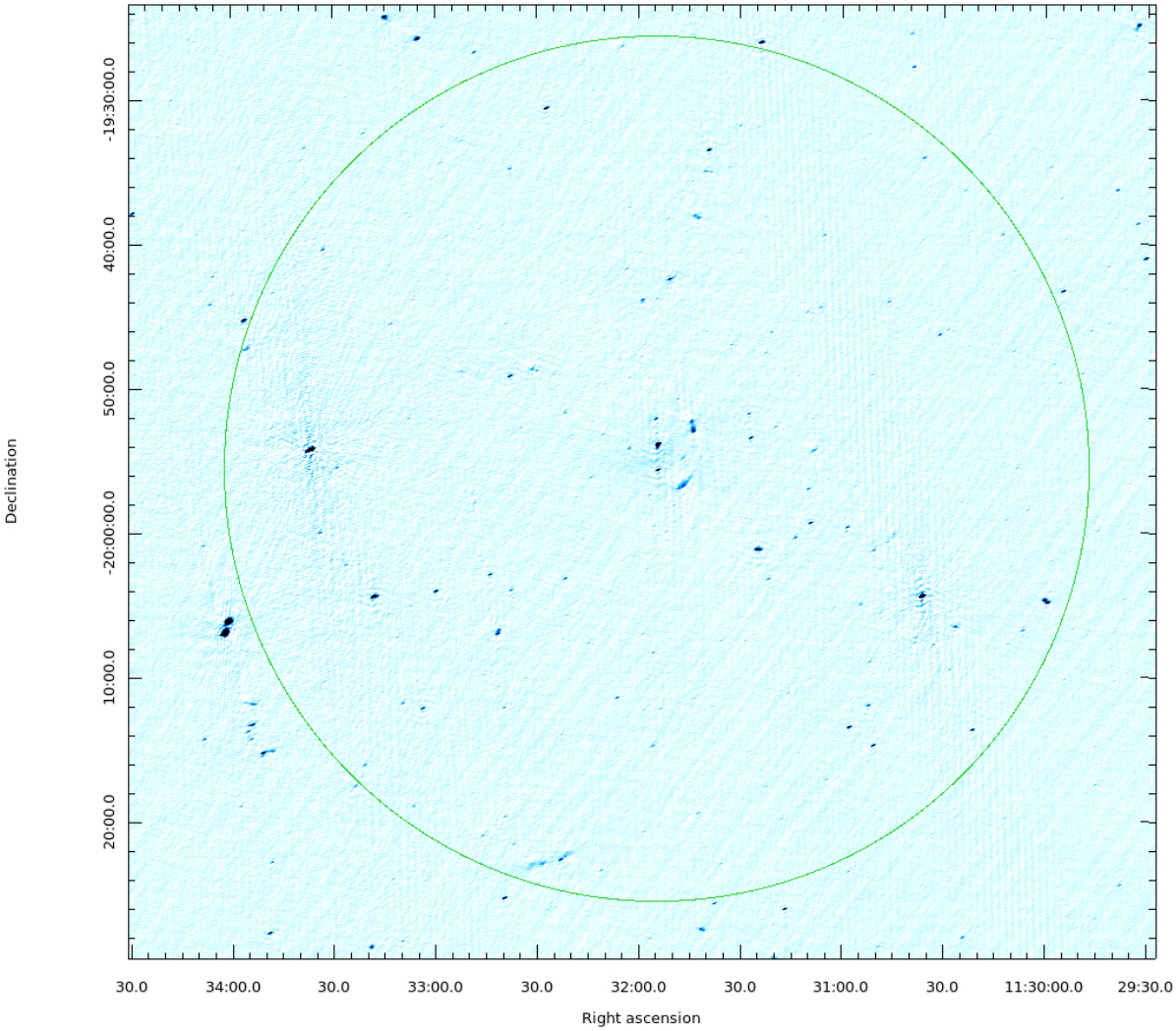

Figure 6.2: The image shows blue-scale view of the MeerKAT field which encompasses an area of 0.785 deg^2 (i.e. 30 arcmin radius, green circle). This is the area within which we extracted our catalogues. The noise is 0.04 mJy/b, with resolution 12 $\times$ 5 arcsec in p.a. $\sim 113°$.

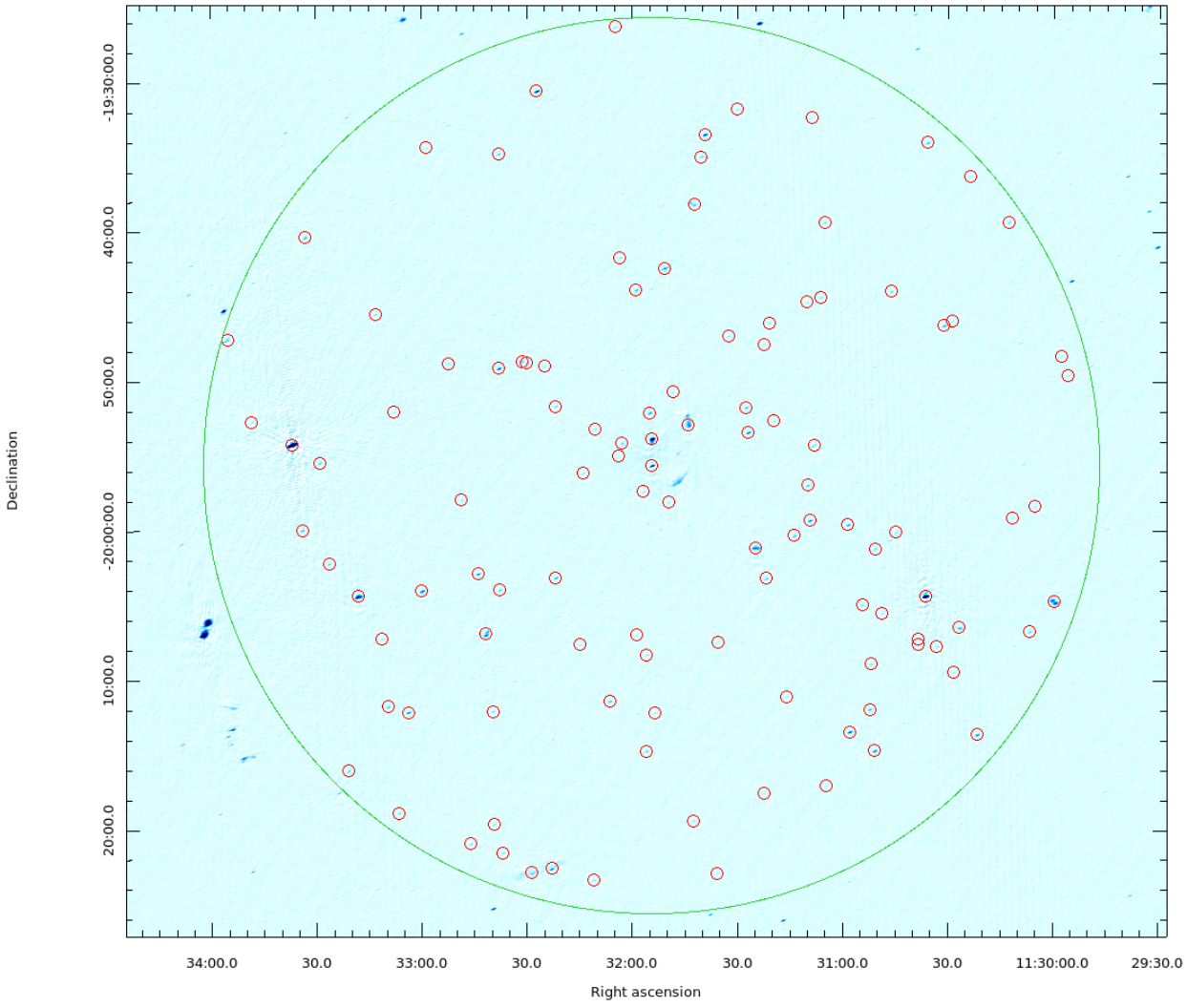

Figure 6.3: The image shows blue-scale view of the same area of 0.785 deg^2 (i.e. 30 arcmin radius, green circle). The red circles indicate the radio sources detected over a threshold of 5σ (i.e. 0.2 mJy/b).

Table 6.5: A1300 MeerKAT radio catalogue

Name	RA_{J2000}	DEC_{J2000}	$F_{1.2GHz}$ (mJy)	ΔF	Morphology
J1129-1949	11:29:55.75	-19:49:35.6	0.53	0.06	unresolved
J1129-1948	11:29:57.58	-19:48:18.1	1.01	0.10	barely
J1129-2004	11:29:59.64	-20:04:44.1	27.0	2.70	**FRII**?
J1130-1958	11:30:05.22	-19:58:22.5	0.33	0.05	barely
J1130-2006a	11:30:06.58	-20:06:44.2	1.46	0.15	unresolved
J1130-1959a	11:30:11.69	-19:59:06.1	0.20	0.02	barely
J1130-1939	11:30:12.66	-19:39:19.9	1.16	0.12	unresolved
J1130-2013a	11:30:21.47	-20:13:38.3	4.84	0.48	unresolved
J1130-1936	11:30:23.56	-19:36:16.2	0.47	0.06	barely
J1130-2006b	11:30:26.59	-20:06:29.3	2.29	0.23	unresolved
J1130-2009	11:30:28.22	-20:09:28.0	0.62	0.07	barely
J1130-1945	11:30:28.87	-19:45:56.9	0.54	0.06	unresolved
J1130-1946	11:30:31.14	-19:46:16.2	1.94	0.19	unresolved
J1130-2007a	11:30:32.98	-20:07:45.0	0.80	0.09	unresolved
J1130-1934	11:30:35.86	-19:34:01.7	1.50	0.15	unresolved
J1130-2004a	11:30:36.32	-20:04:23.1	118.0	11.8	unresolved
J1130-2007b	11:30:38.29	-20:07:36.3	1.48	0.15	barely
J1130-2007c	11:30:38.29	-20:07:14.4	0.80	0.09	barely
J1130-2000	11:30:44.64	-20:00:05.7	1.11	0.11	barely
J1130-1943	11:30:46.08	-19:43:59.3	1.28	0.13	unresolved
J1130-2005	11:30:48.71	-20:05:31.9	0.31	0.05	barely
J1130-2001	11:30:50.61	-20:01:12.1	1.13	0.12	unresolved
J1130-2014	11:30:50.75	-20:14:43.7	4.80	0.48	unresolved
J1130-2008	11:30:51.72	-20:08:55.6	0.72	0.08	unresolved
J1130-2011	11:30:52.15	-20:11:56.9	1.91	0.19	unresolved
J1130-2004b	11:30:54.36	-20:04:58.3	0.84	0.09	unresolved
J1130-2013b	11:30:57.85	-20:13:27.6	6.48	0.64	unresolved
J1130-1959b	11:30:58.41	-19:59:36.6	2.22	0.22	unresolved
J1131-2017a	11:31:04.67	-20:17:05.3	0.36	0.05	barely
J1131-1939	11:31:05.14	-19:39:22.6	1.19	0.12	unresolved
J1131-1944a	11:31:06.17	-19:44:23.2	0.87	0.09	unresolved
J1131-1954	11:31:08.12	-19:54:17.0	2.38	0.24	barely
J1131-1932	11:31:08.71	-19:32:20.0	0.79	0.08	barely
J1131-1959	11:31:09.25	-19:59:19.1	4.18	0.42	unresolved
J1131-1956	11:31:09.93	-19:56:58.1	1.32	0.13	unresolved
J1131-1944b	11:31:10.11	-19:44:42.4	0.62	0.07	barely
J1131-2000	11:31:13.72	-20:00:20.5	1.69	0.17	unresolved
J1131-2011	11:31:15.76	-20:11:06.2	0.26	0.04	barely
J1131-1952a	11:31:19.49	-19:52:39.7	0.60	0.07	unresolved
J1131-1946a	11:31:20.84	-19:46:06.6	0.80	0.09	unresolved
J1131-2003	11:31:21.67	-20:03:11.8	1.39	0.14	unresolved

Table 6.6: A1300 MeerKAT radio catalogue (continued)

Name	RA_{J2000}	DEC_{J2000}	$F_{1.2GHz}$ (mJy)	ΔF	Morphology
J1131-2017b	11:31:22.33	-20:17:34.0	0.36	0.05	barely
J1131-1947	11:31:22.47	-19:47:31.5	0.37	0.05	unresolved
J1131-2001	11:31:24.77	-20:01:09.5	10.7	1.07	barely
J1131-1953a	11:31:26.88	-19:53:26.1	3.90	0.39	unresolved
J1131-1951	11:31:27.49	-19:51:46.1	1.62	0.16	unresolved
J1131-1931	11:31:29.91	-19:31:48.9	0.59	0.07	unresolved
J1131-1946b	11:31:32.52	-19:46:59.5	0.51	0.06	unresolved
J1131-2007a	11:31:35.54	-20:07:27.8	0.31	0.05	barely
J1131-2022	11:31:35.78	-20:22:56.9	0.46	0.06	barely
J1131-1933	11:31:39.27	-19:33:29.7	9.20	0.92	unresolved
J1131-1934	11:31:40.34	-19:34:59.0	0.82	0.09	unresolved
J1131-1938	11:31:42.31	-19:38:11.5	6.49	0.65	**FRII**?
J1131-2019	11:31:42.42	-20:19:25.5	0.74	0.08	unresolved
J1131-1952b	11:31:43.92	-19:52:54.2	10.0	1.00	**WAT**
J1131-1950	11:31:48.36	-19:50:43.9	0.70	0.08	unresolved
J1131-1958	11:31:49.49	-19:58:06.5	0.39	0.05	unresolved
J1131-1942	11:31:50.73	-19:42:26.8	3.08	0.31	unresolved
J1131-2012	11:31:53.44	-20:12:11.0	0.60	0.07	barely
J1131-1953b	11:31:54.29	-19:53:53.5	37.4	3.74	**TAIL**
J1131-1955	11:31:54.30	-19:55:39.0	12.1	1.21	unresolved BCG
J1131-1952c	11:31:54.85	-19:52:07.6	2.30	0.23	unresolved
J1131-2008	11:31:55.72	-20:08:18.6	0.78	0.08	unresolved
J1131-2014	11:31:55.77	-20:14:45.5	1.27	0.13	unresolved
J1131-1957	11:31:56.69	-19:57:22.7	0.39	0.05	barely
J1131-2007b	11:31:58.71	-20:07:00.4	0.48	0.06	unresolved
J1131-1943	11:31:58.83	-19:43:53.1	1.55	0.16	unresolved
J1132-1954a	11:32:02.78	-19:54:09.3	1.02	0.1	unresolved
J1132-1941	11:32:03.40	-19:41:43.2	0.76	0.08	unresolved
J1132-1954b	11:32:03.80	-19:54:59.7	0.46	0.06	barely-bias-halo?
J1132-1926	11:32:04.75	-19:26:17.7	1.02	0.11	barely
J1132-2011	11:32:06.33	-20:11:26.0	1.66	0.17	unresolved
J1132-1953	11:32:10.36	-19:53:11.1	0.70	0.08	unresolved
J1132-2023	11:32:10.97	-20:23:23.3	0.77	0.08	unresolved
J1132-1956	11:32:14.00	-19:56:09.7	0.68	0.07	unresolved
J1132-2007	11:32:14.76	-20:07:38.9	0.58	0.07	unresolved
J1132-2003a	11:32:21.68	-20:03:09.9	1.87	0.19	unresolved
J1132-1951	11:32:21.69	-19:51:41.1	1.15	0.12	unresolved
J1132-2022a	11:32:22.75	-20:22:35.6	4.59	0.46	unresolved
J1132-1949	11:32:24.86	-19:49:01.2	0.41	0.05	barely
J1132-1930	11:32:27.09	-19:30:35.8	14.7	1.47	unresolved
J1132-2022b	11:32:28.57	-20:22:54.7	24.0	2.40	**ext**. – **blending**?

Table 6.7: A1300 MeerKAT radio catalogue (continued)

Name	RA_{J2000}	DEC_{J2000}	$F_{1.2GHz}$ (mJy)	ΔF	Morphology
J1132-1948a	11:32:30.06	-19:48:46.9	0.81	0.09	unresolved
J1132-1948b	11:32:31.30	-19:48:40.1	2.17	0.22	barely
J1132-2021	11:32:36.80	-20:21:33.9	0.80	0.08	unresolved
J1132-2003b	11:32:37.60	-20:03:57.8	1.26	0.13	unresolved
J1132-1949	11:32:37.88	-19:49:08.7	5.59	0.56	unresolved
J1132-1934a	11:32:37.91	-19:34:47.5	1.55	0.16	unresolved
J1132-2019	11:32:39.38	-20:19:39.1	1.05	0.11	unresolved
J1132-2012	11:32:39.69	-20:12:06.1	1.28	0.13	unresolved
J1132-2006	11:32:41.55	-20:06:54.6	5.55	0.55	unresolved
J1132-2002	11:32:43.84	-20:02:53.8	3.47	0.34	unresolved
J1132-2020	11:32:45.96	-20:20:58.1	1.10	0.11	barely
J1132-1957	11:32:48.52	-19:57:56.6	0.52	0.06	unresolved
J1132-1948	11:32:52.18	-19:48:50.0	1.19	0.12	barely
J1132-1934b	11:32:58.47	-19:34:22.1	0.69	0.07	unresolved
J1132-2004	11:32:59.85	-20:04:02.7	7.49	0.75	unresolved
J1133-2012	11:33:03.79	-20:12:09.8	4.48	0.45	unresolved
J1133-2018	11:33:06.42	-20:18:55.7	1.40	0.14	unresolved
J1133-1952a	11:33:07.68	-19:52:04.2	0.59	0.07	barely
J1133-2011	11:33:09.55	-20:11:47.6	1.93	0.19	unresolved
J1133-2007	11:33:11.23	-20:07:14.3	0.71	0.08	unresolved
J1133-1945	11:33:13.05	-19:45:31.2	1.07	0.11	unresolved
J1133-2004	11:33:18.07	-20:04:24.7	33.1	3.31	barely
J1133-2016	11:33:20.75	-20:16:03.6	1.71	0.17	barely
J1133-2002	11:33:26.25	-20:02:13.3	1.63	0.16	unresolved
J1133-1955	11:33:28.86	-19:55:28.0	1.59	0.16	unresolved
J1133-1940	11:33:32.95	-19:40:22.5	2.99	0.3	unresolved
J1133-1959	11:33:33.90	-19:59:58.8	4.36	0.43	unresolved
J1133-1954	11:33:36.89	-19:54:14.6	932.0	93.2	barely
J1133-1952b	11:33:48.22	-19:52:44.1	1.15	0.12	barely
J1133-1947	11:33:55.12	-19:47:13.7	2.41	0.24	barely

6.4 The uGMRT radio catalogue

The total number of sources detected at 640 MHz with the uGMRT interferometer, within an area of 30 arcmin radius, above the catalogue threshold of 0.15 mJy (5 sigma), is 318. The list of the sources is given in Tab. 6.8 and following, where we report respectively their name, position (J2000), integrated flux density at 640 MHz, flux error and indication on the radio morphology. All flux densities given are corrected for the primary beam attenuation. The primary beam correction is obtained by the task PBCOR in AIPS giving the PBPARM parameters for the uGMRT updated at December 1st 2018 (courtesy Ruta Kale; NCRA).
All flux densities are extracted with PYBDSF (Mohan & Rafferty, 2015), whereas we measured by AIPS TVSTAT the flux density of the extended sources. The flux errors are estimated, as for MeerKAT, according to the formula from Klein et al. (2003). The dominant term is the residual calibration error, conservatively assumed of the order of 10%.
We adopted the same method that we used for the MeerKAT sample to determine the morphology of the sources reported in the catalogues. As visible from Tab. 6.8 and following, the majority of the sources is unresolved (i.e. pointlike) or barely resolved; the BCG, of coordinates RA=11:31:54.31 δ=-19:55:40.53, has a flux density of F=30.6 $\pm$ 3.1 mJy. It is barely resolved at 640 MHz.
Eleven sources are extended in the uGMRT catalogue. We remand to Sect. 6.10 for a description of the extended radio sources detected.

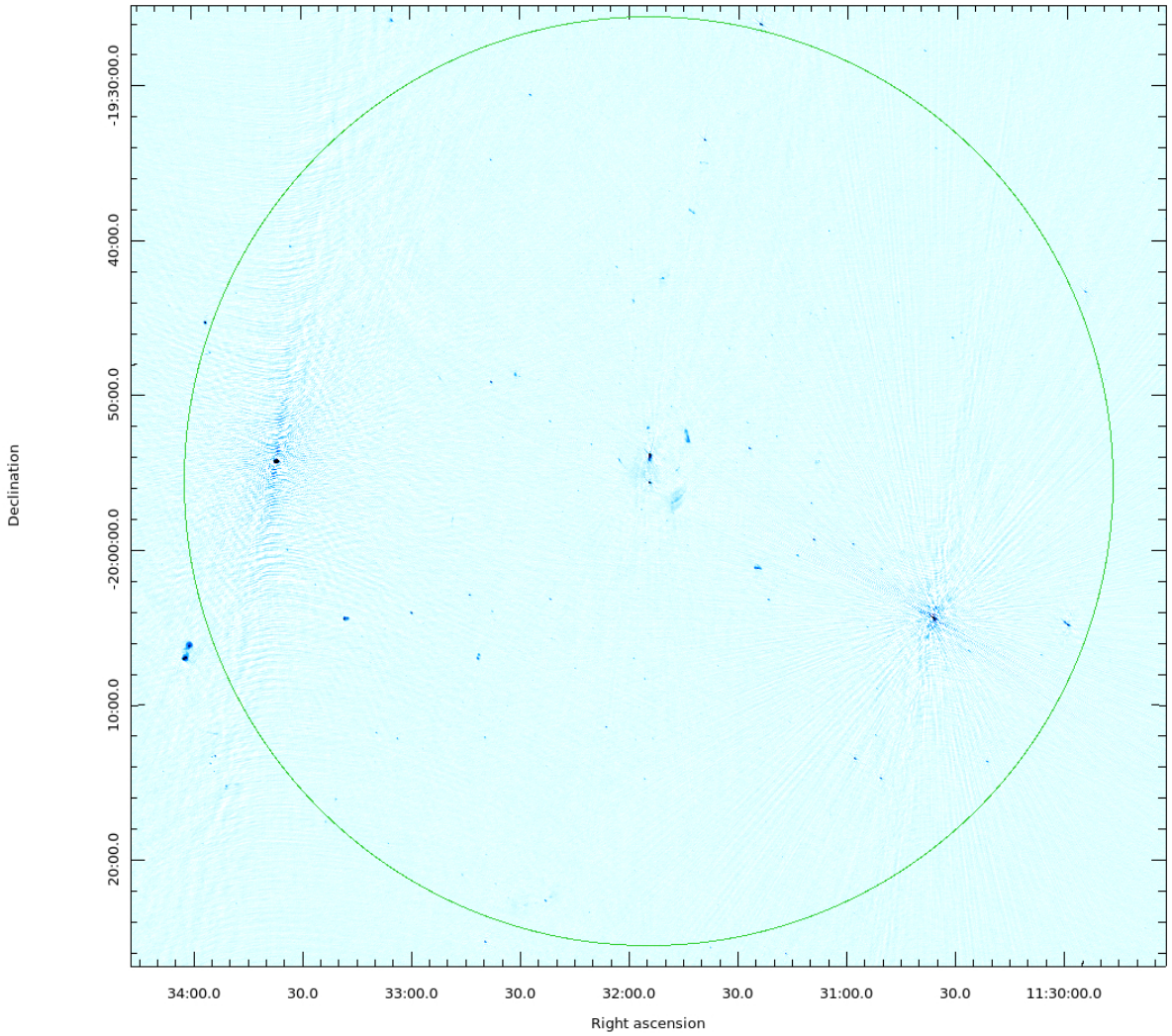

Figure 6.4: The image shows blue-scale view of the uGMRT field which encompasses an area of 0.785 deg^2 (i.e. 30 arcmin radius, green circle). This is the area within which we extracted our catalogues. The noise of the image is 0.03 mJy/b, with resolution of 5 $\times$ 3 arcsec, p.a. $\sim$ 43°. We are aware that the relic is not totally cleaned, this is due to the fact that we did not perform the amplitude self-calibration in order to not introduce amplitude errors. However, the relic is not part of the catalogue.

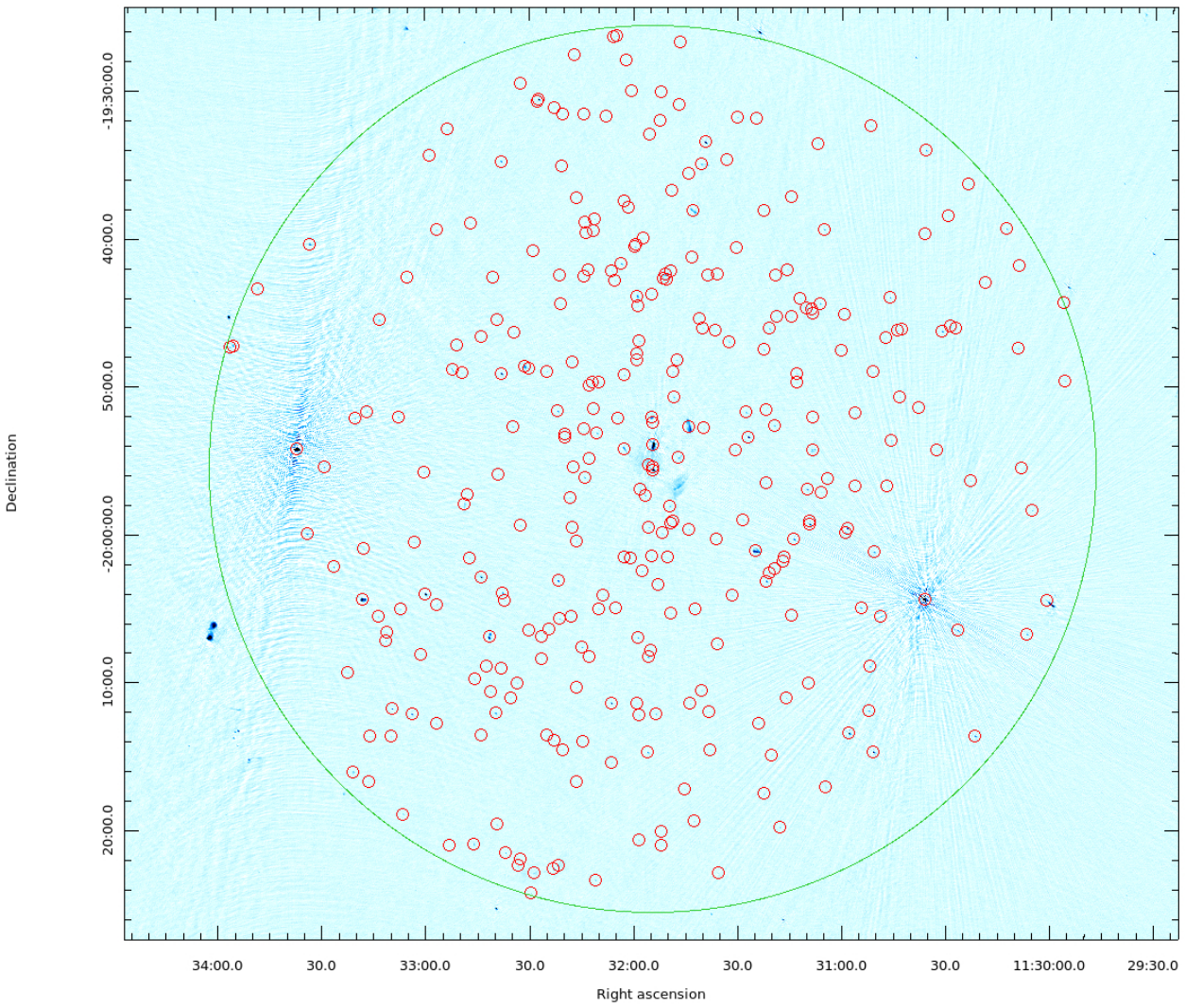

Figure 6.5: The image shows blue-scale view of the same area of 0.785 deg^2 (i.e. 30 arcmin radius, green circle). The red circles indicate the radio sources detected over a threshold of 5 σ (i.e. 0.15 mJy/b).

Table 6.8: A1300 uGMRT radio catalogue

Name	RA_{J2000}	DEC_{J2000}	F_{640MHz} (mJy)	ΔF	Morphology
J1129-1949	11:29:55.76	-19:49:37.3	1.66	0.16	unresolved
J1129-1944	11:29:56.23	-19:44:19.1	3.56	0.35	barely
J1130-2004a	11:30:00.95	-20:04:27.9	2.41	0.24	barely
J1130-1958	11:30:05.13	-19:58:23.6	1.25	0.12	unresolved
J1130-2006a	11:30:06.56	-20:06:45.8	4.93	0.49	unresolved
J1130-1955	11:30:08.41	-19:55:31.9	0.69	0.07	unresolved
J1130-1941	11:30:09.15	-19:41:51.4	0.81	0.08	barely
J1130-1947	11:30:09.32	-19:47:25.7	1.83	0.18	barely
J1130-1939a	11:30:12.65	-19:39:21.4	3.82	0.38	barely
J1130-1943	11:30:18.68	-19:43:00.3	0.80	0.08	barely
J1130-2013a	11:30:21.39	-20:13:39.8	16.0	1.60	barely
J1130-1956a	11:30:22.96	-19:56:22.1	0.62	0.06	unresolved
J1130-1936	11:30:23.60	-19:36:18.1	1.03	0.10	barely
J1130-2006b	11:30:26.49	-20:06:30.8	7.40	0.74	barely
J1130-1946a	11:30:27.31	-19:46:04.6	0.64	0.07	unresolved
J1130-1945a	11:30:28.82	-19:45:58.3	1.62	0.16	barely
J1130-1938	11:30:29.53	-19:38:27.3	0.60	0.06	barely
J1130-1946b	11:30:31.14	-19:46:17.6	4.09	0.41	barely
J1130-1954	11:30:32.71	-19:54:20.6	0.50	0.05	unresolved
J1130-1934	11:30:35.85	-19:34:03.2	5.70	0.57	barely
J1130-2004b	11:30:36.00	-20:04:24.7	70.0	7.00	barely
J1130-1939b	11:30:36.00	-19:39:42.5	0.77	0.08	barely
J1130-1951a	11:30:37.97	-19:51:26.1	0.34	0.04	unresolved
J1130-1946c	11:30:42.84	-19:46:07.6	0.53	0.06	unresolved
J1130-1950	11:30:43.29	-19:50:45.3	0.38	0.04	unresolved
J1130-1946d	11:30:44.06	-19:46:14.0	0.49	0.05	unresolved
J1130-1953	11:30:45.73	-19:53:41.7	0.59	0.06	barely
J1130-1944	11:30:46.08	-19:44:00.8	2.03	0.20	unresolved
J1130-1956b	11:30:46.85	-19:56:46.7	0.44	0.05	unresolved
J1130-1946	11:30:47.32	-19:46:42.3	0.30	0.04	unresolved
J1130-2005	11:30:48.70	-20:05:34.6	2.00	0.20	barely
J1130-2001	11:30:50.59	-20:01:13.8	2.37	0.23	barely
J1130-2014	11:30:50.69	-20:14:45.0	13.0	1.30	unresolved
J1130-1949	11:30:51.02	-19:49:03.7	0.71	0.07	unresolved
J1130-2008	11:30:51.74	-20:08:57.2	2.23	0.22	barely
J1130-1932	11:30:51.86	-19:32:23.3	1.42	0.14	barely
J1130-2011	11:30:52.10	-20:11:58.2	3.45	0.34	barely
J1130-2004c	11:30:54.39	-20:04:59.8	2.05	0.20	barely
J1130-1956c	11:30:56.07	-19:56:46.7	0.44	0.05	unresolved
J1130-1951b	11:30:56.08	-19:51:50.8	0.41	0.05	barely
J1130-2013b	11:30:57.78	-20:13:29.0	21.7	2.17	unresolved

Table 6.9: A1300 uGMRT radio catalogue (continued)

Name	RA_{J2000}	DEC_{J2000}	F_{640MHz} (mJy)	ΔF	Morphology
J1130-1959a	11:30:58.39	-19:59:37.9	5.15	0.51	unresolved
J1130-1959b	11:30:58.73	-19:59:54.9	0.91	0.09	barely
J1130-1945b	11:30:59.39	-19:45:07.8	0.39	0.04	unresolved
J1131-1947a	11:31:00.21	-19:47:34.1	0.38	0.04	unresolved
J1131-1956a	11:31:04.16	-19:56:18.2	0.47	0.05	unresolved
J1131-2017a	11:31:04.56	-20:17:05.8	1.06	0.11	barely
J1131-1939	11:31:05.14	-19:39:24.1	2.00	0.20	unresolved
J1131-1957	11:31:05.82	-19:57:10.7	0.25	0.03	unresolved
J1131-1944a	11:31:06.22	-19:44:24.9	1.33	0.13	unresolved
J1131-1933a	11:31:06.85	-19:33:35.4	0.84	0.08	barely
J1131-1945a	11:31:08.25	-19:45:04.9	0.42	0.05	unresolved
J1131-1954a	11:31:08.32	-19:54:19.9	7.23	0.72	**ext.** – **blending**?
J1131-1952a	11:31:08.50	-19:52:06.5	0.40	0.05	unresolved
J1131-1944b	11:31:08.77	-19:44:50.0	0.69	0.07	barely
J1131-1959a	11:31:09.21	-19:59:20.5	9.68	0.96	barely
J1131-1959b	11:31:09.22	-19:59:08.2	0.45	0.05	barely
J1131-2010a	11:31:09.54	-20:10:07.9	0.50	0.05	unresolved
J1131-1956b	11:31:09.91	-19:56:59.3	2.31	0.23	unresolved
J1131-1944c	11:31:10.09	-19:44:43.5	2.53	0.25	barely
J1131-1944d	11:31:11.94	-19:44:05.2	0.28	0.04	unresolved
J1131-1949a	11:31:12.91	-19:49:46.4	0.38	0.04	barely
J1131-1949b	11:31:13.02	-19:49:09.2	0.50	0.05	unresolved
J1131-2000a	11:31:13.70	-20:00:21.8	3.38	0.33	barely
J1131-2005a	11:31:14.39	-20:05:32.8	0.49	0.05	barely
J1131-1945b	11:31:14.40	-19:45:19.5	0.39	0.04	unresolved
J1131-1937	11:31:14.48	-19:37:11.7	0.52	0.06	barely
J1131-1942a	11:31:15.63	-19:42:07.6	0.52	0.06	barely
J1131-2011a	11:31:15.81	-20:11:07.3	0.76	0.08	unresolved
J1131-2001a	11:31:16.60	-20:01:32.8	0.38	0.04	unresolved
J1131-2001b	11:31:16.86	-20:01:50.0	0.42	0.05	unresolved
J1131-2019a	11:31:17.74	-20:19:50.8	1.37	0.14	unresolved
J1131-1945c	11:31:18.60	-19:45:20.4	0.27	0.04	unresolved
J1131-1942b	11:31:19.20	-19:42:28.9	0.27	0.04	barely
J1131-2002a	11:31:19.37	-20:02:22.1	0.35	0.04	unresolved
J1131-1952b	11:31:19.46	-19:52:40.9	1.30	0.13	unresolved
J1131-2014a	11:31:20.04	-20:14:58.5	0.59	0.06	unresolved
J1131-1946a	11:31:20.81	-19:46:07.7	1.01	0.10	unresolved
J1131-2002b	11:31:20.93	-20:02:38.7	0.48	0.05	barely
J1131-2003a	11:31:21.62	-20:03:13.3	3.98	0.39	unresolved
J1131-1951a	11:31:21.71	-19:51:36.7	0.26	0.03	unresolved
J1131-1956c	11:31:21.76	-19:56:33.5	0.33	0.04	unresolved

Table 6.10: A1300 uGMRT radio catalogue (continued)

Name	RA_{J2000}	DEC_{J2000}	F_{640MHz} (mJy)	ΔF	Morphology
J1131-2017b	11:31:22.29	-20:17:35.2	1.02	0.10	unresolved
J1131-1947b	11:31:22.46	-19:47:32.8	0.90	0.09	unresolved
J1131-1938a	11:31:22.48	-19:38:09.5	0.41	0.05	unresolved
J1131-2012	11:31:23.90	-20:12:50.1	1.21	0.12	barely
J1131-1931a	11:31:24.62	-19:31:54.6	0.46	0.05	unresolved
J1131-2001c	11:31:24.67	-20:01:10.4	27.8	2.84	**WAT – NAT**?
J1131-1953a	11:31:26.85	-19:53:27.5	7.22	0.72	unresolved
J1131-1951b	11:31:27.50	-19:51:47.4	0.92	0.09	unresolved
J1131-1959c	11:31:28.31	-19:59:02.3	0.44	0.05	unresolved
J1131-1931b	11:31:29.96	-19:31:50.1	1.00	0.10	unresolved
J1131-1940	11:31:30.23	-19:40:38.5	0.41	0.05	barely
J1131-1954b	11:31:30.48	-19:54:22.2	0.43	0.05	unresolved
J1131-2004	11:31:31.43	-20:04:10.8	0.34	0.04	unresolved
J1131-1947c	11:31:32.50	-19:47:00.2	0.75	0.08	unresolved
J1131-1934	11:31:33.10	-19:34:41.7	0.47	0.05	barely
J1131-2022	11:31:35.55	-20:22:56.4	1.22	0.12	unresolved
J1131-2007	11:31:35.62	-20:07:29.4	0.74	0.08	unresolved
J1131-1942c	11:31:35.88	-19:42:25.2	0.26	0.04	unresolved
J1131-2000b	11:31:36.07	-20:00:23.1	0.22	0.03	unresolved
J1131-1946b	11:31:36.44	-19:46:14.1	0.30	0.04	barely
J1131-2014b	11:31:37.74	-20:14:38.7	0.35	0.04	unresolved
J1131-2012	11:31:38.13	-20:12:01.7	0.41	0.05	unresolved
J1131-1942d	11:31:38.64	-19:42:31.7	0.24	0.03	unresolved
J1131-1933b	11:31:39.25	-19:33:31.4	23.1	2.32	barely
J1131-1952c	11:31:39.74	-19:52:51.8	0.52	0.06	unresolved
J1131-1946c	11:31:40.02	-19:46:04.2	0.45	0.05	barely
J1131-2010b	11:31:40.30	-20:10:35.4	0.45	0.05	barely
J1131-1935a	11:31:40.39	-19:35:00.1	4.96	0.27	**FRII**?
J1131-1945d	11:31:40.84	-19:45:25.9	0.24	0.03	unresolved
J1131-2005b	11:31:42.31	-20:05:06.7	0.18	0.03	unresolved
J1131-2019b	11:31:42.42	-20:19:26.9	0.74	0.08	unresolved
J1131-1938b	11:31:42.79	-19:38:09.4	10.9	1.09	**FRII**?
J1131-1941	11:31:43.04	-19:41:19.5	0.22	0.03	unresolved
J1131-2011b	11:31:43.63	-20:11:29.9	0.55	0.06	unresolved
J1131-1959d	11:31:43.92	-19:59:42.6	0.50	0.05	unresolved
J1131-1952d	11:31:43.96	-19:52:44.8	34.3	3.97	**WAT**
J1131-1935b	11:31:44.03	-19:35:40.2	0.44	0.05	barely
J1131-2017c	11:31:45.14	-20:17:17.9	0.38	0.04	unresolved
J1131-1926	11:31:46.61	-19:26:45.2	0.63	0.07	unresolved
J1131-1930a	11:31:46.91	-19:30:56.8	0.37	0.04	unresolved
J1131-1954c	11:31:46.96	-19:54:52.5	1.90	0.21	**FRI – II**?

Table 6.11: A1300 uGMRT radio catalogue (continued)

Name	RA_{J2000}	DEC_{J2000}	F_{640MHz} (mJy)	ΔF	Morphology
J1131-1948a	11:31:47.51	-19:48:14.8	0.42	0.05	unresolved
J1131-1950	11:31:48.38	-19:50:45.3	0.78	0.08	unresolved
J1131-1959e	11:31:48.45	-19:59:08.3	0.25	0.03	unresolved
J1131-1949c	11:31:48.62	-19:49:01.7	0.33	0.04	barely
J1131-1936	11:31:49.05	-19:36:49.3	0.59	0.06	unresolved
J1131-1942e	11:31:49.11	-19:42:15.9	1.01	0.10	barely
J1131-2005c	11:31:49.18	-20:05:22.2	0.23	0.03	unresolved
J1131-1959f	11:31:49.31	-19:59:18.4	0.23	0.03	unresolved
J1131-1958	11:31:49.50	-19:58:07.9	0.82	0.08	unresolved
J1131-2001d	11:31:49.97	-20:01:36.7	0.29	0.04	unresolved
J1131-1942f	11:31:50.30	-19:42:46.9	1.23	0.12	barely
J1131-1942g	11:31:50.83	-19:42:28.5	6.68	0.66	barely
J1131-1942h	11:31:51.27	-19:42:43.0	1.53	0.15	barely
J1131-1959g	11:31:51.71	-19:59:57.2	0.40	0.05	unresolved
J1131-1930b	11:31:51.91	-19:30:07.1	0.33	0.04	unresolved
J1131-2021	11:31:52.00	-20:21:03.3	0.59	0.06	barely
J1131-2020a	11:31:52.07	-20:20:06.4	0.42	0.05	unresolved
J1131-1932a	11:31:52.26	-19:32:04.8	0.30	0.04	unresolved
J1131-2003b	11:31:52.98	-20:03:25.6	0.40	0.05	barely
J1131-2012b	11:31:53.46	-20:12:12.4	1.12	0.11	unresolved
J1131-1955a	11:31:54.28	-19:55:28.9	1.20	0.12	barely
J1131-1953b	11:31:54.29	-19:53:57.5	95.7	9.57	**TAIL**
J1131-1955b	11:31:54.31	-19:55:40.5	30.6	3.16	barely BCG
J1131-1952e	11:31:54.51	-19:52:27.3	0.44	0.05	unresolved
J1131-1943a	11:31:54.58	-19:43:48.7	0.41	0.05	unresolved
J1131-2001e	11:31:54.69	-20:01:32.5	0.34	0.04	unresolved
J1131-1952	11:31:54.81	-19:52:07.9	6.54	0.65	barely
J1131-2007b	11:31:54.90	-20:07:53.2	0.26	0.03	barely
J1131-1932b	11:31:55.26	-19:32:59.8	0.49	0.05	barely
J1131-1959h	11:31:55.48	-19:59:33.9	0.63	0.07	unresolved
J1131-2008	11:31:55.71	-20:08:19.8	1.39	0.14	unresolved
J1131-1955	11:31:55.74	-19:55:19.8	0.92	0.09	barely-halo
J1131-2014c	11:31:55.76	-20:14:46.9	2.09	0.21	unresolved
J1131-1957	11:31:56.62	-19:57:23.8	0.98	0.10	unresolved
J1131-1940b	11:31:57.25	-19:40:01.9	0.37	0.04	barely
J1131-2002	11:31:57.41	-20:02:31.9	0.44	0.05	unresolved
J1131-1956d	11:31:57.99	-19:56:59.9	0.40	0.05	barely
J1131-1946c	11:31:58.19	-19:46:58.3	0.58	0.06	unresolved
J1131-2012c	11:31:58.20	-20:12:16.7	0.66	0.07	unresolved
J1131-2020b	11:31:58.48	-20:20:42.3	0.78	0.08	barely
J1131-1944e	11:31:58.63	-19:44:35.1	0.22	0.03	unresolved

Table 6.12: A1300 uGMRT radio catalogue (continued)

Name	RA_{J2000}	DEC_{J2000}	F_{640MHz} (mJy)	ΔF	Morphology
J1131-2007c	11:31:58.67	-20:07:01.5	1.06	0.11	unresolved
J1131-1943b	11:31:58.82	-19:43:56.4	4.73	0.47	barely
J1131-2011c	11:31:58.86	-20:11:26.4	0.29	0.04	unresolved
J1131-1947d	11:31:58.97	-19:47:49.4	0.55	0.06	unresolved
J1131-1948b	11:31:59.07	-19:48:16.9	0.23	0.03	unresolved
J1131-1940c	11:31:59.16	-19:40:26.8	0.23	0.03	unresolved
J1131-1940d	11:31:59.44	-19:40:36.1	0.66	0.07	unresolved
J1132-1930a	11:32:00.42	-19:30:01.1	0.48	0.05	unresolved
J1132-2001a	11:32:00.65	-20:01:39.9	0.25	0.03	unresolved
J1132-1937a	11:32:01.34	-19:37:58.0	0.30	0.04	unresolved
J1132-1927a	11:32:02.08	-19:27:59.4	0.77	0.08	barely
J1132-1949a	11:32:02.56	-19:49:16.6	0.66	0.07	unresolved
J1132-1937b	11:32:02.58	-19:37:28.9	0.51	0.05	unresolved
J1132-1954a	11:32:02.62	-19:54:14.2	4.12	0.47	**tail**
J1132-2001b	11:32:02.71	-20:01:35.7	0.34	0.04	unresolved
J1132-1941	11:32:03.41	-19:41:44.6	1.67	0.16	unresolved
J1132-1952a	11:32:04.41	-19:52:12.1	0.34	0.04	unresolved
J1132-1926a	11:32:04.79	-19:26:19.3	1.75	0.17	barely
J1132-2005a	11:32:04.98	-20:05:03.3	0.23	0.03	unresolved
J1132-1942a	11:32:05.39	-19:42:51.8	0.27	0.04	unresolved
J1132-1926b	11:32:05.50	-19:26:24.8	0.86	0.09	unresolved
J1132-1942b	11:32:06.15	-19:42:13.4	0.42	0.05	unresolved
J1132-2015	11:32:06.30	-20:15:28.9	0.30	0.04	unresolved
J1132-2011a	11:32:06.32	-20:11:27.2	4.13	0.41	unresolved
J1132-1931a	11:32:07.62	-19:31:45.5	0.36	0.04	unresolved
J1132-2004a	11:32:08.67	-20:04:08.0	0.36	0.04	unresolved
J1132-2005b	11:32:09.95	-20:05:03.7	0.52	0.06	barely
J1132-1949b	11:32:10.02	-19:49:43.9	0.72	0.07	barely
J1132-1953	11:32:10.38	-19:53:12.1	1.29	0.13	unresolved
J1132-2023	11:32:10.94	-20:23:24.4	2.00	0.20	unresolved
J1132-1938a	11:32:11.10	-19:38:42.0	0.39	0.04	unresolved
J1132-1951a	11:32:11.32	-19:51:33.6	0.22	0.03	unresolved
J1132-1939a	11:32:11.38	-19:39:31.3	0.37	0.04	unresolved
J1132-1949c	11:32:11.63	-19:49:44.3	0.19	0.03	unresolved
J1132-1954b	11:32:12.66	-19:54:56.1	0.20	0.03	unresolved
J1132-1949d	11:32:12.67	-19:49:56.5	0.20	0.03	unresolved
J1132-2008a	11:32:12.79	-20:08:18.8	0.19	0.03	unresolved
J1132-1942c	11:32:13.02	-19:42:09.6	0.39	0.04	barely
J1132-1939b	11:32:13.41	-19:39:39.9	0.45	0.05	unresolved
J1132-1938b	11:32:13.79	-19:38:54.8	0.30	0.04	unresolved
J1132-1956a	11:32:14.02	-19:56:10.8	0.88	0.09	unresolved

Table 6.13: A1300 uGMRT radio catalogue (continued)

Name	RA_{J2000}	DEC_{J2000}	F_{640MHz} (mJy)	ΔF	Morphology
J1132-1942d	11:32:14.14	-19:42:35.9	0.22	0.03	unresolved
J1132-1931b	11:32:14.23	-19:31:37.4	0.42	0.05	barely
J1132-1952b	11:32:14.31	-19:52:54.0	0.23	0.03	unresolved
J1132-2014a	11:32:14.46	-20:14:02.4	0.30	0.04	barely
J1132-2007	11:32:14.75	-20:07:40.0	1.05	0.11	unresolved
J1132-2016	11:32:16.26	-20:16:47.1	0.35	0.04	unresolved
J1132-2010a	11:32:16.36	-20:10:22.7	0.27	0.04	unresolved
J1132-2000	11:32:16.37	-20:00:28.9	0.30	0.04	unresolved
J1132-1937b	11:32:16.42	-19:37:16.0	0.46	0.05	barely
J1132-1927b	11:32:17.02	-19:27:38.7	1.17	0.12	unresolved
J1132-1955	11:32:17.32	-19:55:28.6	0.23	0.03	unresolved
J1132-1948a	11:32:17.41	-19:48:25.7	0.31	0.04	unresolved
J1132-1959a	11:32:17.62	-19:59:32.6	0.32	0.04	barely
J1132-2005c	11:32:17.79	-20:05:36.6	0.19	0.03	unresolved
J1132-1957	11:32:18.27	-19:57:32.3	0.51	0.05	barely
J1132-1953b	11:32:19.61	-19:53:17.0	0.35	0.04	unresolved
J1132-1953c	11:32:19.75	-19:53:30.6	0.25	0.03	unresolved
J1132-2014b	11:32:20.29	-20:14:36.1	0.37	0.04	barely
J1132-1931c	11:32:20.38	-19:31:35.6	0.61	0.06	barely
J1132-1935	11:32:20.60	-19:35:09.6	0.44	0.05	unresolved
J1132-1944	11:32:20.79	-19:44:25.9	0.31	0.04	unresolved
J1132-1942	11:32:21.21	-19:42:32.7	0.22	0.03	unresolved
J1132-2005d	11:32:21.23	-20:05:44.6	0.77	0.08	barely
J1132-2022b	11:32:21.64	-20:22:26.0	9.28	0.33	**ext.** – **blending**?
J1132-2003a	11:32:21.67	-20:03:11.1	4.03	0.40	unresolved
J1132-1951b	11:32:21.73	-19:51:42.5	1.58	0.16	unresolved
J1132-1931d	11:32:22.66	-19:31:09.8	0.68	0.07	barely
J1132-2013a	11:32:22.72	-20:13:59.0	0.68	0.07	unresolved
J1132-2022b	11:32:23.02	-20:22:39.9	11.6	1.16	unresolved
J1132-2006b	11:32:24.40	-20:06:28.0	0.35	0.04	barely
J1132-1949e	11:32:24.87	-19:49:02.1	0.43	0.05	unresolved
J1132-2013b	11:32:25.06	-20:13:37.5	0.62	0.06	barely
J1132-2006b	11:32:26.36	-20:06:57.1	0.37	0.04	barely
J1132-2008	11:32:26.54	-20:08:25.8	0.39	0.04	unresolved
J1132-1930b	11:32:27.11	-19:30:37.3	18.8	1.88	unresolved
J1132-1930c	11:32:27.49	-19:30:44.7	0.54	0.06	unresolved
J1132-2022c	11:32:28.63	-20:22:57.5	6.02	0.47	**ext.** – **blending**?
J1132-1940	11:32:28.83	-19:40:52.2	0.30	0.04	barely
J1132-2024	11:32:29.52	-20:24:18.0	1.24	0.12	unresolved
J1132-1948	11:32:30.11	-19:48:48.3	1.14	0.11	barely
J1132-2006c	11:32:30.21	-20:06:31.9	0.28	0.04	unresolved

Table 6.14: A1300 uGMRT radio catalogue (continued)

Name	RA_{J2000}	DEC_{J2000}	F_{640MHz} (mJy)	ΔF	Morphology
J1132-1948b	11:32:31.25	-19:48:41.4	7.25	0.72	barely
J1132-1959b	11:32:32.49	-19:59:25.9	0.45	0.05	barely
J1132-1929	11:32:32.53	-19:29:30.6	0.72	0.07	barely
J1132-2022d	11:32:32.74	-20:22:02.1	0.86	0.09	barely
J1132-2022e	11:32:33.32	-20:22:27.4	1.31	0.13	barely
J1132-2010b	11:32:33.53	-20:10:04.4	0.65	0.07	unresolved
J1132-1946a	11:32:34.29	-19:46:23.1	0.51	0.05	barely
J1132-1952c	11:32:34.74	-19:52:44.8	0.75	0.08	unresolved
J1132-2011b	11:32:35.38	-20:11:04.7	0.42	0.05	unresolved
J1132-2021e	11:32:36.79	-20:21:35.1	1.97	0.19	unresolved
J1132-2004b	11:32:36.99	-20:04:31.9	0.43	0.05	unresolved
J1132-2003b	11:32:37.64	-20:03:59.1	2.12	0.21	unresolved
J1132-1949f	11:32:37.89	-19:49:09.9	9.01	0.90	unresolved
J1132-2009a	11:32:37.93	-20:09:07.6	0.30	0.04	unresolved
J1132-1934	11:32:37.96	-19:34:49.0	4.99	0.49	unresolved
J1132-1956b	11:32:38.91	-19:56:00.4	0.29	0.04	unresolved
J1132-1945	11:32:39.21	-19:45:32.8	0.42	0.05	unresolved
J1132-2019	11:32:39.36	-20:19:40.1	1.58	0.16	unresolved
J1132-2012a	11:32:39.68	-20:12:07.3	3.10	0.31	unresolved
J1132-1942e	11:32:40.47	-19:42:41.4	0.30	0.04	unresolved
J1132-2010c	11:32:41.19	-20:10:40.2	0.48	0.05	unresolved
J1132-2006d	11:32:41.51	-20:06:56.0	21.2	2.18	**FRII**?
J1132-2008b	11:32:42.34	-20:08:59.5	0.34	0.04	unresolved
J1132-2002	11:32:43.68	-20:02:57.3	3.17	0.31	barely
J1132-1946b	11:32:43.83	-19:46:41.1	0.25	0.03	unresolved
J1132-2013c	11:32:43.93	-20:13:38.1	0.41	0.05	unresolved
J1132-2009b	11:32:45.74	-20:09:50.9	0.87	0.09	unresolved
J1132-2020	11:32:45.98	-20:20:59.1	3.82	0.38	barely
J1132-1938c	11:32:46.86	-19:38:57.9	0.73	0.07	unresolved
J1132-2001c	11:32:47.21	-20:01:37.5	0.31	0.04	unresolved
J1132-1957a	11:32:47.78	-19:57:22.1	0.30	0.04	unresolved
J1132-1957b	11:32:48.51	-19:57:58.0	0.87	0.09	barely
J1132-1949g	11:32:49.36	-19:49:07.4	0.40	0.05	unresolved
J1132-1947	11:32:50.86	-19:47:15.0	0.44	0.05	unresolved
J1132-1948	11:32:52.05	-19:48:53.9	2.93	0.29	barely
J1132-2021b	11:32:52.99	-20:21:05.8	0.57	0.06	unresolved
J1132-1932	11:32:53.49	-19:32:38.9	0.91	0.09	barely
J1132-1939	11:32:56.53	-19:39:26.5	0.85	0.09	barely
J1132-2004c	11:32:56.66	-20:04:46.2	0.70	0.07	barely
J1132-2012b	11:32:56.81	-20:12:49.8	0.72	0.07	unresolved
J1132-1934	11:32:58.51	-19:34:24.1	0.98	0.10	unresolved

Table 6.15: A1300 uGMRT radio catalogue (continued)

Name	RA_{J2000}	DEC_{J2000}	F_{640MHz} (mJy)	ΔF	Morphology
J1132-2004d	11:32:59.85	-20:04:04.1	18.2	1.82	barely
J1133-1955a	11:33:00.32	-19:55:49.2	0.52	0.06	unresolved
J1133-2008	11:33:01.31	-20:08:08.9	0.58	0.06	barely
J1133-2000a	11:33:03.15	-20:00:34.2	0.60	0.06	barely
J1133-2012	11:33:03.81	-20:12:11.0	7.25	0.72	unresolved
J1133-1942	11:33:05.00	-19:42:37.0	0.58	0.06	unresolved
J1133-2018	11:33:06.39	-20:18:56.9	3.08	0.30	unresolved
J1133-2005a	11:33:07.10	-20:05:06.1	0.67	0.07	barely
J1133-1952a	11:33:07.66	-19:52:04.9	1.16	0.11	unresolved
J1133-2011	11:33:09.55	-20:11:48.9	4.22	0.42	unresolved
J1133-2013a	11:33:09.86	-20:13:41.7	0.73	0.07	barely
J1133-2006	11:33:11.03	-20:06:40.9	0.56	0.06	unresolved
J1133-2007	11:33:11.22	-20:07:15.2	0.86	0.09	unresolved
J1133-1945	11:33:13.05	-19:45:32.4	2.00	0.20	barely
J1133-2005b	11:33:13.47	-20:05:36.1	1.01	0.10	unresolved
J1133-2013b	11:33:16.07	-20:13:42.0	0.63	0.06	barely
J1133-2016a	11:33:16.42	-20:16:46.0	0.67	0.07	unresolved
J1133-1951	11:33:16.57	-19:51:44.7	1.06	0.11	unresolved
J1133-2000b	11:33:17.81	-20:00:59.9	0.81	0.08	barely
J1133-2004	11:33:18.03	-20:04:25.9	78.3	7.83	barely
J1133-1952b	11:33:20.03	-19:52:11.7	1.18	0.12	unresolved
J1133-2016b	11:33:20.78	-20:16:05.4	7.59	0.76	barely
J1133-2009	11:33:22.30	-20:09:20.9	0.89	0.09	barely
J1133-2002	11:33:26.25	-20:02:14.1	2.09	0.21	unresolved
J1133-1955b	11:33:28.90	-19:55:29.1	2.95	0.29	unrsolved
J1133-1940	11:33:32.96	-19:40:23.9	11.9	1.19	barely
J1133-1959	11:33:33.93	-19:59:59.5	5.81	0.58	unresolved
J1133-1954	11:33:36.93	-19:54:15.9	3199.0	320	barely
J1133-1943	11:33:47.87	-19:43:23.2	2.92	0.29	unresolved
J1133-1947a	11:33:55.15	-19:47:14.6	8.74	0.87	barely
J1133-1947b	11:33:56.07	-19:47:20.1	5.15	0.51	barely

6.5 Summary of the MeerKAT and the uGMRT radio catalogues

In this section we report a summary of the MeerKAT and the uGMRT radio catalogues. Tab. 6.16 and 6.17 report the number (N) of the sources and the percentage (%) of the unresolved, barely resolved or extended sources.
According to our morphological classification, in the MeerKAT radio catalogue the unresolved sources are the 67 %, the barely resolved are 28%, and the extended sources are the 5% of the sample.
In the uGMRT catalogue, the unresolved sources are the 61% of the sample, the barely resolved sources are the 35%, and the extended sources are the 4% of the sample.
In Fig. 6.6 and 6.7 we report the histograms of the integrated flux density distributions from the MeerKAT and uGMRT catalogues respectively. As visible from the plots, there is evidence of statistical incompleteness in both the samples. This is consistent with what is found in the logN-logS distributions.

Table 6.16: A1300 MeerKAT radio catalogue

	Unresolved	**Barely**	**Extended**
N	75	32	5
%	67	28	5

Table 6.17: A1300 uGMRT radio catalogue

	Unresolved	**Barely**	**Extended**
N	197	110	11
%	61	35	4

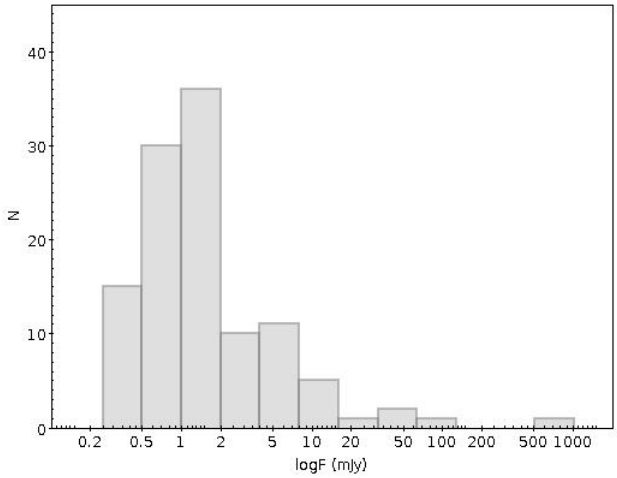

Figure 6.6: The histogram shows the distribution of the integrated flux densities for the sources in the MeerKAT radio catalogue. The incompleteness at low fluxes is consistent with the result from the statistical source counts (logN-logS).

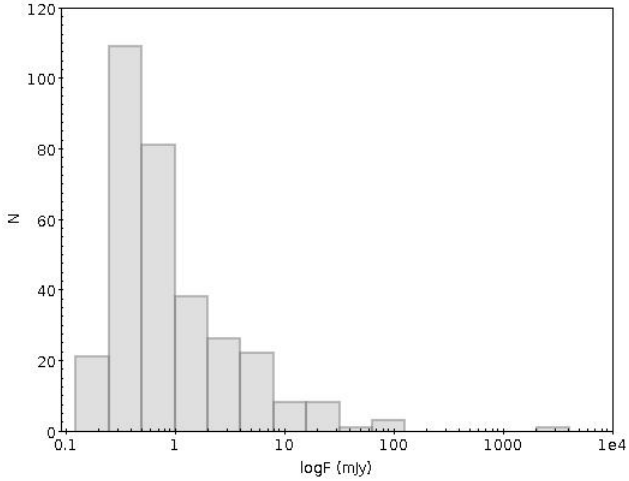

Figure 6.7: The histogram shows the distribution of the integrated flux densities for the sources in the uGMRT radio catalogue. The incompleteness at low fluxes is consistent with the result from the statistical source counts (logN-logS).

6.6 Spectral analysis

In order to get a spectral index information on the radio sources detected in the A1300 field within an area of 30 arcmin radius, we crossmatched our MeerKAT and uGMRT catalogues.
First, we performed the same test as for MACSJ1931-2634, in order to determine the optimal radius for the matches, following the same method adopted in Mahony et al. (2016). We matched our catalogues several times, choosing different separation radii, in order to investigate how the number of matches varies with the separation radius. The optimal matching radius was found to be 10 arcsec, as visible from Fig. 6.8, which corresponds to the radius after which the number of matches drops.

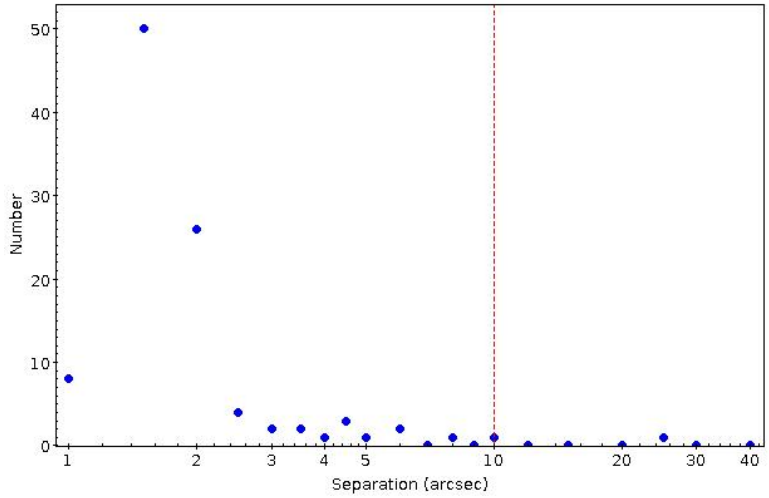

Figure 6.8: The image shows our test to determine the optimal matching radius between the two catalogues. The blue dots are the number of matches as a function of the search radius. The dotted line marks the search radius choosen for the final best match.

We report in Fig. 6.9 the offset between the MeerKAT sources and the uGMRT sources. There is a systematic offset, which is not uncommon when doing phase-only self-calibration (Mahony et al., 2016). The median values of the offset are 0.15 arcsec in right ascension and 1 arcsec in declination. The sources which show a higher offset were further visually inspected to assess the reliability of the cross-match.

To estimate the spectral indices we considered the central frequencies of 1.2 GHz and 640 MHz. First, we report the spectral indices of the sources in common (Tab.6.18 and following), which are 103.
Then, we give an upper limit of the sources detected only at 1.2 GHz, which are 9

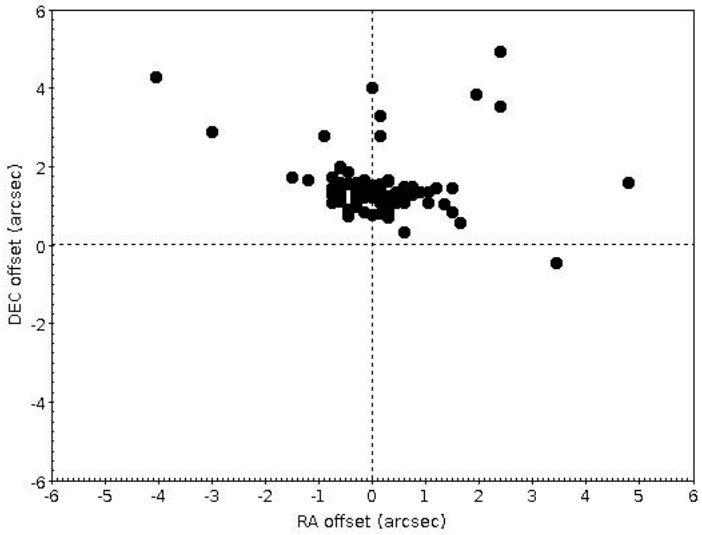

Figure 6.9: The image shows the offset in right ascension and declination between the MeerKAT positions and the uGMRT positions. There is a clear systematic offset, primarly in declination for all sources.

(Tab. 6.21) and the sources detected only at 640 MHz, which are 215 (Tab. 6.22 and following).
To estimate the spectral indices we adopted the convention: $F_\nu \propto \nu^{-\alpha}$.
The values of the spectral indices are estimated by the equation:

$$\alpha = \frac{log_{10}\left(\frac{F_1}{F_2}\right)}{log_{10}\left(\frac{\nu_2}{\nu_1}\right)} \tag{6.1}$$

The errors are estimated according to the formula adopted in Mahony et al. (2016):

$$E_\alpha = \frac{1}{ln\frac{\nu_1}{\nu_2}}\sqrt{\left(\frac{F_{1,err}}{F_1}\right)^2 + \left(\frac{F_{2,err}}{F_2}\right)^2} \tag{6.2}$$

where $\nu_{1,2}$ refers to the frequencies, and $F_{1,2}$ to the corresponding flux densities at those frequencies.
In Figure 6.10 we report the spectral index distribution of the sources in common which has a median spectral index of 1.1 ± 0.2. This value is steeper than what we found from MACSJ1931-2634 field and from previous studies (Williams et al., 2016; Mahony et al., 2016; Intema et al., 2011; Ishwara-Chandra et al., 2010).
According to Mahony et al. (2016), we can separate the sample of the sources in common into three primary categories: sources with $\alpha\ ^{1283}_{640} < 0.5$ are flat, sources with $0.5 < \alpha\ ^{1283}_{640} < 1.2$ are steep, whereas sources with $\alpha\ ^{1283}_{640} > 1.2$ are ultra-steep. According to this separation, the majority of the sources in the sample are steep

sources ($0.5 < \alpha \, ^{1283}_{640} < 1.2$), which is expected at these frequencies. They are the 45% of the sample. The ultra-steep sources are comparable in percentage to the steep sources. They are the 42 % of the sample. Finally, the flat sources are the 13% of the sample.
In Fig. 6.11 and 6.12 are reported the spectral index distributions of the upper limits, i.e. the sources detected at 1.2 GHz only or at 640 MHz only respectively.
The median value of the MeerKAT distribution is -2.4 whereas the median value of the uGMRT distribution is 1.05.
The values reported with an asterisk are extreme cases further visually inspected which could be biased. They are not taken into account in the alpha index distribution.

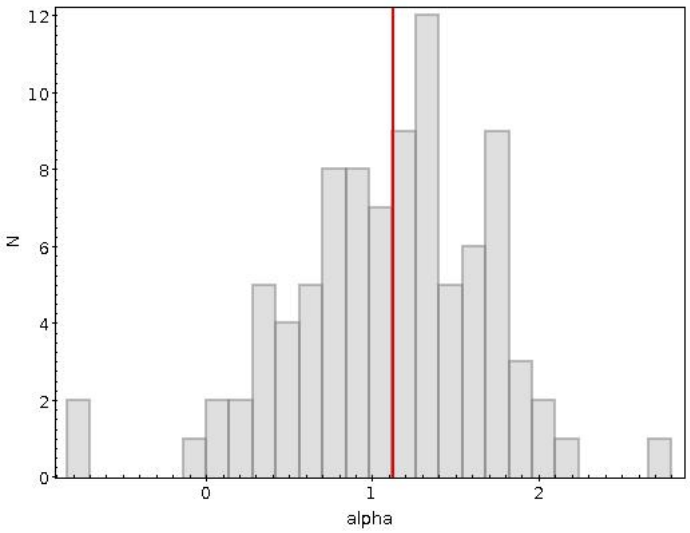

Figure 6.10: Histogram of the spectral indices from 640 MHz-1.2 GHz for sources in the A1300 field detected both at 1.2 GHz and 640 MHz. The red line indicates the median value, steeper in respect to the previous studies, which is 1.1 ± 0.2. The source population is dominated by steep spectra sources.

Table 6.18: Spectral indices of the common sources

RA_{J2000}	DEC_{J2000}	$F_{1.2GHz}$ (mJy)	F_{640MHz} (mJy)	α	E_α
11:29:55.75	-19:49:35.6	0.53	1.66	1.641	0.21
11:30:05.22	-19:58:22.5	0.33	1.25	1.914	0.25
11:30:06.58	-20:06:44.2	1.46	4.93	1.749	0.20
11:30:12.66	-19:39:19.9	1.16	3.82	1.713	0.20
11:30:21.47	-20:13:38.3	4.84	16.0	1.719	0.20
11:30:23.56	-19:36:16.2	0.47	1.03	1.128	0.23
11:30:26.59	-20:06:29.3	2.29	7.40	1.686	0.20
11:30:28.87	-19:45:56.9	0.54	1.62	1.579	0.21
11:30:31.14	-19:46:16.2	1.94	4.09	1.072	0.20
11:30:35.86	-19:34:01.7	1.50	5.70	1.919	0.20
11:30:36.32	-20:04:23.1	118.0	70.0	-0.75	0.20
11:30:46.08	-19:43:59.3	1.28	2.03	0.663	0.20
11:30:48.71	-20:05:31.9	0.31	2.00	2.68	0.27
11:30:50.61	-20:01:12.1	1.13	2.37	1.064	0.20
11:30:50.75	-20:14:43.7	4.80	13.0	1.432	0.20
11:30:51.72	-20:08:55.6	0.72	2.23	1.625	0.21
11:30:52.15	-20:11:56.9	1.91	3.45	0.85	0.20
11:30:54.36	-20:04:58.3	0.84	2.05	1.282	0.20
11:30:57.85	-20:13:27.6	6.48	21.7	1.737	0.20
11:30:58.41	-19:59:36.6	2.22	5.15	1.209	0.20
11:31:04.67	-20:17:05.3	0.36	1.06	1.552	0.24
11:31:05.14	-19:39:22.6	1.19	2.00	0.746	0.20
11:31:06.17	-19:44:23.2	0.87	1.33	0.61	0.20
11:31:08.12	-19:54:17.0	2.38	7.23	1.597	0.20
11:31:09.25	-19:59:19.1	4.18	9.68	1.207	0.20
11:31:09.93	-19:56:58.1	1.32	2.31	0.804	0.20
11:31:10.11	-19:44:42.4	0.62	2.53	2.022	0.21
11:31:13.72	-20:00:20.5	1.69	3.38	0.996	0.20
11:31:15.76	-20:11:06.2	0.26	0.76	1.542	0.26
11:31:19.49	-19:52:39.7	0.60	1.30	1.111	0.22
11:31:20.84	-19:46:06.6	0.80	1.01	0.335	0.21
11:31:21.67	-20:03:11.8	1.39	3.98	1.512	0.21
11:31:22.33	-20:17:34.0	0.36	1.02	1.497	0.24
11:31:22.47	-19:47:31.5	0.37	0.90	1.278	0.24
11:31:24.77	-20:01:09.5	10.7	27.8	1.372	0.21
11:31:26.88	-19:53:26.1	3.90	7.22	0.885	0.21
11:31:27.49	-19:51:46.1	1.62	0.92	-0.81	0.21
11:31:29.91	-19:31:48.9	0.59	1.00	0.758	0.22
11:31:32.52	-19:46:59.5	0.51	0.75	0.554	0.22
11:31:35.54	-20:07:27.8	0.31	0.74	1.251	0.27
11:31:35.78	-20:22:56.9	0.46	1.22	1.402	0.23

Table 6.19: Spectral indices of the common sources (continued)

RA_{J2000}	DEC_{J2000}	$F_{1.2GHz}$ (mJy)	F_{640MHz} (mJy)	α	E_α
11:31:39.27	-19:33:29.7	9.2	23.1	1.323	0.20
11:31:40.34	-19:34:59.0	0.82	4.96	2.587	0.17
11:31:42.31	-19:38:11.5	6.49	10.9	0.745	0.20
11:31:42.42	-20:19:25.5	0.74	0.74	-0.0	0.21
11:31:43.92	-19:52:54.2	10.0	34.3	1.772	0.21
11:31:48.36	-19:50:43.9	0.70	0.78	0.155	0.22
11:31:49.49	-19:58:06.5	0.39	0.82	1.068	0.23
11:31:50.73	-19:42:26.8	3.08	6.68	1.113	0.20
11:31:53.44	-20:12:11.0	0.60	1.12	0.897	0.21
11:31:54.29	-19:53:53.5	37.4	95.7	1.35	0.21
11:31:54.30	-19:55:39.0	12.1	30.6	1.334	0.21
11:31:54.85	-19:52:07.6	2.30	6.54	1.502	0.21
11:31:55.72	-20:08:18.6	0.78	1.39	0.83	0.20
11:31:55.77	-20:14:45.5	1.27	2.09	0.716	0.20
11:31:56.69	-19:57:22.7	0.39	0.98	1.324	0.23
11:31:58.71	-20:07:00.4	0.48	1.06	1.139	0.23
11:31:58.83	-19:43:53.1	1.55	4.73	1.604	0.20
11:32:02.78	-19:54:09.3	1.02	4.12	2.007	0.21
11:32:03.40	-19:41:43.2	0.76	1.67	1.131	0.20
11:32:04.75	-19:26:17.7	1.02	1.75	0.776	0.20
11:32:06.33	-20:11:26.0	1.66	4.13	1.31	0.20
11:32:10.36	-19:53:11.1	0.70	1.29	0.878	0.21
11:32:10.97	-20:23:23.3	0.77	2.0	1.372	0.20
11:32:14.00	-19:56:09.7	0.68	0.88	0.37	0.20
11:32:14.76	-20:07:38.9	0.58	1.05	0.853	0.22
11:32:21.68	-20:03:09.9	1.87	4.03	1.104	0.20
11:32:21.69	-19:51:41.1	1.15	1.58	0.456	0.20
11:32:22.75	-20:22:35.6	4.59	11.6	1.333	0.20
11:32:24.86	-19:49:01.2	0.41	0.43	0.068	0.24
11:32:27.09	-19:30:35.8	14.7	18.8	0.353	0.21
11:32:30.06	-19:48:46.9	0.81	1.14	0.491	0.21
11:32:31.30	-19:48:40.1	2.17	7.25	1.734	0.21
11:32:36.80	-20:21:33.9	0.80	1.97	1.295	0.21
11:32:37.60	-20:03:57.8	1.26	2.12	0.748	0.21
11:32:37.88	-19:49:08.7	5.59	9.01	0.686	0.20
11:32:37.91	-19:34:47.5	1.55	4.99	1.681	0.20
11:32:39.38	-20:19:39.1	1.05	1.58	0.587	0.20
11:32:39.69	-20:12:06.1	1.28	3.1	1.271	0.21
11:32:41.55	-20:06:54.6	5.55	21.2	1.927	0.2
11:32:43.84	-20:02:53.8	3.47	3.17	-0.13	0.21

Table 6.20: Spectral indices of the common sources (continued)

RA_{J2000}	DEC_{J2000}	$F_{1.2GHz}$ (mJy)	F_{640MHz} (mJy)	α	E_α
11:32:45.96	-20:20:58.1	1.10	3.82	1.79	0.21
11:32:48.52	-19:57:56.6	0.52	0.87	0.74	0.22
11:32:52.18	-19:48:50.0	1.19	2.93	1.295	0.20
11:32:58.47	-19:34:22.1	0.69	0.98	0.504	0.21
11:32:59.85	-20:04:02.7	7.49	18.2	1.276	0.21
11:33:03.79	-20:12:09.8	4.48	7.25	0.692	0.20
11:33:06.42	-20:18:55.7	1.40	3.08	1.133	0.20
11:33:07.68	-19:52:04.2	0.59	1.16	0.972	0.21
11:33:09.55	-20:11:47.6	1.93	4.22	1.124	0.20
11:33:11.23	-20:07:14.3	0.71	0.86	0.275	0.22
11:33:13.05	-19:45:31.2	1.07	2.0	0.899	0.20
11:33:18.07	-20:04:24.7	33.1	78.3	1.238	0.21
11:33:20.75	-20:16:03.6	1.71	7.59	2.142	0.21
11:33:26.25	-20:02:13.3	1.63	2.09	0.357	0.21
11:33:28.86	-19:55:28.0	1.59	2.95	0.888	0.22
11:33:32.95	-19:40:22.5	2.99	11.9	1.986	0.21
11:33:33.90	-19:59:58.8	4.36	5.81	0.412	0.21
11:33:36.89	-19:54:14.6	932.0	3199.0	1.773	0.2
11:33:55.12	-19:47:13.7	2.41	8.74	1.852	0.2

Table 6.21: Spectral index upper limits of the MeerKAT (only) sources

RA_{J2000}	DEC_{J2000}	$F_{1.2GHz}$ (mJy)	ΔF	α u.l.
11:29:57.58	-19:48:18.1	1.01	0.10	$<$ -2.74
11:30:11.69	-19:59:06.1	0.20	0.02	$<$ -0.41
11:30:28.22	-20:09:28.0	0.62	0.07	$<$ -2.04
11:30:32.98	-20:07:45.0	0.80	0.09	$<$ -2.40
11:30:38.29	-20:07:14.4	0.80	0.09	$<$ -2.40
11:30:44.64	-20:00:05.7	1.11	0.11	$<$ -2.87
11:31:08.71	-19:32:20.0	0.79	0.08	$<$ -2.38
11:32:03.80	-19:54:59.7	0.46	0.06	$<$ -1.61
11:33:48.22	-19:52:44.1	1.15	0.12	$<$ -2.92

Table 6.22: Spectral index upper limits of the uGMRT (only) sources

RA_{J2000}	DEC_{J2000}	F_{640MHz} (mJy)	ΔF	α u.l.
11:29:56.23	-19:44:19.1	0.21	0.02	< 0.07
11:30:08.41	-19:55:31.9	0.69	0.07	< 1.78
11:30:09.15	-19:41:51.4	0.81	0.08	< 2.01
11:30:09.32	-19:47:25.7	1.83	0.18	< 3.18*
11:30:18.68	-19:43:00.3	0.80	0.08	< 1.99
11:30:22.96	-19:56:22.1	0.62	0.06	< 1.62
11:30:27.31	-19:46:04.6	0.64	0.07	< 1.67
11:30:29.53	-19:38:27.3	0.60	0.06	< 1.57
11:30:32.71	-19:54:20.6	0.50	0.05	< 1.31
11:30:36.00	-19:39:42.5	0.77	0.08	< 1.93
11:30:37.97	-19:51:26.1	0.34	0.04	< 0.76
11:30:42.84	-19:46:07.6	0.53	0.06	< 1.40
11:30:43.29	-19:50:45.3	0.38	0.04	< 0.92
11:30:44.06	-19:46:14.0	0.49	0.05	< 1.28
11:30:45.73	-19:53:41.7	0.59	0.06	< 1.55
11:30:46.85	-19:56:46.7	0.44	0.05	< 1.13
11:30:47.32	-19:46:42.3	0.30	0.04	< 0.58
11:30:51.02	-19:49:03.7	0.71	0.07	< 1.82
11:30:51.86	-19:32:23.3	1.42	0.14	< 2.81
11:30:56.07	-19:56:46.7	0.44	0.05	< 1.13
11:30:56.08	-19:51:50.8	0.41	0.05	< 1.03
11:30:58.73	-19:59:54.9	0.91	0.09	< 2.17
11:30:59.39	-19:45:07.8	0.39	0.04	< 0.96
11:31:00.21	-19:47:34.1	0.38	0.04	< 0.92
11:31:04.16	-19:56:18.2	0.47	0.05	< 1.22
11:31:05.82	-19:57:10.7	0.25	0.03	< 0.32
11:31:06.85	-19:33:35.4	0.84	0.08	< 2.06
11:31:08.25	-19:45:04.9	0.42	0.05	< 1.06
11:31:08.50	-19:52:06.5	0.40	0.05	< 0.99
11:31:08.77	-19:44:50.0	0.69	0.07	< 1.78
11:31:09.22	-19:59:08.2	0.45	0.05	< 1.16
11:31:09.54	-20:10:07.9	0.50	0.05	< 1.31
11:31:11.94	-19:44:05.2	0.28	0.04	< 0.48
11:31:12.91	-19:49:46.4	0.38	0.04	< 0.92
11:31:13.02	-19:49:09.2	0.50	0.05	< 1.31
11:31:14.39	-20:05:32.8	0.49	0.05	< 1.28
11:31:14.40	-19:45:19.5	0.39	0.04	< 0.96
11:31:14.48	-19:37:11.7	0.52	0.06	< 1.37
11:31:15.63	-19:42:07.6	0.52	0.06	< 1.37
11:31:16.60	-20:01:32.8	0.38	0.04	< 0.92

Table 6.23: Spectral index upper limits of the uGMRT (only) sources (continued)

RA_{J2000}	DEC_{J2000}	F_{640MHz} (mJy)	ΔF	α u.l.
11:31:16.86	-20:01:50.0	0.42	0.05	< 1.06
11:31:17.74	-20:19:50.8	1.37	0.14	< 2.76
11:31:18.60	-19:45:20.4	0.27	0.04	< 0.43
11:31:19.20	-19:42:28.9	0.27	0.04	< 0.43
11:31:19.37	-20:02:22.1	0.35	0.04	< 0.80
11:31:20.04	-20:14:58.5	0.59	0.06	< 1.55
11:31:20.93	-20:02:38.7	0.48	0.05	< 1.25
11:31:21.71	-19:51:36.7	0.26	0.03	< 0.37
11:31:21.76	-19:56:33.5	0.33	0.04	< 0.72
11:31:22.48	-19:38:09.5	0.41	0.05	< 1.03
11:31:23.90	-20:12:50.1	1.21	0.12	< 2.58
11:31:24.62	-19:31:54.6	0.46	0.05	< 1.19
11:31:28.31	-19:59:02.3	0.44	0.05	< 1.13
11:31:30.23	-19:40:38.5	0.41	0.05	< 1.03
11:31:30.48	-19:54:22.2	0.43	0.05	< 1.10
11:31:31.43	-20:04:10.8	0.34	0.04	< 0.76
11:31:33.10	-19:34:41.7	0.47	0.05	< 1.22
11:31:35.88	-19:42:25.2	0.26	0.04	< 0.37
11:31:36.07	-20:00:23.1	0.22	0.03	< 0.13
11:31:36.44	-19:46:14.1	0.30	0.04	< 0.58
11:31:37.74	-20:14:38.7	0.35	0.04	< 0.80
11:31:38.13	-20:12:01.7	0.41	0.05	< 1.03
11:31:38.64	-19:42:31.7	0.24	0.03	< 0.26
11:31:39.74	-19:52:51.8	0.52	0.06	< 1.37
11:31:40.02	-19:46:04.2	0.45	0.05	< 1.16
11:31:40.30	-20:10:35.4	0.45	0.05	< 1.16
11:31:40.84	-19:45:25.9	0.24	0.03	< 0.26
11:31:42.31	-20:05:06.7	0.18	0.03	< -0.1
11:31:43.04	-19:41:19.5	0.22	0.03	< 0.13
11:31:43.63	-20:11:29.9	0.55	0.06	< 1.45
11:31:43.92	-19:59:42.6	0.50	0.05	< 1.31
11:31:44.03	-19:35:40.2	0.44	0.05	< 1.13
11:31:45.14	-20:17:17.9	0.38	0.04	< 0.92
11:31:46.61	-19:26:45.2	0.63	0.07	< 1.64
11:31:46.91	-19:30:56.8	0.37	0.04	< 0.88
11:31:46.96	-19:54:52.5	1.90	0.21	< 3.23*
11:31:47.51	-19:48:14.8	0.42	0.05	< 1.06
11:31:48.45	-19:59:08.3	0.25	0.03	< 0.32
11:31:48.62	-19:49:01.7	0.33	0.04	< 0.72
11:31:49.05	-19:36:49.3	0.59	0.06	< 1.55
11:31:49.11	-19:42:15.9	1.01	0.10	< 2.32

Table 6.24: Spectral index upper limits of the uGMRT (only) sources (continued)

RA_{J2000}	DEC_{J2000}	F_{640MHz} (mJy)	ΔF	α u.l.
11:31:49.18	-20:05:22.2	0.23	0.03	< 0.20
11:31:49.31	-19:59:18.4	0.23	0.03	< 0.20
11:31:49.97	-20:01:36.7	0.29	0.04	< 0.53
11:31:50.30	-19:42:46.9	1.23	0.12	< 2.61*
11:31:51.27	-19:42:43.0	1.53	0.15	< 2.92*
11:31:51.71	-19:59:57.2	0.40	0.05	< 0.99
11:31:51.91	-19:30:07.1	0.33	0.04	< 0.72
11:31:52.00	-20:21:03.3	0.59	0.06	< 1.55
11:31:52.07	-20:20:06.4	0.42	0.05	< 1.06
11:31:52.26	-19:32:04.8	0.30	0.04	< 0.58
11:31:52.98	-20:03:25.6	0.40	0.05	< 0.99
11:31:54.28	-19:55:28.9	1.20	0.12	< 2.57*
11:31:54.51	-19:52:27.3	0.44	0.05	< 1.13
11:31:54.58	-19:43:48.7	0.41	0.05	< 1.03
11:31:54.69	-20:01:32.5	0.34	0.04	< 0.76
11:31:54.90	-20:07:53.2	0.26	0.03	< 0.37
11:31:55.26	-19:32:59.8	0.49	0.05	< 1.28
11:31:55.48	-19:59:33.9	0.63	0.07	< 1.64
11:31:55.74	-19:55:19.8	0.92	0.09	< 2.19
11:31:57.25	-19:40:01.9	0.37	0.04	< 0.88
11:31:57.41	-20:02:31.9	0.44	0.05	< 1.13
11:31:57.99	-19:56:59.9	0.40	0.05	< 0.99
11:31:58.19	-19:46:58.3	0.58	0.06	< 1.53
11:31:58.20	-20:12:16.7	0.66	0.07	< 1.71
11:31:58.48	-20:20:42.3	0.78	0.08	< 1.95
11:31:58.63	-19:44:35.1	0.22	0.03	< 0.13
11:31:58.86	-20:11:26.4	0.29	0.04	< 0.53
11:31:58.97	-19:47:49.4	0.55	0.06	< 1.45
11:31:59.07	-19:48:16.9	0.23	0.03	< 0.20
11:31:59.16	-19:40:26.8	0.23	0.03	< 0.20
11:31:59.44	-19:40:36.1	0.66	0.07	< 1.71
11:32:00.42	-19:30:01.1	0.48	0.05	< 1.25
11:32:00.65	-20:01:39.9	0.25	0.03	< 0.32
11:32:01.34	-19:37:58.0	0.30	0.04	< 0.58
11:32:02.08	-19:27:59.4	0.77	0.08	< 1.93
11:32:02.56	-19:49:16.6	0.66	0.07	< 1.71
11:32:02.58	-19:37:28.9	0.51	0.05	< 1.34
11:32:02.71	-20:01:35.7	0.34	0.04	< 0.76
11:32:04.41	-19:52:12.1	0.34	0.04	< 0.76
11:32:04.98	-20:05:03.3	0.23	0.03	< 0.20
11:32:05.39	-19:42:51.8	0.27	0.04	< 0.43

Table 6.25: Spectral index upper limits of the uGMRT (only) sources (continued)

RA_{J2000}	DEC_{J2000}	F_{640MHz} (mJy)	ΔF	α u.l.
11:32:05.50	-19:26:24.8	0.86	0.09	< 2.09
11:32:06.15	-19:42:13.4	0.42	0.05	< 1.06
11:32:06.30	-20:15:28.9	0.30	0.04	< 0.58
11:32:07.62	-19:31:45.5	0.36	0.04	< 0.84
11:32:08.67	-20:04:08.0	0.36	0.04	< 0.84
11:32:09.95	-20:05:03.7	0.52	0.06	< 1.37
11:32:10.02	-19:49:43.9	0.72	0.07	< 1.84
11:32:11.10	-19:38:42.0	0.39	0.04	< 0.96
11:32:11.32	-19:51:33.6	0.22	0.03	< 0.13
11:32:11.38	-19:39:31.3	0.37	0.04	< 0.88
11:32:11.63	-19:49:44.3	0.19	0.03	< -0.07
11:32:12.66	-19:54:56.1	0.20	0.03	< 0.32
11:32:12.67	-19:49:56.5	0.20	0.03	< 0.32
11:32:12.79	-20:08:18.8	0.19	0.03	< -0.07
11:32:13.02	-19:42:09.6	0.39	0.04	< 0.96
11:32:13.41	-19:39:39.9	0.45	0.05	< 1.16
11:32:13.79	-19:38:54.8	0.30	0.04	< 0.58
11:32:14.14	-19:42:35.9	0.22	0.03	< 0.13
11:32:14.23	-19:31:37.4	0.42	0.05	< 1.06
11:32:14.31	-19:52:54.0	0.23	0.03	< 0.20
11:32:14.46	-20:14:02.4	0.30	0.04	< 0.58
11:32:16.26	-20:16:47.1	0.35	0.04	< 0.80
11:32:16.36	-20:10:22.7	0.27	0.04	< 0.43
11:32:16.37	-20:00:28.9	0.30	0.04	< 0.58
11:32:16.42	-19:37:16.0	0.46	0.05	< 1.19
11:32:17.02	-19:27:38.7	1.17	0.12	< 2.53
11:32:17.32	-19:55:28.6	0.23	0.03	< 0.20
11:32:17.41	-19:48:25.7	0.31	0.04	< 0.63
11:32:17.62	-19:59:32.6	0.32	0.04	< 0.67
11:32:17.79	-20:05:36.6	0.19	0.03	< -0.07
11:32:18.27	-19:57:32.3	0.51	0.05	< 1.34
11:32:19.61	-19:53:17.0	0.35	0.04	< 0.80
11:32:19.75	-19:53:30.6	0.25	0.03	< 0.32
11:32:20.29	-20:14:36.1	0.37	0.04	< 0.88
11:32:20.38	-19:31:35.6	0.61	0.06	< 1.60
11:32:20.60	-19:35:09.6	0.44	0.05	< 1.13
11:32:20.79	-19:44:25.9	0.31	0.04	< 0.63
11:32:21.21	-19:42:32.7	0.22	0.03	< 0.13
11:32:21.23	-20:05:44.6	0.77	0.08	< 1.93
11:32:22.66	-19:31:09.8	0.68	0.07	< 1.75

Table 6.26: Spectral index upper limits of the uGMRT (only) sources (continued)

RA_{J2000}	DEC_{J2000}	F_{640MHz} (mJy)	ΔF	α u.l.
11:32:22.72	-20:13:59.0	0.68	0.07	< 1.75
11:32:24.40	-20:06:28.0	0.35	0.04	< 0.80
11:32:25.06	-20:13:37.5	0.62	0.06	< 1.62
11:32:26.36	-20:06:57.1	0.37	0.04	< 0.88
11:32:26.54	-20:08:25.8	0.39	0.04	< 0.96
11:32:27.49	-19:30:44.7	0.54	0.06	< 1.42
11:32:28.83	-19:40:52.2	0.30	0.04	< 0.58
11:32:29.52	-20:24:18.0	1.24	0.12	< 2.62
11:32:30.21	-20:06:31.9	0.28	0.04	< 0.48
11:32:32.49	-19:59:25.9	0.45	0.05	< 1.16
11:32:32.53	-19:29:30.6	0.72	0.07	< 1.84
11:32:32.74	-20:22:02.1	0.86	0.09	< 2.09
11:32:33.32	-20:22:27.4	1.31	0.13	< 2.70
11:32:33.53	-20:10:04.4	0.65	0.07	< 1.69
11:32:34.29	-19:46:23.1	0.51	0.05	< 1.34
11:32:34.74	-19:52:44.8	0.75	0.08	< 1.90
11:32:35.38	-20:11:04.7	0.42	0.05	< 1.06
11:32:36.99	-20:04:31.9	0.43	0.05	< 1.10
11:32:37.93	-20:09:07.6	0.30	0.04	< 0.58
11:32:38.91	-19:56:00.4	0.29	0.04	< 0.53
11:32:39.21	-19:45:32.8	0.42	0.05	< 1.06
11:32:40.47	-19:42:41.4	0.30	0.04	< 0.58
11:32:41.19	-20:10:40.2	0.48	0.05	< 1.25
11:32:42.34	-20:08:59.5	0.34	0.04	< 0.76
11:32:43.83	-19:46:41.1	0.25	0.03	< 0.32
11:32:43.93	-20:13:38.1	0.41	0.05	< 1.03
11:32:45.74	-20:09:50.9	0.87	0.09	< 2.11
11:32:46.86	-19:38:57.9	0.73	0.07	< 1.86
11:32:47.21	-20:01:37.5	0.31	0.04	< 0.63
11:32:47.78	-19:57:22.1	0.30	0.04	< 0.58
11:32:49.36	-19:49:07.4	0.40	0.05	< 0.99
11:32:50.86	-19:47:15.0	0.44	0.05	< 1.13
11:32:52.99	-20:21:05.8	0.57	0.06	< 1.50
11:32:53.49	-19:32:38.9	0.91	0.09	< 2.17
11:32:56.53	-19:39:26.5	0.85	0.09	< 2.08
11:32:56.66	-20:04:46.2	0.70	0.07	< 1.80
11:32:56.81	-20:12:49.8	0.72	0.07	< 1.84
11:33:00.32	-19:55:49.2	0.52	0.06	< 1.37
11:33:01.31	-20:08:08.9	0.58	0.06	< 1.53
11:33:03.15	-20:00:34.2	0.60	0.06	< 1.57
11:33:05.00	-19:42:37.0	0.58	0.06	< 1.53

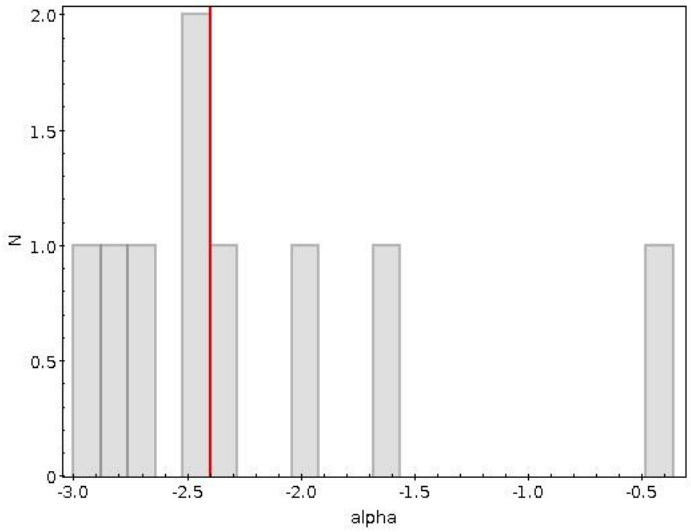

Figure 6.11: Histogram of the upper limits of the spectral indices for sources in A1300 field detected only at 1.2 GHz. For the 640 MHz fluxes we assumed an upper limit of 5σ (i.e. 0.15 mJy). The red line indicates the median value which is -2.4.

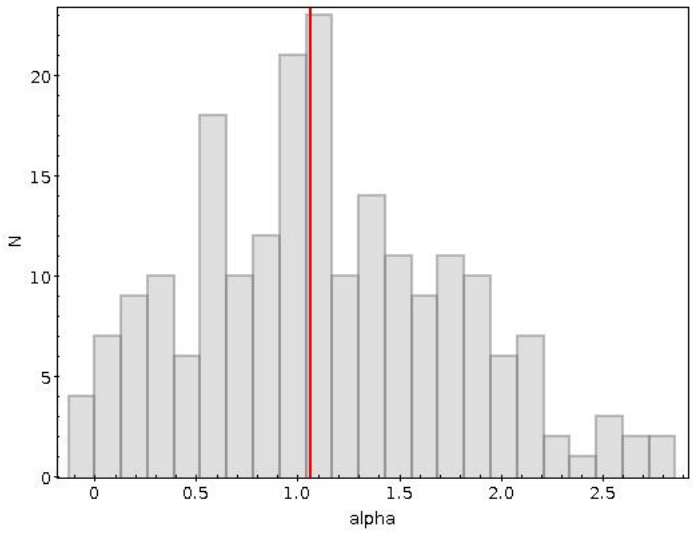

Figure 6.12: Histogram of the upper limits of the spectral indices for sources in A1300 field detected only at 640 MHz. For the 1.2 GHz fluxes we assumed an upper limit of 5σ (i.e. 0.2 mJy). The red line indicates the median value of the distribution which is 1.05.

Table 6.27: Spectral index upper limits of the uGMRT (only) sources (continued)

RA_{J2000}	DEC_{J2000}	F_{640MHz} (mJy)	ΔF	α u.l.
11:33:07.10	-20:05:06.1	0.67	0.07	< 1.73
11:33:09.86	-20:13:41.7	0.73	0.07	< 1.86
11:33:11.03	-20:06:40.9	0.56	0.06	< 1.48
11:33:13.47	-20:05:36.1	1.01	0.10	< 2.32
11:33:16.07	-20:13:42.0	0.63	0.06	< 1.64
11:33:16.42	-20:16:46.0	0.67	0.07	< 1.73
11:33:16.57	-19:51:44.7	1.06	0.11	< 2.39
11:33:17.81	-20:00:59.9	0.81	0.08	< 2.01
11:33:20.03	-19:52:11.7	1.18	0.12	< 2.55
11:33:22.30	-20:09:20.9	0.89	0.09	< 2.14
11:33:47.87	-19:43:23.2	2.92	0.29	< 3.85*
11:33:56.07	-19:47:20.1	5.15	0.51	< 4.67*

6.7 Radio source counts

After the radio analysis performed on the entire sample distributed on an area of 30 arcmin radius centered on the BCG, we restricted the statistical analysis and the radio-optical crossmatch on an area of 12 arcmin radius. Consistently with the analysis performed on MACSJ1931-2634 galaxy cluster, this area corresponds to about 2 virial radii. The A1300 virial radius is 1.53 Mpc as estimated from Ziparo et al. (2012).
We computed the source counts for our radio samples and we compared them with the background in order to study if the dynamical properties of this region result in an enhanced number of radio sources or vice-versa, in a reduced number of radio sources (Venturi et al., 2000, 2001; Prandoni et al., 2006; Mahony et al., 2016). We computed the two logN-logS distributions both for the sources detected with MeerKAT (Fig. 6.13) and those detected with uGMRT (Fig. 6.14).
The MeerKAT logN-logS (black counts) is computed on an area corresponding to 0.125 deg^2. The noise in this area is homogeneus, so we considered a flux limit of F $\geq$ 0.2 mJy, corresponding to 5σ (1σ = 0.04 mJy/b) of the image, which is the source detection threshold of the MeerKAT catalogue. The flux density ranges from 0.2 mJy to 37.4 mJy, which is the flux density of the TAIL radio galaxy in the center.
The total number of sources detected within this area over the flux density threshold is 29. The resulting logN-logS is shown in Figure 6.13. The differential number of sources in each bin is given in N deg^{-2} and the errors are poissonian. The width of each bin is ΔF=F $\times$ log(2.5) (following Venturi et al., 2000, 2001).
For the background estimate (red counts), we considered an integrating area of 0.66 deg^2, obtained by subtracting the 12 arcmin area to the total 30 arcmin area (0.785 deg^2) of our complete sample. In order to take into account the primary beam attenuation at this distance, for the background estimation, we considered a subsample with a flux density limit of 0.25 mJy. The total number of sources in the sub-sample for the background counts is 83.
As visible from Fig.6.13 the counts in the cluster area and in the background do not have the same shape, and we conclude that the number of radio sources in A1300 is not fully in agreement with the background radio source counts. However, it is evident that at fluxes $>$ 10 mJy the sources dominate the background. This result is also true for the uGMRT sample and it is consistent with what we found in previous literature studies (see Venturi et al., 2000, 2001; Giacintucci et al., 2004). The cluster counts are above the background for fluxes F $<$ 0.25 mJy, indicating that there is less statistical incompleteness.
The same method is followed also for the uGMRT sample, integrating over the same total area of 0.125 deg^2, within which the noise is uniform, considering the source detection threshold of 0.15 mJy (5σ). The total number of sources within the integrating area is 96. We plot the background (red counts) for comparison obtained,

as for the MeerKAT sample, by subtracting the integrating area of 12 arcmin radius to the total area of 30 arcmin radius. The total background area is 0.66 deg^2. We take into account the primary beam attenuation at this distance, considering, as we did for the MeerKAT sample, for the background an higher threshold of 0.2 mJy. The number of sources in the reduced sub-sample for the background integration is 222. The resulting logN-logS is shown in Figure 6.14.
The cluster counts and the background have almost the same shape, with the exception of the interval of flux density $2.5 < F < 40$ mJy, within which, the shape is different and the sources dominate the background. The source counts are above the background for flux density $F > 10$ mJy.

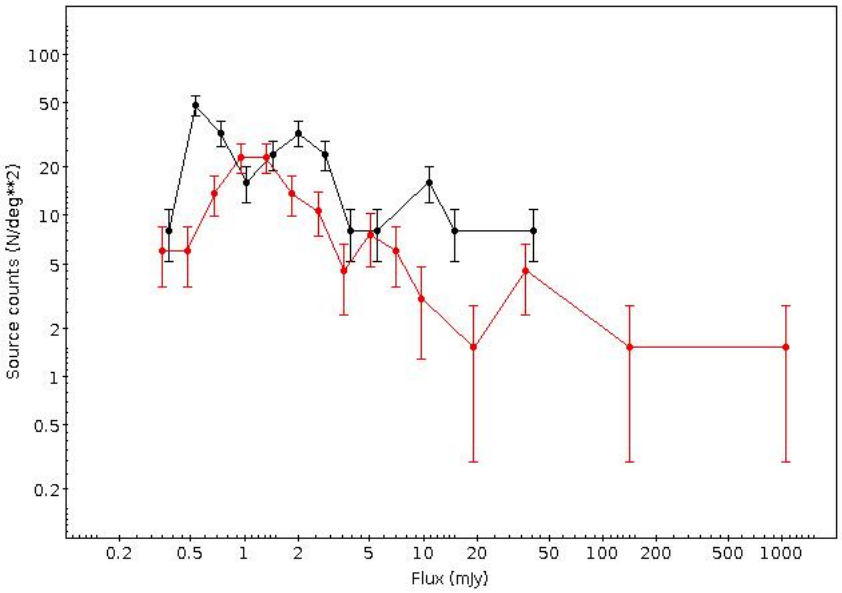

Figure 6.13: Differential radio source counts in A1300 at 1.2 GHz. The total integrating area, equivalent to 2 virial radii, is of 0.125 deg^2 (black counts). The background integrating area is of 0.66 deg^2 (red counts). The sources dominate the background for fluxes > 10 mJy.

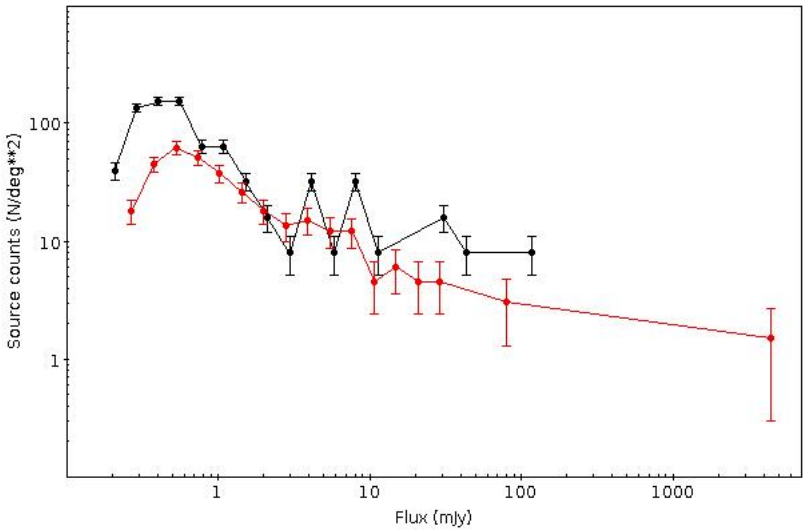

Figure 6.14: Differential radio source counts in A1300 at 640 MHz. The total integrating area, equivalent to 2 virial radii, is of 0.125 deg^2 (black counts). The background integrating area is of 0.66 deg^2 (red counts). The sources dominate the background for fluxes > 10 mJy.

6.8 Optical identifications

We searched for optical counterparts of the radio sources detected in our catalogues using *Subaru*-SuprimeCam photometric catalogues[5], limited by magnitude $m_{g'}$= 25.85 (blue filter) and $m_{r'}$= 26.28 (red filter). The magnitude values are given at 5σ. Magnitudes have been corrected for the galactic extinction. Consistently with the statistical source counts, we performed our search within two virial radii (i.e. 3 Mpc) from the cluster center.
The radio positional error is given by the ratio (HPBW/2×SNR) of the faintest source (5σ) according to the method adopted in Prandoni et al. (2000). In the MeerKAT sample the radio positional error is ~ 1.2 arcsec. In the uGMRT sample the error is ~ 0.5 arcsec. The optical positional error is of the order of ~ 0.02 arcsec. To crossmatch our catalogues, according to the method adopted in Giacintucci et al. (2004), we considered the parameter R, defined as:

$$R^2 = \frac{\Delta^2_{r-o}}{\sigma^2_r + \sigma^2_g} \tag{6.3}$$

Here, Δ^2_{r-o} is the offset between the radio and the optical positions, σ^2_g is the uncertainty in the galaxy position, and σ^2_r is the uncertainty in the radio position. For our radio sources we considered reliable identifications those with R < 3, which

[5]https://archive.stsci.edu/prepds/clash/

corresponds to an offset of the order of 3". In Fig.6.15 we report the offset between the radio and the optical coordinates. After the crossmatch we further visually inspected each source in order to assess the reliability of the matches.

The total number of radio galaxies crossmatched with Suprime r' and g' bands resulted 96. We found 73 optical counterparts in r' and 55 in g', i.e. about ∼75% and ∼57% of our sample respectively. We report upper limits (>) in the blue magnitude for the missing 18 sources.
There are 12 cases of uncertainty in the identification of the optical counterparts in r' and only one case in g'. In these cases we considered the closest source the most reliable counterpart.
Tab. 6.28 and Tab. 6.29 show the result of our cross-match: we report in columns 1 and 2 the Suprime r' coordinates (J2000), in column 3 the radio ID as derived from the original initial catalogue, in 4 and 5 we report the radio coordinates (J2000) and in column 6, 7, 8 the photometric information.
In boldface we report those sources that are consistent with being cluster members. The BCG (source ID 201), of colour 1.4, is reported with an asterisk.
In order to test the reliability of our match, we shifted the radio coordinates of tens arcsec and we repeated the match step. We get on average 12 matching, meaning that about 8-10% of the associations could be random.

The redshift information for the optical counterparts are taken from VIMOS-VLT within the ESO GO Large Programme (PI Böringher), number 169.A-0595 (see Ziparo et al., 2012). We found 21 slits placed on the optical counterparts among which 17 have spectroscopic redshift. Considering also the spectra found from NED database[6], reported with an asterisk in Tab. 6.30 and following, we have a total of 21 redshifts.
We found that 9 galaxies are consistent with being cluster members (7 spectra are extracted from our analysis and 2 spectra are taken from NED database). We considered reliable associations to the cluster A1300 those galaxies with $0.29 < z < 0.31$ using the same interval discussed in Ziparo et al. (2012).
The cluster members are highlighted in boldface.
We report in columns 1 and 2 the radio coordinates (J2000), in column 3 the original radio ID, in 4 and 5 we report the fluxes at 1.2 GHz and 640 MHz respectively, in column 6 the spectral index, in column 7 we report the spectroscopic redshifts that we estimated, or with an asterisk the redshifts from NED database, in columns 8 and 9 we report the radio powers at 1.2 GHz and 0.6 GHz respectively. There is only one source which belongs to the MeerKAT sample only, indicated with radio ID 312*. We can separate between two cases to classify the radio powers: we report for those sources which have the radio flux density and the redshift information a true radio power; we report an upper limit (<) on the radio power at 5σ for those

[6]https://ned.ipac.caltech.edu/

Table 6.28: Optical identifications

RA Suprime (r')	DEC Suprime (r')	Radio ID	RA radio hms	DEC radio dms	g'mag	r'mag	(g'-r')
11:31:04.18	-19:56:18.57	320	11:31:04.16	-19:56:18.25	24.42	23.94	0.47
11:31:05.79	-19:57:11.00	391	11:31:05.82	-19:57:10.75	23.93	22.08	1.85
11:31:08.49	-19:52:06.39	314	11:31:08.50	-19:52:06.55	18.45	18.06	0.38
11:31:09.25	-19:59:19.90	311	11:31:09.21	-19:59:20.55	23.34	22.26	1.07
11:31:09.14	-19:59:10.71	390	11:31:09.22	-19:59:08.28	> 25.55	24.99	> 0.55
11:31:12.90	-19:49:46.14	306	11:31:12.91	-19:49:46.49	> 25.55	24.94	> 0.60
11:31:12.89	-19:49:11.51	305	11:31:13.02	-19:49:09.25	> 25.55	24.48	> 1.06
11:31:13.05	-19:49:09.31	305	11:31:13.02	-19:49:09.25	23.02	21.91	1.10
11:31:13.73	**-20:00:21.51**	**304**	**11:31:13.70**	**-20:00:21.85**	**21.35**	**19.95**	**1.40**
11:31:16.90	-20:01:49.82	296	11:31:16.86	-20:01:50.08	> 25.55	23.10	> 2.44
11:31:16.69	-20:01:49.61	296	11:31:16.86	-20:01:50.08	> 25.55	23.67	> 1.88
11:31:20.91	-20:02:39.67	286	11:31:20.93	-20:02:38.77	22.22	20.54	1.68
11:31:21.72	-19:51:36.17	285	11:31:21.71	-19:51:36.79	21.10	20.51	0.58
11:31:21.78	-19:56:33.76	284	11:31:21.76	-19:56:33.56	> 25.55	24.60	> 0.94
11:31:22.47	-19:47:32.82	280	11:31:22.46	-19:47:32.84	> 25.55	23.21	> 2.33
11:31:24.75	-20:01:10.61	274	11:31:24.67	-20:01:10.40	> 25.55	24.15	> 1.39
11:31:26.90	-19:53:27.30	273	11:31:26.85	-19:53:27.54	21.98	21.95	0.02
11:31:27.52	-19:51:47.89	271	11:31:27.50	-19:51:47.46	> 25.55	23.79	> 1.75
11:31:28.44	-19:59:02.79	270	11:31:28.31	-19:59:02.39	18.85	18.79	0.05
11:31:30.43	-19:54:21.50	267	11:31:30.48	-19:54:22.27	23.17	22.56	0.60
11:31:32.47	-19:46:58.29	265	11:31:32.50	-19:47:00.21	> 25.55	21.69	> 3.85
11:31:32.52	-19:47:00.07	265	11:31:32.50	-19:47:00.21	22.01	20.78	1.22
11:31:36.06	-20:00:22.83	260	11:31:36.07	-20:00:23.18	22.22	20.68	1.53
11:31:36.45	-19:46:14.20	259	11:31:36.44	-19:46:14.19	21.57	20.65	0.91
11:31:39.73	-19:52:51.96	250	11:31:39.74	-19:52:51.83	24.17	22.95	1.22
11:31:40.01	-19:46:03.95	249	11:31:40.02	-19:46:04.27	19.36	18.59	0.77
11:31:40.81	-19:45:26.20	246	11:31:40.84	-19:45:25.99	21.45	20.29	1.15
11:31:43.92	-19:59:42.81	237	11:31:43.92	-19:59:42.69	22.65	22.09	0.56
11:31:43.84	-19:52:45.81	234	11:31:43.96	-19:52:44.86	20.24	18.89	1.34
11:31:47.13	**-19:54:52.77**	**228**	**11:31:46.96**	**-19:54:52.54**	**21.05**	**19.63**	**1.41**
11:31:47.49	-19:48:15.14	227	11:31:47.51	-19:48:14.87	> 25.55	24.06	> 1.48
11:31:48.41	-19:50:45.23	223	11:31:48.38	-19:50:45.30	23.33	22.64	0.69
11:31:48.48	-19:59:08.44	222	11:31:48.45	-19:59:08.30	20.80	20.16	0.64
11:31:48.56	**-19:49:02.21**	**221**	**11:31:48.62**	**-19:49:01.74**	**21.23**	**20.21**	**1.02**
11:31:49.21	-20:05:22.66	219	11:31:49.18	-20:05:22.28	24.00	24.03	-0.03
11:31:49.38	-19:59:17.65	217	11:31:49.31	-19:59:18.43	20.43	19.67	0.75
11:31:49.53	**-19:58:07.66**	**216**	**11:31:49.50**	**-19:58:07.94**	**20.87**	**19.74**	**1.13**
11:31:51.73	-19:59:56.92	212	11:31:51.71	-19:59:57.24	19.80	18.79	1.00
11:31:54.25	-19:55:28.58	204	11:31:54.28	-19:55:28.93	23.06	21.72	1.34
11:31:54.27	**-19:53:50.82**	**200**	**11:31:54.29**	**-19:53:57.53**	**20.86**	**19.41**	**1.45**
11:31:54.18	**-19:55:39.82**	**201***	**11:31:54.31**	**-19:55:40.53**	**20.09**	**18.62**	**1.46**
11:31:54.66	-19:52:25.88	203	11:31:54.51	-19:52:27.36	> 25.55	23.84	> 1.70
11:31:54.49	-19:52:27.61	203	11:31:54.51	-19:52:27.36	23.69	22.29	1.40
11:31:54.96	**-19:52:10.20**	**196**	**11:31:54.81**	**-19:52:07.98**	**20.70**	**19.24**	**1.45**

Table 6.29: Optical identifications (continued)

RA Suprime (r')	DEC Suprime (r')	Radio ID	RA radio hms	DEC radio dms	g'mag	r'mag	(g'-r')
11:31:55.46	-19:59:34.21	194	11:31:55.48	-19:59:33.98	> 25.55	23.12	> 2.43
11:31:55.83	-19:55:19.10	193	11:31:55.74	-19:55:19.82	> 25.55	24.03	> 1.51
11:31:57.40	-20:02:32.14	187	11:31:57.41	-20:02:31.94	21.93	20.78	1.14
11:31:57.88	-19:57:00.00	186	11:31:57.99	-19:56:59.92	> 25.55	24.18	> 1.36
11:31:58.19	-19:46:58.21	185	11:31:58.19	-19:46:58.31	22.09	20.42	1.66
11:31:58.61	-19:44:34.93	182	11:31:58.63	-19:44:35.18	> 25.55	24.67	> 0.87
11:31:58.83	-19:44:35.39	182	11:31:58.63	-19:44:35.18	> 25.55	24.06	> 1.48
11:31:59.02	-19:47:48.84	178	11:31:58.97	-19:47:49.42	22.36	21.32	1.03
11:31:59.06	-19:48:17.49	176	11:31:59.07	-19:48:16.96	> 25.55	22.66	> 2.88
11:31:59.08	-19:48:15.98	176	11:31:59.07	-19:48:16.96	23.22	23.83	-0.61
11:32:02.41	-19:49:15.26	170	11:32:02.56	-19:49:16.61	> 25.55	23.31	> 2.24
11:32:02.57	-19:49:16.62	170	11:32:02.56	-19:49:16.61	22.7218	21.7857	0.9361
11:32:02.82	**-19:54:08.72**	**168**	**11:32:02.62**	**-19:54:14.24**	**21.23**	**19.78**	**1.44**
11:32:02.71	-20:01:35.73	169	11:32:02.71	-20:01:35.78	21.00	20.13	0.87
11:32:04.39	**-19:52:12.41**	**166**	**11:32:04.41**	**-19:52:12.19**	**21.14**	**20.39**	**0.74**
11:32:04.95	-20:05:03.21	164	11:32:04.98	-20:05:03.31	20.69	19.88	0.80
11:32:08.66	-20:04:08.68	157	11:32:08.67	-20:04:08.02	18.75	18.44	0.31
11:32:09.98	-20:05:02.75	156	11:32:09.95	-20:05:03.71	> 25.55	21.51	> 4.03
11:32:09.91	-20:05:04.21	156	11:32:09.95	-20:05:03.71	21.65	21.55	0.10
11:32:10.06	-19:49:43.98	155	11:32:10.02	-19:49:43.93	21.13	19.60	1.52
11:32:10.38	-19:53:12.09	154	11:32:10.38	-19:53:12.11	22.69	22.39	0.29
11:32:11.31	-19:51:33.55	151	11:32:11.32	-19:51:33.61	22.10	20.94	1.15
11:32:11.61	-19:49:44.69	149	11:32:11.63	-19:49:44.38	> 25.55	23.39	> 2.15
11:32:12.69	-19:49:56.11	148	11:32:12.67	-19:49:56.58	22.86	22.03	0.82
11:32:12.49	-19:49:57.94	148	11:32:12.67	-19:49:56.58	> 25.55	23.63	> 1.91
11:32:12.61	-19:49:58.45	148	11:32:12.67	-19:49:56.58	> 25.55	22.78	> 2.76
11:32:14.02	-19:56:10.94	141	11:32:14.02	-19:56:10.87	> 25.55	23.26	> 2.29
11:32:14.26	-19:52:53.98	139	11:32:14.31	-19:52:54.00	22.67	21.26	1.40
11:32:16.35	-20:00:29.02	134	11:32:16.37	-20:00:28.93	> 25.55	24.41	> 1.13
11:32:17.26	-19:55:28.89	131	11:32:17.32	-19:55:28.64	> 25.55	24.20	> 1.34
11:32:17.43	-19:48:25.26	130	11:32:17.41	-19:48:25.77	24.40	23.98	0.41
11:32:18.29	-19:57:32.31	127	11:32:18.27	-19:57:32.37	22.00	21.07	0.93
11:32:19.76	-19:53:30.36	125	11:32:19.75	-19:53:30.65	23.04	22.74	0.29
11:32:21.19	-20:05:44.83	118	11:32:21.23	-20:05:44.68	21.54	20.35	1.19
11:32:21.71	-19:51:42.95	116	11:32:21.73	-19:51:42.58	> 25.55	23.56	> 1.98
11:32:24.85	-19:48:59.57	110	11:32:24.87	-19:49:02.13	23.85	23.60	0.25
11:32:24.84	-19:49:02.35	110	11:32:24.87	-19:49:02.13	24.04	22.19	1.84
11:32:30.08	-19:48:48.46	98	11:32:30.11	-19:48:48.36	23.68	21.96	1.72
11:32:31.30	-19:48:41.84	96	11:32:31.25	-19:48:41.48	23.62	21.87	1.74
11:32:31.07	-19:48:43.01	96	11:32:31.25	-19:48:41.48	> 25.55	23.93	> 1.62
11:32:34.73	-19:52:45.05	89	11:32:34.74	-19:52:44.89	18.27	18.24	0.03
11:32:38.91	-19:56:00.56	81	11:32:38.91	-19:56:00.43	21.53	20.53	1.00

sources with the redshift information but for which the radio flux is undetected; the sources without the redshift information are indicated with a symbol -.

Table 6.30: Redshift identifications and radio powers

RA radio (hms)	DEC radio (dms)	Radio ID	$F_{1.2GHz}$ (mJy)	$F_{0.6GHz}$ (mJy)	α	zspec	$logP_{1.2}$	$logP_{0.6}$
11:31:04.16	-19:56:18.25	320	0.2	0.475	1.243	/	-	-
11:31:05.82	-19:57:10.75	391	0.2	0.258	0.366	/	-	-
11:31:08.32	-19:54:19.98	312	2.3845	7.231	1.595	/	-	-
11:31:08.50	-19:52:06.55	314	0.2	0.402	1.003	/	-	-
11:31:09.21	-19:59:20.55	311	4.1831	9.685	1.207	/	-	-
11:31:09.22	-19:59:08.28	390	0.2	0.459	1.194	/	-	-
11:31:09.91	-19:56:59.35	309	1.324	2.312	0.801	/	-	-
11:31:12.91	-19:49:46.49	306	0.2	0.381	0.926	/	-	-
11:31:13.02	-19:49:09.25	305	0.2	0.506	1.334	/	-	-
11:31:13.70	**-20:00:21.85**	**304**	**1.6916**	**3.381**	**0.995**	**0.303**	**23.72**	**24.02**
11:31:16.60	-20:01:32.81	297	0.2	0.384	0.937	/	-	-
11:31:16.86	-20:01:50.08	296	0.2	0.421	1.07	/	-	-
11:31:19.37	-20:02:22.16	290	0.2	0.356	0.829	/	-	-
11:31:19.46	-19:52:40.98	289	0.6005	1.305	1.116	/	-	-
11:31:20.93	-20:02:38.77	286	0.2	0.489	1.285	/	-	-
11:31:21.62	-20:03:13.30	283	1.3994	3.987	1.505	/	-	-
11:31:21.71	-19:51:36.79	285	0.2	0.261	0.382	/	-	-
11:31:21.76	-19:56:33.56	284	0.2	0.339	0.758	/	-	-
11:31:22.46	-19:47:32.84	280	0.3789	0.9	1.243	/	-	-
11:31:24.67	-20:01:10.40	274	10.788	27.85	1.363	/	-	-
11:31:26.85	-19:53:27.54	273	3.9054	7.22	0.883	3.02	24.15	24.42
11:31:27.50	-19:51:47.46	271	1.627	0.928	-0.8	/	-	-
11:31:28.31	-19:59:02.39	270	0.2	0.446	1.153	0.362	< 22.77	23.12
11:31:30.48	-19:54:22.27	267	0.2	0.439	1.13	/	-	-
11:31:31.43	-20:04:10.89	266	0.2	0.34	0.762	/	-	-
11:31:32.50	-19:47:00.21	265	0.5129	0.755	0.555	/	-	-
11:31:36.07	-20:00:23.18	260	0.2	0.221	0.143	0.465	< 22.93	22.97
11:31:36.44	-19:46:14.19	259	0.2	0.309	0.625	0.525	< 22.86	23.05
11:31:39.74	-19:52:51.83	250	0.2	0.524	1.384	/	-	-
11:31:40.02	-19:46:04.27	249	0.2	0.458	1.191	/	-	-
11:31:40.84	-19:45:25.99	246	0.2	0.241	0.268	/	-	-
11:31:42.31	-20:05:06.79	244	0.2	0.186	-0.1	/	-	-
11:31:43.92	-19:59:42.69	237	0.2	0.504	1.328	/	-	-
11:31:43.96	-19:52:44.68	234	7.7391	34.38	2.144	0.2575*	24.26	24.91
11:31:46.96	**-19:54:52.54**	**228**	**0.2**	**1.907**	**3.242**	**0.3027***	**< 22.81**	**23.51**
11:31:47.51	-19:48:14.87	227	0.2	0.422	1.073	/	-	-
11:31:48.38	-19:50:45.30	223	0.7044	0.786	0.157	/	-	-
11:31:48.45	-19:59:08.30	222	0.2	0.259	0.371	/	-	-
11:31:48.62	**-19:49:01.74**	**221**	**0.2**	**0.334**	**0.737**	**0.302**	**< 22.81**	**23.04**
11:31:49.18	-20:05:22.28	219	0.2	0.231	0.207	/	-	-
11:31:49.31	-19:59:18.43	217	0.2	0.236	0.237	/	-	-

Table 6.31: Redshift identifications and radio powers (continued)

RA radio (hms)	DEC radio (dms)	Radio ID	$F_{1.2GHz}$ (mJy)	$F_{0.6GHz}$ (mJy)	α	zspec	$logP_{1.2}$	$logP_{0.6}$
11:31:49.50	**-19:58:07.94**	**216**	**0.3954**	**0.824**	**1.055**	**0.2956**	**23.08**	**23.40**
11:31:49.97	-20:01:36.71	215	0.2	0.298	0.573	/	-	-
11:31:51.71	-19:59:57.24	212	0.2	0.4	0.996	0.2408	< 22.79	23.09
11:31:52.98	-20:03:25.67	388	0.2	0.408	1.025	/	-	-
11:31:54.28	-19:55:28.93	204	0.2	1.203	2.579	/	-	-
11:31:54.29	**-19:53:57.53**	**200**	**37.883**	**95.7**	**1.332**	**0.3054**	**25.03**	**25.43**
11:31:54.31	**-19:55:40.53**	**201**	**12.147**	**30.63**	**1.329**	**0.3077***	**24.53**	**24.94**
11:31:54.51	-19:52:27.36	203	0.2	0.449	1.162	/	-	-
11:31:54.58	-19:43:48.75	202	0.2	0.413	1.042	/	-	-
11:31:54.69	-20:01:32.50	199	0.2	0.345	0.783	/	-	-
11:31:54.81	**-19:52:07.98**	**196**	**2.3072**	**6.548**	**1.499**	**0.3031**	**23.79**	**24.25**
11:31:55.48	-19:59:33.98	194	0.2	0.632	1.654	0.740	< 22.63	23.13
11:31:55.74	-19:55:19.82	193	0.2	0.924	2.2	/	-	-
11:31:56.62	-19:57:23.80	189	0.3982	0.981	1.296	/	-	-
11:31:57.41	-20:02:31.94	187	0.2	0.448	1.159	/	-	-
11:31:57.99	-19:56:59.92	186	0.2	0.404	1.01	/	-	-
11:31:58.19	-19:46:58.31	185	0.2	0.586	1.545	0.2273	< 22.74	23.21
11:31:58.63	-19:44:35.18	182	0.2	0.222	0.15	/	-	-
11:31:58.67	-20:07:01.54	181	0.4846	1.067	1.134	/	-	-
11:31:58.82	-19:43:56.00	179	1.5523	4.73	1.602	/	-	-
11:31:58.97	-19:47:49.42	178	0.2	0.552	1.459	/	-	-
11:31:59.07	-19:48:16.96	176	0.2	0.23	0.2	/	-	-
11:32:00.65	-20:01:39.93	173	0.2	0.258	0.366	/	-	-
11:32:02.56	-19:49:16.61	170	0.2	0.663	1.723	/	-	-
11:32:02.71	-20:01:35.78	169	0.2	0.345	0.783	/	-	-
11:32:03.62	**-19:54:14.24**	**168**	**1.02**	**4.128**	**2.01**	**0.3067**	**23.38**	**23.99**
11:32:03.80*	-19:54:59.70*	312*	0.464	0.15	-1.62	/	-	-
11:32:04.41	**-19:52:12.19**	**166**	**0.2**	**0.348**	**0.796**	**0.302**	**< 22.81**	**23.05**
11:32:04.98	-20:05:03.31	164	0.2	0.237	0.244	0.3615	< 22.89	22.96
11:32:08.67	-20:04:08.02	157	0.2	0.365	0.864	/	-	-
11:32:09.95	-20:05:03.71	156	0.2	0.523	1.382	/	-	-
11:32:10.02	-19:49:43.93	155	0.2	0.725	1.851	/	-	-
11:32:10.38	-19:53:12.11	154	0.7082	1.293	0.865	/	-	-
11:32:11.32	-19:51:33.61	151	0.2	0.221	0.143	0.612	< 22.97	23.01
11:32:11.63	-19:49:44.38	149	0.2	0.198	-0.017	/	-	-
11:32:12.66	-19:54:56.13	147	0.2	0.208	0.056	/	-	-
11:32:12.67	-19:49:56.58	148	0.2	0.201	0.007	0.675	< 23.01	23.01
11:32:14.02	-19:56:10.87	141	0.6828	0.887	0.376	/	-	-
11:32:14.31	-19:52:54.00	139	0.2	0.232	0.213	/	-	-
11:32:16.37	-20:00:28.93	134	0.2	0.301	0.587	/	-	-
11:32:17.32	-19:55:28.64	131	0.2	0.23	0.2	/	-	-

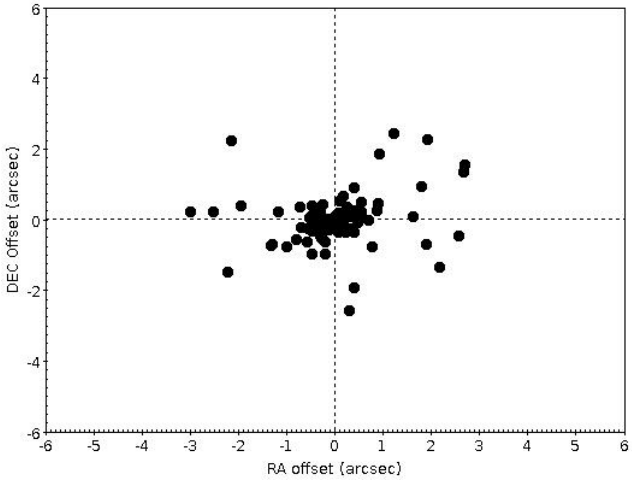

Figure 6.15: The image shows the radio positions compared to the optical positions. We choosed 3" as the reliable distance for the crossmatches further visually inspecting each match.

Table 6.32: Redshift identifications and radio powers (continued)

RA radio (hms)	DEC radio (dms)	Radio ID	$F_{1.2GHz}$ (mJy)	$F_{0.6GHz}$ (mJy)	α	zspec	$logP_{1.2}$	$logP_{0.6}$
11:32:17.41	-19:48:25.77	130	0.2	0.317	0.662	/	-	-
11:32:17.62	-19:59:32.69	129	0.2	0.325	0.698	/	-	-
11:32:17.79	-20:05:36.64	128	0.2	0.196	-0.02	/	-	-
11:32:18.27	-19:57:32.37	127	0.2	0.512	1.351	/	-	-
11:32:19.61	-19:53:17.03	126	0.2	0.35	0.804	/	-	-
11:32:19.75	-19:53:30.65	125	0.2	0.259	0.371	/	-	-
11:32:21.23	-20:05:44.68	118	0.2	0.778	1.953	/	-	-
11:32:21.67	-20:03:11.17	115	1.8784	4.033	1.098	/	-	-
11:32:21.73	-19:51:42.58	116	1.1535	1.581	0.453	/	-	-
11:32:24.87	-19:49:02.13	110	0.4155	0.43	0.049	/	-	-
11:32:30.11	-19:48:48.36	98	0.8198	1.146	0.481	/	-	-
11:32:31.25	-19:48:41.48	96	2.1712	7.25	1.733	/	-	-
11:32:32.49	-19:59:25.99	94	0.2	0.458	1.191	/	-	-
11:32:34.74	-19:52:44.89	89	0.2	0.754	1.908	0.389*	< 22.66	23.24
11:32:38.91	-19:56:00.43	81	0.2	0.296	0.563	/	-	-

6.9 Radio-optical overdensities

In order to explore the properties of the radio galaxies in our sample and the dynamical properties of the environment in which they are located, we analyzed their distribution on the Color-Magnitude diagram (Fig. 6.16) and we analyzed their spatial distribution within a magnitude range $18.0 < m_{r'} < 21.0$ (Fig. 6.17).
The Color-Magnitude diagram shows the distribution of the galaxies (the entire sample belonging to VIMOS-VLT) divided into the red sequence, i.e. (g'-r') higher than 1.2, and the blue sequence. The dotted line represents the central ~ 1.5 value of the red sequence whereas the dashed lines represent a $\pm\ 3\sigma$ scatter from the central value. The green dots are the radio galaxies detected in our samples (either the MeerKAT galaxies and the uGMRT galaxies). The blue diamonds are those galaxies which have redshifts not consistent with being cluster members. The red diamonds represent those galaxies with redshifts consistent with being cluster members: in particular, six are red galaxies, and three are blue galaxies (Fig. 6.17).
The dotted box represents the selection of those galaxies considered for the normalization in the RLF estimation.
In Fig. 6.17 we report the spatial distribution of the galaxies in our sample. The color scale represents the source spatial density, being the white region the densest region. The black lines are isodensity curves. The small black dots indicate all the optical galaxies with the redshift consistent with being cluster members. The radio galaxies lying under the red sequence without the redshifts are represented by the green dots, whereas the radio galaxies which are distributed on the red sequence whithout the redshifts are represented by the cian dots. Among the radio galaxies, nine have redshifts consistent with being cluster members (biggest dots). Six of them are red galaxies whereas three are blue galaxies; the BCG (green dot) is displaced from the center of the distribution, which is consistent with the disturbed dynamical state of the cluster A1300.

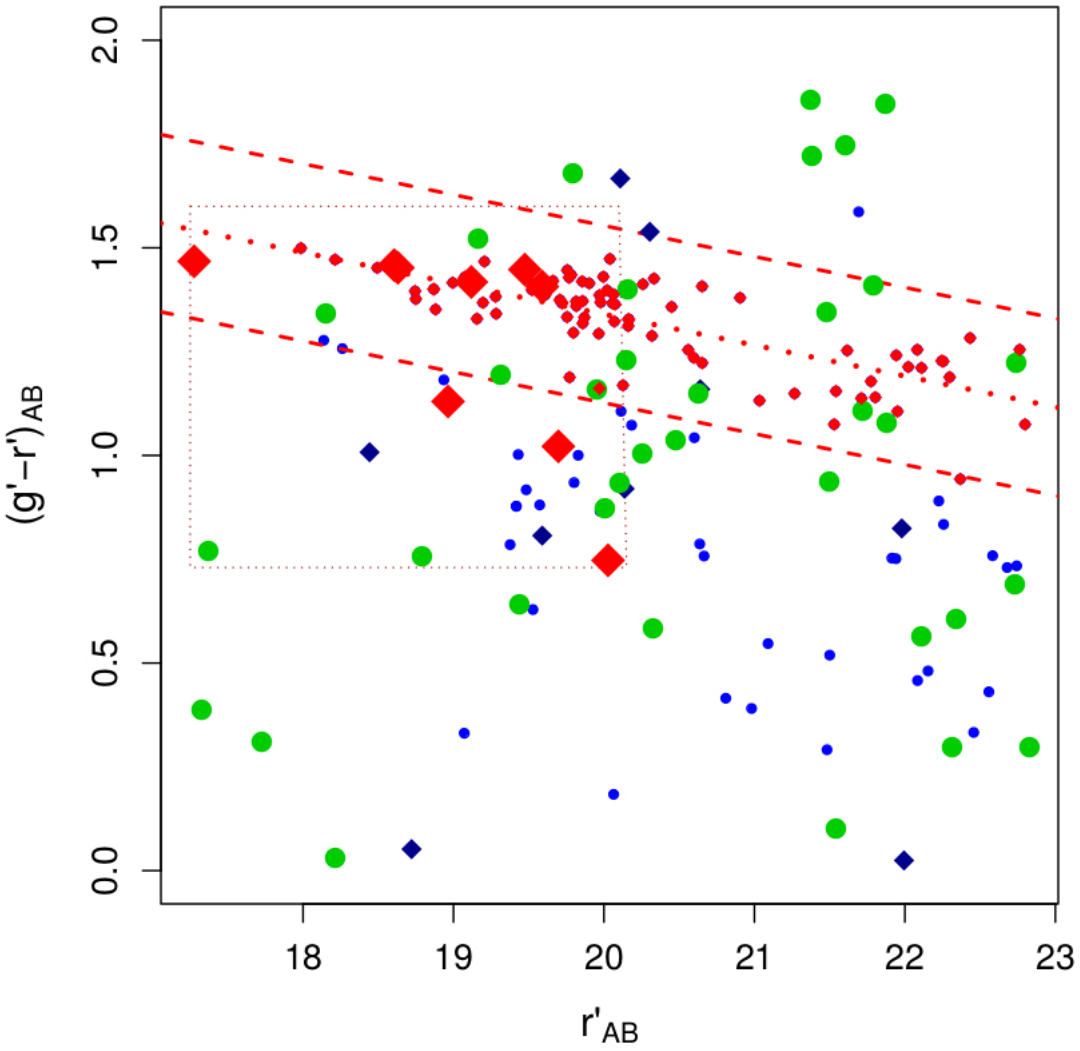

Figure 6.16: The Color-Magnitude diagram shows the galaxies distributed on the red (AGN galaxies) and blue (SF galaxies) sequence. The green dots represent the galaxies from our samples (MeerKAT and uGMRT). The red diamonds are the galaxies with redshift consistent with being cluster members. The blue diamonds are those galaxies with spectroscopic redshift out from the interval $0.29 < z < 0.31$.

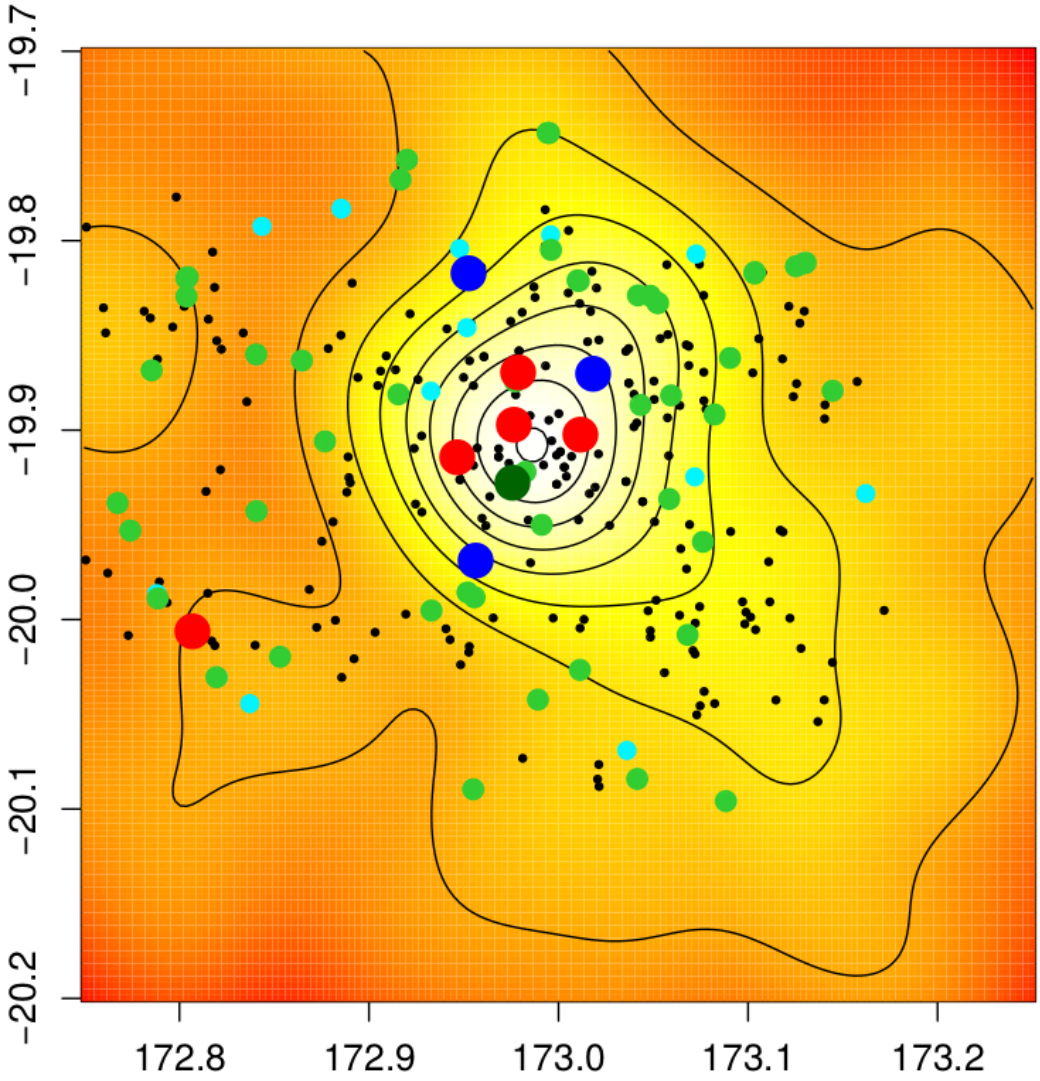

Figure 6.17: Spatial distribution of A1300 galaxies within a magnitude range $18.0 < m_{r'} < 21.0$. The distribution of the optical galaxies (black dots) and of the cluster galaxies could be indicative of the post-merging status of A1300. Indeed, there is an offset of the BCG (green dot) from the center of the distribution.

6.10 Properties of the extended radio galaxies

According to the morphological criterion that we adopted to classify the radio sources in our samples, five radio galaxies are extended in the MeerKAT catalogue, whereas eleven radio galaxies are extended in the uGMRT catalogue. In this Section we report radio-optical overlays by means of optical Suprime and IR GCAV images. The name of the radio sources and the coordinates reported are those from the uGMRT catalogue.

J1131-1954a

This radio galaxy of coordinates RA=11:31:08.32 and δ=-19:54:19.98 is located at a projected linear distance of $\sim$ 2.9 Mpc from the BCG at the cluster redshift towards West direction. Its morphology is difficult to classify, it could be a case of blending. Its flux at 1.2 GHz is 2.38 $\pm$ 0.24 mJy, whereas at 640 MHz is 7.23 $\pm$ 0.72 mJy.

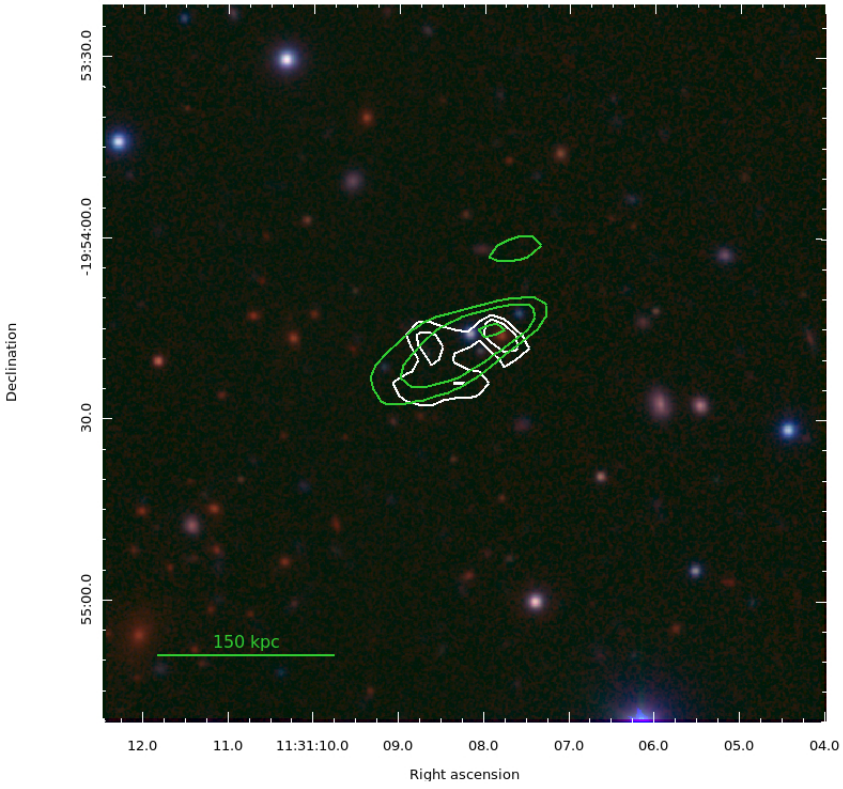

Figure 6.18: **J1131 − 1954a**. Radio contours at 5 sigma from new MeerKAT (i.e. 0.144 mJy/beam) and uGMRT (i.e. 0.135 mJy/beam) data at 1.2 GHz (green) and 640 MHz (white) respectively, overlayed on IR GCAV Ks band, r band CFHT and g' band Suprime (R,G,B).

J1131-2001c

This radio galaxy, located at 2.4 Mpc from the BCG in projected linear distance towards South, could be a distant FRII. However, its morphology is difficult to classify (Fig.6.19). It has coordinates RA=11:31:24.67 and δ=-20:01:10.40. Its integrated flux at 1.2 GHz is 10.7 $\pm$ 1.07 mJy, whereas at 640 MHz the flux is 27.8 $\pm$ 2.8 mJy.

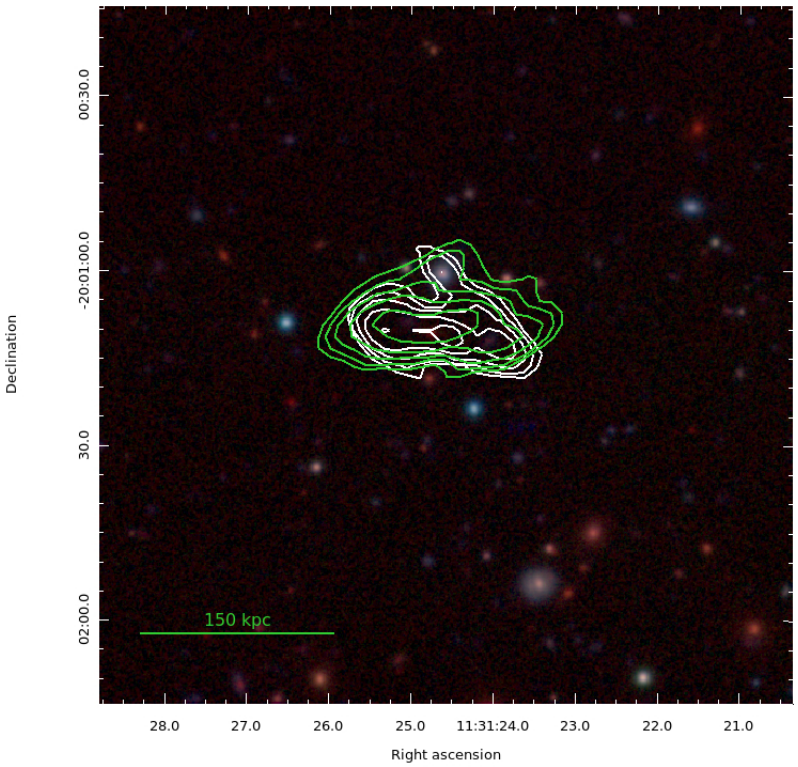

Figure 6.19: **J1131 − 2001c**. Radio contours at 5 sigma from new MeerKAT (i.e. 0.175 mJy/beam) and uGMRT (i.e. 0.165 mJy/beam) data at 1.2 GHz (green) and 640 MHz (white) respectively, overlayed on IR GCAV Ks band, r band CFHT and g' band Suprime (R,G,B).

J1131-1935a

This radio galaxy has coordinates RA=11:31:40.39 and δ=-19:35:00.17. According to the radio contours at 1.2 GHz (green) and at 640 MHz, it could be classified as an FRII radio galaxy (Fig.6.20). It is located at a projected linear distance of 5.6 Mpc, if we consider the cluster scale and cosmology. Its flux density is 0.8 $\pm$ 0.09 mJy at 1.2 GHz whereas at 640 MHz is 4.9 $\pm$ 0.27 mJy.

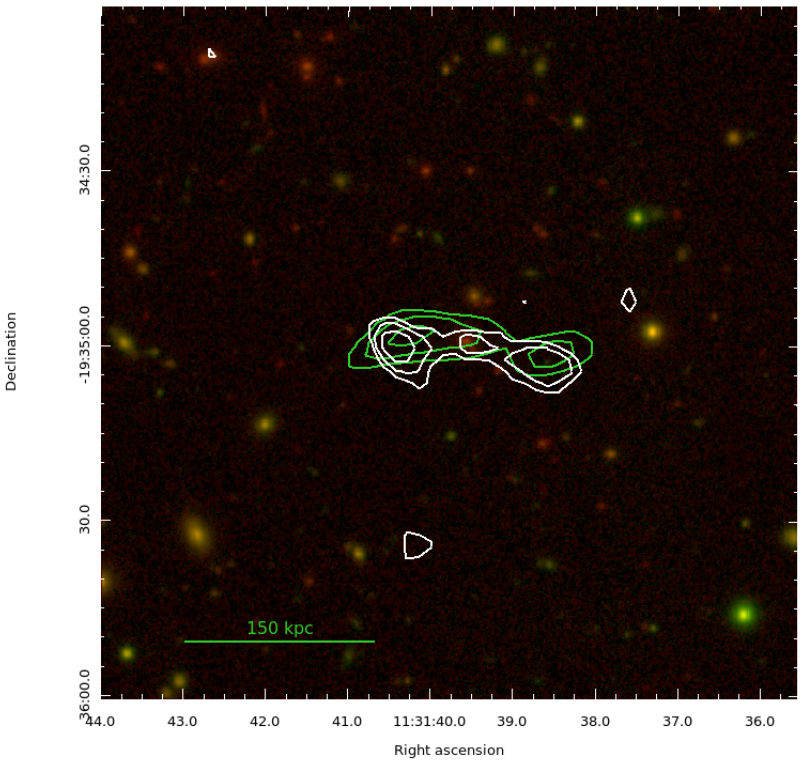

Figure 6.20: **J1131 − 1935a**. Radio contours at 5 sigma from new MeerKAT (i.e. 0.158 mJy/beam) and uGMRT (i.e. 0.119 mJy/beam) data at 1.2 GHz (green) and 640 MHz (white) respectively, overlayed on IR GCAV Ks band, r band CFHT and g' band Suprime (R,G,B).

J1131-1938b

This radio galaxy of coordinates RA=11:31:42.79 and δ=-19:38:09.41 is located at a projected linear distance of $\sim$ 4.7 Mpc from the BCG at the cluster redshift towards North direction. It could be classified as an FRII radio galaxy. Its flux at 1.2 GHz is 6.49 $\pm$ 0.65 mJy, whereas at 640 MHz is 10.9 $\pm$ 1.09 mJy.

J1131-1952d

This radio galaxy of coordinates RA=11:31:43.96 and δ=-19:52:44.86 is located at a projected linear distance of $\sim$ 970 kpc from the BCG at the cluster redshift towards North-West direction. It is classified as a WAT radio galaxy by Reid et al. (1999). They report its redshift at z=0.257, so it is part of a foreground group. Its flux at 1.2 GHz is 10.0 $\pm$ 1.0 mJy, whereas at 640 MHz is 34.3 $\pm$ 3.9 mJy.

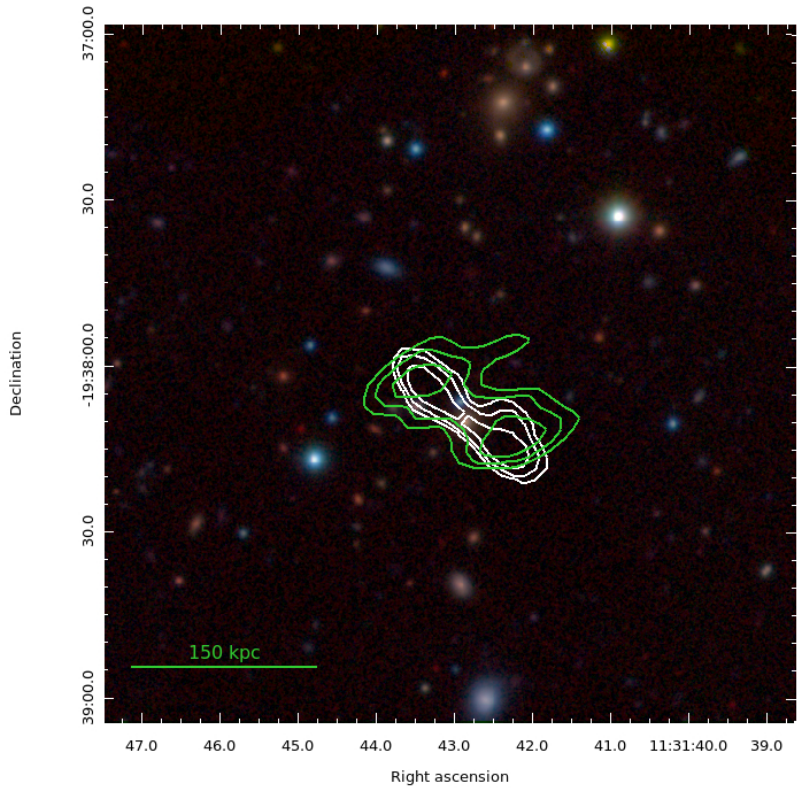

Figure 6.21: **J1131 − 1938b**. Radio contours at 5 sigma from new MeerKAT (i.e. 0.150 mJy/beam) and uGMRT (i.e. 0.115 mJy/beam) data at 1.2 GHz (green) and 640 MHz (white) respectively, overlayed on IR GCAV Ks band, r band CFHT and g' band Suprime (R,G,B).

J1131-1954c

This radio galaxy could be an FRII radio galaxy according to its morphology (Fig.6.23). It has coordinates RA=11:31:46.96 and δ=-19:54:52.54. The radio galaxy J1131-1954c is located at a projected linear distance of $\sim$ 508 kpc towards West from the central BCG. It flux at 1.2 GHz is 0.7 $\pm$ 0.08 mJy, whereas at 640 MHz the integrated flux density is 1.9 $\pm$ 0.21.

J1131-1953b

This galaxy is classified as a tail radio galaxy. Following Reid et al. (1999) nomenclature, it corresponds to the A2 object located towards North in respect to the BCG. It has coordinates RA=11:31:54.31 and δ=-19:53:57.53. It is located at a projected linear distance of $\sim$ 380 kpc only from the BCG. Its flux is 37.4 $\pm$ 3.7 at 1.2 GHz whereas at 640 MHz the integrated flux is 95.7 $\pm$ 9.5 mJy. In Figure 6.24

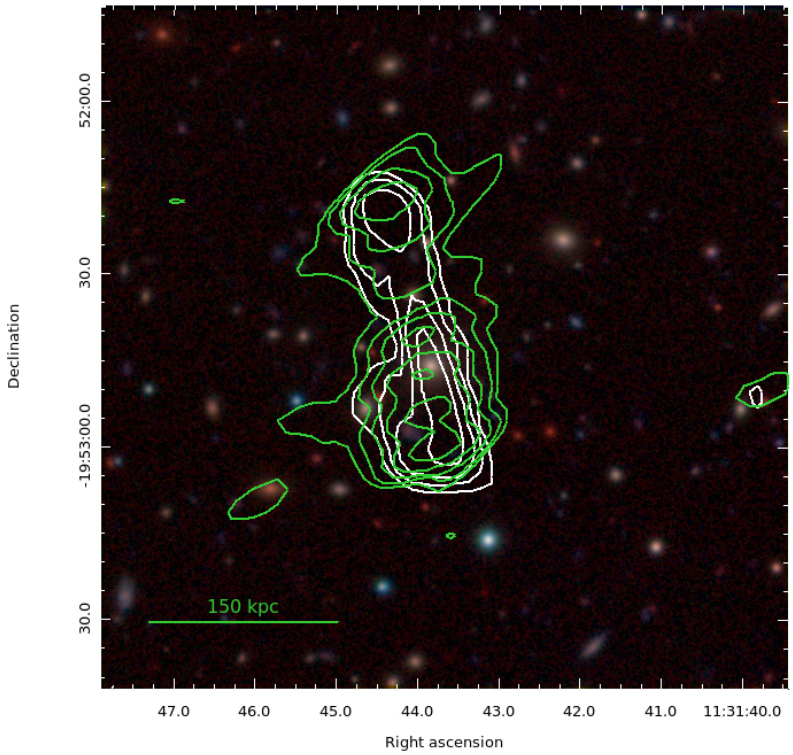

Figure 6.22: **J1131 − 1952d**. Radio contours at 5 sigma from new MeerKAT (i.e. 0.12 mJy/beam) and uGMRT (i.e. 0.17 mJy/beam) data at 1.2 GHz (green) and 640 MHz (white) respectively, overlayed on IR GCAV Ks band, r band CFHT and g' band Suprime (R,G,B).

we indicated with a red cross the central BCG in A1300 galaxy cluster.

J1132-1954a

This galaxy is classified as a tail radio galaxy according to our morphological criterion. It has coordinates RA=11:32:02.62 and δ=-19:54:14.24. It is located at a projected linear distance of $\sim$ 600 kpc from the BCG. Its flux is 1.02 $\pm$ 0.1 at 1.2 GHz whereas at 640 MHz the integrated flux is 4.12 $\pm$ 0.47 mJy. Its extention at 640 MHz is of 120 kpc at the cluster redshift (Figure 6.25).

J1132-2022b and J1132-2022c

This two radio galaxies are challenging to classify: they could represent a case of blending, as visible from Fig.6.26. J1132-2022b has coordinates RA=11:32:21.64

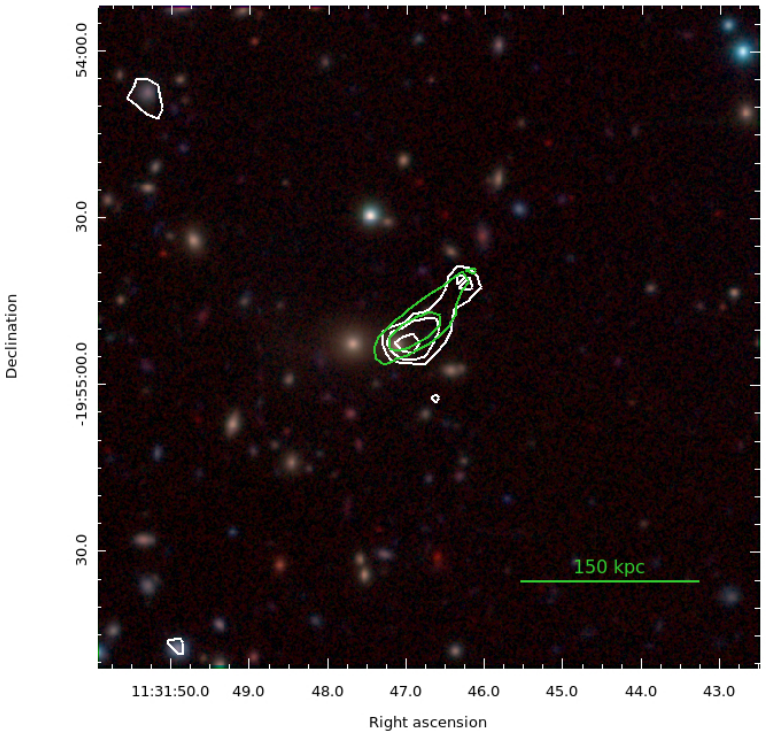

Figure 6.23: **J1131 − 1954c**. Radio contours at 5 sigma from new MeerKAT (i.e. 0.20 mJy/beam) and uGMRT (i.e. 0.187 mJy/beam) data at 1.2 GHz (green) and 640 MHz (white) respectively, overlayed on IR GCAV Ks band, r band CFHT and g' band Suprime (R,G,B).

and δ=-20:22:26.04 and J1132-2022c has coordinates RA=11:32:28.63 and δ=-20:22:57.57. The complex structure is located at a projected linear distance of $\sim$ 7.6 Mpc from the BCG at the cluster redshift towards South direction. Indeed at this distance, the blended structure is covered only by the GCAV Ks band and not from the optical bands. The integrated flux of the total structure is about $\sim$ 16 $\pm$ 0.5 mJy, considering the sum of the two contributions at 640 MHz.

J1132-2006d

This galaxy could be classified as an FRII radio galaxy. It has coordinates RA=11:32:41.51 and δ=-20:06:56.08. It is located at a projected linear distance of $\sim$ 4.3 Mpc from the BCG at the cluster scale. Its flux is 5.55 $\pm$ 0.55 at 1.2 GHz whereas at 640 MHz the integrated flux is 21.2 $\pm$ 2.1 mJy.

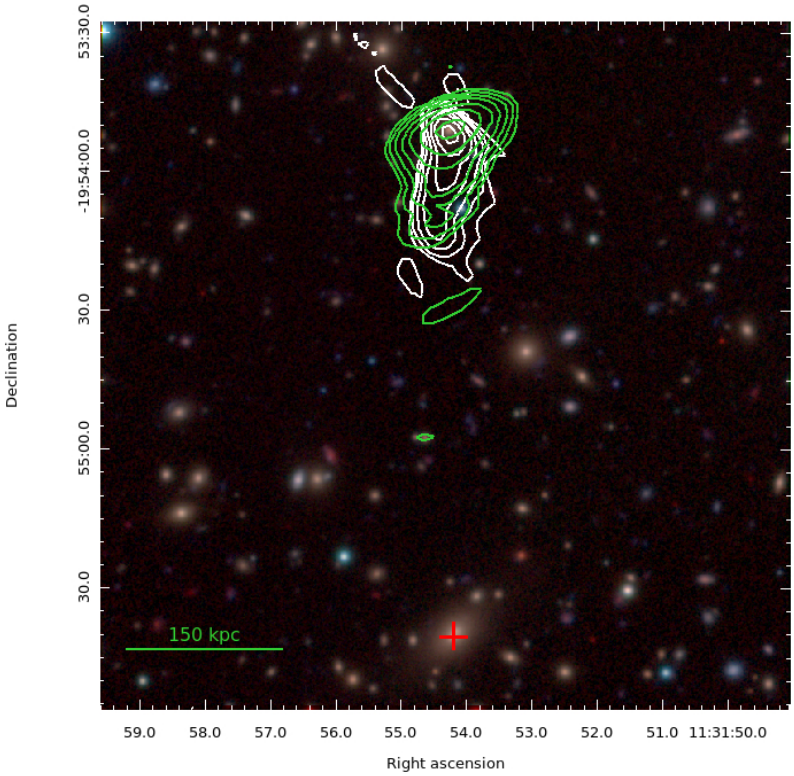

Figure 6.24: **J1131 − 1953b**. Radio contours at 5 sigma from new MeerKAT (i.e. 0.31 mJy/beam) and uGMRT (i.e. 0.33 mJy/beam) data at 1.2 GHz (green) and 640 MHz (white) respectively, overlayed on IR GCAV Ks band, r band CFHT and g' band Suprime (R,G,B).

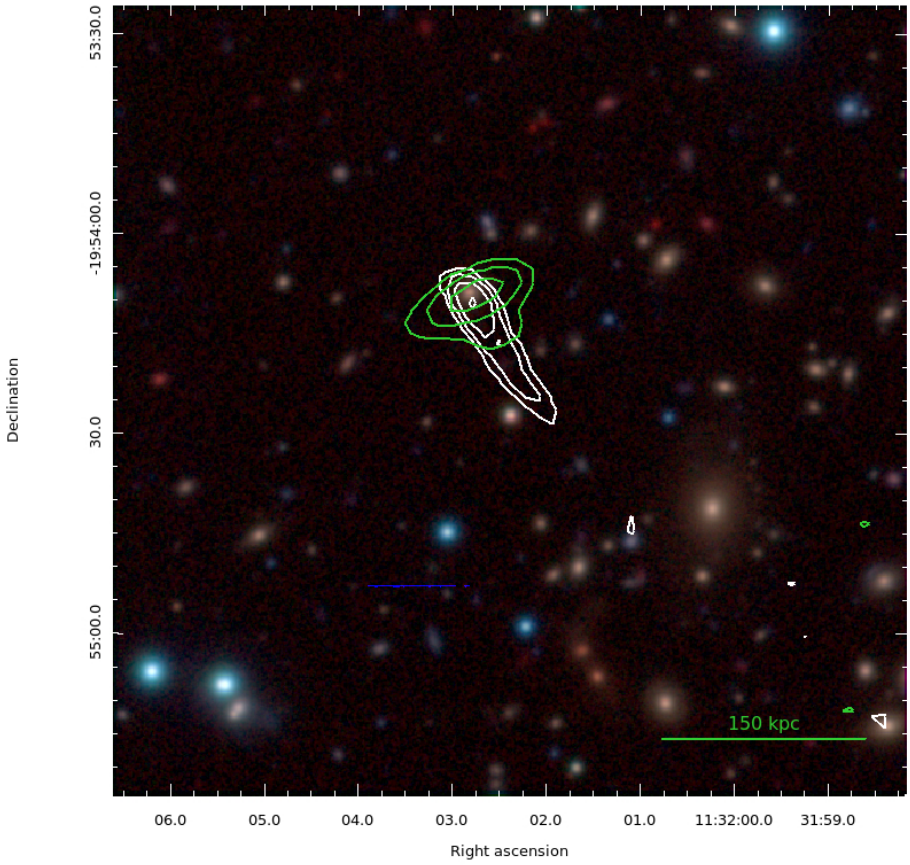

Figure 6.25: **J1132 − 1954a**. Radio contours at 3 sigma from new MeerKAT (i.e. 0.31 mJy/beam) and uGMRT (i.e. 0.33 mJy/beam) data at 1.2 GHz (green) and 640 MHz (white) respectively, overlayed on IR GCAV Ks band, r band CFHT and g' band Suprime (R,G,B).

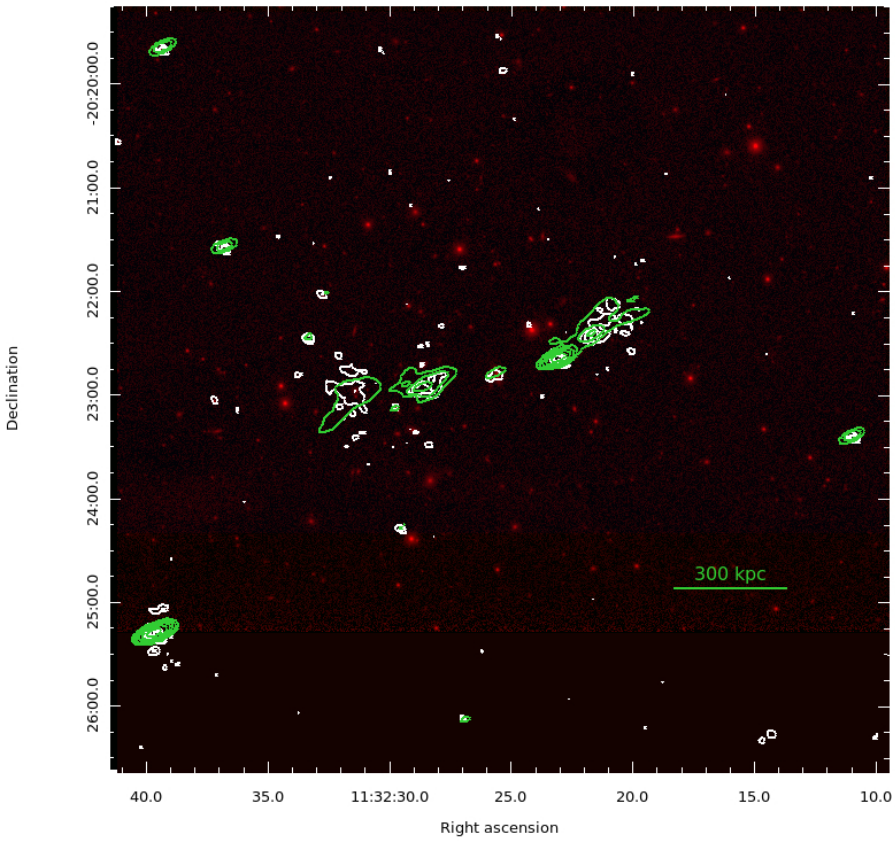

Figure 6.26: **J1132 − 2022b, J1132 − 2022c**. Radio contours at 5 sigma from new MeerKAT (i.e. 0.17 mJy/beam) and uGMRT (i.e. 0.10 mJy/beam) data at 1.2 GHz (green) and 640 MHz (white) respectively, overlayed on IR GCAV Ks band.

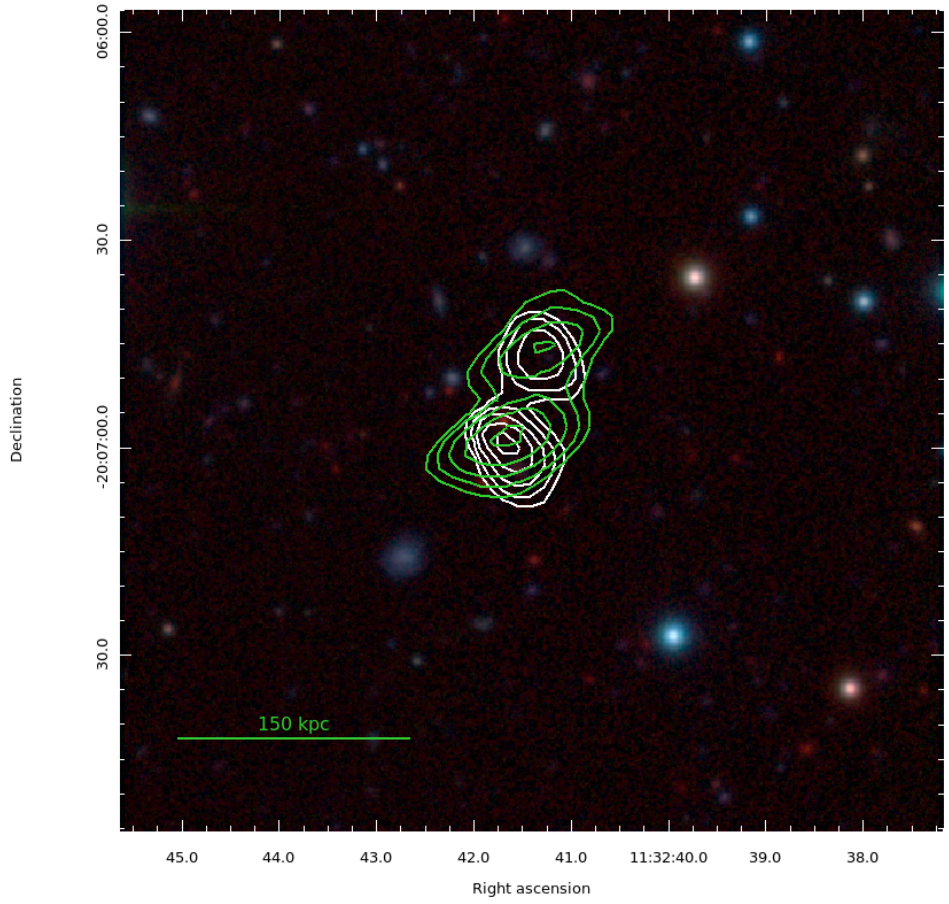

Figure 6.27: **J1132 − 2006d**. Radio contours at 5 sigma from new MeerKAT (i.e. 0.25 mJy/beam) and uGMRT (i.e. 0.2 mJy/beam) data at 1.2 GHz (green) and 640 MHz (white) respectively, overlayed on IR GCAV Ks band, r band CFHT and g' band Suprime (R,G,B).

6.11 The Radio Luminosity Function

The Radio Luminosity Function is a powerful tool for investigating the statistical properties of a population of objects. It provides the probability of a galaxy to be radio loud with a radio power higher than a given value of P. According to the same method adopted for the computation of the RLF for MACSJ1931-2634 sample of galaxies, in this Section, we report the Bivariate Luminosity Function of A1300 sample of galaxies.
We estimated the RLF at 1.2 GHz and at 640 MHz, and we compared the 1.2 GHz result with Venturi et al. (2000), following their same method for the computation and rescaling the result to our cosmology. We also reanalyzed our RLF following the same method adopted in Branchesi et al. (2006), and we compared with them our results. We are aware that our cases are different in terms of detection limits, sample selection and data analysis. However, the comparison with a local (z=0.04) RLF in Venturi et al. (2000) was performed in order to assess a possible evolution with z. The comparison with Branchesi et al. (2006) was performed in order to inspect how the RLF amplitude varies at a comparable redshift (i.e. z=0.3) and within the same logarithmic intervals.
The confirmed cluster members for our computation are nine galaxies which have optical counterparts with magnitude between $18.6 < m_{r'} < 20.3$. The power ranges from $\log P_{1.2GHz}$(W Hz^{-1})= 22.81 to $\log P_{1.2GHz}$(W Hz^{-1})= 25.21 for the MeerKAT sample and from $\log P_{0.6GHz}$(W Hz^{-1})= 22.69 to $\log P_{0.6GHz}$(W Hz^{-1})= 25.49 for the uGMRT sample. Each luminosity interval (ΔlogP) is 0.4 dex in size (Kale et al., 2015). To estimate the Fractional Luminosity Function, we considered the number of elliptical galaxies consistent with being cluster members within the same magnitude interval and the same integrating area. There are 261 galaxies in the same area and with magnitude consistent with our radio sample. Among these, 70 have redshift $0.29 < z < 0.31$, which is the number of objects considered for the normalization.
The resulting Integral Luminosity Functions at 1.2 GHz and at 640 MHz for A1300 radio galaxies are shown in Fig.6.28 and 6.29, compared with Venturi et al. (2000) and Branchesi et al. (2006).
The shape of the Radio Luminosity Function in A1300 is similar to that of A3558 in Venturi et al. (2000) until $\log P_{1.2GHz} \sim 24.0$ (W/Hz), meaning that apparently there is no evolution with z (Stocke et al., 1999); however, it is evident that the amplitude is higher, meaning that statistically there could be higher probability to develop a radio source in A1300.
The amplitude is higher also in respect to the RLF estimated in Branchesi et al. (2006).
The shape of A1300 Radio Luminosity Function at 640 MHz is consistent with the one at 1.2 GHz; apparently, there is a 'jump' in A1300 RLF at $\log P_{0.6GHz} \sim 24.2$ (W/Hz). In literature, they consider the jump as the separation between FRI and

FRII radio galaxies (Ledlow & Owen, 1996).

Table 6.33: A1300 Bivariate Luminosity Function at 1.2 GHz

$\Delta\log P_{1.2}$	Fractional BLF	Integral BLF
22.81-23.21	4/70	0.1284
23.21-23.61	1/70	0.0713
23.61-24.01	2/70	0.0571
24.01-24.41	0/70	0.0285
24.41-24.81	1/70	0.0285
24.81-25.21	1/70	0.0142

Table 6.34: A1300 Bivariate Luminosity Function at 0.6 GHz

$\Delta\log P_{0.6}$	Fractional BLF	Integral BLF
22.69-23.09	2/70	0.128
23.09-23.49	1/70	0.099
23.49-23.89	1/70	0.085
23.89-24.29	3/70	0.071
24.29-24.69	0/70	0.028
24.69-25.09	1/70	0.028
25.09-25.49	1/70	0.014

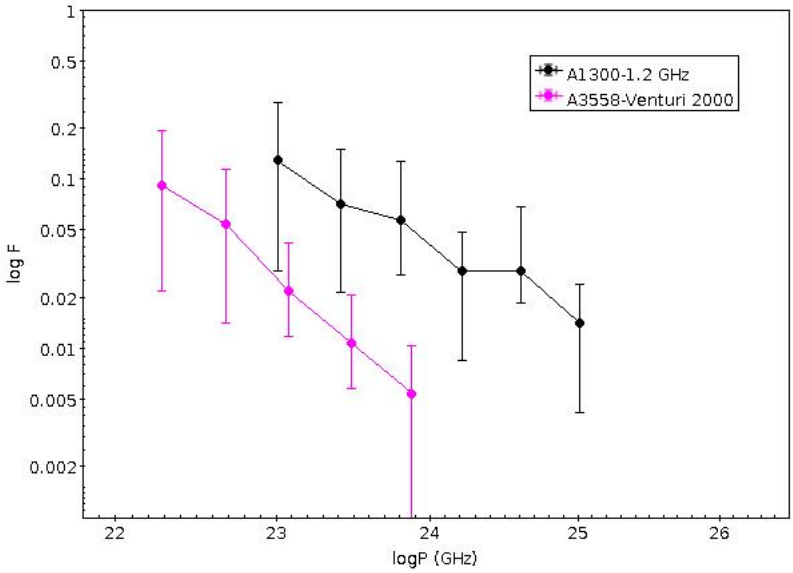

Figure 6.28: Radio integral Luminosity Function, expressed as the fraction of galaxies emitting with radio power $\geq$ logP, for the MeerKAT sample at 1.2 GHz (black) compared with Venturi et al. (2000) Luminosity Function of A3558 (magenta).

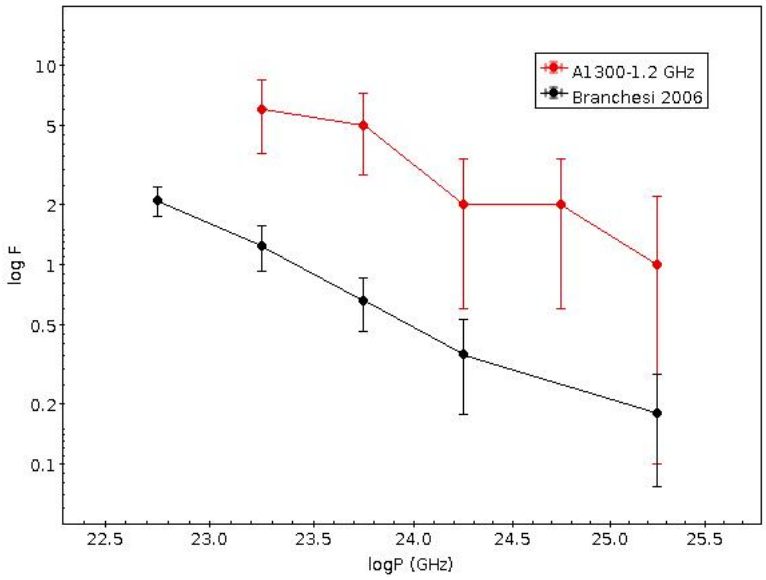

Figure 6.29: Radio integral Luminosity Function, expressed as the fraction of galaxies emitting with radio power $\geq$ logP, for the MeerKAT sample at 1.2 GHz (red) compared with Branchesi et al. (2006) Integral Luminosity Function (black), adopting their method for the RLF estimaton.

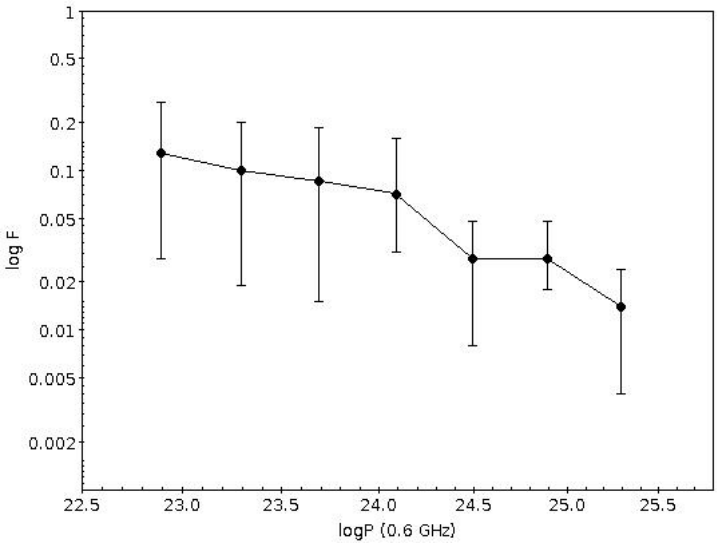

Figure 6.30: Radio integral Luminosity Function, expressed as the fraction of galaxies emitting with radio power $\geq$ logP, for the uGMRT sample at 0.6 GHz.

6.12 The central region of A1300 galaxy cluster: a 'Dumb-bell' BCG

In the radio domain, the central region of A1300 is dominated by a giant diffuse emission consistent with being an ultra-steep radio halo (Venturi et al., 2013). Beyond the halo, a relic is located in the south-western periphery of the cluster and a number of radio galaxies with extended emission are found at the cluster centre (Reid et al., 1999). In this thesis we focused our analysis on the discrete emission from radio galaxies. This cluster hosts a peculiar 'dumb-bell' cD galaxy (i.e. the BCG) which is described in the next Section.

6.12.1 The 'dumb-bell' BCG

The central galaxy in A1300 is a 'dumb-bell' cD galaxy reported for the first time in Pierre et al. (1997). Ziparo et al. (2012) in their X-ray/spectroscopic study on the A1300 galaxy cluster, infer that the two nuclei of the BCG are separated by 1.2 arcsec.
In order to assess the properties of this peculiar object, we extracted the FORS-2 Longslit spectra of the two nuclei of the BCG, taken from an observation of 4 April 2006 (PI A. Edge, Project Number 0.77A-0215). The BCG was observed with two exposures of 450s each, with 300V Grism. We retrived from the archive the data and we reduced them by means of IRAF[7] task. The result of our spectroscopic analysis is reported in Fig.6.31 where we show the spectra of the Northern nucleus (black) and the Southern nucleus (red) respectively. The redshifts are z= 0.3095 (North) and z=0.3098 (South) respectively. The difference in velocity between the two nuclei is of the order of $\sim$ 70 km/s, consistent with the spectroscopic error from the observational setup. The distance between the nuclei is 1" as shown in Fig. 6.32. At the cluster redshift this corresponds to $\sim$ 4.5 kpc.
Our result is consistent with the fact that the BCG consists of two galaxies inside a common halo (see Di Gennaro et al., 2018, for other cases). There is evidence of a third nucleus, which could be probably part of the same system but for which we do not have redshift information.
The two nuclei are consistent with being a merging system, however, there is no evidence of lensing effects (Ziparo et al., 2012).
The radio spectra of A1300 BCG is reported in Fig. 6.33 obtained by means of MeerKAT 1.2 GHz, uGMRT at 640 MHz and archival GMRT at 323 MHz.

We report in Fig. 6.32 the radio contours at 1.2 GHz (green) and at 640 MHz (white) with new MeerKAT and uGMRT data respectively. The contours are drawn at 5 sigma and are overlayed on an optical composite image retrived from HST Relics

[7]https://heasarc.gsfc.nasa.gov/ftools/

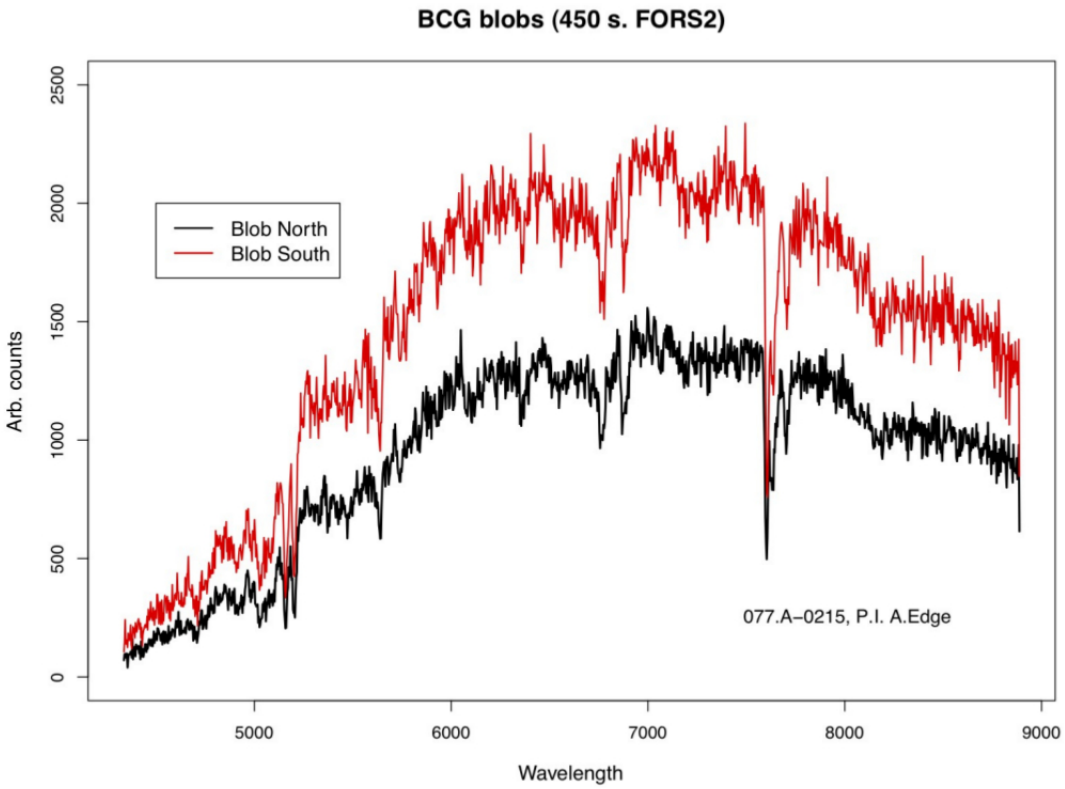

Figure 6.31: The Northern nucleus spectrum (black) and the Southern nucleus spectrum (red) of the 'dumb-bell' BCG in A1300. The difference in velocity resulted 70 km/s, which is the order of the spectroscopic error in the observing setup. The two nuclei are at 1" in distance, which corresponds to 4.5 kpc at the cluster scale. They could be part of a merging system.

archive[8].

[8]https://relics.stsci.edu/

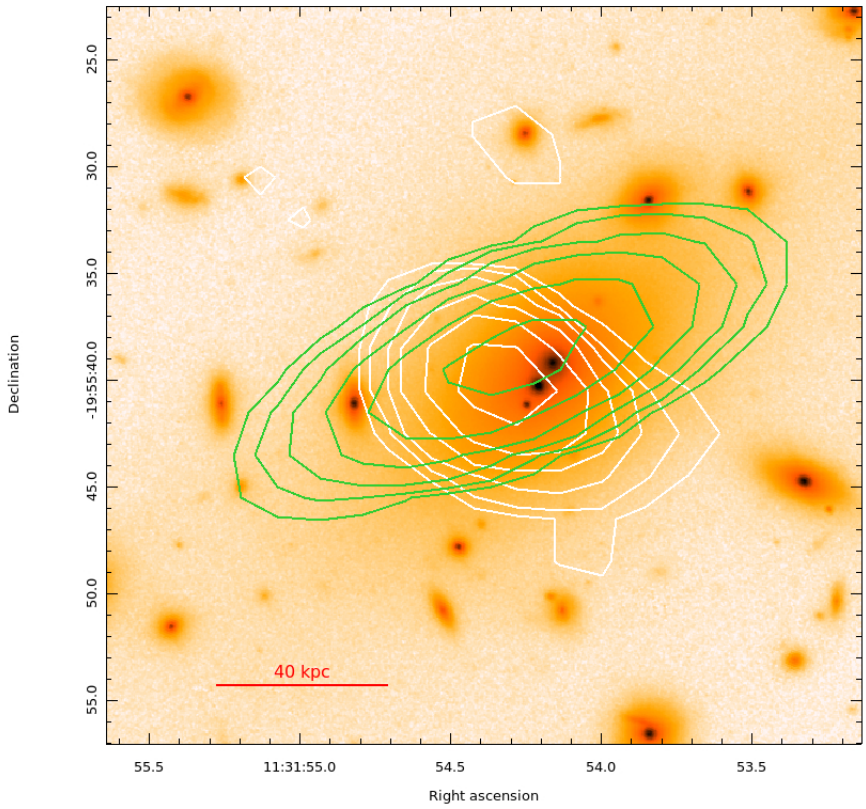

Figure 6.32: The image shows the MeerKAT at 1.2 GHz (green) and the uGMRT at 640 MHz (white) radio contours overlayed on HST Relics composite image of A1300 central BCG. A third nucleus is well visible from the image. The three nuclei could be part of the same merging system. There are no evidence of lensing effects for Ziparo et al. (2012).

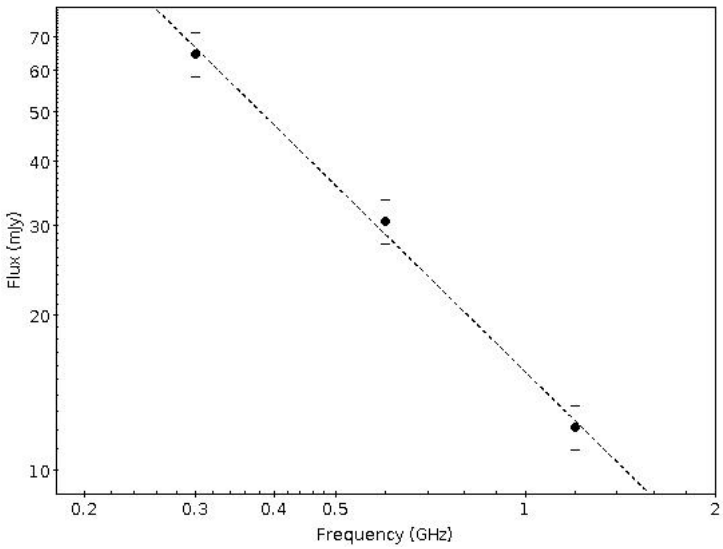

Figure 6.33: The radio spectrum of A1300 central BCG integrated at 1.2 GHz with MeerKAT, 640 MHz with uGMRT and at 323 MHz with GMRT respectively.

Chapter 7

The comparative study of MACSJ1931-2634 and A1300 radio galaxy populations

In this Chapter we review the statistical properties of the radio galaxy populations detected in MACSJ1931-2634 and A1300 galaxy clusters. We compare our statistical results in terms of source detection, spectral properties, statistical source counts over an area wider than the virial radius.
We then compare the properties of the radio galaxies detected within two virial radii from the cluster centre and identified as cluster members from our spectroscopic analysis.
The properties of radio galaxies in relation with the environment in which they are located and in particular, with the dynamical status of the gaseous environment within clusters (the Intra-Cluster Medium), in which they are embedded, is an astrophysical topic which is today still open and much debated.
In particular, understand if the observed properties of radio galaxies arise at formation (nature scenario) or they are an end product of physical processes (nurture scenario) coming into play after galaxies have become part of a 'group' or a 'cluster' is difficult and not yet completely understood (see van Gorkom, 2004, for reviews). The galaxy density changes by orders of magnitude going from the innermost cluster regions to poor groups and to the 'field'. Moreover, the density and the temperature distribution of the ambient medium change dramatically going from small groups, to clusters, to cluster mergers regions (see Feretti & Venturi, 2002). Both factors, however, seem not to affect the probability of early type galaxies to develop an AGN-type radio source.
Owen et al. (1996) suggest that the outer environment is not so different, as it may seem, and all radio galaxies live in a sort of "cluster-like" environment. An alternative hypothesis is that the galaxy density is not a crucial factor in triggering nuclear radio emission in early type galaxies, and the local environment, i.e. the

optical host, plays a much more important role.
The influence of large scale environment, and in particular of cluster merging, on the starburst emission, is still a matter of debate. Numerical simulations in the past (Evrard, 1991) lend support to the idea that the high fraction of starburst galaxies seen in high redshift clusters is due to a single burst of star formation, triggered by compression due to the increasing external pressure as the galaxy falls into the dense intracluster medium. Different results (Fujita et al., 1999) argue that gas stripping during cluster collision is the dominant factor. This leads to a decrease in the star formation rate, hence weakening of the starburst phenomenon during the merger.
The connection between starburst phenomenon and cluster mergers can be obtained at radio wavelengths. Radio sources with $\log P_{1.4GHz}(W/Hz) \lesssim 22$ are dominated by star formation as the mechanism responsible in the production of radio emission (Dwarakanath & Owen, 1999; Burns, 2001).
A detailed study on two clusters at redshift $z \sim 0.25$ was carried out by Owen et al. (1999): A2125 and A2645 have similar intermediate redshift and richness class but different dynamical state. They found a significantly higher number of radio galaxies wih $\log P_{1.4GHz} \lesssim 23$ in A2125 compared to A2645 (27 and 4 respectively). Owen et al. (1999) suggest that the ongoing cluster merger could be responsible for the excess radio source population. The radio emission could be affected by galaxy-galaxy or ICM-galaxy interaction or both.
Different results were obtained from deep observations of the A3558 complex in the central region of the Shapley Concentration ($z \sim 0.05$). Bardelli et al. (1998) proposed that this complex is the result of a cluster-cluster collision. The region of A3558 was uniformely covered by radio observations to a power limit of $\log P_{1.4GHz} \sim 22$ (Venturi et al., 2000, 2001; Giacintucci et al., 2004) and only three candidate starburst radio galaxies were detected.
Nowdays, thanks to new instruments such as LOFAR (van Haarlem et al., 2013), a new window has opened on the low frequency properties of radio galaxy populations (Mahony et al., 2016; Williams et al., 2016; Shimwell et al., 2019) over larger areas. Indeed statistical properties of large samples down to low sensitivity can tell us about evolutionary properties of various source populations (AGN and Star Forming).
New interferometers such as MeerKAT and uGMRT are well suitable for characterizing physical and evolutionary properties of radio sources over wider areas, down to low flux densities thanks to the unprecedent sensitivity.
The study of MACSJ1931-2634 and A1300 radio galaxy populations is inserted within this context. At the time of our observations the instruments used for the analysis in this thesis were totally new. In particular, we performed both a statistical study on the radio galaxy population detected in a wide field of 30 arcmin radius centered on the cluster centre and a radio-optical study on the radio galaxies within the virial radius and consistent with being cluster members.

Our final goal is to compare the statistical properties and the radio-optical features of the galaxy populations of the merging cluster A1300 and the relaxed cluster MACSJ1931-2634, both considered rich clusters and located at the intermediate redshift of ~ 0.3.

7.1 The radio catalogues

We extracted four radio catalogues containing information on the radio galaxy population detected with MeerKAT at 1.2 GHz and uGMRT at 640 MHz.
In order to be consistent with the statistical analysis, we selected the same area of 30 arcmin radius from the cluster centre.
We report the final result in terms of flux density distribution for MACSJ1931-2634 catalogues (Fig. 7.1 and Fig. 7.2), and A1300 catalogues (Fig. 7.3 and Fig. 7.4) respectively; moreover we report the percentage of unresolved, barely resolved and extended sources detected in MACSJ1931-2634 (see Tab. 7.2 and 7.3) and in A1300 (Tab. 7.4 and 7.5), according to the morphological criterion adopted and described in Chapter 5 and 6. The source detection threshold is 5σ(Prandoni et al., 2000) for all the catalogues, i.e 0.20 mJy for MeerKAT catalogues and 0.15 mJy for uGMRT catalogues (see Tab. 7.1).
In MACSJ1931-2634 MeerKAT the flux density distribution peaks within the interval $0.5 < \log F < 1$ mJy. In A1300 MeerKAT there are two peaks between $0.5 < \log F < 1$ mJy and $1 < \log F < 2$ mJy. In MACSJ1931-2634 uGMRT, there is a peak of the distribution between $0.25 < \log F < 0.5$ mJy and also in A1300 uGMRT the peak of the distribution is $0.25 < \log F < 0.5$ mJy. Also the trend of the flux density distribution is consistent with the trend of the source counts, indeed, for $\log F > 1$ mJy there is a drop off due to the decrease of the bright sources. In agreement with Bondi et al. (2008) we observe the upturn at ~ 0.5 mJy and the decline of the flux, corresponding to the decline of the source counts, below ~ 0.5 mJy. This latter could be due to statistical incompleteness of our samples.
If we compare the percentage of the unresolved, barely resolved and extended sources in the two clusters, we can see that MACSJ1931-2634 and A1300 MeerKAT catalogues have almost the same distribution, slightly higher for MACSJ1931-2634. Also, we obtain similar percentage in uGMRT catalogues, but the number of unresolved sources is higher in MACSJ1931-2634 than in A1300 (77% vs 61% respectively).

Table 7.1: MeerKAT and uGMRT radio catalogues

target	frequency (MHz)	threshold(5σ) (mJy)	total area (deg^2)	source total number	area (arcmin)	source final number
A1300	1283	0.20	2.0 × 2.0	339	30	112
MACSJ1931 -2634	1283	0.20	2.0 × 2.0	626	30	192
A1300	640	0.15	1.5 × 1.5	399	30	318
MACSJ1931 -2634	640	0.15	1.5 × 1.5	732	30	623

Table 7.2: Summary on MACSJ1931-2634 MeerKAT radio catalogue

	Unresolved	**Barely**	**Extended**
N	132	56	4
%	69	29	2

Table 7.3: Summary on MACSJ1931-2634 uGMRT radio catalogue

	Unresolved	**Barely**	**Extended**
N	480	137	6
%	77	22	1

Table 7.4: Summary on A1300 MeerKAT radio catalogue

	Unresolved	**Barely**	**Extended**
N	75	32	5
%	67	28	5

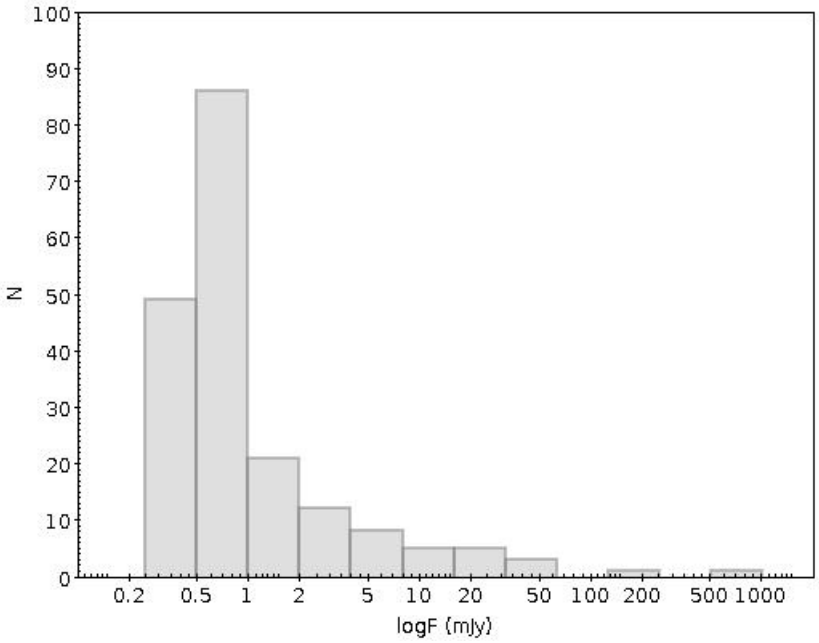

Figure 7.1: **MACSJ1931 − 2634**. The histogram shows the distribution of the integrated flux density for the sources detected at 1.2 GHz in the MACSJ1931-2634 MeerKAT radio catalogue. There is evidence of statistical incompleteness at low fluxes, consistent with the result from the statistical source counts (logN-logS).

Table 7.5: Summary on A1300 uGMRT radio catalogue

	Unresolved	**Barely**	**Extended**
N	197	110	11
%	61	35	4

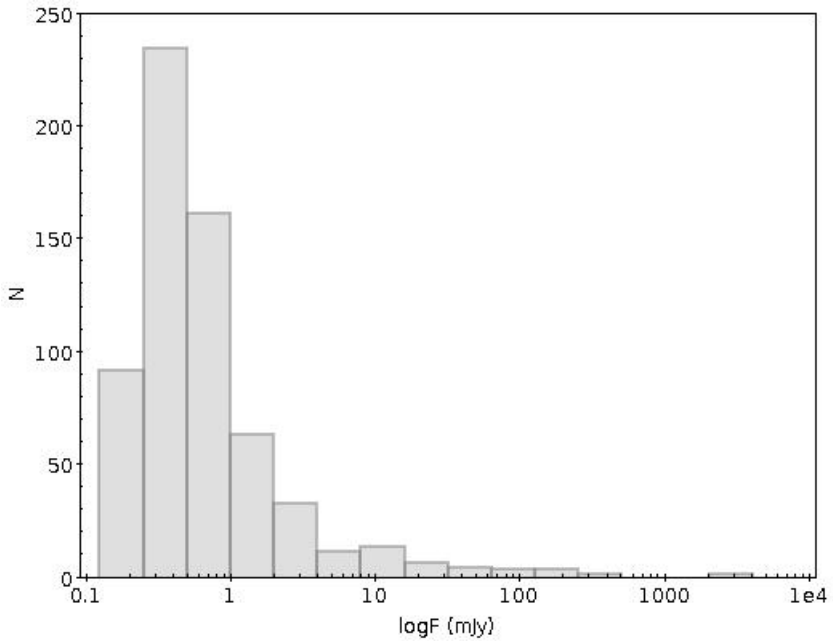

Figure 7.2: **MACSJ1931 − 2634**. The histogram shows the distribution of the integrated flux density for the sources detected at 640 MHz in the MACSJ1931-2634 uGMRT radio catalogue. There is evidence of statistical incompleteness at low fluxes, consistent with the result from the statistical source counts (logN-logS).

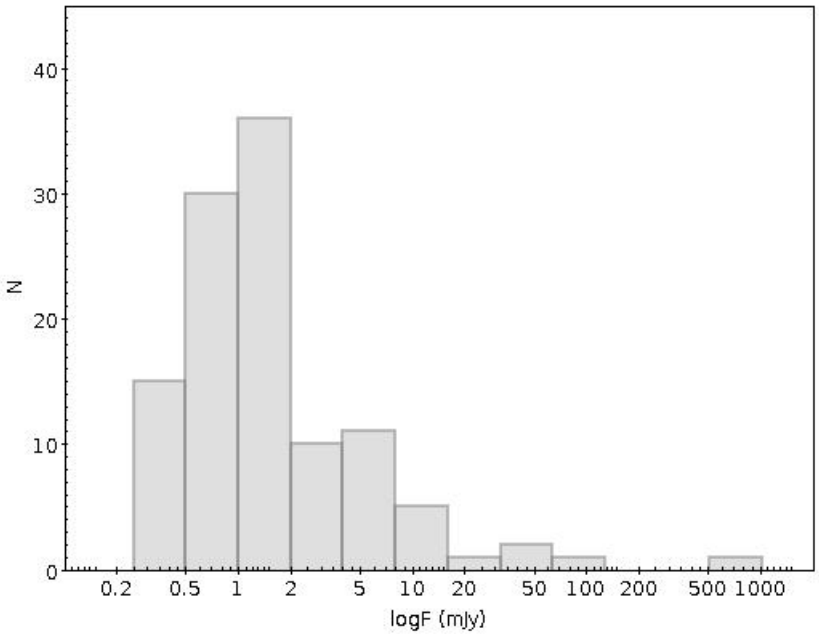

Figure 7.3: **A1300**. The histogram shows the distribution of the integrated flux density for the sources detected at 1.2 GHz in the A1300 MeerKAT radio catalogue. There is evidence of statistical incompleteness at low fluxes, consistent with the result from the statistical source counts (logN-logS).

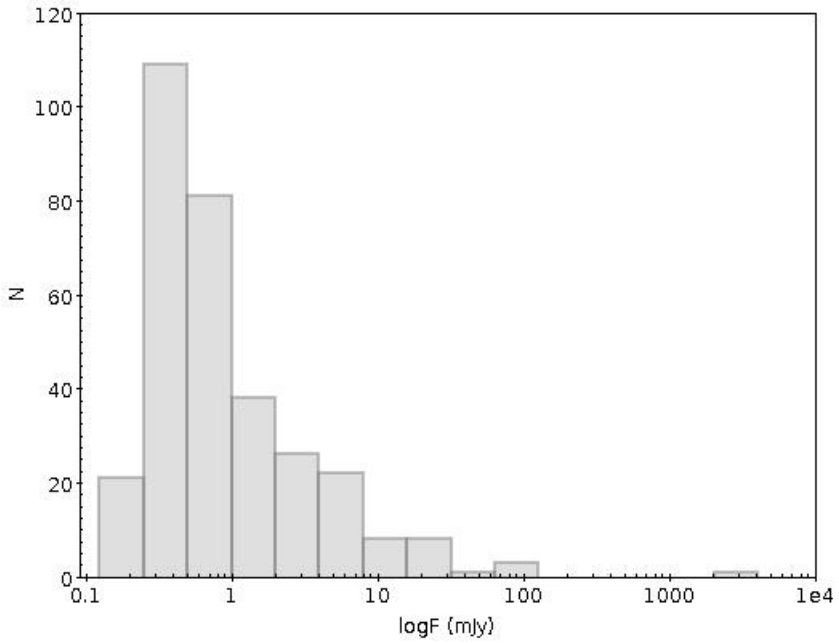

Figure 7.4: **A1300**. The histogram shows the distribution of the integrated flux density for the sources detected at 640 MHz in the A1300 uGMRT radio catalogue. There is evidence of statistical incompleteness at low fluxes, consistent with the result from the statistical source counts (logN-logS).

7.2 Spectral distribution of the common sources

Obtaining large samples of radio galaxies at intermediate-low frequency allows to study the source population in a statistically significant manner and investigate how the properties of radio galaxies evolve over cosmic time (Mahony et al., 2016). In particular, studying the spectral index properties of the radio source population can provide insight into a range of source properties. For example, the spectral index is often used to distinguish between source components in AGN (i.e. flat-spectrum cores versus steep-spectrum lobes), or can also be used to derive approximate ages of the radio source based on spectral ageing models (see Harwood et al., 2013, 2015, and references therein).
Previous studies that have looked at the average spectral index properties of large samples have reported conflicting results as to whether the median spectral index changes as a function of flux density (Prandoni et al., 2006; Randall et al., 2012; Whittam et al., 2013). This studies have been generally carried out at GHz frequencies, with studies of low frequency selected sources typically showing evidence for the median spectral index to become flatter at fainter flux densities (Ishwara-Chandra et al., 2010; Intema et al., 2011; Williams et al., 2013).
We report the result of our spectral analysis in Figure 7.5 and 7.6.
The spectral index distribution of the sources in common between MeerKAT and uGMRT catalogues in MACSJ1931-2634 has a median spectral index $\sim 0.93 \pm 0.2$. This value is steeper than what was found in previous studies (Williams et al., 2016; Intema et al., 2011; Ishwara-Chandra et al., 2010). The typical spectral index over this frequencies is around 0.78, but can ranges from 0.76 to 0.85 (Hardcastle et al., 2016). Mahony et al. (2016) found a steep value of 0.82 ± 0.02 in their work from sources in the Lockman-wide sample between 1.4 GHz and 150 MHz. Steep values are also found in Sirothia et al. (2009) of 0.82 ± 0.01 and in Williams et al. (2013) of 0.87 ± 0.01.
We can separate the sample of the sources in common into three primary categories, according to Mahony et al. (2016): sources with $\alpha\ ^{1283}_{640} < 0.5$ are flat, sources with $0.5 < \alpha\ ^{1283}_{640} < 1.2$ are steep, whereas sources with $\alpha\ ^{1283}_{640} > 1.2$ are ultra-steep.
According to this separation, the sample is dominated by steep sources ($0.5 < \alpha\ ^{1283}_{640} < 1.2$), which is expected at these frequencies (Mahony et al., 2016). They are the 48 % of the sample, whereas the ultra-steep and the flat are the 32% and the 20% of the sample respectively.
In Figure 7.6 we report the spectral index distribution of the sources in common between MeerKAT and uGMRT catalogues in A1300. The median spectral index of the distribution is 1.1 ± 0.2. This value is steeper than what we found for MACSJ1931-2634 field and than what was found from previous studies (Williams et al., 2016; Mahony et al., 2016; Intema et al., 2011; Ishwara-Chandra et al., 2010).
According to the same criterion (Mahony et al., 2016) the majority of the sources in the sample are steep sources ($0.5 < \alpha\ ^{1283}_{640} < 1.2$), which is expected at these fre-

quencies. They are the 45% of the sample. The ultra-steep sources are comparable in percentage to the steep sources. They are the 42 % of the sample. Finally, the flat sources are the 13% of the sample.

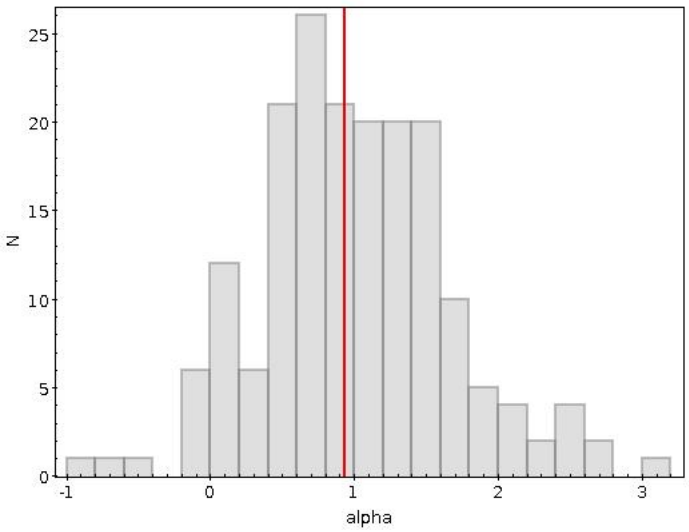

Figure 7.5: Histogram of the spectral indices from 640 MHz-1.2 GHz for sources in the MACSJ1931-2634 field detected both at 1.2 GHz and 640 MHz. The red line indicates the median value, steeper in respect to the previous studies, which is 0.9 $\pm$ 0.2. The source population is dominated by steep spectra sources.

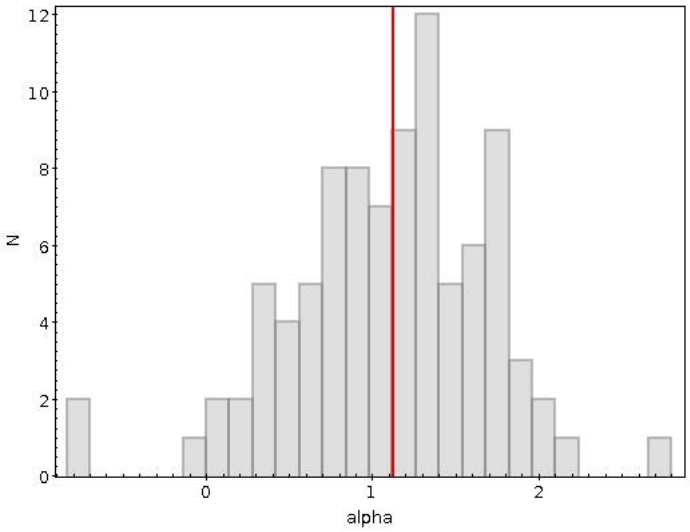

Figure 7.6: Histogram of the spectral indices from 640 MHz-1.2 GHz for sources in the A1300 field detected both at 1.2 GHz and 640 MHz. The red line indicates the median value, steeper in respect to the previous studies, which is 1.1 ± 0.2. The source population is dominated by steep spectra sources.

7.3 Statistical source counts

We computed for both clusters the statistical source counts within an area of 12 arcmin radius, corresponding to about two virial radii. MACSJ1931-2634 virial radius is $\sim$ 1.8 Mpc (Santos et al., 2016) as estimated from lensing; A1300 virial radius is $\sim$ 1.53 Mpc (Ziparo et al., 2012).
We computed the source counts for our radio samples and we compared them with the background in order to study if the dynamical properties of this clusters result in an enhanced number of radio sources or vice-versa, in a reduced number of radio sources (Venturi et al., 2000, 2001; Giacintucci et al., 2004; Bondi et al., 2008).
In Fig. 7.7 and 7.8 we report the logN-logS ditributions for MACSJ1931-2634 and A1300 computed at 1.2 GHz with MeerKAT (black counts) in comparison with the background (red counts). The plots show that in MACSJ1931-2634 cluster, the counts in the cluster area and in the background have the same shape, suggesting that the number of sources found in the cluster area are consistent with those predicted for the background. In A1300 the counts in the cluster area and in the background do not have the same shape. The number of sources detected in the cluster area is not fully in agreement with the number of sources predicted for the background. However, it is evident that for F $>$ 10 mJy the cluster counts are significantly above the background for both the clusters.
There is difference in the counts for F between 1-5 mJy, indeed in A1300 the cluster counts dominate the background within this interval and the two distributions do not have the same shape, whereas in MACSJ1931-2634 the cluster counts are partly

below the background and the distributions have the same trend.
Finally, for F < 0.5 mJy there is a drop off in both the clusters, even if in MACSJ1931-2634 the counts go significantly below the background for F < 0.25 mJy confirming that our sample is incomplete below this limit; source counts in A1300 remain over the background for F < 0.25 mJy, indicating less statistical incompleteness.
The plots show good agreement with previous literature results, indeed there is the upturn in both for F > 0.5 mJy (Bondi et al., 2008). The distributions of both clusters have the same detection threshold of 0.2 mJy (i.e. 5σ), and the noise over the integrating cluster area is uniform. Moreover, the majority of the sources in the cluster counts is unresolved. Avoiding the noise bias and the resolution bias (see Bondi et al., 2008), the different trend between A1300 and MACSJ1931-2634, detected at low fluxes, could be, at least in part, related to the different dynamical state of the clusters.

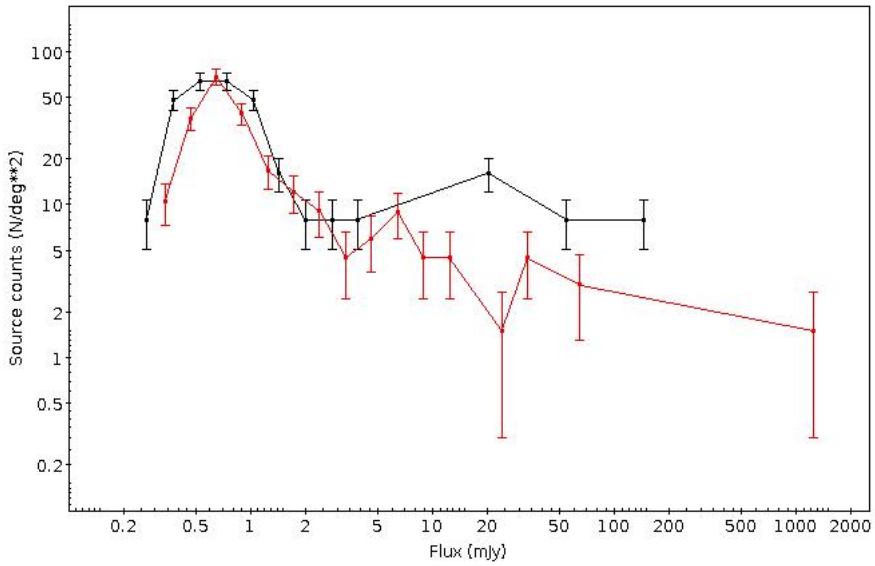

Figure 7.7: **MACSJ1931 − 2634**: Differential radio source counts in MACSJ1931-2434 field at 1.2 GHz. The total integrating area, equivalent to 2 virial radii, is of 0.125 deg^2 (black counts). The background integrating area is of 0.66 deg^2 (red counts). The sources dominate the background for fluxes > 10 mJy.

In Fig. 7.9 and 7.10 we report the logN-logS distributions of MACSJ1931-2634 and A1300 integrated at 640 MHz with the uGMRT. We computed the source counts (black counts) in comparison with the background (red counts) in order to assess if the dynamical properties of this clusters reflect in the enhanced number of radio sources or vice-versa, in a reduced number of radio sources with respect to the background. The plots show that in MACSJ1931-2634, the counts in the cluster area and in the background have almost the same shape, suggesting that the number of sources detected in the cluster area are consistent with those predicted

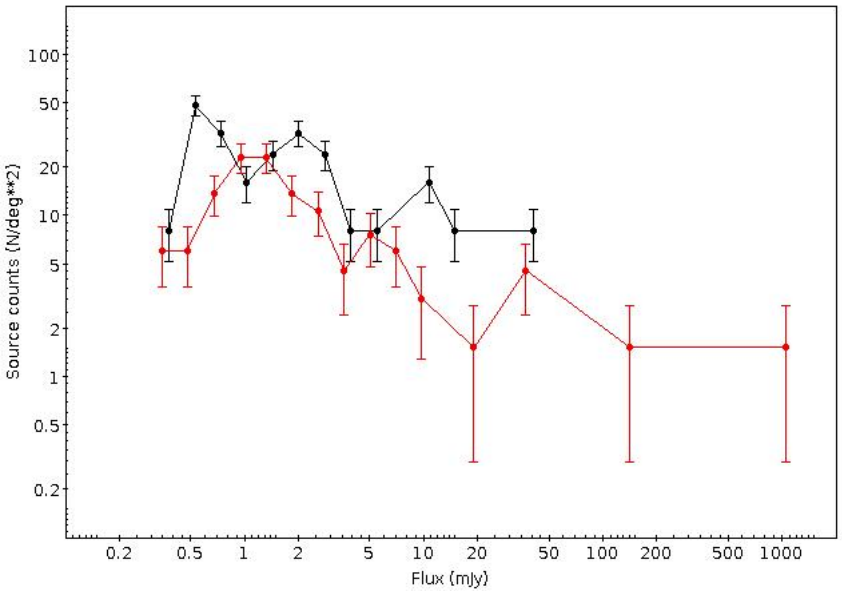

Figure 7.8: **A1300**: Differential radio source counts in A1300 field at 1.2 GHz. The total integrating area, equivalent to 2 virial radii, is of 0.125 deg^2 (black counts). The background integrating area is of 0.66 deg^2 (red counts). The sources dominate the background for fluxes > 10 mJy.

for the background. For $0.2 < F < 0.5$ mJy, the sources dominate the background, and the upturn is visible at $F \sim 0.2$ mJy, below which the counts go under the background indicating the statistical incompleteness of our sample below this limit. As for the MeerKAT plot at 1.2 GHz, the sources dominate the background for fluxes $F > 10$ mJy.
In A1300 the cluster counts and the background have almost the same shape, with the exception of the interval of flux density $2.5 < F < 40$ mJy, within which, the shape is different and the sources dominate the background. For $F < 0.5$ mJy the sources dominate the background, indicating less statistical incompleteness.
The distributions have the same detection threshold of 0.15 mJy (i.e. 5σ), and the noise over the integrating cluster area is uniform. Moreover, the majority of the sources in the cluster counts is unresolved. The different trend between A1300 and MACSJ1931-2634, detected at low fluxes, could be, at least in part, associated to the different dynamical status of the clusters.

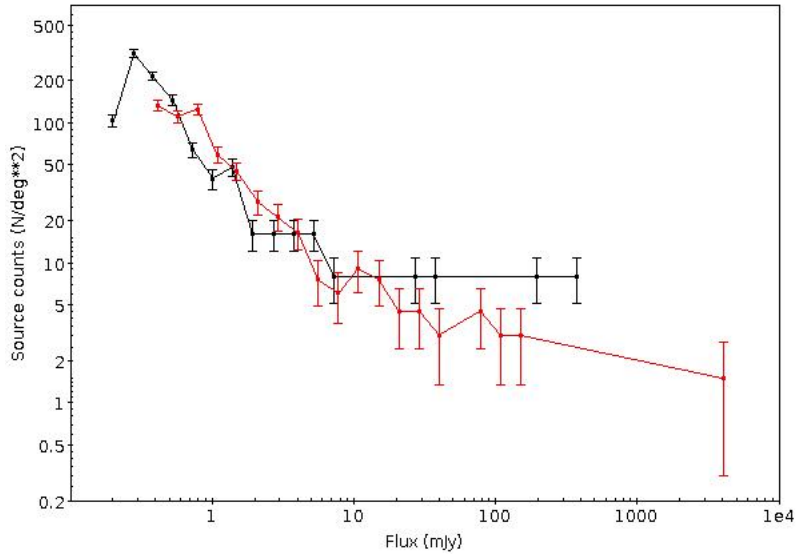

Figure 7.9: **MACSJ1931 − 2634**: Differential radio source counts in MACSJ1931-2434 field at 640 MHz. The total integrating area, equivalent to 2 virial radii, is of 0.125 deg^2 (black counts). The background integrating area is of 0.66 deg^2 (red counts). As for MeerKAT, the sources dominate the background for fluxes > 10 mJy.

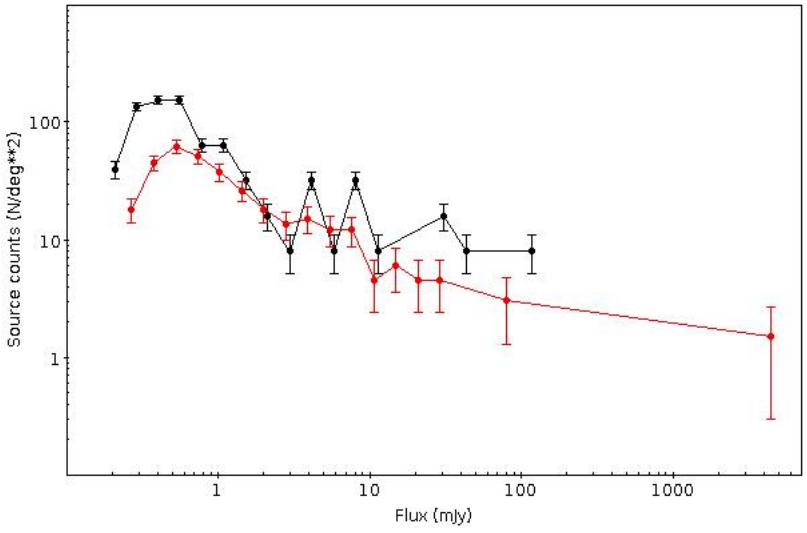

Figure 7.10: **A1300**: Differential radio source counts in A1300 field at 640 MHz. The total integrating area, equivalent to 2 virial radii, is of 0.125 deg^2 (black counts). The background integrating area is of 0.66 deg^2 (red counts). The sources dominate the background for fluxes > 10 mJy.

7.4 The Radio Luminosity Functions

The Radio Luminosity Function is a powerful statistical tool to investigate the radio properties of galaxies in relation with the environment. The influence of the environment should reflect in the shape of the RLF, in its amplitude or both (Venturi et al., 2000; Branchesi et al., 2006).
In Fig. 7.11 we compare the RLF estimated for MACSJ1931-2634 and A1300 (z=0.3) at 1.2 GHz with MeerKAT and the RLF computed by Venturi et al. (2000) for A3558 at z=0.04. We made this comparison in order to assess the properties of radio sources both in relation with the dynamical state of the cluster (i.e. merging vs relaxed) and in relation with the redshift (i.e. evolution).

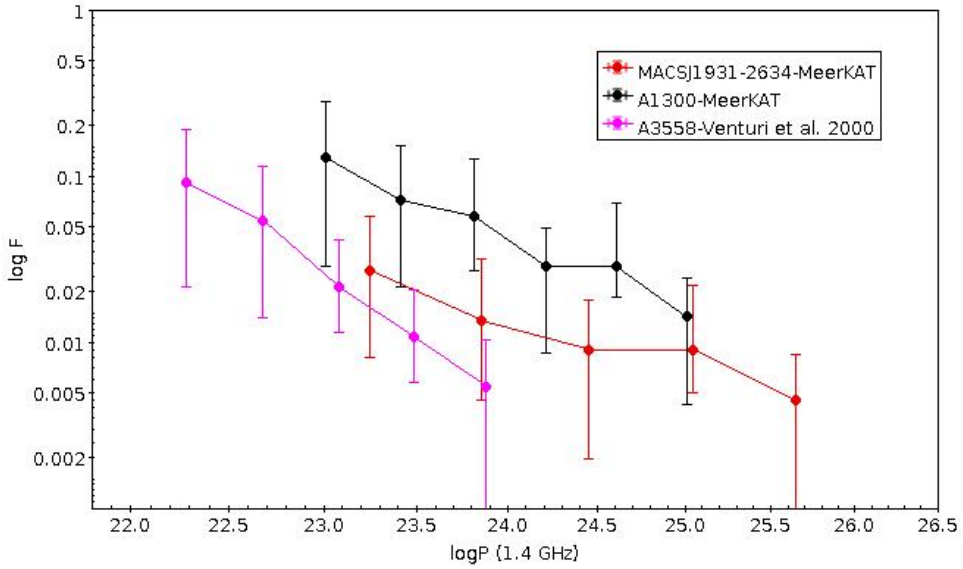

Figure 7.11: Radio integral Luminosity Function, expressed as the fraction of galaxies emitting with radio power $\geq$ logP, for A1300 MeerKAT sample at 1.2 GHz (black), MACSJ1931-2634 MeerKAT (red), compared with Venturi et al. (2000) Luminosity Function of A3558 (magenta) rescaled to our cosmology.

Even though in A3558 the power interval is lower (and this could be the reason of the steeper slope as explained in Branchesi et al. 2006), down to $\log P_{1.4GHz} \sim 22.2$ (W/Hz), and the power interval in MeerKAT is up to $\log P_{1.2GHz} > 25.6$ (W/Hz), there is an overlap in terms of power intervals between $22.9 < \log P_{1.4GHz} < 23.9$ for the three distributions.
The shape of the RLF looks similar until $\log P_{1.4GHz} \sim 23.9$, and it seems to confirm that, apparently, there is no evolution with z, consistent with previous literature results (Stocke et al., 1999).
If we compare the RLF at the same redshift of z $\sim$ 0.3 but in different environments, the amplitude of A1300 RLF is a factor $\sim$ 2 higher than the RLF of MACSJ1931-

2634, indicating that the probability of developing a radio source is higher in a merging cluster (as for example for A2255 by Miller & Owen 2003). Since merger processes might be important in the triggering of radio emission, increased signs of activity are expected at earlier epochs. Our result goes in this direction.
On the contrary, but at local z, in A3558, which is a merging complex, it seems that the unrelaxed environment does not increase the probability for elliptical galaxies to develop a radio source (Bardelli et al., 1998; Venturi et al., 2000, 2001).
The slope of the local RLF appears steeper than MeerKAT RLF, this result is in contrast with Branchesi et al. (2006), which found that the slope of their NEP RLF is steeper than the one found in the local samples (i.e. Ledlow & Owen 1996).
Even though the poor statistics, one can see that there could be a power breaks at $\log P_{1.4GHz} \sim 24.6$ in A1300 and at $\log P_{1.4GHz} \sim 25.1$ in MACSJ1931-2634. According to literature results, the P break corresponds to the transition between FRI and FRII radio galaxies; it is higher for higher optical magnitudes (Owen & Ledlow, 1994; Ledlow & Owen, 1996).
In Fig. 7.12 we report the comparison between the RLF estimated for A1300 and MACSJ1931-2634 at 640 MHz. Also at low frequency the shape of the two RLFs is similar for $\log P_{1.4GHz} \sim < 24.1$. At higher radio power the A1300 RLF shows a P break, whereas the MACSJ1931-2634 RLF seems to remain constant.
Also at low frequency the amplitude of A1300 RLF is a factor ~ 2 higher than MACSJ1931-2634, indicating higher probability to develop a radio source in a merging cluster.
In absence of more data these are only speculations awaiting to be confirmed by a much better statistics. The main result of this study is that the amplitude and the slope of the RLF are different between local and distant clusters and from merging and relaxed clusters.

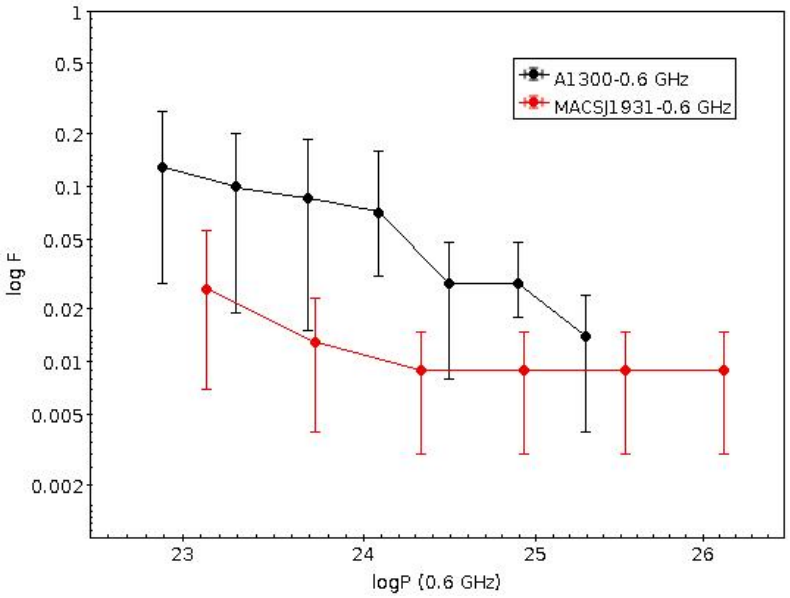

Figure 7.12: Radio integral Luminosity Function, expressed as the fraction of galaxies emitting with radio power $\geq$ logP, for A1300 MeerKAT sample at 640 MHz (black), compared with MACSJ1931-2634 at 640 MHz (red).

7.5 Radio-optical features and spatial densities

In this section we summarize the radio-optical properties of those radio galaxies that, according to our spectroscopic analysis, resulted cluster members. We found that six galaxies are consistent with being cluster members in MACSJ1931-2634 galaxy cluster and nine galaxies are consistent with being cluster members in A1300 respectively.
In Tab. 7.6 and 7.7 we report their name, radio coordinates (J2000), the spectroscopic redshift, their magnitudes and color, the spectral index and the radio power at 1.2 GHz.

In Fig. 7.13 we report the comparison between the Color-Magnitude (C-M) diagram for MACSJ1931-2634 and A1300 galaxy clusters respectively. In MACSJ1931-2634 C-M diagram, cluster members are represented with triangles (the blue is the BCG and the black triangle is the NAT galaxy); in A1300 C-M diagram the cluster members are represented with red diamonds. In MACSJ1931-2634 cluster members are equally distributed on the red and blue sequence (i.e. 3 AGN and 3 SF), in A1300 the AGN population dominate (i.e. 6 AGN and 3 SF).
This result is confirmed in Fig. 7.14 where we report the comparison of the logP-color diagram for MACSJ1931-2634 and A1300 respectively.
If we associate this result to the dynamical state of the cluster, we can confirm the result also found in Dwarakanath & Owen (1999): A1300 is defined post-merging,

Table 7.6: Summary on the radio-optical properties of the MACSJ1931-2634 cluster member radio galaxies

name	RA (hms)	DEC (° ' ")	z	Bmag	Rmag	(B-R)	$\alpha_{0.6}^{1.2}$	$\log P_{1.2GHz}$ (W/Hz)
J1931-2637	19:31:46.60	-26:37:31.7	0.342	21.95	19.67	2.28	-1.3	23.22
J1931-2634	19:31:49.62	-26:34:32.6	0.352	18.84	18.14	0.70	1.9	25.31
J1931-2635	19:31:50.02	-26:35:17.2	0.351	21.54	19.27	2.27	1.2	25.81
J1931-2630	19:31:54.88	-26:30:57.1	0.351	21.66	19.46	2.20	0.6	23.60
J1931-2645	19:31:58.33	-26:45:34.4	0.359	20.85	19.33	1.52	1.7	<22.98
J1932-2625	19:32:07.42	-26:25:16.4	0.349	20.52	19.22	1.30	1.4	<22.95

Table 7.7: Summary on the radio-optical properties of the A1300 cluster member radio galaxies

name	RA (hms)	DEC (° ' ")	z	g'mag	r'mag	(g'-r')	$\alpha_{0.6}^{1.2}$	$\log P_{1.2GHz}$ (W/Hz)
J1131-2000	11:31:13.70	-20:00:21.8	0.303	21.35	19.95	1.40	0.9	23.72
J1131-1954	11:31:46.96	-19:54:52.5	0.302	21.05	19.63	1.41	3.2	<22.81
J1131-1949	11:31:48.62	-19:49:01.7	0.302	21.23	20.21	1.02	0.7	<22.81
J1131-1958	11:31:49.50	-19:58:07.9	0.295	20.87	19.74	1.13	1.05	23.08
J1131-1953	11:31:54.29	-19:53:57.5	0.305	20.86	19.41	1.45	1.3	25.03
J1131-1955	11:31:54.31	-19:55:40.5	0.307	20.09	18.62	1.46	1.3	24.53
J1131-1952	11:31:54.81	-19:52:07.9	0.303	20.70	19.24	1.45	1.4	23.79
J1132-1954	11:32:03.62	-19:54:14.2	0.306	21.23	19.78	1.44	2.0	23.38
J1132-1952	11:32:04.41	-19:52:12.1	0.302	21.14	20.39	0.74	0.7	<22.81

however, the cluster could still undergoing a merger activity. As a consequence, most of the cluster members retain their gas content, which is responsible for radio emission, bot in Star Forming galaxies and in non Star Forming (through fueling the AGN). If MACSJ1931-2634 is already virialized, most of the cluster members would have lost their gas to the intracluster medium, resulting in reduced gas supply and radio emission (see Dwarakanath & Owen, 1999, for comparison).
In Fig. 7.15 we report the spatial distribution of cluster members projected in the plane of the sky.
It is evident from the plots that there is difference in terms of spatial distribution. In both cases, as expected, the densest region is the central region indicating segregation (white-yellow color), but the density distribution in MACSJ1931-2634 results elongated along the North-South direction, and decreases by moving away from the centre; the density distribution in A1300 results roundish, and the galaxies seem almost randomly distributed without an elongated shape.
In both the images the BCG is indicated with a green circle. It results that the BCG in MACSJ1931-2634 is centrally located, whereas the BCG in A1300 is 'shifted' from the centre of the spatial density distribution and there is a spatial offset which could be a footprint of the merging phase.
The distribution of MACSJ1931-2634 and A1300 cluster members as a function of radio luminosity at 1.2 GHz is shown in Fig. 7.16. The median value of the distribution is $\log P_{1.2GHz} \sim 23.5$ for A1300 cluster members and ~ 23.8 for MACSJ1931-2634 cluster members. Even though we have poor statistics, the distribution appears bimodal for both clusters, with two classess centered at $\log P \sim 23.5$ and 25.5 W/Hz (see Dwarakanath & Owen, 1999, for comparison). The lower cutoff in the distribution is due to the detection limit of the radio observations.

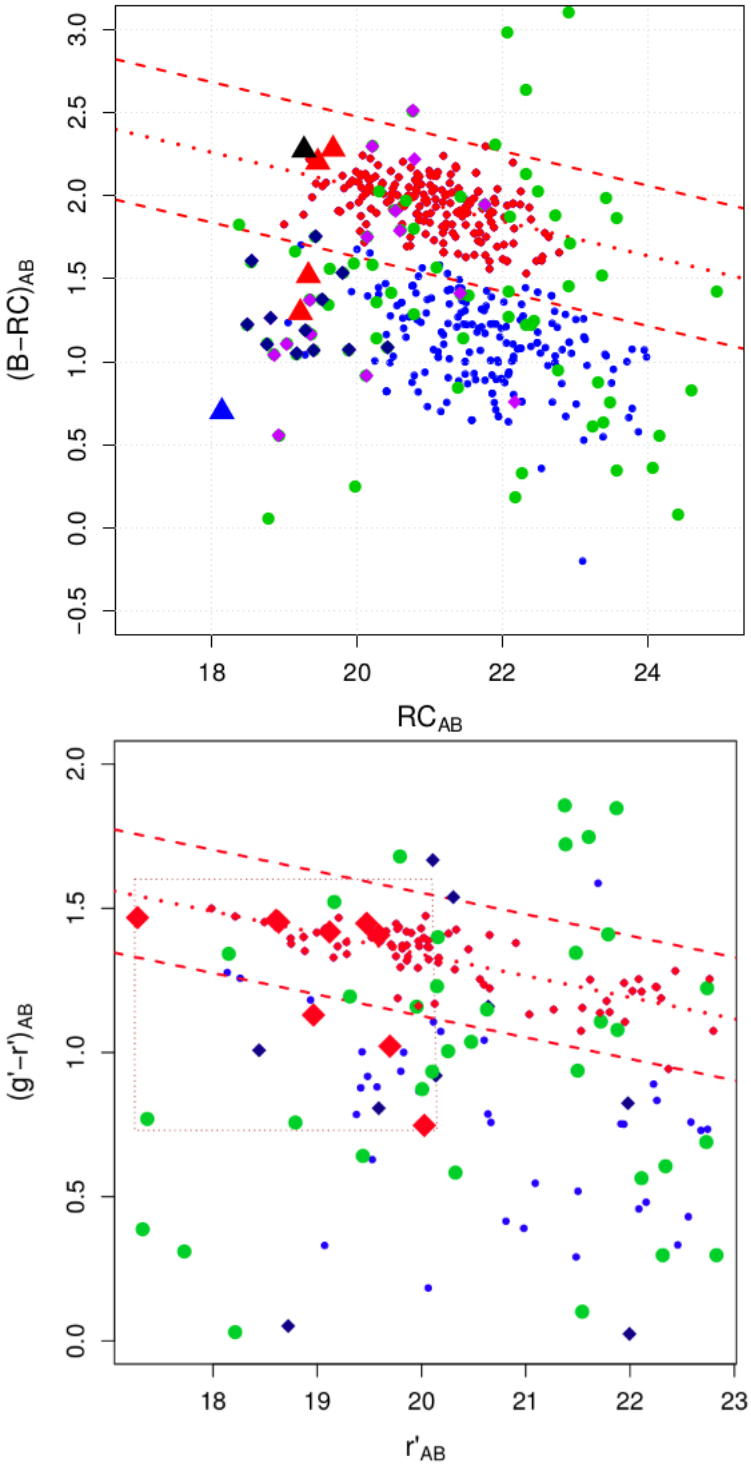

Figure 7.13: The figure shows the Color-Magnitude diagrams for MACSJ1931-2634 (top panel) and A1300 (bottom panel) galaxy clusters. The cluster members are indicated with triangles in MACSJ1931-2634 and red diamonds in A1300.

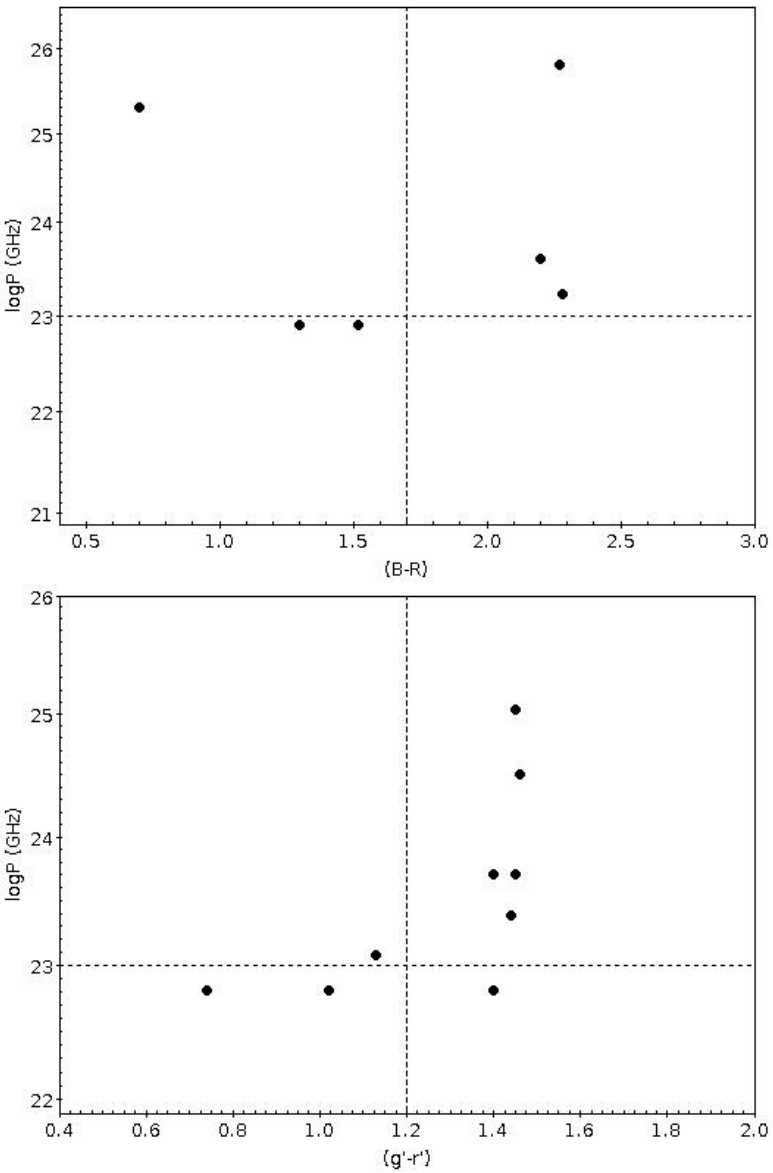

Figure 7.14: The figure shows logP-color diagrams of MACSJ1931-2634 (top panel) and A1300 (bottom panel). Even though with poor statistics, our results seem to confirm that the merging could be a trigger for the radio emission.

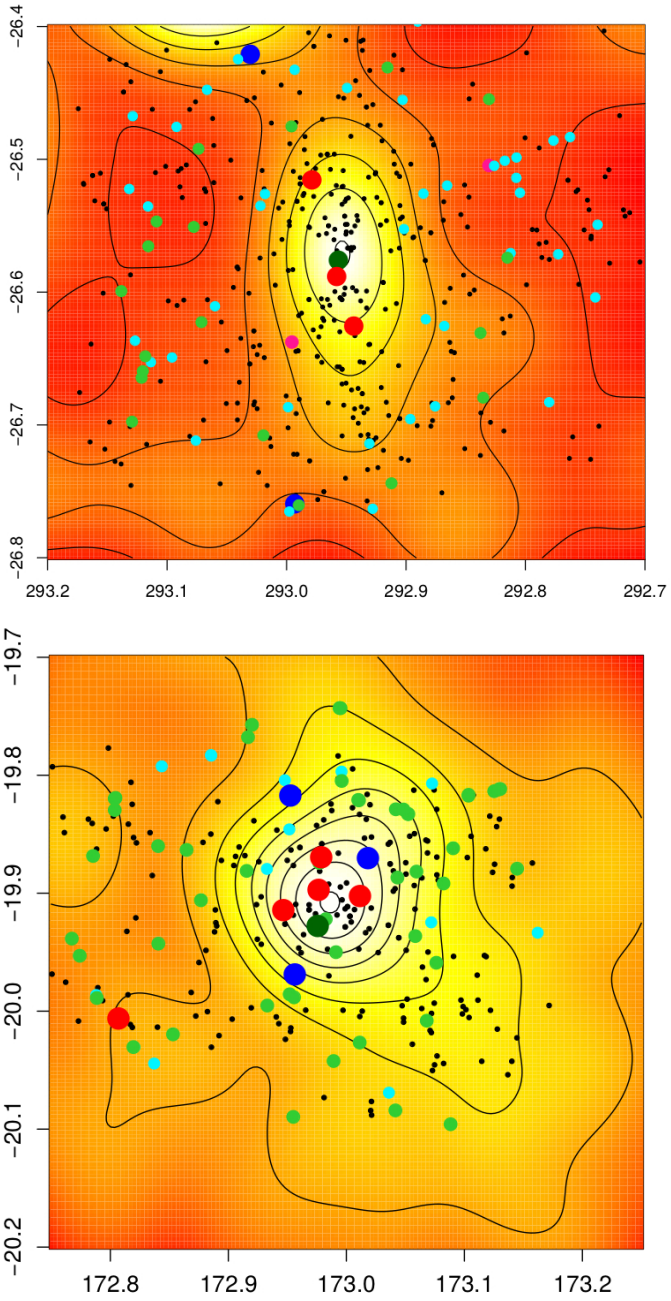

Figure 7.15: The figure shows the spatial distribution of galaxies of MACSJ1931-2634 (top panel) and A1300 (bottom panel). The spatial ditribution seems to confirm that the merging is related to the increase of the density in the central regions (meaning white color higher density) of clusters and, as a consequence, enhance the probability of galaxy-galaxy interactions.

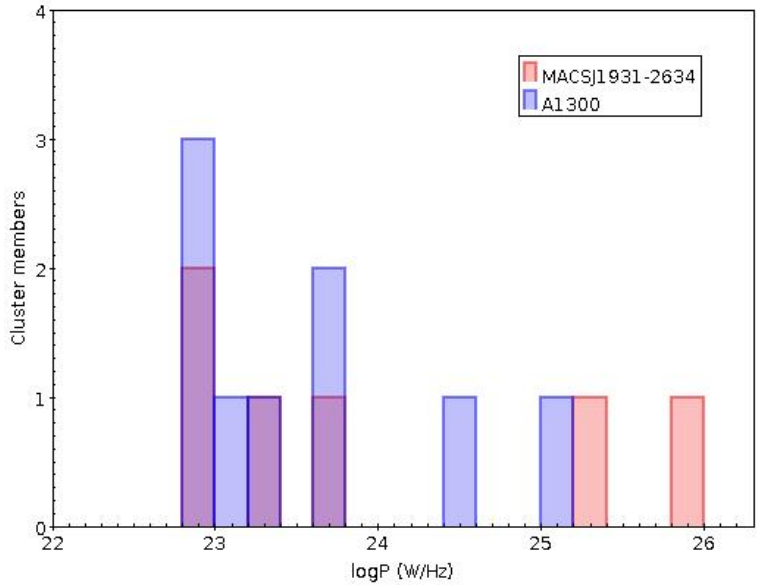

Figure 7.16: The figure shows the distribution of A1300 (blue) and MACSJ1931-2634 (red) cluster members as a function of radio luminosity at 1.2 GHz. The peak of the ditribution is $\log P_{1.2GHz} \sim 23.5$ (W/Hz) for A1300 and $\log P_{1.2GHz} \sim 23.8$ (W/Hz) for MACSJ1931-2634 cluster members. Even though with little statistics, the distribution appears bimodal for both clusters, according to Dwarakanath & Owen (1999).

7.6 SFR and Stellar Mass

We estimated the stellar masses of the cluster members and the specific star formation rate (sSFR; which is the SFR normalized by the stellar mass) by means of MAGPHYS (Cunha et al., 2008) as explained in Chapter 4. The Tables 7.8 and 7.10 report our results. The SFR reported here must be interpreted as the result of the best fitting model, in particular, for MACSJ1931-2634, the high values of the SFR have to be considered as indicative of star formation activity but with high error due to the fitting result (highly skewed). In Tab. 7.9 and 7.11 we report the errors of the fit (percentile 2.5% and 97.5%).
We report in Fig. 7.17 the radio power-stellar mass correlation for A1300 member galaxies and MACSJ1931-2634 member galaxies. Even though the large scatter, in A1300 the trend confirms what it is found in previous literature result: the radio power from the galaxy is dependent on the mass of the galaxy, i.e. less massive galaxies appear to be capable of hosting more low power radio sources (Kauffmann et al., 2003; Best et al., 2005; Best, 2007). No correlation is found instead in the galaxies of MACSJ1931-2634, indeed the most massive galaxy in the sample ($M \sim 9.79 \times 10^{11}$ $M_{\odot}$) has a value of radio power consistent with being a Star Forming galaxy ($\log P_{1.2GHz} \sim 22.9$ W/Hz).

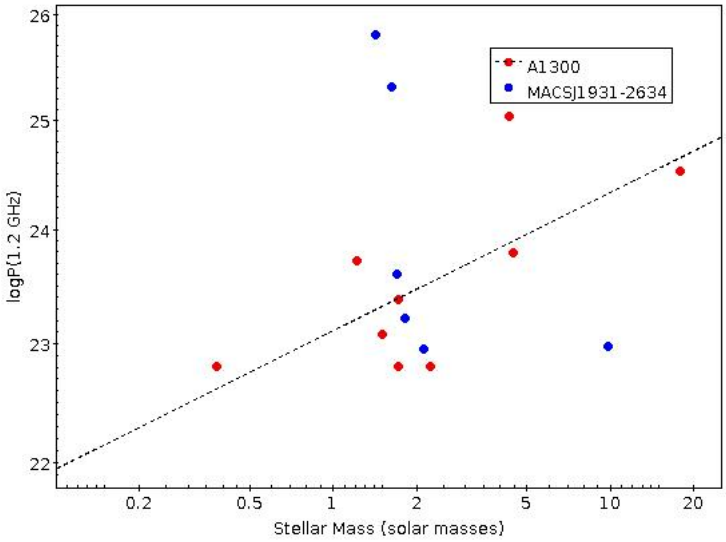

Figure 7.17: The figure shows the Mass-logP correlation of MACSJ1931-2634 (blue dots) and A1300 (red dots). The plot seems to confirm that the correlation in valid for A1300 cluster member galaxies, whereas there is no correlation for MACSJ1931-2634 galaxies.

In Fig. 7.18 we show the radio power vs SFR for A1300 (red), MACSJ1931-2634 (blue) galaxies and for the BCG (black crosses) galaxies analyzed in this work. We can compare our result with the Figure 4 in Cooke et al. (2016). The radio powers

observed are, on average, up to five orders of magnitude above the radio powers expected if solely due to star formation estimated following Bell 2003 (dashed line). This suggests that the radio emission is mainly being powered by the AGN both in BCGs and in the other cluster galaxies. In addition, at least for A1300 the average observed radio power increases with galaxy mass. This suggest that the source of fuel for AGN activity increases with galaxy mass. Apparently, there is no correlation in MACSJ1931-2634 radio galaxies between radio power and stellar mass. Our results go in the direction of confirming that the cold gas could be the source for both the AGN activity and the Star Formation activity (Pizzolato & Soker, 2005; Gaspari et al., 2013; Cooke et al., 2016).
However, we are aware that we need more statistics to confirm and make more robust our results.
In Fig. 7.19 we report the correlation between SFR with stellar mass (expressed as $\times$ 10^{11} $M_{\odot}$), compared with the correlation of the BCGs analyzed in this work and with Cooke et al. (2016). No SFMS is observed, according to the result from Cooke et al. (2016).

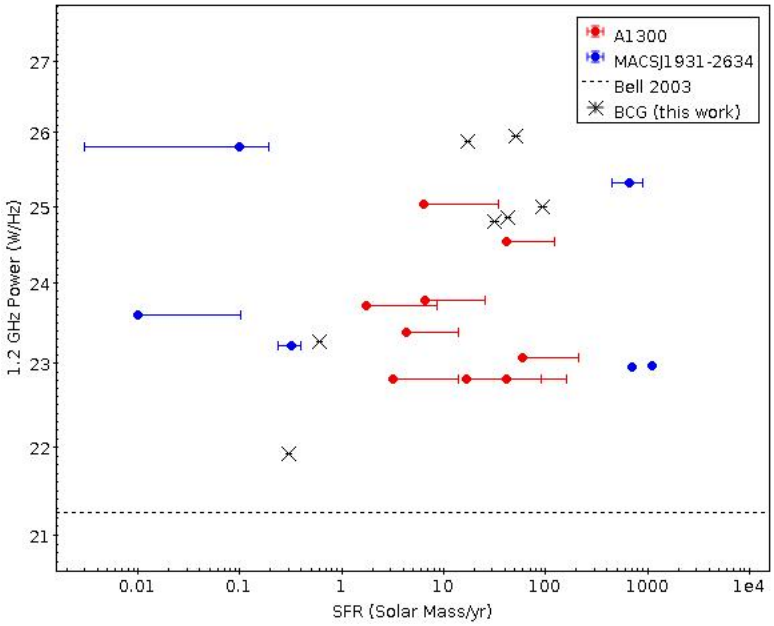

Figure 7.18: The figure shows the SFR-logP correlation of MACSJ1931-2634 (blue dots) and A1300 (red dots) galaxies compared with the BCGs analyzed in this work. The plot shows that the radio powers are, on average, up to five orders of magnitude above the radio powers expected if solely due to Star Formation estimated following Bell 2003 (dashed line).

Table 7.8: Stellar Masses and SFR for A1300 cluster member radio galaxies

name	Stellar Mass ($\times 10^{11}$ $M_\odot$)	SFR $M_\odot$ yr^{-1}	sSFR ($\times 10^{-11}$ yr^{-1})	$logP_{1.2GHz}$ (W/Hz)
J1131-2000	1.22	1.75	1.44	23.72
J1131-1954	2.25	3.17	1.41	<22.81
J1131-1949	1.72	16.82	9.78	<22.81
J1131-1958	1.51	59.5	39.4	23.08
J1131-1953	4.30	6.27	1.46	25.03
J1131-1955	17.8	41.4	2.33	24.53
J1131-1952	4.46	6.51	1.46	23.79
J1132-1954	1.71	4.24	2.48	23.38
J1132-1952	0.38	41.07	108.1	<22.81

Table 7.9: Stellar Mass and SFR fit errors at 2.5 % and 97.5 % respectively for A1300 cluster member radio galaxies

name	Stellar Mass error 2.5 %	Stellar Mass error 97.5 %	SFR error 2.5 %	SFR error 97.5 %
J1131-2000	10.76	11.16	0.078	6.871
J1131-1954	10.99	11.40	0.121	10.764
J1131-1949	10.61	11.23	2.704	73.621
J1131-1958	11.02	11.45	5.649	153.815
J1131-1953	11.29	11.74	0.267	27.990
J1131-1955	11.99	12.30	0.619	80.724
J1131-1952	11.28	11.66	0.205	18.707
J1132-1954	10.90	11.28	0.122	9.484
J1132-1952	10.01	10.61	1.648	118.032

Table 7.10: Stellar Masses and SFR for MACSJ1931-2634 cluster member radio galaxies

name	Stellar Mass ($\times 10^{11}$ $M_\odot$)	SFR $M_\odot$ yr^{-1}	sSFR ($\times 10^{-11}$ yr^{-1})	$logP_{1.2GHz}$ (W/Hz)
J1931-2637	1.81	0.32	0.18	23.22
J1931-2634	1.63	660.1	405.6	25.31
J1931-2635	1.43	0.10	0.07	25.81
J1931-2630	1.69	0.01	0.01	23.60
J1931-2645	9.79	1119	114.3	<22.98
J1932-2625	2.13	707.9	330.2	<22.95

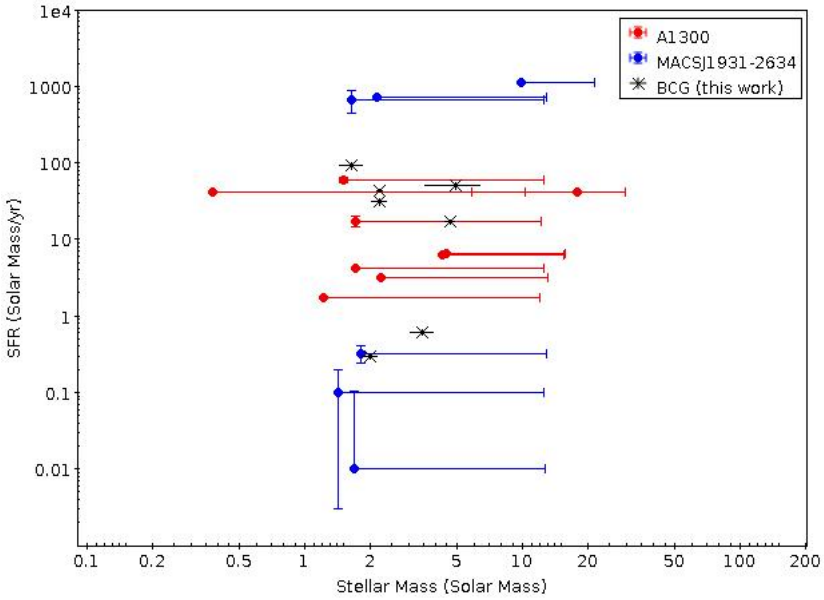

Figure 7.19: The figure shows the SFR-Stellar Mass correlation of MACSJ1931-2634 (blue dots) and A1300 (red dots) galaxies compared with the BCGs analyzed in this work. The plot shows that, according to Cooke et al. (2016) there is no correlation and no SFMS is observed.

Table 7.11: Stellar Mass and SFR fit errors at 2.5 % and 97.5 % respectively for MACSJ1931-2634 cluster member radio galaxies

name	Stellar Mass error 2.5 %	Stellar Mass error 97.5 %	SFR error 2.5 %	SFR error 97.5 %
J1931-2637	11.10	11.58	0.08	24.10
J1931-2634	10.89	11.75	219.78	1294.2
J1931-2635	11.08	11.58	0.097	34.83
J1931-2630	11.03	11.51	0.092	25.23
J1931-2645	11.45	11.96	26.36	1037.53
J1932-2625	10.75	11.27	16.218	1011.69

7.7 Summary and future perspectives

The main aim of this work is to investigate the properties of the radio galaxies in galaxy clusters in relation with the environment in which they are located. In particular, one of the most debated topic is to understand whether or not the merging dynamical state of the cluster influences the radio emission, both triggering the Star Formation and fueling the AGN activity.
We analyzed first a sample of eleven BCGs in order to examine the radio properties of these 'special' centrally located galaxies. We found that, in agreement with literature results, the radio emission is mainly AGN powered in these galaxies. We estimated the q parameter as defined in Condon et al. (2002) to discriminate between the AGN and SF contribution and we found that all the BCGs in our sample have $q < 1.8$ except A209, which is a merging cluster.
We estimated the SFR in the FIR band and we found that there is good agreement with Fogarty et al. (2015). Even though the values are estimated in different bands, the trend seems to confirm that the Star Formation emission, which is not the dominating mechanism, is present and not negligible especially in cool cores.
We selected two targets from our initial sample in order to investigate the properties of radio galaxies into two environments considered 'opposite' in terms of dynamics. A1300 is defined a post-merging cluster Lemonon et al. (1997); Pierre et al. (1997) and MACSJ1931-2634 is considered a cool core cluster (Ehlert et al., 2011; Giacintucci et al., 2017). Moreover, the two selected clusters in our sample are at the same $z\sim0.3$ and classified with the same richness class.
We investigated from a statistical point of view the properties of the fields surrounding the two cluster within an area of 30 arcmin radius extracting two catalogues at 1.2 GHz and two at 640 MHz. We then considered a restricted area of two virial radii to study the source counts and the Radio Luminosity Functions.
We are aware that we need more robust statistics, however, we highlight the fact that we performed the entire analysis based on two completely new instruments which were still in a preliminary stage of construction. Moreover, the radio observations of MACSJ1931-2634 and A1300 were obtained much later than the spectroscopic campaigns. However, our preliminary results show that the logN-logS and the RLF estimated could both confirm that in A1300 the radio emission could be triggered by the merging. Indeed in A1300 the source counts are overall higher than the background, both at 1.2 GHz and at 640 MHz; the RLF of A1300 is a factor ~ 2 higher than that of MACSJ1931-2634, meaning that there is higher probability in A1300 to develop a radio source (see Miller & Owen, 2003, for comparison).
We entirely characterized the radio-optical properties of the radio galaxies resulted consistent with being cluster members from our spectroscopic analysis: we estimated their spatial distribution, their location on the Color Magnitude diagrams and we derived their radio luminosities and Stellar Masses.
Apparently, there is correlation between the Mass and the radio power for the galax-

ies in A1300 and no significant correlation is found in MACSJ1931-2634 galaxies. Moreover, comparing the SFR for the galaxies in our samples, it results that the radio powers observed are up to five orders of magnitude above the radio powers expected if due solely to star formation (see Condon, 1992; Bell, 2003; Cooke et al., 2016). No correlation is found and no SFMS is evident in the SFR-Stellar Mass relation, this is consistent with Cooke et al. (2016).
Our results go in the direction of confirming that the cold gas could be the source for both the AGN activity and the Star Formation activity.
In absence of more data, our results are speculations awaiting to be confirmed by a much better statistics. The future aim and perspective are to enlarge our statistics by means of more spectroscopical information and analyze a wider sample of clusters in different dynamical state.

Bibliography

Abell G. O., 1958, ApJS, 3, 211

Abell G. O., Corwin Harold G. J., Olowin R. P., 1989, ApJS, 70, 1

Adam R., et al., 2017, A&A, 606, A64

Adam R., et al., 2018, A&A, 614, A118

Akamatsu H., Kawahara H., 2013, PASJ, 65, 16

Allen S., 2008, in A Decade of Dark Energy. p. 18

Allen S. W., Schmidt R. W., Ebeling H., Fabian A. C., van Speybroeck L., 2004, MNRAS, 353, 457

Angulo R. E., Springel V., White S. D. M., Jenkins A., Baugh C. M., Frenk C. S., 2012, MNRAS, 426, 2046

Annunziatella M., et al., 2014, A&A, 571, A80

Annunziatella M., et al., 2016, A&A, 585, A160

Asad K. M. B., et al., 2019, arXiv e-prints, p. arXiv:1904.07155

Ascaso B., Aguerri J. A. L., Varela J., Cava A., Bettoni D., Moles M., D'Onofrio M., 2011, ApJ, 726, 69

Auriemma C., Perola G. C., Ekers R. D., Fanti R., Lari C., Jaffe W. J., Ulrich M. H., 1977, A&A, 57, 41

Bardelli S., Pisani A., Ramella M., Zucca E., Zamorani G., 1998, MNRAS, 300, 589

Bartelmann M., Meneghetti M., Perrotta F., Baccigalupi C., Moscardini L., 2003, A&A, 409, 449

Bauer F., 2005, arXiv General Relativity and Quantum Cosmology e-prints,

Baum S. A., O'Dea C. P., 1991, MNRAS, 250, 737

Begelman M. C., Rees M. J., Blandford R. D., 1979, Nature, 279, 770

Bell E. F., 2003, ApJ, 586, 794

Bennett C. L., et al., 1996, ApJ, 464, L1

Bernardi G., et al., 2017, arXiv e-prints, p. arXiv:1708.07728

Best P. N., 2007, in Metcalfe N., Shanks T., eds, Astronomical Society of the Pacific Conference Series Vol. 379, Cosmic Frontiers. p. 213

Best P. N., Heckman T. M., 2012, MNRAS, 421, 1569

Best P. N., Kauffmann G., Heckman T. M., Brinchmann J., Charlot S., Ivezić Ž., White S. D. M., 2005, MNRAS, 362, 25

Birzan L., Rafferty D. A., McNamara B. R., Carilli C. L., Wise M. W., Nulsen P. E. J., 2004, in AAS/High Energy Astrophysics Division #8. p. 905

Biviano A., 2001, arXiv e-prints, pp astro–ph/0110053

Bliton M., Rizza E., Burns J. O., Owen F. N., Ledlow M. J., 1998, MNRAS, 301, 609

Bonafede A., 2015, in The Many Facets of Extragalactic Radio Surveys: Towards New Scientific Challenges. p. 63

Bonafede A., et al., 2009, A&A, 503, 707

Bonafede A., Feretti L., Murgia M., Govoni F., Giovannini G., Vacca V., 2010, arXiv e-prints, p. arXiv:1009.1233

Bonafede A., Govoni F., Feretti L., Murgia M., Giovannini G., Brüggen M., 2011, A&A, 530, A24

Bonafede A., et al., 2012, MNRAS, 426, 40

Bonafede A., et al., 2014, MNRAS, 444, L44

Bonafede A., et al., 2017, MNRAS, 470, 3465

Bonafede A., et al., 2018, MNRAS, 478, 2927

Bond J. R., Cole S., Efstathiou G., Kaiser N., 1991, ApJ, 379, 440

Bondi M., Ciliegi P., Schinnerer E., Smolčić V., Jahnke K., Carilli C., Zamorani G., 2008, ApJ, 681, 1129

Booth R. S., de Blok W. J. G., Jonas J. L., Fanaroff B., 2009, arXiv e-prints, p. arXiv:0910.2935

Botteon A., Gastaldello F., Brunetti G., Kale R., 2016, MNRAS, 463, 1534

Bourdin H., Sauvageot J. L., Slezak E., Bijaoui A., Teyssier R., 2004, A&A, 414, 429

Bower R. G., 1991, MNRAS, 248, 332

Boylan-Kolchin M., Springel V., White S. D. M., Jenkins A., Lemson G., 2009, MNRAS, 398, 1150

Branchesi M., Gioia I. M., Fanti C., Fanti R., Perley R., 2006, Astronomische Nachrichten, 327, 571

Brentjens M. A., de Bruyn A. G., 2005, A&A, 441, 1217

Briel U. G., et al., 1991, A&A, 246, L10

Brough S., Collins C. A., Burke D. J., Lynam P. D., Mann R. G., 2005, MNRAS, 364, 1354

Brown S., Rudnick L., 2011, MNRAS, 412, 2

Brüggen M., van Weeren R. J., Röttgering H. J. A., 2011, Mem. Soc. Astron. Italiana, 82, 627

Brüggen M., Bykov A., Ryu D., Röttgering H., 2012, Space Sci. Rev., 166, 187

Brüggen M., et al., 2018, MNRAS, 477, 3461

Brunetti G., Jones T. W., 2014, International Journal of Modern Physics D, 23, 1430007

Brunetti G., Venturi T., Dallacasa D., Cassano R., Dolag K., Giacintucci S., Setti G., 2007, ApJ, 670, L5

Brunetti G., et al., 2008, Nature, 455, 944

Brunetti G., Cassano R., Dolag K., Setti G., 2009, A&A, 507, 661

Buote D. A., 2001, ApJ, 553, L15

Burke C., Hilton M., Collins C., 2015, MNRAS, 449, 2353

Burn B. J., 1966, MNRAS, 133, 67

Burns J. O., 1998, Science, 280, 400

Burns J. O., 2001, in American Astronomical Society Meeting Abstracts #198. p. 66.05

Butcher H., Oemler A. J., 1978a, ApJ, 219, 18

Butcher H., Oemler A. J., 1978b, ApJ, 226, 559

Butcher H., Oemler A. J., 1984, ApJ, 285, 426

Camilo F., et al., 2018, ApJ, 856, 180

Carilli C. L., Walter F., 2013, ARA&A, 51, 105

Carlstrom J. E., 2002, in APS April Meeting Abstracts. p. E2.001

Cassano R., Ettori S., Giacintucci S., Brunetti G., Markevitch M., Venturi T., Gitti M., 2010, ApJ, 721, L82

Cassano R., et al., 2013, ApJ, 777, 141

Cavagnolo K. W., Donahue M., Voit G. M., Sun M., 2008, ApJ, 683, L107

Cavagnolo K. W., Donahue M., Voit G. M., Sun M., 2009, ApJS, 182, 12

Cavaliere A., Fusco-Femiano R., 1976, A&A, 500, 95

Chengalur J. N., Kanekar N., 2003, Phys. Rev. Lett., 91, 241302

Chung A., et al., 2007, Cluster Environmental Effects on Galaxy Evolution at z=0.2 (Abell 963 vs. Abell 2192), Spitzer Proposal

Clarke D. A., Norman M. L., Burns J. O., 1986, ApJ, 311, L63

Colberg J. M., White S. D. M., Jenkins A., Pearce F. R., 1999, MNRAS, 308, 593

Cole S., 1991, ApJ, 367, 45

Cole S., Aragon-Salamanca A., Frenk C. S., Navarro J. F., Zepf S. E., 1994, MNRAS, 271, 781

Coles P., Lucchin F., 1995, Journal of the British Astronomical Association, 105, 284

Coles P., Lucchin F., 2002, Cosmology: The Origin and Evolution of Cosmic Structure, Second Edition

Condon J. J., 1992, ARA&A, 30, 575

Condon J. J., Cotton W. D., Greisen E. W., Yin Q. F., Perley R. A., Taylor G. B., Broderick J. J., 1998, AJ, 115, 1693

Condon J. J., Cotton W. D., Broderick J. J., 2002, AJ, 124, 675

Cooke K. C., O'Dea C. P., Baum S. A., Tremblay G. R., Cox I. G., Gladders M., 2016, ApJ, 833, 224

Cornwell T. J., Wilkinson P. N., 1981, MNRAS, 196, 1067

Cornwell T. J., Voronkov M. A., Humphreys B., 2012, in Proc. SPIE. p. 85000L (arXiv:1207.5861), doi:10.1117/12.929336

Cunha E., Charlot S., Elbaz D., 2008, MNRAS, 388, 1595

Dallacasa D., et al., 2009, ApJ, 699, 1288

Darling J., Giovanelli R., 2002, AJ, 124, 100

Davé R., 2008, MNRAS, 385, 147

Davis D. S., Keel W. C., Mulchaey J. S., Condon J. J., 1995, in American Astronomical Society Meeting Abstracts. p. 48.13

De Grandi S., Molendi S., 2001, ApJ, 551, 153

De Lucia G., Blaizot J., 2007, MNRAS, 375, 2

De Lucia G., Springel V., White S. D. M., Croton D., Kauffmann G., 2006, MNRAS, 366, 499

De Lucia G., et al., 2007, MNRAS, 374, 809

De Propris R., Phillipps S., Bremer M. N., 2013, MNRAS, 434, 3469

Deo D. K., Kale R., 2017, Experimental Astronomy, 44, 165

Di Gennaro G., et al., 2018, A&A, 620, A25

Diaferio A., 1999, MNRAS, 309, 610

Diaferio A., Geller M. J., Rines K. J., 2005, ApJ, 628, L97

Diehl S., Li H., Fryer C. L., Rafferty D., 2008, ApJ, 687, 173

Donahue M., Voit G. M., 2004, in Mulchaey J. S., Dressler A., Oemler A., eds, Clusters of Galaxies: Probes of Cosmological Structure and Galaxy Evolution. p. 143 (arXiv:astro-ph/0308006)

Donahue M., de Messières G. E., O'Connell R. W., Voit G. M., Hoffer A., McNamara B. R., Nulsen P. E. J., 2011, ApJ, 732, 40

Donahue M., et al., 2015, ApJ, 805, 177

Dong R., Rasmussen J., Mulchaey J. S., 2010, ApJ, 712, 883

Doria A., Gitti M., Ettori S., Brighenti F., Nulsen P. E. J., McNamara B. R., 2012, ApJ, 753, 47

Douglass E. M., Blanton E. L., Clarke T. E., Rand all S. W., Wing J. D., 2011, ApJ, 743, 199

Dressler A., 1980, ApJ, 236, 351

Dwarakanath K. S., Owen F. N., 1999, AJ, 118, 625

Ebeling H., Barrett E., Donovan D., Ma C. J., Edge A. C., van Speybroeck L., 2007, ApJ, 661, L33

Ebeling H., Edge A. C., Mantz A., Barrett E., Henry J. P., Ma C. J., van Speybroeck L., 2010, MNRAS, 407, 83

Eckert D., Jauzac M., Vazza F., Owers M. S., Kneib J. P., Tchernin C., Intema H., Knowles K., 2016, MNRAS, 461, 1302

Ehlert S., et al., 2011, MNRAS, 411, 1641

Eilek J. A., Burns J. O., O'Dea C. P., Owen F. N., 1984, ApJ, 278, 37

Ellingson S. W., et al., 2013, IEEE Transactions on Antennas and Propagation, 61, 2540

Ettori S., Donnarumma A., Pointecouteau E., Reiprich T. H., Giodini S., Lovisari L., Schmidt R. W., 2013, Space Sci. Rev., 177, 119

Evrard A. E., 1991, MNRAS, 248, 8P

Fabian A. C., 2002, Philosophical Transactions of the Royal Society of London Series A, 360, 2035

Fabian A. C., Johnstone R. M., Daines S. J., 1994, MNRAS, 271, 737

Fabian A. C., Sanders J. S., Allen S. W., Crawford C. S., Iwasawa K., Johnstone R. M., Schmidt R. W., Taylor G. B., 2003, MNRAS, 344, L43

Fabian A. C., Sanders J. S., Taylor G. B., Allen S. W., Crawford C. S., Johnstone R. M., Iwasawa K., 2006, MNRAS, 366, 417

Fall S. M., Efstathiou G., 1980, MNRAS, 193, 189

Fanaroff B. L., Riley J. M., 1974, MNRAS, 167, 31P

Fanti R., 1984, in Mardirossian F., Giuricin G., Mezzetti M., eds, Astrophysics and Space Science Library Vol. 111, Clusters and Groups of Galaxies. p. 185, doi:10.1007/978-94-009-6412-9_38

Fasano G., et al., 2010, MNRAS, 404, 1490

Feretti L., Giovannini G., 1996, in Ekers R. D., Fanti C., Padrielli L., eds, IAU Symposium Vol. 175, Extragalactic Radio Sources. p. 333

Feretti L., Giovannini G., 2008, Clusters of Galaxies in the Radio: Relativistic Plasma and ICM/Radio Galaxy Interaction Processes. p. 24, doi:10.1007/978-1-4020-6941-3_5

Feretti L., Venturi T., 2002, in Feretti L., Gioia I. M., Giovannini G., eds, Astrophysics and Space Science Library Vol. 272, Merging Processes in Galaxy Clusters. pp 163–195, doi:10.1007/0-306-48096-4_6

Feretti L., Giovannini G., Govoni F., Murgia M., 2012, A&ARv, 20, 54

Ferrari C., Govoni F., Schindler S., Bykov A. M., Rephaeli Y., 2008, Space Sci. Rev., 134, 93

Finn R. A., et al., 2018, ApJ, 862, 149

Fogarty K., Postman M., Connor T., Donahue M., Moustakas J., 2015, ApJ, 813, 117

Fogarty K., et al., 2019, ApJ, 879, 103

Fomalont E. B., Kellermann K. I., Cowie L. L., Capak P., Barger A. J., Partridge R. B., Windhorst R. A., Richards E. A., 2006, ApJS, 167, 103

Fujita Y., Takizawa M., Nagashima M., Enoki M., 1999, PASJ, 51, L1

Gaspari M., Ruszkowski M., Oh S. P., 2013, MNRAS, 432, 3401

Gaspari M., Brighenti F., Temi P., 2015, A&A, 579, A62

Geller A. M., de Grijs R., Li C., Hurley J. R., 2013, ApJ, 779, 30

Giacintucci S., Venturi T., 2009, A&A, 505, 55

Giacintucci S., Venturi T., Bardelli S., Dallacasa D., Zucca E., 2004, A&A, 419, 71

Giacintucci S., Markevitch M., Brunetti G., Cassano R., Venturi T., 2011, A&A, 525, L10

Giacintucci S., Markevitch M., Brunetti G., ZuHone J. A., Venturi T., Mazzotta P., Bourdin H., 2014, ApJ, 795, 73

Giacintucci S., Markevitch M., Cassano R., Venturi T., Clarke T. E., Brunetti G., 2017, ApJ, 841, 71

Gioia I. M., Henry J. P., Mullis C. R., Böhringer H., Briel U. G., Voges W., Huchra J. P., 2003, ApJS, 149, 29

Giovannini G., Feretti L., 2002, Highlights of Astronomy, 12, 513

Giovannini G., Feretti L., Venturi T., Kim K. T., Kronberg P. P., 1991, in Colless M. M., Babul A., Edge A. C., Johnstone R. M., Raychaudhury S., eds, Clusters and Superclusters of Galaxies. p. 71

Giovannini G., Feretti L., Venturi T., Kim K. T., Kronberg P. P., 1993, ApJ, 406, 399

Giovannini G., Tordi M., Feretti L., 1999, New Astronomy, 4, 141

Giovannini G., Bonafede A., Feretti L., Govoni F., Murgia M., Ferrari F., Monti G., 2009, A&A, 507, 1257

Girardi M., Giuricin G., Mardirossian F., Mezzetti M., Boschin W., 1998, ApJ, 505, 74

Gitti M., 2015, in The Many Facets of Extragalactic Radio Surveys: Towards New Scientific Challenges. p. 43

Gitti M., Brunetti G., Setti G., Feretti L., 2004, in Reiprich T., Kempner J., Soker N., eds, The Riddle of Cooling Flows in Galaxies and Clusters of galaxies. p. 35 (arXiv:astro-ph/0309791)

Gitti M., Feretti L., Schindler S., 2006, A&A, 448, 853

Gitti M., Piffaretti R., Schindler S., 2007, A&A, 475, 441

Gomez P. L., Ledlow M. J., Burns J. O., Pinkey J., Hill J. M., 1997, AJ, 114, 1711

Gonzalez A. H., et al., 2019, ApJS, 240, 33

Govoni F., Murgia M., Markevitch M., Feretti L., Giovannini G., Taylor G. B., Carretti E., 2009, A&A, 499, 371

Hardcastle M. J., Worrall D. M., Birkinshaw M., 1998, MNRAS, 296, 1098

Hardcastle M. J., Sakelliou I., Worrall D. M., 2005, MNRAS, 359, 1007

Hardcastle M. J., et al., 2016, MNRAS, 462, 1910

Harwood J. J., Hardcastle M. J., Croston J. H., Goodger J. L., 2013, MNRAS, 435, 3353

Harwood J. J., Hardcastle M. J., Croston J. H., 2015, MNRAS, 454, 3403

Hausman M. A., Ostriker J. P., 1978, ApJ, 224, 320

Hennig C., et al., 2017, MNRAS, 467, 4015

Henry J. P., Briel U. G., 1991, A&A, 246, L14

Hoang D. N., et al., 2017, MNRAS, 471, 1107

Hoang D. N., et al., 2018, MNRAS, 478, 2218

Hoessel J. G., 1980, PhD thesis, California Institute of Technology, Pasadena.

Hoffer A. S., Donahue M., Hicks A., Barthelemy R. S., 2012, ApJS, 199, 23

Hudson D. S., Mittal R., Reiprich T. H., Nulsen P. E. J., Andernach H., Sarazin C. L., 2010, A&A, 513, A37

Intema H. T., van Weeren R. J., Röttgering H. J. A., Lal D. V., 2011, A&A, 535, A38

Ishwara-Chandra C. H., Sirothia S. K., Wadadekar Y., Pal S., Windhorst R., 2010, MNRAS, 405, 436

Jonas J., MeerKAT Team 2016, in Proceedings of MeerKAT Science: On the Pathway to the SKA. 25-27 May. p. 1

Jones T. W., Owen F. N., 1979, ApJ, 234, 818

Kale R., 2018, arXiv e-prints, p. arXiv:1808.09140

Kale R., Venturi T., Giacintucci S., Dallacasa D., Cassano R., Brunetti G., Macario G., Athreya R., 2013, A&A, 557, A99

Kale R., Venturi T., Cassano R., Giacintucci S., Bardelli S., Dallacasa D., Zucca E., 2015, A&A, 581, A23

Kale R., Parekh V., Dwarakanath K. S., 2018, MNRAS, 480, 5352

Katz N., Weinberg D. H., Hernquist L., 1996, ApJS, 105, 19

Kauffmann G., White S. D. M., Guiderdoni B., 1993, MNRAS, 264, 201

Kauffmann G., et al., 2003, MNRAS, 346, 1055

Kent S. M., Gunn J. E., 1982, AJ, 87, 945

Kenyon J. S., Smirnov O. M., Grobler T. L., Perkins S. J., 2018, MNRAS, 478, 2399

Klein U., Mack K. H., Gregorini L., Vigotti M., 2003, A&A, 406, 579

Korngut P., Dicker S., Reese E. D., Mason B. S., Devlin M. J., Mroczkowski T., Sarazin C. L., Sun M., 2011, in American Astronomical Society Meeting Abstracts #217. p. 227.05

Lacey C., Cole S., 1993, MNRAS, 262, 627

Large M. I., Mathewson D. S., Haslam C. G. T., 1959, Nature, 183, 1663

Lauer T. R., 1988, in BAAS. p. 1103

Lauer T. R., et al., 2007, ApJ, 662, 808

Lauer T. R., Postman M., Strauss M. A., Graves G. J., Chisari N. E., 2014, ApJ, 797, 82

Le Fèvre O., et al., 2003, The Messenger, 111, 18

Ledlow M. J., Owen F. N., 1996, AJ, 112, 9

Lemonon L., Pierre M., Hunstead R., Reid A., Mellier Y., Boehringer H., 1997, A&A, 326, 34

Li Y., Bryan G. L., Ruszkowski M., Voit G. M., O'Shea B. W., Donahue M., 2015, ApJ, 811, 73

Lindner R. R., et al., 2014, ApJ, 786, 49

Liuzzo E., Giovannini G., Giroletti M., Taylor G. B., 2009, A&A, 505, 509

Łokas E. L., Wojtak R., Gottlöber S., Mamon G. A., Prada F., 2006, MNRAS, 367, 1463

Loken C., Roettiger K., Burns J. O., Norman M., 1995, ApJ, 445, 80

Longair M. S., 1966, MNRAS, 133, 421

Ma C.-J., McNamara B. R., Nulsen P. E. J., 2013, ApJ, 763, 63

Macario G., Venturi T., Brunetti G., Dallacasa D., Giacintucci S., Cassano R., Bardelli S., Athreya R., 2010, A&A, 517, A43

Macario G., et al., 2013, Searching for radio halos in the Macs-Planck X-ray luminous cluster sample (III): final stage, ATNF Proposal

Mahony E. K., et al., 2016, MNRAS, 463, 2997

Makhathini S., 2018, PhD thesis, Rhodes University, Drosty Rd, Grahamstown, 6139, Eastern Cape, South Africa

Markevitch M., Vikhlinin A., 2007, Phys. Rep., 443, 1

Markevitch M., Vikhlinin A., Forman W. R., Sarazin C. L., 1999, ApJ, 527, 545

Martel H., Robichaud F., Barai P., 2014, ApJ, 786, 79

Mauch T., Sadler E. M., 2007, MNRAS, 375, 931

Mauch T., et al., 2020, ApJ, 888, 61

Maughan B. J., Giles P. A., Rines K. J., Diaferio A., Geller M. J., Van Der Pyl N., Bonamente M., 2016, MNRAS, 461, 4182

Mazzotta P., Giacintucci S., 2008, ApJ, 675, L9

McNamara B., 2006, A Critical Test for the Existence of Cooling Gas in the Cores of Galaxy Clusters, XMM-Newton Proposal

McNamara B. R., Nulsen P. E. J., 2007, ARA&A, 45, 117

McNamara B. R., et al., 2000, ApJ, 534, L135

McNamara B., et al., 2004, in 35th COSPAR Scientific Assembly. p. 2940

Menanteau F., et al., 2012, ApJ, 748, 7

Merritt D., 1985, ApJ, 289, 18

Miley G., 1980, ARA&A, 18, 165

Miley G. K., Perola G. C., van der Kruit P. C., van der Laan H., 1972, Nature, 237, 269

Miller N. A., Owen F. N., 2003, AJ, 125, 2427

Miller N. A., Hornschemeier A. E., Mobasher B., Bridges T. J., Hudson M. J., Marzke R. O., Smith R. J., 2009, AJ, 137, 4450

Miniati F., Ryu D., Kang H., Jones T. W., 2001, ApJ, 559, 59

Mohan N., Rafferty D., 2015, PyBDSF: Python Blob Detection and Source Finder (ascl:1502.007)

Molendi S., Pizzolato F., 2001, ApJ, 560, 194

Morganti R., Oosterloo T., Oonk J. B. R., Frieswijk W., Tadhunter C., 2015, A&A, 580, A1

Murgia M., Eckert D., Govoni F., Ferrari C., Pand ey-Pommier M., Nevalainen J., Paltani S., 2010, A&A, 514, A76

Muzzin A., et al., 2009, ApJ, 698, 1934

Nipoti C., Londrillo P., Ciotti L., 2003, in Bender R., Renzini A., eds, The Mass of Galaxies at Low and High Redshift. p. 70 (arXiv:astro-ph/0112133), doi:10.1007/10899892_18

O'Dea C. P., Owen F. N., 1985, AJ, 90, 954

O'Donoghue A. A., Owen F. N., Eilek J. A., 1990, in BAAS. p. 802

O'Donoghue A. A., Eilek J. A., Owen F. N., 1993, ApJ, 408, 428

Oemler A. J., 1977, in Clusters of Galaxies, Cosmology and Intergalactic Matter. pp 253–260

Offringa A. R., de Bruyn A. G., Zaroubi S., 2012, MNRAS, 422, 563

Offringa A. R., et al., 2013, A&A, 549, A11

Offringa A. R., et al., 2014, MNRAS, 444, 606

Oguri M., et al., 2018, PASJ, 70, S20

Ostriker J. P., Tremaine S. D., 1975, ApJ, 202, L113

Owen F. N., Laing R. A., 1989, MNRAS, 238, 357

Owen F. N., Ledlow M. J., 1994, in Bicknell G. V., Dopita M. A., Quinn P. J., eds, Astronomical Society of the Pacific Conference Series Vol. 54, The Physics of Active Galaxies. p. 319

Owen F. N., Morrison G. E., 2008, AJ, 136, 1889

Owen F. N., Rudnick L., 1976, ApJ, 205, L1

Owen F. N., Dwarakanath K. S., Smith C. C., Ledlow M. J., Keel W. C., Morrison G. E., Voges W., Burns J. O., 1996, in Hardee P. E., Bridle A. H., Zensus J. A., eds, Astronomical Society of the Pacific Conference Series Vol. 100, Energy Transport in Radio Galaxies and Quasars. p. 353

Owen F. N., Ledlow M. J., Keel W. C., Morrison G. E., 1999, AJ, 118, 633

Parma P., Murgia M., Morganti R., Capetti A., de Ruiter H. R., Fanti R., 1999, A&A, 344, 7

Patra N. N., et al., 2019, MNRAS, 483, 3007

Peebles P. J. E., 1980, in Longair M. S., Warner J. W., eds, Scientific Research with the Space Telescope.

Peebles P. J. E., 1983, in Jones B. J. T., Jones J. E., eds, The Origin and Evolution of Galaxies. pp 143–169

Peterson K. C., Gallagher S. C., Muno M. P., Hornschemeier A. E., 2004, in American Astronomical Society Meeting Abstracts. p. 178.02

Pierre M., Boehringer H., Ebeling H., Voges W., Schuecker P., Cruddace R., MacGillivray H., 1994, A&A, 290, 725

Pierre M., Oukbir J., Dubreuil D., Soucail G., Sauvageot J. L., Mellier Y., 1997, A&AS, 124, 283

Pinkney J., 1993, in American Astronomical Society Meeting Abstracts. p. 98.01D

Pizzolato F., Soker N., 2005, Advances in Space Research, 36, 762

Planck Collaboration et al., 2016, A&A, 596, A104

Poggianti B. M., Smail I., Dressler A., Couch W. J., Barger A. J., Butcher H., Ellis R. S., Oemler Augustus J., 1999, ApJ, 518, 576

Postman M., Geller M. J., 1984, ApJ, 281, 95

Postman M., et al., 2012, ApJS, 199, 25

Prandoni I., Gregorini L., Parma P., de Ruiter R. H., Vettolani G., Wieringa M. H., Ekers R. D., 1999, in Morganti R., Couch W. J., eds, Looking Deep in the Southern Sky. p. 114

Prandoni I., Gregorini L., Parma P., de Ruiter H. R., Vettolani G., Wieringa M. H., Ekers R. D., 2000, A&AS, 146, 41

Prandoni I., Parma P., Wieringa M. H., de Ruiter H. R., Gregorini L., Mignano A., Vettolani G., Ekers R. D., 2006, A&A, 457, 517

Pratt G. W., Croston J. H., Arnaud M., Böhringer H., 2009, A&A, 498, 361

Press W. H., Schechter P., 1974, ApJ, 187, 425

Prestage R. M., Peacock J. A., 1988, MNRAS, 230, 131

Rafferty D., Birzan L., McNamara B., Wise M. W., Nulsen P. E. J., 2004, in APS Ohio Sections Spring Meeting Abstracts. p. B6.004

Randall K., Hopkins A. M., Norris R. P., Zinn P., Middelberg E., Mao M. Y., Sharp R. G., 2012, in American Astronomical Society Meeting Abstracts #219. p. 131.02

Rasia E., et al., 2015, ApJ, 813, L17

Reid A. D., Hunstead R. W., Lemonon L., Pierre M. M., 1999, MNRAS, 302, 571

Reynolds J., 1994, ATNF Internal

Richstone D. O., 1975, ApJ, 200, 535

Roettiger K., Burns J., Loken C., 1993, ApJ, 407, L53

Roettiger K., Burns J. O., Loken C., 1996, ApJ, 473, 651

Rood H. J., Sastry G. N., 1971, Publications of the Astronomical Society of the Pacific, 83, 313

Rosati P., et al., 2014, The Messenger, 158, 48

Rossetti M., Molendi S., 2011, in Ness J.-U., Ehle M., eds, The X-ray Universe 2011. p. 139

Rossetti M., et al., 2016, MNRAS, 457, 4515

Roy N., Kanekar N., Chengalur J. N., 2013, MNRAS, 436, 2366

Rozo E., Rykoff E. S., Becker M., Reddick R. M., Wechsler R. H., 2015, MNRAS, 453, 38

Rudnick L., Owen F. N., 1976, in BAAS. p. 553

Rudnick L., Owen F. N., 1977, AJ, 82, 1

Sanchis T., Łokas E. L., Mamon G. A., 2004, MNRAS, 347, 1198

Sanders J. S., 2006, MNRAS, 371, 829

Santini P., et al., 2009, A&A, 504, 751

Santos J. S., et al., 2016, MNRAS, 456, L99

Sarazin C. L., 1986, Reviews of Modern Physics, 58, 1

Sarazin C. L., 2002a, in Feretti L., Gioia I. M., Giovannini G., eds, Astrophysics and Space Science Library Vol. 272, Merging Processes in Galaxy Clusters. pp 1–38 (arXiv:astro-ph/0105418), doi:10.1007/0-306-48096-4_1

Sarazin C. L., 2002b, in Feretti L., Gioia I. M., Giovannini G., eds, Astrophysics and Space Science Library Vol. 272, Merging Processes in Galaxy Clusters. pp 1–38 (arXiv:astro-ph/0105418), doi:10.1007/0-306-48096-4_1

Schlafly E. F., Finkbeiner D. P., 2011, ApJ, 737, 103

Schombert J. M., 1988, ApJ, 328, 475

Shimwell T. W., Markevitch M., Brown S., Feretti L., Gaensler B. M., Johnston-Hollitt M., Lage C., Srinivasan R., 2015, MNRAS, 449, 1486

Shimwell T. W., et al., 2016, MNRAS, 459, 277

Shimwell T. W., et al., 2019, A&A, 622, A1

Shin J., Woo J.-H., Mulchaey J. S., 2016, ApJS, 227, 31

Sirothia S. K., Saikia D. J., Ishwara-Chandra C. H., Kantharia N. G., 2009, MNRAS, 392, 1403

Springel V., Frenk C. S., White S. D. M., 2006, Nature, 440, 1137

Steinmetz M., Muller E., 1995, MNRAS, 276, 549

Stocke J. T., Perlman E. S., Gioia I. M., Harvanek M., 1999, AJ, 117, 1967

Stroe A., van Weeren R. J., Intema H. T., Röttgering H. J. A., Brüggen M., Hoeft M., 2013, A&A, 555, A110

Stroe A., Harwood J. J., Hardcastle M. J., Röttgering H. J. A., 2014, MNRAS, 445, 1213

Stroe A., et al., 2016, MNRAS, 455, 2402

Sunyaev R. A., Zeldovich Y. B., 1972, Comments on Astrophysics and Space Physics, 4, 173

Swarup G., 1991, Current Science, 60, 106

Terni de Gregory B., Feretti L., Giovannini G., Govoni F., Murgia M., Perley R. A., Vacca V., 2017, A&A, 608, A58

Thierbach M., Klein U., Wielebinski R., 2003, A&A, 397, 53

Tingay S. J., et al., 2013, Publ. Astron. Soc. Australia, 30, e007

Tremblay G. R., et al., 2016, Nature, 534, 218

Trümper J., 1984, MPE Report, 184, 254

Vaddi S., O'Dea C. P., Baum S. A., Whitmore S., Ahmed R., Pierce K., Leary S., 2016, ApJ, 818, 182

Vazza F., Brunetti G., Gheller C., 2009, Memorie della Societa Astronomica Italiana Supplementi, 13, 151

Venturi T., Bardelli S., Morganti R., Hunstead R. W., 2000, MNRAS, 314, 594

Venturi T., Bardelli S., Zambelli G., Morganti R., Hunstead R. W., 2001, MNRAS, 324, 1131

Venturi T., Giacintucci S., Brunetti G., Cassano R., Bardelli S., Dallacasa D., Setti G., 2007, A&A, 463, 937

Venturi T., Giacintucci S., Dallacasa D., Cassano R., Brunetti G., Bardelli S., Setti G., 2008, A&A, 484, 327

Venturi T., Giacintucci S., Dallacasa D., Kale R., Macario G., Brunetti G., Cassano R., 2013, in SnowCLUSTER 2013, Physics of Galaxy Clusters. p. 29

Vikhlinin A., 1999, Study of a New Class of Mass Concentrations in the Universe, Chandra Proposal

Vogelsberger M., et al., 2014, MNRAS, 444, 1518

Voges W., et al., 1999, VizieR Online Data Catalog, p. IX/10A

Voit G. M., Donahue M., O'Shea B. W., Bryan G. L., Sun M., Werner N., 2015, ApJ, 803, L21

Voit G. M., Meece G., Li Y., O'Shea B. W., Bryan G. L., Donahue M., 2017, ApJ, 845, 80

Walker S., et al., 2019, in BAAS. p. 218

Wellington K. J., Miley G. K., van der Laan H., 1973, Nature, 244, 502

Wen Z. L., Han J. L., Liu F. S., 2009, ApJS, 183, 197

White S. D. M., Frenk C. S., 1991, ApJ, 379, 52

White S. D. M., Rees M. J., 1978, MNRAS, 183, 341

White G. J., et al., 2010, A&A, 517, A54

Whittam I. H., et al., 2013, MNRAS, 429, 2080

Wilber A., et al., 2018, MNRAS, 473, 3536

Williams W. L., Intema H. T., Röttgering H. J. A., 2013, A&A, 549, A55

Williams W. L., et al., 2016, MNRAS, 460, 2385

Willson M. A. G., 1970, MNRAS, 151, 1

Wu X.-P., Xue Y.-J., Fang L.-Z., 1999, ApJ, 524, 22

Yu H., et al., 2018, The Astrophysical Journal, 853, 100

Yuan Z. S., Han J. L., Wen Z. L., 2016, MNRAS, 460, 3669

Yun M. S., Reddy N. A., Condon J. J., 2001, ApJ, 554, 803

Zenteno A., et al., 2016, MNRAS, 462, 830

Ziparo F., Braglia F. G., Pierini D., Finoguenov A., Böhringer H., Bongiorno A., 2012, MNRAS, 420, 2480

ZuHone J. A., Markevitch M., Brunetti G., 2011, in American Astronomical Society Meeting Abstracts #218. p. 408.25

ZuHone J., Markevitch M., Brunetti G., Giacintucci S., 2013, in SnowCLUSTER 2013, Physics of Galaxy Clusters. p. 39

Zwicky F., 1937, ApJ, 86, 217

Zwicky F., Herzog E., Wild P., Karpowicz M., Kowal C. T., 1961, Catalogue of galaxies and of clusters of galaxies, Vol. I

de Gasperin F., van Weeren R. J., Brüggen M., Vazza F., Bonafede A., Intema H. T., 2014, MNRAS, 444, 3130

de Gasperin F., Intema H. T., van Weeren R. J., Dawson W. A., Golovich N., Wittman D., Bonafede A., Brüggen M., 2015, MNRAS, 453, 3483

de Gasperin F., et al., 2017, Science Advances, 3, e1701634

de Ruiter H. R., Parma P., Fanti C., Fanti R., 1990, A&A, 227, 351

van Gorkom J. H., 2004, in Mulchaey J. S., Dressler A., Oemler A., eds, Clusters of Galaxies: Probes of Cosmological Structure and Galaxy Evolution. p. 305 (arXiv:astro-ph/0308209)

van Haarlem M. P., et al., 2013, A&A, 556, A2

van Weeren R. J., Röttgering H. J. A., Brüggen M., Cohen A., 2009, A&A, 505, 991

van Weeren R. J., Röttgering H. J. A., Brüggen M., Hoeft M., 2010, Science, 330, 347

van Weeren R. J., de Gasperin F., Akamatsu H., Brüggen M., Feretti L., Kang H., Stroe A., Zandanel F., 2019, Space Sci. Rev., 215, 16